

Optochemical Approaches for Controlling Protein Dimerization and Protein Function

by

Taylor Marie Courtney

B.S. Biochemistry, B.S. Biology, B.A. Chemistry, North Carolina State University, 2015

Submitted to the Graduate Faculty of the
Dietrich School of Arts and Sciences in partial fulfillment
of the requirements for the degree of
Doctor of Philosophy

University of Pittsburgh

2020

UNIVERSITY OF PITTSBURGH

DIETRICH SCHOOL OF ARTS AND SCIENCES

This dissertation was presented

by

Taylor Marie Courtney

It was defended on

October 22, 2020

and approved by

W. Seth Childers, Assistant Professor, Department of Chemistry

Stephen G. Weber, Professor, Department of Chemistry

Nathan A. Yates, Associate Professor, Department of Cell Biology

Dissertation Advisor: Alexander Deiters, Professor, Department of Chemistry

Copyright © by Taylor Marie Courtney

2020

Optochemical Approaches for Controlling Protein Dimerization and Protein Function

Taylor Marie Courtney, PhD

University of Pittsburgh, 2020

Light activation of small molecules, peptides, and proteins is a useful tool for the precise, spatiotemporal control of various biological processes. The incorporation of light-responsive amino acids into proteins in cells and organisms with an expanded genetic code has enabled the precise activation/deactivation of numerous, diverse proteins, such as kinases, nucleases, proteases, and polymerases. Herein, I describe my contributions toward: (1) the application of genetically encoded, photo-activatable cysteine and lysine derivatives for improved understanding of the Ras/Raf/MEK/ERK pathway (specifically, using the dual-specificity phosphatase, MKP3) in mammalian cells, (2) the development of a site-specific light-induced oxidation approach for targeted protein inactivation, and (3) development and application of new, photoswitchable amino acids for future use in controlling metal complex formation.

In addition to the regulation of protein function using light-controlled amino acids, I have contributed to the development of photo-controlled small molecules for manipulating protein dimerization. Rapamycin is a small molecule which dimerizes two proteins, FKBP and FRB, and has been applied for the conditional control of protein-protein interactions. To provide additional levels of control, three different approaches were developed and applied in this thesis: (1) red-shifted caged rapamycin analogs for light-activation of dimerization, (2) ROS-generating analogs for light-inactivation of the ternary complex, and (3) photoswitchable analogs which undergo a configurational change to allow for preferential ternary complex of one isomer over another. The

development of these various optically controlled dimerizers expands the range of tools available to chemical biologists for conditional control of protein dimerization.

Table of Contents

List of Abbreviations	xxii
Preface.....	xxvii
1.0 Introduction to Optical Control and Genetic Code Expansion	1
1.1 Introduction to Genetic Code Expansion	1
1.2 Introduction to Photocaged Amino Acids	4
1.2.1 Caged Lysines	5
1.2.2 Caged Cysteines and Caged Selenocysteine.....	6
1.2.3 Caged Tyrosines	9
1.2.4 Select Applications of Caged Amino Acids.....	10
1.2.4.1 Optical Control of Nucleic Acid Processing	10
1.2.4.2 Optical Control of Cell Signaling	12
1.2.4.3 Optical Control of Protein-Protein Interactions.....	14
1.2.4.4 Optical Control of other Enzymatic Processes	15
1.3 Summary	16
2.0 Optical Activation of Protein Function.....	18
2.1 Optical Control of Dual Specific Phosphatase 6 (DUSP6 or MKP3).....	18
2.2 Introduction to MAPK Signaling and MKP3.....	18
2.3 Optical Control through Active Site Caging.....	21
2.4 Optical Control through Protein-Protein Interaction Caging	29
2.5 Summary and Outlook.....	36
2.6 Methods	37

3.0 Optical Deactivation of Protein Function	50
3.1 Introduction to Light-Induced Protein Inactivation Approaches.....	50
3.2 Introduction to Bioconjugation Reactions and Genetically Encoded Handles.....	58
3.3 Mapping of Protein Oxidation via Light-Induced Localized Oxidation	62
3.4 Ongoing Efforts and Future Work	80
3.5 Methods	81
4.0 Reversible Optical Switching of Protein Function.....	91
4.1 Introduction to Photoswitchable Amino Acids	91
4.2 Development of an Arylazopyrazole Photoswitchable Amino Acid (AAPF)	94
4.2.1 Control of Gene Expression Using AAPF	101
4.2.2 Optimization of Incorporation Efficiency for AAPF	108
4.3 Introduction to Natural and De Novo Metalloproteins.....	115
4.3.1 Introduction to Phenylazopyridines as Metal Chelators and Photoswitches	121
4.3.2 Toward Control of Metal Complex Formation using Photoswitchable Amino Acids	127
4.4 Summary and Outlook.....	136
4.5 Methods	137
5.0 Optical Activation of Rapamycin-Induced Protein Dimerization.....	159
5.1 Introduction to Chemical Inducers of Dimerization	159
5.1.1 Brief History of Rapamycin	163
5.1.2 Optical Control of Rapamycin-Induced Protein Dimerization	165
5.1.3 Optical Control of Other Chemical Inducers of Dimerization	170

5.1.4 Optogenetic Approaches to Control Protein Dimerization	174
5.2 Toward the Development of Optically Controlled, Bioorthogonal Rapalogs	179
5.2.1 Validation of Bioorthogonal Rapalogs and FRB Pairs	180
5.2.2 Methods	188
5.3 Introduction to Caged Rapamycin Analogs with Improved Photochemical Properties	190
5.4 BIST-caged Rapamycin Analogs.....	191
5.4.1 Methods	205
5.5 ANB-caged Rapamycin Analogs	212
5.5.1 Methods	225
6.0 Optical Deactivation of Rapamycin-Induced Protein Dimerization	235
6.1 Development and Application of Optically-Deactivated Rapamycin Analog.....	236
6.2 Summary and Outlook.....	247
6.3 Methods	248
7.0 Reversible Optical Switching of Rapamycin-Induced Protein Dimerization.....	254
7.1 Arylazopyrazole-modified Rapamycin Analogs	254
7.2 Spiropyran-modified Rapamycin Analog	263
7.3 Methods	267
8.0 Expanded Methods	271
8.1 General Techniques – Molecular Biology	271
8.1.1 Polymerase Chain Reaction (PCR)	271
8.1.2 Introduction of Point Mutations (Site-Directed Mutagenesis and QuikChange).....	272

8.1.3 Restriction Enzyme Digest	274
8.1.4 Plasmid Assembly – Ligation	275
8.1.5 Plasmid Assembly – Gibson Isothermal Assembly	276
8.1.6 PCR Screen	276
8.1.7 Calcium Competent Cell Preparation (for Cloning).....	278
8.1.8 KCM Competent Cell Preparation (for Protein Expression)	280
8.1.9 Transformation of Calcium Competent Cells	280
8.1.10 Transformation of KCM Competent Cells	282
8.1.11 Plasmid Purification.....	282
8.1.12 Sanger Sequencing	283
8.1.13 Agarose Gel Electrophoresis	284
8.2 General Techniques – Cell Biology	285
8.2.1 Protein Expression (and UAA incorporation) in <i>E. coli</i>	285
8.2.2 Lysis of Bacterial Cells – for sfGFP Mutants	286
8.2.3 Lysis of Bacterial Cells – for Non-sfGFP Proteins	287
8.2.4 Ni-NTA Protein Purification	288
8.2.5 SDS-PAGE Preparation and Electrophoresis	290
8.2.6 Mammalian Cell Maintenance.....	292
8.2.7 Poly-D-Lysine Treatment	294
8.2.8 Mammalian Cell Transfection – Linear Polyethyleneimine	295
8.2.9 Mammalian Cell Transfection – Lipofectamine 2000.....	296
8.2.10 Mammalian Cell Lysis	297
8.2.11 Western Blot Analysis.....	298

8.2.12 AmidoBlack 10B Staining	300
8.3 Common Buffers and Solutions Recipes	300
8.3.1 10X Phosphate Buffered Saline (PBS)	301
8.3.2 10X Tris Buffered Saline (TBS).....	301
8.3.3 1X Tris Buffered Saline + Tween-20 (TBST)	302
8.3.4 10X Tris-Boric Acid-EDTA (TBE).....	302
8.3.5 0.5 M EDTA pH 8.0 Solution	303
8.3.6 10X SDS-PAGE Running Buffer	303
8.3.7 20X MES-SDS-PAGE Running Buffer	304
8.3.8 Radioimmunoprecipitation Assay (RIPA) Lysis Buffer – for Mammalian Cells	304
8.3.9 4X Laemmli Sample Buffer	305
8.3.10 Coomassie Stain Solution	305
8.3.11 Coomassie Destain Solution	306
8.3.12 10X Western Blot Transfer Buffer	306
8.3.13 1X Western Blot Transfer Buffer	306
8.3.14 Amido Black 10B Stain (for PVDF Membrane).....	307
8.3.15 Amido Black 10B Destain (for PVDF Membrane).....	307
8.3.16 DMEM (for Culturing Mammalian Cells).....	307
8.3.17 Transformation Storage Buffer (TSB)	308
8.3.18 5X KCM Solution (for KCM Transformations)	308
8.3.19 5X Isothermal Gibson Assembly Buffer	309
8.3.20 Gibson Assembly Master Mix	309

8.3.21 Lysis Buffer (for Bacterial Protein Expression)	309
8.3.22 Wash Buffer (for Bacterial Protein Expression)	310
8.3.23 Elution Buffer (for Bacterial Protein Expression)	310
8.3.24 FKBP/FRB Storage and Assay Buffer	310
8.3.25 TEV Protease Lysis and Storage Buffer	311
8.3.26 1 M Dithiothreitol (DTT) – for Gel Band Sample Preparation	311
8.3.27 450 mM Iodoacetamide (IAA) – for Gel Band Sample Preparation	311
Appendix A – Plasmid Maps.....	312
Appendix B – Synthetase Panel Mutants.....	318
Appendix C – ITC Binding Curves	319
Appendix D – Description of LEDs	322
Bibliography	323

List of Tables

Table 2-1 Representative examples of light controlled kinases and phosphatases for studying cell signaling.....	19
Table 2-2 List of primers used for MKP3 experiments	39
Table 3-1 Small molecule photosensitizers	53
Table 3-2 Amino acids susceptible to oxidation via reaction with singlet oxygen	58
Table 3-3 Primers used for generating plasmids used in this chapter.....	83
Table 4-1 Structures of literature reported photoswitchable amino acids	93
Table 4-2 Structures and photophysical properties of azoheteroarenes.....	95
Table 4-3 Properties of metal ions found in biological systems.....	117
Table 4-4 Assembly of error-prone PCR.....	140
Table 4-5 DNA sequences and primers used for photoswitchable amino acid incorporation....	141
Table 5-1 Optogenetic dimerizer systems sorted by increasing wavelength.....	176
Table 5-2 List of primers used to generate FRB mutants in YFP-FRB.....	189
Table 5-3 Primer sequences for cloning constructs used with caged rapamycin 53	226
Table 7-1 Characterization of the PSS at 365 nm and 530 nm irradiation and thermal stability of the AAP-rapamycin analogs	256
Table 7-2 List of primers used to generate constructs for AAP-rapamycin analogs testing	268
Table 8-1 Antibiotic stocks and dilutions	282
Table 8-2 Preparation of various percentage of SDS-PAGE gels	290
Table 8-3 LPEI transfection reagent volumes for various plate formats	295
Table 8-4 Lipofectamine 2000 transfection reagent volumes for various plate formats	296

Table 8-5 Volumes of antibody solution and wash steps for various membrane box sizes	299
Table 8-6 Preparation of UAA stock solutions.....	301

List of Figures

Figure 1-1 Schematic overview of unnatural amino acid (UAA) mutagenesis	3
Figure 1-2 Three commonly utilized tRNA/synthetase pairs	4
Figure 1-3 Genetically encoded, photocaged amino acids	6
Figure 1-4 Optical control of TEV protease function and intein splicing using photocaged cysteine	8
Figure 1-5 Optical control of nucleic acid processing via caged CRISPR/Cas9 and T7 RNA polymerase	11
Figure 1-6 Optical control of kinase activity via genetic incorporation of the caged lysine HCK and optical control of nuclear translocation through caging of a protein-protein interaction ..	14
Figure 2-1 Schematic representation of the domain structures of the three groups of MAP kinase phosphatases.	20
Figure 2-2 Overview of the MAPK/MKP3 signaling pathway	21
Figure 2-3 The active site of MKP3 and structure of caged cysteine NVC	22
Figure 2-4 Western blots for incorporation of NVC into MKP3.....	23
Figure 2-5 Biochemical phosphatase assay with catalytically caged MKP3.....	24
Figure 2-6 Overview of ERK2-mCherry reporter	24
Figure 2-7 Optical control of the MKP3 catalytic site in the ERK2-mCherry reporter	26
Figure 2-8 Overview of the ERK-KTR-mCherry reporter	27
Figure 2-9 Optical control of the MKP3 catalytic site in the ERK-KTR-mCherry reporter	28
Figure 2-10 Crystal structure of the MKP3 KIM peptide bound to ERK2 reveals four targetable residues	30

Figure 2-11 Optical control of the phosphatase-kinase interaction motif (KIM).	31
Figure 2-12 MKP3 R64K and R65K mutants retain near wild-type activity	32
Figure 2-13 ERK activity in response to optical activation of the MKP3 kinase interaction motif	33
Figure 2-14 Analysis of ERK activity in response to different doses of growth hormone stimulation and optically tuned phosphatase function	35
Figure 2-15 UV control experiments with ERK-mCherry and ERK-KTR-mCherry reporters....	36
Figure 3-1 Overview of chromophore-assisted light inactivation	50
Figure 3-2 Jablonski diagram describing reactive oxygen species (ROS) generation.....	51
Figure 3-3 Fusion proteins for ROS production	55
Figure 3-4 Chemoselective labeling of proteins using bioorthogonal reactions.....	59
Figure 3-5 Structures of representative unnatural amino acids bearing bioorthogonal handles...	60
Figure 3-6 Schematic of localized ROS production for protein oxidation and inactivation	63
Figure 3-7 Overview of protein-protein mapping approaches.....	64
Figure 3-8 Turn-on tetrazine-BODIPY ROS generators	66
Figure 3-9 Validation of turn-on ROS generation	67
Figure 3-10 MS/MS coverage of sfGFP peptides using trypsin and chymotrypsin	68
Figure 3-11 MS/MS analysis of NorK -modified sfGFP	69
Figure 3-12 MS/MS analysis of the conjugated product of NorK -sfGFP and 5	70
Figure 3-13 Bioconjugation reactions of NorK -sfGFP with iodo-BODIPY-tetrazines 2 and 3 ..	71
Figure 3-14 Tandem MS/MS/MS analysis of a 3-NorK -sfGFP peptide.....	72
Figure 3-15 Light-induced oxidation of 3-NorK -sfGFP	74
Figure 3-16 Background DNP-labeling of NorK -sfGFP	75

Figure 3-17 Fenton oxidation of BSA and 6 -labeling/detection.....	76
Figure 3-18 Analysis of TEV protease crystal structure for unnatural amino acid incorporation sites	77
Figure 3-19 Protein and peptide-based TEV protease sensors	79
Figure 4-1 Synthetase screen of <i>MbPylRS</i> variants with AAPF	97
Figure 4-2 AAPF was successfully incorporated in <i>E. coli</i> and confirmed by ESI-MS	98
Figure 4-3 AAPF was successfully incorporated in mammalian cells and confirmed via fluorescence microscopy and western blotting	99
Figure 4-4 Determination of photostationary states and thermal stability of AAPF	100
Figure 4-5 Overview of translational control using AAPF	102
Figure 4-6 Validation of a dual mCherry-sfGFP reporter for UAA incorporation in <i>E. coli</i>	103
Figure 4-7 Integrated peak areas of flow cytometry analysis emphasizes differences between the conditions	104
Figure 4-8 Thermal stability of AAPF in <i>E. coli</i> and mammalian growth media	105
Figure 4-9 Thermal stability of <i>cis</i> - AAPF in the presence and absence of glutathione.....	106
Figure 4-10 Pulsed irradiations help maintain <i>cis</i> - AAPF over a longer time period	107
Figure 4-11 Comparison of pBK and pEVOL systems for AAPF incorporation	110
Figure 4-12 Comparison of various promoter arrangements for bacterial UAA incorporation .	112
Figure 4-13 PylRS selections using EP-PCR library against AAPF	114
Figure 4-14 Structures of genetically encoded metal chelating unnatural amino acids	119
Figure 4-15 Control of protein self-assembly using BpyA	120
Figure 4-16 Computationally designed metalloproteins reported by the Baker lab	121
Figure 4-17 Structures of 4-(2-pyridylazo)resorcinol (7) and 1-(2-pyridylazo)-2-naphthol (8).	122

Figure 4-18 Photoswitching and metal ion chelation of a self-assembled monolayer containing a phenylazopyridine.....	123
Figure 4-19 A bowl-equipped 4-(phenylazo)pyridine for control of zinc chelation	124
Figure 4-20 Phenylazopyridines as photodissociable ligands for Ni-porphyrins	125
Figure 4-21 Structures of phenylazopyridine-based amino acids.....	126
Figure 4-22 Computationally designed metalloproteins bearing AAPF modifications	127
Figure 4-23 Synthetase screen of <i>MbPylRS</i> variants with <i>o</i>-PyrAzoF	128
Figure 4-24 <i>o</i>-PyrAzoF was successfully incorporated in <i>E. coli</i> and confirmed by ESI-MS ..	129
Figure 4-25 Determination of photostationary states and thermal stability of <i>o</i>-PyrAzoF	130
Figure 4-26 Absorbance spectra of <i>o</i>-PyrAzoF in the presence and absence of metal ions	132
Figure 4-27 Test substrates for <i>o</i>-PyrAzoF metal chelation	133
Figure 4-28 ITC binding studies of 13 , 14 , and 15 with four different metal ions.....	134
Figure 4-29 Pyrazole test substrate as putative divalent chelate.....	135
Figure 5-1 Prominent chemical inducers of dimerization and their respective protein partners	159
Figure 5-2 Structures of homodimerizers 18 and 19	160
Figure 5-3 Structures of 20 and 21 function as heterodimerizers.....	161
Figure 5-4 Crystal structure of FKBP- 21 -FRB and mechanisms of binding.....	162
Figure 5-5 Role of rapamycin in mTOR signaling	164
Figure 5-6 Application of caged rapamycin 22 toward control of FAK kinase	166
Figure 5-7 Application of caged rapamycin 23 toward Rac localization	167
Figure 5-8 Application of caged rapamycin 25 toward control of split TEV protease.....	169
Figure 5-9 Application of caged rapamycin 26 for inhibition of endogenous mTOR signaling	170
Figure 5-10 Application of caged HaloTag-TMP ligand 27	171

Figure 5-11 Application of the photocleavable SNAP-tag/HaloTag ligand 28	172
Figure 5-12 Structures of caged abscisic acid 29 and gibberellic acid 30	173
Figure 5-13 Schematic of various optogenetic dimerizers	177
Figure 5-14 Schematic representation of multi-wavelength bio-orthogonal rapamycin dimerization	180
Figure 5-15 Rapalogs and FRB pairs.....	181
Figure 5-16 Validation of membrane reporter with varying concentrations of rapamycin	183
Figure 5-17 TIRF imaging analysis of rapalog and FRB pairs.....	185
Figure 5-18 TIRF analysis of 31 and 32 with KTW and PLF mutants.....	187
Figure 5-19 Attempted synthesis of a coumarin-modified rapamycin	191
Figure 5-20 Structure of a new bisstyrylthiophene caging group and the absorbance spectrum	192
Figure 5-21 Attempted synthesis of a BIST-dRap 42	193
Figure 5-22 Synthesis of a second-generation BIST-dRap 44	194
Figure 5-23 Schematic representation of a split luciferase with rapamycin.....	195
Figure 5-24 Determination of optimal FKBP:FRB ratios in the split luciferase reporter for dRap analogs	196
Figure 5-25 Attempts to photoactivate 44 in a split luciferase reporter assay.....	197
Figure 5-26 Structures of BIST-dRap 46 and BIST-Rap 47	198
Figure 5-27 HPLC analysis of BIST-dRap 46 decaging with 450 nm LED irradiation.....	199
Figure 5-28 HPLC decaging of 46 in the presence of 1,3-cyclohexadiene (48).....	201
Figure 5-29 Background dimerization comparison of dRap 25 and BIST-dRap 46	202
Figure 5-30 HPLC analysis of decaging of BIST-Rap 47	203
Figure 5-31 Photoactivation of BIST-Rap 47 in the split luciferase reporter.....	204

Figure 5-32 Structures of nitrobiphenyl caging groups and 53	213
Figure 5-33 HPLC decaging analysis of caged rapamycin 53 with 405, 415, and 450 nm LEDs	214
Figure 5-34 Gel shift assays with caged rapamycin 53 and previous caged analogs	215
Figure 5-35 Photoactivation of caged rapamycin 53 in the split luciferase reporter assay	216
Figure 5-36 Structure of Shield-1 (54) and schematic of destabilized FKBP reporter.....	218
Figure 5-37 Optimization of a destabilized FKBP reporter for use with rapamycin.....	219
Figure 5-38 Photoactivation of caged rapamycin 53 in a destabilized FKBP reporter	220
Figure 5-39 Photoactivation of caged rapamycin 53 in a nuclear translocation reporter	221
Figure 5-40 Optical control of 53 inhibition of mTOR signaling in HeLa cells.....	222
Figure 5-41 Assessment of background activity of 53 in zebrafish embryos.....	223
Figure 5-42 Demonstration of light activation of 53 in zebrafish embryos.....	224
Figure 6-1 Schematic representation of ROS-induced ternary complex disruption.....	235
Figure 6-2 Structure of BODIPY-rapamycin 55 and testing in split luciferase reporter	236
Figure 6-3 Structures of 56 and PEG-BODIPY-rapamycin 57	237
Figure 6-4 Testing of 57 with the singlet oxygen sensor 4	238
Figure 6-5 HPLC analysis of 57 stability in physiological buffers	239
Figure 6-6 Gel shift assays using 21 , 56 , and 57	240
Figure 6-7 Application of 57 in a split luciferase reporter.....	241
Figure 6-8 Validation of the dimerization efficiency of 57 in the membrane translocation reporter	242
Figure 6-9 Light-induced deactivation of fluorescent membrane reporter proteins using 57	243

Figure 6-10 Western blot analysis of light-induced oxidation using 57 in a membrane reporter	244
Figure 6-11 Western blot analysis of 57 in the membrane reporter with a proteasome inhibitor	245
Figure 6-12 Determination of type of ROS being generated upon light-induced oxidation in the membrane reporter	246
Figure 6-13 XTT cell viability assay with 57 in non-transfected and membrane reporter transfected cells	247
Figure 7-1 Five arylazopyrazole-modified rapamycin analogs were synthesized.....	256
Figure 7-2 A split luciferase reporter was used to test the efficacy of the photoswitchable rapamycin analogs	257
Figure 7-3 Split luciferase variant (iFKBP) was used for testing 58	258
Figure 7-4 Split luciferase variants (point mutations made in FKBP) were used for testing 58	259
Figure 7-5 The photocycling stability of 58 was analyzed.....	260
Figure 7-6 Assessment of reversibly controlled ternary complex formation with 58 in the split luciferase assay	261
Figure 7-7 The spiropyran photoswitch exists in both a spiropyran and merocyanine form	264
Figure 7-8 Structure of the spiropyran-modified rapamycin 63	265
Figure 7-9 Absorbance spectra of spRap in the spiropyran and merocyanine forms	265
Figure 7-10 A split luciferase reporter was used to test the spiropyran-modified rapamycin analog 63	266
Figure A-1 Plasmids used in Chapter 2	313
Figure A-2 Plasmids used in Chapter 3	314

Figure A-3 Plasmids used in Chapter 4	315
Figure A-4 Plasmids used in Chapters 5 and 6	316
Figure A-5 Plasmids used in Chapter 7	317
Figure A-6 Synthetase panel mutations	318
Figure A-7 Raw data corresponding to the heat maps shown in Figure 4-27.....	319
Figure A-8 Raw data corresponding to the heat maps shown in Figure 4-28.....	320
Figure A-9 Raw data corresponding to the heat maps shown in Figure 4-29.....	321

List of Abbreviations

2-TCOK	2- <i>trans</i> -cyclooctene-lysine
4-TCOK	4- <i>trans</i> -cyclooctene-lysine
AAP	arylazopyrazole
AAPF	arylazopyrazole phenylalanine
ACN	acetonitrile
AllocK	allyloxycarbonyl lysine
AmBic	ammonium bicarbonate buffer
AP	antarctic phosphatase
APEX	ascorbate peroxidase
APS	ammonium persulfate
ATP	adenosine triphosphate
AzoF	azobenzene phenylalanine
BCNK	bicyclo[6.1.0]nonyne lysine
BioID	proximity-dependent biotin identification
BIST	bisstyrylthiophene
BODIPY	boron-dipyrromethene
bp	base pair
BSA	bovine serum albumin
<i>C. elegans</i>	<i>Caenorhabditis elegans</i>
C/N	cytoplasmic/nuclear ratio
CALI	chromophore assisted light inactivation
CFP	cyan fluorescent protein
CHD	1,3-cyclohexadiene
CID	collision-induced dissociation
CID	chemical inducer of dimerization
Cluc	C-terminus fragment of firefly luciferase
CpK	cyclopropene-lysine
CuAAC	copper(I)-catalyzed azide alkyne cycloaddition
DCM	dichloromethane
ddFKBP	destabilized mutant of FKBP
DEACM	diethyl amino coumarin
DiFMUP	6,8-difluoro-4-methylumbelliferyl phosphate
DMAP	4-dimethylaminopyridine

DME	dimethoxyethane
DMEM	Dulbecco's modified Eagle's medium
DMF	dimethylformamide
DMSO	dimethyl sulfoxide
DNA	deoxyribonucleic acid
DNP	2,4-dinitrophenyl
DNPH	2,4-dinitrophenyl hydrazine
dNTPs	deoxyribonucleotide triphosphate mix
DPBF	1,3-diphenylisobenzofuran
DTT	dithiothreitol
DUSP6	dual specificity phosphatase 6
<i>E. coli</i>	<i>Escherichia coli</i>
EDTA	ethylenediaminetetraacetic acid
EGF	epidermal growth factor
EGFP	enhanced green fluorescent protein
ERK	extracellular regulated kinase
ESI	electrospray ionization
FAK	focal adhesion kinase
FeBABE	iron bromoacetamidobenzyl-EDTA
FKBP	FK506 binding protein
FLuc	firefly luciferase
FRB	FKBP rapamycin binding domain of mTOR
FRET	fluorescence energy transfer
GABA	gamma-aminobutyric acid
GAPDH	glyceraldehyde 3-phosphate dehydrogenase
HCK	hydroxycoumarin lysine
HCl	hydrochloric acid
HEK293T	human embryonic kidney 293T cells
HPLC	high pressure liquid chromatography
HRP	horseradish peroxidase
IAA	iodoacetamide
IEDDA	inverse electron demand Diels-Alder
IPTG	isopropyl B-D-1-thiogalactopyranoside
IRES	internal ribosome entry site
ISC	intersystem crossing
kb	kilobases
KCM	potassium, calcium, magnesium solution for transformation
K_d	dissociation constant

kDa	kilodalton
KIM	kinase interaction motif
KR	KillerRed
KTR	kinase translocation reporter
LC	liquid chromatography
LCIS	live cell imaging solution
LCK	lymphocyte-specific protein tyrosine kinase
LED	light-emitting diode
LeuRS	leucyl tRNA synthetase
Lipo2K	Lipofectamine 2000
LPEI	linear polyethyleneimine
LTQ	linear trap quadrupole
MAPK	mitogen-activated protein kinase
MBP	maltose-binding protein
<i>MbPylRS</i>	<i>M. barkeri</i> pyrrolysyl tRNA synthetase
MC	merocyanine
MCA	methoxycoumarin
MeCN	acetonitrile
MEK	MAPK/ERK kinase or mitogen-activated protein kinase kinase
MB	methylene blue
MG	malachite green
MGI	iodinated malachite green
MKK6	mitogen-activated protein kinase kinase 6
MKP3	MAPK phosphatase 3
<i>MmPylRS</i>	<i>M. mazei</i> pyrrolysyl tRNA synthetase
MS	mass spectrometry
MS/MS	tandem mass spectrometry or MS2
MS/MS/MS	MS3
mTOR	mammalian target of rapamycin
N/C	nuclear/cytoplasmic ratio
NB	nitrobenzyl
NES	nuclear export sequence
NHS	<i>N</i> -hydroxysuccinimide
NLS	nuclear localization sequence
Nluc	N-terminus fragment of firefly luciferase
NMR	nuclear magnetic resonance spectroscopy
NorK	norbornene lysine
NPOM	6-nitropiperonyloxymethyl caging group

nt	nucleotide
NT	non-treated
NVC	nitroveratryl cysteine
OD	optical density
ONBY	nitrobenzyl caged tyrosine
P/S	penicillin-streptomycin
PAGE	polyacrylamide gel electrophoresis
pAzF	para-azidophenylalanine
PBS	phosphate-buffered saline
PBST	phosphate-buffered saline + 0.1% Tween-20
PCR	polymerase chain reaction
PES	polyethersulfone
PKC- γ	protein kinase C - gamma
PVDF	polyvinylidene difluoride
PylT	pyrrolysyl tRNA
PyrAzoF	pyridinylazobenzene phenylalanine
RB	Rose Bengal
RIPA	radioimmunoprecipitation assay
RNA	Ribonucleic acid
ROS	reactive oxygen species
RS	tRNA synthetase
SDM	site-directed mutagenesis
SDS	sodium dodecyl sulfate
sfGFP	superfolder green fluorescent protein
shRNA	short hairpin RNA
siRNA	small interfering RNA
SOG	miniSOG or mini singlet oxygen generator
SP	spiropyran
SPAAC	strain-promoted azide alkyne cycloaddition
ssDNA	single-stranded DNA
ssRNA	single-stranded RNA
TBE	tris base, boric acid, EDTA buffer
TBET	through-bond energy transfer
TBS	tris buffered saline
TBST	tris buffered saline + 0.1% Tween-20
TCA	trichloroacetic acid
TCEP	tris(2-carboxyethyl)phosphine
TCO	<i>trans</i> -cyclooctene

TEMED	tetramethylethylenediamine
TEVp	Tobacco Etch Virus protease
TIRF	total internal reflection fluorescence microscopy
T_m	melting temperature
TPP	three-phase partitioning
tRNA	transfer RNA
UAA	unnatural amino acid
UV	ultraviolet light
WT	wild-type
XTT	2,3-Bis-(2-methoxy-4-nitro-5-sulphenyl)-2 <i>H</i> -tetrazolium-5-carboxanilide
YFP	yellow fluorescent protein

Preface

I would like to thank my advisor, Alex Deiters, for his support, his enthusiasm for science, and his high expectations. All of these have significantly contributed to making me a better scientist than I was five years ago. I would also like to thank my committee members Steve Weber, Seth Childers, and Nathan Yates for their continued guidance and support over the last few years.

A special thanks to former Deiters lab members Jessica Torres-Kolbus, Kalyn Brown, and Colleen Connelly for mentoring me as an undergraduate at NCSU (it was a taxing time for all of us), for contributing to my decision to attend grad school (sometimes I question why I ever listened), and for keeping me sane these last few years. Thanks to former lab member Nick Ankenbruck for his mentorship and friendship, and to Trevor Horst for synthesizing a majority of the compounds (amino acids and rapamycin analogs) that are described here. To current lab members Mary Cacace, Kristie Darrah, Chasity Hankinson, and Amy Ryan (it's in alphabetical order guys, it's not ranked), you all have made the last several years bearable. Thanks for putting up with my shenanigans, the "would you rathers," and the endless sarcasm and snark.

I would also like to thank the Yates lab (Jim Boslett and Matt Fagerburg) and the BioMS Core (Xuemei Zhou, Pam Cantrell, and Jackie Jones-Laughner) for training me and answering my endless questions as I entered the world of proteomics. Thanks to the Childers and Islam labs for use of shared instruments and for troubleshooting assistance.

Finally, I would like to thank my family and Sam for their continuous support throughout this marathon of a process. Leila, you've brightened up the last three years with your crazy antics and Taylor Jr behavior.

1.0 Introduction to Optical Control and Genetic Code Expansion

This chapter was reprinted in part from: **Courtney, T.**; Deiters, A. *Curr. Opin. Chem. Biol.* **2018**, *46*, 99-107 and **Courtney, T.**; Deiters, A. *Cell Chem. Biol.* **2019**, *26*, 1481-1483.

1.1 Introduction to Genetic Code Expansion

Proteins are required for all cellular processes and participate in a wide range of cellular functions such as signal transduction, cellular structure, enzymatic catalysis, and many others. Nature utilizes 20 canonical amino acid building blocks that are genetically encoded by 64 triplet codons. Deoxyribonucleic acid (DNA) is transcribed into messenger ribonucleic acid (mRNA), which is the template used for protein synthesis in the cell through the process of translation. Translation requires several components to generate a full-length, functional protein. Protein synthesis occurs in ribosomes located in the cytoplasm of the cell. The mRNA template, which codes for specific amino acids, binds to the ribosome to initiate translation. Transfer RNAs (tRNAs) are aminoacylated (“charged”) by amino-acyl tRNA synthetases and carry the amino acids to the ribosome. The mRNA sequence is read in three-base sequences known as codons, which base pair with the anticodon loop of the charged tRNA to incorporate a specific amino acid into the growing polypeptide chain. Upon reaching one of three codon sequences (UAG, UGA, or UAA), a release factor is recruited to the ribosomal machinery to terminate translation.

While these natural 20 amino acids provide a diverse set of proteins that can be synthesized, nature requires additional modifications beyond the 20 amino acids. The endogenous chemical

functionality of amino acids is limited to alcohols, thiols, amines, aromatics, acids/bases, and hydrophobic groups. To date, more than 25 unique post-translational modifications have been identified in prokaryotes and eukaryotes combined, including, in order from most to least frequent: phosphorylation, acetylation, N-linked glycosylation, amidation, hydroxylation, methylation, O-linked glycosylation, and ubiquitylation, to name just a few.¹ This indicates the need for more diversity than the 20 amino acids alone. In certain prokaryotes and archaea, it was found that selenocysteine (21st amino acid) or pyrrolysine (22nd amino acid) are incorporated using the UGA or UAG codon, respectively.²⁻³ The discovery of pyrrolysine incorporation into the UAG amber codon paved the way for the development of some UAA mutagenesis machinery components that are widely utilized today.⁴⁻⁵

Wang and Schultz demonstrated that an engineered *M. jannaschii* tyrosyl-tRNA/synthetase pair could be used to suppress translational termination at the UAG stop codon by incorporating *o*-methyl tyrosine into that position in *E. coli* (Figure 1-1).⁶ This approach relies on evolution of the tRNA synthetase to charge the cognate tRNA exclusively with the unnatural amino acid and no other endogenous amino acid. Additionally, mutations were made to the tRNA such that the *E. coli* machinery would not recognize it as an endogenous tRNA. This initial, orthogonal tRNA/synthetase pair has been widely utilized to incorporate ~40 amino acids in *E. coli* over the last several years.⁷

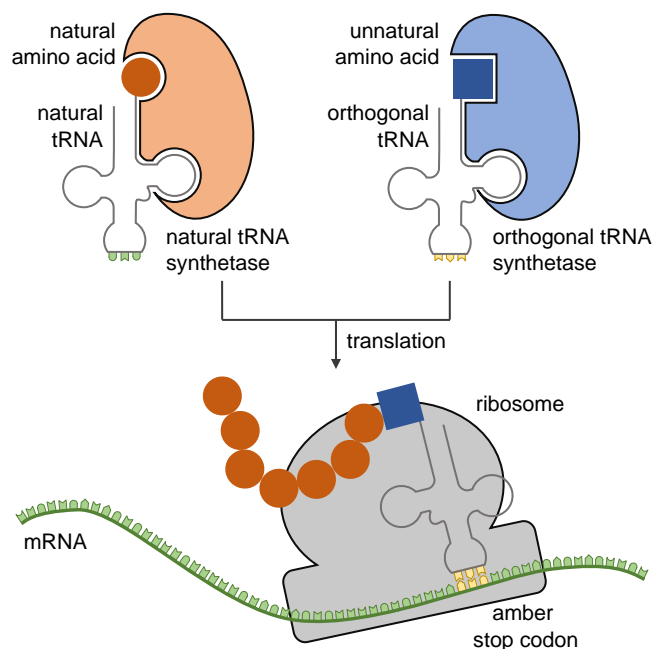


Figure 1-1 Schematic overview of unnatural amino acid (UAA) mutagenesis

The tRNA and the synthetase (light blue) need to be orthogonal to all endogenous tRNA/synthetase (light orange) pairs, and the synthetase needs to be engineered to exclusively recognize the UAA (blue) as a substrate. The aminoacylated tRNA is then used by the ribosome to deliver the UAA site-specifically into the growing polypeptide chain in response to an amber stop codon (yellow). Reprinted from Courtney and Deiters, *Cell Chem. Biol.* **2019**, 26, 1481-1483. Copyright 2019 Elsevier Ltd.

Unfortunately, this original pair is not orthogonal in mammalian cells, thus alternative pairs have been explored for expanding this approach to mammalian cells.⁸ The two commonly utilized pairs for mammalian cells are PylRS/tRNA and *EcTyrRS*/tRNA (Figure 1-2).⁹ Due to the high degree of orthogonality observed for the PylRS/tRNA system in bacterial, yeast, and mammalian cells, our lab primarily uses this system for incorporation of unnatural amino acids into proteins. The UAA work presented in this document primarily utilized the *M. barkeri* PylRS/tRNA pair, except where noted in various cases.

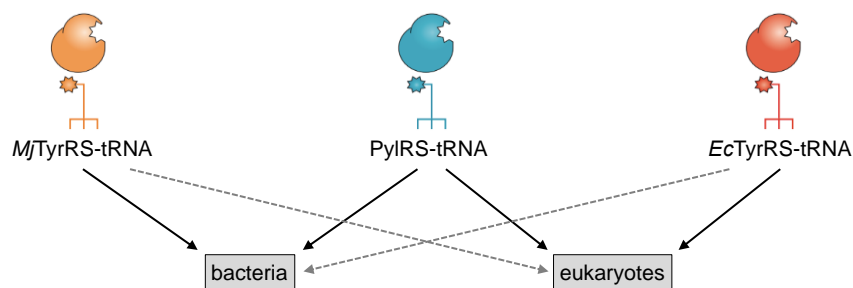


Figure 1-2 Three commonly utilized tRNA/synthetase pairs
 Black lines correspond to systems where the tRNA/synthetase pair has been utilized and the dotted, gray line represents non-orthogonal systems. Adapted from Davis *et al.*, *Nat. Rev. Mol. Cell Biol.* **2012**, *13*, 168-182. Copyright 2012 Macmillan Publishers Ltd.

1.2 Introduction to Photocaged Amino Acids

In order to study and manipulate biological processes with the same precision as nature, chemical biologists have developed a number of optical tools.¹⁰ The use of light to control protein activity provides non-invasive, precise, spatiotemporal control and allows for more acute perturbation than other methods (such as RNA interference or gene editing). Optical control of protein function in live systems has primarily been achieved through two approaches: genetic encoding of light-responsive amino acids or optogenetic methods using natural photo-responsive protein domains. Over the last two decades, more than a hundred non-canonical amino acids have been genetically encoded in a range of organisms to provide functionalities not found in the common set of 20 amino acids.⁴ The incorporation of light-triggered amino acids into proteins has been used to control a wide range of biological processes in cells and animals,¹¹ and this introduction highlights prominent examples from recent years in order to demonstrate the versatility of this approach. Important methodologies, such as protein bioconjugation of photoswitchable ligands,¹²⁻¹³ and purely optogenetic approaches are outside the scope of the work presented herein.¹⁴⁻¹⁷

1.2.1 Caged Lysines

Optical control of lysine, which plays an essential role in enzymatic catalysis of many biological processes, has been instrumental in gaining a deeper understanding of living systems at the molecular level. The photocaged lysine **PCK** (Figure 1-3) has been applied toward optical triggering of Cas9 nuclease,¹⁸ T7 RNA polymerase,¹⁹ Cre recombinase,²⁰ MEK,²¹⁻²² and LCK²³ kinases, isocitrate dehydrogenase,²⁴ and protein-protein interactions.²⁵⁻²⁶ This photocaged lysine utilizes 365 nm light for activation and may be incompatible with certain experiments performed in *E. coli* due to the abundance of nitroreductases. In order to develop a system that is compatible with a range of organisms and to provide activation with blue (405 nm) and near-IR (two-photon 760 nm) light, the coumarin-caged lysines **HCK** and **BHCK** were developed.²⁷ Both were applied in mammalian cells for the optical control of luciferase function and of GFP folding and the different decaging wavelengths for **HCK** (405 nm) and **BHCK** (760 nm) enable sequential, wavelength-selective activation. Additionally, the coumarin chromophore provides fluorescent tracking of the incorporated amino acid prior to decaging, thus **HCK** and **BHCK** can act as both fluorescent and photo-activatable probes in live cells. Introduction of the additional methylene group in **HC₂K**, blocks photolysis and provides a stable and small fluorophore that can be site-specifically placed into proteins. The caged lysine **HCK** has subsequently been applied to control MEK kinase in zebrafish embryos²² and DNA helicase.²⁸

While lysine often plays an essential role in enzymatic catalysis, replacement of the ϵ -carbon with oxygen generates an amino-oxy functionality which can undergo bio-orthogonal oxime ligation with a ketone or aldehyde. The Virdee group generated the corresponding lysine analog **PAOK** with a nitrobenzyl caging group to render it unreactive until UV-induced photolysis and encoded it using the same synthetase/tRNA pair engineered for **PCK**.²⁹

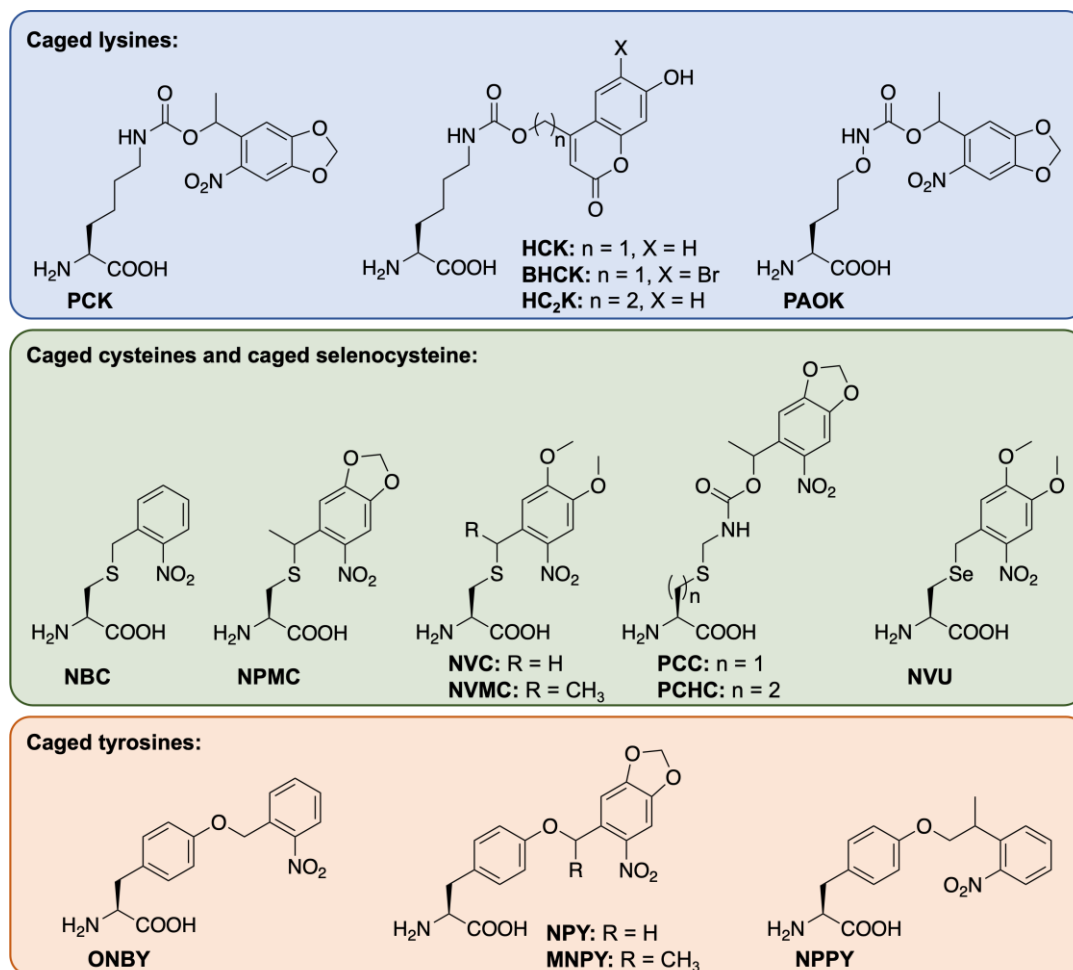


Figure 1-3 Genetically encoded, photocaged amino acids. These include caged lysines (**PCK**, **HCK**, **BHCK**, **HC₂K**), caged cysteines (**NBC**, **NPMC**, **NVC**, **NVMC**, **PCC**, **PCHC**), caged selenocysteine (**NVU**), and caged tyrosines (**ONBY**, **NPY**, **MNPY**, and **NPPY**). Figure modified from Courtney and Deiters, *Curr. Opin. Chem. Biol.* **2018**, 46, 99-107. Copyright 2018 Elsevier Ltd.

1.2.2 Caged Cysteines and Caged Selenocysteine

Although it is the least abundant amino acid found in proteins, cysteine plays an essential role in nucleophilic catalysis, redox signaling, metal binding, and structural support through disulfide formation.³⁰ In order to optically control these different functions, several caged cysteine analogs have emerged in the last few years. Schultz genetically encoded **NBC** in yeast using an *E. coli* leucyl synthetase/tRNA pair to cage the active site of caspase-3.³¹ More recently, the Chin lab

developed the caged cysteine **NPMC**, which was incorporated by an engineered pyrrolysine tRNA synthetase/tRNA pair and applied in mammalian cells for the photo-activation of TEVp (Figure 1-4a).³²

Photoactivated proteins are typically generated through replacement of an essential amino acid with a caged analog. In contrast, the Ai lab developed an approach that can be utilized in cases where such a critical amino acid residue is not available, by developing a light-triggered intein.³³ Inteins are protein segments which can self-cleave and excise, thereby rejoining the cleaved N- and C-terminal fragments to form a new, truncated protein. This cleavage event often utilizes a nucleophilic cysteine residue, making it amenable to optical control through incorporation of the caged cysteines **NVC** and **NVMC**. As proof-of-concept, a caged *Nostoc punctiforme* DnaE intein (splicing occurs with a reaction half-life of one minute) was placed in the middle of the mCherry protein sequence such that an inactive, non-fluorescent protein was expressed. Following UV irradiation and protein splicing, full-length, active mCherry was generated. In a second application, the caged intein was placed into the catalytic domain of Src kinase in order to control its enzymatic activity and downstream phosphorylation (Figure 1-4b). One limitation of the approach is the necessity of a cysteine residue at the splice site; which, if not naturally present, will leave a scar following intein excision. In addition, optically controlled inteins have been applied to protein splicing in yeast³⁴ and generation of cyclic peptides in *E. coli*.³⁵

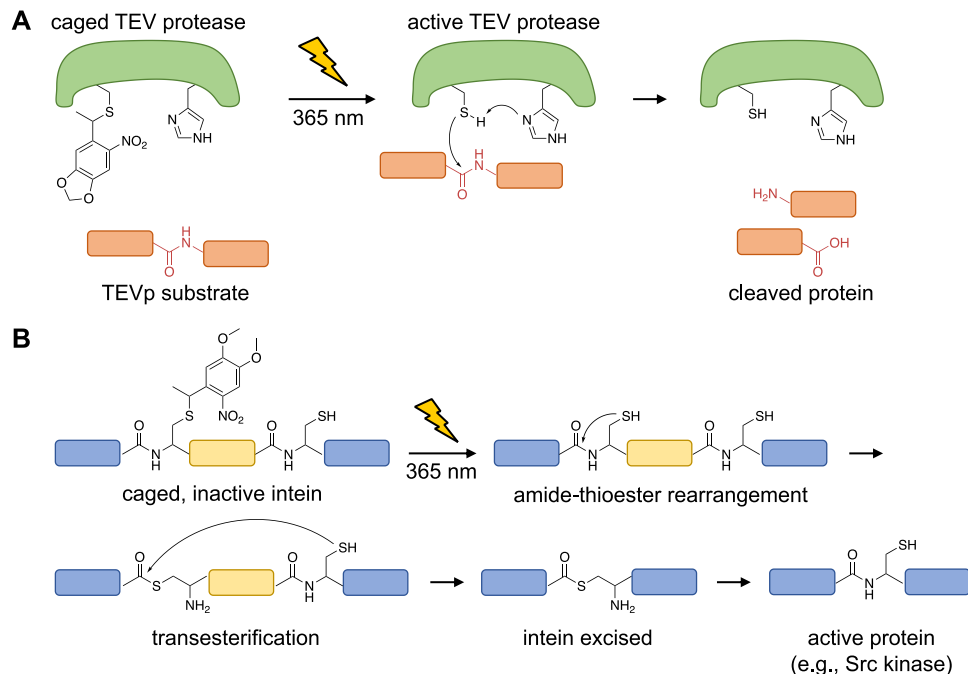


Figure 1-4 Optical control of TEV protease function and intein splicing using photocaged cysteine
 a) Upon caging of TEVp, the catalytic activity is blocked until photolysis of the caged, catalytically active cysteine, which performs a nucleophilic attack onto the protein target to generate cleaved protein fragments. b) A caged intein, indicated by the region in yellow, can be strategically placed within a protein (shown in blue; e.g., mCherry or Src kinase) such that it is misfolded and inactive prior to irradiation. Upon photo-activation, the native cysteine is generated and the intein is excised, leading to full-length, active protein (with only a cysteine scar). Reprinted from Courtney and Deiters, *Curr. Opin. Chem. Biol.* **2018**, 46, 99-107. Copyright 2018 Elsevier Ltd.

The light-activated cysteines discussed above required tRNA synthetase engineering for genetic encoding. Alternatively, the Deiters lab engineered the caged cysteine structure and developed the caged cysteine **PCC** and the homocysteine **PCHC**, which structurally mimic the caged lysine **PCK** and serve as substrates for the corresponding tRNA synthetase.³⁶ Not surprisingly, the homocysteine **PCHC** was incorporated as efficiently as caged lysine **PCK**, while incorporation of **PCC** was slightly less efficient. Light activation of **PCC** and **PCHC** was demonstrated through optical control of *Renilla* luciferase. While both **PCC** and **PCHC** showed an increase in luminescence following UV irradiation, the activity of the homocysteine containing enzyme was substantially lower. Thus, site-specific incorporation of homocysteine through light-

activation of **PCHC** may enable perturbation of an active site with single-atom resolution due to the introduction of an additional methylene unit.

Selenocysteine (Sec) is structurally and functionally similar to its periodic neighbor cysteine. Recently, the role of Sec in functional proteins and enzymes has received much attention³⁷ and clever approaches to its introduction have been developed.³⁸⁻⁴⁰ The Klimasauskas group masked the nucleophilic selenium with a nitrobenzyl moiety to generate **NVU** and incorporated it into sfGFP.⁴¹ Following UV irradiation, native Sec was generated and reacted with maleimide-modified biotin.

1.2.3 Caged Tyrosines

The tyrosine side chain plays important roles in catalysis when found in an enzyme active site and in cell signaling as it is a widely utilized substrate for protein kinases for signal propagation. Photocaged tyrosine **ONBY** was genetically encoded a decade ago and has been applied to the optical control of several enzyme classes;⁴²⁻⁴⁷ however, in order to facilitate decaging through red-shifting of the chromophore's absorption maximum, the Deiters group developed three additional photocaged tyrosine derivatives **MNPY**, **NPY**, and **NPPY**.⁴⁸ Use of a dual-luciferase reporter allowed for simultaneous assessment of incorporation and decaging efficiency. While **MNPY** delivered the most efficient optical activation of protein function, the caged tyrosine **NPY** proved to be the better analog when both incorporation efficiency and decaging efficiency are considered. Thus, caged tyrosine **NPY** was subsequently applied to the demonstration of spatial control of luciferase activity and the efficient optical triggering of TEV protease (TEVp) activity in mammalian cells. Optical control of TEVp may enable the engineering of precise spatiotemporal activation/deactivation of a protein of interest at a desired subcellular region or protein

translocation through light-triggered peptide cleavage. Furthermore, caged amino acids may be applicable to the photocontrol of other proteases.³¹

1.2.4 Select Applications of Caged Amino Acids

In addition to technical advances involving the development of new photocaged amino acids with improved photochemical properties, advancements in applications have been made in recent years. The photocaged amino acids described above have been applied for controlling various enzymes involved in DNA and RNA processing, for controlling essential enzymes involved in signaling cascades, and for regulating protein-protein interactions.

1.2.4.1 Optical Control of Nucleic Acid Processing

The CRISPR/Cas9 system is a highly versatile genome-editing tool that enables modification, insertion, or deletion of sequences of genomic DNA.⁴⁹⁻⁵¹ While natural Cas9 is constitutively active, conditional control of its function enables applications with spatio-temporal precision and may minimize off-target effects.⁵¹ The Deiters group developed the first optically controlled CRISPR/Cas9 system by replacing a lysine residue in the HNH nuclease domain with the photocaged lysine **PCK**, in order to prevent the conformational change necessary for nuclease activity (Figure 1-5a).¹⁸ Using a dual fluorescent reporter, which relies on the excision of mCherry and the subsequent expression of GFP, spatial and temporal control of Cas9 activity was achieved in mammalian cells. Additionally, light-triggered gene silencing of an endogenous target, the cell surface receptor CD71, was demonstrated.

In order to expand the toolkit of optically controlled DNA-processing enzymes, the Deiters group developed a caged helicase (UvrD)²⁸ and a caged DNA recombinase²⁰ for spatiotemporal

control of DNA unwinding and recombination, respectively. UvrD was rendered light responsive through the installation of the photocaged lysine **HCK** at a conserved lysine residue within the ATPase domain. In conjunction with optical control of kinase function,^{21, 23} this indicates the possibility of universal photochemical triggering of ATP-dependent processes. Cre recombinase was initially photocaged at an active-site tyrosine with **ONBY**; however, in order to improve enzyme expression levels in mammalian cells, a conserved lysine residue was replaced with **PCK**. Excellent off to on photocontrol of Cre recombinase was achieved and the potential for performing knock-in/knock-out experiments with high spatiotemporal resolution was demonstrated in developing zebrafish embryos.⁵²

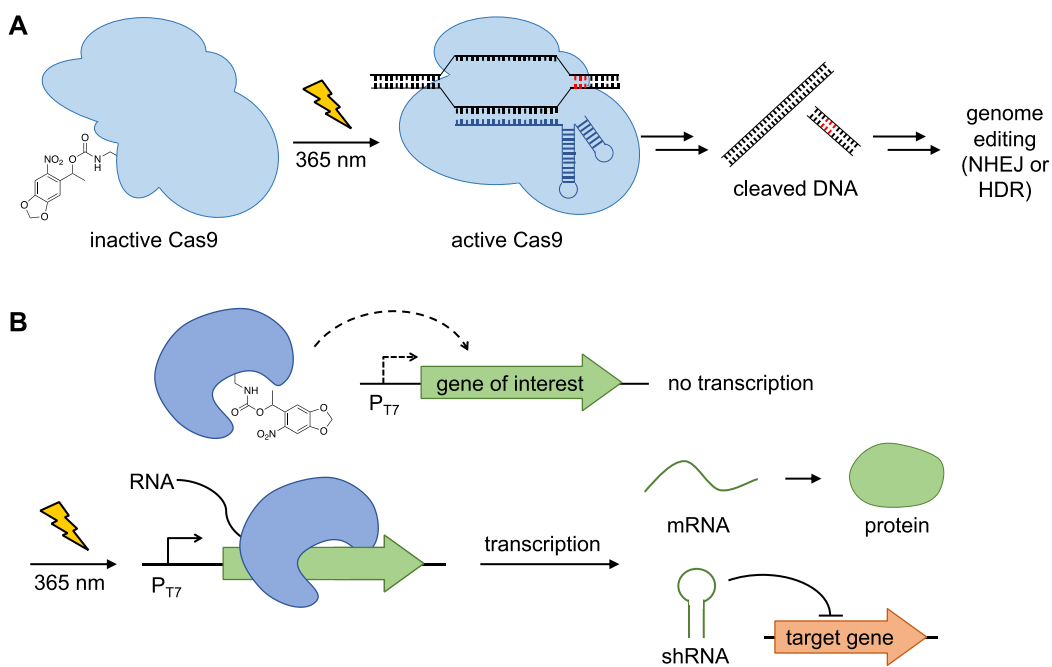


Figure 1-5 Optical control of nucleic acid processing via caged CRISPR/Cas9 and T7 RNA polymerase
a) CRISPR/Cas9 was rendered inactive by the incorporation of the photocaged lysine **PCK**, which blocks HNH nuclease activity. UV irradiation generates active Cas9, which results in DNA double strand cleavage and subsequent genomic editing. b) Caged T7 RNA polymerase is catalytically inactive, preventing transcription of genes under control of the T7 promoter. Upon UV-induced decaging, wild-type T7 RNA polymerase is restored and T7-promoter induced genes (e.g., mRNAs to code for protein or shRNA for gene silencing) are transcribed. Reprinted from Courtney and Deiters, *Curr. Opin. Chem. Biol.* **2018**, 46, 99-107. Copyright 2018 Elsevier Ltd.

In order to optically control transcription in mammalian cells, the Deiters group developed a photocaged T7 RNA polymerase in which an active site lysine was replaced with the caged lysine **PCK** (Figure 1-5b).¹⁹ This enables light-activation of a transcriptional pathway (gene of interest placed under the T7 promoter) that is orthogonal to the endogenous cellular machinery, and the caged T7 RNA polymerase was applied to the triggering of gene expression (control of EGFP mRNA as a proof-of-concept), as well as, gene silencing (control of shRNA targeting the motor protein Eg5 as a proof-of-concept) with spatial and temporal resolution.

1.2.4.2 Optical Control of Cell Signaling

Cell signaling networks exhibit a high degree of spatial and temporal dynamics, suggesting light as a preferred external control element. Unlike genetic tools, which require days or hours to knock down or inhibit signaling proteins, light activation of caged amino acids enables one to study the acute effects of kinase function. Since the caged amino acids are genetically directed to their incorporation site in cell signaling proteins, they provide an unmatched specificity that is difficult to achieve with small molecule inhibitors.

LCK (lymphocyte-specific protein tyrosine kinase) is responsible for initiating the T-cell receptor (TCR) signaling pathway, following MHC protein recognition by the TCR. The Chin and James groups used the photocaged lysine **PCK** to place LCK function under optical control by following the general strategy of blocking an essential and conserved lysine residue in the ATP binding pocket.²³ Through light-triggering of kinase function, they were able to quantify the phosphorylation kinetics of LCK and identified its ability to stimulate its own activation. This work nicely showcases that acute optical activation of kinase function allows for uncovering of mechanistic details of cell signaling activity.

Using a similar strategy with the caged lysine **PCK**, the Deiters and Haugh groups developed a light responsive MKK6, a MAPK kinase within the p38 pathway responsible for stress-induced apoptosis.⁵³ Light-activation of MKK6 was validated by monitoring cellular morphology for typical markers of apoptosis (*e.g.*, blebbing and shrinkage) and the release of fluorescently tagged cytochrome *c* from mitochondria, both of which were shown to be p38-dependent processes. Interestingly, when exploring cross-talk with the ERK pathway, the light activated MKK6 inhibited ERK kinase activity both in the presence and absence of p38 inhibitors suggesting a new, p38-independent mechanism of negative regulation. Additionally, the caged MKK6 was successfully activated in a murine melanoma cell line overexpressing high levels of the oncogenic B-Raf mutant (V600E), thus demonstrating that light activated kinases can be employed as tools for dissecting both normal and disease states.

The photocaged lysine **PCK** has previously been utilized to render the MEK/ERK pathway light-responsive in mammalian cells.²¹ More recently, MEK kinase was placed under light control using the more sensitive caged lysine **HCK** in zebrafish embryos (Figure 1-6a).²² Temporal control of MEK function in the developing animal revealed an essential time window in which hyperactive MEK affects dorsal/ventral patterning, a discovery that is relevant to human birth defects caused by Ras/MAPK pathway mutations. The expansion of optical control of cell signaling to multicellular model organisms will enable investigations in complex systems through more precise perturbation of enzymes/pathways required for normal/mutant embryonic development.

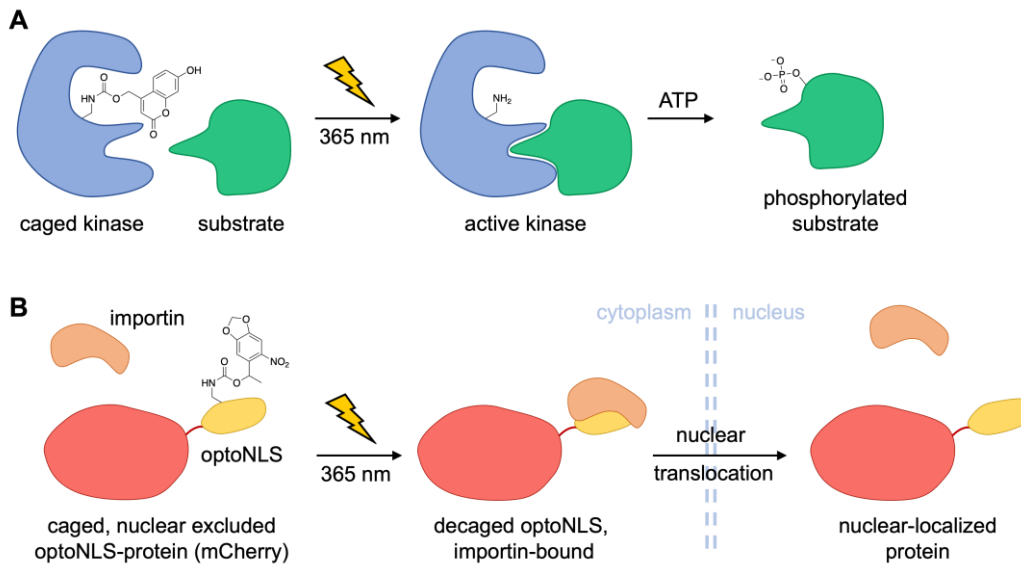


Figure 1-6 Optical control of kinase activity via genetic incorporation of the caged lysine **HCK** and optical control of nuclear translocation through caging of a protein-protein interaction

a) Upon replacement of an essential lysine in the ATP-binding site of a kinase with the caged lysine **HCK**, the enzyme is rendered catalytically inactive. Following UV irradiation, the native, active kinase is generated and is capable of phosphorylating its downstream substrate. b) Replacement of the endogenous nuclear localization sequence (NLS) in the transcription factor FOXO3 (mCherry labeled) with an optoNLS sequence from SatB1 (indicated in yellow), containing a single caged lysine residue enables optical triggering of nuclear translocation. Reprinted from Courtney and Deiters, *Curr. Opin. Chem. Biol.* **2018**, 46, 99-107. Copyright 2018 Elsevier Ltd.

Control of neural circuits with light has been extensively explored via optogenetic approaches using light-responsive ion channels.¹⁴ In addition to classical optogenetic methods, the use of unnatural amino acid mutagenesis has been utilized by the Wang group by genetically incorporating the caged cysteine **NVC** into an inward rectifying potassium channel in mouse neocortex tissue slices in order to obtain precise activation of neuronal suppression as measured by patch-clamp recordings.⁵⁴⁻⁵⁵

1.2.4.3 Optical Control of Protein-Protein Interactions

Most examples of using photocaged amino acids for optical control of protein function target enzymatic processes through caging of an essential residue within the active site. However, even a relatively small nitrobenzyl caging group can be efficiently used in the regulation of protein-protein interactions when strategically placed into the protein binding interface. The Engelke and

Deiters groups replaced an important lysine residue in the nuclear localization sequence (NLS) of the transcription factor SatB1 with caged lysine **PCK**.²⁵ This led to sequestration of NLS fusion protein in the cytoplasm until UV irradiation generated the native NLS sequence, followed by translocation into the nucleus (Figure 1-6b). This optical NLS approach was applied to controlling FOXO3 transcription factor-DNA binding and TEVp-nuclear substrate interaction. Due to the small size of this optical NLS (20 amino acids), it can easily be appended to any protein of interest to modulate cytoplasmic to nuclear localization. One limitation of the approach is the relatively slow rate of translocation to the nucleus compared to other NLS.

A similar strategy was applied for optically controlling a virus-host protein-protein interaction using the caged lysine **PCK**.²⁶ The Chatterjee group incorporated **PCK** into VP1, a surface protein, of the adeno-associated virus (AAV) capsid. This blocked interaction with human heparin sulfate proteoglycan (HPSG) and prevented viral infection of HEK293T cells, until photolysis released the caging group, forming the native capsid. This approach provides an innovative tool to probe the cellular entry process of human viruses by disrupting the interactions between the virus and the host cell through introduction of photocaged residues and should be broadly applicable to viruses that utilize Lys/Arg, Cys/Ser/Thr, or Tyr as critical regulatory residues at the binding interface.

1.2.4.4 Optical Control of other Enzymatic Processes

Isocitrate dehydrogenase (IDH) is an essential enzyme in the citric acid cycle, and has been found mutated through an active site arginine to lysine mutation in various cancers. In order to better study the effects of mutant IDH2 activation, the Chin group replaced an active site lysine with the photocaged lysine **PCK** to block substrate binding until UV induced decaging.²⁴ Upon

photoactivation of IDH2, a decrease in 5-hydroxymethylcytosine was observed, validating a previously proposed sequence of events in cancer cell epigenetic modifications.

The study of pathogenic bacteria has increased over the last several years as the result of a spike in MRSA-related illnesses. Traditionally, it has been challenging to purify *S. aureus* toxin-antitoxin proteins due to the toxicity caused in *E. coli* upon overexpression. The Hergenrother group developed a strategy to overcome this limitation by replacing the active site tyrosine with **ONBY**, rendering the toxin inactive until a defined activation time-point post-expression and purification.⁵⁶ This approach of expressing toxic proteins as their benign, caged precursors may constitute a general method for obtaining otherwise hard-to-isolate proteins.

1.3 Summary

Optical control of proteins in cells and organisms with an expanded genetic code has provided precise, spatiotemporal regulation of a diverse range of protein functions.¹⁰⁻¹¹ These include optical control of proteolysis,^{31-32, 48} genome editing,¹⁸ protein splicing,^{33, 35} phosphorylation,^{21-23, 53} DNA recombination,²⁰ RNA polymerization,¹⁹ neuronal activity,⁵⁴ and protein translocation.²⁵ In many of the applications discussed above, replacement of an essential residue with a photocaged analog in either an active site or a binding interface rendered the protein inactive. In instances where an essential residue cannot be identified, incorporation of a photocaged intein into the protein may provide an alternative approach for optical control. However, requirements and kinetics of the splicing event will need to be considered in experimental designs. In recent years, photocaged amino acids with improved optical properties,

e.g., red-shifted excitation maxima, have been developed, further broadening the scope of this approach.

Compared to other means to optically controlling protein function (*e.g.*, optogenetic tools, see Chapter 5.1.4),¹⁵⁻¹⁷ the site-specific, genetic encoding of photocaged and photoswitchable amino acids in cells and animals has several unique advantages: (i) the small size of the various caging groups (~150 – 250 Da) results in modification of only the most essential site of the protein of interest; (ii) the location of the caged residue can often be predicted based on structural and mechanistic protein data, thereby minimizing the need for extensive trial-and-error experiments; (iii) light-triggered removal of the caging group yields the native, wild-type protein; and (iv) only the photocaged/-switchable amino acid needs to be synthesized and the unnaturally modified protein is generated by the biosynthetic machinery within the cell or organism. For structurally complex unnatural amino acids, protein yields can (depending on the protein and the site of incorporation) be significantly reduced, leaving room for improvement of the existing tRNA/tRNA synthetase expression systems. This is particularly important for expansion of photocaged amino acid mutagenesis into multicellular model organisms such as zebrafish, fruit flies, and mice which will enable enhanced developmental studies with spatio-temporal precision in order to better understand the complex underpinnings of metazoan development.

2.0 Optical Activation of Protein Function

2.1 Optical Control of Dual Specific Phosphatase 6 (DUSP6 or MKP3)

This chapter was reprinted in part with permission from **Courtney, T.**; Deiters, A., *Nat Commun.* **2019**, *10*, 4384.

2.2 Introduction to MAPK Signaling and MKP3

Protein phosphorylation is an essential post-translational modification that plays a key role in signal transduction.⁵⁷ The transfer of a single phosphate group from ATP to a protein substrate is catalyzed by protein kinases, while the reverse process of removing a phosphate group is catalyzed by protein phosphatases. A typical signaling event results in a cascade of phosphorylations by protein kinases; however, protein phosphatases play an equally important regulatory role in all cell signaling networks by reversing kinase action through phosphate removal from target proteins.⁵⁸ Over the last few decades, several optically controlled protein kinases have been developed and applied in gaining a deeper understanding of the extensive regulatory mechanisms involved in signaling pathways;^{21-23, 59-69} however, optical control of protein phosphatase function has not been achieved (Table 2-1).⁷⁰

Both optochemical and optogenetic approaches have been used to render various kinases light responsive. In the case of kinases, use of an unnatural amino acid containing a photocaging group to block the ATP binding site is a broadly applied strategy.²¹⁻²³ For obtaining reversible

control of kinase activity, optogenetic tools have been employed.⁶⁰⁻⁶¹ Less commonly, a photocaged rapamycin analog has been used to control the activation of different kinases fused to a rapamycin binding protein⁷¹ (caged rapamycin analogs are discussed in extensive detail in Chapter 5). A single example of a light responsive phosphatase with a phospho-sugar substrate has been developed using optogenetic tools.⁷⁰ Protein phosphatases are often difficult to study due to: i) the necessity of detecting a negative signal (removal of a phosphate; which, obviously, needs to be installed first), and ii) the highly conserved, shallow active site, which renders the development of specific inhibitors nearly impossible.⁷²

Table 2-1 Representative examples of light controlled kinases and phosphatases for studying cell signaling

Enzyme Class	Enzyme Name	Optochemical/genetic	Approach
Kinases	MEK1	optochemical	Photocaged UAA to block ATP binding site
	LCK	optochemical	Photocaged UAA to block ATP binding site
	SOS	optogenetic	PhyB:PIF fusion for upstream activation of MEK/ERK pathway
	MEK1, c-Raf, CDK	optogenetic	Dronpa
	FAK, Src	optochemical	Photocaged rapamycin analog
Phosphatase	Phosphatidylinositol 5-phosphatase	optogenetic	CRY2PHR:CIBN fusion

Mitogen-activated protein kinases (MAPKs) are serine/threonine kinases that convert extracellular stimuli (input) into a range of cellular responses (output). The three conventional MAPK families that have been extensively studied are ERK, JNK, and p38.⁷³ MAPK signaling is implicated in a number of pathological phenotypes, which generally result from MAPK upregulation or MAPK phosphatase (MKP) down-regulation.⁷⁴ MKP3, one of ten MKPs, has high specificity for ERK over JNK or p38 (Figure 2-1).⁷⁵⁻⁷⁶ Unlike the inducible class of MKPs, the cytoplasmically localized MKPs are constitutively expressed and in the case of MKP3 undergoes activation upon substrate binding and subsequent conformational change.

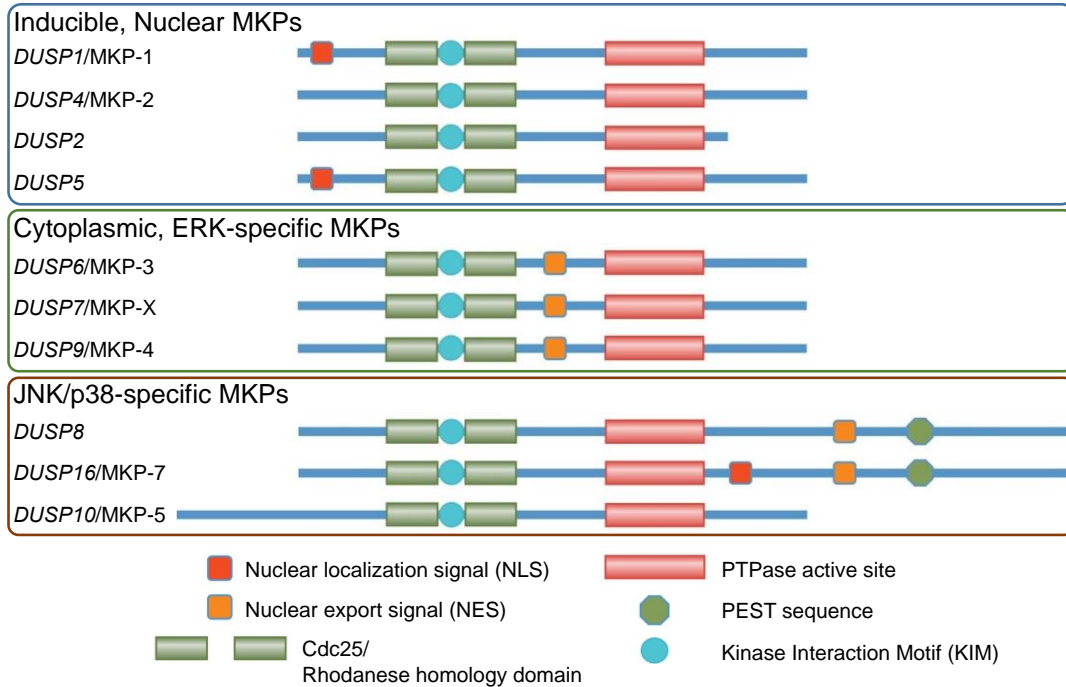


Figure 2-1 Schematic representation of the domain structures of the three groups of MAP kinase phosphatases. The three classes of MAP kinase phosphatases (MKPs) are inducible, nuclear MKPs (blue), cytoplasmic, ERK-specific MKPs (green), and JNK/p38-specific MKPs (orange). Key features and domains are indicated with varying shapes. Figure adapted from Seternes *et al.*, *Biochim. Biophys. Acta, Mol. Cell Res.* **2019**, 1866, 124-143. Copyright 2018 The Authors.

MKP3 is a dual-specificity (it acts on both phosphorylated Thr and Tyr) cytoplasmic phosphatase that recognizes dually-phosphorylated ERK (pERK) and rapidly dephosphorylates it, thus preventing nuclear translocation and activation of downstream targets (Figure 2-2). Aberrant MKP3 levels (both over-expression and down-regulation) have been linked, without a clear mechanistic understanding, to both oncogenic and tumor-suppressive roles in numerous forms of cancer, including pancreatic, lung, colorectal, and thyroid cancer.^{74, 77-78} Within the same cancer, varying levels of MKP3 expression have been observed, demonstrating the complexity of the role that protein phosphatases play in disease pathology. Thus, an improved understanding of the mechanisms and dynamics of phosphatase-mediated effects on signaling pathways will yield a better understanding of human physiology and disease.

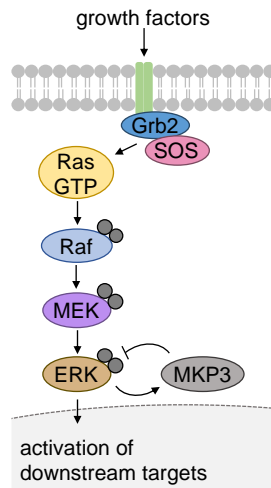


Figure 2-2 Overview of the MAPK/MKP3 signaling pathway
 Reprinted from Courtney and Deiters, *Nat. Commun.* **2019**, 10, 4384.

We aimed to generate the first light-activated protein phosphatase and selected MKP3 as a target due its link to the well-understood substrate pERK. This work lays the foundation to investigate other, poorly characterized phosphatases through placement under optical control. We envisioned two distinct approaches for generating a photocaged MKP3: (i) caging of the catalytic cysteine to completely abolish enzymatic activity until photo-activated and (ii) caging of the protein-protein binding interface between MKP3 and ERK2 to abrogate phosphatase-substrate interaction until photoactivation.

2.3 Optical Control through Active Site Caging

The catalytic domain of MKP3 contains the conserved PTPase sequence HCX₅R, in which the cysteine acts as a nucleophile in the dephosphorylation reaction of pERK and the arginine interacts with the phosphate group to stabilize the transition state (Figure 2-3a). An aspartate facilitates a proton transfer and is essential for efficient catalysis. We hypothesized that

replacement of the catalytic cysteine with caged cysteine **NVC** (Figure 2-3b) would mask the nucleophilicity through a thioether bond and block enzymatic activity until UV irradiation removes the caging group (Figure 2-3c). Due to the flexibility of the active site pocket, incorporation of **NVC** is expected to have no effect on protein folding thereby enabling rapid activation of enzymatic function after photolysis.

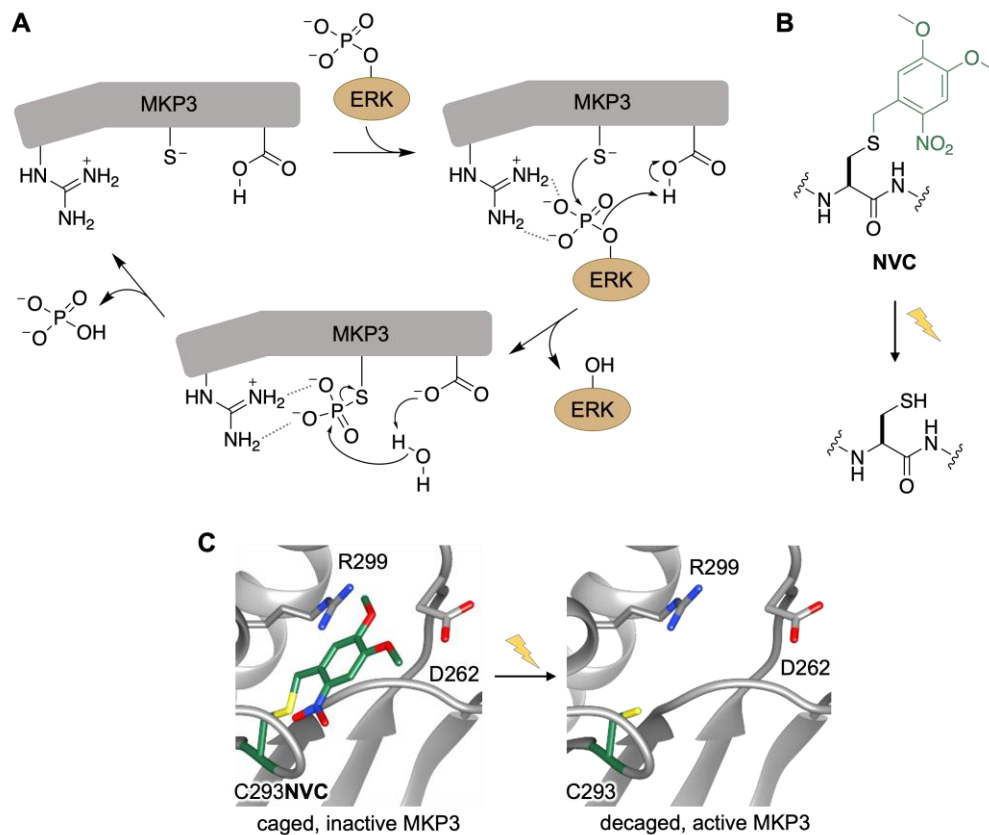


Figure 2-3 The active site of MKP3 and structure of caged cysteine **NVC**

a) The mechanism of MKP3-catalyzed ERK dephosphorylation. Dashed lines indicate electrostatic and/or hydrogen-bond interactions. b) Irradiation of **NVC** removes the nitrobenzyl caging group (green) and restores a native cysteine residue. c) The crystal structure of MKP3 (PDB: 1MKP) is shown with the three critical active site residues labeled in black. On the left, the catalytic cysteine was replaced with **NVC**, which sterically blocks the active site and prevents catalysis, until exposed to 365 nm light. Reprinted from Courtney and Deiters, *Nat. Commun.* **2019**, 10, 4384.

We utilized the *E. coli* LeuRS/tRNA pair (pMAH-CageCys) for genetic encoding of the caged cysteine **NVC** in human cells and incorporation into MKP3.³³ In our initial testing with pMKP3(C293TAG-EGFP)-HA, we were unable to detect the caged protein via western blot. Therefore, we used the pMAH-CageCys plasmid, which contains the LeuRS and three copies of

LeuT, to cut out the LeuRS and replace with the MKP3-EGFP-HA coding sequence of the wild-type, catalytically dead, and TAG mutants, thus effectively doubling the copies of tRNA. When transiently expressing the LeuRS/tRNA pair with the new pMAH-MKP3-EGFP-HA constructs in HEK293T cells, full-length MKP3(C293NVC)-EGFP-HA was detected by western blot only in the presence of NVC (Figure 2-4).



Figure 2-4 Western blots for incorporation of NVC into MKP3
Western blot analysis confirms expression of caged MKP3 only in the presence of NVC (1 mM) using an anti-GFP antibody. Reprinted from Courtney and Deiters, *Nat. Commun.* **2019**, 10, 4384.

In order to validate that the catalytic activity was blocked by the nitroveratryl group, we performed an *in vitro* biochemical assay. Unfortunately, the synthetase/tRNA pair used for NVC incorporation is incompatible with bacterial protein expression of the caged proteins. Thus, MKP3-EGFP-HA variants were immunoprecipitated from HEK293T cells and phosphatase activity of the immobilized enzymes was measured using the fluorogenic substrate DiFMUP (**1**). MKP3 undergoes an activating conformational change upon binding to ERK2 and previous *in vitro* analysis has shown a 50 – 70 fold increase in activity (comparing k_{cat}/K_m) in the presence vs absence of ERK2.⁷⁹⁻⁸⁰ Thus, we recombinantly expressed GST-ERK2 in *E. coli*⁸¹ and used this in our enzyme assays. In the absence of irradiation, the caged sample displayed similar activity to the catalytically dead (C293S) mutant; however, following UV activation, phosphatase enzymatic function was fully restored (Figure 2-5), indicating excellent OFF to ON switching behavior.

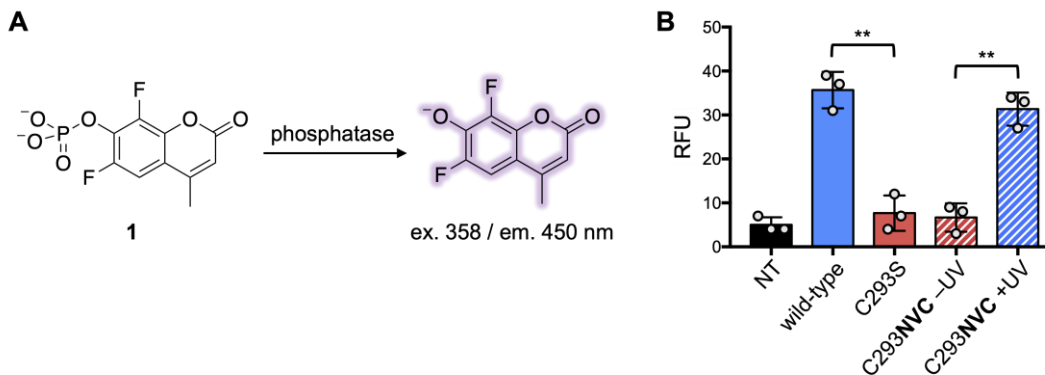


Figure 2-5 Biochemical phosphatase assay with catalytically caged MKP3

a) The phosphatase sensor **1** is non-fluorescent until an active phosphatase generates the phenolate to turn on fluorescence. b) Biochemical phosphatase assays show complete loss of activity for the caged enzyme, until 365 nm irradiation restores the wild-type enzyme. Error bars denote standard deviation from three biological replicates; **, $p < 0.01$ from unpaired two-tailed Student's t test. Reprinted from Courtney and Deiters, *Nat. Commun.* **2019**, 10, 4384.

To apply our photocaged MKP3 in live cells, we utilized an ERK2-mCherry nuclear translocation reporter (Figure 2-6).⁸² In a resting cellular state, ERK2 is primarily found in its dephosphorylated form. Upon phosphorylation and activation by upstream kinases, ERK2 translocates to the nucleus. Once in the nucleus, endogenous phosphatases dephosphorylate ERK and the reporter fusion translocates back to the cytoplasm.

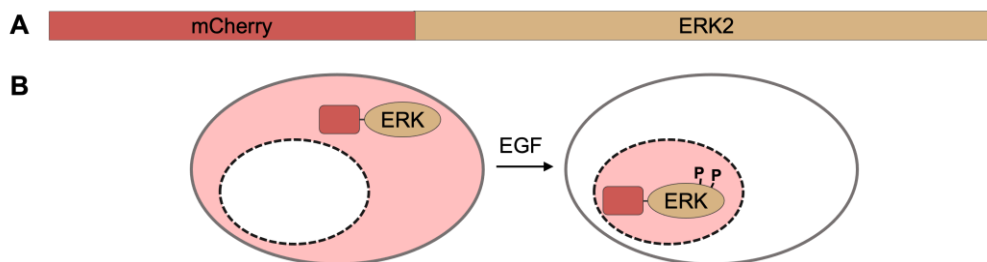


Figure 2-6 Overview of ERK2-mCherry reporter

a) Gene sequence of the ERK-mCherry reporter. b) When expressed in cells, ERK-mCherry resides primarily in the cytoplasm in the absence of growth factor stimulation (inactive MAPK signaling); however, following activation with EGF, ERK is phosphorylated and translocates to the nucleus. Reprinted from Courtney and Deiters, *Nat. Commun.* **2019**, 10, 4384.

When HEK293T cells expressed ERK2-mCherry alone, cytoplasmic accumulation of ERK was observed until stimulation with epidermal growth factor (EGF, 100 ng/mL) induced nuclear translocation (Figure 2-7a, top row).⁸² Upon co-expression of wild-type MKP3, ERK2 remains in the cytoplasm before and after pathway stimulation with EGF (Figure 2-7a, second row).⁸³⁻⁸⁴ This

is a result of the rapid dephosphorylation of pERK2 by MKP3, which prevents any significant nuclear accumulation and thus dampens the EGF signal. Next, we tested whether the active site C293NVC caged MKP3 would have an effect on EGF-induced ERK translocation to the nucleus. When the caged MKP3 and ERK2-mCherry were co-expressed in HEK293T cells, complete cytoplasmic localization was again observed before and after EGF stimulation (Figure 2-7a, third row), regardless of UV activation (Figure 2-7a, bottom row). The affinities of wild-type and catalytically dead MKP3 for dually-phosphorylated ERK2 are essentially the same (22 and 31 nM, respectively),⁸⁵ thus sequestration of pERK2 by catalytically dead (or catalytically caged) MKP3 anchors pERK2 in the cytoplasm and prevents nuclear translocation regardless of its dephosphorylation activity (\pm UV).⁸³ These results indicate that the introduction of a bulky caging group has no effect on the MKP3:ERK2 interaction. Due to the inherent sequestration of ERK2-mCherry by MKP3 variants, we concluded that a different reporter was needed to study the optical triggering of enzymatic dephosphorylation activity in live cells. Additionally, to avoid any potential issues with the imbalance of MEK/ERK signaling components due to the overexpression of ERK2, we sought to utilize a live cell reporter that monitors endogenous ERK levels.⁸⁶ Moreover, these results also indicated that control of the phosphatase:substrate protein-protein interaction may be a second, complementary approach to optically control the cellular function of phosphatases (see Optical Control through Protein-Protein Interaction Caging).

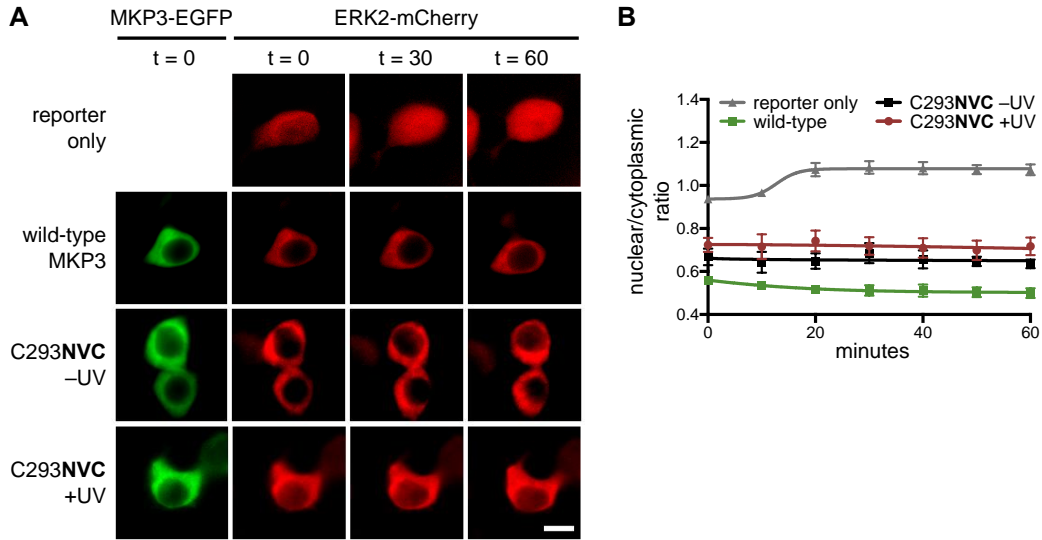


Figure 2-7 Optical control of the MKP3 catalytic site in the ERK2-mCherry reporter

a) Using an ERK2-mCherry reporter, the activity of wildtype, caged (at the catalytic cysteine), and photoactivated MKP3 was investigated in HEK293T cells. Following pathway stimulation, nuclear exclusion of an ERK2-mCherry reporter is observed for all MKP3 variants. Scale bar 10 μ m. b) Quantification of nuclear/cytoplasmic ratios shows successful nuclear translocation for the reporter only control; however, none of the MKP3 variants show any significant change. Error bars represent standard error of the mean from nine individual cells combined from three biological replicates. One-way ANOVA tests at the 60-minute time point results in $p < 0.0001$ for the reporter compared to all MKP3 samples, indicating this a significant difference. Comparing C293NVC -UV to C293NVC +UV results in $p > 0.1$, indicating no significant difference. Reprinted from Courtney and Deiters, *Nat. Commun.* **2019**, 10, 4384.

Since the binding of MKP3:ERK2 is a dynamic process⁵⁸ and imaging only depicts an average state of ERK2 localization within the cell, we hypothesized that utilization of a reporter that reports on a downstream target of ERK2 (instead of directly detecting ERK2 localization) might enable live-cell monitoring of MKP3 photoactivation. For this, we applied an ERK-KTR-mCherry reporter which utilizes the ERK binding region of Elk-1 fused to a bipartite NLS and NES sequence and is localized in the nucleus in the absence of active pERK, but translocates to the cytoplasm when active pERK is present (Figure 2-8).⁸⁷

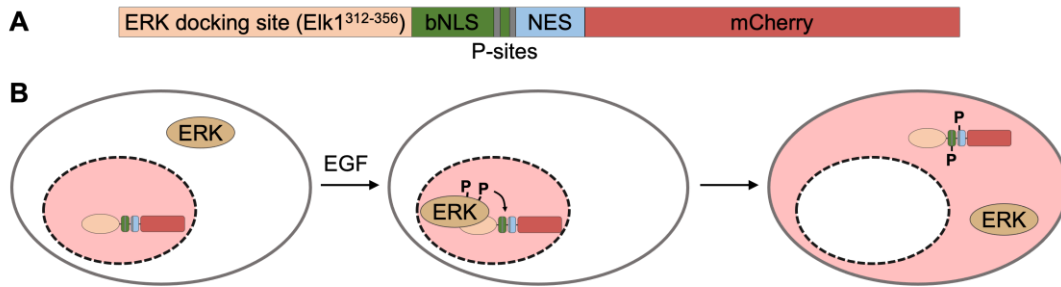


Figure 2-8 Overview of the ERK-KTR-mCherry reporter

a) Gene sequence of the ERK-KTR-mCherry reporter.⁸⁷ The ERK docking site of the transcription factor Elk1 (residues 312 – 356) is fused to a bipartite nuclear localization sequence (bNLS) and a nuclear export sequence (NES), followed by mCherry. The two “P-sites” indicate residues in the NLS and NES which are phosphorylated by pERK. b) Prior to stimulation of the MAPK/ERK pathway with external growth factors, the reporter resides in the nucleus. Upon ERK phosphorylation, pERK translocates to the nucleus where it binds the docking domain and phosphorylates both P-sites. Phosphorylation of the reporter represses the nuclear localization signal and activates the nuclear export sequence, resulting in transport of mCherry to the cytoplasm. Unlike other FRET-based kinase reporters (e.g., EKARs), the KTR technology requires only a single fluorescent protein, has excellent dynamic range, and can be activated/deactivated faster. Reprinted from Courtney and Deiters, *Nat. Commun.* **2019**, 10, 4384.

Importantly, this reporter couples ERK (and pERK) translocation with pERK activity, thus overcoming the inherent limitations of using the direct ERK2-mCherry reporter. HEK293T cells expressing the ERK-KTR-mCherry reporter alone displayed nuclear accumulation prior to EGF addition; however, 60 minutes after pathway stimulation, complete nuclear exclusion occurred (Figure 2-9a, top row). Upon co-expression of the reporter and wild-type MKP3, we observed maintenance of nuclear localization before and after stimulation (Figure 2-9a, second row), due to signal dampening through MKP3 dephosphorylation of pERK2. When the active site-caged C293NVC MKP3 was expressed together with the ERK-KTR-mCherry reporter, we observed significant nuclear exclusion following pathway stimulation (Figure 2-9a, third row). This reflects the dynamic nature of the MKP3:ERK interaction in that pERK is still capable of dissociating from MKP3 and triggering the reporter, while imaging of ERK localization indicates that, on average, the majority of pERK is anchored in the cytoplasm. Upon irradiation of the caged MKP3, nuclear localization of the reporter is maintained, thus demonstrating successful optical control of phosphatase enzymatic function in live cells (Figure 2-9a, fourth row).

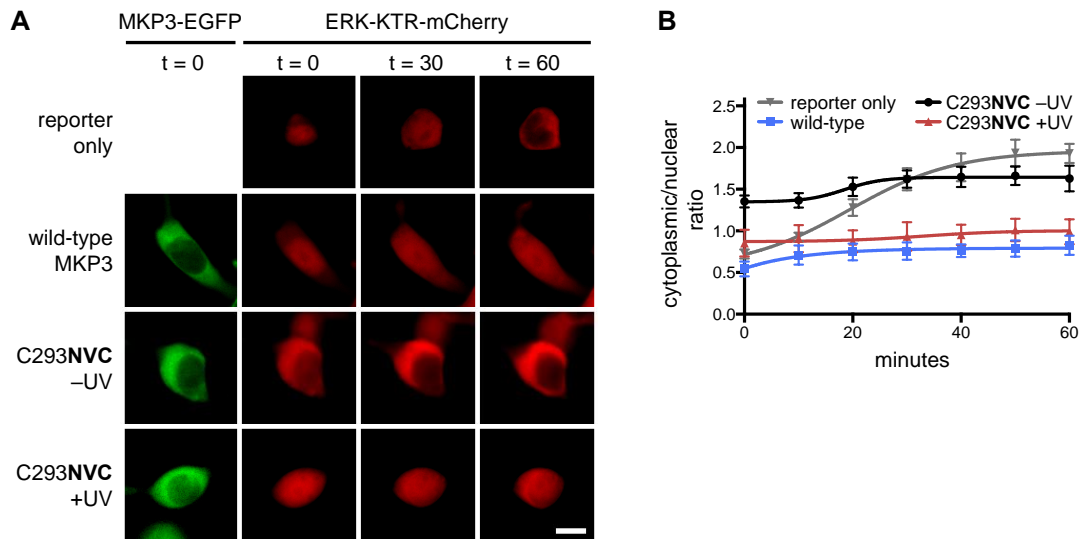


Figure 2-9 Optical control of the MKP3 catalytic site in the ERK-KTR-mCherry reporter

a) An ERK-KTR-mCherry reporter was utilized to report on the activity of endogenous ERK2 levels in the presence of wild-type, caged, and photo-activated MKP3 variants in HEK293T cells. Wild-type MKP3 prevents EGF-induced triggering of the reporter, while the caged MKP3 is only active following UV exposure (365 nm, 2 min). Scale bar 10 μm . b) Quantification of the cytoplasmic/nuclear ratio for the MKP3 variants shows successful photoactivation of MKP3. Error bars represent standard error of the mean for nine individual cells combined from three biological replicates. One-way ANOVA tests at the 60-minute time point resulted in $p < 0.0005$ when comparing C293NVC -UV to C293NVC +UV, and reporter only to WT. No significant difference ($p > 0.1$) was observed between WT and C293NVC +UV or reporter only and C293NVC -UV. Reprinted from Courtney and Deiters, *Nat. Commun.* **2019**, 10, 4384.

Unlike our results with the ERK2-mCherry reporter, utilization of the ERK-KTR-mCherry reporter allowed for successful demonstration of optical OFF to ON switching of MKP3. While the ERK2-mCherry reporter exclusively measures ERK (or pERK) localization, the ERK-KTR-mCherry construct actually reports on the enzymatic activity of ERK (or pERK). Thus, these two reporters allow for two different functions/outputs to be observed. Additionally, it has been reported that working with physiologically-relevant ERK concentrations is essential for investigating this highly dynamic pathway;⁸⁶ therefore, the ERK-KTR reporter presumably reflects biologically relevant findings more accurately. In light of these observations, all remaining experiments were performed with the ERK-KTR-mCherry reporter.

2.4 Optical Control through Protein-Protein Interaction Caging

In order to abrogate any potential for substrate sequestration by a caged phosphatase, we next explored the possibility of optically controlling the phosphatase:substrate interface. While optical control of protein active sites through site-specific caging group installation has been used to study a wide range of enzymatic functions (*e.g.*, kinase,^{21-23, 59} polymerase,⁴⁴ nuclease,⁴⁶ recombinase,⁸⁸ helicase,²⁸ and others),⁸⁹ optical control of protein-protein interactions has remained underexplored. In this context of transitioning from optical control of enzymatic function to optical control of protein-protein interactions, caged amino acid mutagenesis represents an advantage over other optogenetic approaches, since the position of the caging group is simply defined by the position of the TAG codon and thus can be readily moved to other sites on the protein, *e.g.*, from the active site to the protein surface.

The kinase interaction motif (KIM) of MKP3 is the region responsible for binding to both ERK and pERK with equal affinity and for conferring a high degree of selectivity for ERK over other MAP kinases. Upon binding of ERK, MKP3 undergoes a conformational change in which a loop in the active site becomes positioned for efficient catalysis; therefore, in the absence of ERK binding, MKP3 catalytic activity is greatly diminished.⁷⁹ We hypothesized that caging an essential residue at the MKP3:ERK interface would provide a complementary approach to optically controlling MKP3 function in cells. By blocking the KIM with a light-removable protecting group, both ERK and pERK binding, and thus enzymatic activity and pERK dephosphorylation would be blocked.

For caging the protein-protein interaction, analysis of the crystal structure of ERK2 bound to the 17 amino acid KIM peptide of MKP3 (residues 60-76) revealed several positions that could be targeted.⁹⁰ The MKP3 KIM peptide contains four basic amino acid sites that we hypothesized

could be replaced with a caged lysine to sterically block the protein-protein interaction and abrogate electrostatic interaction, until light exposure removes that sterically demanding caging group and restores a positive charge (Figure 2-10). The optimal scenario would be replacement of K68 with a caged lysine in order to generate the native phosphatase upon light activation. Whereas, replacement of R64, R65, or R74 would require confirmation that an R-to-K mutation retained substrate recognition and enzymatic activity. We tested all four of these positions in the cell-based KTR assay and found that caging at K68 and R74 was not sufficient to inhibit the phosphatase-kinase interaction. Oddly, we were unable to incorporate a caged lysine at R64; however, successful caging at R65 is described below.

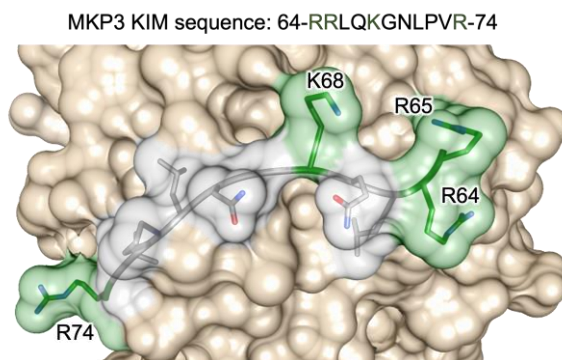


Figure 2-10 Crystal structure of the MKP3 KIM peptide bound to ERK2 reveals four targetable residues. The KIM peptide sequence is provided above the crystal structure. The MKP3 KIM peptide is shown in gray with basic residues indicated in green, while ERK2 is tan. PDB: 2FYS

Two electrostatic interactions between R64 and R65 of MKP3 with D316 and D319, respectively, of ERK2 play a major role in the high affinity binding of these proteins (Figure 2-11a). We speculated that optically controlling the electrostatics (positive charge) at either the R64 or R65 site, plus introducing significant steric hindrance, would allow us to optically control the phosphatase:substrate interaction. The photocaged lysine **HCK**²⁷ enables light-induced ammonium ion generation under physiological conditions, since the carbamate greatly reduces the

basicity of the ϵ -amino group, thus providing a potential switch for this protein-protein interaction (Figure 2-11b-c).

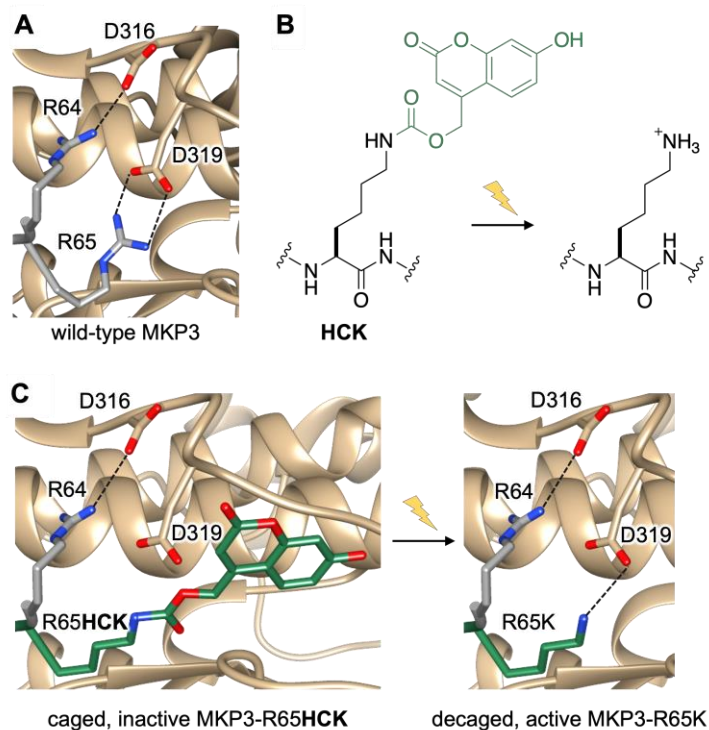


Figure 2-11 Optical control of the phosphatase-kinase interaction motif (KIM).

a) The crystal structure of ERK2 (tan) bound to the KIM peptide of MKP3 (grey) shows essential electrostatic interactions of R64 and R65 with D316 and D319 (PDB: 2FYS). b) Irradiation of **HCK** removes the coumarin caging group (green) and restores a native lysine residue. c) Replacement of R65 with **HCK** generates steric hindrance and prevents electrostatic interaction until light exposure release K65, which enables the ERK2-MKP3 interaction. Reprinted from Courtney and Deiters, *Nat. Commun.* **2019**, 10, 4384.

It has been reported that replacement of R64 with lysine had no effect on ERK2 binding affinity; however, an R65K mutation resulted in a 50-fold lower affinity for ERK2 compared to wild-type MKP3.⁹¹ Interestingly, almost identical MKP3 phosphatase activity was reported for both mutants. Based on these results, we tested both the R64K and R65K mutants using the ERK-KTR-mCherry reporter in HEK293T and compared their activity to wild-type MKP3. Not surprisingly, both lysine mutants showed similar phosphatase activity (Figure 2-12) and were only slightly less active than wild-type in the KTR reporter assay.

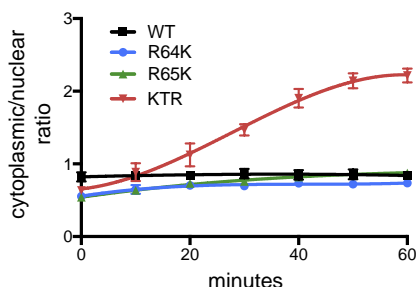


Figure 2-12 MKP3 R64K and R65K mutants retain near wild-type activity

Co-expression of wild-type MKP3, R64K MKP3, or R65K MKP3 with the ERK-KTR-mCherry reporter demonstrates that both R64K and R65K closely mimic the activity of the wild-type phosphatase. The cytoplasmic/nuclear ratio over time for the four conditions shows significant nuclear exclusion in the case of the reporter alone; however, upon co-expression of wild-type (WT), R65K, or R64K MKP3, minimal change in reporter localization is observed due to similar levels of phosphatase activity under all three conditions. Error bars indicate standard deviation of five individual cells per condition from two biological replicates. Reprinted from Courtney and Deiters, *Nat. Commun.* **2019**, 10, 4384.

Since R65 is reported to be the more critical residue for ERK2 binding, we incorporated **HCK** at that position (Figure 2-13a). We again utilized the ERK-KTR-mCherry reporter for exploring photoactivation of the caged KIM. HEK293T cells expressing only the reporter showed complete nuclear exclusion after EGF stimulation (Figure 2-13b, first row), while cells co-expressing the R65K mutant led to mostly nuclear reporter accumulation, as expected (Figure 2-13b, second row). When the reporter and KIM-caged R65**HCK** MKP3 were co-expressed, we observed complete nuclear exclusion following EGF stimulation, indicating inactivity of the phosphatase (Figure 2-13b, third row). Upon irradiation and activation of the caged MKP3, nuclear localization of the reporter is maintained, thus demonstrating that the cellular function of the phosphatase, specifically its ability to engage its substrate, was optically triggered (Figure 2-13b, fourth row). Quantification of the micrograph fluorescence clearly displays the ability to optically control the ERK2-MKP3 interaction via caging of the phosphatase KIM, thereby enabling light-triggered substrate binding and dephosphorylation (Figure 2-13c). As in the case of active site cysteine caging, introduction of a caging group into the phosphatase:substrate interface also provides excellent optical OFF to ON switching behavior.

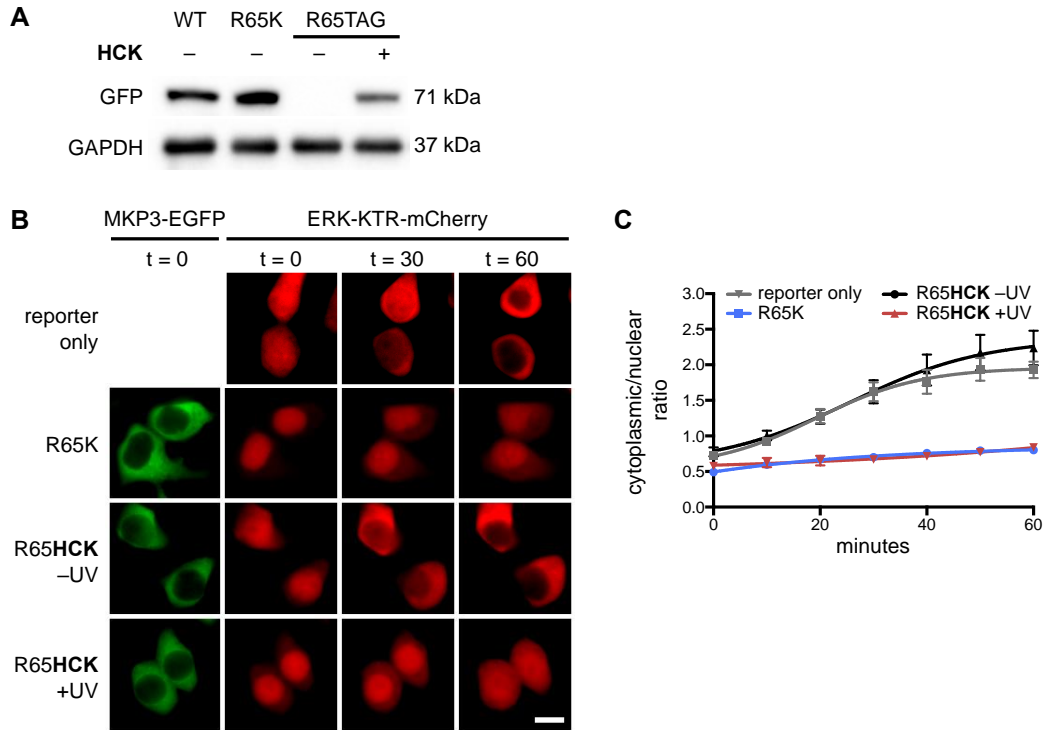


Figure 2-13 ERK activity in response to optical activation of the MKP3 kinase interaction motif
a) Western blot of wild-type, R65K, and caged MKP3 shows full-length expression only in the presence of 0.25 mM **HCK**. b) KIM-caged MKP3 cannot efficiently bind to and dephosphorylate pERK until UV irradiation (365 nm, 2 min) generates an active enzyme. Scale bar 10 μ m. c) Quantification of cytoplasmic-to-nuclear (C/N) ratios support the micrograph findings. Error bars represent standard error of the mean of nine individual cells from three biological replicates. One-way ANOVA tests at the 60-minute time point resulted in $p < 0.0001$ when comparing R65**HCK** -UV to R65**HCK** +UV, and reporter only to R65K. No significant difference ($p > 0.1$) was observed between R65K and R65**HCK** +UV or reporter only and R65**HCK** -UV. Reprinted from Courtney and Deiters, *Nat. Commun.* **2019**, 10, 4384.

After demonstrating that we could successfully photo-activate the MKP3:ERK interaction and subsequently control phosphatase activity, we sought to explore the effect of titrating the level of active vs inactive phosphatase in order to further characterize the role of MKP3 in downregulating the ERK pathway. It is well established that ERK phosphorylation occurs in a graded manner, meaning pERK levels increase almost proportionally to an increase in external stimulus.⁹²⁻⁹³ However, downstream targets of the ERK pathway often act in a switch-like manner, meaning there is an all-or-nothing response. This has been reported for the nuclear translocation of ERK2 monitored as an ERK2-EGFP fusion in both HeLa and PC12 cells.⁹⁴ We utilized the ERK-KTR-mCherry reporter to characterize ERK nuclear translocation behavior in HEK293T

cells and observed a graded response upon varied EGF stimulation (Figure 2-14a-b). For classification as a graded or switch-like response, the cytoplasmic/nuclear ratio for increasing EGF concentrations was fitted with a Hill function to calculate the Hill slope. A slope of approximately 1 indicates a graded response, while a slope of $\gg 1$ is representative of switch-like behavior.⁹⁴ A slope of 1.5 was calculated, thus indicating a graded response. Unlike the monitoring with an ERK2-GFP fusion which only reports protein localization, this reporter couples nuclear translocation with reporting of nuclear activity of pERK. Our results showcase the complexity and variability of the ERK signaling pathway within different cell types. We were curious how titrating MKP3 phosphatase levels would affect the ERK activity response in the KTR reporter. We observed a graded reporter response to increasing MKP3 activity upon increasing UV exposure (Figure 2-14c). Almost complete activation is achieved with a two-minute irradiation, thus irradiation for shorter times is expected to allow for titration of increasing levels of active versus inactive phosphatase. With shorter irradiation times, a partial response was observed where only a small amount of pERK is dephosphorylated and results in incomplete exclusion of the reporter. This graded response indicates that MKP3 functions to dampen the response to growth factor stimulation like a rheostat rather than completely blocking signal propagation above a certain threshold like a switch. The MKP family has been considered more of a modulator of MAPK signal intensity and duration, rather than an ‘off switch’,⁵⁸ thus the graded response observed by us supports those previous hypotheses.

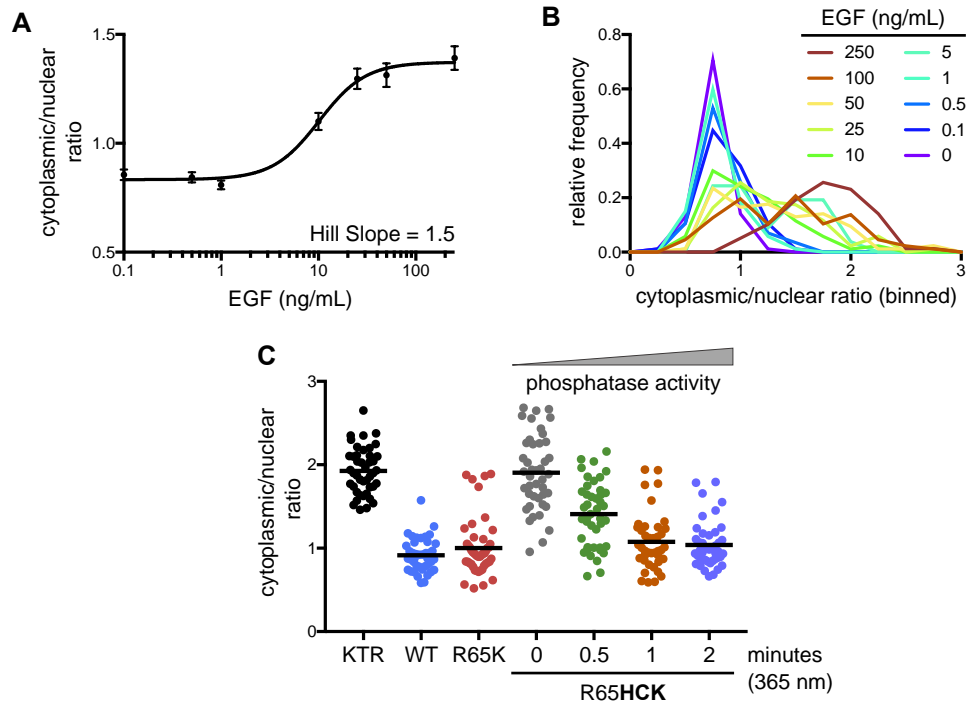


Figure 2-14 Analysis of ERK activity in response to different doses of growth hormone stimulation and optically tuned phosphatase function

a) The cytoplasmic/nuclear ratios for the ERK-KTR-mCherry reporter in HEK293T cells were plotted for a range of EGF concentrations and fitted with a Hill function. Based on the calculated Hill slope, a graded response is observed. Error bars represent the standard error of the mean of 85-90 cells per condition pooled from three biological replicates. b) Histogram representation of the obtained data more clearly depicts the graded response as seen by a unimodal distribution. c) Optical activation of KIM-caged MKP3 shows a graded response for the regulation of pERK translocation upon increased UV irradiation and cell surface stimulation with EGF (100 ng/mL), and thus increased levels of active MKP3. Each dot represents a single cell, black lines represent the mean, $n = 40-45$. Quantified cells were pooled from three biological replicates. One-way ANOVA tests showed $p < 0.0001$ comparing 0 minute to 0.5 minute irradiation, $p = 0.0002$ for 0.5 minute to 1 minute irradiation, and $p > 0.1$ for 1 minute to 2 minute irradiation, indicating a significant difference for the first two comparisons and no significant difference for the third. Reprinted from Courtney and Deiters, *Nat. Commun.* **2019**, 10, 4384.

In order to validate that the responses we observed were due to light activation of the caged phosphatase (and not due to light alone), we conducted a few control experiments. Cells expressing either the ERK-mCherry or ERK-KTR-mCherry reporter were treated with or without EGF both in the presence and absence of a two-minute UV irradiation (Figure 2-15a-b). No significant difference was observed when comparing the irradiated versus non-irradiated samples. Additionally, although we observed no phototoxicity throughout our time course imaging, we wanted to validate that the UV exposure did not adversely affect cell viability (Figure 2-15c). In

an XTT assay, we observed no change in cell viability upon a two-minute UV irradiation, followed by a 72-hour incubation.

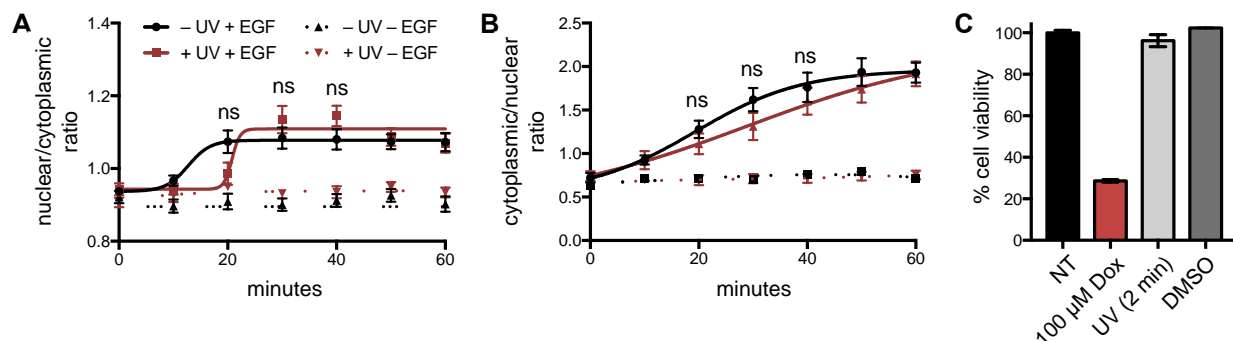


Figure 2-15 UV control experiments with ERK-mCherry and ERK-KTR-mCherry reporters

a) The nuclear/cytoplasmic ratio over time for the ERK-mCherry reporter in the presence or absence of UV irradiation with or without EGF treatment (100 ng/mL) shows no significant difference between the irradiated and non-irradiated samples. b) The cytoplasmic/nuclear ratio over time for the ERK-KTR-mCherry reporter in the presence or absence of UV irradiation with or without EGF treatment (100 ng/mL) shows no significant difference between the irradiated and non-irradiated samples. Error bars represent standard error of the mean for nine individual cells obtained from three biological replicates. One-way ANOVA was used to compare the +/-UV samples; $p > 0.05$ equals ns. c) HEK293T cells were left non-treated (NT), treated with 100 μ M doxorubicin (as a positive control for toxicity), irradiated for 2 minutes with UV light, or treated with 0.1% DMSO, then incubated for 72 hours. An XTT cell viability assay was performed and values were normalized to the non-treated sample. No effect on cell viability was observed with the UV irradiation. Reprinted from Courtney and Deiters, *Nat. Commun.* **2019**, 10, 4384.

2.5 Summary and Outlook

These results represent the first example of photo-activation of a protein phosphatase. Unlike traditional methods employed for studying phosphatases (*e.g.*, gene knockdown), the optochemical approaches developed here allow for acute triggering of enzyme activity, generation of tunable levels of activity depending on the length of light exposure, and temporal control of activation. Two complementary approaches were developed in order to render the dual-specific phosphatase MKP3 light-activatable, thereby enabling independent optical control of catalytic function and of phosphatase-substrate interaction. In the first approach, incorporation of caged cysteine into the active site enabled direct control of catalytic activity by blocking an essential

catalytic residue. Based on the extensive active site conservation of dual-specificity phosphatases, this approach is generalizable and can be used to optically control other members of the DUSP family. In addition to DUSPs, most tyrosine phosphatases utilize a catalytic cysteine, enabling expansion of our strategy to many of the 200 protein phosphatases. In addition, we applied a second approach by strategic caging of lysine-mediated electrostatic interaction in the MKP3:ERK protein-protein interface. Optical control of the kinase interaction motif will be useful for placing other phosphatase-MAPK interactions under optical control since electrostatic interactions are most often the main determinants of these high affinity interactions. More broadly, light-regulation of catalytic sites through introduction of caged amino acids has been demonstrated numerous times; however, the use of caged amino acids to control protein-protein interactions remains underdeveloped^{25-26, 59, 95} and extension of this approach to other scaffolding proteins will further facilitate the optical dissection of cell-signaling networks.

2.6 Methods

Reagents. The photocaged amino acids **NVC** and **HCK** were synthesized as previously reported.^{27, 33} Reagents used for synthesis were obtained from commercial vendors and used without additional purification. Recombinant animal-free human epidermal growth factor (EGF) was purchased from PeproTech (AF-100-15) and reconstituted per the manufacturer's recommendation. Live Cell Imaging Solution (LCIS) was purchased from Molecular Probes/Invitrogen (A14291DJ). All antibodies used in western blots and immunoprecipitations were purchased from ProteinTech: GFP (50430-2-AP), GAPDH (10494-1-AP), and goat anti-rabbit HRP (SA00001-2).

DNA constructs. All cloning was performed using chemically-competent Top10 cells. The synthetase plasmid (pMAH2-CageCys) used for caged cysteine (NVC) incorporation was a gift from Hui-wang Ai (UVA).³³ The MKP3 gene was PCR-amplified using primers P1 and P2 from Addgene plasmid #27975 and ligated into EGFP-N1 (Clontech 6085-1) using restriction sites HindIII and BamHI to generate pMKP3-EGFP. Plasmid sequence was confirmed by Genewiz Sanger sequencing with their CMV-forward primer. An HA epitope tag was added to the C-terminus of the MKP3-EGFP fusion using primers P3 and P4 following a site-directed mutagenesis method⁹⁶ with pMKP3-EGFP as the template to yield pMKP3-EGFP-HA which was confirmed by sequencing at Genewiz with their SV40 polyA reverse primer.

To improve incorporation levels for caged cysteine, the MKP3-EGFP-HA coding sequence was PCR amplified with primers P5 and P6 and ligated into the pMAH vector following digestion with SacI and PmeI to remove the synthetase (doubling the number of tRNAs genes in a given experiment), thus generating pMAH-MKP3-EGFP-HA-WT. Site-directed mutagenesis⁹⁶ was performed to generate pMAH-MKP3-EGFP-HA-C293TAG (primers P7 and P8) and pMAH-MKP3-EGFP-HA-C293S (primers P9 and P10) mutations using the pMAH-MKP3-EGFP-HA-WT construct. All pMAH constructs were confirmed by Sanger sequencing (Genewiz) using their CMV forward primer and BGH polyA reverse primer.

The pMKP3-EGFP-HA construct was used for generating pMKP3-EGFP-HA-R65K (primers P11 and P12), pMKP3-EGFP-HA-R65TAG (primers P13 and P14), and pMKP3-EGFP-HA-R64K (primers P15 and P16) mutants via site-directed mutagenesis.⁹⁶ Sanger sequencing (Genewiz) was performed to confirm successful mutagenesis with their CMV-forward primer. Two PylRS HCKRS/tRNA vectors were utilized: pU6-PylT-H1-PylT-HCKRS and p(U6-PylT)_{x4}-HCKRS.⁹⁷ Due to the significant difference in size of these two plasmids, the smaller plasmid,

pU6-PyIT-H1-PyIT-HCKRS, was used in live cell imaging experiments as triple transfections were required, while the larger plasmid, p(U6-PyIT)_{x4}-HCKRS, was used for western blot analysis after double transfections.

The pERK2-mCherry reporter was a gift from Jason Haugh (NCSU).⁹⁸ The pERK-KTR-mCherry reporter was generated by PCR amplifying the ERK-KTR fragment from Addgene plasmid #59150 with primers P17 and P18 and the backbone fragment was generated by PCR amplifying from an mCherry-N1 construct (gift from Gerry Hammond, University of Pittsburgh) with primers P19 and P20. The two fragments (ERK-KTR and mCherry) underwent Gibson assembly⁹⁹ to generate pERK-KTR-mCherry. Plasmid sequence was confirmed by Genewiz using their CMV-forward primer. For a list of all primer sequences, see Table 2-2. For maps of all plasmids, see Appendix A.

Table 2-2 List of primers used for MKP3 experiments

Restriction site sequences are indicated in **bold**, base mutations are indicated with CAPITALIZATION, and the HA tag DNA sequence is highlighted in gray.

Primer	Sequence (5' → 3')
P1	aga aa gcttatgatagatacgctcagacccg tg ccc
P2	tct ggat ccccgtagattgcagagag tg ccacc
P3	gcatggacgagctgtacaag ta ccatac g atgtccagattacgcttaaagcggccg cg actctagatcataatcagc
P4	ctgtacagctcg tc catg cc gagagtgatcc gg cg gc ggtc
P5	gcat gag ctctcaagcttatgatagatac g
P6	cgtag tt aaactaagc g ta at ctggaacat
P7	caagaactgtggtgtcttggtacatTAG tt ggctggc
P8	g cg gcta at g cc ag cc aaCTA at gtacc
P9	gtacatAG C ttggctggcattag cc gctca
P10	ag cc aa G CTatgtaccaagacaccacag tt cttg
P11	ctgc gg AAGctgcagaagg g ta ac ctg cc ggtg c
P12	ctgcag CT ccgcagcatgatg cc cg g gatg gc
P13	ctgc gg TAGctgcagaagg g ta ac ctg cc ggtg c
P14	ctgcag CT Accgcagcatgatg cc cg g gatg gc
P15	atgctgAAG gc cctgcagaagg g ta ac ctg cc ggt
P16	cag gc g CT Tcagcatgatg cc cg g gatg cc ac
P17	gatccaccggtcgccaccatgaagg gc gaaagcct
P18	ctc gc ctgtctaccatactagtg g atg g gaattg
P19	caattccatccactagtatggtgagcaagg gc gag
P20	aggctt tc ggcccttc at g tg ggcgaccggtg g atc

General cell culture and transfection. HEK293T cells (ATCC, CRL-11268) were maintained at 37 °C in 5% CO₂ atmosphere in DMEM High Glucose with 4.5 mM L-glutamine (GE Life Sciences, SH30003.03) supplemented with 1 mM sodium pyruvate (Alfa, A11148), 10% fetal bovine serum (Sigma, F0926), and 1% penicillin-streptomycin (Corning, 30-002-CI). For a 96-well format used in all imaging-based experiments, 100 µL of media was used for culturing, whereas for a 12-well plate used for western blot or biochemical assays, 1 mL of media was used. Cells were monitored every 3 months to confirm the absence of mycoplasma contamination (Genlantis, MY01100). Cells were transiently transfected with LPEI (Polysciences, 23966) using a 0.5 mg/mL solution at a 5:1 LPEI:DNA (w/w) ratio in antibiotic-free DMEM. Following overnight transfection, the media was removed and the cells were gently washed once with regular DMEM to remove any excess unnatural amino acid. Cells were serum-starved (DMEM with 0.1% FBS, without antibiotics) for 4 h. The media was replaced with 90 µL of LCIS immediately prior to irradiation. Irradiation was performed on a UV transilluminator (VWR Dual Transilluminator at 365 nm) for two minutes (unless specified otherwise).

General live cell imaging. HEK293T cells were imaged at ambient temperature with an Axio Observer Z1 microscope using a 20x Plan Apochromat objective equipped with an AxioCam MRm camera using Zen 2 Blue Edition software. Growth factor stimulation was performed by diluting a 10X (1 µg/mL) stock directly into media containing cells on the microscope stage to a final concentration of 100 ng/mL. Images were acquired using EGFP and mCherry filter sets (Zeiss 38HE and 43HE, respectively). All image analysis and quantification was performed using FIJI and specific details are provided in the corresponding sections.

Expression of MKP3 with a caged catalytic site. To validate the expression of wild-type, catalytically dead, and caged MKP3 via western blot, HEK293T cells were plated at ~200,000

cells per well in a 12-well clear bottom plate (Greiner). At ~80% confluence, cells were transfected as follows: (1) 1000 ng of pMAH-MKP3-EGFP-HA-WT and 1000 ng of pMAH2-CageCys, (2) 1000 ng of pMAH-MKP3-EGFP-HA-C293S and 1000 ng of pMAH2-CageCys, or (3) 1000 ng of pMAH-MKP3-EGFP-HA-C293TAG and 1000 ng of pMAH2-CageCys with 20 μ L of LPEI using 100 μ L of OptiMEM. The transfection mix (OptiMEM, DNA, and LPEI) was incubated at room temperature for 20 minutes, then the entire volume was added to wells containing 1 mL of DMEM (antibiotic-free). For **NVC**-containing wells, 10 μ L of **NVC** stock solution (100 mM in DMSO) were diluted into 990 μ L of DMEM for a final 1 mM **NVC** concentration. Cells were incubated for ~24 hours prior to harvesting for western blot analysis (see next section).

Western blot analysis. Proteins were expressed in HEK293T cells as described (see Expression of MKP3 with a caged catalytic site or Expression of MKP3 with a caged kinase interaction motif) and the 12-well plate was placed on ice, the media was removed, and the cells were washed with 200 μ L of ice-cold phosphate buffer saline (PBS), then lysed with 100 μ L of ice-cold RIPA lysis buffer (150 mM NaCl, 1.0% NP-40, 0.5% sodium deoxycholate, 0.1% SDS, 50 mM Tris pH 8.0) supplemented with 1X protease inhibitor cocktail (Thermo Scientific, 78429). Cellular debris was pelleted at 21,000 g for 15 minutes at 4 °C and the supernatant was collected and mixed with 4X Laemmli sample buffer (12 μ L lysate + 4 μ L 4X buffer). Samples were heated at 95 °C for 10 minutes, then frozen at -80 °C. The samples (all 16 μ L per condition) were resolved on a 10% SDS-PAGE (60 V for 20 minutes, 150 V for 1.25 hours), then transferred to a 0.45 μ m PVDF membrane (Millipore, IPVH00010) at 80 V for 1.5 hours using Towbin buffer (25 mM Tris-HCl, 192 mM glycine, pH 8.3, 20% methanol [v/v]). The membrane was blocked for 2 hours with 5% milk in TBST (0.1% Tween-20 in 1X TBS) at room temperature with rocking. After blocking, the membrane was cut in half horizontally. The top half was probed with anti-GFP, while the bottom

half was probed with anti-GAPDH. Anti-GFP was diluted 1:5000 and anti-GAPDH was diluted 1:5000 in 5% milk in 6 mL of TBST and the membranes were incubated with primary antibodies overnight with rocking at 4 °C. The following day, membranes were washed thrice with TBST (~10 mL), then probed with goat anti-rabbit HRP using 1:10,000 dilution in 6 mL of TBST for 2 hours. The membranes were again washed thrice with TBST (~10 mL). Membranes were developed with SuperSignal West Pico PLUS Chemiluminescent Substrate (Thermo Scientific, 34580) and imaged on a BioRad ChemiDoc using the Chemi setting. Images were exported using the “auto scale” feature in the BioRad Image Lab software.

Biochemical phosphatase assays. MKP3 variants were expressed in a 12-well format identical to the method used above for western blot analysis. The plate was chilled on ice, the media was removed, and cells were gently washed with 1 mL of ice-cold PBS. Cells were gently lysed with 100 μ L of GE Mammalian Protein Extraction Buffer (28941279) on ice. The plate (still on ice) was placed on a rotary shaker and shaken at 250 rpm for 15 minutes. The lysate was collected, and cellular debris was pelleted at 21,000 g for 10 minutes at 4 °C. The supernatant (~90 μ L to avoid disturbing the pellet) was collected into a fresh tube. Anti-GFP antibody was added to each sample (0.1 μ g) and incubated for 1 hour at 4 °C. Protein A resin (SCBT, sc-2001) was added to each sample (10 μ L) and rocked for 2 hours in a cold room. The resin was gently pelleted at 100 g for 5 minutes at 4 °C. The supernatant was removed (and discarded) and the resin was washed twice (500 μ L each time) with chilled phosphatase assay buffer (25 mM HEPES, 50 mM NaCl, 2.5 mM EDTA, 10 mM DTT, pH 7.2). To activate MKP3 for *in vitro* assays, 5 μ g of purified GST-ERK2 was added to each sample (see below for its expression in *E. coli*). DiFMUP (**1**, Invitrogen – D6567) was added to a final concentration of 50 μ M (from a 10 mM stock prepared in DMSO) and reactions were incubated at 37 °C for 30 minutes. Fluorescence was measured using a Tecan

M1000 pro with settings of 358/5 nm for excitation and 450/5 nm for emission. Background hydrolysis was measured in buffer plus **1** and was subtracted from all data points. Expression and immunoprecipitation were performed in biological triplicates and fluorescence readings were averaged with error bars representing standard deviations.

To generate GST-ERK2 protein, Addgene plasmid pGEX-4T-1 3xFlag-ERK2 (#47573) was transformed into BL21(DE3) using LB broth supplemented with ampicillin (100 µg/mL) and protein expression was performed following a literature procedure at a 100 mL scale.⁸¹ In short, a 100 mL LB culture (plus ampicillin) was prepared by inoculating with 1 mL of saturated overnight culture, then grown to OD₆₀₀ of 0.6 at 37 °C with shaking. At this point, expression was induced by the addition of IPTG (using a 1 M stock solution prepared in water) to a final 2 mM concentration, and the culture was shaken for 5 hours at 37 °C. Cells were harvested by centrifugation at 4200 g at 4 °C for 10 minutes, and purification commenced by resuspending the cell pellet in 20 mL of ice-cold PBS containing 1X protease inhibitor (Sigma, P8849). Cell lysis was performed using an EmulsiFlex C3 Homogenizer (Avestin). Cells were passed through without pressure for 5 minutes, then cycled through with pressure (20,000 psi) for 15 minutes. Cellular debris was pelleted at 21,000 g for 15 minutes at 4 °C, and the soluble protein fraction was transferred to a fresh tube. GST-ERK2 was purified using Pierce Glutathione Agarose (PI16100) following the manufacturer's protocol. Purified protein was buffer exchanged thrice using centrifuge filters (Amicon Ultra 10 kDa, 0.5 mL) into phosphatase assay buffer prior to use in the *in vitro* assays and diluted to a final concentration of 1 µg/µL. Protein concentration was determined using a Coomassie-stained SDS-PAGE gel with a BSA standard curve.

Catalytic site-caged MKP3 and ERK2-mCherry reporter. HEK293T cells were plated at ~50,000 cells per well in a black, poly-D-lysine coated 96-well clear bottom plate (Greiner). At

~80% confluence, cells were transfected as follows: (1) 75 ng of pERK2-mCherry and 300 ng of pMAH2-CageCys, (2) 75 ng of pERK2-mCherry, 150 ng of pMAH-MKP3-EGFP-HA-WT, and 150 ng of pMAH2-CageCys, or (3) 75 ng of pERK2-mCherry, 150 ng of pMAH-EGFP-HA-C293TAG, and 150 ng of pMAH2-CageCys using 3.75 μ L of LPEI (0.5 mg/mL) in 20 μ L of OptiMEM. Transfection mix was added to wells containing 100 μ L of DMEM. For NVC-containing wells, DMEM was prepared as above to yield 1 mM NVC. Cells were incubated with the transfection mix for ~24 hours prior to serum starving. Cells were serum-starved (DMEM with 0.1% FBS, without antibiotics) for 4 hours. The media was replaced with 90 μ L of LCIS and the cells were irradiated for 2 minutes with a UV transilluminator (from the bottom of the plate), then immediately placed on the microscope stage for fluorescence imaging. EGF activation was performed as described previously (see General live cell imaging) using a final concentration of 100 ng/mL. Images were acquired every 10 minutes for 60 minutes using GFP and mCherry filters.

Circular ROIs were selected using the EGFP channel in order to discriminate between nuclear and cytoplasmic signal. Mean fluorescence was used for determining nuclear/cytoplasmic (N/C) ratios. For comparison of the MKP3 mutants over time, nine cells were analyzed at each time point from 0 to 60 from the three biological replicates and the average values \pm standard error of the mean were plotted against time. One-way ANOVA tests were performed to evaluate the statistical significance of the data.

Catalytic site-caged MKP3 and ERK-KTR-mCherry reporter. HEK293T cells were plated at ~50,000 cells per well in a black, poly-D-lysine coated 96-well clear bottom plate. At ~80% confluence, cells were transfected as follows: (1) 150 ng of pERK-KTR-mCherry and 300 ng of pMAH2-CageCys, (2) 150 ng of pERK-KTR-mCherry, 150 ng of pMAH-MKP3-EGFP-HA-WT, and 150 ng of pMAH2-CageCys, or (3) 150 ng of pERK-KTR-mCherry, 150 ng of pMAH-MKP3-

EGFP-HA, and 150 ng of pMAH2-CageCys using 4.5 μ L of LPEI in 20 μ L of OptiMEM. Transfection mix was added to wells containing 100 μ L of DMEM. For **NVC**-containing wells, DMEM was prepared as above for 1 mM final concentration. Cells were incubated with the transfection mix for ~24 hours prior to serum starving. Serum starvation, light activation, EGF stimulation, and image acquisition were performed identical to section Catalytic site-caged MKP3 and ERK2-mCherry reporter.

Circular ROIs were selected using the EGFP channel in order to discriminate between nuclear and cytoplasmic signal. Mean fluorescence was used for determining cytoplasmic/nuclear (C/N) ratios. For comparison of the MKP3 mutants over time, nine cells were analyzed at each time point from 0 to 60 from the three biological replicates and the average values \pm standard error of the mean were plotted against time. One-way ANOVA tests were performed to evaluate the statistical significance of the data.

Expression of MKP3 with a caged kinase interaction motif. To validate the expression of wild-type, R65K, and caged MKP3 via western blot, HEK293T cells were plated at ~200,000 cells per well in a 12-well clear bottom plate. At ~80% confluence, cells were transfected as follows: (1) 1000 ng of pMAH-MKP3-EGFP-HA-WT and 1000 ng of p(U6-PyIT)_{x4}-HCKRS, (2) 1000 ng of pMKP3-EGFP-HA-R65K and 1000 ng p(U6-PyIT)_{x4}-HCKRS, or (3) 1000 ng of pMKP3-EGFP-HA-R65TAG and 1000 ng of p(U6-PyIT)_{x4}-HCKRS with 20 μ L of LPEI using 100 μ L of OptiMEM. The transfection mix (OptiMEM, DNA, and LPEI) was incubated at room temperature for 20 minutes, then the entire volume was added to wells containing 1 mL of DMEM (antibiotic-free). For **HCK**-containing wells, 2.5 μ L of **HCK** (100 mM stock in DMSO) was diluted in 998 μ L of DMEM for a final 0.25 mM **HCK** concentration. Cells were incubated for ~24 hours prior to harvesting for western blot analysis (see section above).

KIM-caged MKP3 and ERK-KTR-mCherry reporter. HEK293T cells were plated at ~50,000 cells per well in a black, poly-D-lysine coated 96-well clear bottom plate. At ~80% confluence, cells were transfected as follows: (1) 150 ng of pERK-KTR-mCherry and 300 ng of pU6-PyIT-H1-PyIT-HCKRS, (2) 150 ng of pERK-KTR-mCherry, 150 ng of pMKP3-EGFP-HA-R65K, and 150 ng of pU6-PyIT-H1-PyIT-HCKRS, (3) 150 ng of pERK-KTR-mCherry, 150 ng of pMKP3-EGFP-HA-R65TAG, and 150 ng of pU6-PyIT-H1-PyIT-HCKRS using 4.5 μ L of LPEI in 20 μ L of OptiMEM. Transfection mix was applied to wells containing 100 μ L of DMEM. **HCK** in DMEM was prepared as above and 100 μ L was added per well. Serum starvation, light activation, EGF stimulation, and image acquisition were performed identical to section Catalytic site-caged MKP3 and ERK2-mCherry reporter.

Circular ROIs were selected using the EGFP channel in order to discriminate between nuclear and cytoplasmic signal. Mean fluorescence was used for determining cytoplasmic/nuclear (C/N) ratios. For comparison of C/N ratios over time for the MKP3 mutants, nine cells were analyzed at each time point from 0 to 60 from the three biological replicates and the average values \pm standard error of the mean were plotted against time. One-way ANOVA tests were performed to evaluate the statistical significance of the data.

Tunability of ERK activity. HEK293T cells were plated at ~50,000 cells per well in a black, poly-D-lysine coated 96-well plate. At ~80% confluence, cells were transfected with 150 ng of pERK-KTR-mCherry using 1.5 μ L of LPEI (0.5 mg/mL) in 20 μ L of OptiMEM. Transfection mix (OptiMEM, DNA, and LPEI) was incubated at room temperature for 20 minutes, then the entire volume was added to wells containing 100 μ L of DMEM (antibiotic-free). Cells were incubated with the transfection mix for ~24 hours prior to serum starvation. Cells were starved for 4 hours in DMEM with 0.1% FBS (without antibiotics), then the media was replaced with 90 μ L of LCIS.

A range of EGF concentrations (from 2500 ng/mL to 1 ng/mL, for final range of 250 ng/mL to 0.1 ng/mL after 1:10 dilution upon addition to cells) was generated starting with a 10 μ g/mL stock and diluting into LCIS. Following EGF addition, a 60-minute time point image was acquired for all ten EGF concentrations.

Circular ROIs were used to measure mean fluorescence in the nucleus and cytoplasm. C/N ratios were calculated for 85-90 cells per condition (combined from three biological replicates) and the averages \pm standard error of the mean (s.e.m.) were plotted. A curve was fitted using the settings “[agonist] versus response – variable slope (four parameters)” in GraphPad Prism 7. The Hill slope was computed to be 1.534.

Tunability of KIM-caged MKP3 activity. For exploring the tunability of photo-activation, irradiation times of 30, 60, and 120 seconds were utilized on cells transfected as described above (section KIM-caged MKP3 and ERK-KTR-mCherry reporter). Irradiation was performed as previously described (see General cell culture and transfection) and cells were immediately placed on the microscope stage for imaging. EGF activation was performed as described previously using 100 ng/mL final concentration. A 60-minute time point image was acquired.

Circular ROIs were selected using the EGFP channel in order to discriminate between nuclear and cytoplasmic signal. Mean fluorescence was used for determining cytoplasmic/nuclear (C/N) ratios. C/N ratios were determined for 40-45 cells per condition from a combined three biological replicates. A dot plot representation shows the C/N for each of the analyzed cells and a horizontal bar indicates the average. Histogram representation used a bin range of 0 to 3 with a bin size of 0.25. One-way ANOVA tests were performed to evaluate the statistical significance of the data.

Effect of UV irradiation on cell signaling reporters. HEK293T cells were plated at ~50,000 cells per well in a black, poly-D-lysine coated 96-well clear bottom plate. At ~80% confluence, cells were transfected with either: (1) 150 ng of pERK-KTR-mCherry or (2) 75 ng of pERK2-mCherry using 1.5 μ L or 0.75 μ L of LPEI, respectively, in 20 μ L of OptiMEM (note: a working solution of transfection mix was prepared for four wells in a single tube). Transfection mix was applied to wells containing 100 μ L of DMEM. Cells were incubated with the transfection mix for ~24 hours prior to serum starving. Cells were starved for 4 hours in DMEM with 0.1% FBS (without antibiotics), then the media was replaced with 90 μ L of LCIS. Following starvation and media change, a subset of wells was irradiated for 2 minutes with a UV transilluminator, then immediately placed on the microscope stage for fluorescence imaging. EGF activation was performed as described previously using 100 ng/mL final concentration (a subset of wells was left unstimulated). Images were acquired every 10 minutes for 60 minutes. Mean fluorescence from circular ROIs was used for determining cytoplasmic/nuclear (C/N) ratios for the ERK-KTR reporter or nuclear/cytoplasmic (N/C) ratios for the ERK2-mCherry reporter. Nine cells were analyzed at each time point from 0 to 60 minutes combined from three biological replicates and the average values \pm standard error of the mean were plotted against time. One-way ANOVA tests were performed to evaluate the statistical significance of the data.

Effect of UV irradiation on cell viability. HEK293T cells were plated at ~25,000 cells per well in a white, poly-D-lysine coated 96-well clear bottom plate. The next day, four different treatments were performed in triplicate: (1) non-treated, (2) 100 μ M doxorubicin, (3) UV irradiation for 2 minutes, or (4) 0.1% DMSO, all in regular DMEM. Cells were maintained at 37 $^{\circ}$ C and 5% CO₂ atmosphere for 72 hours. An XTT cell viability assay¹⁰⁰ was performed by adding 40 μ L of the activated XTT reagent (8 μ L of 1.7 mg/mL menadione diluted into 1 mL of 1 mg/mL XTT reagent

solution) to each well. Absorbance was measured at 450 nm and 630 nm (background) on a Tecan M1000 pro plate reader immediately following reagent addition. Cells were placed back in the incubator for four hours, then final absorbance measurements were taken. The background absorbance was subtracted from each well, then absorbance was normalized such that the non-treated sample equaled 100% cell viability.

3.0 Optical Deactivation of Protein Function

3.1 Introduction to Light-Induced Protein Inactivation Approaches

As detailed in earlier sections, light is a powerful external tool that has been applied for the activation of various biological processes. Analogously, light has been harnessed for inducing protein and cell inactivation through a technique known as chromophore-assisted light inactivation (CALI).¹⁰¹⁻¹⁰² CALI utilizes reactive oxygen species (ROS) generating photosensitizers that are either (a) genetically encoded as a protein fusion or (b) small molecule based probes that are post-translationally conjugated to the biomolecule of interest (Figure 3-1).¹⁰³

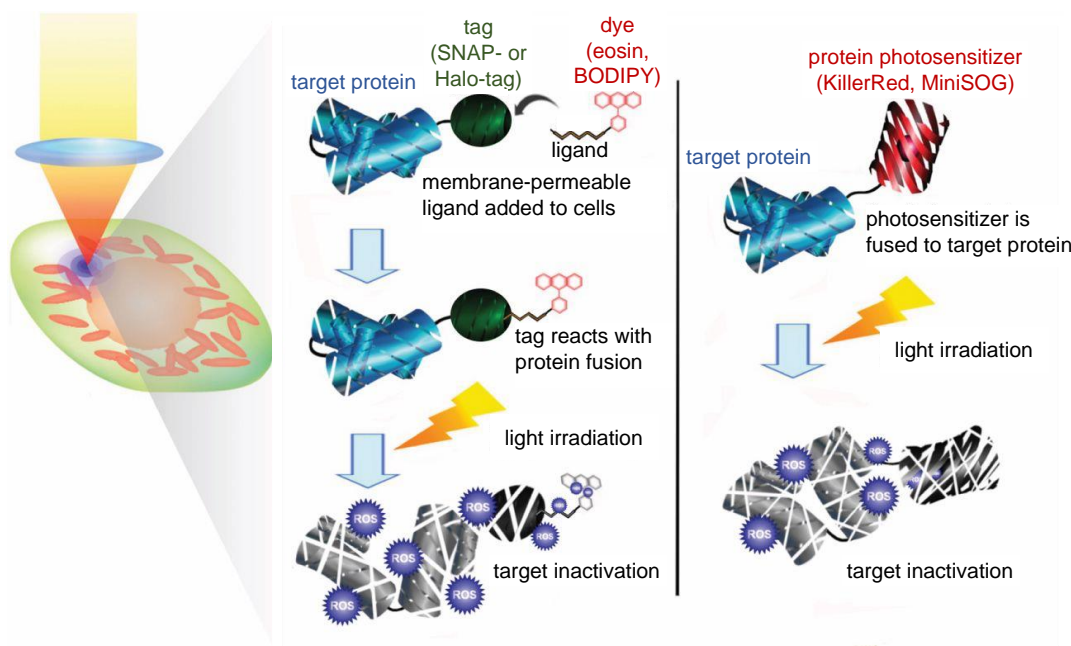


Figure 3-1 Overview of chromophore-assisted light inactivation

Chromophore-assisted light inactivation (CALI) can utilize a small molecule-based photosensitizer that reacts with a tagged fusion protein to covalently attach the ROS generator to the fusion (left) or a protein-based photosensitizer that can be genetically encoded and expressed as a fusion protein with the target protein (right). Figure adapted from Sano *et. al.*, *J. Cell. Sci.* **2014**, 127, 1621-1629. Copyright 2014 The Company of Biologists Ltd

Upon irradiation with light of an appropriate wavelength, these photosensitizers are excited to the S_1 singlet state, then undergo intersystem crossing to an excited triplet state (3O_2) at which point they react with oxygen through one of two pathways (Figure 3-2). The Type I pathway (electron transfer) generates superoxide radical anion, $O_2^{\cdot-}$, while the Type II pathway (energy transfer) produces singlet oxygen, 1O_2 . In the case of superoxide radical anion, additional reactions can occur to generate hydrogen peroxide (H_2O_2) and hydroxyl radical (HO^{\cdot}), both of which can also react with and modify biomolecules (both DNA and proteins).¹⁰⁴ Energy and electron transfer are competing processes and in most cases the rate constant for energy transfer is greater, thus most photosensitizers predominantly generate singlet oxygen (Type II); however, this is not always the case.¹⁰⁵⁻¹⁰⁶

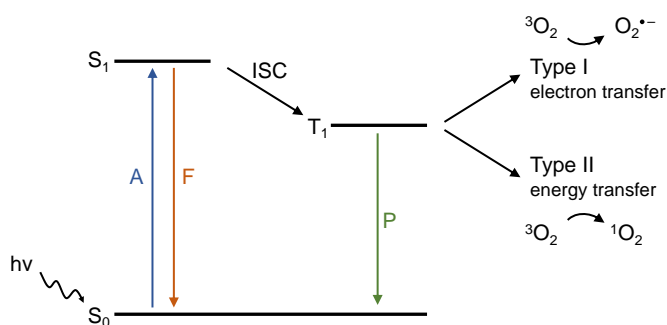


Figure 3-2 Jablonski diagram describing reactive oxygen species (ROS) generation

Absorbance (blue – A), fluorescence (orange – F), and phosphorescence (green – P) processes are indicated with the appropriate lines. In the case of photosensitizers, once excited to the singlet (S_1) state, intersystem crossing (ISC) can result in a transition to a triplet state (T_1) in which the photosensitizer can react with oxygen via two different pathways: Type I – electron transfer or Type II – energy transfer to generate superoxide radical anions or singlet oxygen, respectively. Figure adapted from Trewin *et. al.*, *Free Radic. Biol. Med.*, 128, 157-164. Copyright 2018 Elsevier Ltd.

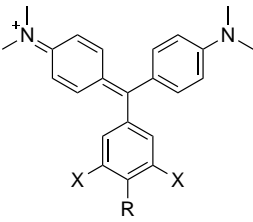
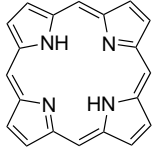
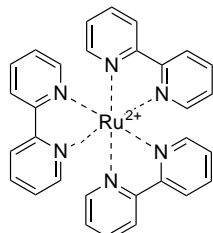
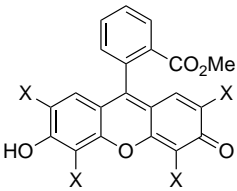
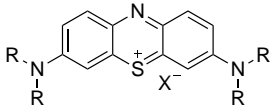
An important aspect to consider when generating ROS for targeted approaches is the lifetime and the distance traveled before quenching; unfortunately, there are several factors that affect these values and the literature remains somewhat controversial in regard to these measured parameters. Singlet oxygen lifetime measurements acquired in Hela cells yielded 30 to 40 μs ,¹⁰⁷ while measurements in L1210 leukemia cells showed 0.17 to 0.3 μs ,¹⁰⁸ and measurements acquired

around synthetic lipid membranes were ~ 3 ns,¹⁰⁹ thus demonstrating the wide range of values depends on the system tested. The distance traveled by singlet oxygen reportedly ranges between 10 nm to 3 μ m when measured in various cell lines or at the cell membrane.¹¹⁰⁻¹¹⁵

Small molecule photosensitizers have been developed using a wide range of core motifs (Table 3-1). The first example of protein inactivation using a small molecule photosensitizer was described by Daniel Jay in 1988.¹¹⁶ In this work, malachite green was attached to streptavidin and used to target biotinylated alkaline phosphatase and β -galactosidase. Upon irradiation with light (620 nm), enzyme activities were reduced by 75 to 85 percent. Jay initially attributed this localized inactivation to heat release proximal to the chromophore that dissipated over longer distances; however, in follow up reports, he elucidated the mechanism of inactivation to involve hydroxyl radicals and singlet oxygen.¹¹⁷⁻¹¹⁸ As malachite green is a poor ROS-generating chromophore, subsequent applications focused on the use of porphyrin, phthalocyanine, xanthene (Rose Bengal – RB) derivatives, and phenothiazinium (methylene blue – MB) motifs,¹¹⁹ while bis(bipyridyl) ruthenium (II) and boron-dipyrromethene (BODIPY) cores have become more common in recent years.¹²⁰⁻¹²² Early CALI reports utilized xanthene derivatives, FAsH and ReAsH, comprised of fluorescein and rhodamine cores bearing arsenic tags that react with tetracysteine sequences appended on the N- or C-terminus of the protein target.¹²³ Unfortunately, these ROS generators suffered from non-specific interaction with cysteine-rich proteins thus limiting their utility, and the use of fluorescein and rhodamine motifs resulted in low quantum yields for ROS generation. Ruthenium (II) motifs have been used for inducing oxidation in DNA/RNA¹²⁴ or conjugated to peptide derivatives (peptoids) for inhibition and inactivation of cell surface receptors.¹²⁵

Table 3-1 Small molecule photosensitizers

Structures of small molecule photosensitizers are shown. X represents positions for halogenation, typically bromine or iodine. R represents hydrocarbon additions, either aliphatic or aromatic. Wavelength ranges and quantum yields of singlet oxygen generation are included.

name	structure	wavelength	quantum yield
malachite green		X = H; 620 – 640 nm X = I; 640 – 670 nm	X = H; N.D. X = I; 0.13
porphyrin		620 – 640 nm	0.20 – 0.63
bis(bipyridyl) ruthenium (II)		460 – 480 nm	0.30 – 0.82
xanthene		RB: 540 – 580 nm Eosin: 500 – 550 nm	RB: 0.75 – 0.86 Eosin: 0.28 – 0.57
phenothiazinium		MB: 550 – 700 nm	0.49 – 0.60
BODIPY		440 – 580 nm	0.26 – 0.96

A tetrabrominated xanthene derivative, Eosin Y, has been used in conjunction with a HaloTag protein fusion for inactivation of two kinases, PKC γ and Aurora B.¹²⁶ An unmodified fluorescein conjugated to an O⁶-benzylguanine moiety was used to covalently label SNAP-tag fusions of both α - and γ -tubulin enabling inactivation of mitosis.¹²⁷ The BODIPY core shows very

low ROS generation until functionalization with heavy atoms (bromine or iodine). The heavy atom effect is known to promote intersystem crossing, producing more efficient ROS generators.¹²⁸ Several reports have demonstrated that iodinated-BODIPYs can be used in photodynamic therapy for the inactivation of target cells (typically cancer cells) without damaging neighboring, healthy cells.¹²⁸⁻¹³² Although the quantum yield determination for singlet oxygen generation is highly dependent on solvent, iodinated-BODIPY analogs tend to be the most efficient (0.26 to 0.96),^{122, 133} followed by bis(bipyridyl) ruthenium (II) complexes (0.30 to 0.82)¹³⁴ and eosin (0.28 to 0.57).¹³⁵ While these small molecule photosensitizers have shown significant promise in photodynamic therapy applications, controlling oxidation within a confined region of interest remains challenging due to the potential for unbound small molecule diffusion (if not washed out sufficiently). When selecting a ROS generator for CALI applications, one should consider the following: (1) ensure that the wavelength needed for ROS generation does not overlap or interfere with any fluorescent protein fusions or intended fluorescent readout probes and (2) synthetic accessibility of generating a modified ROS chromophore bearing the necessary reactive handle for target labeling.

The Bruchez lab developed a strategy which capitalizes on the advantages of both small molecule- and protein-based ROS generators. First, an engineered protein dL5** that selectively binds to malachite green with low nanomolar affinity was developed as a turn-on fluorophore strategy in which fluorescence is only achieved when MG is complexed with dL5** (fused to the protein of interest).¹³⁶ The Bruchez lab later generated an iodinated-MG (MGI) such that the capacity for ROS generation was only possible upon MGI complex formation with dL5**.¹³⁷ Among the many applications, they demonstrated that this approach could be used to achieve targeted cell ablation of cardiac muscle cells in zebrafish.

Several genetically encoded proteins such as KillerRed, miniSOG, and SuperNova have been developed to induce inactivation of their fusion proteins in cells (Figure 3-3).¹³⁸⁻¹⁴¹ Early examples demonstrated that GFP could be used for CALI applications to inactivate α -actinin¹⁴² and myosin;¹⁴³ however, the use of GFP as a ROS generator is not ideal given its common utilization as a marker of subcellular localization during fluorescence microscopy. A fusion protein composed of KillerRed and the protein of interest can be expressed in cells, and upon irradiation, Killer Red generates superoxide ions, which degrade the fusion protein to inactivate its function or induce phototoxicity and subsequent cell death. Typically, KillerRed is applied as an optogenetic tool for total cell ablation as opposed to targeted enzymatic inactivation.¹⁴⁴⁻¹⁴⁶ More recently, monomeric variants, such as Supernova, have been developed in order to address issues associated with using a dimeric fusion protein,^{141, 147} and point mutations have been introduced to generate KillerOrange expanding the wavelength options available for ablation.¹⁴⁸

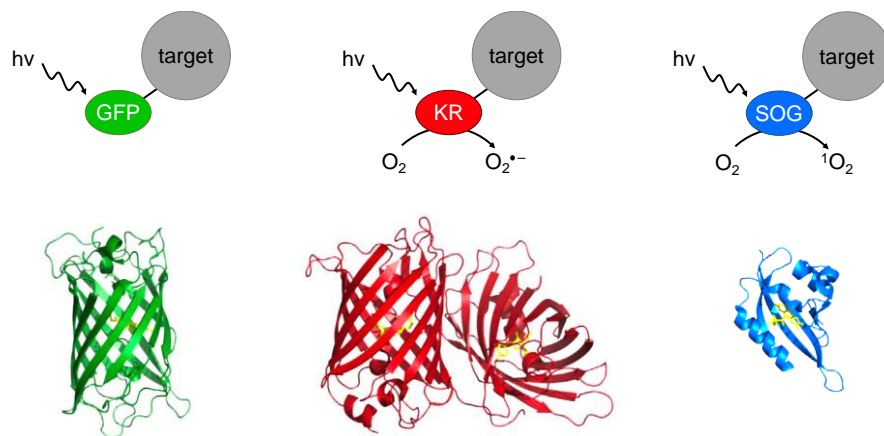


Figure 3-3 Fusion proteins for ROS production

Unlike green fluorescence protein (GFP) which is predominantly used as a fluorescent marker of subcellular localization in cells, Killer Red (KR) and miniSOG (SOG) generate reactive oxygen species upon excitation with the appropriate wavelength of light. Figure adapted from Foster *et al.*, *Redox Biol.*, 2, 368-376. Copyright 2014 Elsevier Ltd.

MiniSOG (mini singlet oxygen generator) was derived from the LOV domain of *Arabidopsis thaliana* phototropin 2 and is often advantageous over the KillerRed series due to its significantly smaller size of ~15 kDa.¹³⁹ It has been employed for cell ablation studies in *C.*

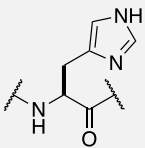
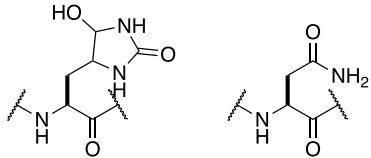
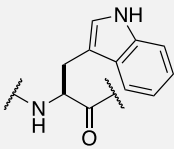
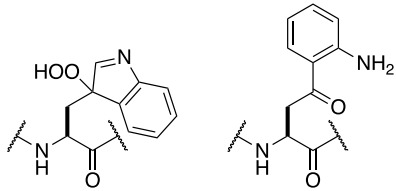
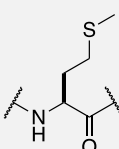
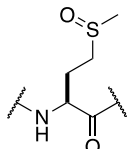
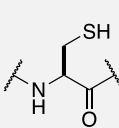
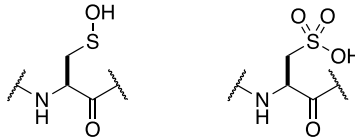
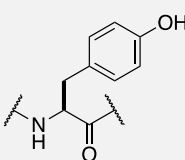
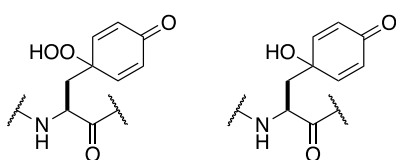
elegans, *Drosophila*, *E. coli*, and various mammalian cell lines,¹⁴⁹⁻¹⁵³ and in a few cases has been used for targeted inactivation of mitochondrial protein complexes and synaptic proteins (VAMP2) in neurons.¹⁵⁴⁻¹⁵⁵ These protein based ROS generators suffer from significantly lower quantum yields (of both singlet oxygen and superoxide radical anion) ranging from $7 - 20 \times 10^{-3}$.¹⁵⁶ In addition, in most cases attachment of the chromophore is limited to the N- or C-termini, thus the fused ROS generator may be oriented in an imperfect manner. Although the quantum yields are much lower and orientation of the chromophore is not exact, this type of ROS generator is advantageous in that the localization and proximity of the chromophore to the protein of interest is pre-defined during experimental design of the fusion protein. While small molecule ROS generators can diffuse throughout the cell, requiring washout of any unbound ROS generator, this is a non-issue with protein-based ROS generators.

In addition to ROS generation resulting from irradiation of photosensitizers, there are several endogenous sources of ROS, primarily the byproducts of aerobic respiration. A significant amount of research has been performed to study the effects of both exogenous and endogenous sources of ROS and the roles that they play in cell signaling, redox homeostasis, and healthy versus disease states.¹⁵⁷⁻¹⁶⁰ Due to the reactive nature, these species are capable of reacting with a range of biomacromolecules such as DNA, RNA, lipids, and proteins.¹⁶¹⁻¹⁶² In particular, singlet oxygen is consumed by these molecules with a distribution of 69:12:19 (protein:DNA/RNA:lipids/small molecules), which roughly matches the cellular abundance of these macromolecules.¹⁰⁶

For the work discussed in this document, we focus on the effects of ROS reacting with proteins. At physiological pH, singlet oxygen reacts preferentially with histidine, tryptophan, tyrosine, methionine, and cysteine; however, under high pH conditions, lysine and arginine can undergo modification.¹⁶³ Table 3-2 shows some representative products of singlet oxygen

reactivity with these different side chains.¹⁰⁶ In many cases, peroxide intermediates are formed; however, these often rapidly decompose into more stable products. For example, the peroxide intermediate of tryptophan is converted to N-formylkynurenine then further reduced to kynurenin (shown on the right), while the peroxide generated from tyrosine is converted to the more stable alcohol product (a dienone alcohol) that has been reported to undergo Michael additions with cellular thiols.¹⁰⁶ The sheer number of potential products that can be generated upon reaction with singlet oxygen (and other ROS) makes characterization a challenge. Although less common, backbone oxidation and fragmentation, as well as protein cross-linking has been reported as a product of ROS reaction with proteins.¹⁶⁴⁻¹⁶⁵

Table 3-2 Amino acids susceptible to oxidation via reaction with singlet oxygen
The rate constants, amino acid structures and representative products are shown.

amino acid	rate constant ($\text{dm}^3 \text{mol}^{-1} \text{s}^{-1}$)	structure	representative oxidized products
histidine	3.2×10^7		
tryptophan	3.0×10^7		
methionine	1.6×10^7		
cysteine	8.6×10^6		
tyrosine	8.0×10^6		

3.2 Introduction to Bioconjugation Reactions and Genetically Encoded Handles

First described by Carolyn Bertozzi, “bioorthogonal chemistry” refers to the introduction of a unique chemical handle into a biomacromolecule such that upon addition of an exogenous probe, a highly selective reaction will occur between the modified macromolecule and the probe.¹⁶⁶⁻¹⁶⁷ A “bioorthogonal reaction” must fulfill several key requirements: (1) the reactive handles that are appended to the biomolecule should not react with undesired biomolecules (or

small molecules) in the cell, (2) the reactive handle and the added probe must react with each other under physiologically relevant conditions (aqueous environment at pH 7.4), (3) the product of the reaction must generate a stable linkage that is not susceptible to hydrolysis, and (4) the reactive handle and probe should not be cytotoxic.¹⁶⁸⁻¹⁶⁹ Although the list of requirements is lengthy, several bioorthogonal reactions have been developed and applied in the last few decades. Further, these handles have been converted into unnatural amino acids that have been genetically encoded in *E. coli* and mammalian systems.¹⁷⁰⁻¹⁷¹ Upon genetic encoding, these handles can undergo chemoselective reactions to label the protein with fluorophores, PEG linkers, and even additional proteins (Figure 3-4a). Depending on the bioorthogonal moiety selected, the reaction rates vary drastically between the different chemistries, covering several orders of magnitude (Figure 3-4b).

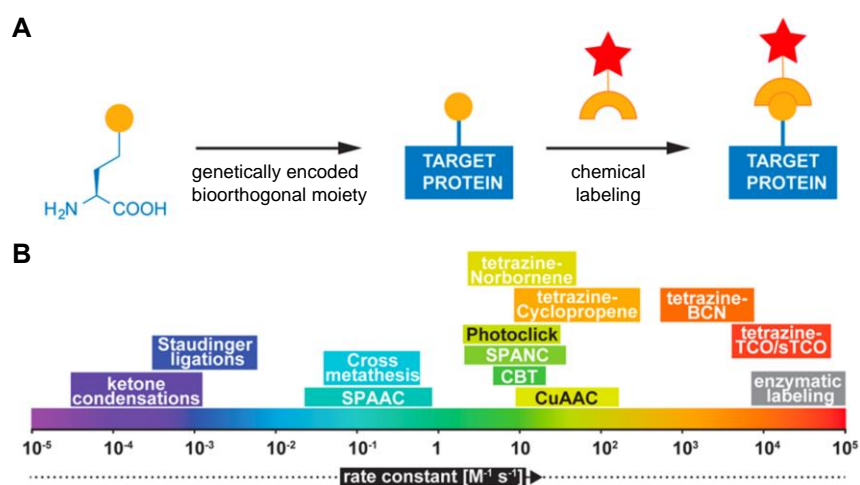


Figure 3-4 Chemoselective labeling of proteins using bioorthogonal reactions

a) Following genetic encoding of a bioorthogonal moiety, chemoselective reactions can be applied for targeted labeling of the protein of interest. b) The different chemistries exhibit a wide range of reaction rates, which are shown for the commonly utilized techniques. Figure was taken from Lang, K and Chin, J. *Chem. Rev.* **2014**, 114, 4764–4806. Copyright 2014 American Chemical Society.

Copper-mediated [3+2] cycloadditions (CuAAC) utilize aliphatic or aromatic alkynes and azides but requires the addition of copper (II). Strain promoted copper-free [3+2] cycloadditions (SPAAC) are slower than traditional click reactions; however, they do not require a catalyst and are advantageous in scenarios where addition of copper is not favorable or can contribute to

cytotoxicity. Inverse-electron demand Diels-Alder cycloadditions (IEDDA) are the fastest bioconjugation reaction reported thus far and utilize tetrazines and strained alkenes and occasionally, strained alkynes (Figure 3-5a).

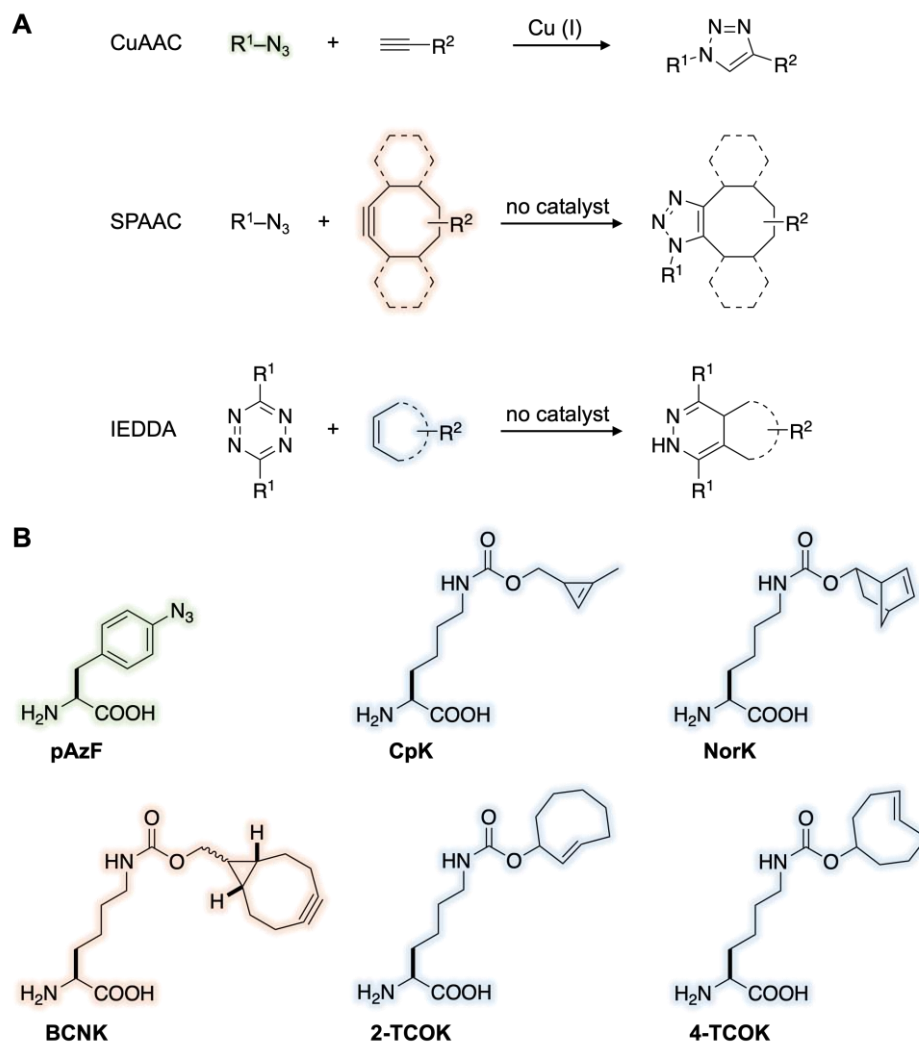


Figure 3-5 Structures of representative unnatural amino acids bearing bioorthogonal handles

a) The reaction partners for three common cycloadditions are shown. b) Representative UAAs with bioorthogonal reactive handles are shown. Color coding of the amino acids are matched to the reaction type, with the exception that **BCNK** can undergo both SPAAC and IEDDA reactions.

Representative bioorthogonal amino acids are discussed here; however, this is by no means a comprehensive discussion of these UAAs. A *p*-azidophenylalanine, **pAzF**, was genetically encoded by the Schultz lab (Figure 3-5b) and utilized for copper-mediated cycloadditions with various fluorophores to demonstrate site-specific protein labeling,¹⁷²⁻¹⁷³ and was later applied for

a Staudinger ligation using an appropriate phosphine.¹⁷⁴ A cyclopropene-containing lysine, **CpK**, was encoded and used in photoclick reactions with tetrazoles.¹⁷⁵ The Chin lab later applied **CpK** for tetrazine ligations and applied this for proteome labeling in mammalian cells and fruit flies.¹⁷⁶ Addition of norbornene to lysine produced **NorK**, which was genetically encoded by our lab, in collaboration with the Chin lab, in both *E. coli* and mammalian cells, and labeling of cell surface modified proteins with tetrazine-fluorophore conjugates was performed and showed near quantitative and rapid labeling.¹⁷⁷ A strained cyclooctyne (bicyclo[6.1.0]nonyne) was attached to lysine to generate **BCNK** that then reacted with an azide-fluorophore.¹⁷⁸ In addition to reacting with azides, **BCNK** can undergo Diels-Alder reactions with tetrazines that occur even faster.¹⁷⁹ A strained cyclooctene in the *trans*-configuration conjugated to lysine at the 4-position resulted in generation of **4-TCOK** that was incorporated separately by the Lemke and Chin labs and used for cell surface labeling with a variety of tetrazine-modified fluorophores.¹⁷⁹⁻¹⁸⁰ The Lemke lab later developed a **2-TCOK** that is more stable,¹⁸¹ however, tetrazine conjugations with **2-TCOK** have been shown to undergo β -elimination, leading to generation of a native lysine.¹⁸² Follow up applications with both the **2-** and **4-TCOK** analogs showed that they could be used for attachment of super resolution imaging probes.¹⁸³⁻¹⁸⁵

While tetrazine-TCO ligations are the fastest, there are some limitations of these reactions when applied in cell-based experiments. The **4-TCOK** is susceptible to attack by cellular thiols, while the **2-TCOK** seems to be protected from this side reactivity as a result of the alkene proximity to the carbamate. Isomerization to the *cis*-isomer produces a non-reactive tagged-protein that cannot be separated from the desired TCOK-modified sample, thus in these cases, quantitative conversion becomes impossible.¹⁷⁹ In recent years, the Fox lab developed a clever silver(I) complexation strategy for improving the shelf-life and stability of the *trans*-isomer without

affecting reaction rates toward tetrazines.¹⁸⁶⁻¹⁸⁷ An alternative strategy to improve TCO stability is the introduction of a water-soluble vitamin E analog, Trolox, to prevent undesired thiol side reactions.¹⁸⁶ For the purpose of the work detailed here, we chose to utilize **NorK** as it does not suffer from the side reactivity observed by the other strained alkenes, while still affording sufficiently fast reaction rates with a variety of tetrazines. Additionally, **NorK** is more synthetically accessible than the more reactive alkene-containing UAAs, thus making it an attractive starting point.

3.3 Mapping of Protein Oxidation via Light-Induced Localized Oxidation

We envisioned that the incorporation of a bioorthogonal unnatural amino acid would enable the site-specific attachment of a small molecule ROS generator, affording more precise control of targeted protein oxidation/inactivation as compared to existing methodologies. Although the exact mechanism of ROS generation is not fully characterized, ROS are thought to travel through an inner channel of protein-based photosensitizers, thus producing multiple “clouds” of ROS at opposite ends of the protein barrel (Figure 3-6a). As a result, the ROS are not optimally positioned at the desired site of inactivation, here denoted as an enzyme active site. In contrast, our design aims to utilize an unnatural amino acid proximal to the desired inactivation site, which can undergo a bioorthogonal reaction with a ROS generator fused to the appropriate reactive handle such that the ROS generator is spatially confined (Figure 3-6b).

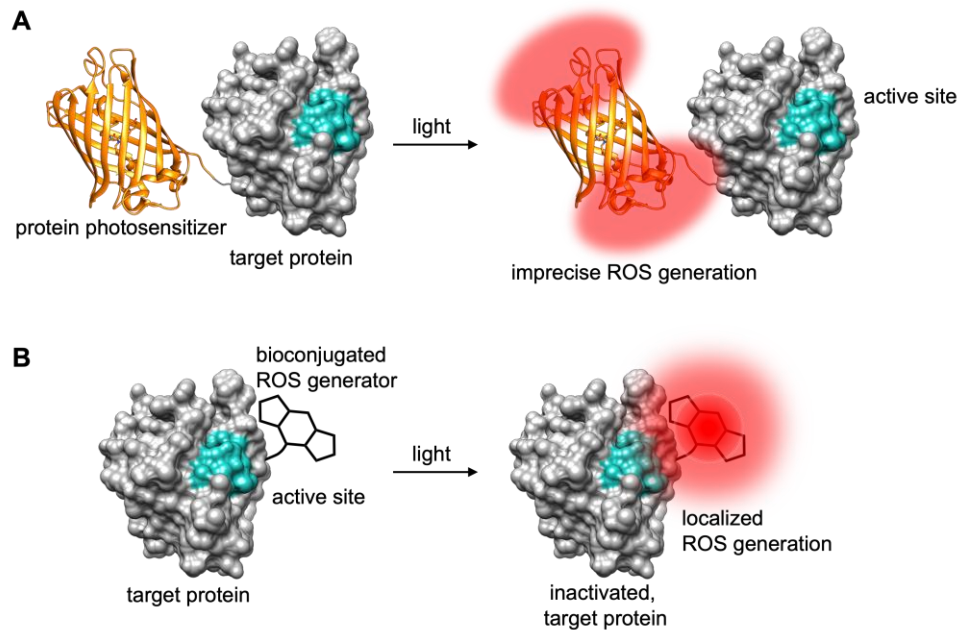


Figure 3-6 Schematic of localized ROS production for protein oxidation and inactivation

a) With traditional protein photosensitizers, generated ROS travels out the inner channel as indicated by the red cloud and depending on the site of attachment, may or may not reach the active site of the target protein prior to being quenched. b) Through the introduction of the ROS generator via a bioconjugation reaction with a UAA-bearing target protein, the ROS generator can be proximally located near the desired site, such that the generated ROS cloud is capable of reacting with nearby side chains.

In preliminary studies, which are the focus of this document, we aimed to generate targeted ROS in order to simply oxidize and inactivate proteins of interest in a proof-of-concept manner. However, upon development of the technology, the long-term goal is to apply the approach for protein-protein mapping as overviewed in Figure 3-7. Current technologies such as APEX¹⁸⁸ and BioID¹⁸⁹ use enzymes fused to the “bait” protein such that upon addition of biotin-phenol and hydrogen peroxide or simply biotin, respectively, these enzymes are activated and label nearby proteins with a biotin handle (Figure 3-7a,b).¹⁹⁰ These approaches have been widely explored for the goal of protein-protein mapping; however, background labeling has been observed and both approaches suffer from similar issues as protein photosensitizer fusions in that the positioning of the enzyme on the bait protein can interfere with protein function/localization due to the large size (28 – 35 kDa). An alternative strategy employs a small molecule iron-based sensor (FeBABE)

which alkylates surface cysteines and can induce protein side chain oxidation upon addition of hydrogen peroxide (Figure 3-7c).¹⁹⁰⁻¹⁹¹ In our design (Figure 3-7d), the small molecule ROS generator will be localized to a user defined site such that upon irradiation, both the target protein (blue) and any interacting proteins (orange) will undergo oxidation, which can be stably trapped with a tagged hydrazine,¹⁹²⁻¹⁹³ followed by LC-MS/MS analysis to determine sites of oxidation/labeling. All three of the existing approaches are limited in their temporal resolution in that upon addition of the biotin or hydrogen peroxide reagents, the reaction will proceed until the cells are lysed (and in the case of BioID, this reaction typically proceeds for ~24 hours); whereas with our approach, ROS will only be generated at a user-defined time and several pulses of irradiation can be performed for controlling different levels of oxidation/mapping with spatial control.

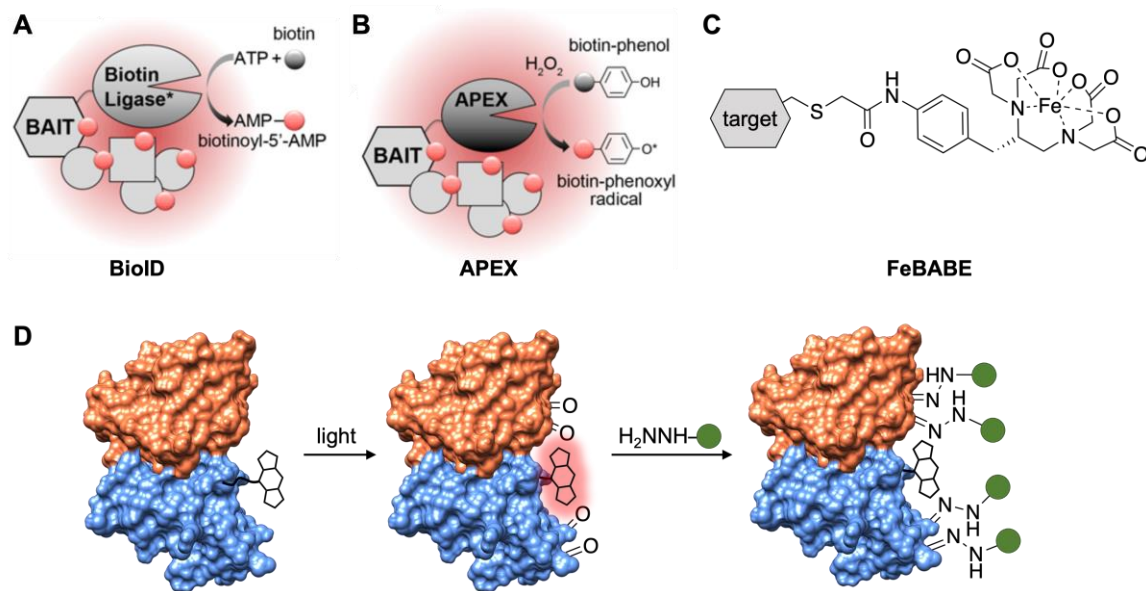


Figure 3-7 Overview of protein-protein mapping approaches

a) BioID utilizes a biotin ligase enzyme which upon addition of high concentrations of biotin will label neighboring proteins with biotin. b) APEX uses an ascorbate peroxidase which is activated upon addition of hydrogen peroxide and biotin to generate a biotin-phenoxyl radical which labels nearby proteins. c) FeBABA uses the reagent Fe(III) (S)-1-(*p*-bromoacetamido-benzyl)ethylene diamine tetraacetic acid to alkylate cysteine residues such that in the presence of hydrogen peroxide and ascorbic acid, protein side chains are oxidized. d) Our strategy uses a site-specific ROS-generator to induce localized oxidation that can be trapped with various hydrazines, which can be subsequently identified via LC-MS/MS. Panels (a) and (b) are adapted from Trinkle-Mulcahy, L. *F1000*, **2019**, 8, Faculty Rev-135. Copyright 2019 Laura Trinkle-Mulcahy.

In order to overcome an inherent limitation of existing small molecule photosensitizers, we hypothesized the use of a turn-on ROS generator would help to minimize background, undesired ROS generation due to incomplete removal of unbound probe. Several turn-on fluorescent probes have been developed in recent years using a variety of reactive groups such as the reduction of an azide to an amine to trigger a self-immolative release, nucleophilic attack of a closed-form xanthene derivative to generate the open-form, and oxidative cleavage of boronates with hydrogen peroxide.¹⁹⁴⁻¹⁹⁷ However, for the purpose of this work, we focus on the tetrazine-fluorophore moiety.¹⁹⁸ These probes contain a tetrazine functionality either in direct conjugation or proximally linked to a fluorophore such that the fluorescence is quenched via through-bond energy transfer (TBET) or fluorescence resonance energy transfer (FRET), respectively. Following a successful bioconjugation reaction, the tetrazine is converted to a dihydropyridazine which no longer functions as a quencher, turning on fluorescence. This approach has been utilized for the turn-on control of coumarin, rhodamine, and BODIPY dyes and has enabled protein labeling and super resolution imaging in mammalian cells.^{194, 198-199} We hypothesized that the same approach could be applied to iodinated-BODIPY analogs in order to generate “turn-on” ROS generators (Figure 3-8). Both TBET and FRET analogs **2** and **3** were synthesized by Anirban Bardhan, as there are (dis)advantages to both types of quenchers. TBET quenching is more efficient than FRET due to the rigid, conjugated linker; however, the rigidity and short nature of this linker may lead to steric interactions that preclude the bioconjugation reaction from occurring.²⁰⁰⁻²⁰¹ Additionally, TBET does not require spectral overlap for efficient quenching, while FRET (as the name implies) does require spectral overlap.

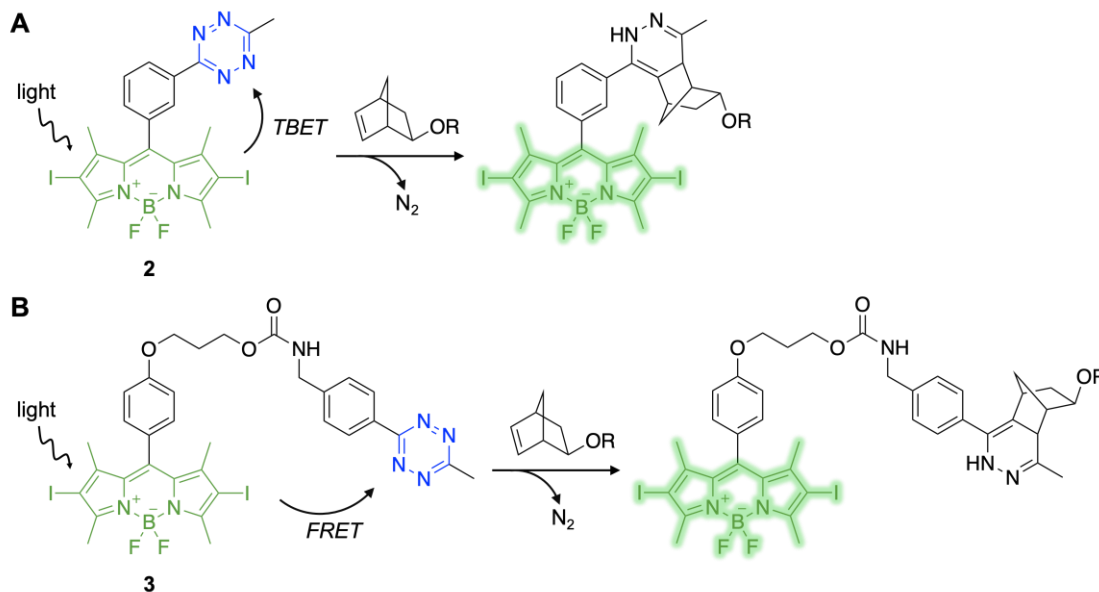


Figure 3-8 Turn-on tetrazine-BODIPY ROS generators

Two different quenched iodo-BODIPY-tetrazine ROS generators were synthesized by Anirban Bardhan. Tetrazine **2** utilizes TBET quenching, while **3** utilizes FRET. Upon successful cycloaddition (shown with norbornene here), a dihydropyridazine is generated, which no longer functions as a quencher, enabling ROS generation.

Anirban Bardhan tested the turn-on nature of tetrazine **2** using the singlet oxygen sensor 1,3-diphenylisobenzofuran (DPBF, **4**). This fluorescent sensor readily reacts with singlet oxygen to form a peroxide intermediate that decomposes to the non-fluorescent dibenzoylbenzene (Figure 3-9a), thus, in the presence of high levels of ROS, a loss of fluorescence is observed. Irradiation of the sensor alone showed no change (black trace), while the iodo-BODIPY-tetrazine **2** showed minimal background ROS generation, indicating incomplete quenching (blue trace); however, upon reaction with **NorK**, the ROS generation roughly doubled (orange trace) showcasing that **2** can be used as a turn-on ROS generator (Figure 3-9b).

Around the same time, the Vázquez lab reported similar findings using tetrazine **2** and a different FRET-quenched tetrazine.²⁰² They report changes in quantum yield for **2** of 0.217 to 0.505 upon reaction with norbornene, which is a 2.3-fold increase in ROS generation. Unfortunately, for their FRET-based quencher, the quantum yield changes were 0.440 to 0.473, which only corresponds to a 1.08-fold increase, implicating very poor FRET-based quenching.

They utilized **2** to show light-induced phototoxicity only upon treatment with *trans*-cyclooctenol in HeLa cells. In a follow up study, they treated cells with 5-vinyl-2'-deoxyuridine which was incorporated into DNA by endogenous cellular machinery during cell division, then following a bioconjugation reaction with **2**, they demonstrated light-induced DNA damage. Based on their work and our preliminary DPBF assay, use of tetrazine **2** would be the best option for proceeding with a turn-on ROS generator.

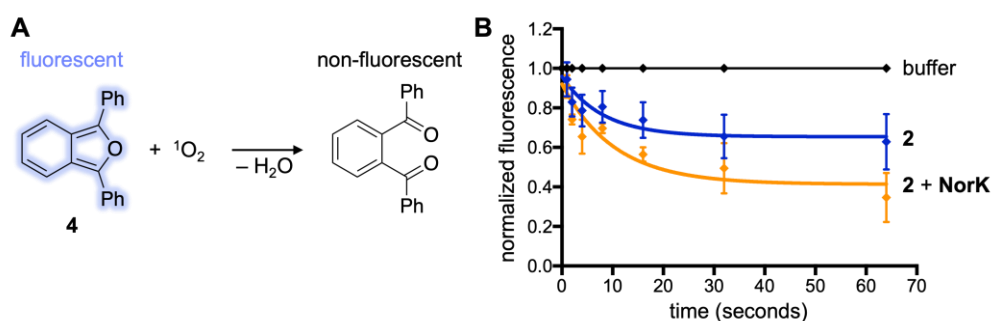


Figure 3-9 Validation of turn-on ROS generation

a) The DPBF sensor **4** reacts with singlet oxygen to generate an unstable peroxide intermediate which rapidly decomposes to a non-fluorescent product. b) The sensor alone (black) shows no change upon increased irradiation with 530 nm light. The tetrazine **2** showed some background ROS generation (blue); however, upon treatment with **NorK**, an even greater ROS generating capability was observed (orange), thus demonstrating the turn-on nature of **2**. Experiment was conducted by Anirban Bardhan.

Given the previous success using **NorK** as a genetically encoded bioorthogonal handle in our lab (in collaboration with the Chin lab) and its ease of synthesis, we proceeded with the encoding of **NorK** into sfGFP as a proof-of-concept target protein. We selected sfGFP for the following reasons: (1) high yielding expression for many different UAAs, and (2) simple, functional readout of protein inactivation via GFP fluorescence measurements on a plate reader or via in-gel fluorescence. Bacterial protein expression and genetic encoding of **NorK** into sfGFP was performed by Anirban Bardhan.

Because our long-term goal is to determine the specific sites of oxidation, we first performed in-gel analyses to characterize the native and modified sfGFP sequences and locate the site-specific incorporation of **NorK**. In collaboration with the Yates lab (Cell Biology, University

of Pittsburgh), in-gel digestions were carried out using trypsin and chymotrypsin, followed by LC-MS/MS analysis on a nano-flow liquid chromatography system (Dionex RSLC) coupled to an ion trap mass spectrometer (Finnigan LTQ). Protein sequence identification was achieved via a database search engine (Matrix Science MASCOT) and a modified database (Uniprot-Jellyfish, with in-house modifications). The database search considered a fixed modification of cysteine (Cys – carbamidomethyl) and three variable modifications (Met – oxidation, N-terminal – acetylation, and Tyr – NorborneneLysine). A tolerance of 1.4 and 0.8 Da was used for the precursor and product ion m/z ratios, respectively. Figure 3-10 shows the identified sfGFP peptides (shaded with blue and green coloring) mapped onto the sfGFP protein crystal structure. High sequence coverage was observed with both trypsin and chymotrypsin, and the amino acid residues proximal to **NorK** (and the eventual ROS generator) were covered in both the wild-type and **NorK**-sfGFP samples. These data support the feasibility of detecting site-specific modifications of **NorK**-sfGFP in future experiments.

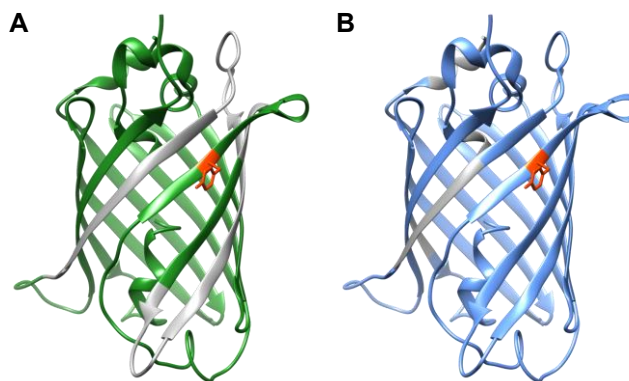


Figure 3-10 MS/MS coverage of sfGFP peptides using trypsin and chymotrypsin
The peptide matches from a MASCOT database search were mapped onto the structure of sfGFP (PDB: 2B3P) to illustrate which regions were detectable upon enzymatic digestion with trypsin (a) and chymotrypsin (b).

Next, the MS/MS spectrum for the triply charged **NorK**-incorporated peptide LEYNFNSHNVXITADK (where **X** = **NorK**) was reviewed to confirm the sequence. Briefly, collision activated dissociation of an ion at m/z 677.3 was carried out using an ion trap mass

spectrometer (Finnigan LTQ) to produce a tandem mass spectrum that is dominated with b-type and y-type fragment ions. *In silico* fragmentation (Protein Prospector MS-product – UCSF) was used to generate a list of possible product ions, which were then manually compared to the experimental spectrum (Figure 3-11). Observation of the b_{10}^+ , b_{11}^{2+} , y_5^+ , and y_8^+ confirm the site-specific incorporation of **NorK** in the sfGFP tryptic peptide.

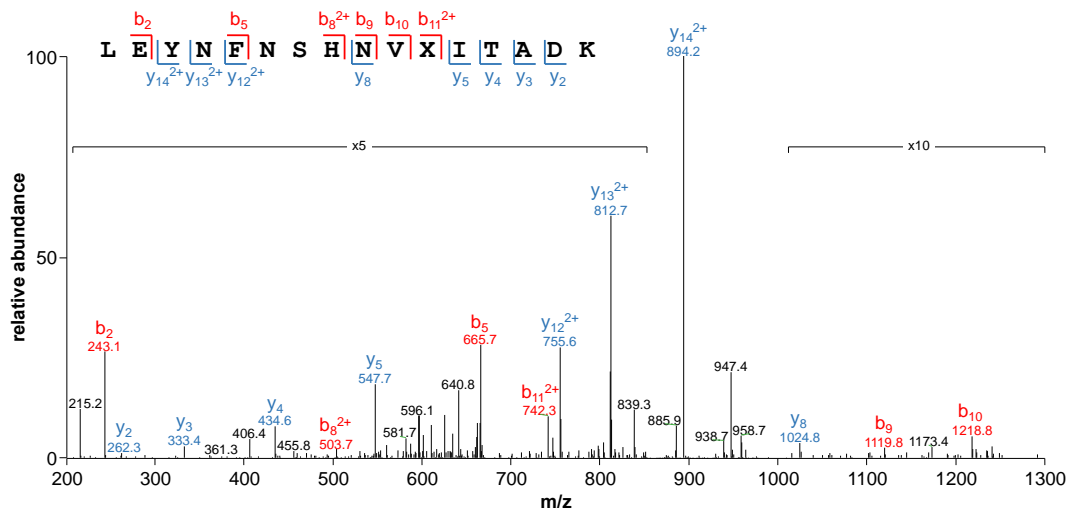


Figure 3-11 MS/MS analysis of **NorK**-modified sfGFP
Tandem mass spectrum of **NorK**-modified peptide with b and y ions denoted in red and blue, respectively.

After identifying the **NorK**-containing peptide in sfGFP, we wanted to validate that we could detect the product following a bioconjugation reaction. For this preliminary study, Anirban incubated **NorK**-sfGFP with the dipyrindyl-tetrazine **5** (Figure 3-12a) at room temperature overnight in phosphate-buffered saline (PBS) at a final DMSO concentration of 10%. Following SDS-PAGE analysis and subsequent in-gel tryptic digestion, the sample was analyzed by LC-MS/MS in the same manner as before. Figure 3-12b shows the CAD spectrum for the **NorK**-incorporated peptide LEYNFNSHNVZITADK at m/z 746.8 where **Z** = **NorK-5** side chain. The presence of the b_{10}^+ and y_5^+ ions support the successful bioconjugation reaction.

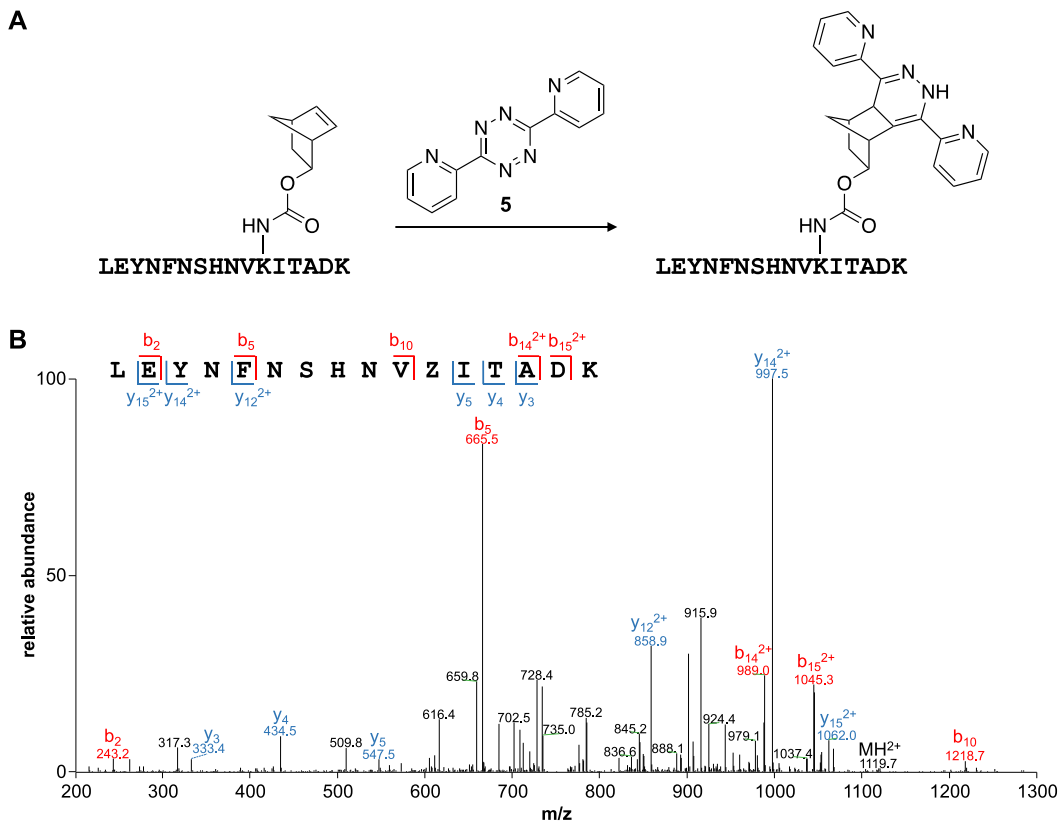


Figure 3-12 MS/MS analysis of the conjugated product of **NorK**-sfGFP and **5**

a) **NorK**-sfGFP was incubated with dipyrrolyl-tetrazine **5**, performed by Anirban. b) Tandem mass spectrum of a **5-NorK**-modified sfGFP peptide. Here **Z** refers to the **NorK-5** side chain.

We proceeded with testing the bioconjugation reactions of **NorK**-sfGFP with iodo-BODIPY-tetrazines **2** and **3** by varying the incubation time (Figure 3-13 – conducted by Anirban). Samples were again analyzed using a standard in-gel protein procedure. Unexpectedly, in the reaction with **2**, the expected product peptide was not detected via LC-MS/MS analyzed in a data-dependent (DDA) manner. A targeted method was designed to search for the m/z corresponding to the 2+ and 3+ charge states of the non-reacted **NorK**-peptide and the **2-NorK**-peptide conjugated product peptide. In DDA, if the desired peptide (and m/z) was of low abundance, it might not have been isolated for fragmentation in the typical Top8 method used for all previous analyses, thus a targeted method has the potential for improving the sensitivity in this case. Unfortunately, the target peptide was not confirmed using a targeted method either. The unreacted **NorK**-peptide was

observed with similar relative abundance in samples collected before and after reaction, and may suggest that the reaction efficiency was low. Additional experiments would need to be conducted in order to attempt to quantify the conversion in this type of experiment.

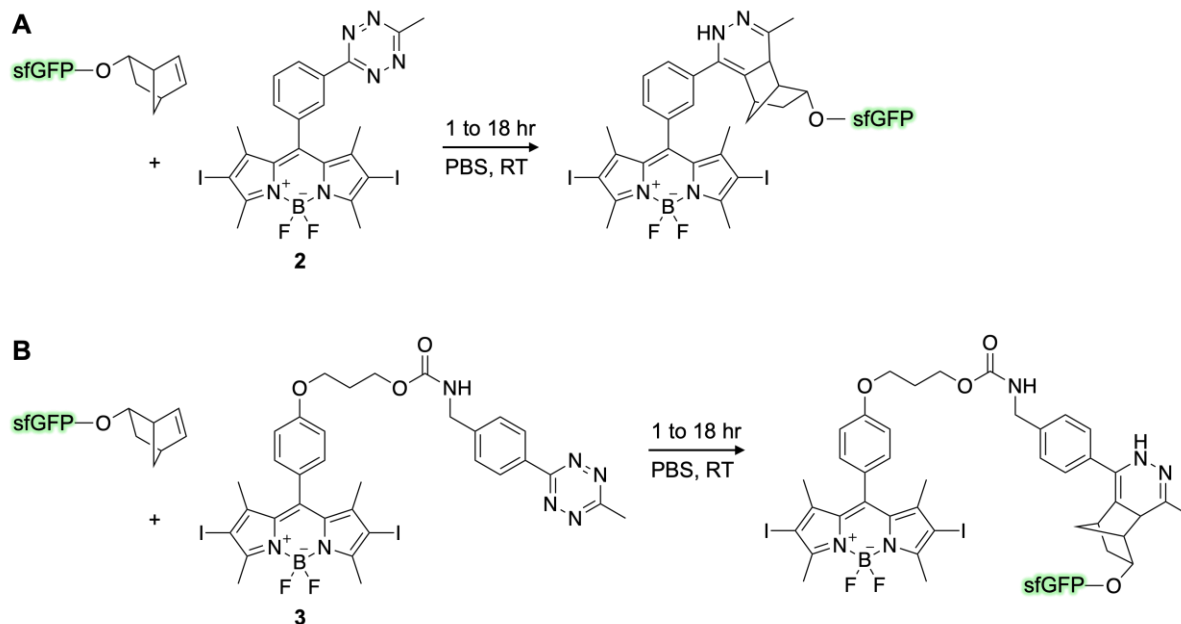


Figure 3-13 Bioconjugation reactions of **NorK-sfGFP** with iodo-BODIPY-tetrazines **2** and **3**
 Bioconjugation reactions between **NorK-sfGFP** and two different iodo-BODIPY tetrazines **2** and **3** were assembled by Anirban Bardhan. Reaction time was varied from one hour to overnight. Samples were analyzed via SDS-PAGE, and tryptic digestion was performed from excised gel bands.

For the reaction between **3** and **NorK-sfGFP**, the LC-MS data showed a qualitative decrease in signal intensity for the m/z corresponding to the starting **NorK**-peptide; however, the corresponding CAD spectrum (Figure 3-14a) did not contain matching fragment ions for the **3-NorK**-peptide. Interestingly, several of the observed product ions closely matched the spectra acquired in Figure 3-11 for the starting **NorK**-peptide and the most intense fragment ion matched the mass of the 2+ charge state of the starting **NorK**-peptide (Figure 3-14b). Thus, it seemed that the bioconjugation product might be undergoing an unexpected gas phase fragmentation to generate a product that closely matched the starting **NorK**-peptide.

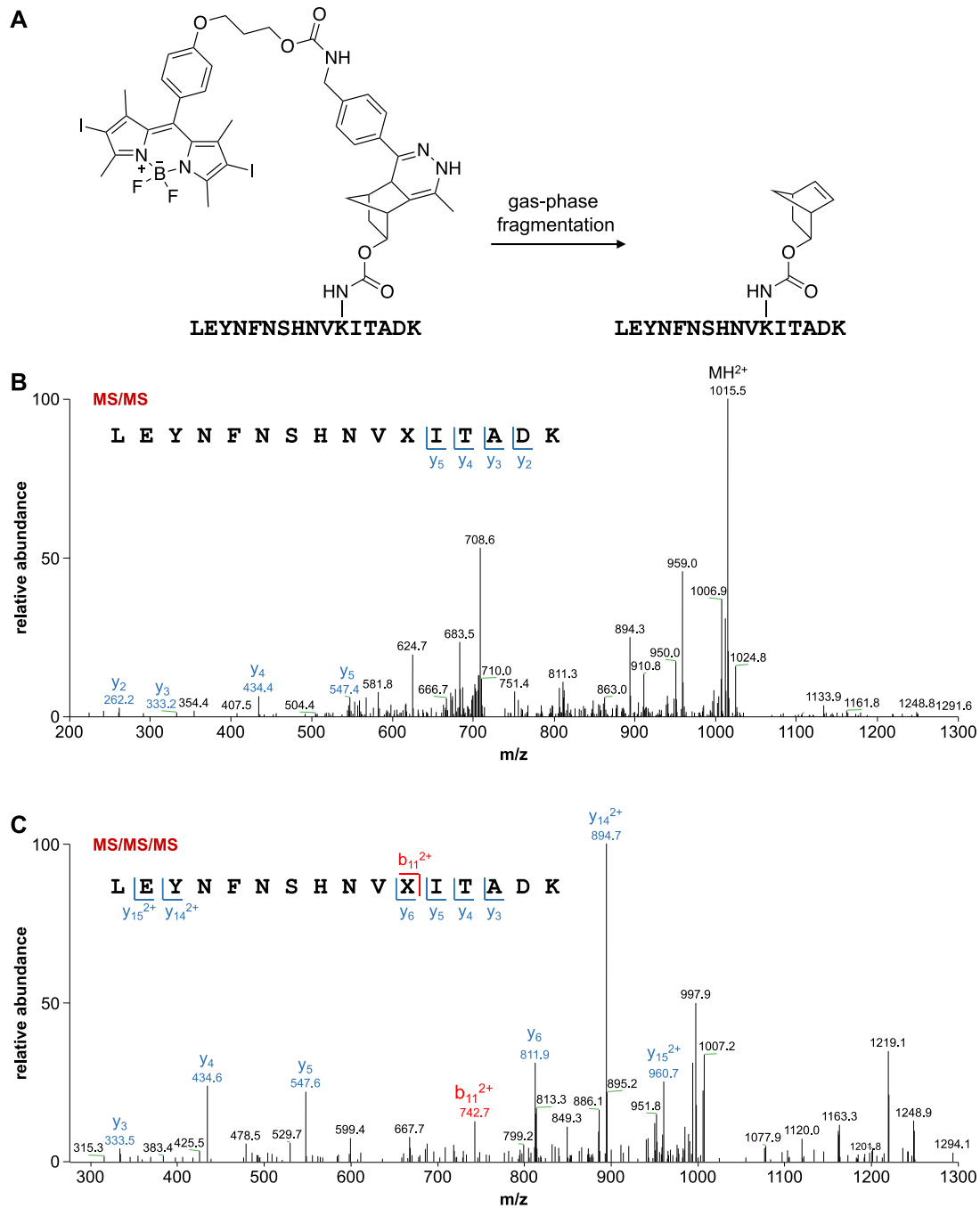


Figure 3-14 Tandem MS/MS/MS analysis of a **3-NorK**-sfGFP peptide

a) The expected product peptide may potentially undergo gas phase fragmentation to regenerate the **NorK**-peptide, based on the daughter ions generated in (b) and (c). b) The product **3-NorK**-peptide was selected at m/z 720.3 and fragmented; however, the observed ions do not match *in silico* predictions. c) The most intense ion from (b) was selected at m/z 1015.5 and fragmented. This produced a spectrum that closely matched the starting **NorK**-peptide.

To further explore this, we designed an MS/MS/MS experiment that first isolated the bioconjugation product **3-NorK**-peptide (m/z 720.3), followed by isolation and fragmentation of

an m/z corresponding to the starting **NorK**-peptide (m/z 1015.5). The spectrum (Figure 3-14c) closely matches that of the starting **NorK**-peptide from Figure 3-11, further supporting the possibility that we generated the product peptide. Unfortunately, in order to validate this, the **3-NorK**-peptide needs to be synthesized and analyzed in an identical manner in order to compare the MS2 and MS3 spectra from both samples.

In the absence of mass spectrometry confirmation of the bioconjugation product, we proceeded to test this in a functional assay in hopes that if the functional assay were successful, we could show the conjugation reaction must have been successful. To do this, **NorK**-sfGFP was reacted with an excess of tetrazine **3** (10 equivalents) for four hours, then unreacted **3** was removed by extraction with diethyl ether. The protein samples were then irradiated with a 530 nm LED for various times, then SDS-PAGE analysis was performed (Figure 3-15a,b). No change was observed via Coomassie staining, while a decrease in GFP signal was observed via in-gel fluorescence imaging. Based on these preliminary results, it appeared that the conjugation reaction occurred, and light-induced protein oxidation was successful. Next, we attempted to validate these results using biochemical methods to detect protein carbonylation. The most widely utilized method involves the reaction of 2,4-dinitrophenylhydrazine (DNPH, **6**) with protein carbonyls to generate the corresponding hydrazones (Figure 3-15c), which can be detected using antibodies against the dinitrophenyl moiety.²⁰³⁻²⁰⁶ The same experiment was repeated, the samples were separated on SDS-PAGE, then transferred to a PVDF membrane which was incubated with **6** to label any side chain oxidation. Western blot analysis against the DNP-epitope showed an unexpected result (Figure 3-15d) in that all samples were labeled to a similar degree, including the non-**3** treated sfGFP sample (lane 1).

In an effort to analyze the degree of oxidation, these samples were analyzed by in-gel protein identification. Following a MASCOT search for various side chain oxidations, the level of oxidation was assessed by summation of the number of oxidized peptides divided by the total number of peptides identified. Unfortunately, in this analysis, high levels of background oxidation in the non-BODIPY treated samples and the BODIPY-treated non-irradiated samples (lanes 1 and 2) were observed. Future analyses should analyze the relative abundance of the identified oxidized peptides between the different conditions in order to determine the extent of oxidation since the spectral counting method used previously did not account for prevalence or abundance of signal.

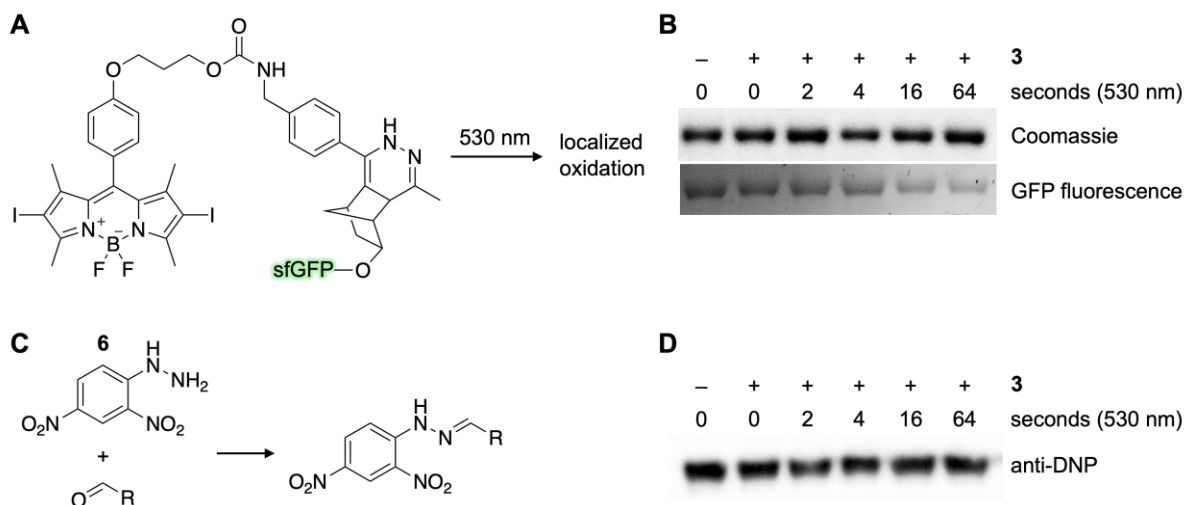


Figure 3-15 Light-induced oxidation of **3-NorK**-sfGFP

a) **NorK**-sfGFP was reacted with tetrazine **3**, followed by ether extraction to remove unbound compound. Samples were irradiated for increasing times with 530 nm light, then analyzed by Coomassie staining and in-gel fluorescence (b). c) Biochemical methods to detect protein carbonylation utilize the hydrazine **6** to generate a DNP-hydrazone which can be detected using an anti-DNP antibody. d) The experiment in (b) was repeated, samples were analyzed via SDS-PAGE, then transferred to PVDF membrane, followed by incubation with **6**. Western blot analysis against the DNP-epitope showed equivalent labeling for all samples.

In an effort to elucidate what was contributing to the background DNP-labeling of the **NorK**-sfGFP sample, we decided to test a few additional sfGFP variants under similar conditions. The wild-type sfGFP protein contains a tyrosine at position 151, thus to determine whether the labeling was inherent to sfGFP, we used this as a control. Additionally, we hypothesized that the carbamate or strained alkene of the **NorK** side chain might be reacting with the hydrazine, thus

we opted to compare this with an aliphatic alkene found in **AllocK** (Figure 3-16a). The three sfGFP protein samples were electrophoresed, followed by transfer to a PVDF membrane, then incubation with **6**. Anti-DNP western blot analysis showed a substantially higher degree of labeling for the **NorK**-sfGFP, indicating that the strained alkene might somehow be reacting with **6** (Figure 3-16b). Additional experiments should be conducted in order to confirm these findings and to determine the structure of the product being generated between the reaction of **NorK** (or the simpler norbornene alcohol) and **6**.

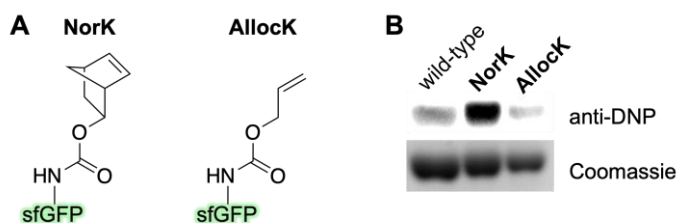


Figure 3-16 Background DNP-labeling of **NorK**-sfGFP

a) **NorK**-sfGFP and **AllocK**-sfGFP side chains are shown for comparison. b) Wild-type sfGFP, **NorK**-sfGFP and **AllocK**-sfGFP were electrophoresed, transferred to PVDF, and incubated with **6**. Prominent labeling of **NorK**-sfGFP versus the other two samples was observed.

To further validate and optimize the DNP-labeling for future oxidation studies, we decided to generate a positive control for protein carbonylation based on literature reports.²⁰⁷ A metal-catalyzed Fenton oxidation was performed (Figure 3-17a) using BSA as a test protein with two different conditions that were reported to yield low and high degrees of protein carbonylation (obtained by varying the concentrations of iron and hydrogen peroxide in the reaction).²⁰⁷ In this reaction, hydrogen peroxide and iron (II) generate hydroxyl radical ions which react with protein side chains in a similar manner as singlet oxygen. We compared two different **6**-labeling approaches: (1) immobilized, on-membrane labeling, post electrophoresis and transfer and (2) in-solution **6**-labeling, followed by the standard electrophoresis and transfer (Figure 3-17b). We were only able to detect protein carbonylation using the in-solution method, and the extent of labeling correlates with the low and high degrees of oxidation. The slight decrease observed in the

Coomassie loading control can be attributed to the decreased affinity of the Coomassie G-250 reagent toward oxidized proteins, as has been reported in the literature.²⁰⁷ Further, these samples were analyzed by SDS-PAGE, and subsequent in-gel digestions were performed. Following a MASCOT search for several side chain oxidations, the level of oxidation was assessed by summation of the number of oxidized peptides divided by the total number of peptides identified (as done for the sfGFP samples above). Unfortunately, in this analysis, high levels of background oxidation in the non-treated (no oxidation) sample were observed. Future analyses should identify oxidized peptides, then compare the relative abundance between the different conditions utilizing high resolution LC-MS in order to determine the extent of oxidation.

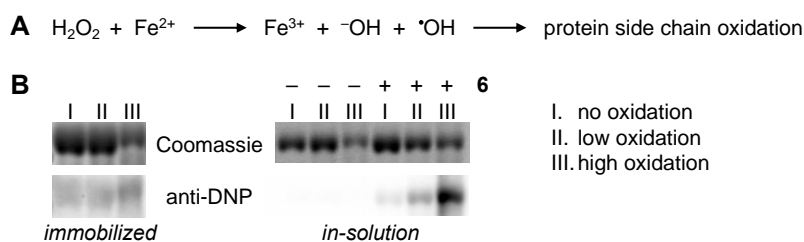


Figure 3-17 Fenton oxidation of BSA and **6**-labeling/detection

a) Fenton oxidation utilizes iron (II) in the presence of hydrogen peroxide (H_2O_2) to generate hydroxyl radical ($\text{}^*\text{OH}$) and a hydroxide ion ($\text{}^-\text{OH}$). Hydroxyl radical can further react with hydrogen peroxide to generate peroxide radicals, both of which can react with protein side chains. b) **6**-labeling was compared using immobilized (on-membrane) versus in-solution approaches in order to determine which approach worked best in our hands.

In addition to sfGFP, we are concurrently applying these strategies to other enzymes that will allow for additional functional readouts. When selecting a new target, we aimed to fulfill a few requirements: (1) established bacterial protein expression protocols in order to obtain sufficient material, (2) readily available substrates or sensors for use as readout of enzymatic function, and (3) availability of a crystal structure in order to select residues proximal to the active site. We selected TEV protease (TEVp) as it met all of the above requirements and also contains a catalytic cysteine that can be readily oxidized.²⁰⁸⁻²⁰⁹ A bacterial protein expression construct was generated by former lab member, Dr. Jihe Liu, in which a maltose-binding protein (MBP) was

fused to a TEV recognition sequence, followed by a His-tagged TEV protease sequence.²¹⁰ In this design, during expression, the MBP tag is post-translationally cleaved such that following nickel purification, a His-tagged TEVp is isolated. Protein expression of this construct was validated and shown to generate sufficient quantities of the wild-type enzyme (data not shown). Next, we analyzed the crystal structure of a catalytically dead (C151A) TEVp bound to the peptide substrate²¹¹ and selected six different residues that were located proximally to the active site, but distal enough (hypothetically) to avoid interfering with enzyme activity or substrate binding (Figure 3-18a). Site-directed mutagenesis was performed to independently generate six different TAG constructs at the selected residues, and plasmids were confirmed by Sanger sequencing. Bacterial protein expression was first performed with **AlloK** at all six mutation sites in order to validate these sites were amenable to UAA incorporation and that the mutants retained enzymatic activity (if TEVp were inactive, a full length MBP-TEVp would be observed). Representative SDS-PAGE images (Figure 3-18b) are included for the two mutants that showed the greatest incorporation efficiency and highest protein yield; however, all six of the mutants retained activity and were successfully expressed with slightly differing yields.

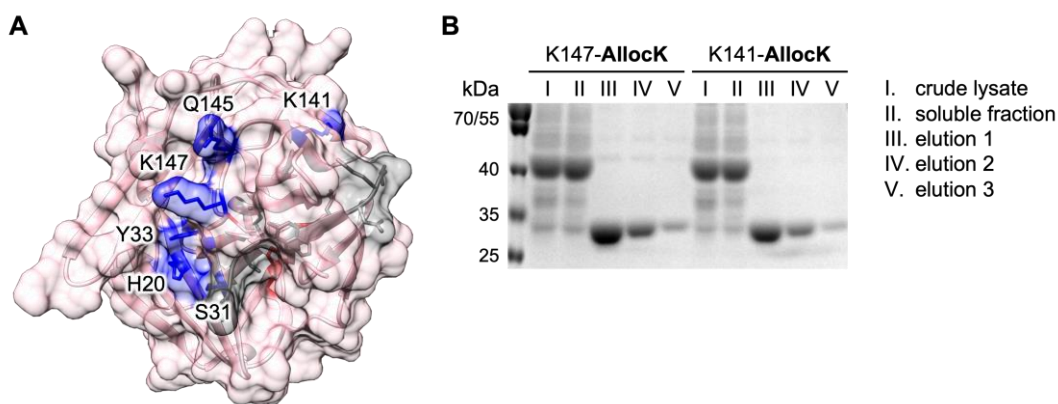


Figure 3-18 Analysis of TEV protease crystal structure for unnatural amino acid incorporation sites
a) The crystal structure of a catalytically dead TEV protease (pink) bound to a TEV peptide substrate (grey) was used for selecting various sites for the incorporation of an unnatural amino acid (PDB: 1LVB). Residues indicated in blue were mutated independently to the amber stop codon TAG. b) Small scale bacterial expressions were performed to (1) confirm protein expression and (2) validate retention of TEV protease activity at the various sites. SDS-PAGE

analysis of two of the mutants (TEV-K147TAG and TEV-K141TAG) shows successful incorporation of **AllocK** and demonstrates that both of these sites allow for retention of enzymatic activity.

A commonly utilized TEV sensor is a circularly permuted luciferase which is inactive in the absence of TEVp; however, in the presence of TEVp, the sensor is cleaved and luminescence can be measured (Promega TEV-GloSensor).^{48,212} Unfortunately, this sensor has only been applied in mammalian cells and has not been expressed and utilized as a purified recombinant sensor. In our preliminary experiments, it would be beneficial to have a sufficient quantity of the substrate for use in experimental and optimization studies. Thus, we decided to generate a protein-based TEV sensor that was originally designed as a caspase sensor by replacing the caspase recognition sequence (DEVD) with the TEVp recognition sequence (ENLYFQG). This sensor utilizes a quenching peptide fused to the C-terminus of GFP, which forms a tetramer in solution and prevents GFP maturation.²¹³ Upon cleavage of the sensor, the quenching peptide is released and GFP matures to produce a fluorescent signal (Figure 3-19a). Kristie Darrah generated a mammalian expression construct of this GFP-TEV-quencher protein fusion and verified the functionality of this sensor in HEK293T cells (data not shown). The coding sequence from this construct was then assembled into a pBAD bacterial expression construct and a C-terminal 6x-histidine tag was added, and the construct was confirmed by Sanger sequencing. Several attempts to generate a soluble protein preparation under different expression conditions were unsuccessful and the protein was always identified in the insoluble fraction following different lysis conditions. Western blot analysis of crude material was performed to verify successful expression using a GFP antibody and expression was confirmed. Future work to explore inclusion body isolation and purification²¹⁴ might enable the production of a soluble TEV protein-based sensor.

Concurrently, we synthesized a TEV fluorophore-quencher peptide sensor. A variety of fluorophore-quencher pairs are available in the literature; however, we wanted to avoid any

spectral overlap with the iodo-BODIPY that would be immobilized on the enzyme, thus we selected methoxycoumarin (MCA) and 5-amino-2-nitrobenzoic acid (ANA). We synthesized a TEV peptide based on a literature reported design (Figure 3-19b) and validated quenching and subsequent turn-on of fluorescence using recombinant TEV protease (0.34 μM) at room temperature and at 37 $^{\circ}\text{C}$ with 1 μM of the TEV peptide substrate (Figure 3-19c-d). A control solution of 1 μM of MCA was analyzed in order to estimate the extent of peptide cleavage. Cleavage assays performed in TEV storage buffer resulted in 44 to 48% cleavage, while assays performed in Glo Lysis Buffer (from Promega) resulted in 73 to 76% cleavage.

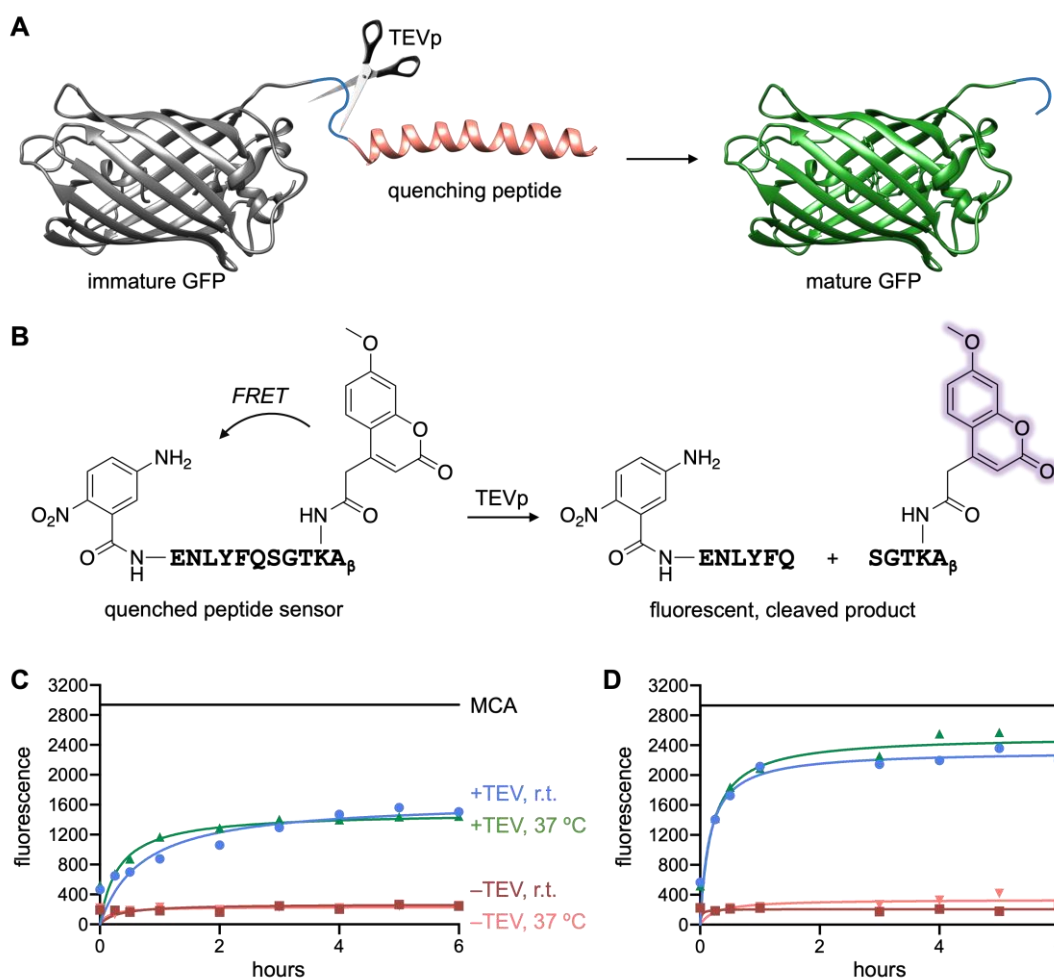


Figure 3-19 Protein and peptide-based TEV protease sensors

a) A protein-based TEV sensor is comprised of GFP fused to a quencher peptide that forms a tetramer to inhibit GFP maturation, until protease cleavage removes the quenching peptide and turns on fluorescence. b) A fluorophore-

quencher TEV peptide substrate was designed such that in the absence of protease fluorescence is quenched; however, in the presence of protease, the sensor is cleaved and fluorescence is turned on. Synthesis was performed by Kristie Darrah. c-d) The TEV peptide substrate (1 μM) was incubated in the presence or absence of recombinant TEV protease (0.34 μM) and fluorescent measurements were acquired over the course of six hours. Both room temperature (r.t.) and 37 °C incubations were tested in two different buffers: TEV storage buffer (c) and Glo Lysis Buffer (d).

3.4 Ongoing Efforts and Future Work

While we were able to detect the bioconjugation product of **NorK**-sfGFP reactions with various tetrazines, we are in the process of exploring alternative UAAs with more reactive handles in order to facilitate quantitative conversion to the ROS generator-modified proteins. Future studies will be conducted using **BCNK** as the reactivity with tetrazines is significantly faster, thus hopefully providing increased product formation within minutes, thereby making it more amenable for future cellular studies. Once the bioconjugation reactions have been established, the immediate next steps are to incorporate **BCNK** into TEVp at either of the two positions (K147TAG or K141TAG), followed by a functional readout of enzymatic activity. If successful, in order to demonstrate the targeted nature of this approach, the ROS-generator should be installed at a distal residue and an analogous experiment performed, in which enzymatic activity should hopefully be unaffected (or minimally inhibited).

For determining sites of modification, in addition to detection of oxidized side chains via the carbonyl-hydrazine reaction with **6**, we could also employ a FOX assay to quantify the extent of side chain peroxide formation following incubation with iron-xylene orange as a colorimetric readout.²¹⁵ While our initial efforts to use mass spectrometry for the identification of oxidized side chains was unsuccessful, there are several avenues for future optimization. Detection of side chain oxidation (or protein carbonylation) by mass spectrometry is not a trivial process as some of the oxidations are quite labile. An additional complication is adventitious oxidation which occurs

during sample handling and processing (*e.g.*, methionine oxidation is a prominent modification introduced during a typical workflow), thus care must be taken during sample preparation to minimize this introduction of background oxidation.²¹⁶ It is common to react oxidized protein samples with hydrazines, hydrazides, or hydroxylamines, followed by reduction (often with sodium cyanoborohydride) to generate stable cross-links.²¹⁷⁻²¹⁸ These can be directly analyzed following tryptic digestion or can be used for enrichment of modified samples prior to analysis.²¹⁹⁻

220

3.5 Methods

Reagents. A 100 mM solution (in water) of **NorK** was provided by Anirban Bardhan. Tetrazines **2** and **3** were synthesized by Anirban Bardhan. **AllocK** was purchased from Chem-Impex (06129). Recombinant EZcut TEV protease was purchased from BioVision as a 1 mg/mL (or 34 μ M) solution (VWR – 10835-726). An anti-DNP antibody was purchased from Millipore Sigma (D9656-2ML). Unlike all other antibodies used, this one was provided in antiserum and upon the initial thaw, aliquots (5 μ L) were prepared in 0.2 mL tubes. When needed for western blot detection, a fresh aliquot was thawed and the remaining volume was discarded. A secondary goat anti-rabbit-HRP antibody was purchased from ProteinTech (SA00001-2).

Cloning of new plasmids. All primers used for cloning are included in Table 3-3. To generate a bacterial expression construct for the GFP-TEV sensor, parent plasmid pCS2-GFP-TEVsensor was obtained from fellow lab member, Kristie Darrah. Primers GFP-TEV-QP-His F/R were used to PCR amplify the coding sequence of the gene, followed by gel extraction and purification. The pBAD backbone fragment was generated by double digestion of pBAD-sfGFPY151TAG-PylT

using NcoI and NdeI, followed by gel extraction and purification. A Gibson assembly was performed using a 3:1 ratio of insert:backbone, and the resulting plasmid was confirmed by sequencing at Genewiz using their pBAD forward and reverse primers.

For the sake of brevity, discussion of **NorK** incorporation into myoglobin was excluded from the results section above (a general protocol is provided in 8.2.1); however, two different TAG sites were cloned into the myoglobin sequence and are described here. The parent wild-type pBAD-myo-pylT plasmid was used as template for a QuikChange mutagenesis reaction (using primers A74TAG F/R) or site-directed mutagenesis reaction (using primers D126TAG F/R) to generate both pBAD-myoA74TAG-pylT and pBAD-myoD126TAG-pylT following protocols in 8.1.2, which were confirmed by sequencing using pBAD forward and reverse primers by Genewiz.

Six different plasmids were generated with TAG sites at various residues. Parent plasmid from Dr. Jihe Liu, pBAD-MBP-TEVp, was used as the template for the six site-directed mutagenesis reactions (using the appropriate combination of F/R primers from Table 3-3). All plasmids were confirmed using pBAD reverse sequencing primers from Genewiz and a custom C-term MBP seq F primer to ensure full coverage of the TEVp region.

Table 3-3 Primers used for generating plasmids used in this chapter

Nucleotide mutations are indicated with CAPITALIZATION and histidine tags are highlighted in grey. These primers were used to generate TAG mutations in pBAD-myo-PyIT and pBAD-MBP-TEVp-PyIT (see Appendix A).

Primer Name	Sequence (5' → 3')
GFP-TEV-QP-His F	aattaaccatggtgagcaagggcgaggagc
GFP-TEV-QP-His R	actgcatatgtaaatggtgatggtgatggtgcagacgatccagaat
A74TAG F	atgatgccctttttcctaaggatctaaccTAGggcagttaacacggtaac
A74TAG R	gttaccgtgtaactgccCTAggtagatccttaagaaaaagggcatcat
D126TAG F	ggtgctTAGgctcaggggtgctatgaacaaagctctcg
D126TAG R	ctgagcCTAagcaccgaagtcacctggatgctagaatg
K147TAG F	caaaccTAGgatgggcagtggtggcagtcattagat
K147TAG R	cccatcCTAggttgaaatccaatgctccagaatagc
K141TAG F	ttctggTAGcattggattcaaaccaaggatgggca
K141TAG R	ccaatgCTAccagaatagccatcagatgaaggggaatg
Y33TAG F	tcgttgTAGggtattggattggcccttcatt
Y33TAG R	aataccCTAcaacgatgttggtgcccacag
S31TAG F	acaacaTAGttgtatggtattggattggccctt
S31TAG R	atacaaCTAtgttggtgcccacagattcattc
H20TAG F	attgtTAGttgacgaatgaatctgatgggcacac
H20TAG R	cgtcaaCTAcaaatggtgctcgatcgggt
Q145TAG F	tggattTAGaccaaggatgggcagtggtggca
Q145TAG R	cttggCTAaatccaatgctccagaatagccatcag
C-term MBP seq F	gggatcgaggggaagggga

Protein identification via in-gel digestion. This protocol is minimally modified from one provided by the BioMS Center. Mass spectrometry grade proteases were purchased from ThermoFisher: trypsin (90057) and chymotrypsin TLCK-treated (90056). Once resuspended, protease solutions were stored at $-20\text{ }^{\circ}\text{C}$ and used for up to one month. DNA synthesizer-grade MeCN (BP1170-4) and Honeywell Burdick & Jackson HPLC-grade water (60-026-52) were purchased from Fisher. All reagents and solutions were prepared using the B&J water. Pipette tips (important: *non-autoclaved*) were used for all volume transfers. Following Coomassie staining/destaining (see 8.3.10 and 8.3.11), gel bands were excised using a scalpel and cut into 1 mm cubes (typically 4 cubes/band), then transferred to a 1.5 mL LoBind Eppendorf tube (Eppendorf 022431081). Bands were destained overnight in freshly prepared 25 mM ammonium bicarbonate in 50:50 MeCN:water (1 mL) in a room temperature shaker (250 rpm). The solution was discarded and a fresh aliquot of destain solution (1 mL) was added and shaken for an additional

one hour. The gel pieces were centrifuged at 13,000 g for 2 minutes, then residual destain solution was aspirated. The bands were dehydrated by the addition of 200 μ L of 100% MeCN, followed by a five-minute incubation at room temperature. MeCN was discarded, the samples were centrifuged at 13,000 g for 2 minutes and residual MeCN was removed. Tubes were placed in a 37 °C incubator for 10 minutes with the caps open to dry any remaining MeCN. Fresh solutions of 25 mM ammonium bicarbonate (referred to as AmBic) in water were prepared daily. A working solution of 10 mM dithiothreitol (DTT) was prepared in AmBic from a 1 M solution in water (see 8.3.26). Fifty microliters were added to each tube and tubes were placed in a 55 °C heat block for one hour. Excess DTT solution was removed and discarded. A working solution of 55 mM iodoacetamide was prepared in AmBic from a 450 mM solution in water (see 8.3.27). Fifty microliters of iodoacetamide were added, and the reaction was allowed to proceed at room temperature in the dark for one hour. Excess solution was removed and discarded. Gel bands were washed with AmBic (150 μ L), vortexed for 5 minutes, then centrifuged at 13,000 g for 10 seconds. The supernatant was discarded, and the gel pieces were dehydrated using MeCN (150 μ L) with a 5-minute vortexing. The solution was discarded and the process was repeated. After removing the solvent, gel pieces were dried for 20 minutes in a 37 °C incubator with the caps open. A 20 μ g vial of trypsin was resuspended in 1 mL of AmBic to afford 20 ng/ μ L of Trypsin. To each tube, 10 μ L of the Trypsin solution was added and tubes were kept on ice for 30 minutes to rehydrate the gel pieces. An additional 50 μ L of AmBic was added to the tubes to ensure that gel pieces were completely covered, then samples were placed in the 37 °C shaker set to 250 rpm overnight. Chymotrypsin digestions were performed in an analogous manner except the 20 μ g vial of chymotrypsin was resuspended in 1 mL of 1 mM HCl and digestions were placed in a 30 °C shaker overnight to minimize Chymotrypsin autolysis. The following day, the digest solution was

collected and transferred to a fresh 1.5 mL LoBind Eppendorf tube. Extraction buffer comprised of 70% MeCN, 5% formic acid, and 25% water was prepared monthly. To each tube, 150 μ L of extraction buffer was added, tubes were vortexed for 5 minutes, sonicated in a bath sonicator for 15 minutes, centrifuged at 13,000 g for 1 minute, then the solution was combined with the overnight digest solution. This cycle was repeated for a total of 3 extractions with a combined final volume of \sim 500 μ L. These solutions were frozen at -80 $^{\circ}$ C for at least 45 minutes (or they can be stored for a few days, if needed), then dried in a speed-vac centrifuge. The dried peptides were resuspended in 18 μ L of 0.1% formic acid in water.

Mass spectrometry. Reversed-phase nano-flow high performance liquid chromatography was performed on an UltiMate 3000 RSLCnano HPLC (Thermo Scientific) coupled to an LTQ ion trap mass spectrometer (Finnigan Corp). Mobile phases A and B were 0.1% formic acid in Burdick & Jackson water and 0.1% formic acid in MS-grade acetonitrile, respectively. A PicoChip (New Objective) Reprisil-Pur C₁₈-AQ column (3 μ m, 120A; 105 mm) was used for the separation of peptides. An autosampler was used for the injection of 1 μ L of sample per run. A 120 minute gradient method was employed with percentages indicating solvent B: 0 to 8 minutes – fixed 2%, 8 to 95 minutes – 2 to 40%, 95 to 97 minutes – 40 to 95%, 97 to 98 minutes – fixed 95%, 98 to 100 minutes – 95 to 2%, 100 to 120 minutes – fixed 2%. The eluent was directed into the LTQ using a nanoflow electrospray source (New Objective). The data-dependent acquisition parameters were: MS precursor scan (m/z of 375 – 1800), with the top eight most intense peaks being isolated and fragmented with CAD (normalized collision energy setting of 35%) and isolation width of 2 m/z . Dynamic exclusion was enabled with the following settings: count – 1, duration – 30 seconds, and list size – 150. A reject mass list with m/z of 371.10 and 445.12 corresponding to polysiloxane contaminants was included.

When a targeted method was necessary, the same LC parameters were employed and a mass list with the appropriate m/z was generated. Isolation widths of 2 m/z were used and normalized collision energy was maintained at 35%. A full MS was acquired for visual inspection of the quality of chromatography and the spectra.

Data analysis. All .raw files were visually inspected using the Xcalibur software to assess quality of the generated chromatogram and spectra. Files were loaded into MASCOT Daemon in order to perform database searches. The following parameters were used in database searches: enzyme – trypsin (or chymotrypsin, in rare cases), max. missed cleavages – 2, peptide charge – 2+ and 3+, average vs monoisotopic – average, peptide tolerance – 1.4 Da, MS/MS tolerance – 0.8 Da, fixed modifications – carbamidomethyl (C), and variable modifications – oxidation (M) and acetyl (N-term). With sfGFP samples, the Uniprot-Jellyfish database was utilized. However, for other custom sequences, a small database “tagged myoglobin” was generated by Mai Sun (BioMS Center) and was employed for various searches.

Analysis of 3-NorK-sfGFP protein oxidation. A 15 μM solution of NorK-sfGFP in 1X PBS and a 20 mM solution of **3** in DMSO were provided by Anirban. A working solution of **3** (0.5 mM) was prepared in DMSO. For a single reaction, final concentrations of 10 μM of protein and 100 μM of **3** were used. In a 0.2 mL PCR tube, 60 μL of 15 μM NorK-sfGFP, 18 μL of 0.5 mM **3**, and 12 μL of 1X PBS were combined and incubated in the dark for four hours. To remove unbound **3**, 100 μL of diethyl ether was added to the reaction mixture, followed by vigorous shaking, then removal of the ether layer (top). This process was repeated six times until the ether layer no longer appeared colored (pink) to the eye. The conjugated protein solution was then split into five 15 μL aliquots in five 0.2 mL PCR tubes. Five irradiation conditions (0, 2, 4, 16, and 64 seconds) were tested using a 530 nm LED (set to 5 mW, as measured by a light power meter). For a control

reaction lacking tetrazine **3**, 10 μL of 15 μM **NorK**-sfGFP, 3 μL of DMSO, and 2 μL of 1X PBS were combined. After irradiation, 6 μL of 4X loading buffer was added to each sample (and to the control reaction), followed by heating at 95 $^{\circ}\text{C}$ for 15 minutes. SDS-PAGE analysis (10% gel) was performed using 6 μL of each sample (two identical gels were loaded – one for Coomassie staining, another for DNP-labeling), and samples were separated using 60 V for 20 minutes, then 175 V for 70 minutes. On-membrane labeling with DNPH and anti-DNP detection was performed as described below in “DNP-labeling on membrane.”

Fenton oxidation of BSA for use as positive control in DNP-labeling. This procedure is closely following a literature report.²⁰⁷ A 0.15 mM (10 mg/mL) BSA stock solution was prepared in milliQ water. Fenton oxidation solutions were prepared as follows: 25 mM FeCl_2 (49.7 mg in 10 mL milliQ water), 25 mM EDTA (0.5 mL of a 0.5 M stock into 9.5 mL of milliQ water), and 50 mM H_2O_2 (51 μL of a commercial 30% solution into 10 mL of milliQ water). Three reactions were assembled: no oxidants, low oxidation, and high oxidation. No oxidants – 333 μL of 0.15 mM BSA solution and 667 μL of 1X PBS; low oxidation – 333 μL of 0.15 mM BSA solution, 2 μL of 25 mM iron (II) chloride, 2 μL of 25 mM EDTA, 2 μL of 50 mM hydrogen peroxide, and 660 μL of 1X PBS; and high oxidation – 333 μL of 0.15 mM BSA solution, 10 μL of 25 mM iron (II) chloride, 10 μL of 25 mM EDTA, 10 μL of 50 mM hydrogen peroxide, and 636 μL of 1X PBS. Reactions were incubated at 37 $^{\circ}\text{C}$ for eight hours, acidified by the addition of 10 μL of concentrated TFA (1% final), then stored at -80°C . A quenching step (performed prior to acidification) using thiourea has been reported in some biological applications of the Fenton oxidation.²²¹

In-solution DNP-labeling. A literature procedure was used as a starting point²⁰⁶ for the modified protocol below. Protein samples were dialyzed for a buffer to water exchange using a 10 kDa spin

column (VWR PES Centrifugal Filters – 82031-348) and milliQ water (3 x 500 μ L). Protein concentrations of all samples were determined via Bradford assay, then diluted to 1 μ g/ μ L in milliQ water. A 10 mM DNPH solution was freshly prepared in 2.5 M HCl. Forty microliters (40 μ g) of protein solution was mixed with 160 μ L of the DNPH solution for a total 200 μ L reaction volume. Samples were incubated in the dark for one hour at room temperature. A non-labeled negative control reaction was prepared by mixing 40 μ L of protein with 160 μ L of 2.5 M HCl alone. A 100% trichloroacetic acid (TCA) solution was prepared by dissolving 2.2 g of TCA in 1 mL of milliQ water. To the 200 μ L labeling reaction, 50 μ L of 100% TCA was added and samples were incubated on ice for one hour to facilitate protein precipitation (note: no visible precipitate was observed, potentially due to low protein amounts used). Precipitated proteins were pelleted at 10,000 g for 5 minutes at 4 $^{\circ}$ C, and the supernatant was discarded. The pellets were washed with 200 μ L of 1:1 ethyl acetate:ethanol, followed by centrifugation at 10,000 g for 5 minutes at 4 $^{\circ}$ C, and two wash cycles were performed. Pellets were dried by leaving tube lids open and incubating for 30 minutes at room temperature, then resuspended in 40 μ L of 1X PBS (assuming full recovery to yield 1 μ g/ μ L again).

Labeling efficiency was measured both via dot blot and western blot. For the dot blot, 0.45 μ m nitrocellulose membrane was cut to 0.5 x 1.5-inch pieces. Two microliters were directly spotted onto the membrane and allowed to dry (two membranes were prepared identically, one for dot blot and one for total protein staining). The membranes were blocked overnight with 3 mL of 5% milk in PBST (1X PBS + 0.1% Tween-20) in a cold room with rocking. The following day, both were washed thrice for 5 minutes each time with PBST (6 mL). One membrane was stained with AmidoBlack 10B (see 8.2.12), while the other was incubated with anti-DNP antibody at 1:20,000 (1 μ L in 20 mL of 5% milk in PBST) for one hour at room temperature with rocking.

Three 5-minute washes with PBST (6 mL) were performed, then a goat anti-rabbit secondary antibody was applied at 1:10000 in PBST (10 mL) for one hour at room temperature. Following three 5-minute PBST (6 mL) washes, the membrane was developed using a chemiluminescent substrate, then imaged on a ChemiDoc.

For western blot analysis, samples were prepared by mixing 10 μ L (10 μ g) of DNP-labeled protein with 4 μ L of 4X loading buffer. Samples were heated for 10 minutes at 95 $^{\circ}$ C, then cooled on ice. Six microliters of each sample were loaded onto a 10% SDS-PAGE gel in duplicate (two wells), and electrophoresed at 60 V for 20 minutes and 175 V for 80 minutes. The gel was cut in half vertically – one half was Coomassie stained for total protein levels and the other half was transferred to a PVDF membrane at 80 V for 105 minutes. Following transfer, the membrane was blocked, incubated with primary and secondary antibodies as described in the preceding paragraph.

DNP-labeling on membrane. A literature procedure was used as a starting point²⁰⁶ for the protocol below. Protein samples (10 μ g) were resolved on a 10% SDS-PAGE gel following typical electrophoresis settings (60 V – 20 min, 175 V – 60 min), then transferred to a PVDF membrane at 80 V for 105 minutes. All labeling steps were performed with rocking at room temperature. Immediately following transfer, the membrane was washed twice for 5 minutes each time with PBST (10 mL), then incubated with 2 M HCl (10 mL) for 10 minutes. A fresh 10 mg/mL DNPH solution was prepared in 2 M HCl, then diluted to 0.05 mg/mL in 2 M HCl (50 μ L of 10 mg/mL into 10 mL of 2 M HCl). The membrane was incubated with 0.05 mg/mL DNPH (5 mL) for 2 minutes, then the labeling solution was discarded and the membrane was quickly rinsed with 2 M HCl (10 mL), followed by two longer 5-minute washes with 2 M HCl (10 mL). The membrane was then washed seven times for 5 minutes each time with methanol (10 mL), then washed twice

for 5 minutes each time with PBST (10 mL). The membrane was blocked, incubated with primary and secondary antibodies as described in section “In-solution DNP-labeling.”

4.0 Reversible Optical Switching of Protein Function

Material in Section 4.1 was reprinted in part with permission from **Courtney, T.**; Deiters, A. *Curr. Opin. Chem. Biol.*, **2018**, *46*, 99-107.

4.1 Introduction to Photoswitchable Amino Acids

The amino acids described above in Chapter 2 have enabled optical control of a wide range of protein functions, but they are limited to an irreversible activation event. Since many biological processes undergo cycles of activation and deactivation, tools that mimic this reversibility may be better suited for studying these systems.²²²⁻²²⁷ Additionally, the use of photoswitchable tools allows for enhanced spatial resolution due to protein activity confined within an illuminated area since diffusion outside of the light beam will lead to reversible off switching.²²⁸ The photoswitchable azobenzene amino acid **AzoF** was first genetically encoded in bacteria in 2006 and applied to controlling catabolite activator protein binding²²⁹ and GFP fluorescence.²³⁰ Additional photoswitchable amino acids have been genetically encoded, in order to provide improved photostationary states, red-shifted wavelengths for photoisomerization, and increased modulation of protein conformation through azo-bridging.²³¹⁻²³² Table 4-1 includes the structures of azobenzene amino acids that have been incorporated and used for controlling protein function, and includes photostationary states and thermal stability (if available). The Wang group developed three azobenzene-derived photoswitchable amino acids **PSCaa**, **keto-PSCaa**, and **Cl-PSCaa** (photoswitchable, click amino acids) with thiol-reactive handles and demonstrated their function

in the control of calmodulin conformation.²³²⁻²³³ Upon thiol attack of the electrophilic handle, an azobridge is generated within an α -helix such that isomerization from the *trans*- to *cis*-state results in a decrease in helical content. This bridging strategy induces a more dramatic protein conformational change than a single side chain isomerization. Later, the Wang group applied **PSCaa** to the reversible control of glutamate receptors in mammalian cells without utilizing the inherent cross-linking capabilities.²³⁴ Subsequently, the pentafluoro-azobenzene derivative **F-PSCaa** with red-shifted isomerization wavelength and improved azo-bridging efficiency was reported.²³¹

Table 4-1 Structures of literature reported photoswitchable amino acids

Seven photoswitchable UAAs have been incorporated into *E. coli* or mammalian cells and have been used to control protein function. The structures with a gray background undergo attack of nearby cysteine residues to form an azo-bridge to induce an even greater protein conformational change. ^aNot measured for the amino acid, but for the non-substituted azobenzene core. N.D. indicates that the value was not reported.

trans $\xrightleftharpoons[hv_2, \text{thermal}]{hv_1}$ cis

compound	structure	<i>trans:cis</i> ($h\nu_1$)	<i>trans:cis</i> ($h\nu_2$)	thermal stability of <i>cis</i> -isomer
AzoF		22:78 (365 nm)	76:24 (450 nm)	23 °C: 12.8 h ^a
PSCaa		N.D. (330–365 nm)	N.D. (405–470 nm)	N.D.
keto-PSCaa		N.D. (330–365 nm)	N.D. (405–470 nm)	N.D.
Cl-PSCaa		N.D. (330–365 nm)	N.D. (405 nm)	N.D.
F-PSCaa		22:78 (540 nm)	73:27 (405 nm)	N.D.
F₂AzoF: X ¹ = F, X ² = H		18:82 (530 nm)	70:30 (405 nm)	N.D.
F₄AzoF: X ¹ = F, X ² = F		9:91 (530 nm)	84:16 (405 nm)	25 °C: 2 years ^a

The Lin group synthesized and genetically encoded a full set of fluorinated azobenzene analogs with improved photoswitching properties; however, these amino acids have yet to be applied to the control of protein function.²³⁵ Most recently, our lab published compounds **F₂AzoF**

and **F4AzoF** that showed a dramatic improvement in *trans*-to-*cis* conversion; however, light-induced conversion to the more stable *trans*-isomer was comparable to previously reported analogs. These analogs were used to reversibly control luciferase enzyme activity through computationally-predicted sites for UAA incorporation.²³⁶ **F2AzoF** was used as the L-isomer, while the synthetic route for **F4AzoF** produced a racemic mixture, thus both isomers were included for cell based studies.

The approaches presented above have established a foundation for obtaining reversible, spatiotemporal control of biological processes in living systems through unnatural amino acid mutagenesis; however, the field is still in its early stages and further work is underway to improve this technology. One key area that seems to be overlooked thus far is the development of photoswitches with high thermal stability of the *cis*-isomer.

4.2 Development of an Arylazopyrazole Photoswitchable Amino Acid (AAPF)

Replacement of one phenyl ring with various *N*-heterocycles has extensively been explored in recent years to develop new and improved photoswitches. Functionalities such as pyrroles, pyrazoles, imidazoles, triazoles, and tetrazoles have all been appended to generate azoheteroarenes (Table 4-2) and their photoswitching capabilities have been characterized.²³⁷⁻²³⁹ Each of these groups impact photoswitching parameters, such as isomerization wavelengths, *cis*-isomer thermal stabilities, and photostationary states for *cis*-to-*trans* or *trans*-to-*cis* conversions in different manners. With the goal of increased *cis*-isomer thermal stability and near-quantitative photostationary states, the methylated 4-pyrazole modification fit both of these criteria.

Table 4-2 Structures and photophysical properties of azoheteroarenes

Replacement of a single phenyl ring of an azobenzene with N-heterocycles has been extensively explored. The numbers represent the position of attachment to the heterocycle, H and Me denote whether a given heterocycle was methylated at position X, and the functionalities pyrrole (py), pyrazole (pz), imidazole (im), triazole (tri), and tetrazole (tet) are abbreviated. Table adapted from Calbo *et. al.*, *J. Am. Chem. Soc.* **2017**, 139, 1261-1274.

R =	abbreviation	<i>trans</i> : <i>cis</i> ($h\nu_1$)	<i>trans</i> : <i>cis</i> ($h\nu_2$)	thermal stability of <i>cis</i> -isomer
	2pyH , X = H	16:84 (415 nm)	82:18 (532 nm)	12 hours
	2pyMe , X = Me	15:85 (415 nm)	98:2 (532 nm)	21 seconds
	3pyH , X = H	23:77 (355 nm)	85:15 (532 nm)	3.7 days
	3pyMe , X = Me	15:85 (355 nm)	98:2 (532 nm)	0.25 hours
	3pzH , X = H	2:98 (355 nm)	97:3 (532 nm)	74 days
	3pzMe , X = Me	4:96 (355 nm)	87:13 (532 nm)	7.8 days
	4pzH , X = H	2:98 (355 nm)	70:30 (532 nm)	1000 days
	4pzMe , X = Me	2:98 (355 nm)	98:2 (532 nm)	10 days
	5pzH , X = H	2:98 (355 nm)	79:21 (532 nm)	11 days
	5pzMe , X = Me	6:94 (355 nm)	86:14 (532 nm)	12 hours
	2im	2:98 (363 nm)	–	9 hours
	4im	5:95 (365 nm)	–	2.4 days
	5im	2:98 (365 nm)	45:55 (455 nm)	6.5 days
	3tri	10:90 (355 nm)	84:16 (532 nm)	21 days
	tet	24:76 (355 nm)	72:28 (532 nm)	39 days

We envisioned that the azobenzene amino acid **AzoF** could undergo a similar replacement of one phenyl ring with a 4-pyrazole to generate an arylazopyrazole (AAP) amino acid **AAPF** (Figure 4-1a). Arylazopyrazoles utilize switching wavelengths of *trans*-to-*cis* (365 nm) and *cis*-to-*trans* (530 nm) and display improved photophysical properties of their azobenzene counterpart. We chose to utilize a 3,5-dimethylated AAP since those display near quantitative switching between the two isomers; however, the non-methylated AAPs provide longer thermal stability (1000 days with 3,5-H vs 10 days with 3,5-CH₃).²⁴⁰ *N*-methylation was utilized based on literature reports where DFT predictions showed rapid *cis*-to-*trans* isomerization of N-H variants. Trevor Horst synthesized **AAPF**, then a synthetase panel screen was performed.

Previous lab members (primarily Dr. Jihe Liu and Xinyu Chen) have assembled a small library of *MbPylRS* mutants with several mutations in the amino acid binding pocket (see Appendix B for a list of the corresponding mutations). These mutants were each doubly transformed with an sfGFP reporter bearing a TAG site at position 151 and stored as glycerol stocks to generate a panel used for screening. Briefly, the doubly transformed glycerol stocks for EV mutants previously shown to incorporate tyrosine and phenylalanine derivatives were grown in liquid culture. Small scale (200 μ L) cultures were prepared with and without **AAPF** (**ONBY** was used as a positive control for the screen since it is incorporated by many of the PylRS mutants that were included) to assess whether any current synthetase could utilize the new UAA. Cultures were grown to OD₆₀₀ of 0.5 at 37 °C and induced with 0.1% arabinose, followed by the addition of amino acid. Cultures were grown overnight with shaking at 37 °C to allow for incorporation and protein expression, then the following day an aliquot (100 μ L) was transferred to a 96-well plate and sfGFP fluorescence (ex. 488/5 and em. 510/5 nm) and optical density (absorbance at 600 nm) were measured using a plate reader. To adjust for variation in optical density, the fluorescence

values were divided by OD₆₀₀ and plotted for all combinations of synthetases and amino acids (Figure 4-1b). Unfortunately, the majority of the synthetases showed no increase in fluorescence upon introduction of **AAPF**; however, EV16-5 and EV20 showed a >2-fold increase in the presence of **AAPF**. This result was somewhat expected since both EV16-5 and EV20 were previously reported to incorporate **AzoF**, **F₂AzoF**, and **F₄AzoF**, all of which are structurally similar.²³⁶

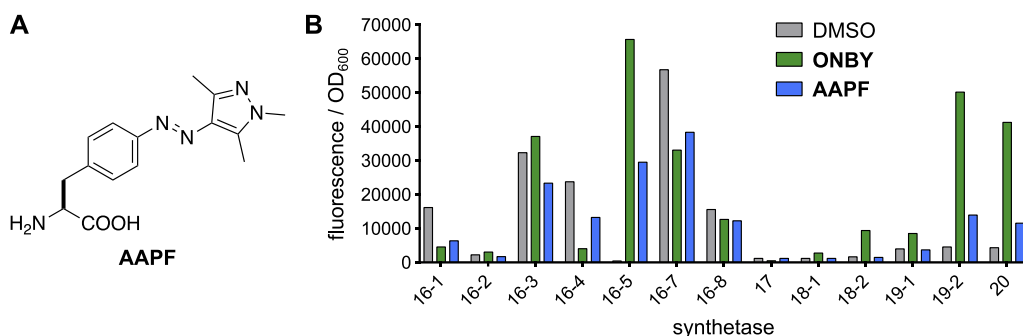


Figure 4-1 Synthetase screen of *MbPylRS* variants with **AAPF**

a) Structure of **AAPF**, which was synthesized by Trevor Horst. b) A small panel of *MbPylRS* mutants was screened using an sfGFP reporter to assess whether an existing synthetase would be capable of utilizing **AAPF** as a substrate.

To further validate incorporation, larger expression cultures (5 mL) were prepared in an analogous method used for the screen, except only synthetases EV16-5 and EV20 were used (constructs are detailed in Figure 4-2a). Following expression, the samples were lysed using a three-phase partitioning (TPP) method,²⁴¹ then purified using Ni-NTA resin. Samples were analyzed via SDS-PAGE, followed by Coomassie staining (Figure 4-2). Here, EV16-5 showed a significant level of background incorporation in the absence of UAA, while EV20 showed a dependence on the presence of **AAPF** for protein expression. The purified sample from the EV20 expression was submitted to the Department of Chemistry Mass Spectrometry facility for ESI analysis (Figure 4-2c). Following deconvolution, a mass of 28382.063 was observed, which closely matches the expected mass of 28382.178 ($\Delta -0.115$ Da). Two lower abundance species were also identified. These may represent background phenylalanine incorporation (expected

28246.018, $\Delta -0.711$ Da) and reduction of the azo group to yield *p*-aminophenylalanine (expected 28261.035, $\Delta 1.979$ Da); however, the error in these two contaminants is greater than that observed for **AAPF** incorporation. Bacteria (and even mammalian cells) possess azoreductases which reduce the azo bond to the corresponding anilines, thus providing one explanation as to the presence of the *p*-aminophenylalanine incorporation.²⁴²⁻²⁴³ In hindsight, the samples from EV16-5 incorporation should have been analyzed to check whether the plus **AAPF** condition was able to efficiently outcompete the background phenylalanine incorporation which is a common issue with this specific synthetase mutant.

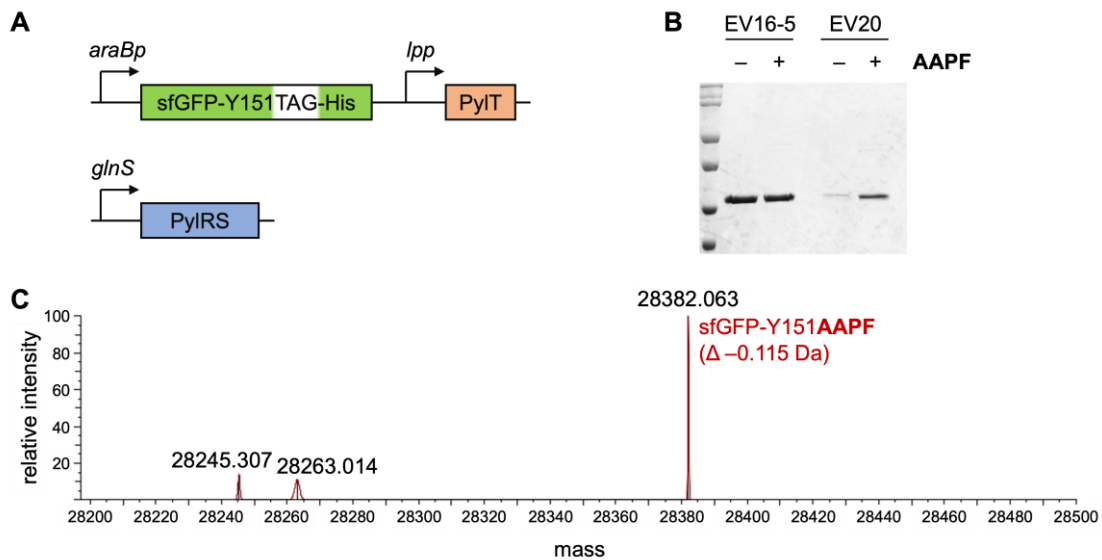


Figure 4-2 **AAPF** was successfully incorporated in *E. coli* and confirmed by ESI-MS

a) The two plasmids used for *E. coli* incorporation are shown. The gene of interest (here, sfGFP) is under arabinose control, while the tRNA is controlled by a constitutive *lpp* promoter. The *MbPylRS* is constitutively expressed using a bacterial glutamine synthetase promoter, *glnS*. b) SDS-PAGE analysis of purified sfGFP-Y151**AAPF** shows significant background when using EV16-5, while EV20 results in protein expression only in the presence of **AAPF**. c) ESI-MS analysis of the EV20 sample shows successful incorporation, with two lower abundance contaminants.

Next, we validated expression and incorporation in mammalian cells using HEK293T cells utilizing a two-plasmid system. One plasmid contained the mCherry-TAG-EGFP-HA reporter under CMV control, while the other plasmid contained the mammalian codon optimized synthetase (with the same mutations as EV20) under CMV control and four copies of the *pylT* under U6

control (Figure 4-3a). HEK293T cells co-transfected with both plasmids were treated with and without **AAPF** for 48 hours to monitor for incorporation. Fluorescence micrographs show low levels of incorporation; however, western blotting does confirm incorporation with only low background incorporation in the absence of UAA (Figure 4-3b,c).

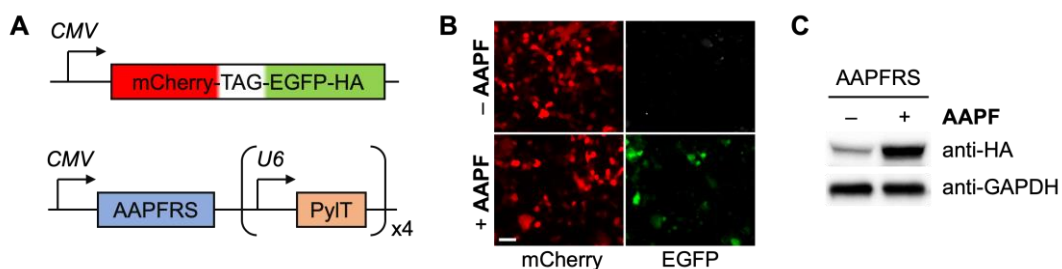


Figure 4-3 **AAPF** was successfully incorporated in mammalian cells and confirmed via fluorescence microscopy and western blotting

a) The two plasmids used for mammalian incorporation are shown. The mCherry-TAG-EGFP-HA reporter and the AAPFRS are both under CMV control and there are four copies of PyIT. b) Fluorescence micrographs of HEK293T cells co-expressing the mCherry-TAG-EGFP-HA reporter, AAPFRS, and PyIT in the presence and absence of **AAPF**. Scale bar = 50 μ m. c) Western blot analysis of mCherry-**AAPF**-EGFP-HA using an anti-HA antibody and anti-GAPDH as a loading control.

After confirming incorporation into protein in both *E. coli* and mammalian cells, we characterized the photophysical properties of **AAPF** to see how it compares to previously reported photoswitchable amino acids. Irradiation of a 0.1 mM solution prepared in PBS at pH 7.4 using 530 nm light to generate the *trans*-isomer and 365 nm light to generate the *cis*-isomer shows distinct spectra for each form (Figure 4-4a,b). We determined the photostationary state ratios using HPLC to separate the two isomers and integrated the peak areas of each when measuring at the isosbestic point (280 nm). In this experiment, a 0.1 mM solution in acetonitrile was prepared. The dark state was analyzed (black trace) and a 365 nm irradiated sample was analyzed (blue trace) to yield *trans*:*cis* ratios of 96:4 and 9:91, respectively (Figure 4-4c). Next, we determined the thermal stability of the *cis*-isomer at 37 $^{\circ}$ C. First, a solution in acetonitrile was prepared the same as for photostationary state determination, and aliquots were collected each hour and analyzed via HPLC. Integration of the peak area of the *cis*-isomer was plotted over time and an exponential decay

model was fit to the data to determine a $t_{1/2}$ of 2.5 hours (Figure 4-4d). Since this showed a significantly more rapid reversion than expected, this experiment was repeated using PBS at pH 7.4 to more closely mimic a biological setting. This time, when fitting with an exponential decay model, we calculated a $t_{1/2}$ of 36 hours which is much closer to reported thermal stabilities of other AAPs.²⁴⁴ Significant stabilization of the *cis*-isomer was obtained when switching from acetonitrile to water (PBS), which is consistent with literature reported effects of solvent polarity on increased thermal stability.²⁴⁵⁻²⁴⁶

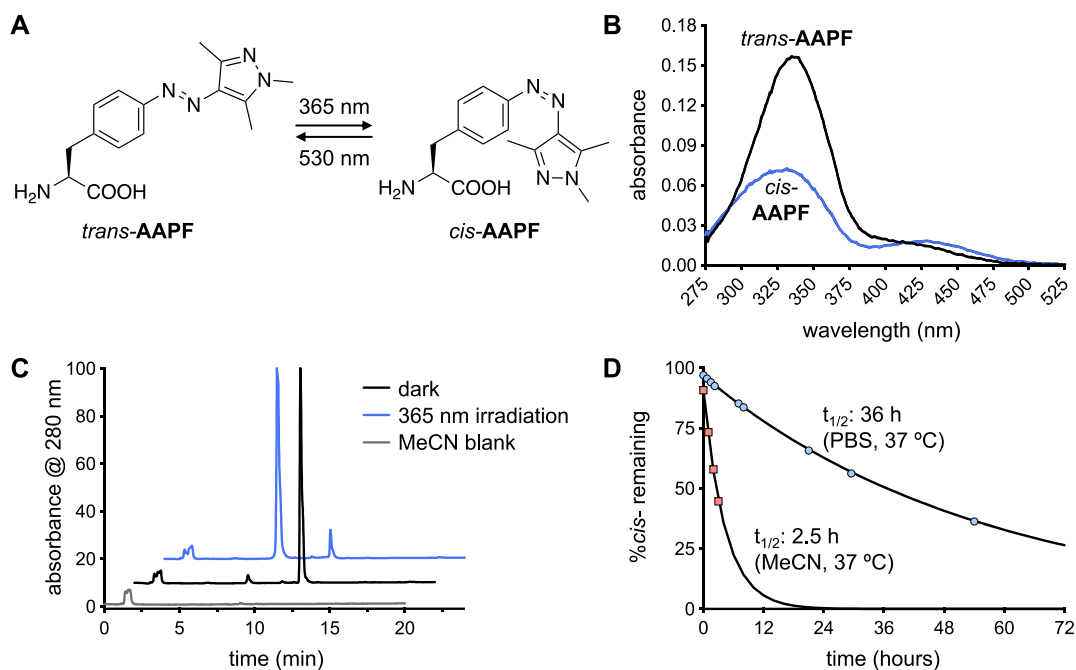


Figure 4-4 Determination of photostationary states and thermal stability of **AAPF**

a) Structures of both *cis*- and *trans*-**AAPF** are shown. b) Absorbance spectra of *cis*- and *trans*-isomers at 100 μ M in PBS. c) HPLC analysis to determine photostationary states showed distinct peaks for each isomer. d) Thermal stability of *cis*-**AAPF** was tested in acetonitrile (coral) and PBS at pH 7.4 (blue) and analyzed via HPLC.

Our preliminary studies confirmed that **AAPF** was successfully incorporated in both *E. coli* and HEK293T cells. Photochemical characterization of **AAPF** was comparable to existing arylazopyrazoles reported in the literature.^{244, 247} Since this UAA exhibited improved

photostationary states and thermal stability of the *cis*-isomer relative to azobenzene analogs, we next wanted to use **AAPF** for controlling protein function in a biological setting.

4.2.1 Control of Gene Expression Using AAPF

Due to high thermal stability of *cis*-AAPF in an aqueous environment, we decided to apply this UAA for the regulation of gene expression, more specifically through control of translation. Optical control of translation has previously been achieved through indirect methods using caged and photoswitchable short-interfering RNA (siRNA) and antisense agents to interfere with or trigger for degradation target mRNA transcripts.²⁴⁸⁻²⁵¹ Direct methods using light have been developed such that the mRNA is modified with caging or photoswitchable groups to allow for activation or reversible control of mRNA recognition by translational machinery.²⁵²⁻²⁵⁵ Additionally, direct control of translation has been achieved through the use of photocaged tRNAs that cannot interact with the elongation factor due to the presence of a nitrobenzyl or a coumarin caging group on the NH₂-group of the amino acid,²⁵⁶⁻²⁵⁷ however, these existing methods allow only for a single activation of translation. We envisioned that **AAPF** could be utilized as a direct method for controlling translation through the regulation of tRNA charging. We hypothesized that **AAPF** would be recognized by the engineered synthetase only in the *trans*-form and that generation of the *cis*-isomer would abolish tRNA charging by the synthetase. Thus, if we introduced **AAPF** as the *cis*-isomer, upon exposure to 530 nm light (to generate the active, *trans*-isomer) we could generate a pool of charged tRNAs that could be used by the ribosome to synthesize our protein of interest (Figure 4-5). Upon depletion of the pool, translation would be halted until another pulse of irradiation generates more of the active isomer that can be used by the synthetase for another round of tRNA charging.

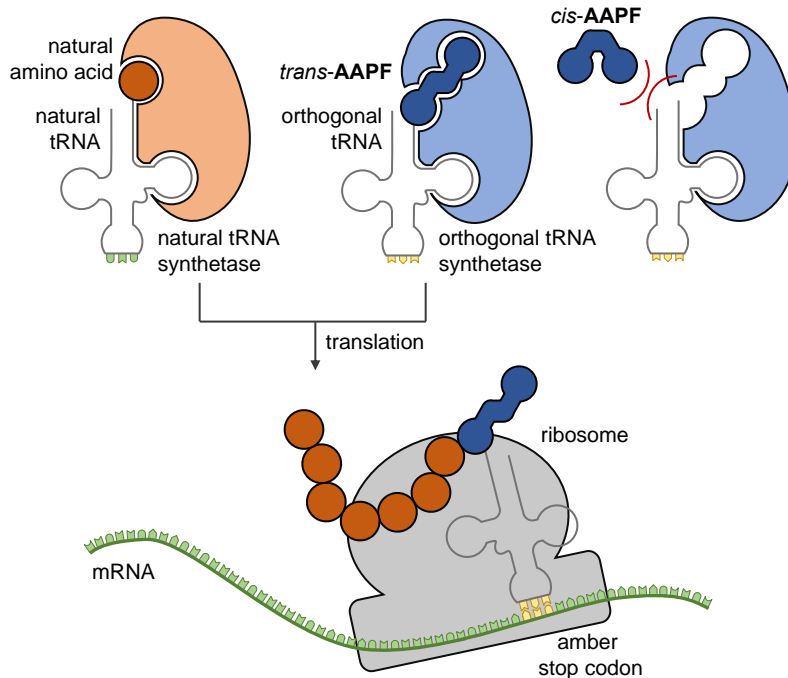


Figure 4-5 Overview of translational control using **AAPF**

Only the trans-isomer of **AAPF** is in a configuration that can be recognized by the orthogonal synthetase. Generation of the *cis*-isomer would inhibit synthetase binding and tRNA charging, thus enabling us to control translation using different wavelengths of light.

To explore the ability of **AAPF** to be utilized as a tool for regulating translation, we generated a dual reporter in order to have a way of validating induction and generation of an mRNA transcript in these experiments. This bacterial dual reporter is slightly different than the dual reporter commonly used in our mammalian cell experiments, but functions in the same manner. Here, mCherry is fused to sfGFP-Y151TAG using a flexible GSG linker followed by a C-terminal histidine tag (Figure 4-6a). Upon induction but in the absence of UAA (or absence of tRNA charged with this UAA), mCherry fluorescence is expected but a truncated sfGFP fusion remains non-fluorescent; however, upon incorporation of the UAA, both red and green fluorescence is expected. This reporter was first validated using the wild-type PylRS which accepts the commercially available allyloxycarbonyl-lysine (**AlloCk**). Comparison of three conditions: (i) no induction, no **AlloCk**, (ii) with induction, no **AlloCk**, and (iii) with induction, with **AlloCk**

revealed that the reporter was functioning as expected when using a plate reader to measure bulk fluorescence intensity (Figure 4-6b). We proceeded with testing the ability to regulate translation using **AAPF** in this dual reporter in conjunction with AAPFRS (or EV20). Top10 cells co-transformed with both plasmids were grown to OD₆₀₀ of 0.5 at 37 °C, then the cells were pelleted and resuspended in LB broth containing either *cis*- (irradiated with 365 nm) or *trans*-**AAPF** (maintained in the dark, so ~98% *trans*) at various concentrations. Aliquots were removed at 1, 2, and 4 hours post-induction and the samples were analyzed via flow cytometry to obtain fluorescence data at the single cell level. The non-induced sample was used to determine the gating criteria, meaning that cells with mCherry values higher than the non-induced sample were included in the plots. Histogram analysis of the sfGFP channel shows a dose dependence on the concentration of **AAPF** used; however, the differences between the dark and UV (*trans*- and *cis*-forms) is very subtle in this representation (Figure 4-6c).

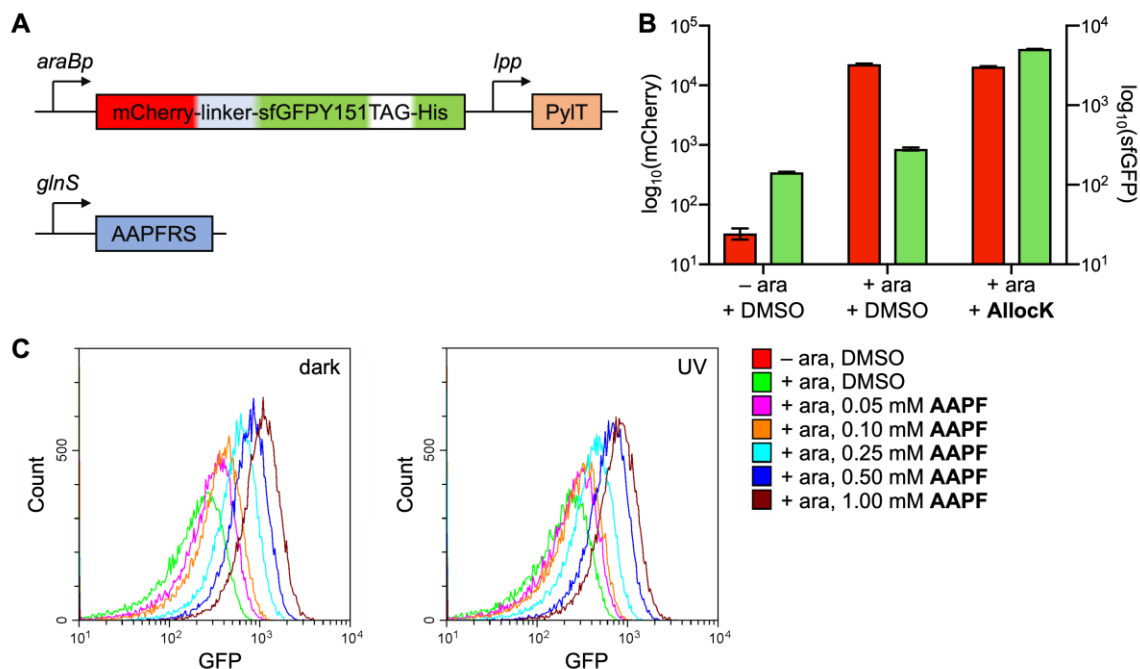


Figure 4-6 Validation of a dual mCherry-sfGFP reporter for UAA incorporation in *E. coli*

a) The dual reporter consists of mCherry fused to sfGFP-Y151TAG using a GSG linker and contains a C-terminal His-tag. For UAA incorporation, a second plasmid containing the desired PylRS (here, shown as AAPFRS or EV20)

is required. b) A significant increase in mCherry fluorescence is observed upon addition of arabinose (ara), and a dependence on the presence of UAA (here, **AlloCk**) is required for an increase in sfGFP fluorescence. Plate reader analysis of bulk fluorescence in living cells validates that the new dual reporter responds as expected. c) Top10 cells co-transformed with the reporter and AAPFRS (EV20) were grown at 37 °C to an OD₆₀₀ of 0.5, then the cells were resuspended in the appropriate concentration of **AAPF** that was pre-irradiated to generate the *cis*-isomer or maintained in the dark to retain the *trans*-isomer. Flow cytometry analysis of the 4-hour post-induction sample shows a dose dependence in response to increasing UAA concentration; however, the difference between dark and UV states is minimal.

In an effort to tease out the difference in incorporation levels of the two isomers, we integrated the peak area of the flow cytometry histogram plots to obtain the total sfGFP fluorescence of ~25,000 cells per condition (while an uncommon method, this was performed to elucidate if there were any subtle differences). When plotting the 1-, 2-, and 4-hour time points in this manner, it became more apparent that there were differences between the dark and UV conditions (Figure 4-7). At the 1- and 2-hour time points, the background incorporation in the UV, *cis*-form remained mostly the same for all concentrations of **AAPF**; however, after 4 hours a significant degree of background *cis*-isomer incorporation was observed for all concentrations. Based on our thermal stability assessment, we would expect ~90% *cis*-**AAPF** remaining after 4 hours, but this is not consistent with the high background incorporation we observed. We predicted that this background could be due to two potential factors: (i) faster thermal reversion to the *trans*-isomer in the more complex cellular environment, or (ii) unanticipated activity of the synthetase for the *cis*-isomer (a less likely explanation).

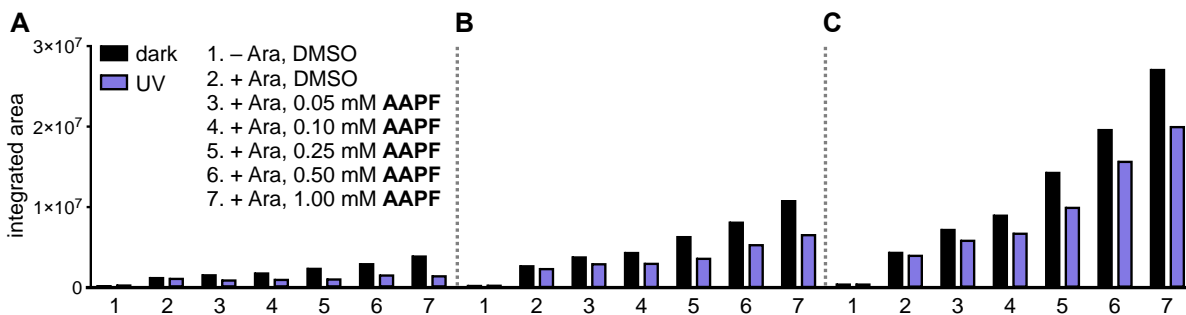


Figure 4-7 Integrated peak areas of flow cytometry analysis emphasizes differences between the conditions. The total sfGFP fluorescence of each condition was generated by the summation of sfGFP signal from all cells with an mCherry values > 0 for each of the three time points: 1 hour (a), 2 hours (b), and 4 hours (c). In this manner, a

preference for incorporation of the dark, *trans*-isomer was observed; however, significant background incorporation of the UV-generated, *cis*-isomer was also observed, in particular at 4 hours post-induction.

Since our initial thermal stability study was conducted in PBS, we decided to repeat the thermal stability using several different growth media for both *E. coli* and mammalian cells to see how those compared to PBS. We tested four bacterial growth broths (GMML – glycerol-based minimal media supplemented with leucine, auto-induction media, LB, and 2xYT listed in increasing richness), and included a DMEM media which has been optimized to have low background autofluorescence for live cell imaging. **AAPF** was diluted to 250 μM in each of these six diluents and converted to the *cis*-isomer using 365 nm irradiation, and absorbance spectra were acquired over several hours (Figure 4-8a). The change in absorbance of each sample at 335 nm (maximum for the *trans*-isomer) was plotted for each different media and minimal deviation from the PBS control was observed (Figure 4-8b). The gray line represents the average change in absorbance expected for complete reversion back to the *trans*-isomer. Based on this experiment, it does not appear that some component of the media is the causative agent of the faster-than-expected thermal reversion.

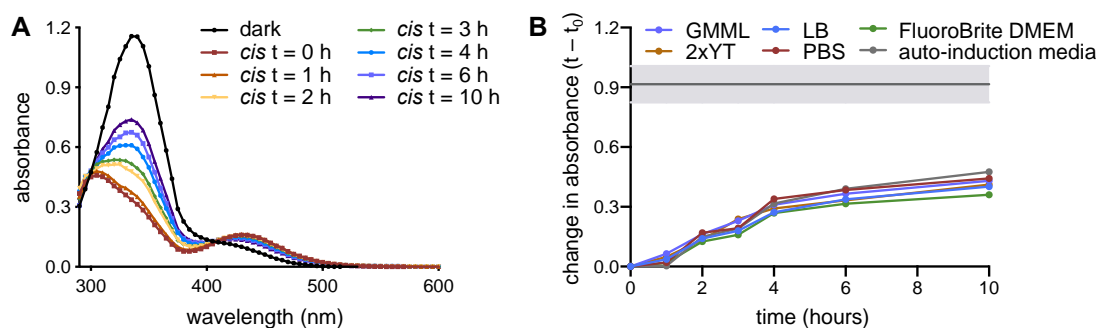


Figure 4-8 Thermal stability of **AAPF** in *E. coli* and mammalian growth media

Solutions of **AAPF** in six buffers/media were prepared at 250 μM and the *cis*-isomer was generated using 365 nm irradiation. a) An absorbance spectrum was acquired every few hours and a representative plot in LB is shown. b) The change in absorbance at 335 nm was plotted over time for all 6 samples and minimal difference is observed between

Azobenzene photoswitches have previously been reported to undergo attack by glutathione at the azo-group²⁵⁸⁻²⁵⁹ and several ortho-modified analogs have been developed to prevent this

from happening.²⁶⁰ The stability of sixteen different arylazopyrazoles containing various modifications to the phenyl ring toward glutathione was explored in the *trans*-state with no change observed over 24 hours; however, the stability of the *cis*-isomers of those analogs was not conducted.²⁴⁴ We tested the stability of *cis*-**AAPF** toward glutathione in LB broth by monitoring absorbance over the course of three hours (Figure 4-9). In the presence of 10 mM glutathione, rapid reversion to the *trans*-isomer was observed in less than one hour, which is consistent with the azobenzene literature,²⁵⁸⁻²⁵⁹ but has not been observed for **AAPF**.²³⁷ Fortunately, no shift in the absorbance maximum or change in shape of the spectrum was observed suggesting the compound remains intact, as changes in the spectrum would be expected upon glutathione-adduct formation and loss of conjugation. The intracellular concentration of reduced glutathione in *E. coli* has previously been reported to reach up to 10 mM,²⁶¹ while the concentration reported in mammalian cells is in the low mM range.²⁶² Based on this, it is likely that the half-life of *cis*-**AAPF** inside of *E. coli* during these experiments is significantly lower than expected, which is attributing to the higher background observed with increasing time.

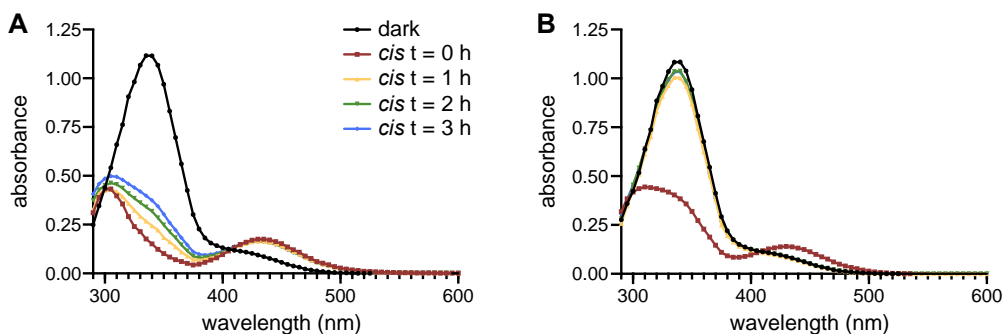


Figure 4-9 Thermal stability of *cis*-**AAPF** in the presence and absence of glutathione
A 250 μ M solution of **AAPF** was prepared in LB broth in the absence (a) and presence (b) of 10 mM glutathione and irradiated with 365 nm light to generate the *cis*-isomer. An absorbance spectrum was acquired every hour. In the presence of 10 mM glutathione, rapid reversion to the *trans*-isomer was observed.

We hypothesized performing additional cycles of 365 nm irradiation would increase the effective concentration of the *cis*-isomer, thereby improving the difference between the dark and

UV states over a longer time period. We tested this again using the dual reporter in Top10 cells. Cells co-transformed with both plasmids were grown to an OD₆₀₀ of 0.5 at 37 °C, then the cells were pelleted and resuspended in LB broth containing either *cis*- (irradiated with 365 nm) or *trans*-**AAPF** (maintained in the dark) at various concentrations. Every hour post-induction, the cells in the UV-irradiated media were irradiated for an additional 10 minutes at 365 nm prior to collecting samples for analysis. Aliquots were removed at 1, 2, and 4 hours post-induction and the samples were analyzed via flow cytometry. Area under the curve analysis was performed again to better ascertain any differences between the dark and UV samples. Analysis of the four-hour time point shows a greater separation between the dark and UV samples when utilizing multiple cycles of 365 nm irradiation to help maintain the *cis*-isomer (Figure 4-10a). When comparing the 1 mM data, the fold change of dark/UV decreases upon increased induction and expression time (black bars) as a result of the faster reversion of the *cis*-isomer; however, by adding repeated cycles of irradiation, the fold change remain consistent over time (gray bars), suggesting that the additional irradiation functions to convert **AAPF** back to the inactive *cis*-isomer (Figure 4-10b).

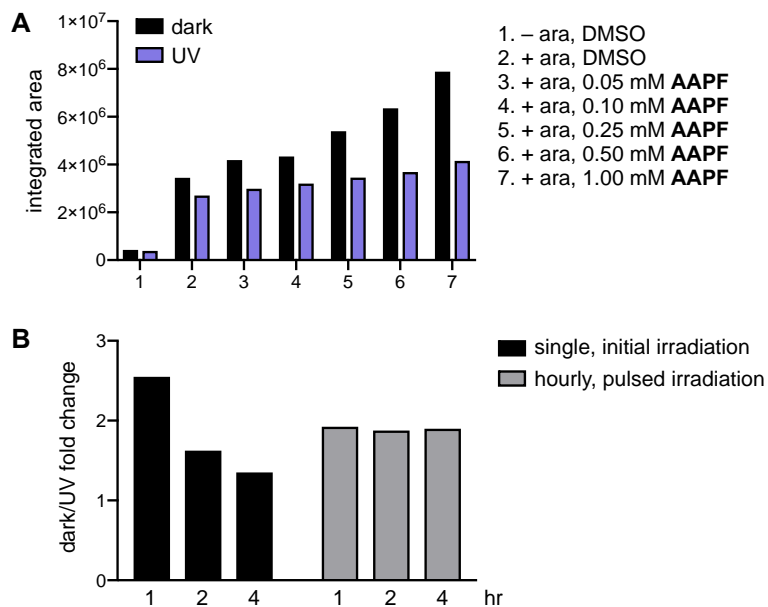


Figure 4-10 Pulsed irradiations help maintain *cis*-**AAPF** over a longer time period

a) The total sfGFP fluorescence of each condition was generated by the summation of sfGFP signal from all cells with mCherry values > 0. The four-hour time point data is shown here. b) The fold change of dark/UV sfGFP signal for the 1 mM data shows a significant decrease over time when only an initial irradiation is performed; however, introduction of repeated cycles of irradiation maintains the fold change over time.

Although we observed an improvement in lower background activity when using additional cycles of irradiation, we concluded the use of **AAPF** to control translation needed significantly more optimization to be a useful tool. Although no significant change in optical density was observed over the four hour experiments we conducted here, there is plenty of literature precedence demonstrating the adverse effects of prolonged UVA irradiation on bacteria.²⁶³⁻²⁶⁴ Thus, in order for this to be a useful tool in the field, optimization to minimize the need for repeated UV irradiations of **AAPF** would be requisite. Although not a trivial task, we could engineer a synthetase variant that only recognizes the *cis*-isomer, such that the more thermally stable *trans*-isomer would be the inactive form. In this design, short irradiations would only need to be conducted to activate the system, rather than maintained persistently to keep the system inactive (as in our current design). Alternatively, we could perform these experiments using the previously published **4FAzoF** since generation of the *cis*-isomer is performed using 530 nm light, which avoids any potential for UV-induced toxicity. To further validate that the background incorporation is due to fast thermal reversion, and not just enzymatic activity of the synthetase toward the “inactive” isomer, the PylRS should be recombinantly expressed and utilized for determining kinetic parameters for tRNA charging with both *cis*- and *trans*-**AAPF** in a spectrophotometric enzyme assay.²⁶⁵

4.2.2 Optimization of Incorporation Efficiency for AAPF

In an effort to improve the yield of **AAPF**-modified protein from a bulk *E. coli* expression, we decided to test whether **AAPF** would serve as a substrate for the *Mj*TyrRS system previously

used by the Schultz lab for **AzoF** incorporation.²²⁹ We performed a side-by-side comparison of the traditional *MbPylRS* (EV20 mutations – L270F, L274M, Y349F, N311G, and C313G) system in Top10 cells in LB broth versus the *MjTyrRS* (AzoPheRS mutations – Y32G, L65E, F108A, Q109E, D158G, and L162H) in BL21(DE3) cells in both LB broth and GMML (a minimal media to suppress background). A key difference between the two systems is the use of promoters for each of the components. Their system – Schultz pEVOL – encodes two copies of the synthetase, with one under arabinose induction and the other is constitutively expressed using the *E. coli* glutamine synthetase (*glnS*) promoter, while the tRNA is driven by a *proK* promoter. Historically, the gene of interest would be sub-cloned into a pET vector for IPTG induction (as done by Schultz), but in this experiment, we utilized a pBAD-sfGFP-Y151TAG construct. Our standard system – pBK – utilizes a single copy of the PylRS under constitutive expression using the *glnS* promoter. The gene of interest is controlled by arabinose induction and the PylT is driven by an *lpp* promoter, which is reportedly weaker than the *proK* promoter used with pEVOL.²⁶⁶

First, we cloned the necessary pEVOL-AzoFRS construct by sequential T4 DNA ligations of the AzoFRS – obtained by PCR amplifying from a synthetic gene fragment – into a pEVOL backbone already containing the Tyr-tRNA. The pylT sequence in pBAD-sfGFP-Y151TAG-PylT was removed by linearizing the plasmid with two restriction enzymes flanking the pylT, followed by generation of blunt ends, and subsequent T4 DNA ligation to yield pBAD-sfGFP-Y151TAG for use with the pEVOL system. Double transformation of pEVOL-AzoFRS with pBAD-sfGFP-Y151TAG in BL21(DE3) was performed, and a glycerol stock of doubly transformed Top10 containing pBK-EV20 and pBAD-sfGFP-Y151TAG-PylT was used. Expression cultures were grown to an OD₆₀₀ of 0.5 in LB broth or GMML, then induced with arabinose and supplemented with **AzoF**, **AAPF**, **ONBY**, or DMSO. After 20 hours of expression, aliquots were removed and

analyzed on a plate reader to measure sfGFP fluorescence and optical density. As observed previously, the pBK system incorporated **AAPF** at 1.9-fold over the DMSO control, while both **ONBY** and **AzoF** were incorporated with even higher fold changes (Figure 4-11a). When the pEVOL system was used in LB broth, very high background incorporation was observed in the absence of UAA, and no incorporation was detected (Figure 4-11b). However, by switching to GMML, much lower background was observed and **AzoF** was incorporated most efficiently of the three UAAs, and **AAPF** incorporation was only improved to 2.1-fold over DMSO (Figure 4-11c).

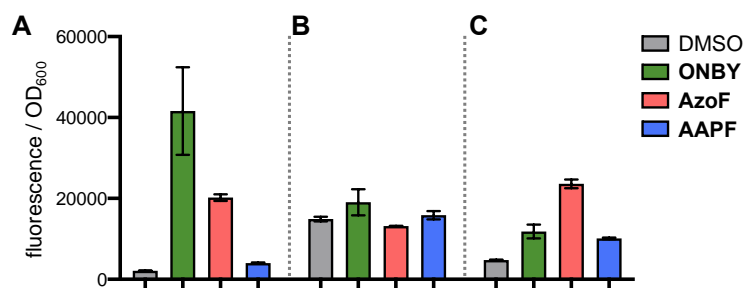


Figure 4-11 Comparison of pBK and pEVOL systems for **AAPF** incorporation

a) Top10 cells expressing pBAD-sfGFP-Y151TAG-PylT and pBK-EV20 were grown in LB broth and induced with arabinose, then supplemented with the specified amino acid. b-c) BL21 (DE3) cells expressing pBAD-sfGFP-Y151TAG and pEVOL-AzoFRS were grown in LB broth (b) or GMML (c) and induced with arabinose, then supplemented with different UAAs.

Unfortunately, based on this preliminary experiment, the Schultz pEVOL system did not result in a dramatic improvement in incorporation efficiency; however, we could follow this up with larger scale expressions such that purification and SDS-PAGE analysis could be performed to calculate the expression yields since fluorescence measurements do not always correlate with gel-based analyses.

In the last several years, prominent players in the UAA mutagenesis field transitioned from the pBAD/pBK system (the primary system employed in our lab) and which is used for PylRS selections, to one of two optimized and improved systems referred to as pEVOL/pET or pUltra/pET (Figure 4-12a). Key differences between these systems is the use of promoters (indicated in italics – inducible promoters are shown in red, while constitutive promoters are in

black) for sfGFP versus the PylRS, and replacement with a stronger promoter for the production of pylT. The pEVOL/pET system utilized by the Wenshe Liu lab is modified from the Schultz pEVOL system described above in that there is a single, arabinose-inducible copy of the PylRS and the gene of interest is induced using IPTG.²⁶⁷ The pUltra/pET system utilized by Abhishek Chatterjee uses IPTG-induction for both the PylRS and the gene of interest.²⁶⁶ For a side-by-side comparison of the various systems utilized in the field, a pET-His-sfGFP-Y151TAG was generated via Gibson assembly using the typical pET28 backbone for inclusion of the T7 promoter. The *MbPylRS* sequence containing EV20 mutations was Gibson assembled into pEVOL and pUltra plasmids (gifts from Liu and Chatterjee, respectively) to generate pEVOL-EV20 and pUltra-EV20. The pBAD/pBK was co-transformed into Top10 cells, while the pEVOL/pET and pUltra/pET systems were co-transformed into BL21(DE3). In our initial testing, optimized conditions (37 °C, overnight) were used for the pBAD/pBK system, while two standard conditions (high IPTG, short expression – six hours at 37 °C, or low IPTG, long expression – overnight at 25 °C) for IPTG-induction were compared for the pEVOL/pET and pUltra/pET systems (Figure 4-12b). **ONBY** was employed since it typically results in the highest incorporation efficiency with this PylRS mutant. A plate reader was used for measuring sfGFP fluorescence and the optical density at 600 nm, and the ratio of the two measurements is reported. Unfortunately, neither of the pET systems showed any improvement, but rather showed a marked decrease in sfGFP fluorescence compared to the pBAD/pBK system. **Thus, for incorporation into sfGFP, future work should continue to utilize the pBAD/pBK system with 37 °C, overnight expression.** However, in some cases, the target protein may not be stable for extended periods of time at 37 °C or may aggregate during longer expressions, so we performed a side-by-side comparison of the pBAD/pBK system with the literature reported conditions for each of the other systems (Figure 4-12c). These experiments

revealed that short expressions conducted at 37 °C using the pEVOL system resulted in much higher expression of sfGFP than the pBAD/pBK system. Unfortunately, the pUltra system still underperformed relative to the pBAD/pBK system with twelve hour, 30 °C expressions. **Based on these results, for protein expression of targets that benefits from a shorter expression time, the pEVOL system should be employed.** Similar experiments should be conducted with additional protein targets to further validate these trends. Additionally, it might be useful to compare moderate and weak incorporating UAAs with these three EV20 systems to see if similar trends emerge.

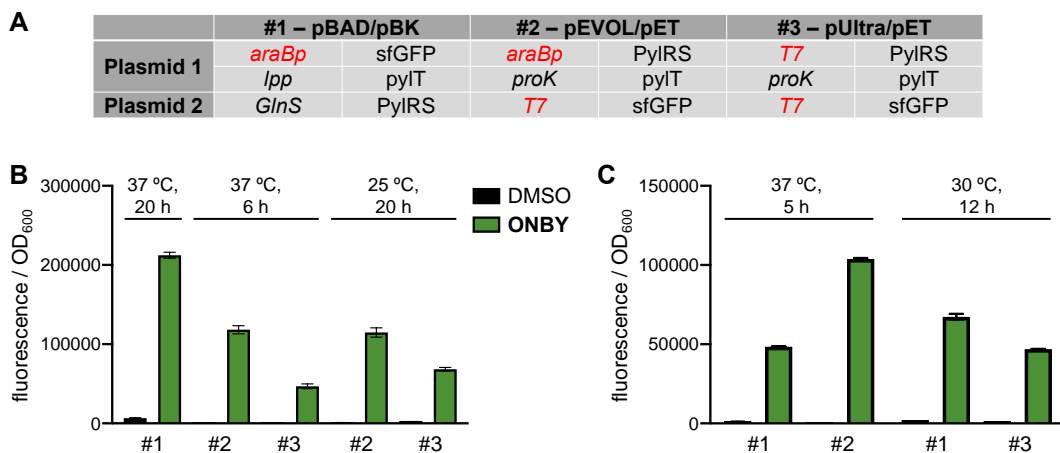


Figure 4-12 Comparison of various promoter arrangements for bacterial UAA incorporation

a) Three different plasmid systems were compared for bacterial UAA incorporation. Promoters are indicated with italics and the red color indicates inducible promoters (*araBp*, induced with L-arabinose; *T7*, induced with IPTG). System 1 (pBAD/pBK) utilizes an arabinose-inducible promoter for sfGFP, while the PylRS is constitutively expressed using an E. coli glutamine synthetase promoter (*glnS*) and the *pyIT* is under a weak, constitutive *lpp* promoter. In Systems 2 (pEVOL/pET) and 3 (pUltra/pET), sfGFP is under IPTG control and the *pyIT* is transcribed using the stronger *proK* promoter. In System 2, the PylRS is induced with arabinose, while in System 3 the PylRS is IPTG-inducible. b-c) Various expression conditions were utilized for direct comparison of the three systems.

Furthermore, we are in the early stages of evolving an improved PylRS that will utilize **AAPF** more efficiently than EV20 currently does. Unlike the traditional approach of performing saturation mutagenesis at the residues directly positioned within the UAA binding pocket, we chose to utilize an unbiased error-prone polymerase chain reaction (EP-PCR) approach to generate a library of mutant PylRS.²⁶⁸⁻²⁷³ Based on these reports, multiple rounds (3-4) of EP-PCR

mutagenesis were required for the identification of an efficient synthetase, and in rarer instances, initial error prone libraries were further mutagenized using either targeted mutagenesis (*e.g.*, NNK randomization at one or two sites) or DNA shuffling. We selected EV20 as the template for mutagenesis since it already contained mutations that enabled moderate levels of incorporation. After performing a literature reported EP-PCR protocol,²⁷⁴ the synthetase library was Gibson assembled into the pBK vector and transformed into commercial chemically competent *E. coli*. Individual colonies were selected for Sanger sequencing in order to analyze the diversity of the clones. Twenty cycles of EP-PCR afforded ~6.9 mutations per kilobase pair within the entire synthetase sequence (~1200 bp). Typically, between 4.5-9 mutations per kilobase is desirable since the introduction of greater than 9 mutations often results in a significant number of inactive mutants (through introduction of frameshifts or internal stop codons) that must be screened or undergo genetic selection to find improved, active mutants.²⁷⁵ This library (~55,000 clones) was co-transformed into *E. coli* containing the pRep selection plasmid (gift from the Cropp Lab). This selection plasmid expresses chloramphenicol acetyltransferase with D111TAG, as well as a T7 polymerase containing a TAG site, with a GFP_{UV} under T7 promoter control. In the case of successful UAA incorporation, resistance to chloramphenicol is achieved and colonies are fluorescent; however, in the absence of incorporation, the *E. coli* do not survive on chloramphenicol plates. Selections for **AAPF** were initially performed using 20 µg/mL chloramphenicol (as this concentration was sufficient for a successful **ONBY** test selection); however, after 72 hours, no colonies were obtained. In a second attempt, less stringent selection conditions were employed (10 µg/mL) and after 72 hours of growth at 37 °C, appearance of colonies was observed. Several of these colonies were isolated and tested in liquid culture (without chloramphenicol) both in the presence and absence of **AAPF** (Figure 4-13). Sanger sequencing of

three clones (#2, #6, and #8 in Figure 4-13b) exhibiting a high ratio of **AAPF** over DMSO fluorescence revealed that all three clones were identical and contained an additional amino acid mutation, Y65N, in the N-terminal domain compared to the parent EV20 sequence. This was surprising since there were slight differences in the fluorescence-based assay between these three clones and suggests that this assay may not always be reflective of incorporation efficiency. This synthetase mutant referred to as AAPFRS contains the mutations Y65N, L270F, L274M, N311G, C313G, and Y349F from the wild-type PylRS. The Y65N mutation has not previously been reported as a site for PylRS mutagenesis; however, in directed evolution work performed by David Liu's group, they evolved a PylRS with four mutations in the N-terminal domain.²⁷⁶ Interestingly, these mutations (referred to as IPYE) resulted in a 40-fold improvement in the catalytic efficiency (k_{cat}/K_M^{tRNA}); however, only a modest improvement (2- to 9-fold) in incorporation efficiency was observed.

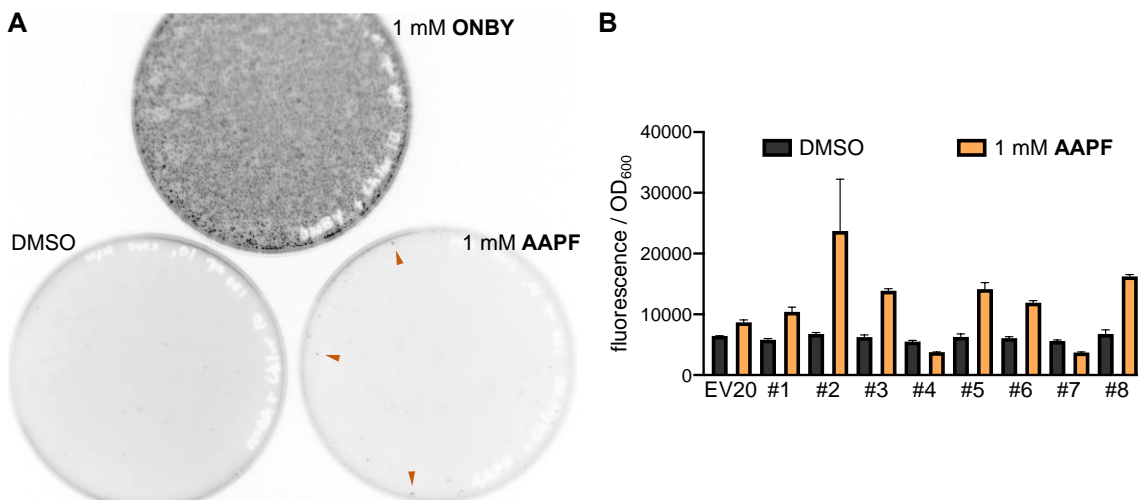


Figure 4-13 PylRS selections using EP-PCR library against **AAPF**

a) Doubly transformed *E. coli* containing the error prone pBK-EV20 library and pRep selection plasmid were selected using 10 μ g/mL chloramphenicol with **AAPF** (and **ONBY** as a control). Orange arrows indicate representative colonies that were selected and tested in liquid culture. b) Comparison of 8 clones in the presence and absence of AAPF show a dependence on the presence of UAA for sfGFP expression.

The pBK-AAPFRS plasmid was isolated separately from the pRep plasmid via gel extraction from a 1% agarose gel. In the future, this AAPFRS should be further tested with the

pBAD-sfGFPY151TAG-PylT construct for expression and purification of **AAPF**-modified protein in order to further validate whether this new synthetase outperforms EV20. Based on literature results using error prone PCR for directed evolution methodologies, multiple rounds of EP-PCR are often required, and in some cases, additional methods for introducing diversity (*e.g.*, DNA shuffling) are used in conjunction.²⁷⁷⁻²⁷⁸

Continued efforts to improve the incorporation efficiency of **AAPF** will facilitate its utility in follow-up application experiments. Once an improved synthetase is evolved, those mutations can also be introduced into the mammalian codon optimized system. For the photoswitchable metal chelation studies discussed in Section 4.3.2, an improved incorporation system will be essential for obtaining enough protein to use in characterization studies and functional assays.

4.3 Introduction to Natural and De Novo Metalloproteins

Approximately half of all proteins for which there is structural data require binding of at least one metal ion and ~40% of all proteins utilize a metal within its catalytic center.²⁷⁹⁻²⁸⁰ Metals play a role in providing structural support, facilitating protein-protein interactions between domains (both inter- and intra-), and functioning as cofactors in enzyme catalysis, through electron transfer processes or by acting as a Lewis acid.²⁸¹ Metalloproteins (or any protein that binds a metal) are involved in a wide array of biological processes and can be categorized into three classes based on their function (storage/transport, metalloenzymes, and signal transduction metalloproteins). Common examples include hemoglobin/myoglobin, cytochromes, carbonic anhydrase, superoxide dismutase, and calmodulin. There are many different metal ions that bind to proteins in various oxidation states, with different preferences for ligand atoms, and in a wide

range of geometries (Table 4-3).²⁸¹ Six naturally occurring amino acids contain sidechains that can complex with these metals: histidine, cysteine, methionine, tyrosine, glutamate, and aspartate.²⁸² Less frequently, the backbone amide can be found in coordination complexes.²⁸³ Interestingly, the cellular concentration of these metal ions does not directly correlate with the occupancy of these metals within proteins (*e.g.*, zinc is the second least abundant metal in Table 4-3, but is the second most prevalent metal found in enzymes with known structures). Although a complete understanding of how proteins/enzymes select for a specific metal ion is still lacking, significant effort has been aimed toward understanding the design principles employed by Nature to create or engineer designer metalloprotein and metalloenzymes.²⁸⁴⁻²⁸⁶

Table 4-3 Properties of metal ions found in biological systems

Geometry abbreviations are as follows: O_h – octahedral, T_d – tetrahedral, C_{4v} – square pyramidal, D_{3h} – trigonal bipyramidal, D_{4h} – square planar). Table adapted from Andreini *et. al.*, *J. Biol. Inorg. Chem.* **2008**, *13*, 1205–1218.

Metal	Common oxidation states	Common coordination numbers	Common coordination geometries	Preferred donors	Redox	Concentration in cells (M)
Mg	2	6	O_h	O	No	10^{-3}
Ca	2	6	O_h	O	No	10^{-7}
		7	Irregular			
		8	Irregular			
Zn	2	4	T_d	N, S, O	No	10^{-11}
		5	C_{4v}/D_{3h}			
		6	O_h			
Mn	2	4	T_d	N, O, S	Yes	10^{-7}
		5	D_{3h}			
		6	O_h			
	3	5	C_{4v}/D_{3h}	O		
		6	O_h			
Fe	2	4	T_d/D_{4h}	N, S, O	Yes	10^{-7}
		5	C_{4v}/D_{3h}			
		6	O_h			
	3	4	T_d	O, N		
		5	C_{4v}			
		6	O_h			
Cu	1	2	Linear	S, N	Yes	10^{-15}
		3	Trigonal			
		4	T_d			
	2	4	T_d/D_{4h}	N, O, S		
		5	C_{4v}/D_{3h}			
		6	O_h			
Co	2	4	T_d	N, O, S	Yes	10^{-8}
		5	C_{4v}/D_{3h}			
		6	O_h			
	3	6	O_h	N, O		
Mo	4	6	O_h	O	Yes	10^{-6}
	6	4	T_d	O		
		6	O_h			

Although only a fraction of the natural amino acids is suitable for efficient metal chelation, many examples of artificial and *de novo* metalloproteins/enzymes have been developed in recent years using only amino acids found in nature.²⁸⁷⁻²⁹⁰ Design of a di-heme four-helix bundle resulted in a complex that binds oxygen more tightly than carbon monoxide (the opposite trend of natural hemoglobin).²⁹¹ Alpha helical bundles have been designed to bind non-native metals such as arsenic, mercury, and cadmium and can be applied as sensors of these toxic metals.²⁹²⁻²⁹³ Using a native scaffold of a DNA-binding protein, the native nickel (II) ligand was swapped out for dioxouranium (II) such that DNA binding was induced only upon exogenous ligand addition.²⁹⁴ Impressively, this early work was conducted with significant trial-and-error through testing of many different designs, and without the aid of computational approaches.

The development of metal binding proteins using unnatural amino acids has also been explored (Figure 4-14).²⁹⁵⁻²⁹⁷ The (2,2'-bipyridin-5-yl)alanine (**BpyA**) was introduced by Imperiali for utilization in designing metal binding peptides,²⁹⁸ and was first genetically encoded by the Schultz group where they showed that T4 lysozyme containing **BpyA** bound copper (II).²⁹⁹ The Schultz group later developed 8-hydroxyquinolinylalanine (**HqA**) and demonstrated that proteins bearing this chelator showed increased fluorescence upon the introduction of zinc (II).³⁰⁰ The Opella group expanded the utility of **HqA** by applying it as a paramagnetic probe in membrane proteins and demonstrated superiority over traditional nitroxide probes.³⁰¹ The Lee group incorporated the more structurally rigid phenanthrolylalanine (**PheA**) into GFP but no discussion of metal chelation was provided.³⁰² In addition to pyridine-based metal chelating UAAs, a pyrazolylytyrosine (**PyY**) was developed by Wang and applied as an electron transfer probe by complexing copper to regulate the quenching of GFP fluorescence.³⁰³ All four of these UAAs

utilize the *Mj*TyrRS/Tyr tRNA pair for incorporation and therefore cannot be applied in mammalian cells.

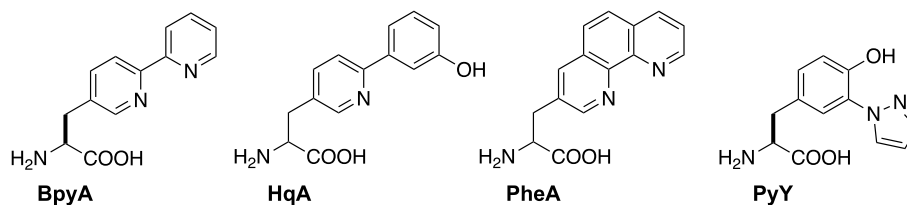


Figure 4-14 Structures of genetically encoded metal chelating unnatural amino acids. Structures of 2,2'-bipyridylalanine (**BpyA**), 8-hydroxyquinolinylalanine (**HqA**), and 1,10-phenanthrolylalanine (**PheA**), 1-pyrazolyltyrosine (**PyY**) are shown.

More recent work has focused on applications involving **BpyA** and extend beyond a simple demonstration of metal chelation. In a follow up report, the Schultz lab demonstrated that **BpyA** could be used to convert an *E. coli* catabolite binding protein into a sequence-specific nuclease through introduction of copper (II) or iron (II) which induced oxidative cleavage of the protein-bound DNA.³⁰⁴ Most recently, the Song lab used **BpyA** to control the self-assembly of symmetrical protein complexes (Figure 4-15). In this work, they introduced **BpyA** at various positions within a D3 symmetry homohexamer (*B. anthracis* acetyltransferase) and showed control of both one- and two-dimensional protein assembly depending on the incorporation site and combination of point mutations. They demonstrated these assemblies resulted in approximately a 20 °C increase in thermal stability compared to the individual subunits and that enzymatic activity was retained even at elevated temperatures.

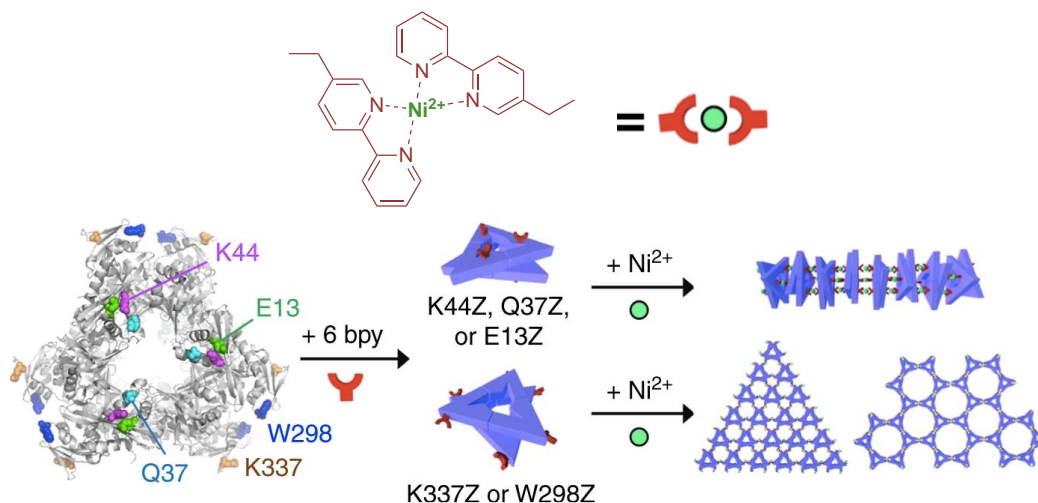


Figure 4-15 Control of protein self-assembly using **BpyA**

The driving force of this self-assembly is the formation of a $[\text{Ni}(\text{bpy})_2]^{2+}$ complex where the red shape represents **BpyA**. Different combinations of point mutants allow for 1D assembly (top) or 2D assembly (bottom). Adapted from Yang *et. al.*, *Nat. Commun.* **2019**, *10*, 5545.

Pioneering work by the Baker lab has capitalized on the power of computational approaches to predict and design *de novo* proteins and enzymes using the natural 20 amino acids.³⁰⁵⁻³⁰⁷ More recently, they have also utilized **BpyA** to computationally introduce a novel metal binding site in a protein initially lacking that functionality³⁰⁸ (Figure 4-16a) and later designed a homotrimer comprised of a trisbipyridyl core (Figure 4-16b).³⁰⁹ In their first design, they introduced **BpyA** (or **Bpy-Ala** in their figure) to function as a bidentate chelator and utilized two natural residues plus two water molecules to comprise their octahedral metal binding site, which was capable of binding several different divalent metal cations with mid picomolar affinities. Their second approach relied upon a scaffold set of *de novo* protein designs (previously developed by their lab) that contained threefold symmetry, in which they introduced **BpyA** at the interface such that metal complexation facilitated assembly of the trimer. These two approaches relied extensively on the computational tool, ROSETTA, that was developed decades ago by the Baker lab for protein structure predictions.³¹⁰

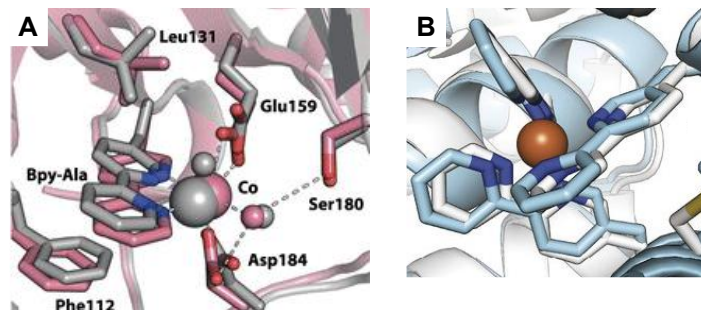


Figure 4-16 Computationally designed metalloproteins reported by the Baker lab

a) A computationally designed protein containing **BpyA** allows for metal binding of copper (II). The design (gray) closely matches the crystal structure (pink). b) Introduction of **BpyA** in a surface exposed helix enabled computational design of a homotrimer with the trisbipyridyl core that chelates iron (II). Again, the prediction (gray) matches the elucidated crystal structure (blue). Panel a is taken from Mills *et. al.*, *J. Am. Chem. Soc.* **2013**, *135*, 13393-13399 and panel b is taken from Mills *et. al.*, *Proc. Natl. Acad. Sci. USA.* **2016**, *113*, 15012-15017.

Based on these previous successes of computationally designed metalloproteins using **BpyA**, we envisioned that a similar methodology could be applied to incorporate photoswitchable metal-chelating amino acids to generate novel metalloproteins that can be regulated with light.

4.3.1 Introduction to Phenylazopyridines as Metal Chelators and Photoswitches

Two phenylazopyridine analogs 4-(2-pyridylazo)resorcinol (**7**) and 1-(2-pyridylazo)-2-naphthol (**8**) shown in Figure 4-17 have extensively been used as colorimetric indicators for the presence of various metal ions as measured by a bathochromic shift in the absorption maximum.³¹¹ These sensors have been found to chelate many biologically relevant transition metals such as manganese (II), iron (II), cobalt (II), copper (II), and nickel (II) in a tridentate manner with two equivalents of ligand per metal.³¹²⁻³¹⁴

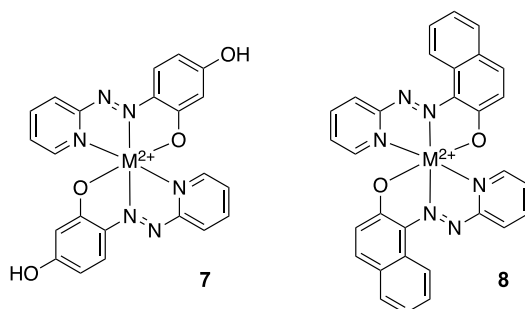


Figure 4-17 Structures of 4-(2-pyridylazo)resorcinol (**7**) and 1-(2-pyridylazo)-2-naphthol (**8**)
 Both 4-(2-pyridylazo)resorcinol (**7**) and 1-(2-pyridylazo)-2-naphthol (**8**) can form tridentate complexes with a variety of divalent transition metals and typically form in a 1:2 ratio.

Additionally, the non-modified phenylazopyridine core has been shown to function as a bidentate ligand in complexes with ruthenium (II), nickel (II), cobalt (II) and zinc (II) in organic solvents.³¹⁵⁻³¹⁸ Interestingly, in many reported examples, there is no discussion of the ability to use light to regulate chelation or complex formation using differences in *cis*- versus *trans*-isomers. In most examples, the *trans*-isomer functioned as a bidentate ligand; however, in some cases, the *cis*-isomer was used as a monodentate ligand.

A thiol-modified phenylazopyridine analog was developed by the Russell lab and used to generate a self-assembled monolayer on a thin gold film (Figure 4-18).³¹⁹ When the ligand was incubated with nickel (II) or cobalt (II) in the free thiol (unconjugated) form, both the *cis*- and *trans*-isomers were found to bind with similar affinities. However, when they tested metal binding capabilities of the self-assembled monolayer, they observed slightly reduced binding in the immobilized *trans*-form relative to the in-solution affinity; however, no binding to the *cis*-isomer was detected. Unfortunately, a discussion of the ability to reverse the metal:*trans*-isomer coordination was not included.

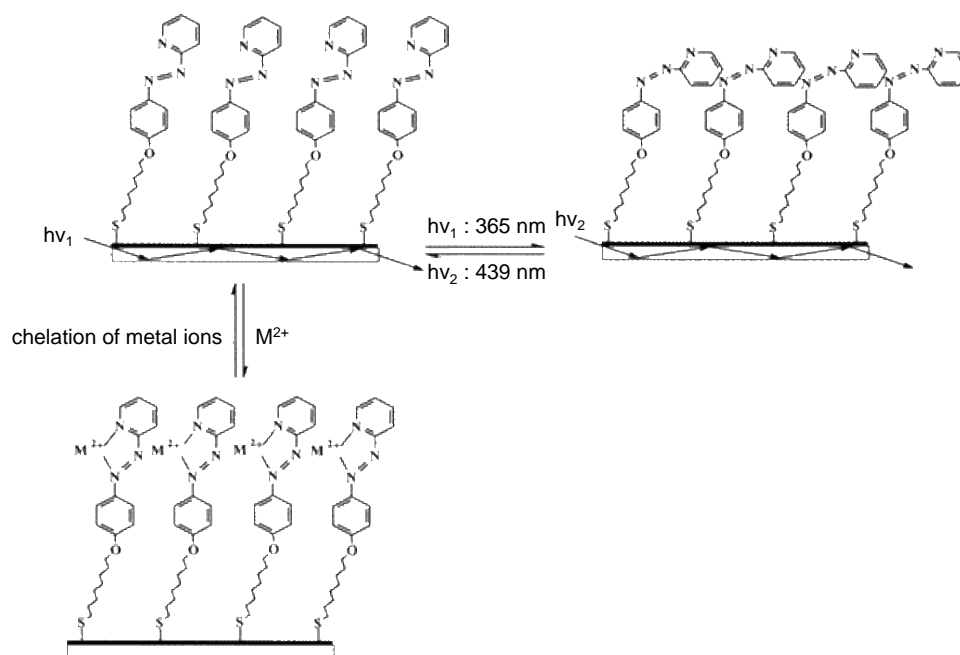


Figure 4-18 Photoswitching and metal ion chelation of a self-assembled monolayer containing a phenylazopyridine. A thiol-modified phenylazopyridine was used to generate a self-assembled monolayer on a gold film. The photoswitching properties of the phenylazopyridine were retained in the immobilized monolayer. Additionally, metal chelation of nickel (II) and cobalt (II) were only observed in the *trans* configuration. Figure taken from Wang *et. al*, *Langmuir*. **2003**, 19(9), 3779-3784.

The Goto lab developed a bowl-shaped framework using a bis-terphenyl core with a 4-(phenylazo)pyridine moiety protruding outward from the core.³²⁰ They demonstrated that the *trans*-isomer bound to a zinc-porphyrin, while the *cis*-isomer was too sterically hindered to form a complex (Figure 4-19). When they tested just the 4-(phenylazo)pyridine core, no differences in *trans*- and *cis*-isomer binding to zinc was observed, thus indicating the importance of steric bulk. Although they demonstrate that the bowl-shaped structure successfully undergoes cycles of photoswitching, they do not provide any discussion as to whether the interaction with the zinc-porphyrin can be reversed using light.

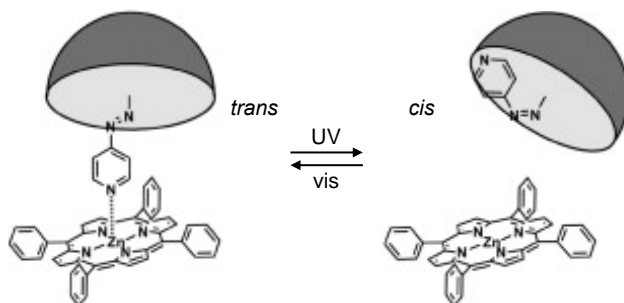


Figure 4-19 A bowl-equipped 4-(phenylazo)pyridine for control of zinc chelation

Introduction of a phenylazopyridine into a bis-terphenyl structure generated a bowl-shaped framework which was found to chelate zinc (II) only in the *trans* configuration as the *cis*-isomer was sterically precluded from metal binding. Reversion in response to visible light was not demonstrated although it is depicted in the figure. Figure taken from Suwa *et. al.*, *Tetrahedron Lett.* **2009**, 50(18), 2106-2108.

Follow-up work by the Herges lab developed several phenylazopyridines analogs that undergo reversible complex formation with a Ni-porphyrin core.³²¹ Many transition metals can exist in different spin states as a result of their coordination number, and in this change in spin state can be measured via NMR. In the case of nickel (II) used here, the square planar coordination observed with the porphyrin complex is diamagnetic; however, upon coordination at either one or both of the axial sites generates square-pyramidal or octahedral geometries which are both paramagnetic. In this work, various designs using 2-, 3-, or 4-substituted phenylazopyridines can be generated such that either the *cis*- or *trans*-isomers favorably interact with the metal center while the other isomer results in an unfavorable interaction that disrupts the complex (Figure 4-20a-b). They demonstrated that introduction of bulky *tert*-butyl groups onto the phenyl ring allowed for significantly improved switching over the unmodified phenyl ring (labeled parent system) when measuring changes in spin state of the associated metal center (Figure 4-20c). To do this, a solution containing the Ni-porphyrin (0.1 mM) was treated with the various phenylazopyridine (160 mM) in toluene and alternating cycles of irradiation with 365 and 440 nm LEDs were performed, followed by analysis of NMR in order to determine changes in the para- and diamagnetic nature of the complex.

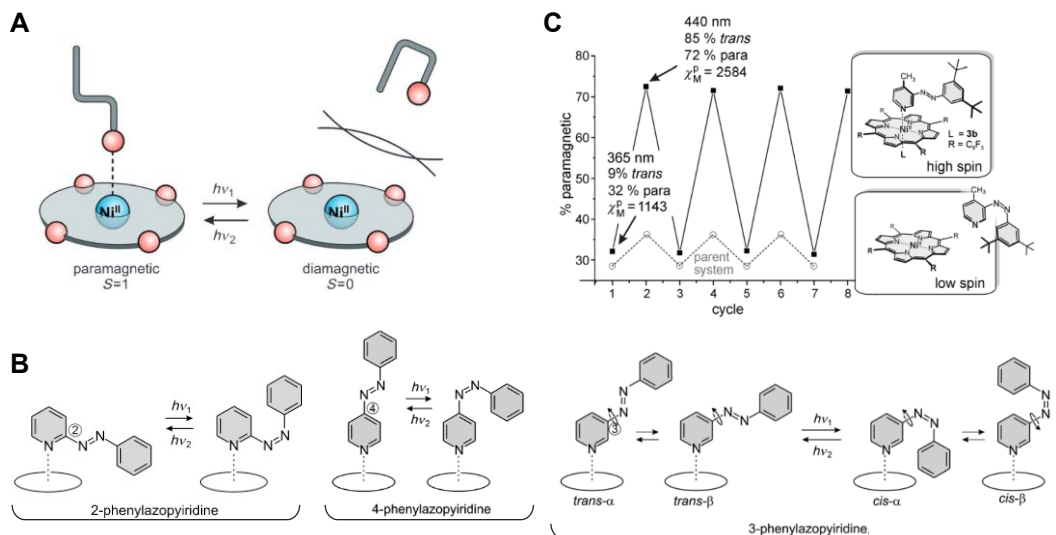


Figure 4-20 Phenylazopyridines as photodissociable ligands for Ni-porphyrins

a) Schematic of the photodissociable ligand strategy where the *trans*-isomer binds to the axial position of a Ni-porphyrin, while the *cis*-isomer results in unfavorable interactions that prevent complex formation. b) Various arrangements of 2-, 3-, and 4-phenylazopyridines allow for different design strategies. c) Irradiation with different wavelengths of light allowed for reversible complex formation between a bulky 3-phenylazopyridine analog and a Ni-porphyrin core as determined by spin state changes from dia- to paramagnetic nickel centers. Figure adapted from Thies *et. al.*, *Chem. Eur. J.* **2012**, 18(51), 16358-16368.

Based on these literature reports, we envisioned that the phenylazopyridine core could be used to generate three different phenylalanine derivatives with *ortho*-, *meta*-, and *para*-azopyridine substitutions (Figure 4-21) that would allow for the development of non-natural metal chelation sites which could potentially allow for light regulation of complex formation. We hypothesized the *ortho*-substituted analog might function similarly to the self-assembled monolayer in that we could use light to convert the immobilized, inactive *cis*-isomer to the active *trans*-isomer, thereby enabling control of bidentate metal binding. The *para*- (and presumably the *meta*-) substituted analogs are predicted to bind in a monodentate fashion as observed with the bowl-containing analog developed by Goto. While their work required introduction of bulky substituents to achieve selective binding, in our case, the steric bulk and rigidity imposed by the protein macromolecule should have a similar effect. Depending on the stability of the metal complex generated with each of these three analogs, using light to break open the complex might be more feasible for the

monodentate ligands over the bidentate ones; however, due to a lack of literature reports discussing this conversion, ligand preference will need to be experimentally determined.

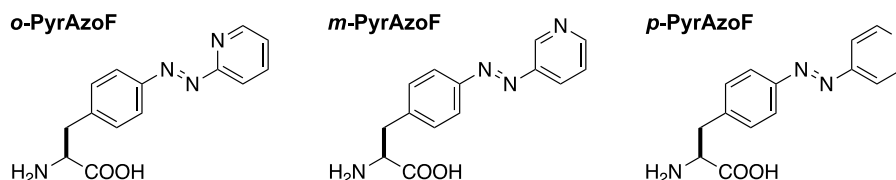


Figure 4-21 Structures of phenylazopyridine-based amino acids
Potential metal chelating amino acids composed of phenylazopyridine motifs. Synthesis of **o-PyrAzoF** was performed by Trevor Horst, while synthesis of **m-PyrAzoF** and **p-pyrAzoF** is currently underway by Olivia Shade.

In collaboration with the Khare lab (a computational biology lab at Rutgers University), we are utilizing **AAPF** and **o-PyrAzoF** to computationally design novel metalloproteins. We are planning to incorporate **AAPF** at a position such that the *trans*-isomer will function to coordinate an essential metal ion to produce an active enzyme, while irradiation to generate the *cis*-isomer will either break the coordination (Figure 4-22a) or move the metal site and perturb enzyme function. In a similar manner, we eventually aim to use **o-PyrAzoF** as a bidentate ligand to replace two of the natural ligands; however, computationally, this a much more challenging goal. Additionally, the Khare lab has provided us with designs to generate novel metal binding sites within several different protein targets. In this approach, trimeric proteins with C₃ symmetry were selected and *trans*-**AAPF** was introduced at the trimer interface to form a tetrahedral coordination site (here, with zinc in mind), leaving one site open for a water molecule (Figure 4-22b). Upon isomerization to the *cis*-form, we hypothesize the geometry will be disrupted and the metal ion will no longer be complexed.

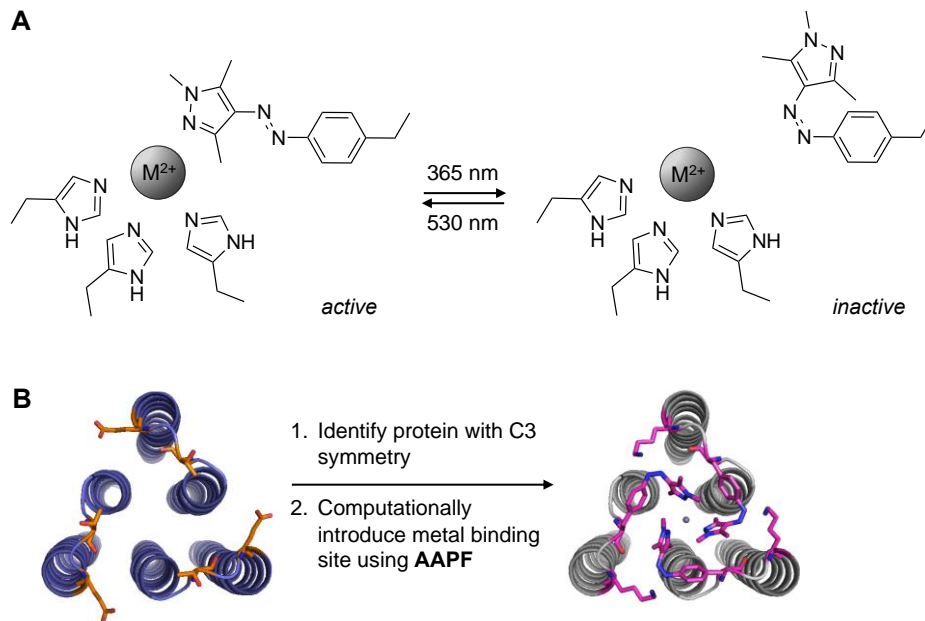


Figure 4-22 Computationally designed metalloproteins bearing **AAPF** modifications

a) Replacement of a chelating ligand (potentially cysteine, histidine, or aspartate) with *trans*-**AAPF** generates a near-native, active enzyme. Upon irradiation and generation of the *cis*-isomer, the metal site is perturbed resulting in enzyme inactivation. b) Trimeric proteins with C3 symmetry were selected and a novel metal binding site was introduced at the trimer interface using *trans*-**AAPF** to generate a tetrahedral coordination site. Conversion to the *cis*-isomer will disrupt the coordination geometry and is predicted to release the metal ion.

4.3.2 Toward Control of Metal Complex Formation using Photoswitchable Amino Acids

We hypothesized generation of an *ortho*-substituted pyridinylazophenylalanine (***o*-PyrAzoF**) analog would generate a metal chelating amino acid similar to **BpyA**, but with the potential for photoswitchable control. Trevor Horst synthesized ***o*-PyrAzoF** and a synthetase panel screen was performed as in Section 4.2 to find candidate synthetases that could incorporate this new UAA (Figure 4-23). Small scale (200 μ L) cultures were prepared with and without ***o*-PyrAzoF** (**ONBY** and **AzoF** were used as controls) to assess whether any of our existing synthetases could utilize this new UAA. Cultures were grown to an OD₆₀₀ of 0.5 at 37 °C and induced with 0.1% arabinose, followed by the addition of unnatural amino acid. Cultures were grown overnight with shaking at 37 °C to allow for incorporation and protein expression, then the

following day an aliquot (100 μ L) was transferred to a 96-well plate and sfGFP fluorescence (ex. 488/5 and em. 510/5 nm) and optical density (absorbance at 600 nm) were measured using a plate reader. The sfGFP fluorescence was normalized to the OD₆₀₀ and was plotted for all of the synthetases with each amino acid (Figure 4-23). Only EV16-5 and EV20 showed a greater than 2-fold increase in the presence of ***o*-PyrAzoF**, which is consistent with previous findings that those two synthetases efficiently incorporate the traditional **AzoF**.

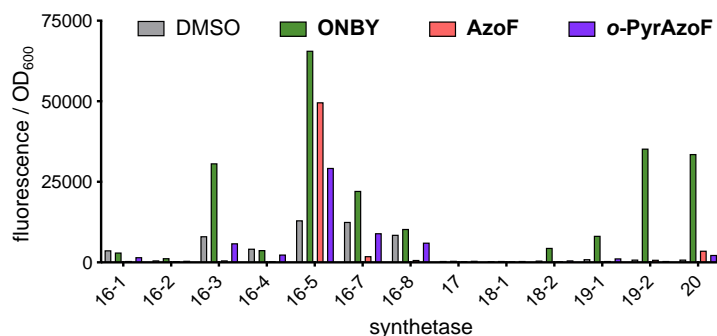


Figure 4-23 Synthetase screen of *MbPylRS* variants with ***o*-PyrAzoF**

A small panel of *MbPylRS* mutants was screened using an sfGFP reporter to assess whether an existing synthetase would be capable of utilizing ***o*-PyrAzoF** as a substrate.

Larger expression cultures (5 mL) were prepared in an analogous method used for the screen – only synthetases EV16-5 and EV20 were included – in order to confirm incorporation via gel and mass spectrometry. Following expression, lysis, and Ni-NTA purification, the samples were analyzed via SDS-PAGE, followed by Coomassie staining (Figure 4-24a). Compared to the **AzoF** control, both synthetases showed a lesser degree of incorporation with ***o*-PyrAzoF**. EV16-5 resulted in the highest level of incorporation in the presence of ***o*-PyrAzoF** and the purified sample was submitted to the Department of Chemistry Mass Spectrometry facility for ESI analysis (Figure 4-24b). Following deconvolution, a mass of 28350.920 was observed, which closely matches the expected mass of 28351.119 ($\Delta -0.185$ Da). Significant background incorporation of phenylalanine was observed (28245.957 Da), which closely matches the expected mass of 28246.019 ($\Delta -0.062$ Da). This is consistent with previous reports of unnatural amino acids

incorporated with this specific synthetase mutant. In an effort to improve the yield of modified protein, we tried increasing the ***o*-PyrAzoF** concentration from 1 mM to 5 mM; however, this concentration resulted in moderate toxicity as observed by a reduction of total cell volume after 20 hours of expression.

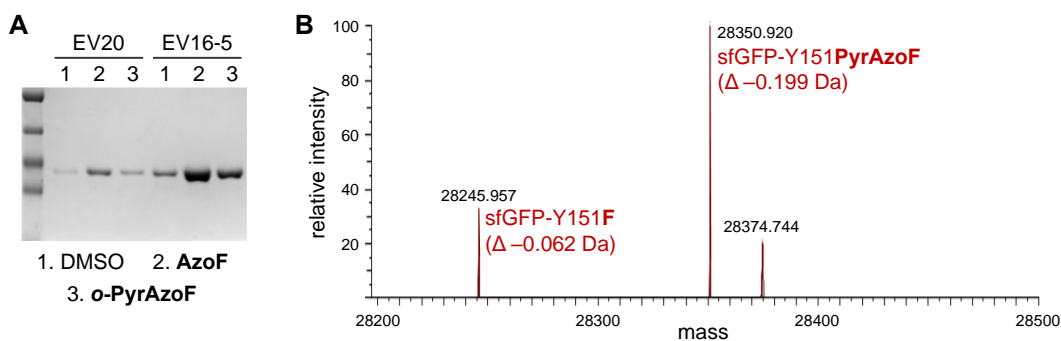


Figure 4-24 ***o*-PyrAzoF** was successfully incorporated in *E. coli* and confirmed by ESI-MS

a) SDS-PAGE analysis of purified sfGFP-Y151***o*-PyrAzoF** more efficient incorporation with EV16-5 than EV20 in the presence of ***o*-PyrAzoF**. b) ESI-MS analysis of the EV16-5 sample shows successful incorporation; however, significant background phenylalanine incorporation was observed and an additional unidentified contaminant was present.

Initial attempts to incorporate ***o*-PyrAzoF** into mammalian cells were unsuccessful, even though the transfection was successful, as observed by mCherry fluorescence (data not shown). Additionally, cellular toxicity at concentrations above 0.5 mM was observed for ***o*-PyrAzoF**. Optimization of transfection reagent or transfection/expression time, as well as further UAA purification, might enable ***o*-PyrAzoF** incorporation in mammalian cells and should be pursued in the future.

Next, we characterized the photophysical properties of ***o*-PyrAzoF** in an analogous manner as performed previously for **AAPF**. Irradiation of a solution (0.1 mM) prepared in PBS at pH 7.4 using 365 nm light to generate the *cis*-isomer shows distinct spectra from the dark-adapted *trans*-isomer (Figure 4-25a,b). We determined the photostationary state ratios using HPLC (monitored at 280 nm) to separate the two isomers and the peak areas of each isomer were integrated (Figure 4-25c). The dark state, a 365 nm irradiated sample, and a subsequent 530 nm irradiated sample

resulted in PSS ratios of *trans*:*cis* of 99:1, 13:87, and 71:29, respectively. Then, we determined the thermal stability of the *cis*-isomer of ***o*-PyrAzoF** at 37 °C using PBS at pH 7.4 since our studies with **AAPF** showed improved thermal stability in the more physiological solvent. When fit with an exponential decay model, a $t_{1/2}$ of 87 hours was calculated, suggesting that this analog has even greater thermal stability than **AAPF** (Figure 4-25d). This aligns favorably with literature reported phenylazopyridine analogs in which the *cis*-isomer thermal stability ranges from 13 minutes to 300 hours, depending on the phenyl substituents and solvent used.

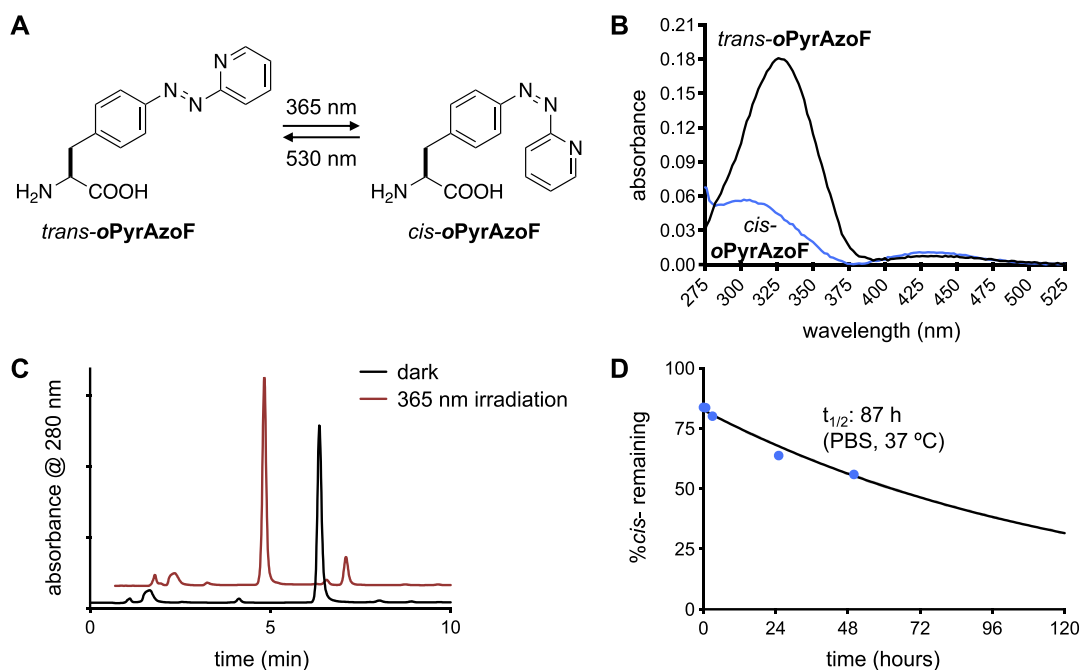


Figure 4-25 Determination of photostationary states and thermal stability of ***o*-PyrAzoF**

a) Structures of both *cis*- and *trans*-***o*-PyrAzoF** are shown. b) Absorbance spectra of *cis*- and *trans*-isomers at 100 μ M in PBS. c) HPLC analysis to determine photostationary states showed distinct peaks for each isomer. d) Thermal stability of *cis*-***o*-PyrAzoF** was tested in PBS at pH 7.4 and analyzed via HPLC.

Next, we proceeded to test whether ***o*-PyrAzoF** would function to chelate/complex various metal ions. Metal complexes consisting of one or more phenylazopyridines functioning as a bidentate chelate have been reported for cobalt (II), nickel (II), copper (II), zinc (II), and ruthenium (II); however, all of these examples were synthesized using organic solvents followed by crystallization and subsequent characterization.³²²⁻³²⁴ Because these conditions are quite different

from what we can assemble in a biological setting, we first tested whether any change in the absorbance spectrum would be detected upon introduction metal ions and subsequent complex formation. Literature reports indicate that metal complexes typically result in a shift (either hypso- or bathochromic) in absorbance maxima compared to the ligand alone and in many cases appearance of an additional peak in the 500 to 700 nm range is observed.³²⁵⁻³²⁹ We combined ***o*-PyrAzoF** in 1:1 molar ratios with eleven different metal chloride salts covering various oxidation states. While this does not match the stoichiometry of common complexes, a shift in the absorbance maximum should still be observed. An absorbance spectrum was acquired for each combination and the background absorbance of the metal ion alone in buffer was subtracted. A bathochromic shift for both nickel (II) and copper (II) was observed, shifting from λ_{max} of 326 nm to 330 and 342 nm, respectively (Figure 4-26a,b). Additionally, in the presence of copper, a broad peak with a λ_{max} of 536 nm was detected. None of the alkali or alkaline earth metals showed any significant change in absorbance (and presumably chelation), which was expected due to the preferential complex formation of (bi)pyridines with transition metals.³³⁰⁻³³¹

We performed an identical experiment using the **AzoF** isostere which lacks the pyridinyl nitrogen necessary to form a bidentate chelate and may or may not be able to coordinate a metal with either of the azo nitrogens, expecting this to function as a negative control. Unlike with ***o*-PyrAzoF** no shift in the λ_{max} was observed for any of the metals; however, both nickel (II) and copper (II) showed a significant decrease in absorbance at the maximum (Figure 4-26c,d), suggesting an interaction could be occurring between an azo nitrogen and the metal ion. To further characterize the stoichiometry of complex formation, we should titrate increasing amounts of metal ion against ***o*-PyrAzoF** or **AzoF** in order to generate a Job plot.³³²⁻³³³ By maintaining a constant sum of molar concentration of both metal and ligand while varying the molar ratio of the two

components, one can extrapolate the binding stoichiometry as the maximum of a plot of UV absorbance versus mole fraction. Further complicating matters, α -amino acids have been reported to chelate metal ions, thus, we may be observing chelation of these metal ions with the carboxylate and amine.³³⁴⁻³³⁶ To avoid this, these experiments should be repeated with just the chromophore alone.

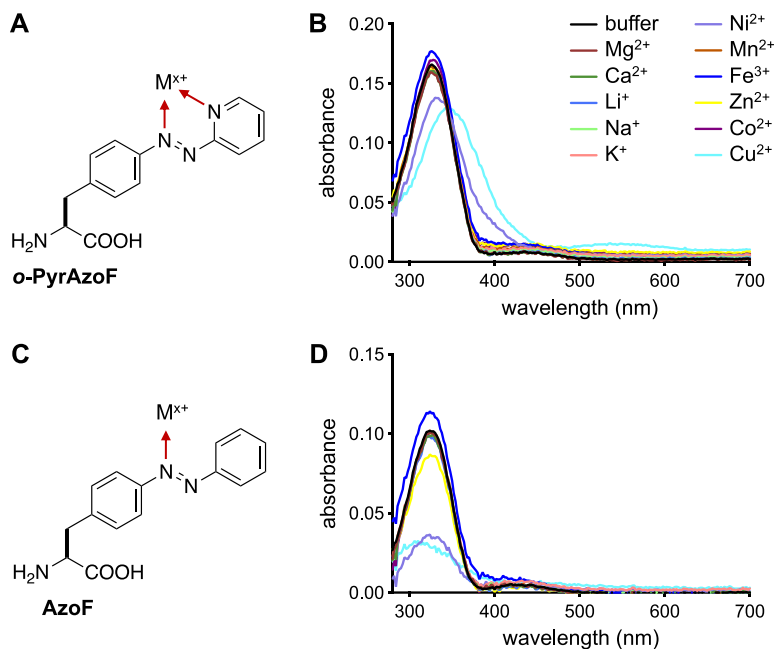


Figure 4-26 Absorbance spectra of *o*-PyrAzoF in the presence and absence of metal ions
a) *o*-PyrAzoF is predicted to form a bidentate chelate in the presence of metal ions. b) A 1:1 molar ratio of metal ion to *o*-PyrAzoF was prepared at 50 μ M (in 25 mM HEPES at pH 7.5) and the absorbance spectrum for each combination was recorded. c) AzoF has the potential to form a monodentate chelate. d) Same experiment in (b) was repeated using AzoF.

To avoid the influence of the amino acid moiety, test substrates were synthesized for use in follow-up isothermal calorimetry (ITC) studies. Removal of the amino acid and β -carbon to yield the core phenylazopyridine (**9**) is the most relevant substrate (Figure 4-27). The corresponding imines with either C=N or N=C connectivity would allow us to confirm bidentate chelation as **11** is unexpected to form a chelate since literature reported 2-aminopyridine complexes with transition metals all utilize a tridentate ligand,³³⁷⁻³³⁸ while **10** is expected to show a similar binding affinity as **9**. Unexpectedly, preliminary ITC binding experiments showed that **9**

interacted with copper (II) similarly to **11** rather than **10** when comparing heat released (ΔH in cal/mol) under identical experimental condition, thus invalidating our anticipated mode of binding. Additional ITC studies need to be performed in order to elucidate the binding stoichiometry (N) and the K_a of these ligands with copper (II) since early saturation resulted in incomplete curves in these current experiments. Testing of additional metal ions for complex formation should also be explored.

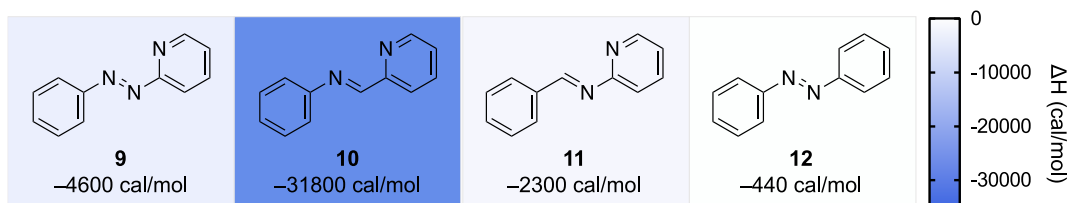


Figure 4-27 Test substrates for *o*-PyrAzoF metal chelation

Structures of phenylazopyridine **9**, imines **10** and **11**, and azobenzene **12**. Compounds **9** – **11** were synthesized by Olivia Shade. ITC binding studies were conducted using 1.2 mM of ligand in the cell with 18 mM of copper (II) sulfate in the syringe. A heat map displaying the relative enthalpy where dark blue represents a large heat release, while light blue indicates a low value.

Concurrently, we explored the potential for **AAPF** to function as a metal chelator. In literature examples of pyrazole-metal complexes, a bidentate ligand is often utilized, as seen in **PyY**. Examples of monodentate pyrazole ligand metal complexes have been reported; however, these were typically formed in boiling organic solvents.³³⁹⁻³⁴⁰ These complexes were usually characterized by NMR and X-ray crystallography, and in some cases, molar conductance and IR spectrum are provided. For preliminary testing, we chose to utilize just the pyrazole moiety to avoid any potential interaction from either of the azo nitrogens or the amino acid functionalities since the designs in Figure 4-22 rely solely on the pyrazole. To represent **AAPF**, we used 1,3,5-trimethylpyrazole (**15**) in ITC binding studies. Attempts to optimize concentrations of metal in the cell or syringe versus concentrations of **15** in the cell or syringe were conducted; however, we were unable to detect any heat release. We compared using Tris versus HEPES buffers since reports have shown slight differences in thermodynamic parameters depending on the pH and

buffer; however, no difference was observed.³⁴¹⁻³⁴² Next, we employed imidazole (**13**) as a control compound for histidine, which has extensively been explored in ITC and other assays for metal binding studies.^{341, 343-344} We used 2 mM of metal ion in the cell and a 90 mM solution of ligand in the syringe³⁴¹ prepared in Tris buffer at pH 7.5. The values for ΔH (in cal/mol) for **13** with four metal ions and different counter anions are summarized in Figure 4-28. These values are slightly lower than literature reported values where histidine was titrated against various transition metal ions, but show the same trend for the different metals.³⁴⁴ To explore whether the *N*-methyl group of **15** was preventing metal binding, we tested 3,5-dimethylpyrazole (**14**) under the same conditions used for **13**. Unfortunately, no binding was observed with this test substrate either. Based on these results, it does not appear that **AAPF** will function to chelate metal ions in its current form; however, there is a chance that upon pre-arrangement of the trimeric interface, that a pseudo-tridentate chelate could still form.

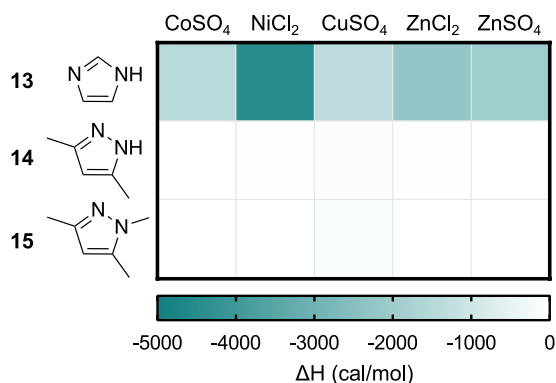


Figure 4-28 ITC binding studies of **13**, **14**, and **15** with four different metal ions. Solutions of **13**, **14**, and **15** were prepared at 90 mM in Tris buffer, while the metal ion solutions were prepared at 2 mM and were placed in the syringe and cell, respectively. The ΔH (in cal/mol) for each of the combinations is plotted.

Additionally, we could modify **AAPF** to contain *N*-propargyl instead of *N*-methyl, such that a subsequent click reaction would generate a triazole which might function as a bidentate chelator. Unfortunately, this would require completely new protein designs, but may be necessary to generate a stable metal complex. Prior to synthesizing the new UAA, we first decided to prepare

the analogous test substrates for ITC binding studies. The 1-propargyl-3,5-dimethylpyrazole (**16**) was synthesized following a literature protocol,³⁴⁵ and was provided to former Deiters lab member Filippo Gentile for modification via a click reaction with benzyl azide to generate **17** (Figure 4-29a). To date, similar pyrazole-triazole substructure cores have been shown to function as bidentate chelators of rhodium (II), iridium (II) and Cu₄I₄,³⁴⁶⁻³⁴⁷ so this test substrate might allow for complex formation with similar divalent transition metals. ITC studies were performed in a similar manner as before where 20 mM metal ion solutions were injected into the cell containing 2 mM ligand (Figure 4-29b). Relative to imidazole, very weak binding was observed for the pyrazole-triazole structure with the three metal ions tested here. Based on these results, synthesis of the corresponding propargylated amino acid is unlikely to afford an efficient metal chelator, and will likely lead to even lower incorporation efficiency upon introduction of a bulkier *N*-substituent. Due to differences in the pi-donor and pi-acceptor nature of various N-heterocycles, it might prove beneficial to connect pyrazoles to bipyridine or terpyridine ligands for improved metal complex formation.³⁴⁸

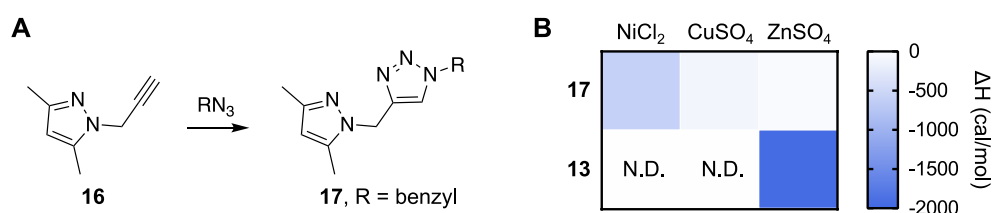


Figure 4-29 Pyrazole test substrate as putative divalent chelate

a) The propargylated dimethylpyrazole **16** was subjected to a click reaction with benzyl azide (performed by Filippo Gentile) to generate **17**. b) ITC binding studies were performed by injecting 20 mM solutions of **17** (with **13** used as a control) into 2 mM metal ion solutions. Combinations not tested are indicated with N.D.

4.4 Summary and Outlook

We have successfully incorporated two new photoswitchable amino acids in *E. coli* that provide improvements in photoswitching properties and introduce functionalities not found in previously developed analogs. Preliminary experiments suggest that ***o*-PyrAzoF** can form complexes with nickel (II) and copper (II); however, additional experiments need to be conducted to validate this and to determine the stoichiometry of binding. In initial efforts to demonstrate metal chelation with **AAPF** test substrates, none of the metals tested showed any complex formation with the various ligands tested via ITC. Similar experiments could be conducted with other transition metals such as ruthenium (II), iron (II), and manganese (II) since these metals show preferential complex formation with *N*-based ligands (Table 4-3). Additionally, we could consider synthesizing a test substrate that would mimic the tridentate arrangement of the three *trans*-**AAPFs** at the trimer interface to test for metal complex formation.

Additionally, PylRS selections using an error-prone PCR library produced one new synthetase mutant that will undergo additional validation to determine its efficiency relative to EV20. This library can also be mutagenized further through DNA shuffling or subsequent rounds of EP-PCR in order to identify improved synthetase mutants for AAPF and *o*-PyrAzoF. Lastly, the protocols developed during these selection efforts can be applied for the generation of mutant libraries with different starting PylRS sequences for improving the incorporation of other unnatural amino acids within the lab.

4.5 Methods

Reagents. Unnatural amino acids **AAPF**, ***o*-PyrAzoF**, and **AzoF** were synthesized by Trevor Horst. **ONBY** was synthesized by Dr. Jessica Torres-Kolbus. All amino acids were provided as HCl salts. The three photoswitchable analogs were prepared as 100 mM solutions in DMSO, while the caged tyrosine was prepared at 100 mM in 0.25 M NaOH. The propargyl pyrazole **16** was synthesized following a literature reported procedure,³⁴⁵ then provided to Filippo Gentile for further modification.

Cloning of PylRS constructs in the pEVOL and pUltra systems. To generate pEVOL-AzoFRS, the *Mj*TyrRS sequence published by the Schultz lab was ordered from Twist Bioscience (see Table 4-5).²²⁹ Primers AzoFRS1 F/R and AzoFRS2 F/R were used to PCR amplify the gene fragment and introduce the necessary restriction sites on both the 5' and 3' ends, then the gene fragments were digested with the appropriate enzymes following protocols in 8.1.1 and 8.1.3. pEVOL-VSFRS (cloned for use with VSF – vinylsulfonamide phenylalanine – from parent Addgene plasmid pEVOL-AzF - #31186) was used as the backbone and was linearized with NdeI and PstI. Standard T4 DNA ligation cloning (see 8.1.4) was used to generate pEVOL-VSFRS1-AzoFRS2, which was confirmed by sequencing at Genewiz using the TyrRS2 forward sequencing primer. This plasmid was utilized as the backbone and was linearized with BglII and SalI, then the AzoFRS1 fragment was ligated using T4 DNA ligase (see 8.1.3 and 8.1.4). pEVOL-AzoFRS (now containing both copies of AzoFRS) was confirmed by sequencing at Genewiz using their pBAD forward sequencing primer.

Two different improved *E. coli* UAA expression systems were assembled for use with the pET-sfGFP constructs described above. The parent plasmids pEVOL-AckRS and pUltra-MmPylRS-optPylT were kindly provided by Wenshe Liu (Texas A&M University) and Abhishek

Chatterjee (Boston College). Backbone pieces were PCR amplified using primers EVOL-bb F/R and Ultra-bb F/R primers, respectively, while the PylRS pieces were amplified using EVOL-EV20 F/R and Ultra-EV20 F/R with pBK-EV20 used as the template following protocols in 8.1.1. Gel purified pieces were Gibson assembled using a 1:3 ratio of backbone:insert as described in 8.1.5. Both constructs were verified by sequencing at Genewiz: pEVOL-EV20 used pBAD forward and reverse sequencing primers, pUltra-EV20 used UltraRS seqF/R primers provided in the table.

Cloning of a His-tagged PylRS. For generation of a His-tagged *MbPylRS* expression construct, the *MbPylRS* containing EV20 mutations was PCR amplified using His-EV20 F/R primers with pEV20 as the template (see 8.1.1). An N-terminal histidine tag was added using the forward primer. Plasmid pCFP-FRB_{x5}-His (from Chapter 5) was used as the backbone since it already contained an IPTG-inducible promoter and it was linearized with NcoI and XhoI to remove the unwanted insert (see 8.1.3). A Gibson assembly was performed following 8.1.5 to assemble the His-*MbPylRS* into the pET backbone, yielding pHis-*MbPylRS*. This construct was confirmed by sequencing at Genewiz using their T7 forward and T7 term reverse sequencing primers.

Cloning of bacterial expression constructs for UAA incorporation. To generate a bacterial dual reporter plasmid for UAA incorporation, a bacterial codon optimized mCherry gene sequence was obtained from the Childers lab (pXCHYC-2a). The mCherry fragment was PCR amplified using mCherry F/R primers in Table 4-5 following protocols in 8.1.1. The sfGFP-Y151TAG piece was obtained by PCR amplifying from pBAD-sfGFP-Y151TAG-PylT using sfGFP F/R primers. A C-terminal histidine tag was added through introduction in the reverse sfGFP primer. The pBAD-sfGFP-Y151TAG-PylT plasmid was doubly digested with NcoI and NdeI to generate the backbone fragment as detailed in 8.1.3. A two-insert Gibson assembly was performed in order to assemble

pBAD-mCherry-sfGFP-Y151TAG-6xHis-PylT as described in 8.1.5. The plasmid sequence was confirmed by Genewiz using their pBAD-forward and reverse primers.

The pBAD-sfGFPY151TAG-PylT plasmid was modified to remove the PylT sequence for use in conjunction with the Schultz pEVOL system. The plasmid was linearized with PstI and NotI to remove the PylT (see 8.1.3), then the sticky ends were blunted using a Quick Blunting Kit (NEB E1201) following the manufacturer's protocol, and a T4 DNA ligation reaction was performed to recircularize the plasmid (see 8.1.4). Successful removal was confirmed by sequencing at Genewiz using their M13F sequencing primer.

To generate sfGFP constructs under IPTG-inducible control, two different plasmids were assembled: pET-His-sfGFP-Y151TAG and pET-sfGFP-Y151TAG-His. Primers His-sfGFP F/R were used to PCR amplify His-sfGFP-Y151TAG and primers sfGFP-His F/R were used to amplify sfGFP-Y151TAG-His (the histidine tag was included in the reverse primer) using pBAD-sfGFP-Y151TAG-PylT as the template for both reactions following the protocols in 8.1.1. Plasmid pCFP-FRB_{x5}-His was used as the backbone since it already contained an IPTG-inducible promoter and it was linearized with NcoI and BamHI to remove the unwanted insert (see 8.1.3). Gibson assemblies were performed to assemble pET-His-sfGFP-Y151TAG and pET-sfGFP-Y151TAG-His using backbone:insert ratios of 1:3 as described in 8.1.5. Both constructs were confirmed by sequencing at Genewiz using their T7 forward and T7 term reverse sequencing primers.

Generation of a mutagenized library based on pBK-EV20 using EP-PCR. Error-prone PCR was performed using the pBK-EV20 plasmid as the starting template following a literature protocol which is detailed here.²⁷⁴ A 100 μ L error prone PCR reaction was assembled as described in Table 4-4 using primers EP-EV20 F/R from Table 4-5. PCR cycling conditions were performed as for standard PCR (see 8.1.1) except only 20 PCR extension cycles were used. The PCR product

was purified by gel extraction (8.1.13); however, a low yield was obtained (~15 ng/ μ L). A standard 50 μ L DreamTaq PCR reaction was performed as described in 8.1.1 in order to generate sufficient material for Gibson assembly. Following gel purification, a concentrated PCR product of ~90 ng/ μ L was obtained.

Table 4-4 Assembly of error-prone PCR

Volume	Reagent	Final Concentration
10 μ L	100 mM Tris-HCl pH 8	10 mM
2.5 μ L	2 M KCl	50 mM
3.5 μ L	200 mM MgCl ₂	7 mM
4 μ L	25 mM dCTP	1 mM
4 μ L	25 mM dTTP	1 mM
4 μ L	5 mM dATP	0.2 mM
4 μ L	5 mM dGTP	0.2 mM
2 μ L	100 μ M forward primer	2 μ M
2 μ L	100 μ M reverse primer	2 μ M
10 μ L	200 pg/ μ L template	20 pg/ μ L
2 μ L	25 mM MnCl ₂	0.5 mM
1 μ L	DreamTaq DNA pol.	0.05 U/ μ L
51 μ L	water	

A 100 μ L Phusion PCR reaction was utilized for generating the backbone EV20 fragment using primers pBK-bb F/R in Table 4-5, followed by gel extraction to yield ~300 ng/ μ L of purified product. Gibson assembly was performed using 300 ng of the backbone fragment with 180 ng of the EP-EV20 insert (this is approximately 6x more DNA than normal) using the Gibson mix described in 8.1.5. It was essential to use commercial chemically competent *E. coli* (MAX Efficiency DH5 α – Invitrogen 18258012) for transformation of the Gibson assembled library, following the manufacturer's protocol. Ten microliters (1/100th of the cell suspension) were diluted into 40 μ L of LB broth and the entire 50 μ L were plated on LB agar containing kanamycin (50 μ g/mL). The remaining 990 μ L of cell suspension was used to inoculate 50 mL culture of LB broth containing 30 μ g/mL kanamycin. The plate and culture were incubated at 37 $^{\circ}$ C for 20 hours. The

number of colonies (~5500, counted by portioning the plate) was multiplied by 100 (to account for the dilution factor) in order to calculate a library size of ~55,000 clones.

Table 4-5 DNA sequences and primers used for photoswitchable amino acid incorporation
Restriction sites are denoted with **bold** font, the histidine tag is highlighted, and site mutations are CAPITALIZED.

Name	Sequence (5' → 3')
mCherry F	taacaggaggaatta ccatgg tgagcaagggcgag
mCherry R	ccttgctcattccactgccctgtacagctcgtcc
sfGFP F	tacaagggcagtggaatgagcaagggcgaagaac
sfGFP R	tccaatt ccat gtgtagtggtgatggtgatggtttatacagttcatccatgc
AzoFRS1 F	gaatt agatc tatggacgaattgaaat
AzoFRS1 R	gatgat ggtcg actataatctcttc
AzoFRS2 F	gaatcc catatg gacgaattgaaat
AzoFRS2 R	cgttgaa actgc agttataatctcttc
TyrRS2 seqF	aacagttgtcagcctgtccc
AzoFRS	atggacgaattgaaatgataaagagaaacacatctgaaattatcagcgaggaagagtaagagaggttttaa aaaagatgaaaatctgctGGCataggtttgaaccaagtgtgtaaaatacatttagggcattatctccaaataa aaaagatgattgattacaaaatgctgatttgatataattataGAAttggctgattacacgcctattaaaccaga aaggagagttggatgagattagaaaataggagattatacaaaaaagttttgaagcaatggggtaaaggc aaaatatgttatggaagtgaCGGAActgataaggattatacactgaatgtctatagattggcttaaaaaac taccttaaaaagagcaagaaggagatggaacttatagcaagagaggatgaaaatccaaaggtgctgaagt atctatccaataatgcaggttaatGGCattcattatCATggcgttgatgtgcagttggaggatggagcagag aaaaatacacatgttagcaagggagctttacaaaaagggtgtttgattcacaacctgtctaacgggttg atggagaaggaaagatgagttctcaaaaggaatttatagctgttgatgactctccagaagagattagggcta agataaagaaagcactactgccagctggagttgtgaaggaaatccaataatggagatagctaaatactcctg aatatccttaaccataaaaagggccagaaaaatgtgtggagattgacagttatagctatgaggagttagaga gtttatttaaaaataaggaattgcatccaatggatttaaaaaatgctgtagctgaagaactataaagatttagagc caattagaaagagattataa
His-EV20 F	gaaggagatataccatgggtcatcaccaccatcaccatattggataaaaaaccgctg
His-EV20 R	tggtggtggtgctcaggttacaggttcgtgctaag
sfGFP-His F	taagaaggagatata ccatgg ggagcaagggcgaagaactg
sfGFP-His R	ctagatccggt ggatc ttagtgatggtgatggtgatggtttatacagttcatccatgcc
His-sfGFP F	taagaaggagatata ccatgg ggggtctcatcatcat
His-sfGFP R	tatctagatccggt ggatc ttattatacagttcatccatgc
EVOL-EV20 F	aacaggaggaattactagtagtggataaaaaaccgctg
EVOL-EV20 R	tgatgatggtcgacttacaggttcgtgctaag
EVOL-bb F	gcacgaacctgtaagtcgaccatcatcatcat
EVOL-bb R	catccagcggttttatccatactagtaattcctcctgt
Ultra-EV20 F	ggaggtgcccgcgatggataaaaaaccgctg
Ultra-EV20 R	gaccgttaaacgcccgccttacaggttcgtgctaag
Ultra-bb F	gcacgaacctgtaagcggccgcttaaacggctc
Ultra-bb R	gcggtttttatccatcggccgcacctcctttgtg
UltraRS seqF	tcgtataatgttggaattg
UltraRS seqR	ctcatccgcaaacag
EP-EV20 F	acgcttgaggaatcccatatggataaaaaaccgctg
EP-EV20 R	caatttagcgtttgaaactgcagttacaggttcgtgctaag
pBK-bb F	cattagcacgaacctgtaactgcagttcaaacgct
pBK-bb R	cagcggttttatccatagggtcctcaaagcgtaaa

Synthetase panel screen using AAPF. The doubly transformed glycerol stock panel that is stored in a 96-well deep well plate in the $-80\text{ }^{\circ}\text{C}$ freezer was utilized for generating starter cultures. A pipette tip was gently stabbed into the frozen stock and used to inoculate 1 mL of LB broth containing kanamycin ($50\text{ }\mu\text{g/mL}$) and tetracycline ($25\text{ }\mu\text{g/mL}$). Cultures were grown overnight at $37\text{ }^{\circ}\text{C}$ with 250 rpm shaking to reach saturation. The next day, 2 mL cultures for each synthetase mutant were prepared by diluting the saturated starter culture 1:100 in LB broth (+ kanamycin, + tetracycline). Expression cultures were grown at $37\text{ }^{\circ}\text{C}$ with 250 rpm shaking until the OD_{600} reached 0.5, then 200 μL was transferred to a 96-well deep well plate in triplicate per synthetase (for DMSO, positive control, and **AAPF** – a single replicate each). To the appropriate well, 2 μL of DMSO, **ONBY**, or **AAPF** was added for a final 1 mM concentration. All wells were induced by the addition of 10 μL of 2% arabinose for a final 0.1% arabinose concentration. The deep well plate was covered with aluminum foil, and the plate was secured to the platform of the shaker and shaken overnight at 250 rpm at $37\text{ }^{\circ}\text{C}$. After ~ 20 hours, 100 μL of each culture was transferred to a black 96-well plate and the OD_{600} (absorbance at 600 nm) and sfGFP fluorescence (ex. 488/5, em. 510/5 nm) was measured using a Tecan M1000 Pro plate reader. The raw fluorescence values were divided by the corresponding OD_{600} measurement to correct for any variation in cell density and the fluorescence/ OD_{600} is plotted for all synthetase mutants screened with each of the three conditions.

Validation of AAPF incorporation by ESI-MS. The doubly transformed glycerol stock panel was utilized for generating 2 mL starter cultures for EV16-5 and EV20, separately. Cultures were grown overnight at $37\text{ }^{\circ}\text{C}$ with 250 rpm shaking to reach saturation. The next day, 20 mL cultures for both synthetase mutants were prepared by diluting the saturated starter culture 1:100 in LB broth containing kanamycin ($50\text{ }\mu\text{g/mL}$) and tetracycline ($25\text{ }\mu\text{g/mL}$). These cultures were grown

at 37 °C with 250 rpm shaking until the OD₆₀₀ reached 0.5, then 5 mL of culture was aliquoted to 15 mL conical tubes (two per synthetase mutant). The 5 mL cultures were treated with either 50 µL of DMSO or **AAPF**, followed by the addition of 25 µL of 20% arabinose for a final 0.1% arabinose concentration. The cultures were incubated with 250 rpm shaking at 37 °C for ~20 hours to allow for protein expression. The next day, cells were pelleted at 4000 g for 10 minutes and the cell pellets were lysed following a three-phase partitioning protocol and purified over Ni-NTA resin (see 8.2.2 and 8.2.4 for a detailed protocol). The samples were analyzed via SDS-PAGE following the protocols in 8.2.5. An aliquot of sfGFP-Y151**AAPF** from the EV20 sample (along with wild-type sfGFP) was submitted to the Department of Chemistry Mass Spectrometry facility for intact ESI-MS analysis. The raw file was analyzed using Protein Deconvolution 2.0 (Thermo Scientific) software using the “Manual ReSpect” algorithm with the following parameters: negative charge – false, charge carrier – H⁺, relative abundance threshold – 10%, *m/z* range – 800-2,000, output mass range – 28,200-30,000, mass tolerance – 10, target mass – 30,000, charge state range – 10-50, choice of peak model – intact protein.

Incorporation of AAPF into proteins in mammalian cells. HEK293T cells were plated in a black 96-well plate (for imaging) and a 6-well plate (for western blot analysis) at 50,000 and 200,000 cells per well, respectively, and grown at 37 °C/5% CO₂. At ~80% confluence, cells were co-transfected with pmCherry-TAG-EGFP-HA (provided by Dr. Kalyn Brown) and pAAPFRS-4xPyIT (provided by Dr. Ji Luo) at a 1:1 plasmid ratio using 200 ng or 2000 ng total, for each plate format respectively, following the LPEI protocol detailed in Section 8.2.8. The media was replaced with DMEM (+ 10% FBS, – antibiotics) containing 0.75 mM **AAPF** (or DMSO). The transfection solution was added to the wells, and the plates were incubated overnight at 37 °C/5% CO₂ for ~20 hours to allow for protein expression. The following day, the 96-well plate was imaged using the

Zeiss microscope equipped with EGFP (ex. 470/40, em. 525/50 nm) and mCherry (ex. 550/25, em. 605/70 nm) filter cubes through a 10X Plan-Apochromat objective. The 6-well plate was processed as detailed in Sections 8.2.10 and 8.2.11 for cell lysis and western blot analysis. An anti-HA antibody (Cell Signaling Technology – 3724S) was used at a 1:1000 dilution in TBST + 5% milk and an anti-GAPDH antibody (ProteinTech – 10494-1-AP) was used at 1:5000 dilution in TBST + 5% milk (6 mL volume each). A goat anti-rabbit HRP-conjugated secondary antibody (ProteinTech – SA00001-2) was used at a 1:10,000 dilution in TBST (10 mL).

Determination of photostationary states and thermal stability of AAPF. A solution of AAPF at 250 μ M was prepared by diluting 12.5 μ L of a 10 mM solution into 488 μ L of acetonitrile. Fifty microliters of this solution were transferred to an HPLC vial and analyzed as the dark state. A 365 nm irradiated sample was prepared by irradiating a ½ dram clear glass vial containing 50 μ L of the 250 μ M solution for 10 minutes on a UV transilluminator (with the vial directly touching the glass) set to 365 nm, then the solution was transferred to an HPLC vial for analysis. A 50 μ L aliquot of the 250 μ M solution was transferred to a ½ dram vial, irradiated for 10 minutes on a UV transilluminator (365 nm), followed by an irradiation with a 530 nm LED (output set to 300 mA, LED source directly touching the vial) for 5 minutes, then the solution was transferred to an HPLC vial for analysis. A Shimadzu HPLC equipped with an analytical scale column (Agilent, Zorbax SB-C18, 3.5 μ m, 4.6 x 100 mm) was used. Solvent A was milliQ water and Solvent B was HPLC-grade acetonitrile. A gradient method of 5 – 95% acetonitrile over 30 minutes with a 1.0 mL/minute flow rate was utilized. An autosampler was utilized for injections and 20 μ L of sample was injected per analysis. The UV detector was set to 280 nm. The raw data was extracted from the Lab Solutions (Shimadzu) software and analyzed in Prism. To determine the photostationary states, the peak area at 7.5 minutes (corresponding to the *cis*-isomer) and peak area at 11.0 minutes

(corresponding to the *trans*-isomer) were extracted. The “% *cis*-isomer” was determined by: (peak area at 7.5 minutes)/(summation of peak areas of 7.5 and 11.0 minutes)*100.

For determining thermal stability of the *cis*-isomer, a 250 μ M solution of **AAPF** was prepared in acetonitrile as above and irradiated for 10 minutes with 365 nm light. The vial was wrapped in aluminum foil and maintained in a 37 °C incubator for the duration of the experiment. Aliquots (50 μ L) were removed hourly for three hours and analyzed via HPLC using the same analytical method detailed above. The thermal stability in 1X PBS at pH 7.4 was performed exactly as detailed for the acetonitrile sample, except aliquots were taken at the following time points: 0, 0.75, 1.5, 2.25, 7, 8, 21, 30, and 54 hours. The raw data was extracted from the Lab Solutions (Shimadzu) software and analyzed in Prism as above. An exponential model was fit to the data to obtain half-life values for the *cis*-isomer in both solvents.

Validation of dual reporter in Top10 cells. Top10 cells were doubly transformed with pBAD-mCherry-sfGFP-Y151TAG-6xHis-PylT and pEV1 (wild-type *MbPylRS*) and plated on LB agar containing kanamycin (50 μ g/mL) and tetracycline (25 μ g/mL). A 5 mL starter culture was prepared by isolating a single colony and growing to saturation in LB broth containing both kanamycin (50 μ g/mL) and tetracycline (25 μ g/mL) at 37 °C with 250 rpm shaking. A 25 mL expression culture was inoculated using a 1:100 dilution of the saturated starter culture in LB broth containing kanamycin (50 μ g/mL) and tetracycline (25 μ g/mL) and grown at 37 °C with 250 rpm shaking until the OD₆₀₀ reached 0.5. At this point, the culture was split into 5 mL cultures in 15 mL conical tubes (for each of 3 samples). Three expression conditions were generated by adding the following to the appropriate 5 mL culture: (i) no induction, noAA (25 μ L of water + 50 μ L of DMSO), (ii) induction, noAA (25 μ L of 20% arabinose + 50 μ L of DMSO), and (iii) induction, **AllocK** (25 μ L of 20% arabinose + 50 μ L of 100 mM **AllocK**). The expression cultures were

incubated at 37 °C overnight at 250 rpm shaking to allow for protein expression and UAA incorporation. After ~20 hours, 100 µL of culture was transferred to a black, 96-well plate (in duplicate per condition) and fluorescence measurements were acquired using a Tecan M1000 Pro to collect sfGFP (ex. 485/5, em. 510/5 nm) and mCherry (ex. 581/5, em. 610/5 nm) readings. Averages of technical duplicates were plotted in GraphPad Prism 8 with error bars representing standard deviation.

Control of translation using AAPF – a single, pre-irradiation. A 2 mL starter culture in LB broth containing kanamycin (50 µg/mL) and tetracycline (25 µg/mL) was prepared from a glycerol stock of Top10 cells doubly transformed with pBAD-mCherry-sfGFP-Y151TAG-6xHis-PylT and pEV20. The following day, a 25 mL expression culture was prepared by back diluting the saturated starter culture 1:25 in LB broth containing kanamycin (50 µg/mL) and tetracycline (25 µg/mL). This culture was incubated at 37 °C with 250 rpm shaking until the OD₆₀₀ reached 0.5, then 500 µL of this culture was transferred into each of fourteen 1.7 mL tubes. The cells were pelleted at 10,000 g for 5 minutes, then the supernatant was removed and discarded. The following seven solutions were prepared at 1 mL volume in LB broth (without antibiotics) and maintained in the dark: (i) LB broth only, (ii) LB broth + DMSO, (iii) LB broth + 0.05 mM **AAPF**, (iv) LB broth + 0.10 mM **AAPF**, (v) LB broth + 0.25 mM **AAPF**, (vi) LB broth + 0.50 mM **AAPF**, and (vii) LB broth + 1.0 mM **AAPF**. Using 500 µL from each of these solutions, half of the cell pellets (7) were resuspended and labeled with the appropriate concentration and denoted as the dark-state. The remaining 500 µL of each LB broth solution was transferred to a clear, ½ dram vial and each vial was irradiated for 10 minutes using a dual UV transilluminator set to 365 nm (with the vials touching the glass). After irradiation, the remaining half of the cell pellets were resuspended in these pre-irradiated LB broth samples and labeled as the “UV” sample. Twelve of the cultures

were induced by adding 2.5 μ L of 20% arabinose, and the two non-induced cultures received 2.5 μ L of milliQ water. All fourteen expression cultures were placed back in the 37 °C shaker at 250 rpm. After 1, 2, and 4 hours of induction, aliquots were removed for analysis by flow cytometry and were processed in the same manner. For each of the fourteen samples, 50 μ L of culture was transferred to a 1.7 mL tube and cells were pelleted at 10,000 g for 2 minutes. The supernatant was removed and discarded, then cell pellets were resuspended in 200 μ L of syringe-filtered, 1X PBS + 0.5 mM EDTA (to prevent cell clumping). Samples were maintained on ice prior to analysis. A CytoFlex S (N-V-B-Y) flow cytometer equipped with 488 and 561 nm laser lines and 510/20 and 610/20 nm band pass filters was used for analysis. *Note: Ensure that the 510/20 nm filter is in slot 3 of the 488 nm laser since the software may not accurately reflect which filter is physically in place.* The default laser settings were utilized and a manual threshold of FSC-H >1000 was employed. A dot plot of FSC-H versus SSC-H was generated, and a square gate encompassing FSC-H 1,000-10,000 and SSC-H 1,000-10,000 was drawn and labeled as “live.” Data acquisition was conducted using the “Events to Record” set at 25,000 events in the “live” gate. These settings allowed for the analysis of 25,000 events (or cells, in this case) only in the region indicative of live *E. coli*. Histogram representation of GFP-A and mCherry-A were plotted in the CytExpert Software using “live” and “induced” gates. The “live” gate was described above, the “induced” gate is based on the mCherry-A histogram and consists of a line-segment gate selecting all mCherry signal greater than the non-induced sample. To utilize a double gate, the “combo population” feature was employed to create an AND Boolean relationship between “live” and “induced” gates.

For integrating the area under the curve, the raw data was exported to FSC 3.0 files using the CytExpert software. For analysis, the open-source FlowingSoftware 2.5.1 was employed. Two

dot plots were opened under the “visualization tools” header and set to FSC-H versus SSC-H and GFP-A and mCherry-A, then a connector between the plots was formed. Each .fcs file was opened and the raw data was extracted by right clicking on a dot plot, then selecting “export to clipboard,” then pasting into an Excel sheet. This was done for both dot plots for each of the fourteen conditions at each of the three time points. Within Excel, the data was sorted by the FSC-H column and all rows <1,000 and >10,000 were removed, then the data was sorted by the mCherry-A column. Summation of the GFP-A column where mCherry value was >0 were performed for each condition. This sum was treated as the integrated area and was plotted in GraphPad Prism.

Analysis of AAPF thermal stability in more complex solutions. A 250 μ M solution of AAPF was prepared in six different diluents (1X PBS, LB broth, 2xYT, GMML, auto-induction media, and FluoroBrite DMEM) at a 1 mL final volume. Aliquots of GMML³⁴⁹ and auto-induction media³⁵⁰ were obtained from Joshua Wesalo and the components of each can be found in the corresponding references. Absorbance spectra of the dark state for each sample was acquired on a Tecan M1000 Pro plate reader using 100 μ L of each sample in a black, 96-well plate. The remaining 900 μ L was transferred to a 12-well plate and the plate was irradiated for 10 minutes using a dual UV transilluminator set to 365 nm (the plate was directly placed on the glass). A time zero aliquot was removed and analyzed on the plate reader, while the remaining volume was transferred to a 1.7 mL tube, then maintained in the dark at 37 °C. Every few hours, a 100 μ L aliquot was removed and an absorbance spectrum was acquired. An absorbance spectrum of each of the buffers/media alone was acquired and the background absorbance was subtracted from each time point. Qualitative analysis of the spectra was performed and no calculation of *cis*- and *trans*-isomer ratios was performed. All data was plotted in GraphPad Prism.

For determining the effect of glutathione on *cis*-isomer thermal stability, a 1 M solution of glutathione reduced-form was prepared in water. Two solutions (250 μ M) of **AAPF** were prepared with and without the addition of 10 mM glutathione in LB broth. Absorbance spectra were acquired for the dark state, the *cis*-isomer, and hourly time points. Background subtraction was performed by measuring the absorbance of LB broth alone or with 10 mM glutathione. Data analysis was performed as detailed above.

Control of translation using AAPF – pulsed, cycles of irradiation. A 2 mL starter culture in LB broth containing kanamycin (50 μ g/mL) and tetracycline (25 μ g/mL) was prepared from a glycerol stock of Top10 cells doubly transformed with pBAD-mCherry-sfGFP-Y151TAG-6xHis-PylT and pEV20. The following day, a 25 mL expression culture was prepared by back diluting the saturated starter culture 1/25 in LB broth containing kanamycin (50 μ g/mL) and tetracycline (25 μ g/mL). This culture was incubated at 37 °C with 250 rpm shaking until the OD₆₀₀ reached 0.5, then 500 μ L of this culture was transferred into each of fourteen 1.7 mL tubes. The cells were pelleted at 10,000 g for 5 minutes, then the supernatant was removed and discarded. The following seven solutions were prepared at 1 mL volume in LB broth (without antibiotics) and maintained in the dark: (i) LB broth only, (ii) LB broth + DMSO, (iii) LB broth + 0.05 mM **AAPF**, (iv) LB broth + 0.10 mM **AAPF**, (v) LB broth + 0.25 mM **AAPF**, (vi) LB broth + 0.50 mM **AAPF**, and (vii) LB broth + 1.0 mM **AAPF**. Using 500 μ L of each of these solutions, half (7) of the cell pellets were resuspended and labeled with the appropriate concentration and denoted as the dark-state. The remaining 500 μ L of each LB broth solution was transferred to a clear, ½ dram vial and the vials were irradiated for 10 minutes using a dual UV transilluminator set to 365 nm. After irradiation, the remaining half of the cell pellets were resuspended in these pre-irradiated LB broth samples and labeled as the “UV” samples. Twelve of the cultures were induced by adding 2.5 μ L of 20%

arabinose, and the two non-induced cultures received 2.5 μL of milliQ water. All fourteen expression cultures were placed back in the 37 °C shaker at 250 rpm. After 1, 2, and 4 hours of induction, aliquots were removed for analysis by flow cytometry and were processed in the same manner as described previously. Additionally, at every hour post-induction, the UV pre-irradiated cultures were transferred to a 24-well plate and irradiated for an additional 10 minutes (the plate was propped such that there was ~2 cm gap between the bottom of the plate and the glass of the transilluminator), then transferred back to culture tubes for continued expression. Flow cytometry data collection and analysis was performed exactly as detailed above.

Comparison of pBK and pEVOL systems with AAPF. The pBK system was prepared similarly to the screen, where a starter culture was generated in LB broth containing kanamycin (50 $\mu\text{g}/\text{mL}$) and tetracycline (25 $\mu\text{g}/\text{mL}$) from a doubly transformed glycerol stock of Top10 cells containing pBK-EV20 and pBAD-sfGFP-Y151TAG-pylT. The pEVOL system (pEVOL-AzoFRS and pBAD-sfGFP-Y151TAG) was doubly transformed into BL21(DE3) cells and plated on LB agar plates containing chloramphenicol (25 $\mu\text{g}/\text{mL}$) and tetracycline (25 $\mu\text{g}/\text{mL}$). Starter cultures were prepared in LB broth and GMML, separately, both containing chloramphenicol and tetracycline. Once starter cultures reached saturation (~20 hours for the two in LB broth and ~72 hours for GMML), 10 mL expression cultures were prepared by back-diluting in fresh media containing the appropriate combination of antibiotics to obtain a starting OD_{600} of 0.2. Expression cultures were grown at 37 °C with 250 rpm shaking until the OD_{600} reached 0.5, then the cultures were split into four 2 mL cultures in 15 mL conical tubes. The four conditions represent: no UAA control (DMSO), 1 mM **ONBY**, 0.5 mM **AzoF**, 1 mM **AAPF**. To obtain 1 mM from a 100 mM stock, 20 μL of stock solution was used, and for the 0.5 mM sample, 10 μL of a 100 mM stock was used. All samples were induced with 20 μL of 20% arabinose for a final 0.2% concentration. All cultures

were incubated with 250 rpm shaking at 37 °C for ~20 hours to allow for expression and UAA incorporation. sfGFP fluorescence and optical density were measured for each of the conditions using 100 µL of the expression cultures in a black, 96-well plate in technical triplicate with the same settings described previously for the plate reader assay.

Side-by-side comparison of improved *E. coli* UAA systems. Three different UAA systems were tested side-by-side: (1) pBAD/pBK, (2) pEVOL/pET, and (3) pUltra/pET. The two plasmids for system 1 were doubly transformed into Top10 cells, while the two appropriate plasmids for systems 2 and 3 were doubly transformed into BL21(DE3). A single colony was used to inoculate a 2 mL starter culture with the appropriate antibiotics: system 1 – tetracycline (25 µg/mL) and kanamycin (50 µg/mL), system 2 – chloramphenicol (25 µg/mL) and kanamycin (50 µg/mL), and system 3 – spectinomycin (50 µg/mL) and kanamycin (50 µg/mL). Expression cultures (5 mL) in LB broth containing the appropriate combination of antibiotic were grown to OD₆₀₀ of 0.5. The cultures were induced as follows: system 1 – 0.2% arabinose, system 2 – 0.2% arabinose and 0.5 mM IPTG, and system 3 – 0.5 mM IPTG. System 1 cultures were shaken at 37 °C for 20 hours, system 2 cultures were shaken at 37 °C for 6 hours, and system 3 cultures were shaken at 25 °C for 20 hours. After expression, 100 µL was transferred to a black 96-well plate in duplicate and sfGFP fluorescence and absorbance at 600 nm were measured on a Tecan M1000 plate reader.

PylRS selections using EP-PCR library. The pBK-EV20 error prone library (diversity of 55,000) was transformed into chemically competent Top10 cells containing the pRep selection plasmid (provided by Ashton Cropp, VCU). Ten microliters (1/30th) of the cell suspension was plated on LB agar containing kanamycin (30 µg/mL) and tetracycline (12 µg/mL), and the remainder (290 µL) was diluted into 15 mL of LB broth containing kanamycin (30 µg/mL) and tetracycline (12

$\mu\text{g/mL}$). The plate and culture were incubated at 37 °C, and the following day, colony counting x the dilution factor (30x) revealed coverage of 40,000 clones.

The saturated overnight culture was diluted 1:10 (100 μL into 900 μL of LB broth) and 100 μL was plated on selection plates (10 cm petri dishes) using sterile plating beads. Selection plates contained the following per plate: 10 mL of LB agar, kanamycin (30 $\mu\text{g/mL}$), tetracycline (12 $\mu\text{g/mL}$), chloramphenicol (10 $\mu\text{g/mL}$), arabinose (0.2% w/v), and **AAPF** (1 mM). As controls, a plate lacking **AAPF** (supplemented with DMSO) was prepared and a plate containing 1 mM **ONBY** (in place of **AAPF**) was prepared. Plates were incubated at 37 °C for 72 hours, followed by imaging on a ChemiDoc using the GFP settings.

Surviving colonies (that were also green under UV light) were used to inoculate 1 mL starter cultures in LB broth containing kanamycin (30 $\mu\text{g/mL}$) and tetracycline (12 $\mu\text{g/mL}$). At saturation, these cultures were diluted 1:25 in 1 mL of LB broth containing kanamycin (30 $\mu\text{g/mL}$) and tetracycline (12 $\mu\text{g/mL}$) and grown to OD_{600} of 0.5. At this point, the cultures were split into a 96 deep-well plate with 200 μL per well and replicates of four (two used for DMSO and two used for **AAPF**). Arabinose was added to 0.2% final concentration and either DMSO or 1 mM **AAPF** was added to the appropriate wells. The deep well plate was secured to the platform of the shaker and incubated for 20 hours at 37 °C. After, 100 μL of each well was transferred to a black, 96-well plate and sfGFP fluorescence and absorbance at 600 nm were acquired on a Tecan M1000 plate reader.

Synthetase panel screen with *o*-PyrAzoF. A synthetase panel screen was performed as detailed in “Synthetase panel screen with **AAPF**” with only minor modifications denoted here. Once the bulk expression culture reached an OD_{600} of 0.5, then 200 μL was transferred to a 96-well deep well plate in quadruplicate per synthetase (for four different conditions). To the appropriate well,

2 μ L of DMSO, **ONBY**, or ***o*-PyrAzoF** was added for a final 1 mM concentration. An **AzoF** control was also included this time by adding 1 μ L of 100 mM **AzoF** for a 0.5 mM final concentration. The remainder of the experiment was conducted as described above. The fluorescence/OD₆₀₀ is plotted for all synthetase mutants screened with each of the four conditions.

Confirmation of *o*-PyrAzoF incorporation by ESI-MS. The doubly transformed glycerol stock panel was utilized for generating 2 mL starter cultures for EV16-5 and EV20, separately. Cultures were grown overnight at 37 °C with 250 rpm shaking to reach saturation. The next day, 20 mL cultures for both synthetase mutants were prepared by diluting the saturated starter culture 1:100 in LB broth containing kanamycin (50 μ g/mL) and tetracycline (25 μ g/mL). These cultures were grown at 37 °C with 250 rpm shaking until the OD₆₀₀ reached 0.5, then 5 mL of culture was aliquoted to 15 mL conical tubes (three per synthetase mutant). The 5 mL cultures were treated with either 50 μ L of DMSO, 50 μ L of 100 mM **AAPF**, or 25 μ L of 100 mM **AzoF**, followed by the addition of 25 μ L of 20% arabinose for a final 0.1% arabinose concentration. The cultures were incubated with 250 rpm shaking at 37 °C for ~20 hours to allow for protein expression. The next day, cells were pelleted at 4000 g for 10 minutes and the cell pellets were lysed following a three-phase partitioning protocol and purified over Ni-NTA resin (see Sections 8.2.2 and 8.2.4 for a detailed protocol). The samples were analyzed via SDS-PAGE following the protocols in 8.2.5. An aliquot of sfGFP-Y151***o*-PyrAzoF** from the EV16-5 sample was submitted to the Department of Chemistry Mass Spectrometry facility for intact ESI-MS analysis. The raw file was analyzed using Protein Deconvolution 2.0 (Thermo Scientific) software using the “Manual ReSpect” algorithm with the following parameters: negative charge – false, charge carrier – H⁺, relative abundance threshold – 20%, m/z range – 800-2000, output mass range – 28200-30000, mass

tolerance – 10, target mass – 30000, charge state range – 10-50, choice of peak model – intact protein.

Determination of photostationary states and thermal stability of *o*-PyrAzoF. A solution of *o*-PyrAzoF at 250 μ M was prepared by diluting 12.5 μ L of a 10 mM solution into 488 μ L of 1X PBS pH 7.4. Fifty microliters of this solution were transferred to an HPLC vial and analyzed as the dark state. A 365 nm irradiated sample was prepared by irradiating a ½ dram clear glass vial containing 200 μ L of the 250 μ M solution for 15 minutes on a UV transilluminator set to 365 nm, then 50 μ L was transferred to an HPLC vial for analysis. This sample was then irradiated with a 530 nm LED with the bulb touching the bottom of the vial for 10 minutes, then a 50 μ L aliquot was removed for analysis. A 50 μ L aliquot of the 250 μ M solution was transferred to a ½ dram vial, irradiated for 10 minutes on a UV transilluminator (365 nm), followed by an irradiation with a 530 nm LED (output set to 300 mA, LED source directly touching the vial) for 20 minutes (in 5 minute intervals), then the solution was transferred to an HPLC vial for analysis. A Shimadzu HPLC equipped with an analytical scale column (Agilent, Zorbax SB-C18, 3.5 μ m, 4.6 x 100 mm) was used. Solvent A was milliQ water and Solvent B was HPLC-grade acetonitrile. A gradient method of 5 – 95% acetonitrile over 30 minutes with a 1.0 mL/minute flow rate was utilized. An autosampler was utilized for injections and 20 μ L of sample was injected per analysis. The UV detector was set to 280 nm. The raw data was extracted from the Lab Solutions (Shimadzu) software and analyzed in Prism. To determine the photostationary states, the peak area at 5.9 minutes (corresponding to the *cis*-isomer) and peak area at 8.1 minutes (corresponding to the *trans*-isomer) were extracted. The “% *cis*-isomer” was determined by: (peak area at 5.9 minutes)/(summation of peak areas of 5.9 and 8.1 minutes)*100.

To determine the thermal stability of the *cis*-isomer, another solution of ***o*-PyrAzoF** at 250 μM was prepared by diluting 12.5 μL of a 10 mM solution into 488 μL of 1X PBS pH 7.4. The entire sample (in a $\frac{1}{2}$ dram vial) was irradiated for 15 minutes at 365 nm using a UV transilluminator. Fourty microliters was transferred to an HPLC vial for analysis as the initial *cis*-isomer, $t = 0$ sample. The vial was wrapped in aluminum foil and maintained at 37 $^{\circ}\text{C}$, and 40 μL aliquots were removed at 0.75, 3, 25, and 50 hours post-irradiation. All samples were analyzed using the same HPLC system and conditions as in the previous paragraph. The raw data was extracted from the Lab Solutions (Shimadzu) software and analyzed in Prism as above. An exponential model was fit to the data to obtain half-life values for the *cis*-isomer.

Absorbance-based metal chelation study with *o*-PyrAzoF. One molar solutions of MgCl_2 , CaCl_2 , LiCl , NaCl , KCl , NiCl_2 , MnCl_2 , FeCl_3 , ZnCl_2 , CoCl_2 , and CuCl_2 were prepared individually using milliQ water. Working solutions of 100 μM were prepared by diluting 0.5 μL of the 1 M solution into 5 mL of milliQ. Next, buffer only, **AzoF** and ***o*-PyrAzoF** solutions were prepared by diluting 4 μL of DMSO or UAA (from a 100 mM stock solution, for a 100 μM final concentration) into 3.996 mL of 25 mM HEPES pH 7.5 buffer. Each of the metal ion solutions (11 metals + water control = 12 total) were combined with the buffer only, **AzoF**, or ***o*-PyrAzoF** for 36 total combinations with 1:1 molar ratios of 50 μM of each component (200 μL metal solution + 200 μL buffer/UAA solution). The solutions were incubated at room temperature for 30 minutes, then 100 μL of each solution were transferred into a clear, 96-well plate and absorbance scans were acquired from 250 – 700 nm. The background absorbance of metal ion in buffer was subtracted from the **AzoF** and ***o*-PyrAzoF** samples, then the data was graphed in GraphPad Prism 8.

ITC binding studies of AAPF test substrates. The potential chelating ligands (**13**, **14**, and **15**) were prepared at 200 mM concentrations in autoclaved milliQ water. Five metal ion solutions were

prepared at 500 mM concentrations in autoclaved milliQ water from the following salts: ZnCl_2 , $\text{ZnSO}_4 \cdot 7\text{H}_2\text{O}$, $\text{CuSO}_4 \cdot 5\text{H}_2\text{O}$, $\text{CoSO}_4 \cdot 7\text{H}_2\text{O}$, and NiCl_2 . Working solutions of 2 mM of metal solution and 90 mM of ligand were prepared fresh for each ITC run. To prepare 2 mM metal solutions, 20 μL of 1 M metal solution was combined with 125 μL of 1 M Tris-HCl pH 7.5 and 4.855 mL of autoclaved milliQ water. To prepare 90 mM ligand solutions, 2.25 mL of 200 mM ligand was combined with 125 μL of 1 M Tris-HCl pH 7.5 and 2.625 mL of autoclaved milliQ water.

A MicroCal iTC200 was used for all binding studies. To prepare the instrument, the cell was washed with 20% Contrad70 using the “Detergent Soak and Rinse (Long)” feature. After the wash cycle, the cell was rinsed twice with milliQ water, then primed once with the metal solution. Carefully, 200 μL of metal solution was added without introducing bubbles by filling a syringe to the 250 μL mark and ejecting to the 50 μL mark. The syringe was washed by filling and emptying the syringe (using the “Syringe Fill” command) twice with milliQ water, then once with the appropriate ligand solution. The syringe was filled using the ligand solution, then carefully inserted into the cell. The following method was utilized for all runs: 1st injection – 0.4 μL , 2nd – 18th injections – 2.0 μL , and a 2-minute equilibration time between injections. Between runs of the same metal ion, but different ligands, the cell was rinsed three times with milliQ water, then primed again with the same metal solution. The remaining ligand in the syringe was discarded, the syringe was rinsed three times with milliQ water, then primed with the next ligand, and filled for an experiment with the next ligand. When a different metal ion was to be used, a detergent wash cycle was performed first. At the end of the day (or end of a reserved time slot), the cell was soaked for 1 hour with 100 mM EDTA, followed by a detergent wash cycle, then leaving the cell filled with milliQ water.

The values reported in the figure are directly taken from the “rawITC” window in the Origin analysis software. The first injections were discarded and reported values correspond to the “NDH” data from the second injection peak.

ITC binding studies of putative bidentate AAPF test substrate. A solution of **17** was prepared in 1:1:1 water:DMSO:methanol at 33 mM (because of poor aqueous solubility, likely due to the addition of the benzyl moiety). A 20 mM working solution was prepared by combining 303 μL of the stock with 12.5 μL of 1 M Tris-HCl pH 7.5 and 184.5 μL of milliQ water. As a positive control, a 20 mM solution of imidazole (**13**) was prepared using the identical solvent ratios as for **17**. The metal solutions were prepared at 2 mM, but to avoid heat of mixing/dilution, DMSO/methanol was included at the same final concentration as in the ligand solution. The instrument was operated as described in the previous ITC section.

ITC binding studies of *o*-pyridinylazobenzene analogs. Stock solutions of substrates (**9**, **10**, and **11** – synthesized by Olivia Shade; **12** – purchased from TCI) were prepared at 100 mM in DMSO. In contrast to previous ITC experiments, the contents of the cell and syringe were inverted for these experiments such that the ligand was placed in the cell, while the metal ion solution was placed in the syringe. Due to issues with precipitation of copper sulfate in the presence of high concentrations of DMSO and buffer, buffer-free conditions were used in these experiments with 10% DMSO in milliQ water. Ligands were prepared at 1.2 mM by combining 24 μL of the 100 mM stocks with 176 μL of DMSO in 1800 μL of milliQ water. A working solution of 18 mM copper sulfate was prepared by diluting 360 μL of 100 mM copper sulfate with 200 μL of DMSO in 1440 μL of milliQ water. A control experiment was conducted this time in which the copper solution was injected into a 10% DMSO/water solution to account for any heat release detected

due to injection of metal alone. This reference data was subtracted from the experimental injection traces.

5.0 Optical Activation of Rapamycin-Induced Protein Dimerization

5.1 Introduction to Chemical Inducers of Dimerization

Chemical inducers of dimerization, or CIDs, are small molecule ligands that result in the dimerization of two proteins and are classified as homodimerizers (those which bind the same two proteins) or heterodimerizers (those which bind two different proteins). CIDs play a pivotal role in chemical biology by enabling us to place biological processes under conditional control.³⁵¹⁻³⁵⁵ A wide range of ligands and protein binding partners have been discovered/developed in recent years and are summarized in Figure 5-1. An in-depth discussion of relevant ligands is provided throughout this section.

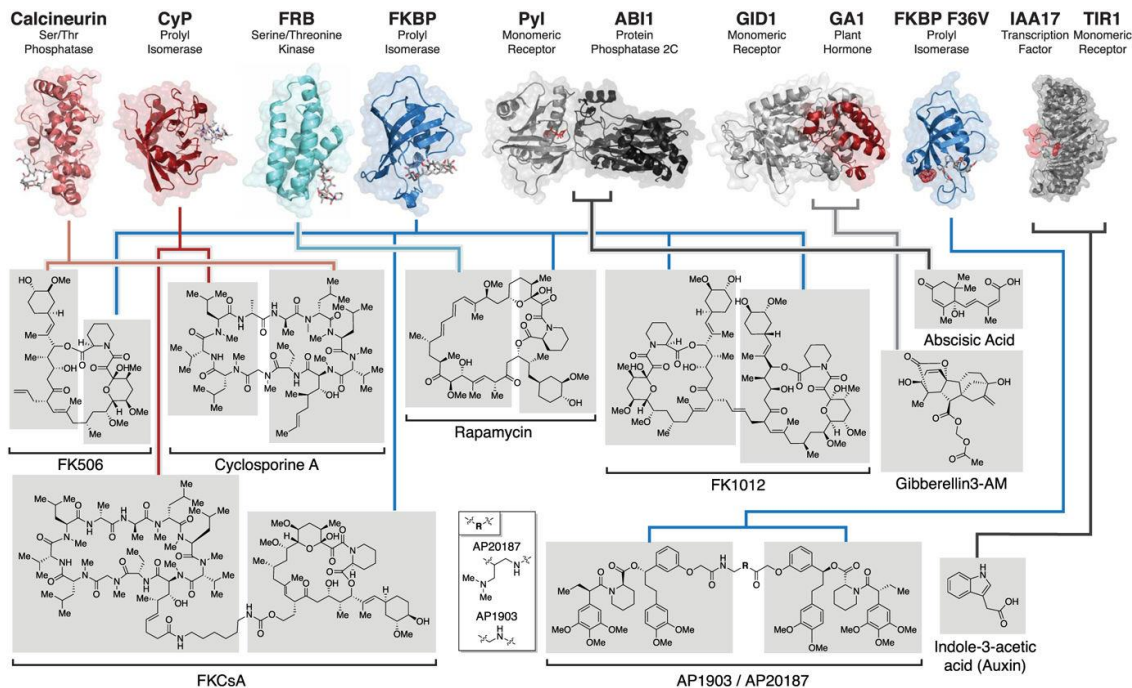


Figure 5-1 Prominent chemical inducers of dimerization and their respective protein partners. Compounds are displayed from left to right in the approximate order in which they were developed. The protein binding partners are shown on top, while the small molecule ligands are shown on bottom with the portion of the

molecule responsible for protein interaction indicated with a gray box. Adapted from Stanton *et. al.*, *Science*, **2018**, 359, 6380.

Homodimerizers have somewhat limited utility as chemical biology tools in that fewer processes require a homodimeric protein species; however, they have been quite useful for controlling receptor dimerization (Figure 5-2). Coumermycin (**18**) is a natural product that consists of two coumarin units joined together by a pyrrole-linker, and was originally discovered as an antibiotic that functioned to inhibit bacterial cell growth through the dimerization of DNA gyrase B (GyrB), a topoisomerase involved in DNA replication.³⁵⁶ It has been employed as a CID to study both the Raf and JAK/STAT signal transduction pathways.³⁵⁷ Another well characterized homodimerizer is FK1012 (**19**), which is a synthetic dimerizer derived from FK506. In pioneering work by Stuart Schreiber, they controlled several other dimeric receptors (TGF- β , insulin, and T-cell) through introduction of **19** in cells and animals.³⁵⁸⁻³⁶¹

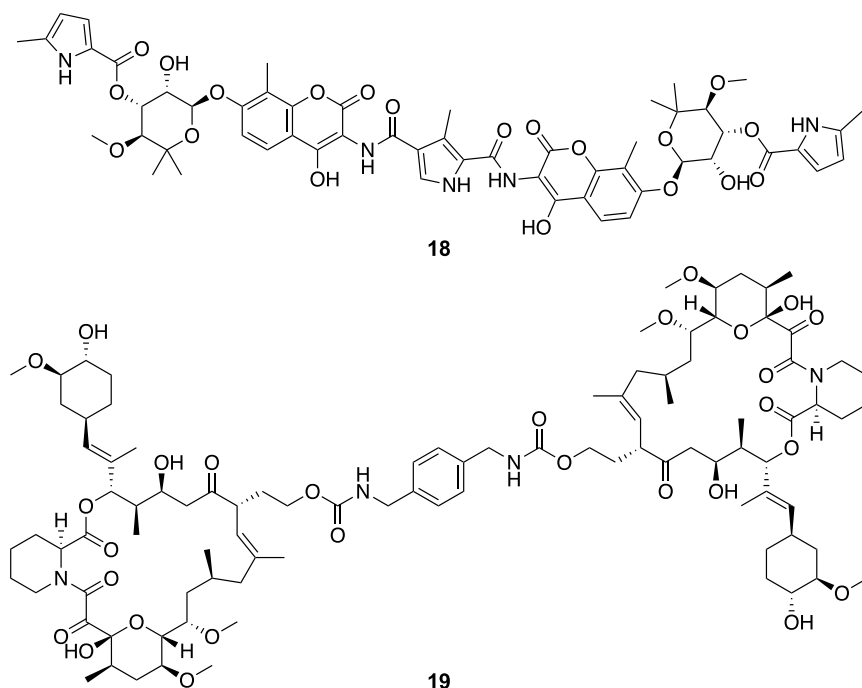


Figure 5-2 Structures of homodimerizers **18** and **19**
Coumermycin (**18**) and FK1012 (**19**) are commonly utilized homodimerizers for controlling receptor activation.

Arguably, the discovery and development of heterodimerizers was transformative for the chemical biology field. Rather than being limited to bringing together the same two proteins, heterodimerization allowed researchers to bring together any proteins of interest that were fused to the appropriate dimerization domains. FK506 (**20**) is an immunosuppressant that functions through dimerizing FKBP12 and calcineurin to inhibit calcium/calmodulin-dependent signaling (Figure 5-3).³⁶² Derivatization into **19**, as discussed above, led to the more common dimerizer.

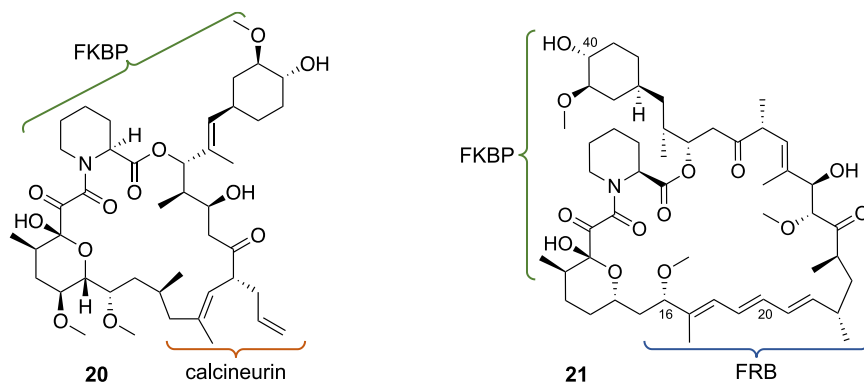


Figure 5-3 Structures of **20** and **21** function as heterodimerizers

FK506 (**20**) and rapamycin (**21**) both interact with FKBP12 to form a complex, which generates a ternary complex with calcineurin and FRB, respectively. The region responsible for binding to FKBP, calcineurin, and FRB are indicated with brackets. Derivatization of rapamycin at positions C-40, C-20, and C-16 have been explored and are discussed within.

The discovery of rapamycin (**21**), which functions to dimerize FKBP12 and the FKBP-rapamycin binding domain of mTOR (FRB) has afforded endless opportunities to control protein dimerization processes and has been commercialized for widespread use throughout the scientific community (Figure 5-3, 5-4a).³⁶³ Rapamycin binds to FKBP with a dissociation constant of 0.2 nM. This FKBP-rapamycin complex then binds to FRB, forming a ternary complex with a K_d of 12 nM (Figure 5-4b).³⁶⁴

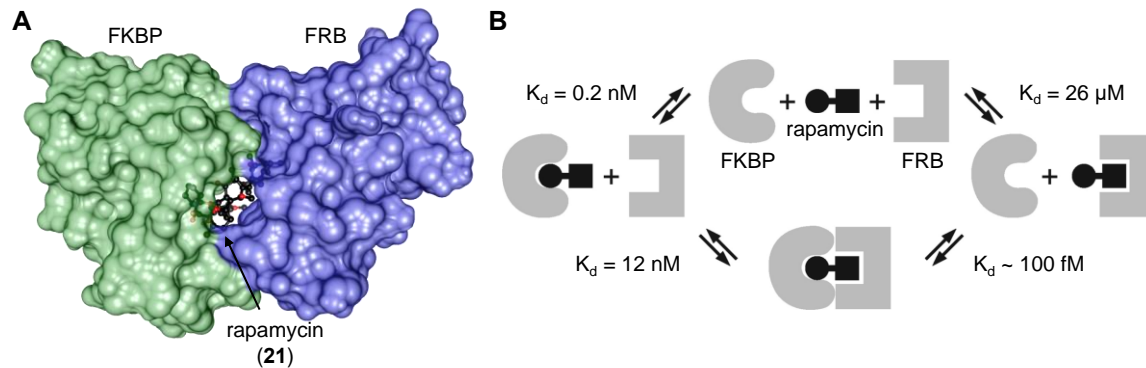


Figure 5-4 Crystal structure of FKBP-21-FRB and mechanisms of binding

a) FKBP and FRB, in green and blue, form a ternary complex with rapamycin tightly bound in the middle (PDB: 1FAP). The ternary complex is stabilized by several protein–protein interactions, as well as, protein–small molecule interactions. b) The affinities of each monomeric and dimeric species toward complex formation was determined. Adapted from Banazynski *et. al.*, *J. Am. Chem. Soc.*, 127, 4715-4721. Copyright 2005 American Chemical Society.

Due to the small size of FKBP and FRB (only 12 and 11 kDa, respectively) and their strong binding affinity for complexation by rapamycin – essentially forming an irreversible interaction – these two domains have been extensively utilized as tools to control the protein-protein interaction of FKBP/FRB fusion proteins of interest. Moreover, the fast cellular diffusion and favorable pharmacokinetics of rapamycin in animals has led to a wide range of processes being placed under rapamycin-inducible control, including (i) regulation of protein translocation (*e.g.*, Golgi/endoplasmic reticulum association,³⁶⁵ endocytic trafficking,³⁶⁶ protein sequestration to the mitochondria,³⁶⁷ recruitment of an inositol phosphatase to the plasma membrane,³⁶⁸ and cell surface glycosylation³⁶⁹), (ii) reconstitution of split proteins or enzymes for activation (*e.g.*, Abl-kinase,³⁷⁰ Cas9 nuclease,³⁷¹ tobacco etch virus protease,³⁷²⁻³⁷³ green fluorescent protein,³⁷⁴ beta-lactamase,³⁷⁵ Cre recombinase,³⁷⁶ BS2 esterase,³⁷⁷ and firefly luciferase³⁷⁸), and (iii) regulation of ubiquitin-modified proteolytic stability.³⁷⁹ This CID has been extensively utilized by our lab (and many others) and is the central theme of the next three chapters.

5.1.1 Brief History of Rapamycin

First discovered in the 1970s by Suren Sehgal, rapamycin was initially reported to be an antifungal antibiotic.³⁸⁰⁻³⁸² It was isolated from *Streptomyces hygroscopicus* on the island of Rapa Nui (or Easter Island), hence the trade name Rapamune or rapamycin. Further research found that rapamycin could inhibit cell proliferation and showed immunosuppressive activity.³⁸³ Elucidating the role of rapamycin as an immunosuppressive agent led to the FDA-approval of rapamycin as an organ transplant drug in the 1990s.³⁸⁴⁻³⁸⁵ As such, Wyeth Pharmaceuticals marketed Rapamune for treatment in conjunction with corticosteroids for prevention of kidney rejection. Through his own investigations at Ayerst Research Lab, Sehgal was convinced that rapamycin possessed additional therapeutic properties beyond its immunosuppressive role. Thus in collaboration with the National Cancer Institute (NCI), rapamycin was screened for anti-tumor activity and showed growth inhibition in many of the cell lines tested.³⁸⁶ As a result, this prompted the NCI to advance rapamycin as a priority drug. In the following years, many analogs of rapamycin were generated in the pharmaceutical industry and some of the analogs have been approved for use in the treatment of various cancers.³⁸⁷⁻³⁹¹

Independent work by both Sabatini and Schreiber, led to characterization of the mammalian target of rapamycin (mTOR) function, regulation, and significance for disease.³⁹²⁻³⁹⁴ It was shown that rapamycin inhibits cell growth through direct inhibition of kinase activity of TOR proteins in eukaryotes. In human cells, this inhibition is the result of FKBP-rapamycin interacting with a small domain in mTOR to inhibit mTOR complex formation. The prevention of mTOR to form an active complex, either mTORC1 or mTORC2, is the mechanism through which cell division and a number of other pathways is impacted by rapamycin (Figure 5-5).

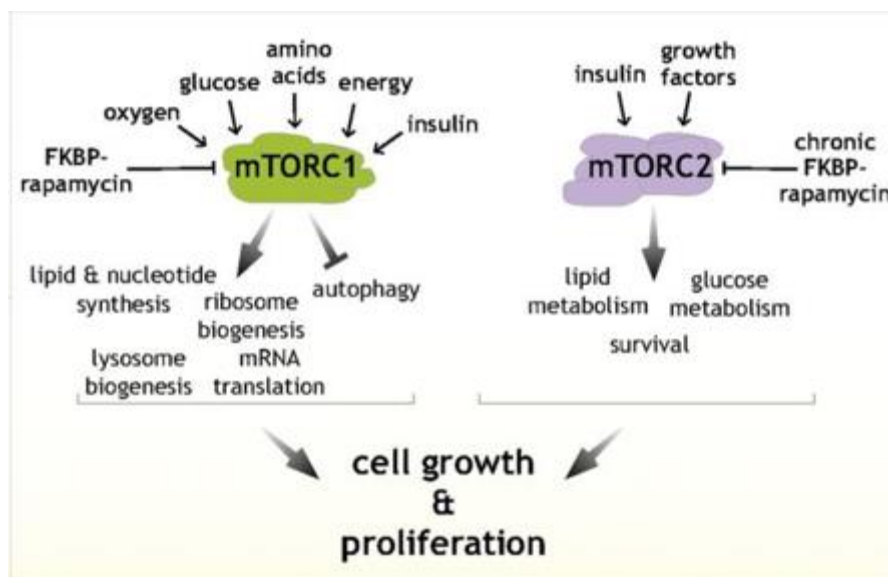


Figure 5-5 Role of rapamycin in mTOR signaling

Schematic showing the signals sensed by mTORC1/2 and the downstream processes they modulate for control of cell growth. Figure used with permission from Sabatini, *Proc. Natl. Acad. Sci. U.S.A.*, 114, 11818-11825.

The University of Pittsburgh has a long-standing tradition of rapamycin and mTOR research dating back to the 1980s work of Thomas E. Starzl (for whom Institutes and campus buildings are named in honor of) who advanced the use of rapamycin and cyclosporin from an experimental to an established clinical treatment following early transplant surgeries.³⁹⁵⁻³⁹⁶ Research in the Thomson group at Pitt focuses on understanding the mechanism of mTORC1/2 inhibition in T lymphocytes³⁹⁷⁻³⁹⁸ and additional efforts by Oertel and Monga have explored the effects of mTOR inhibition in hepatoblastoma tumor models.³⁹⁹ Decades of research has established mTOR as a master regulator, yet there are still areas of mTOR signaling that are not fully characterized; however, the work herein focuses solely on the development and application of rapamycin analogs as tools for chemical biology, rather than biological studies for an improved understanding of the mTOR pathway.

5.1.2 Optical Control of Rapamycin-Induced Protein Dimerization

The material in sections 5.1.2 and 5.1.3 was reprinted in part from Ankenbruck, N.; Courtney, T.; Naro, Y.; Deiters, A. *Angew. Chem. Int. Ed.* **2018**, *56*, 2768-2798.

Caged rapamycin analogs allow for the placement of numerous biological processes under optical control in order to enhance temporal and spatial resolution. The photocaged rapamycin analog **22** was generated through installation of a nitrobenzyl caging group at the C-40 position (Figure 5-6a).⁷¹ When applied to cells, **22** still induced FKBP-FRB dimerization, indicating that the caging group alone wasn't sufficient to abrogate protein-small molecule interaction, which is consistent with previous modifications at C-40.³⁶⁴ However, work by the Hahn lab had shown that a truncated FKBP, termed iFKBP,⁴⁰⁰ exhibited increased flexibility in the loop that interacts with the C-40 position of rapamycin. This flexibility increased contacts for interaction with **2** and resulted in a distorted binding conformation that prevented formation of the ternary complex consisting of iFKBP, FRB, and **22**. This system was then applied to the optical activation of focal adhesion kinase (FAK), using an engineered iFKBP-FAK fusion which rendered the kinase inactive until UV irradiation lead to rapamycin decaging, FAK activation, and an expected cell ruffling phenotype (Figure 5-6b). While **22** was readily synthesized, the need for FKBP truncation required protein engineering.

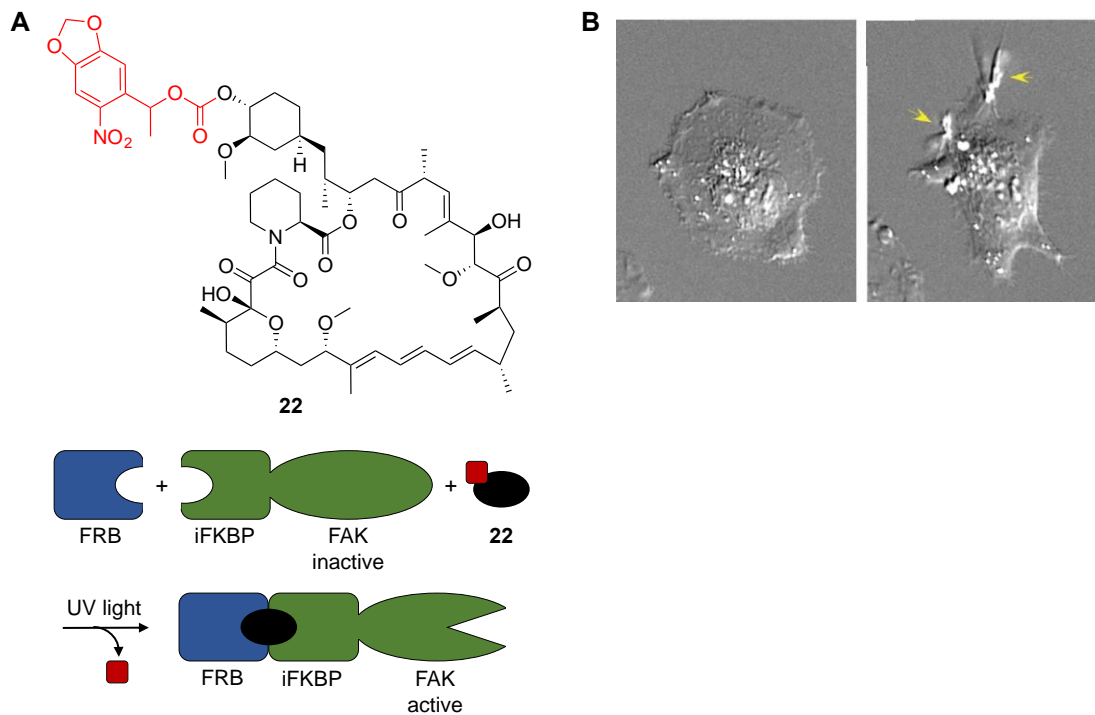


Figure 5-6 Application of caged rapamycin **22** toward control of FAK kinase

a) The structure of **22** is shown with the caging group in red. In this system, FAK activity was monitored in the presence of **1** with and without UV exposure. b) Cells treated with **22** alone did not display active FAK (left); however, UV irradiation led to activation of FAK and subsequent cell ruffling (right). Figure taken from Ankenbruck, *et. al.*, *Angew. Chem. Int. Ed.* **2018**, 57, 2768-2798. Copyright 2018 Wiley-VCH.

A concurrent approach by Inoue addressed this limitation, in the form of the photocleavable rapamycin construct **23** consisting of a caging group at the C-40 position of rapamycin conjugated to biotin.⁴⁰¹ Similar to **22**, the biotin moiety was too small to block FKBP interaction, however, when bound to the avidin protein, steric demand was significantly increased and cell permeability was diminished sequestering **23** outside of the cell (Figure 5-7a). A related strategy of using a ligand-protein complex as a caging group, rather than a small synthetic chromophore, was previously reported by Miller.⁴⁰² Upon irradiation, the avidin-biotin moiety was removed generating a cell-permeable hydroxyethyl rapamycin **24**, which led to intracellular dimerization of FKBP and FRB and, for example, membrane recruitment of a protein of interest, such as Tiam, a Rac1 activator. The latter induces cell migration and ruffling at the edge of cells (Figure 5-7b). Overall, **23** enabled the spatiotemporal activation of protein dimerization and can be readily

interfaced with a range of biological systems that have already been placed under control by rapamycin.

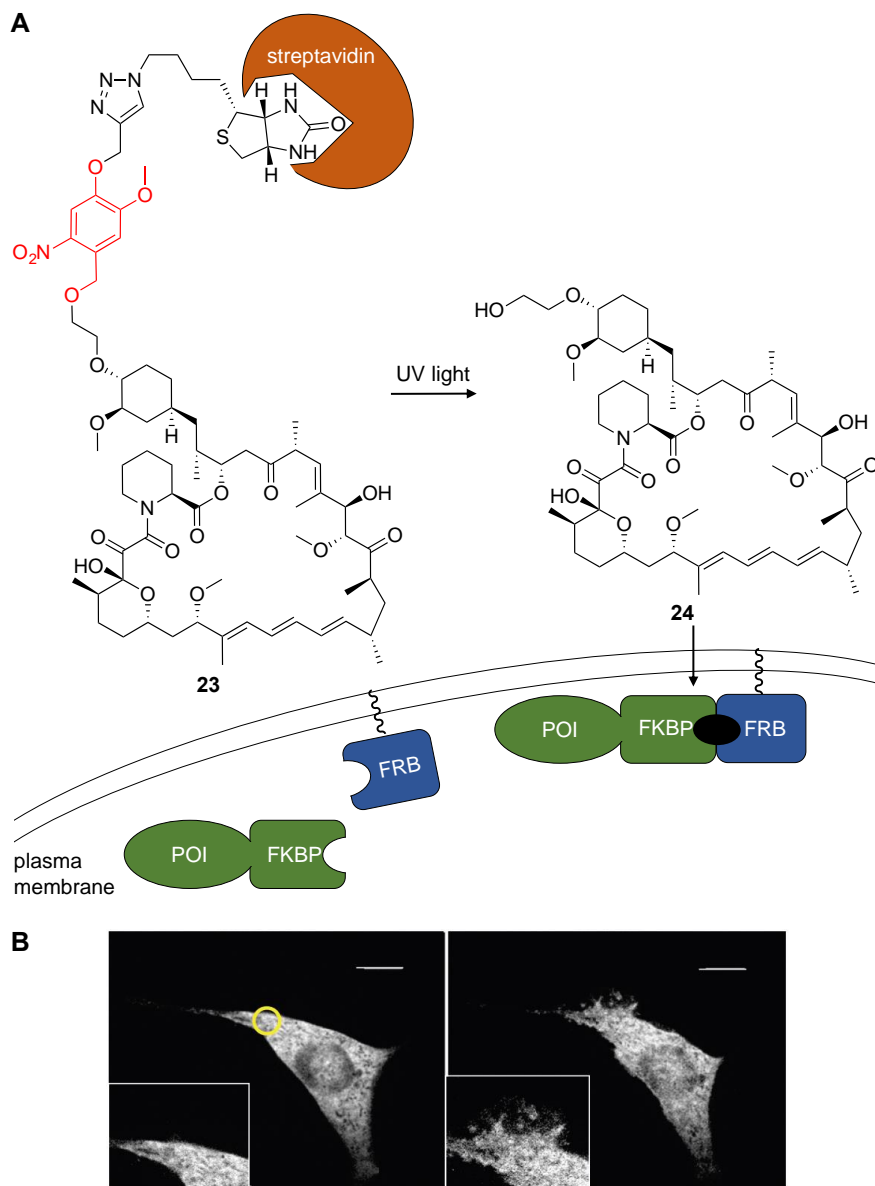


Figure 5-7 Application of caged rapamycin **23** toward Rac localization

a) The **23**-streptavidin complex is unable to enter cells and does not induce protein dimerization until UV irradiation generates **24**. b) Rac-FKBP was used with membrane localized FRB. In the absence of UV light, cells displayed normal cell edges (left); however, upon irradiation and Rac localization cell ruffling is apparent (right). Figure taken from Ankenbruck, *et. al.*, *Angew. Chem. Int. Ed.* **2018**, 57, 2768-2798. Copyright 2018 Wiley-VCH.

In order to alleviate the need for an external avidin protein, while still capitalizing on the dramatic steric demand provided through recruitment of a protein to the caging group, a second

rapamycin molecule was attached to generate the symmetric dimer **25** (Figure 5-8a).²¹² Computational and experimental studies confirmed that the formation of an FKBP-4-FKBP homodimer conformationally blocked binding of FRB. Thus, **25** did not require the use of an engineered iFKBP or the use of an exogenous protein, such as avidin, demonstrating a more practical engineering approach for light-triggered dimerization. The broad applicability of light-activated **25** was demonstrated via optical control of mTOR kinase, TEV protease, and Cre recombinase function through protein dimerization (Figure 5-8b,c).

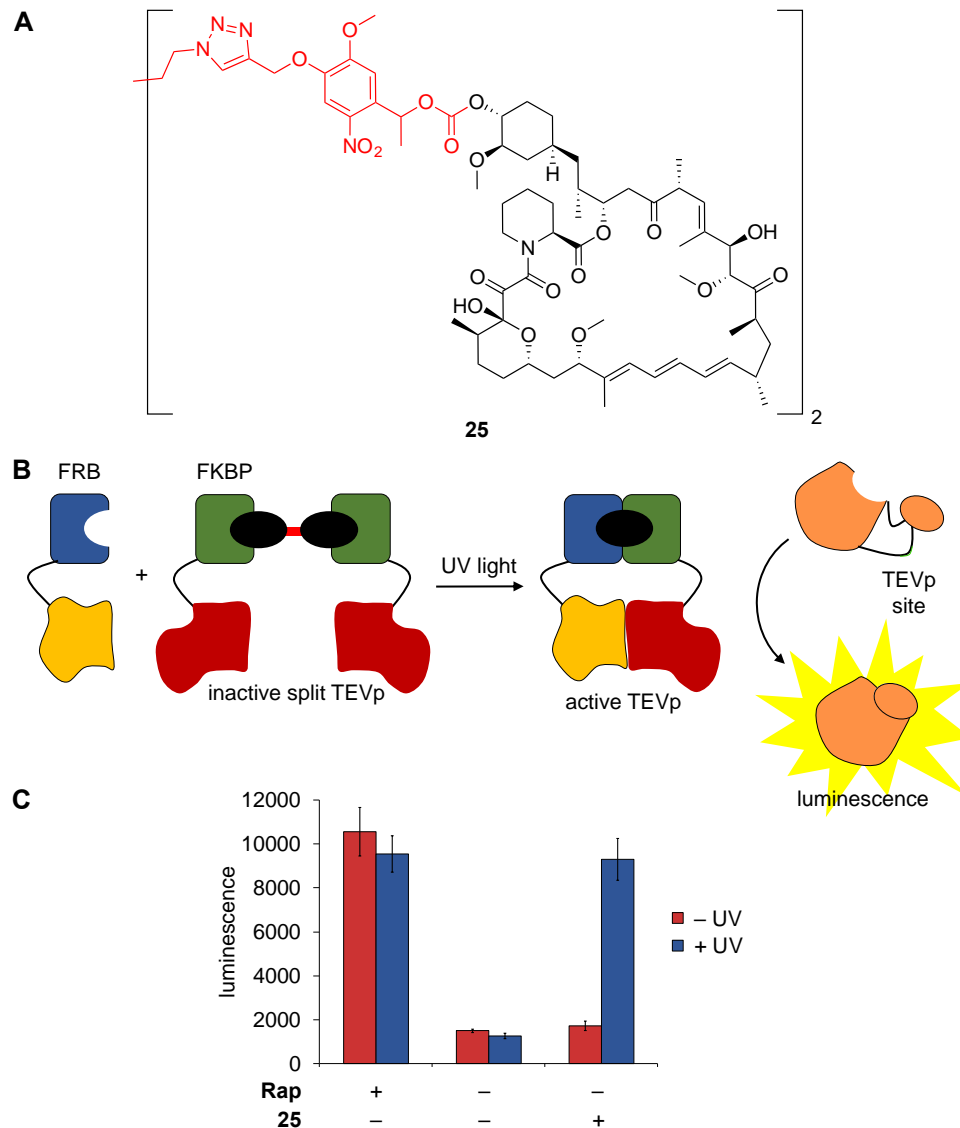


Figure 5-8 Application of caged rapamycin **25** toward control of split TEV protease

a) The structure of **25** is shown with the caging group highlighted in red. b,c) The caged rapamycin dimer **25** was applied to a split TEV protease system consisting of FRB-TEVp (N-terminus) and FKBP-TEVp (C-terminus) to demonstrate optical control. In the presence of **25**, no protease activity is detected. However, after UV irradiation and dimerization of split TEV, a luciferase reporter is proteolytically cleaved and luminescence is generated. Figure taken from Ankenbruck, *et. al.*, *Angew. Chem. Int. Ed.* **2018**, *57*, 2768-2798. Copyright 2018 Wiley-VCH.

Although not applied as a tool for controlling protein dimerization of two fusion proteins, the Woolley group developed the first caged rapamycin **26** in 2010 and demonstrated that this analog can be used for controlling inhibition of the endogenous mTOR signaling pathway (Figure 5-9).⁴⁰³ Rapamycin functions to inhibit the mTORC1 pathway by dimerizing FKBP to the FRB domain of mTOR, which blocks downstream phosphorylation of 4EBP1, ribosomal protein S6

kinase (S6K), and ribosomal protein S6 (S6). While UV irradiation does not generate the native rapamycin but instead a C16-OH analog, this product still retains full inhibitory activity. Using **26**, they were able to show successful light activation as observed via a decrease in phospho-S6K and phospho-S6 levels in western blot analysis.

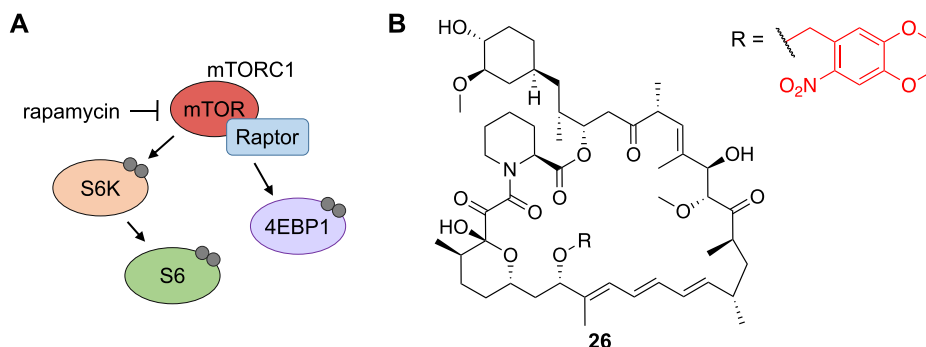


Figure 5-9 Application of caged rapamycin **26** for inhibition of endogenous mTOR signaling

a) An isolated subnetwork of the complex mTOR pathway is provided. Rapamycin inhibits the mTORC1 complex by dimerizing FKBP to the FRB domain of the complex. In the absence of rapamycin, mTORC1 phosphorylates 4EBP1 and ribosomal protein S6 kinase (S6K), which phosphorylates ribosomal protein S6; however, upon treatment with rapamycin, a loss of phosphorylation is observed. Grey filled circles represent phosphorylation. b) The structure of **26** is shown with the caging group highlighted in red.

5.1.3 Optical Control of Other Chemical Inducers of Dimerization

While rapamycin remains the most well-studied CID, other dimerizer systems have been developed and placed under optical control. One limitation of the caged rapamycin system is the generation of free and diffusible rapamycin following UV irradiation, limiting spatial resolution. To address this concern, Chenoweth developed the photoactivatable covalent protein dimerizer **27**, containing a chloro-alkyl moiety for targeting the HaloTag enzyme and a trimethoprim (TMP) group that binds to *E. coli* dihydrofolate reductase (DHFR).⁴⁰⁴⁻⁴⁰⁵ The caging group blocks the TMP/DHFR interaction until irradiation and subsequent ternary complex formation (Figure 5-10a,b). This interaction can be reversed through addition of an excess of TMP which outcompetes the dimerizer ligand. Additionally, the modularity of this approach allows for easy

exchange of components, such as caging groups and binding proteins (e.g., SNAP-tag or cutinase).⁴⁰⁶ The caged TMP-HaloTag ligand has enabled spatial control of protein dimerization in a variety of cellular compartments, including kinetochores, centromeres, and centrosomes (Figure 5-10c). Unlike the rapamycin dimerization system where protein binding and ternary complex formation occur following irradiation, this approach overcomes the diffusion limitation through the covalent tethering of TMP to the HaloTag protein, followed by ternary complex formation after light activation to yield tight spatial control of dimerization.

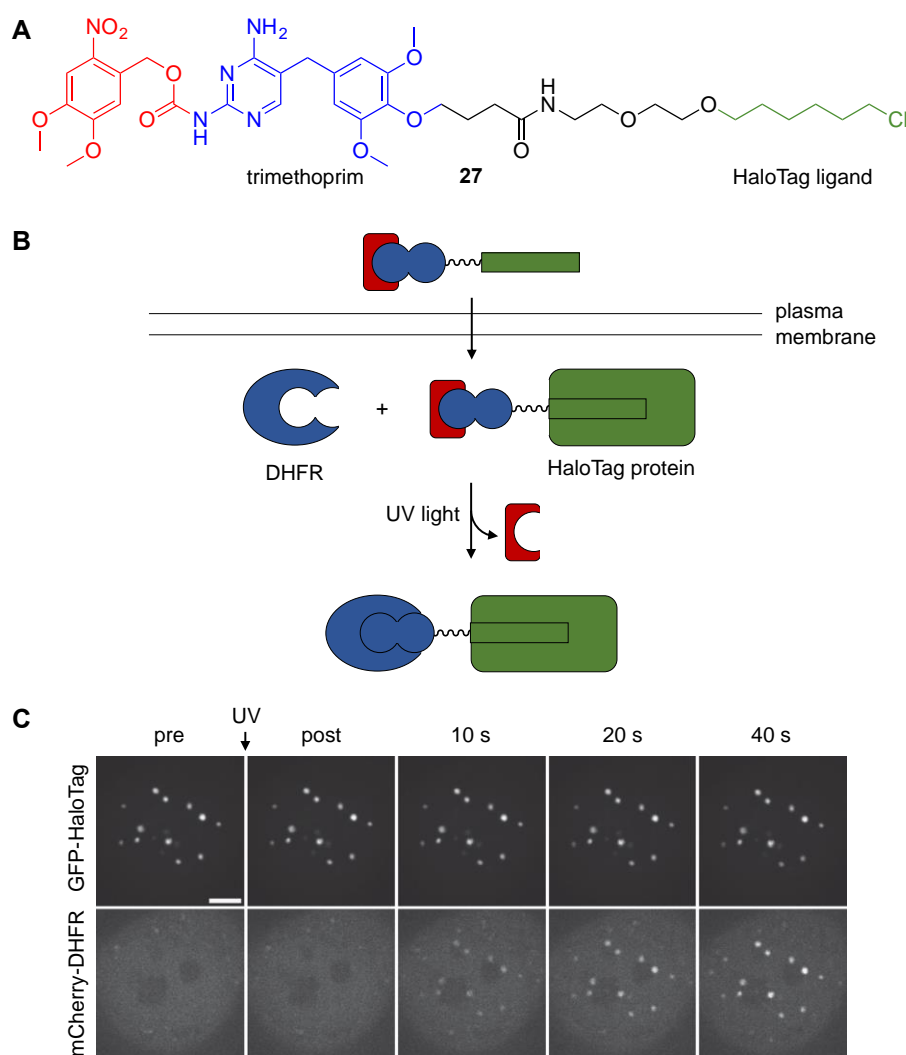


Figure 5-10 Application of caged HaloTag-TMP ligand **27**

a) The structure of **27** is shown with the photolabile group highlighted in red, the trimethoprim group that interacts with DHFR is shown in blue, and the alkyl chloride is shown in green. b) Compound **27** enters cells and covalently

labels HaloTag protein fusions. The removal of the caging group with UV light allows for dimerization with the DHFR protein fusion. c) Recruitment of mCherry to centromere-localized GFP following 387 nm light exposure. Figure taken from Ankenbruck, *et. al.*, *Angew. Chem. Int. Ed.* **2018**, *57*, 2768-2798. Copyright 2018 Wiley-VCH.

In order to complement light-activated CIDs, Wymann developed the light-cleavable CID **28**, enabling the deactivation of protein dimerization.⁴⁰⁷ This approach also utilizes the HaloTag protein and its chloro-alkyl ligand, as well as SNAP-tag technology (Figure 5-11a). The SNAP protein is an engineered mutant of the DNA repair enzyme O⁶-alkylguanine-DNA alkyltransferase and reacts specifically and covalently with benzylguanine analogs. The chloro-alkyl group and the benzylguanine are linked through a photocleavable linker. Delivery into cells induced covalent dimerization of SNAP-tag and HaloTag fusion proteins until the linker is cleaved through UV irradiation (Figure 5-11b,c). Cells expressing NLS-CFP-SNAP (nuclear) and Halo-RFP-giantin (Golgi) were treated with **28**, which induced dimerization and translocation of CFP from the nucleus to the Golgi. Upon UV irradiation and subsequent linker cleavage, CFP translocated back to the nucleus. This approach may enable deactivation of proteins via sequestration to a non-native location until photoactivation triggers protein transport to its native compartment.

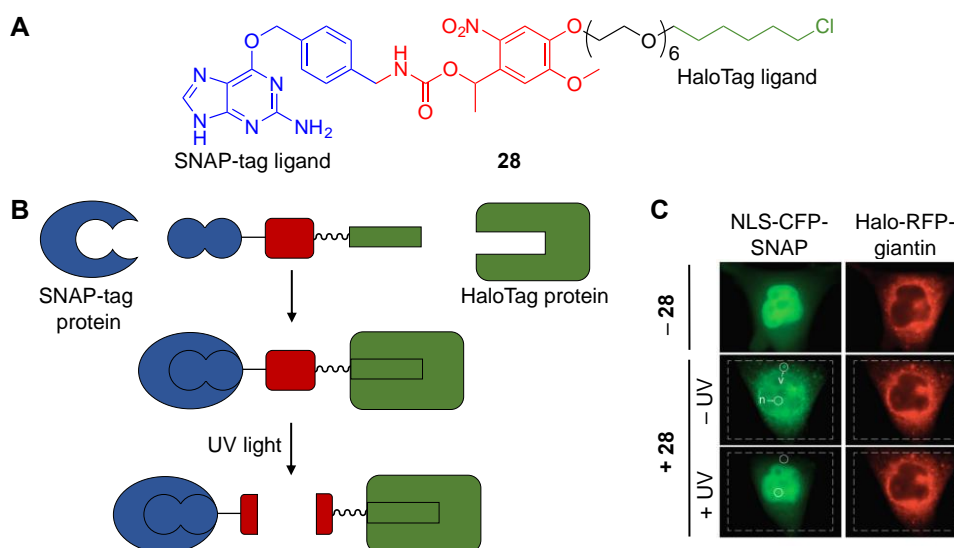


Figure 5-11 Application of the photocleavable SNAP-tag/HaloTag ligand **28**

a) The structure of **28** is shown with the SNAP-tag reactive region in blue, the caging group in red, and the HaloTag ligand in green. b) Upon addition of **28** to cells, the SNAP- and HaloTag moieties react with their respective protein binding partners, thus dimerizing the two proteins. Upon UV irradiation, the linker is cleaved generating free proteins

again. c) Cell micrographs for part b. Figure taken from Ankenbruck, *et. al.*, *Angew. Chem. Int. Ed.* **2018**, 57, 2768-2798. Copyright 2018 Wiley-VCH.

Additionally, two other natural product-inspired caged CIDs have been developed based on abscisic acid⁴⁰⁸ (ABA) and gibberellic acid (Figure 5-12).⁴⁰⁹ ABA is a phytohormone involved in plant adaptation due to environmental stresses, which functions by binding to PYL1, then forming a complex with ABI1.⁴¹⁰ The binding affinity of ABA with PYL1 is reported as 52 and 340 μM from ITC and SPR measurements, respectively, which is ~ 1000 -fold weaker than the rapamycin-FKBP interaction and the binding affinity for ABI1 to generate the ternary complex is not characterized.⁴¹⁰ ABA was previously developed as a CID by Crabtree, and was utilized with rapamycin to orthogonally control two different subcellular localizations.⁴¹¹ The terminal carboxylic acid of ABA was chosen for photocaging with a nitrobenzyl group because an essential hydrogen bond was identified in the crystal structure. Caged ABA **29** was used in regulating gene expression in a split transcriptional activator assay and in regulating cell morphology through induced translocation of Tiam1 to initiate Rac1 signaling and membrane ruffling.

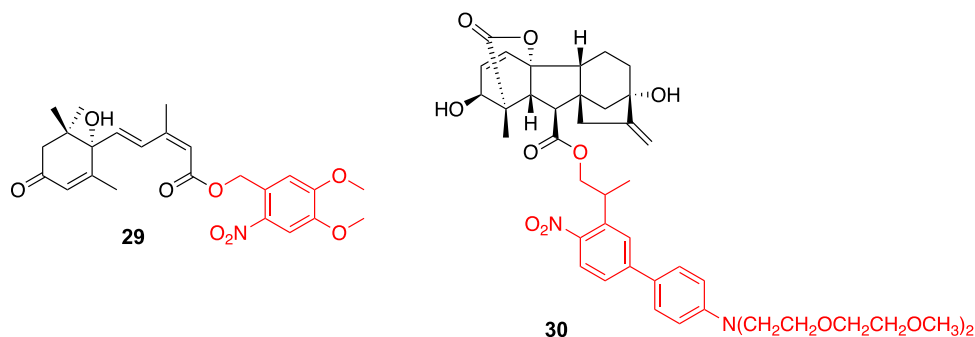


Figure 5-12 Structures of caged abscisic acid **29** and gibberellic acid **30**. Abscisic acid was caged using a dimethoxynitrobenzyl caging group and gibberellic acid was caged with an aminonitrobiphenylpropanol derivative.

Gibberellic acid (GA3), another plant hormone, first binds to GID1 with an estimated K_d value of 4 μM ,⁴¹² inducing a conformational change which enables ternary complex formation with GAI and has been applied as a CID by Inoue.⁴¹³ A series of caged GA3 analogs was developed

using both nitrobenzyl and aminonitrophenyl caging groups to enable one- and two-photon activation, respectively.⁴⁰⁹ Caged GA3 **30** was utilized for two-photon activation of mitochondrial protein localization in mammalian cells. These two methods present alternative CID approaches that do not require protein engineering for efficient optical control and have no endogenous off-target interactions when applied in mammalian cells since the dimerization components are native to plants. Interestingly, in both of these examples, although the caging groups are attached through ester linkages, they are reportedly stable to endogenous esterases with minimal background activation in the absence of light. One disadvantage of these two approaches is the size of the protein components (21 – 38 kDa) required, thus increasing the need for careful design when fusing to proteins of interest to avoid interfering with endogenous protein/enzyme function.

Several photo-controlled CIDs have been developed that enable activation or deactivation of protein-protein dimerization. These tools directly interface with well-established and commercially available systems, such as FKBP/FRB, HaloTag, and SNAP-tag, and thus have the potential to provide optical control for a wide range of cellular processes.

5.1.4 Optogenetic Approaches to Control Protein Dimerization

In addition to the chemical inducers discussed in the previous section, several purely optogenetic approaches have been developed for the regulation of protein dimerization.^{17, 414-418} Optogenetic tools most commonly utilize photo-responsive protein domains derived from photoreceptors found in plants, animals or even fungi. A wide range of systems has been developed and reported thus far, and there are still numerous ongoing efforts to engineer improved versions. Table 5-1 showcases several of the most common systems reported to date and denotes several key features: (i) the association and dissociation wavelengths, (ii) the size of the protein domains

required, (iii) the approximate lifetime of the on-states, and (iv) the necessity of a cofactor. At least one of the protein partners contains a photo-responsive moiety that undergoes a light-induced structural change, which in turn induces a protein conformational change. The light-responsive moiety is sometimes intrinsic to the photoreceptor (as in UVR8 and Dronpa, gray shaded rows in the table) or it is a small molecule cofactor that is conjugated to the protein (LOV domains, phytochromes, and cryptochromes). In most cases, the dark-state refers to a dissociated (or inactive state), which can be converted to the associated (or active state) with irradiation of the appropriate wavelength of light. Systems have been developed to cover the entire visible light spectrum, enabling multiplexing of optogenetic components with various fluorescent reporters when activation/deactivation and imaging wavelengths are carefully considered.⁴¹⁹

Table 5-1 Optogenetic dimerizer systems sorted by increasing wavelength

The various association/dissociation wavelengths, size of each protein partner, and the half-life of different optogenetic systems is summarized. Gray shading indicates the chromophore is intrinsic to the one of the proteins, while the white background systems utilize a small molecule cofactor. Adapted from Spiltoir et al., *Curr. Opin. Struct. Biol.* **2019**, 57, 1-8. Copyright 2019 Elsevier Ltd.

System	Typical/peak excitation wavelength		Size (amino acids)	Approx. lifetime (half-life)
	Association	Dissociation		
UVR8/COP1	280 nm	N/A	440/340	
UVR8/UVR8	dark	280 nm	440	>8 hours
Dronpa	405 nm	488 nm	257	light inducible
CRY2/CIB1	450 nm	dark	612/335	5 minutes
CRY2PHR/CRY2PHR (clustering)	450 nm	dark	498	5 minutes
CRY2olig, CRY2clust	450 nm	dark	498	5 minutes
TULIPs	450 nm	dark	153/194	tunable
iLID/SspB	450 nm	dark	144/110	tunable
FKF1/GI	450 nm	dark	619/1173	62.5 hours
VVD/VVD	450 nm	dark	150	tunable
nMag/pMag (Magnets)	450 nm	dark	150/150	tunable
LOVTRAP	dark	450 nm	143/59	tunable
EL222	450 nm	dark	208	<50 seconds
Aureochrome	450 nm	dark	136	7 minutes (tunable)
PixD/PixE	dark	450 nm	150/380	seconds-minutes
phyB/PIF3	660 nm	740 nm	621/524	light inducible
phyB/PIF6	660 nm	740 nm	908/100	light inducible
BphP1/PpsR2	740 nm	650 nm	732/465	light inducible, dark reversion 15 minutes

These systems function through a variety of different mechanisms as shown in Figure 5-13, thus depending on the biological question being addressed, certain systems should be employed over others. Similar to chemical dimerizers, the most common use of optogenetic dimerizers is the manipulation of protein localization to a desired subcellular compartment (Figure 5-13a), often for

control of cell signaling. Examples include the use of PhyB/PIF6 to control the recruitment of the Tiam catalytic domain to the plasma membrane for regulation of Rac1 kinase activity,⁶³ use of TULIPs and CRY2/CIB1 to control MAPK signaling at the plasma membrane by recruitment of a scaffolding protein Ste5,⁴²⁰⁻⁴²¹ and use of CRY2PHR or PhyB/PIF6 to recruit CRaf or SOS, respectively, for control of the Ras-ERK signaling pathway through varying the duration and frequency of plasma membrane localization.^{61, 422}

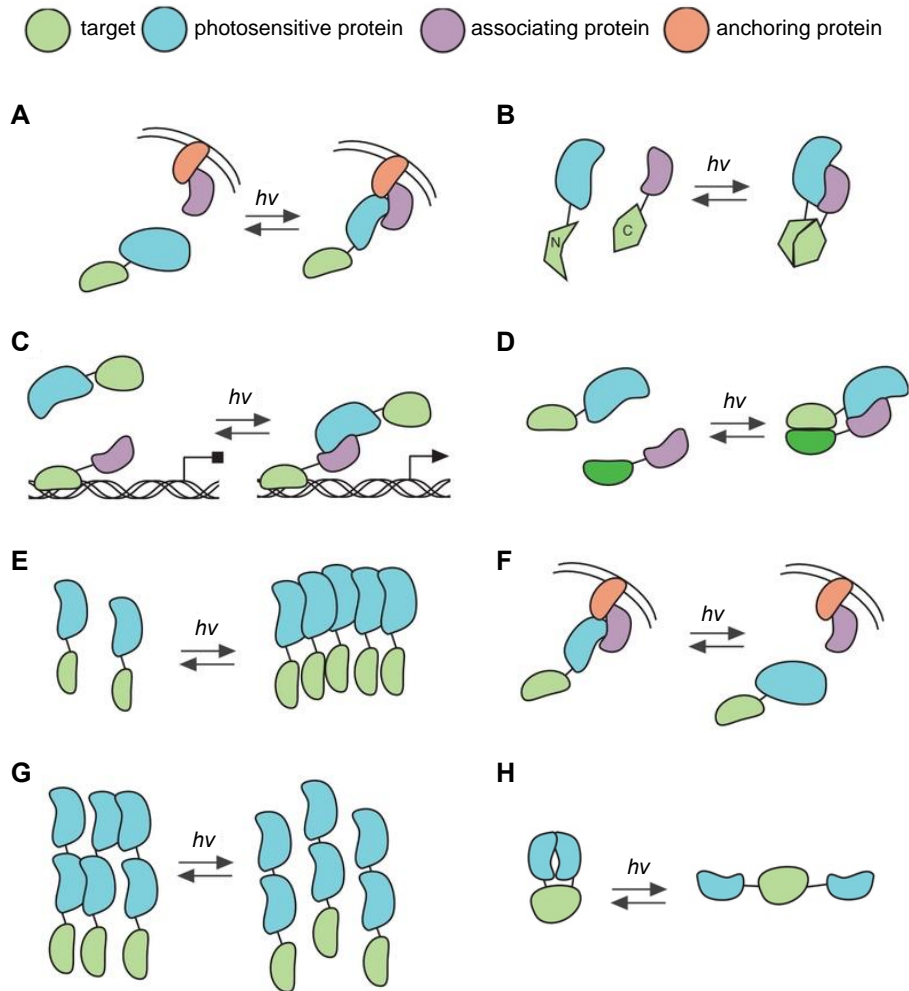


Figure 5-13 Schematic of various optogenetic dimerizers

Eight different optogenetic arrangements are depicted in cartoon form and afford control over a wide range of processes: (a) recruitment of a target to a desired subcellular location, (b) reconstitution of a split protein or enzyme, (c) reconstitution of a split transcription factor to control gene expression, (d) heterodimerization of two different proteins, (e) oligomerization of a target protein, (f) inactivation through sequestration, followed by release and activation, (g) dissociation of protein clusters, and (h) utilization of a protein-protein interaction to block/inhibit target protein function or interaction. Adapted from Spiltoir *et al.*, *Curr. Opin. Struct. Biol.*, 57, 1-8. Copyright 2019 Elsevier Ltd.

Control of split proteins/enzymes or split transcription factors (Figure 5-13b,c) has been performed using PhyB/PIF3 for control of GAL4 DNA binding domains⁴²³ and ATPase intein,³⁴ CRY2/CIB1 to control Cre recombinase,⁴²⁴⁻⁴²⁵ and nMag/pMag for controlling Cre recombinase,⁴²⁶ Cas9,⁴²⁷ and T7 RNA polymerase.⁴²⁸

Similarly to small-molecule dimerization, optogenetic systems have been developed to enable both homo- and heterodimerization of protein fusions that naturally have no or poor-affinity for each other (Figure 5-13d,e). Homodimerization (or oligomerization) using CRY2 clustering has been employed to study DNA damage response due to TopBP1 protein assembly⁴²⁹ and for inducing the B-catenin pathway through clustering of LRP6c.⁴³⁰ Heterodimerization has all been employed in activation of cell signaling pathways through the shuttling of proteins to different subcellular compartments using CRY2PHR/CIBN in TrkB⁴³¹ and FGFR pathways.⁴³²

In contrast to light-induced assembly (as seen in the above examples), systems that function to activate upon disassembly have also been developed (Figure 5-13f-h). Dimers of UVR8/UVR8 fused to an endoplasmic reticulum-processed protein initially sequestered the protein in the ER; however, upon light-induced disassembly of the dimer, the protein fusion was released from the ER and secreted through a series of protein trafficking events. In the LOVTRAP system, proteins of interest, in this example constitutively active signaling enzymes Vav2, Rac1, and PI3K, were fused to the small protein unit Zdk which is tightly bound to the dark-state of AsLOV2 such that the enzymes are inactive due to mis-localization; however, upon irradiation and release of the Zdk-tagged enzymes, the active enzymes translocate to their appropriate cell compartment to perform their functions.⁴³³ Similarly, Dronpa has been fused to Cas9⁴³⁴ and MEK1⁶⁰ in such a manner that the dark-state dimeric form sterically occludes the active site, until light-induced monomer formation exposes the active site enabling catalysis.

The various applications described above using different optogenetic systems should sound familiar since many of these same systems have been placed under optical control using unnatural amino acids (as in Chapter 2.0) or through caged small molecule dimerizers discussed previously in this chapter. This shows how widespread the utility of light is for controlling various biological processes, but also demonstrates there are a wide range of tools in the field for rendering different processes light-responsive. As such, there are advantages and disadvantages of each type of optical tool that need to be considered when designing a new application. Compared to photocaged UAAs and small molecules, optogenetic methodologies offer an advantage of reversibility of interaction through turning the light source on or off. However, the introduction of large photoresponsive proteins often requires careful engineering of the design in particular with regard to removal of undesired background (dark) activity and in many cases, the off-state does not fully block or inhibit activity.⁴³⁵ On the other hand, utilization of optically-controlled dimerizers (typically) abrogates the need for protein engineering and can be utilized with commercial or previously established systems.

5.2 Toward the Development of Optically Controlled, Bioorthogonal Rapalogs

While the combination of rapamycin with other CIDs has enabled orthogonal control of two different biological processes, we envisioned that we could use bio-orthogonal rapamycin analogs with light-orthogonal caging groups to enable multi-wavelength activation of two distinct biological processes (Figure 5-14). All caged rapamycin analogs in the literature use nitrobenzyl-derived caging groups which optimally decay at 365 nm, thus we hypothesized that development of a red-shifted caged rapamycin analog would afford light-orthogonal activation, or at a

minimum, sequential activation. Additionally, rapamycin analogs modified at the region involved in FRB, termed rapalogs, have been developed alongside a panel of FRB mutants to generate bio-orthogonal rapalog/FRB pairs. We concurrently worked to (i) validate that the rapalog/FRB pairs functioned orthogonally in our assays (5.2.1) and (ii) design, synthesize, and assess red-shifted caged rapamycin analogs in a range of biological assays (5.3).

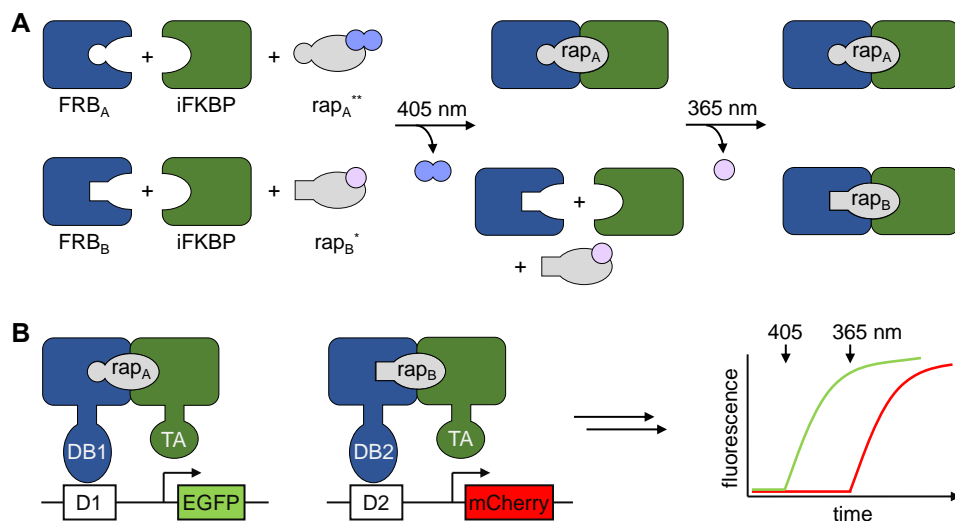


Figure 5-14 Schematic representation of multi-wavelength bio-orthogonal rapamycin dimerization
a) The orthogonal rapalog/FRB pairs – FRB_A/Rap_A** and FRB_B/Rap_B* – can be sequentially activated with 405 (blue caging group) and 365 nm (violet caging group) irradiations. b) Ternary complexes formed after sequential decaging events where the FRB mutants are fused to two different DNA binding domains which recognize two different promoter regions and the iFKBP is fused to a transcriptional activator. In the example shown, sequential irradiation would lead to the generation of GFP, then mCherry which could be readout through fluorescence microscopy or western blot analysis.

5.2.1 Validation of Bioorthogonal Rapalogs and FRB Pairs

Rapamycin interacts with mTOR, which is a kinase responsible for controlling cell growth and metabolism.⁴³⁶ Due to the inherent nature of rapamycin to regulate cell growth, rapalogs and FRB mutants have been developed to minimize the cytotoxic effects of rapamycin, thereby improving the utility of rapamycin as a dimerization tool. BSRap (31), MaRap (32), iRap (33), and aiRap (34) (Figure 5-15a) are examples of rapalogs with modifications at either the C-16 or C-20

position. Pioneering work by Schreiber and later Crabtree and Wandless led to the discovery of specific residues in FRB that provided substantial selectivity toward one rapalog over another (Figure 5-15b).⁴³⁷⁻⁴³⁸ Specific residues 2095, 2098, and 2101 within FRB were randomized to create libraries that were then screened by a secreted alkaline phosphatase (SEAP) assay for specific binding to the rapalog. In addition to being less toxic than rapamycin, the rapalogs also offer the opportunity for orthogonal triggering of two different FKBP/FRB-mutant dimerizations.⁴³⁸ Two rapalog/FRB mutant pairs are marked in blue and orange in the table for clarity. The matching rapalog/FRB mutant is indicated with a solid box, while the mis-matched pair is indicated with a dotted box.

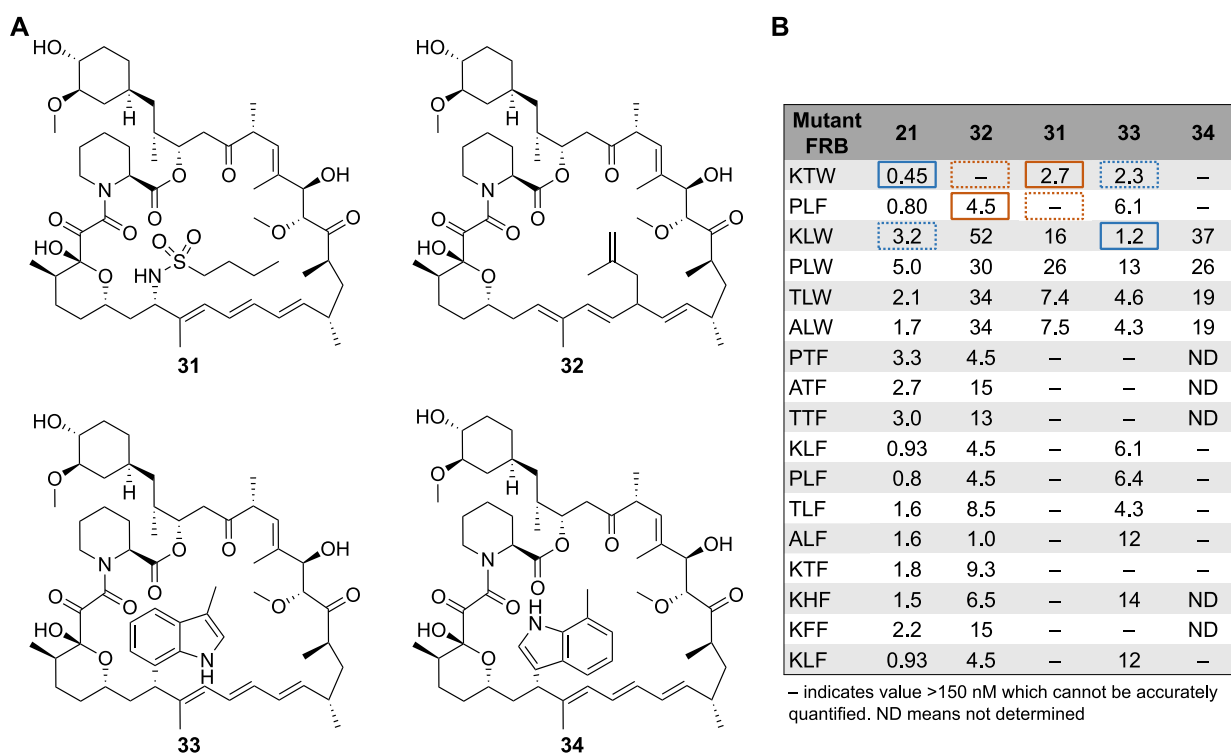


Figure 5-15 Rapalogs and FRB pairs

a) Structures of the C16 or C20 modified rapalogs BSrap (**31**), maRap (**32**), iRap (**33**), and aiRap (**34**) are shown. b) Using a SEAP reporter assay, the EC₅₀ values (in nM) of rapamycin and the four analogs with various FRB mutants are provided in the table. The mutation abbreviations correspond to the residues 2095, 2098, and 2101, respectively. The table is adapted from Bayle, *et al.*, *Chem Biol*, 13, 99-107. Copyright 2006 Elsevier.

Based on the literature reported values, we decided to try using **21** and **33** with KTW and K LW mutants, respectively. In order to test these constructs, a membrane translocation assay was utilized. The constructs for this include Lyn₁₁-FKBP_{x2}-CFP and YFP-FRB, which when expressed in mammalian cells localize to the plasma membrane or remain diffuse throughout the cell, respectively (Figure 5-16a).⁴³⁹ Upon addition of rapamycin or a rapalog, YFP-FRB translocates to the membrane due to ternary complex formation. This assay was imaged on a Nikon A1 using either confocal or total internal reflection fluorescence (TIRF) modes. Initial experiments were conducted with confocal imaging to verify the integrity of the assay to ensure visualization of membrane localization. Rapamycin (**21**) was tested over a range of concentrations (10 nM to 1 μM) with FRB_{KTW} and displayed concentration dependent dimerization over time (Figure 5-16b). When using 1 μM of **21**, complete translocation was observed around 60 minutes after addition of the compound. For both 100 nM and 10 nM of **21**, complete translocation took closer to 2 hours. In order to screen compounds for orthogonality, a 1 μM concentration was selected since complete translocation occurred faster and in a more biologically relevant time frame.

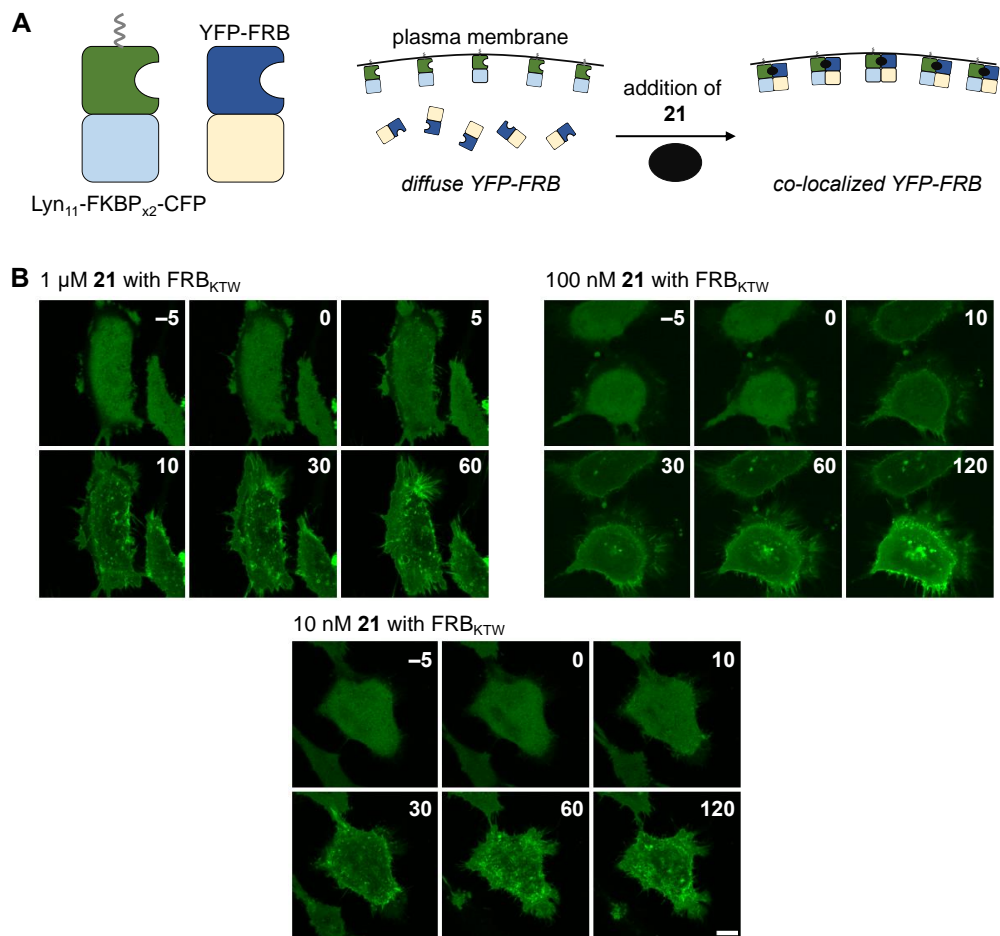


Figure 5-16 Validation of membrane reporter with varying concentrations of rapamycin

a) Cartoon representation of the membrane localization assay. Cells doubly transfected with $\text{Lyn}_{11}\text{-FKBP}_{x2}\text{-CFP}$ and YFP-FRB show the localization patterns indicated on the left prior to addition of compound. However, upon addition of **21** or rapalog, ternary complex formation co-localizes YFP-FRB to the membrane with $\text{Lyn}_{11}\text{-FKBP}_{x2}\text{-CFP}$. b) Higher concentrations ($1\ \mu\text{M}$) of **21** resulted in much faster translocation, while low concentrations ($10\ \text{nM}$) still resulted in translocation but at a slower overall rate. Numbering represents time in minutes relative to compound addition. Scale bar represents $10\ \mu\text{m}$. Note: only the YFP channel is presented in the images above and is pseudo-colored green instead of yellow.

Site-directed mutagenesis was employed to generate the YFP-FRB_{KLW} mutant for use with **33**. Following a published protocol, **33** was synthesized in one step using **21** with TFA and 3-methylindole in DCM in 72% yield.⁴³⁸ After establishing that the membrane translocation assay was working as expected using confocal imaging, we switched to TIRF imaging to enable more facile quantification of membrane localization.

Hela cells were doubly transfected with Lyn₁₁₁-FKBP_{x2}-CFP and YFP-FRB* (the asterisk denotes a mutant FRB) in glass-bottom chamber slides. To investigate the activity of **33**, YFP-FRB_{KLW} was used; whereas, for **21**, YFP-FRB_{KTW} was employed. The following day, cells were imaged for ~30 minutes prior to addition of compound to ensure that minimal fluctuations in TIRF were observed over time. Compound **21** or **33** was carefully added to the wells at the indicated concentration and TIRF images were collected every 2.5 minutes for an hour. Both YFP-FRB_{KTW} and YFP-FRB_{KLW} were tested with 1 μ M and 100 nM of **33** as seen in Figure 5-17a,b. Unfortunately, at both concentrations, similar levels of ternary complex formation and translocation are observed. We also tested **21** with YFP-FRB_{KTW} at 1 μ M (Figure 5-17c) and 100 nM (data not shown). Upon comparison of the “matched” pairs **33**/KLW (black line) and **21**/KTW (blue line) against the “mismatched” pair **33**/KTW (red line), the level of bio-orthogonality was not ideal for activating two different processes (Figure 5-17d). Based on this data, **33** dimerizes both FRB_{KTW} and FRB_{KLW} with similar efficiencies. Thus, we concluded that a different set of FRB/rapalog pairs would need to be explored in order for us to apply this with a high degree of bio-orthogonality.

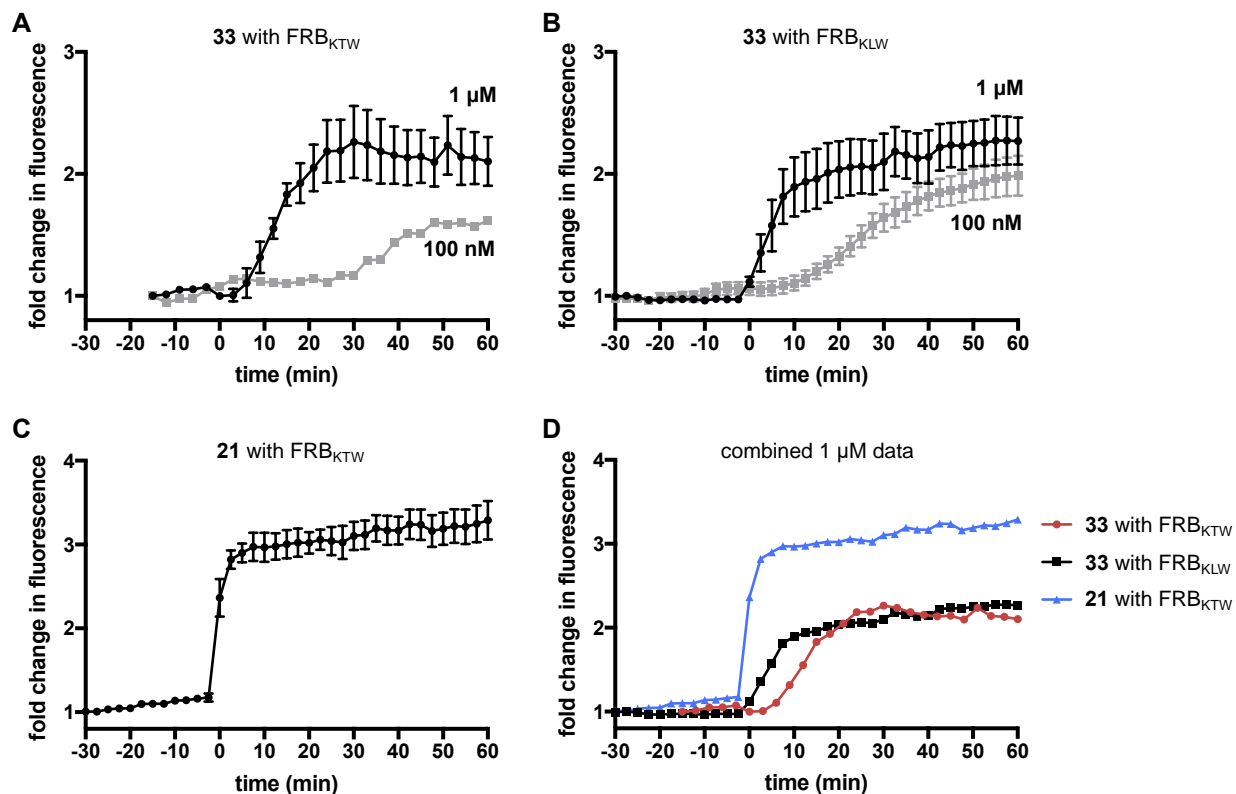


Figure 5-17 TIRF imaging analysis of rapalog and FRB pairs

a,b) TIRF quantification of membrane localization for **33** with YFP-FRB_{KTW} (a) and YFP-FRB_{KLW} (b) at both 1 μM (black line) and 100 nM (gray line) concentrations. c) **21** was tested with YFP-FRB_{KTW} and the TIRF quantification is shown at 1 μM final concentration. d) The 1 μM data from parts a-c were combined into a single graph for comparison of matched and mismatched pairs. The “matched” pairs are **33**/KLW (black line) and **21**/KTW (blue line), while the “mismatched” pair is **33**/KTW (red line). As demonstrated by the graph, these analogs do not display the level of orthogonality that is needed. Note: error bars represent the standard error calculated from an average of three or more cells per condition.

The next rapalog/FRB pairs we decided to test were **31**/FRB_{KTW} and **32**/FRB_{PLF} (Figure 5-15b). Based on the values obtained from the SEAP reporter assay,⁴³⁸ these compounds show more complete orthogonality (see EC₅₀ values from Figure 5-15b; top two rows). Following previously reported procedures, **31** and **32** were synthesized in one step each. For synthesis of **31**, **8** and butylsulfonamide in DCM at -40 °C was treated with trifluoroacetic acid to give **31** in 44% yield after column purification.⁴⁴⁰ Synthesis of **32** started with **8** and trimethylmethylallylsilane in DCM cooled to -40 °C, followed by the addition of boron trifluoride diethyletherate.⁴⁴¹ The reaction generates two regioisomers, a C-16-modified analog and the C-20-modified analog **32**.

Only the C-20-modified analog is biologically active; thus, the isomers needed to be further separated. In the original report, a phenyl stationary phase HPLC column was utilized, but we first tried to optimize conditions using a traditional C18 HPLC column. We were unable to achieve baseline separation of the three isomers (*R*-C-20, *S*-C-20, and *R*-C-16); however, we did collect both the C-20 isomers together and these were used in the biological studies.

Site-directed mutagenesis was utilized for generating the YFP-FRB_{PLF} mutant. With the new rapalogs in hand and the FRB mutants cloned, we were able to test these pairs in cells to determine their bio-orthogonality. Similarly to above, HeLa cells were doubly transfected with Lyn₁₁-FKBP_{x2}-CFP and YFP-FRB mutants in glass-bottom chamber slides. Depending on the specific experiment, either YFP-FRB_{KTW} or YFP-FRB_{PLF} was used for transfection. The next day, cells were imaged for ~20 minutes prior to addition of compound, then **31** or **32** was carefully added to the wells at the desired final concentration and TIRF images were collected every 2.5 minutes for an hour. Based on the previous results with **33** and **21**, we observed fast translocation using 1 μ M; therefore, we used 1 μ M as a starting point for these experiments. When treated with 1 μ M of **31**, YFP-FRB_{KTW} appears to have higher translocation efficiency than YFP-FRB_{PLF} with a 3.4-fold change compared to a 2.3-fold change (Figure 5-18a). Similarly, when treated with 1 μ M of **32**, YFP-FRB_{PLF} shows a fold change of 3.5 compared to 2.6 with YFP-FRB_{PLF} (Figure 5-18b). When the four combinations are overlaid on a single plot (Figure 5-18c), the matched pairs perform better than the mismatched pairs; however, in order to control biological processes with tight control, the mismatched pair should ideally be as close to 1 as possible. We hypothesized that the lack of orthogonality could be due to the high concentrations that we were using compared to the literature reported experiment in which 10 nM was used;⁴³⁸ thus, we decided to test 10 nM. As seen in Figure 5-18d, over the course of an hour, neither mutant appeared to translocate in the

presence of 10 nM of **52**. We concluded that concentrations higher than 10 nM were necessary to see a response with these mutants. Unfortunately, the data presented here does not correlate well with the EC₅₀ values reported from the SEAP assay in the initial publication.

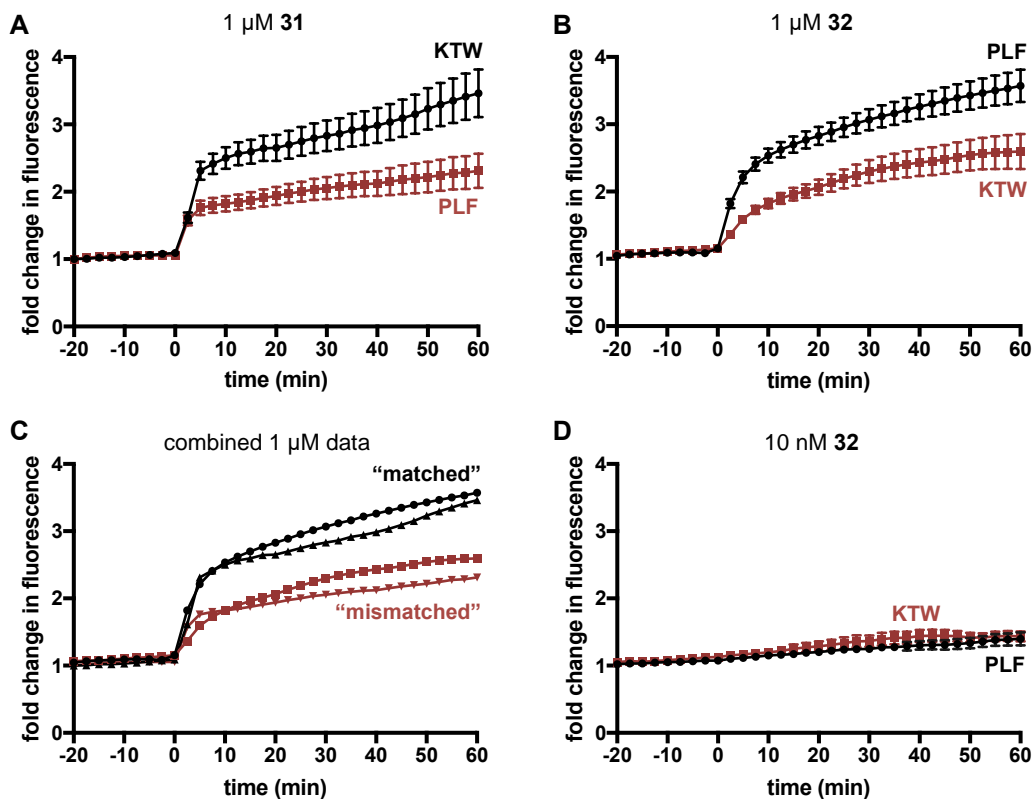


Figure 5-18 TIRF analysis of **31** and **32** with KTW and PLF mutants

a) TIRF quantification using 1 μM **31** with FRB_{KTW} (black) and FRB_{PLF} (red). b) TIRF quantification using 1 μM **32** FRB_{PLF} (black) and FRB_{KTW} (red). c) When combining all four pair options into a single plot, it becomes apparent that the matched and mismatched pairs are not very different. This indicates that these rapalogs/FRB mutants are not fully bio-orthogonal. d) Since 1 μM did not show a high degree of separation, 10 nM was also tested. Unfortunately, at this low concentration, no activation was observed in the time frame that was monitored.

The two different rapalog/FRB pairs that we tested did not display the level of bio-orthogonality (ideally a binary on or off level of control) needed in our translocation assays. At this point, efforts were shifted to focus solely on the development of red-shifted analogs, but in the future, there are two avenues we could further pursue toward developing bio-orthogonal pairs. First, we could retest these current two pairs in a split luciferase reporter (see Figure 5-23) to more closely replicate the SEAP assay and yeast three-hybrid system in which these pairs were

established. Secondly, we could generate the FRB mutants utilized in the initial report (FRB_{TLW} and FRB_{KTF}) for use with **31** and **32**, although based on the table in Figure 5-15b, these FRB mutants exhibit less orthogonality in the SEAP reporter assay than the ones we have previously tested. Although not discussed in the original publication, subsequent publications and work performed by Crabtree *et al.* demonstrated that PLF and other “L” mutants (*e.g.*, KLW, one mutation from wild-type) were unstable unless **32** or rapamycin were present.⁴⁴¹⁻⁴⁴² While substantial work was performed in order to generate these conclusions for PLF and KLW, no mention regarding the stability of TLW can be found; however, in our hands, confocal imaging of the KLW mutant showed no destabilization (no loss of signal was observed in the time frame imaged) relative to that of the KTW mutant. Should a bio-orthogonal pair be found via either approach, introduction of nitrobenzyl and amino-nitrobiphenyl caging groups to the validated rapalogs could be used for generating multi-wavelength activatable bio-orthogonal pairs.

5.2.2 Methods

Synthesis of 31, 32, and 33. All reagents and solvents obtained from commercial sources were used without any additional purification. Literature procedures were followed exactly as written for the synthesis of **31**,⁴³⁸ **32**,⁴⁴⁰ and **33**.⁴⁴³ NMR characterization of **31** and **32** matched literature reported spectra. Purification of **33** via HPLC was performed with an Agilent Zorbax SB-C18 (5 µm particle size, 9.4 x 250 mm) semi-prep column rather than the recommended phenyl stationary phase. Stock solutions of these 3 rapalogs (and rapamycin) were prepared in sterile-filtered DMSO at 5 mM, and samples were stored at -20 °C.

Cloning of DNA constructs. All cloning was performed using Top10 cells. Phusion DNA polymerase was used for site directed mutagenesis following the protocol detailed in 8.1.2.

YFP-FRB purchased from Addgene (#20148) contained the FRB_{KLW} mutant (with KLW referring to K2095, L2098, and W2101; this short-hand nomenclature is used throughout). Site directed mutagenesis was performed using YFP-FRB as the template to generate YFP-FRB_{KTW} using primers L2098T For/Rev to generate the wild-type FRB sequence. YFP-FRB_{PLF} was generated through two sequential rounds of SDM. First, YFP-FRB_{PLW} was generated using primers K2095P For/Rev with YFP-FRB as the template, the YFP-FRB_{PLW} was used as the template to generate YFP-FRB_{PLF} using primers W2101F For/Rev. Both mutations were validated by Sanger sequencing at Beckman Coulter using an “FRB seq For” sequencing primer. All primer sequences are provided in Table 5-2.

Table 5-2 List of primers used to generate FRB mutants in YFP-FRB
Base mutations are indicated with CAPITALIZATION.

Name	Sequence (5' → 3')
L2098T For	gacctcACCcaagcctgggacctctattatcatgtgtccga
L2098T Rev	ggcttgGGTgaggctcctgacattccctgattcatgtactcctg
K2095P For	aatgtcCCGacctcctccaagcctgggacct
K2095P Rev	gaggtcGGGgacattccctgattcatgtactcctgca
W2101F For	caagccTTCgacctctattatcatgtgttccgacgaatctca
W2101F Rev	gaggtcGAAGgcttgaggaggtcggggaca
FRB seq For	atgaaggcctggaagaggcatc

Confocal and TIRF microscopy analysis of membrane translocation. HeLa cells were plated at 20,000 – 30,000 cells per well in a PDK-treated glass-bottomed 8-well chamber slide. At ~70% confluence, cells were transfected with Lyn₁₁-FKBP_{x2}-CFP and the appropriate YFP-FRB mutant (100 ng of each plasmid, 200 ng total/well) using LPEI (protocol 8.2.8). After overnight transfection, the media was removed and replaced with 250 µL of DMEM (– phenol red, + 10% FBS) or LCIS (+ 10% FBS). Compound solutions were prepared from 1 mM solutions (10 µL of 5 mM stock into 40 µL of DMSO) or 0.1 mM solutions (10 µL of 1 mM into 90 µL of DMSO). Working solutions were prepared at 6X of the final desired concentration (6 µM or 600 nM). For

6 μM , 1.2 μL of 1 mM was diluted into 199 μL of media. For 600 nM, 1.2 μL of 0.1 mM was diluted into 199 μL of media.

Chamber slides were imaged on a Nikon TiE inverted microscope equipped with an A1R confocal head and LU-NV laser for 405 and 488 nm excitation (with 425–475 nm and 500–550 nm emission filters, respectively). A 100X 1.45 NA Plan-Apochromatic oil-immersion objective was used. For TIRF, a TIRF illuminator arm fiber coupled to an Oxxius L4C laser with 405 and 488 nm excitation lines was used. The 100X objective was used for objective-based TIRF and images were acquired via epifluorescence on a Zyla (Andor) camera. Image acquisition for Figure 5-16 and 5-17 were acquired on a demo microscope, while data in Figure 5-18 was acquired in the Department of Cell Biology (Gerry Hammond lab). For TIRF imaging, cells were imaged for ~15 – 30 minutes to establish a flat baseline, followed by the addition of 50 μL of 6X compound solution to achieve the desired 1 μM or 100 nM concentration. Post-treatment images were acquired every 2.5 minutes for an hour. TIRF data was directly analyzed using the NIS Elements software by drawing a region of interest (ROI) around a given cell and measuring the mean intensity over time. Normalization to the membrane fluorescence at the beginning of the experiment (set equal to 1) was used to determine the fold change of activation. The mean plus standard error of the mean is reported for 8 – 12 cells per condition.

5.3 Introduction to Caged Rapamycin Analogs with Improved Photochemical Properties

Based on the previous success of controlling a single biological process with temporal control, we envisioned light- and bio-orthogonal rapalogs could be developed to enable wavelength selective activation of multiple biological processes. To do so, after establishing bio-

orthogonal FRB/rapalog pairs, the corresponding rapalogs need to be caged with light-orthogonal caging groups. Our lab has previously developed two nitrobenzyl-caged rapamycin analogs that were activated with 365 nm light, thus developing a red-shifted caged rapamycin should enable orthogonal light activation. We utilized a modified 7-diethylaminocoumarin as our first red-shifted target, which decages upon irradiation with >405 nm light and can be selectively removed in the presence of nitrobenzyl caging groups.^{67, 444-445} A synthetic route established by a former lab member (Yan Zou) was initially utilized toward this goal; however, even with significant optimization of low-yielding steps, the NHS-carbonate **35** was obtained in <2% yield over eight steps. Additionally, the alkynyl-coumarin rapamycin **36** was never isolated even with extended reaction times and optimization efforts (Figure 5-19).

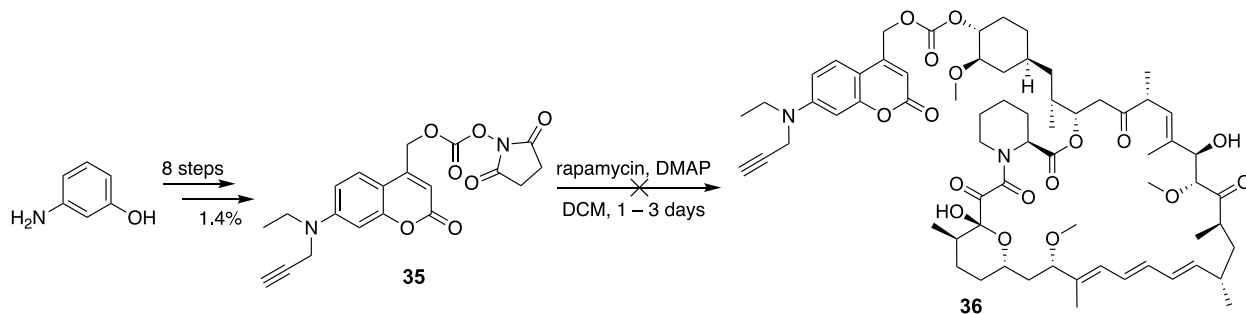


Figure 5-19 Attempted synthesis of a coumarin-modified rapamycin
The 3-aminophenol was converted to the alkynyl-coumarin NHS-carbonate **35** in 8 steps. The desired coumarin-modified rapamycin analog **36** could not be isolated.

5.4 BIST-caged Rapamycin Analogs

Around the same time that we were working to optimize the coumarin-caged rapamycin synthesis, the Ellis-Davies group published a new red-shifted caging group, a dinitro-bisstyrylthiophene (BIST) derivative, BIST-EGTA (Figure 5-20).⁴⁴⁶ The BIST caging group has an absorbance maximum at 440 nm, which is ~100 nm red-shifted of traditional nitrobenzyl caging

groups, and should also be light-orthogonal. In their initial report, they demonstrate the release of calcium using both one- and two-photon activation, with 405 and 810 nm irradiation, in cardiac myocytes. Additionally, based on the linkage between the caging group and EGTA moieties, two different decaging mechanisms were plausible. Using NMR, they confirmed release of the α -substituent, as opposed to fragmentation through the β -elimination pathway.

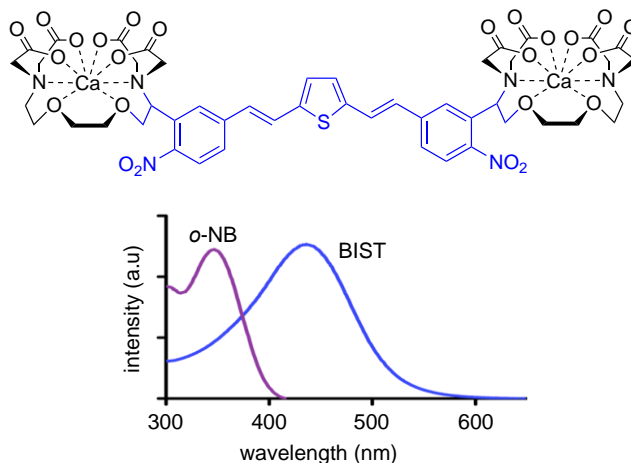


Figure 5-20 Structure of a new bisstyrylthiophene caging group and the absorbance spectrum. The structure of BIST-EGTA is shown with the caging moiety indicated in blue. The absorbance spectra of BIST-EGTA and *o*-NB-EGTA are shown in blue and purple respectively. The BIST caging group exhibits a bathochromic shift of ~100 nm compared to the traditional *ortho*-nitrobenzyl caging group. Adapted with permission from Agarwal *et al.*, *J. Am. Chem. Soc.*, 138(11), 3687-3693. Copyright 2016 American Chemical Society.

We envisioned this BIST caging group could be modified to generate a monomeric-caged BIST-rap or a dimeric BIST-dRap. Thus, the synthetic route in Figure 5-21 was developed for the synthesis of a BIST-dRap. Synthesis of **42** commenced with methylation of 5-bromo-2-nitrobenzaldehyde (**37**) with trimethyl aluminum in ice-cold DCM to yield the alcohol **38** in 73% yield. A Suzuki coupling of a vinyl boronic anhydride pyridine complex and **38** in the presence of catalytic amounts of tetrakis(triphenylphosphine)palladium and potassium carbonate in water/dimethoxyethane under reflux afforded **39** in 88% yield. A double Heck reaction of **39** with 2,5-dibromothiophene in DMF under reflux yielded **40** in 39% yield. The symmetric alcohol **40** was activated with *N,N'*-disuccinimidyl carbonate with triethylamine in acetonitrile to give **41** in

55% yield. Thus, the synthesis of BIST-NHS **41** was achieved over 4 steps in 14% yield. Unfortunately, the subsequent step to generate BIST-dRap **42** using **41** and rapamycin (**21**) in the presence of DMAP in DCM remained elusive. A range of reaction times (1 – 3 days) was screened in an effort to improve the reaction yield; however, minimal increase in generation of **42** was observed with increasing time. Considering that literature reported yields for mono-substitution of rapamycin range from 18% to 41%,⁴⁴⁷ it is not surprising that double addition with rapamycin would be even lower yielding, thus preventing isolation of the small amount actually generated in the reaction. Generation of the desired product was confirmed by HRMS; however, both rapamycin (**21**) and the caging group alcohol (**40**) were the predominant species by mass spectrometry analysis.

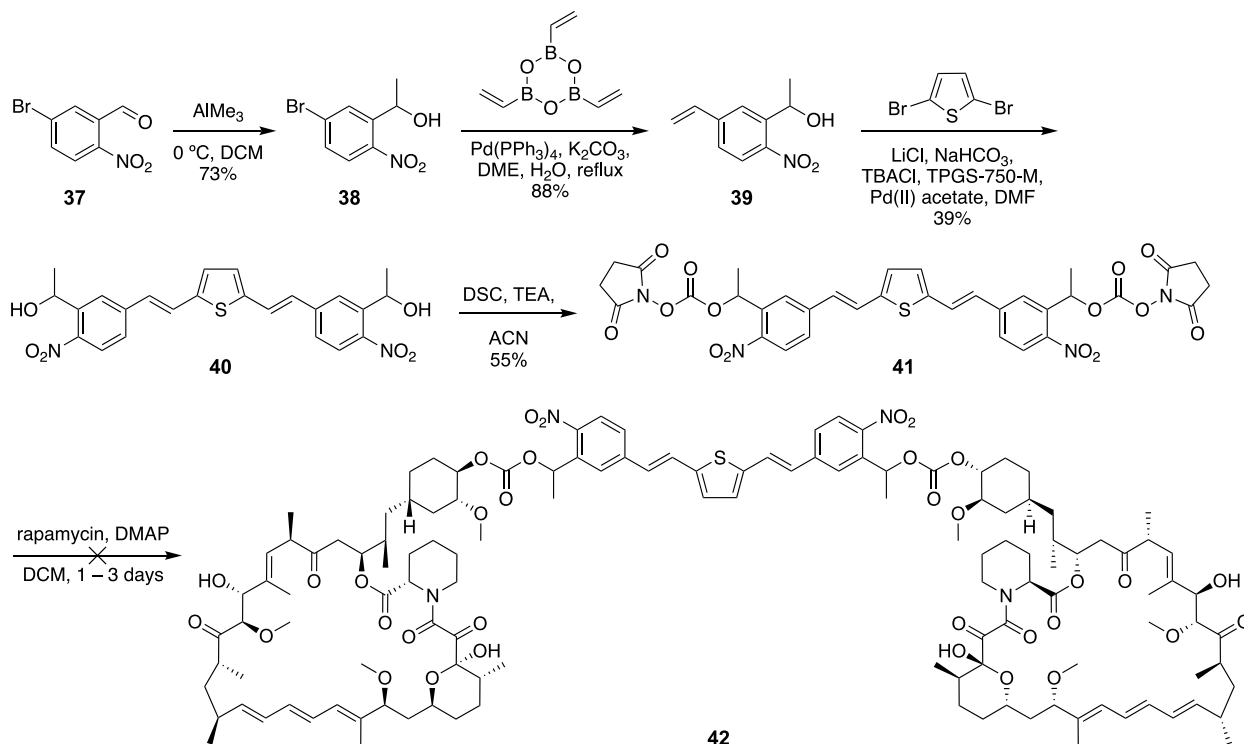


Figure 5-21 Attempted synthesis of a BIST-dRap **42**

The symmetric BIST-NHS **41** was synthesized in four steps from the commercially available 5-bromo-2-nitrobenzaldehyde. Synthesis of the BIST-dRap **42** was unsuccessful.

Since generation of this BIST-dRap variant proved more synthetically challenging than originally planned, we decided to utilize click chemistry to generate a BIST-dRap variant. Numerous examples of copper-catalyzed click reactions can be found in the literature and the yields of these transformations are typically higher than formation of a carbonate using an NHS-carbonate.⁴⁴⁸⁻⁴⁴⁹ The NHS-carbonate **41** from Figure 5-21 was reacted with propargyl alcohol to generate one of the reactive groups needed for click chemistry, **43**.

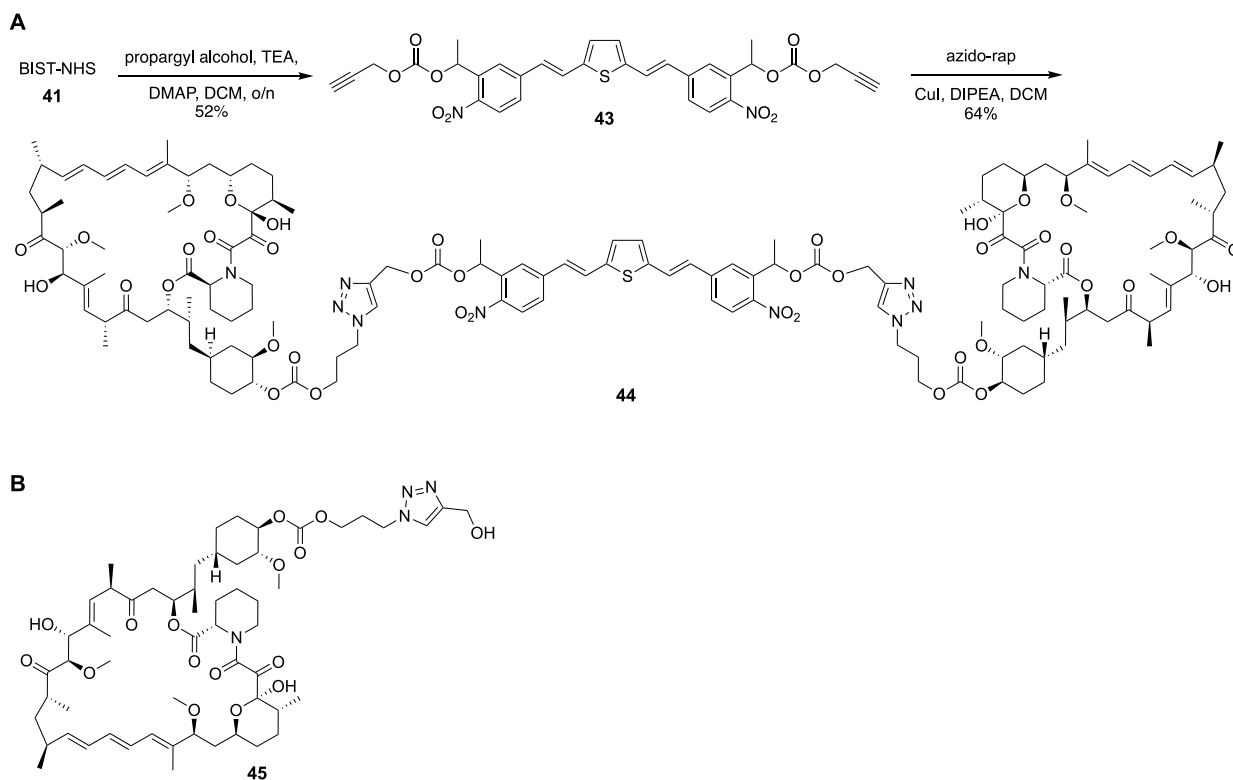


Figure 5-22 Synthesis of a second-generation BIST-dRap **44**

a) The activated NHS-carbonate **41** was reacted with propargyl alcohol to generate **43**. Trevor Horst prepared an azide-modified rapamycin to use in a click reaction with the symmetric alkyne **43** to yield the second generation BIST-dRap **44**. b) As a control compound, the azide-modified rapamycin was coupled with propargyl alcohol to generate the triazole-modified rapamycin **45** that would be released upon decaging.

In collaboration with Trevor Horst, rapamycin was functionalized with an aliphatic azide over three steps to generate an azido-rap. The azido-rap and alkyne **43** underwent a click reaction to generate the second generation BIST-dRap **44** in 64% yield (Figure 5-22a). Additionally, azido-rap was coupled to propargyl alcohol to give triazole-modified rapamycin **45** that mimics the

rapamycin analog that should be released upon decaging (Figure 5-22b). Biological evaluations of BIST-dRap **44** were performed in a luciferase assay below.

Plasmids for a split luciferase FKBP/FRB dimerization assay were obtained from Addgene (#31181 and 31184).³⁷⁸ When transiently expressed in mammalian cells, CLuc-FKBP and FRB-NLuc fragments undergo minimal interaction. However, upon addition of rapamycin to the cell medium, FKBP-rapamycin-FRB ternary complex formation occurs, thereby reconstituting a functional luciferase enzyme that generates a luminescence output (Figure 5-23a). In the literature, this system has exclusively been applied to rapamycin; however, we envisioned that this assay would enable a rapid method for the testing of caged, rapamycin analogs (Figure 5-23b).

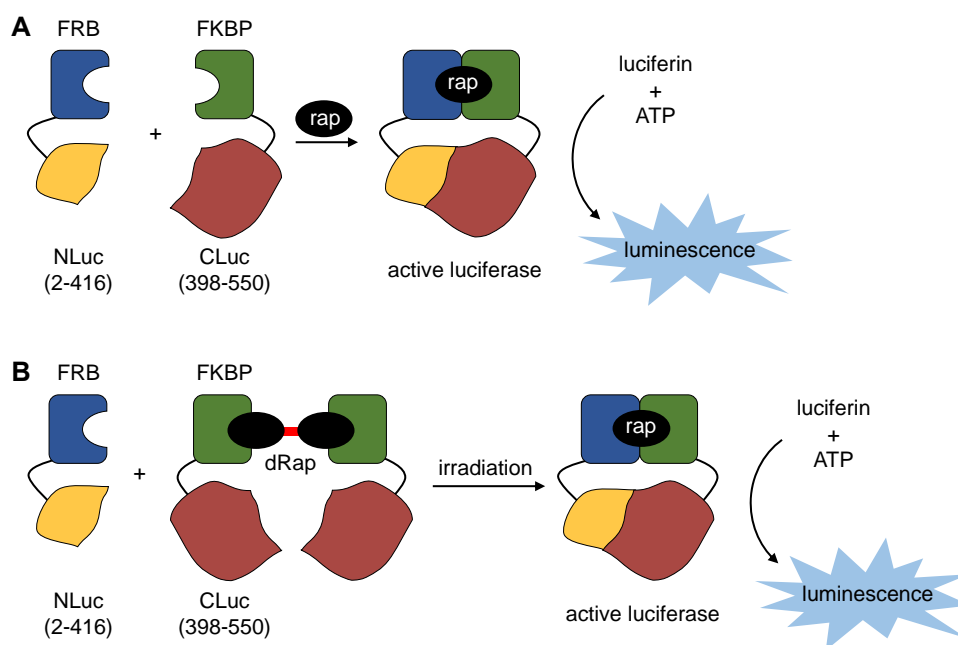


Figure 5-23 Schematic representation of a split luciferase with rapamycin

a) FRB-NLuc and CLuc-FKBP are transiently expressed in mammalian cells, then upon rapamycin addition and ternary complex formation, a functional luciferase enzyme is reconstituted. Following addition of luciferase substrates (luciferin, ATP, etc), luminescence is measured on a plate reader. b) When using the split luciferase assay with dRap analogs, homodimerization of FKBP occurs. After irradiation to generate rapamycin, ternary complex formation results in a functional luciferase enzyme which provides a luminescence output.

Based on previous computational data that supports the formation of a FKBP-**25**-FKBP homodimer prior to irradiation, we decided to try three different ratios of the FKBP:FRB plasmid

amounts during transfection in order to produce more FKBP, thus minimizing background dimerization (Figure 5-24). For all subsequent dimeric rapamycin experiments, a 3:1 FKBP:FRB plasmid ratio was chosen since it showed the greatest fold change between rapamycin (**21**) and published dRap (**25**) and **25** showed minimal background activity relative to DMSO treatment.

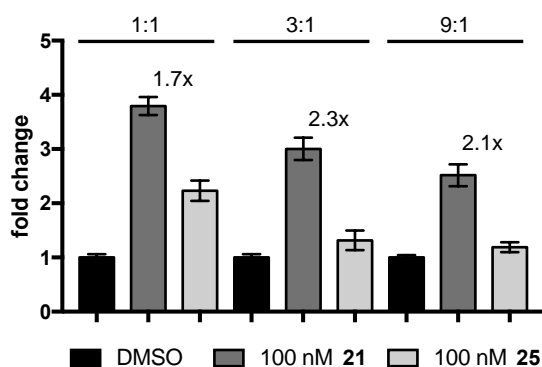


Figure 5-24 Determination of optimal FKBP:FRB ratios in the split luciferase reporter for dRap analogs HEK293T cells were transfected with various plasmid ratios of FKBP:FRB to find optimal conditions to minimize background dimerization with **25**, while still displaying high signal-to-noise values. Cells were treated with 100 nM concentrations of **21** or **25** and incubated at 37 °C for three hours. Based on these results, a 3:1 ratio was chosen for all future dRap analog experiments since minimal background was observed and a moderate signal was obtained. The fold change values comparing **21** to **25** are provided, with the 3:1 plasmid ratio showing the greatest difference. Error bars represent the standard deviation of three independent wells.

Cells expressing the split luciferase constructs were treated with **21**, **44**, or **45** at 25 nM. A subset of wells was irradiated with a Zeiss mercury lamp (filter 47HE, ex. 436/25, em. 480/40) for 0, 30, 60, or 90 seconds (Figure 5-25a). Unfortunately, we did not observe activation of **44** even after 90 seconds of irradiation. Several controls were included to ensure that the longer irradiation times did not impact the integrity of the assay. Additionally, three LEDs were tested for decaging (405, 448, and 470 nm) with no activation of **44** being observed (Figure 5-25b). Unexpectedly, irradiation at 405 nm and 448 nm resulted in a significant decrease in signal, although an increase was expected. The luminescence values obtained were much smaller than even the DMSO control which leads to the hypothesis that the split protein fragments could have been degraded as a result of the extended irradiation. Additional experiments would need to be conducted to elucidate the precise factor that lead to this substantial loss of signal. Irradiation with 470 nm light showed

minimal decrease in signal. Based on this, it appears that the 470 nm LED does not have a detrimental effect on the system and that the compound, however, does not efficiently degrade at this wavelength.

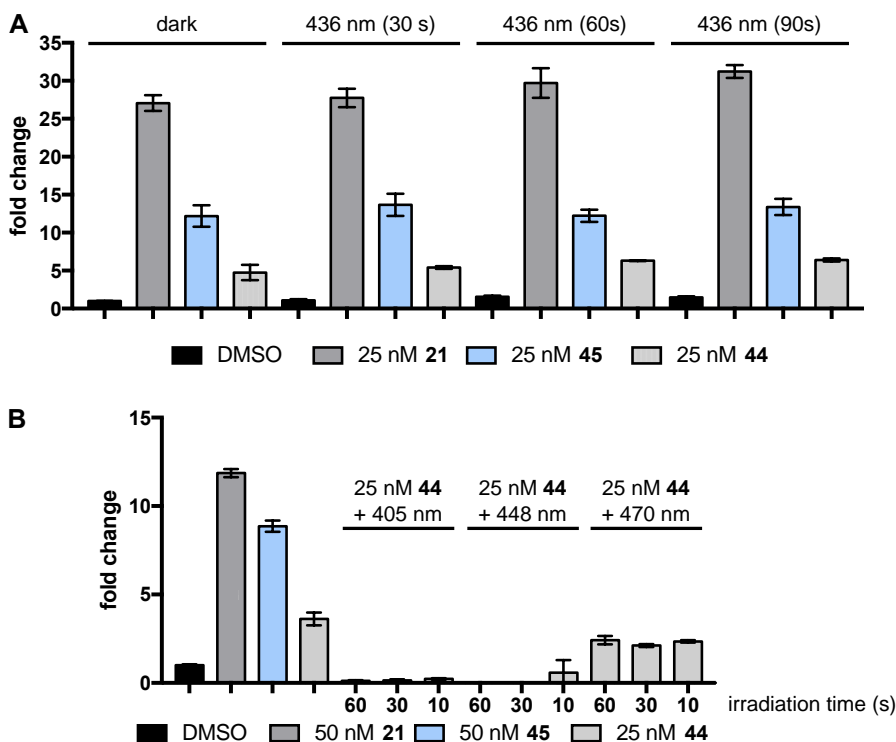


Figure 5-25 Attempts to photoactivate **44** in a split luciferase reporter assay

a) HEK293T cells were transfected with the split luciferase plasmids, then treated with the specified rapalog at 25 nM. A Zeiss CFP filter set was used to irradiate the desired samples for the times given in the graph. Following irradiation, cells were incubated at 37 °C to allow for dimerization, then BrightGlo reagent was added and luminescence was read out. Unfortunately, no activation of **44** was observed in any of these irradiation conditions. b) The same transfection as part (a) was repeated and cells were treated with 50 nM of **21**, 50 nM of **45** or 25 nM of **44** and a subset of wells were irradiated with a 405 nm, 448 nm or 470 nm LED for 60, 30, or 10 seconds. Again, no activation of **44** was observed.

Unfortunately, the BIST-dRap **44** does not appear to readily degrade at any of the wavelengths tested thus far. Additionally, we observed that the triazole-modified rapamycin **45** did not function as efficiently as rapamycin, so if only small percentage of decaying was occurring, it may be difficult to detect. As such, we redesigned the caging group such that native rapamycin would be generated upon photocleavage. We hypothesized that the double substitution of rapamycin onto the double NHS-carbonate **41** (Figure 5-21) suffered from low reactivity due to

the steric bulk from benzylic methyl groups. As such, we envisioned that removal of these methyl groups might allow for the successful synthesis of a BIST-dRap analog that would generate rapamycin following irradiation. Toward this goal, Trevor Horst optimized a synthetic route to generate the BIST-dRap **46** (Figure 5-26). Concurrently, he synthesized a monomeric BIST-Rap **47** (Figure 5-26), since the monomeric BIST caging group had successfully been utilized by Anirban Bardhan in our lab for an unrelated project.

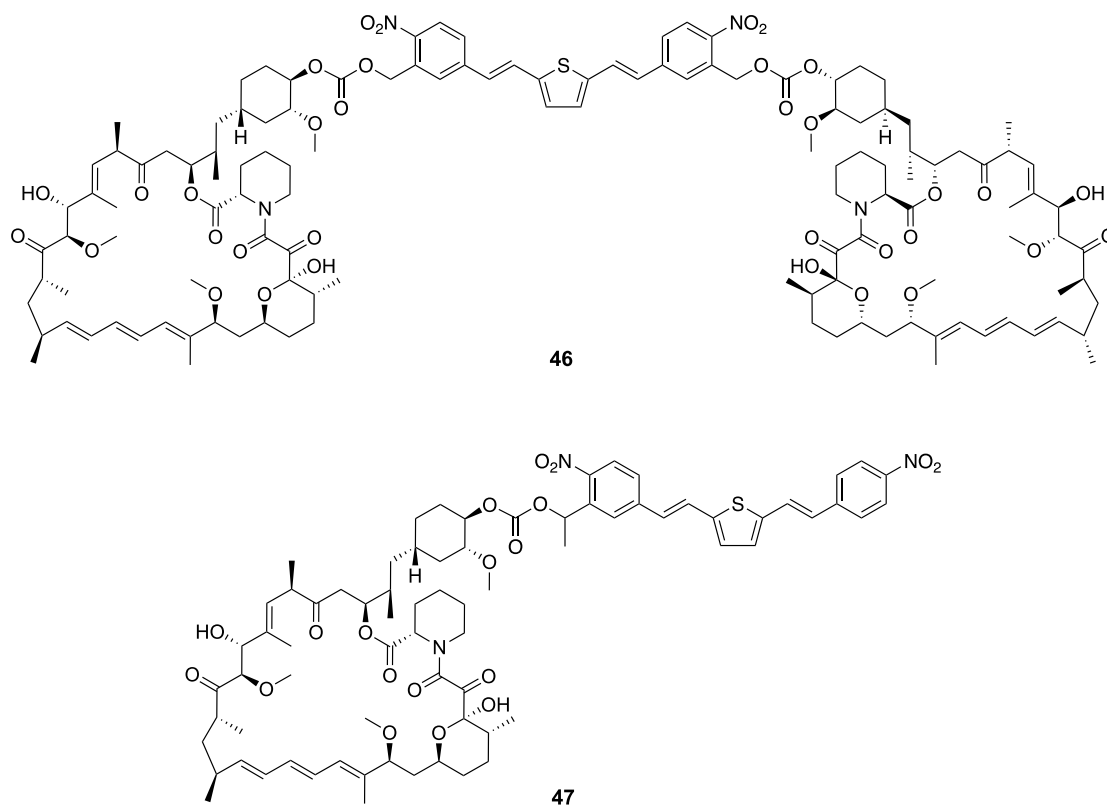


Figure 5-26 Structures of BIST-dRap **46** and BIST-Rap **47**
Both **46** and **47** were synthesized by Trevor Horst.

With these new BIST analogs in hand, we first decided to validate decaging using HPLC. An absorbance spectrum of **46** shows a maximum at 455 nm (Figure 5-27a), so decaging experiments were performed with a 450 nm LED. A 250 μ M solution of BIST-dRap **46** was prepared in methanol (5% DMSO) and an aliquot was collected and analyzed via HPLC as a non-irradiated sample (Figure 5-27b). While there appears to be a small amount of impurity (likely the

monomeric caged rapamycin species that wasn't completely removed during purification), BIST-dRap **46** has a retention time of 44 minutes, while the similarly prepared rapamycin control has a retention time of 20 minutes, suggesting that we can monitor both the disappearance of **46** and the appearance of rapamycin via this approach. The solution of **46** was irradiated in increments of 15 minutes for a total of 45 minutes, with aliquots collected and analyzed via HPLC at each time point. Initially, the samples were monitored at 280 nm (Figure 5-27b), which is maximum for rapamycin; however, almost no appearance of rapamycin was detected. Thus, the experiment was repeated with monitoring at 450 nm, near the maximum for the BIST chromophore, to see if we could detect the by-product following release of a single rapamycin unit (Figure 5-27c). Unfortunately, this still did not show the appearance of any new peak(s), but did further validate the disappearance of **46**.

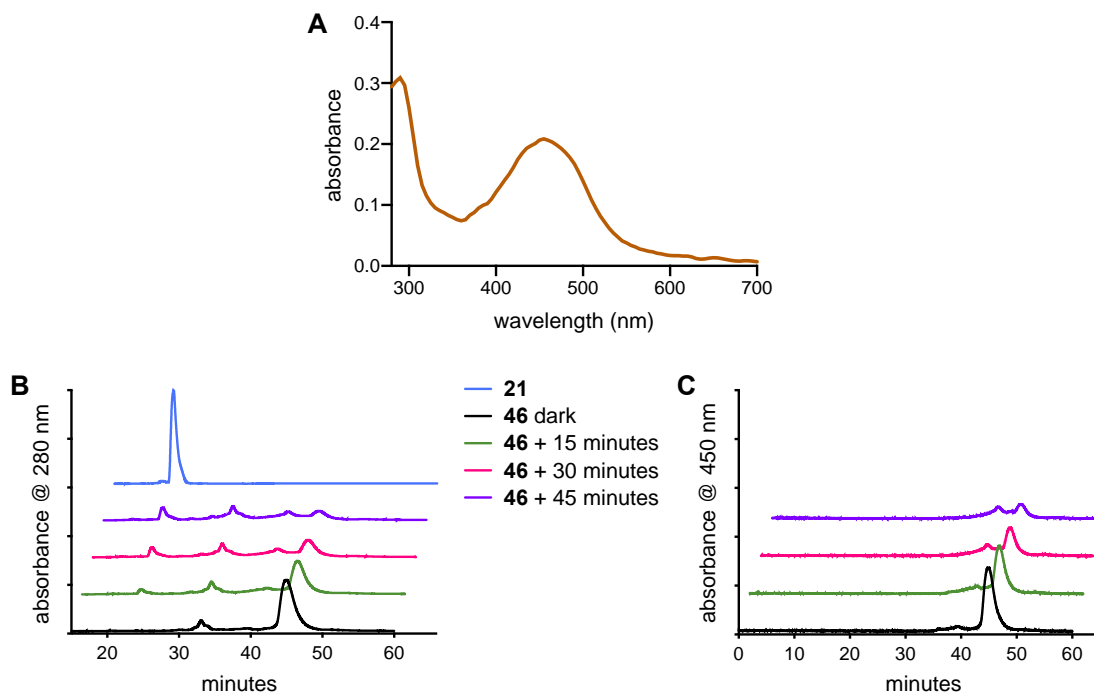


Figure 5-27 HPLC analysis of BIST-dRap **46** decaying with 450 nm LED irradiation

a) A 10 μ M solution of BIST-dRap **46** was prepared in water and the absorbance spectrum was measured. BIST-dRap shows a maximum at 455 nm. b,c) A 250 μ M solution of **46** in methanol (5% DMSO) was prepared. A handheld 450 nm LED was used for decaging studies with irradiation times of 15, 30, and 45 minutes. Monitoring at 280 nm (b), the maximum for rapamycin, shows near complete loss of BIST-dRap; however, only marginal appearance of

rapamycin is observed. Monitoring at 450 nm (c), again shows disappearance of BIST-dRap, but no appearance of a red-shifted decayed byproduct.

Since we were unable to detect the appearance of rapamycin in this study, we explored the possibility that the nitroso byproduct was reacting with the triene of rapamycin, and in doing so, disrupting the conjugation that is required for absorbance at 280 nm. In the literature, there is an example of a Diels Alder reaction occurring with the triene using nitrosobenzene (Figure 5-28a).⁴⁵⁰ Additionally, there have been several examples of nitroso-modified species reacting with dienes of various natural products.⁴⁵¹ Although there is no report of a photo-induced nitroso reaction with rapamycin, we hypothesized that this could account for the lack of rapamycin signal appearance. To test this, we added an excess of 1,3-cyclohexadiene (**48**) to the sample prior to performing the irradiation experiments, to see if the addition of a more reactive diene could quench the nitroso species and enable the detection of rapamycin appearance. An HPLC study was performed as detailed above using 280 nm for detection (Figure 5-28b). Interestingly, in the presence of a significant excess of **48**, a slight improvement in the appearance of rapamycin was observed. Thus, it seems that there may in fact be an undesired side reaction occurring between the nitroso byproduct and rapamycin; however, there is likely something else happening during light irradiation or the decaying process since we were still unable to produce a significant amount of rapamycin upon complete disappearance of **46**.

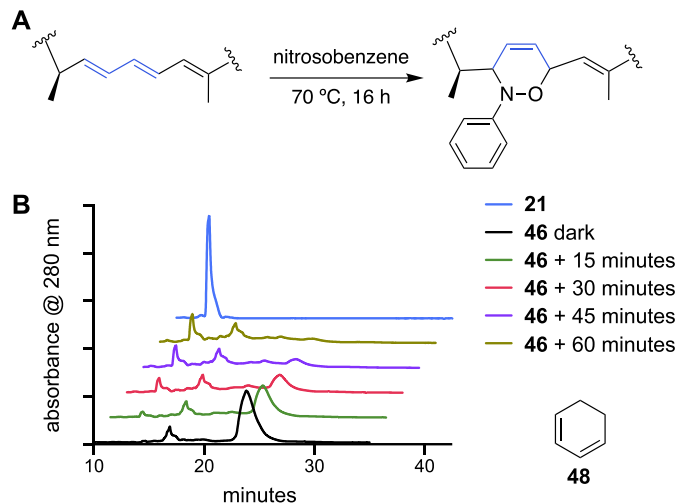


Figure 5-28 HPLC decaging of **46** in the presence of 1,3-cyclohexadiene (**48**)

a) In the literature, rapamycin was reacted with nitrosobenzene at an elevated temperature to generate a cycloaddition product that abolishes conjugation of the triene.⁴⁵⁰ For simplicity, only the triene portion is shown here. b) A 250 μ M solution of **46** (and **21** as a control) were supplemented with 210 mM of **48** (an excess of 840X compared to **46**) prior to performing the irradiations with a 450 nm LED. Irradiations were performed in 15 minute intervals for 60 minutes total with aliquots analyzed by HPLC (at 280 nm) every 15 minutes.

While the introduction of **48** was useful in allowing us to identify one potential side reaction in the decaging process, it did not afford a significant improvement in decaging efficiency, and as such, we concluded that this BIST-dRap analog was not suitable for photoactivation in a cellular context. However, we did still proceed with an initial testing in the split luciferase reporter to see how background dimerization compared to that of the previously reported dRap **25**. HEK293T cells were transiently transfected with CLuc-FKBP and FRB-NLuc in a 3:1 plasmid ratio (the optimal ratio determined previously for dRap **25**) and treated with different concentrations of rapamycin, dRap **25** and BIST-dRap **46** for 2.5 hours, then luciferase substrates were added and luminescence measured. Raw values were normalized to the DMSO negative control (Figure 5-29). A decrease in background dimerization activity was observed with the new BIST-dRap analog compared to the previously reported analog. This is potentially due to the shorter, more rigid linker between the two rapamycin molecules such that the more compact homodimer precludes background FRB binding. To further validate this claim, additional linker

lengths would need to be synthesized and tested to confirm that this trend holds, but unfortunately, that is outside the scope of the current testing.

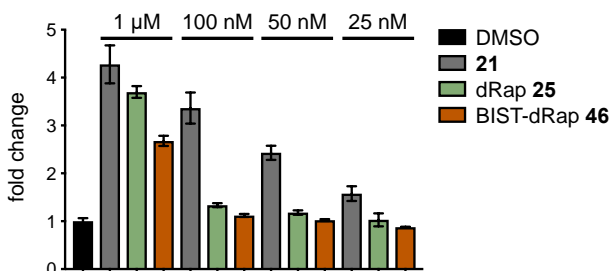


Figure 5-29 Background dimerization comparison of dRap **25** and BIST-dRap **46**

HEK293T cells expressing the split luciferase reporter in a 3:1 FKBP:FRB ratio were treated with a range of concentrations of **21**, dRap **25**, or BIST-dRap **X** for 2.5 hours. Cells were lysed, luciferase substrates were added, and luminescence values were recorded. A reduction in background dimerization activity was observed for **46** compared to the previously published analog.

After demonstrating that BIST-dRap **46** still suffered from poor decaging, we hypothesized that maybe the symmetric BIST caging group was not amenable for rapamycin caging. Additionally, the same BIST caging group in **46** was utilized by Trevor Horst to cage benzyl alcohol as a test substrate. In his HPLC analysis of decaging, complete loss of signal monitoring at 450 nm was observed; however, concomitant of detection of benzyl alcohol when monitoring at 250 nm showed no desired product (data not shown – experiment conducted by Trevor). Thus, we concluded that the symmetric BIST caging group could not be used to cage aromatic or large macrocyclic structures. With the asymmetric BIST-Rap **47** in hand, we first collected an absorbance spectrum and identified a maximum of 455 nm (Figure 5-30a), then Trevor performed the HPLC decaging experiment in a similar manner as before using both a 415 and 450 nm LED (Figure 5-30b,c). While the decaging with either wavelength was not very efficient, it did at least appear that the marginal loss of **47** was accompanied by the appearance of rapamycin (**21**), which was a significant improvement over the dimeric analog.

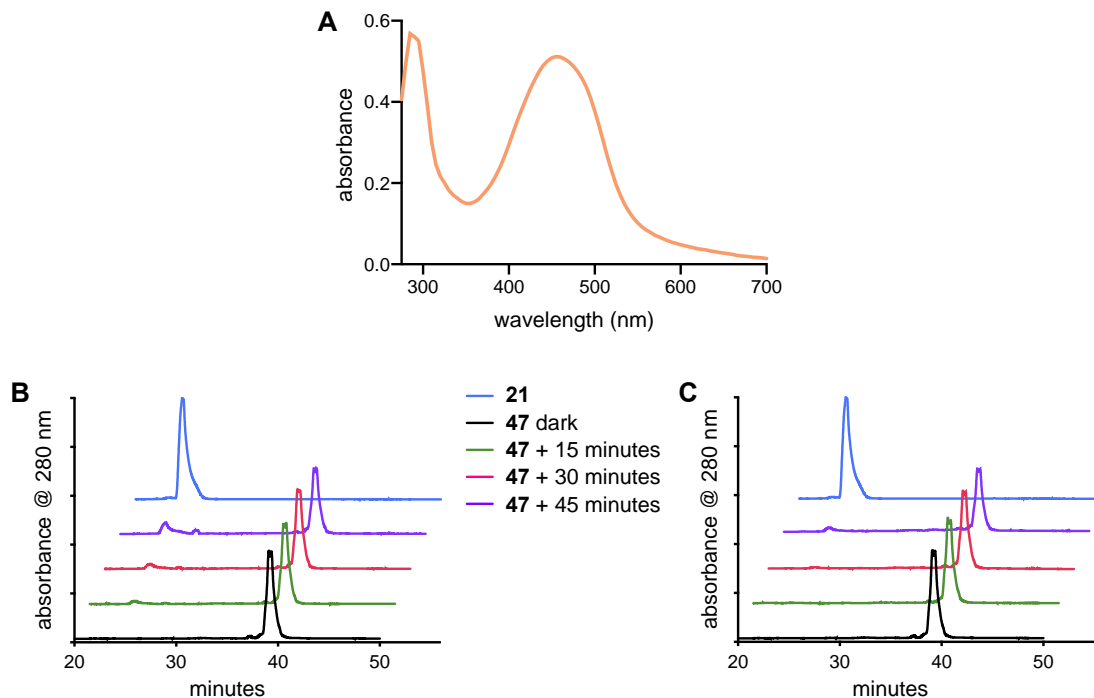


Figure 5-30 HPLC analysis of decaging of BIST-Rap **47**

a) The absorbance spectrum of BIST-Rap **47** at 10 μ M shows a maximum of 455 nm. b,c) Trevor Horst performed decaging experiments with a 415 (b) and 450 nm (c) LED, followed by HPLC analysis for detecting appearance of rapamycin. Unfortunately, poor decaging was observed with either condition.

We were encouraged that BIST-Rap **47** was being decaged to generate rapamycin, albeit with very low efficiency; however, we hypothesized that we might observe more complete decaging if we were using a significantly lower concentration of the compound. For this, we decided to test **47** in the split luciferase reporter using 50 nM compound treatment, which was 5000-fold more dilute than our HPLC studies. HEK293T cells were transiently transfected with the split luciferase reporter in a 1:1 plasmid ratio (optimal ratio for monomeric caged analogs), and were treated with rapamycin or **47** at 50 nM. A subset of samples was irradiated with either a 415 or 450 nm LED for 0 – 180 seconds (Figure 5-31a,b), followed by a 2.5 hour incubation to allow for ternary complex formation. After addition of luciferase substrates and a 2-minute lysis, luminescence values were measured, then normalized to DMSO. Interestingly, we did observe a slightly improved decaging efficiency with 415 nm irradiation than we had in our HPLC study.

Unexpectedly, the amount of rapamycin generated plateaued at ~30% even upon extended irradiation. Irradiation of rapamycin alone for up to 3 minutes showed no detrimental effect, thus it appears that the compound is simply not decaying under these conditions. Irradiation with 450 nm showed no activation of **47**, but also had no negative impact on the rapamycin control alone.

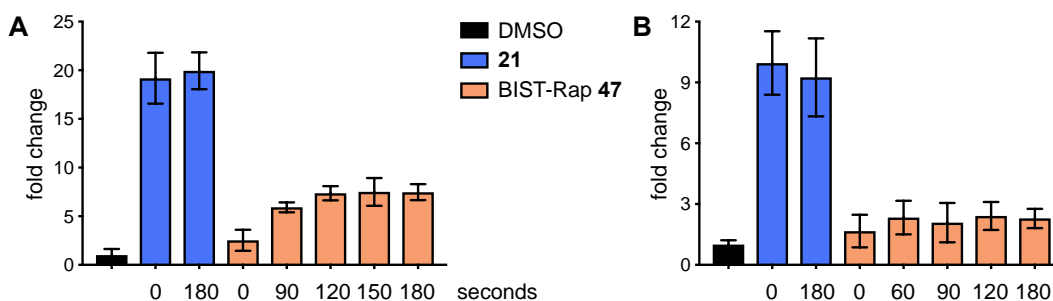


Figure 5-31 Photoactivation of BIST-Rap **47** in the split luciferase reporter HEK293T cells expressing the split luciferase reporter in a 1:1 FKBP:FRB ratio were treated with 50 nM of rapamycin or BIST-Rap **47**, and a subset was irradiated from 0 – 180 seconds with a 415 (a) or 450 nm (b) LED, followed by a 2.5 hour incubation. Cells were lysed, luciferase substrates were added, and luminescence values were recorded. A reduction in background dimerization activity was observed for **47** compared to the previously published analog.

Unfortunately, in our hands, the BIST caging group did not prove viable for generating red-shifted caged rapamycin analogs, thus alternative red-shifted caging groups were explored (see section 5.5). After we had synthesized and tested these four different BIST-caged rapamycin analogs, a second BIST-caged compound was reported in the literature by the Ellis-Davies group. In this report, they developed a symmetric caged γ -aminobutyric acid (GABA) analog cloaked with a G3.5 dendrimer (a branched ethylenediamine core with terminal carboxylate groups to enhance solubility) that was completely resistant to one-photon decaging at 470 nm irradiation (exposure for 2 days at 1.4 W); however, this analog underwent quantitative decaging with two-photon excitation at 780 nm.⁴⁵² Unfortunately, at the time of this report we had already shifted our efforts toward development of an alternate caged analog; however, in the future, it may be worth subjecting these analogs to two-photon activation (potentially in collaboration with the Neurobiology Department) to see how they perform.

5.4.1 Methods

1-(5-Bromo-2-nitrophenyl)ethan-1-ol (38). In a doubly-flame dried round bottom flask, 5-bromo-2-nitrobenzaldehyde (500 mg, 2.17 mmol, 1 eq) was dissolved in DCM (16 mL) and cooled to 0 °C in an ice bath (~ 20 minutes) under argon. AlMe₃ (2 M in hexanes, 1.63 mL, 3.260 mmol, 1.5 eq) was added dropwise over 20 minutes and the reaction was stirred for an additional 3 hours at the same temperature. The reaction was quenched by the slow addition of ice-cold water (2 mL), followed by the slow addition of 1 M NaOH (16 mL). The biphasic solution was stirred vigorously at room temperature for 1 hour, then the phases were separated. The organic layer was collected, the aqueous layer was extracted with DCM (3 x 20 mL), then the organic layers were combined. The combined organic layers were washed with water (100 mL), then brine (50 mL), then dried over sodium sulfate and concentrated under reduced pressure. The crude material was purified over silica with 20% ethyl acetate in hexanes to afford **36** as a pale-yellow solid (389 mg, 73% yield). ¹H NMR spectral data matched literature reported values.⁴⁵³

1-(2-Nitro-5-vinylphenyl)ethan-1-ol (39). The bromide **38** (351 mg, 1.43 mmol, 1 eq) and tetrakis(triphenylphosphine)palladium(0) (35 mg, 0.03 mmol, 0.02 eq) were dissolved in dimethoxyethane (15 mL). A solution of potassium carbonate (197 mg, 1.43 mmol, 1 eq) in water (4 mL) was added to the stirring reaction mixture, followed by the addition 2,4,6-trivinylcyclotriboroxane pyridine complex (120 mg, 0.74 mmol, 0.5 eq). The reaction mixture was refluxed overnight (~20 hours). The solvents were evaporated under reduced pressure and the residue was purified over silica with a 0 – 10 % gradient of ethyl acetate in hexanes to provide **39** as a pale-yellow solid (242 mg, 88% yield). ¹H NMR (400 MHz, CDCl₃) δ 7.934 (d, 1 H, J = 8.4 Hz), 7.846 (d, 1 H, J = 1.6 Hz), 7.447 (dd, 1 H, J = 2, 6.4 Hz), 6.808 (q, 1 H, J = 6.8 Hz), 5.957 (d,

1 H, J = 17.6 Hz), 5.503 (m, 2 H), 2.318 (d, 1 H, J = 4 Hz), 1.592 (d, 3 H, J = 6 Hz). Compound characterization is incomplete since ^{13}C NMR and HRMS data were not collected.

1,1'-(((1E,1'E)-Thiophene-2,5-diylbis(ethene-2,1-diyl))bis(6-nitro-3,1-phenylene))bis(ethane-1-ol) (40). The styrene **39** (211 mg, 1.09 mmol, 3 eq), 2,5-dibromothiophene (45 μL , 0.40 mmol, 1 eq), lithium chloride (52 mg, 1.23 mmol, 3.3 eq), sodium bicarbonate (102 mg, 1.21 mmol, 3.3 eq), and tetrabutylammonium chloride (169 mg, 0.61 mmol, 1.7 eq) were suspended in DMF (7.25 mL) and purged with nitrogen for 20 minutes. TPGS-750 (5 wt % in water, 200 μL) and palladium (II) acetate (20 mg, 0.25 mmol, 0.25 eq) were added, and the reaction was heated to 110 $^{\circ}\text{C}$ for 1 hour. The reaction mixture was poured into water (75 mL), then extracted thrice with ethyl acetate (75 mL each). The organic layer was dried over sodium sulfate, then concentrated under reduced pressure. The crude material was purified over silica with a gradient of 0 – 25% ethyl acetate in hexanes to yield **40** as a red solid (72 mg, 39% yield). ^1H NMR (400 MHz, CDCl_3) δ 7.995 (d, 2 H, J = 8.4 Hz), 7.938 (d, 2 H, J = 2 Hz), 7.500 (dd, 2 H, J = 1.6, 8.8 Hz), 7.389 (d, 2 H, J = 16 Hz), 7.104 (s, 2 H), 6.979 (d, 2 H, J = 16), 5.574 (m, 2 H), 2.302 (d, 2 H, J = 4 Hz), 1.626 (d, 6 H, J = 6.4). Compound characterization is incomplete since ^{13}C NMR and HRMS data were not collected.

Bis(2,5-dioxopyrrolidin-1-yl) (((1E,1'E)-thiophene-2,5-diylbis(ethene-2,1-diyl))bis(6-nitro-3,1-phenylene))bis(ethane-1,1-diyl) bis(carbonate) (41). The alcohol **40** (72 mg, 0.16 mmol, 1 eq) and DSC (159 mg, 4 eq) were dissolved in acetonitrile (775 μL) under nitrogen. TEA (130 μL , 0.93 mmol, 6 eq) was added, and the reaction was stirred overnight at room temperature. The reaction mixture was concentrated, then purified over silica with a gradient of 5 – 10% acetone in DCM to yield **41** as a red solid (64 mg, 55% yield). ^1H NMR (400 MHz, CDCl_3) δ 8.099 (d, 2H, J = 8.4 Hz), 7.780 (d, 2H, J = 1.6 Hz), 7.549 (dd, 2H, J = 2, 8.8 Hz), 7.462 (d, 2H, J = 16 Hz), 7.160

(s, 2H), 7.003 (d, 2H, J = 16 Hz), 6.536 (q, 2H, J = 6.4 Hz), 2.823 (s, 8H), 1.823 (d, 6H, J = 6.4 Hz). Compound characterization is incomplete since ^{13}C NMR and HRMS data were not collected.

Di(prop-2-yn-1-yl) (((((1*E*,1'*E*)-thiophene-2,5-diylbis(ethene-2,1-diyl))bis(6-nitro-3,1-phenylene))bis(ethane-1,1-diyl)) bis(carbonate) (43). The NHS-carbonate **41** (64 mg, 0.09 mmol, 1 eq), propargyl alcohol (10 μL , 0.17 mmol, 2.1 eq), and DMAP (11 mg, 0.09 mmol, 1 eq) were dissolved in anhydrous DCM (900 μL) under a nitrogen atmosphere. TEA (25 μL , 0.18 mmol, 2.1 eq) was added and the reaction was stirred at room temperature overnight. The reaction mixture was concentrated, then purified over silica with 0 – 25% ethyl acetate in DCM to yield **43** as a red-orange solid (27 mg, 52% yield). ^1H NMR (400 MHz, CDCl_3) δ 8.053 (d, 2 H, J = 8.4 Hz), 7.730 (d, 2 H, J = 1.6 Hz), 7.541 (dd, 2 H, J = 1.6, 7.2 Hz), 7.376 (d, 2 H, J = 16 Hz), 7.125 (s, 2 H), 6.965 (d, 2 H, J = 16 Hz), 6.416 (q, 2 H, J = 6.4 Hz), 4.768 (m, 4 H), 2.535 (t, 2 H, J = 2.4 Hz), 1.745 (d, 6 H, J = 6.4 Hz). HRMS calculated for $[\text{M} + \text{Na}]^+$ $\text{C}_{32}\text{H}_{26}\text{N}_2\text{NaO}_{10}\text{S}$ 653.1200, found 653.1222. Compound characterization is incomplete since ^{13}C NMR was not collected.

Optimal FKBP:FRB ratio for dRap analogs in split luciferase reporter. HEK293T cells were plated at 200,000 cells/well in a 6-well clear bottom plate and grown at 37 $^\circ\text{C}$ /5% CO_2 . At ~80% confluence, cells were co-transfected with CLuc-FKBP and FRB-NLuc (2000 ng total per well; 1:1, 1000 ng of each; 3:1, 1500 ng of FKBP:500 ng of FRB; 9:1, 1800 ng of FKBP:200 ng of FRB) using Lipo2K. The two plasmids were diluted into 250 μL of OptiMEM in separate tubes. Three separate tubes of 250 μL of OptiMEM plus 5 μL of Lipo2K were incubated at room temperature for five minutes, then the Lipo/OptiMEM solution was mixed into the DNA/OptiMEM solutions to generate 500 μL solutions for each ratio. Transfection solutions were incubated at room temperature for 20 minutes. Meanwhile, the media in the wells was replaced with 2 mL of DMEM (+ 10% FBS, – antibiotics), then the transfection mix (all 500 μL) was added to the wells and

incubated overnight. After ~18 hours of transfection, the media was removed, the cells were lifted with 0.5 mL of TrypLe and transferred to a 15 mL conical tube, then TrypLe was inactivated by the addition of 4.5 mL of media. Cells were pelleted at 1,000 g for 10 minutes at room temperature. The media was removed, and the cells were resuspended in 1 mL of LCIS. Cells were counted using a hemocytometer in the presence of Trypan Blue to avoid counting dead cells. Subsequently, cells were plated in a white, clear bottom 96-well plate at 30,000 cells per well in 100 μ L of LCIS.

To prepare the compound solutions, 1 mM stocks of rapamycin and **25** were diluted to 0.1 mM in milliQ water (10 μ L of stock solution into 90 μ L). A 1.1 μ M solution of each was prepared in milliQ water by diluting 3.3 μ L of the 100 μ M stock solution into 297 μ L of LCIS. To each well of the 96-well plate containing cells expressing the reporter, 10 μ L of compound was added in triplicate to yield 100 nM and placed in the incubator for 30 minutes. Afterwards, 100 μ L of BrightGlo reagent (Promega) was added to each well and incubated for two minutes, then luminescence was measured on a Tecan M1000. Raw luminescence values were normalized such that DMSO equaled 1. Average fold-change values with error bars representing standard deviation of triplicates are reported.

Attempted activation of BIST-dRap 44 using a CFP filter. HEK293T cells were plated, transfected, counted and re-plated into a 96-well plate in 90 μ L of LCIS exactly as described above using the 3:1 plasmid ratio only for transfection (2-wells transfected identically). Using 1 mM stock solutions in DMSO, 25 μ M solutions of rapamycin, tRap **45**, and dRap **44** were prepared by diluting 1 μ L of the 1 mM stock into 39 μ L of milliQ water. A working solution of 250 nM (10X desired final concentration) was prepared by diluting 3 μ L of 25 μ M into 297 μ L of LCIS. Ten microliters of the 10X solution was added to the 96-well plate containing cells expressing the reporter in triplicate such that a final 25 nM concentration was achieved. The plate was placed in

the plate holder on the Zeiss and the z-plane was adjusted such that the cells were in focus through the 5X objective. The x- and y-positions were adjusted such that the objective was placed in the center of the well. The light path was directed through the eyepiece to avoid any potential damage to the camera upon extended light illumination. Three different irradiation times (30, 60, and 90 seconds) were utilized, each of the triplicate wells was aligned as described, and all four sample conditions (DMSO, rapamycin, tRap **45**, and dRap **44**) were irradiated at all three times. The plate was placed back in the incubator for two hours to allow for ternary complex formation, then 90 μ L of BrightGlo reagent was added per well and incubated for 2 minutes at room temperature, then luminescence values were measured. Raw luminescence values were normalized such that DMSO equaled 1. Average fold-change values with error bars representing standard deviation of triplicates are reported.

Attempted activation of BIST-dRap 44 using blue light LEDs. HEK293T cells were plated, transfected, counted and re-plated into a 96-well plate in 90 μ L of LCIS exactly as described above. Using 1 mM stock solutions in DMSO, 25 μ M solutions of rapamycin, tRap **45**, and dRap **44** were prepared by diluting 1 μ L of the 1 mM stock into 39 μ L of milliQ water. A working solution of 250 nM (10X desired final concentration) of dRap **44** was prepared by diluting 3 μ L of 25 μ M into 297 μ L of LCIS. Working solutions of 500 nM (10X desired final concentration) of rapamycin and tRap **45** were prepared by diluting 6 μ L of 25 μ M solutions into 294 μ L of LCIS. Ten microliters of the 10X solution was added to the 96-well plate containing cells expressing the reporter in triplicate such that a final 25 nM concentration was achieved for the caged analog, while 50 nM was used for rapamycin and tRap **45**. Three different LEDs (405, 447.5, and 450 nm) were utilized for the decaging experiments with the controller box set to the max output of 1000 mA. An aluminum foil mask was used with a cutout the size of a single well, to prevent

unintentional irradiation of neighboring wells. The LED was held directly over the well and irradiation times of 10, 30, and 60 seconds were employed. *Note: All three LEDs were mounted on a “small” heat sink, which did not provide sufficient cooling, thus after every 60 second irradiation, the LED was left off to cool at room temperature for ~2 minutes. All three LEDs have now been mounted on “medium” heat sinks (see Appendix D) allowing up to 15-minute irradiations with no overheating.* After irradiation, the plates were placed back in the incubator for two hours. Then, 90 μL of BrightGlo reagent was added and incubated for 2 minutes, and luminescence was measured. Values were normalized such that DMSO equaled 1, and averages with standard deviation of triplicate wells are reported.

Analysis of BIST-dRap 46 decaging by HPLC. A 250 μM solution of **46** was prepared using a 5 mM stock solution (10 μL of stock solution diluted in 190 μL of methanol) in a $\frac{1}{2}$ dram clear glass vial. A 25 μL pre-irradiation sample was transferred to an HPLC sample vial. The vial was irradiated from the bottom with the LED source touching the glass surface. A handheld 450 nm LED operated at 700 mA output (the manufacturer’s recommendation) was used in increments of 15 minutes to provide 15, 30, and 45-minute irradiation samples (25 μL was removed and transferred to an HPLC vial at each time point). A 250 μM solution of rapamycin was prepared in the same manner to use as a control for retention time and expected product peak area following irradiation. A Shimadzu HPLC equipped with an analytical scale column (Agilent, Zorbax SB-C18, 3.5 μm , 4.6 x 100 mm) was used for analysis. Solvent A was milliQ water and Solvent B was HPLC-grade acetonitrile. A gradient method with 1.0 mL/minute flow rate was developed and percentages listed are for Solvent B (0 minutes – 35%, 35 minutes – 95%, 60 minutes – 95%, 40.05 minutes – 35%, 70 minutes – 35%). An autosampler was utilized for injections and 10 μL of sample was injected per analysis. The UV detector was set to 280 nm (absorbance maximum for

rapamycin) for the first batch of samples (in order, rapamycin, **46** dark, 15 minutes, 30 minutes, 45 minutes), then the method was modified such that the detection wavelength was 450 nm (absorbance maximum for BIST) and the batch was reanalyzed. The raw data was extracted from the Lab Solutions (Shimadzu) software and analyzed in GraphPad Prism 8.

Analysis of BIST-dRap 46 decaging in the presence of 48 by HPLC. A 250 μ M solution of **46** and a 210 mM solution of **48** (gift from the Brummond lab) was prepared using a 5 mM stock solution of **46** (10 μ L of **46** and 4 μ L of **48** were diluted in 186 μ L of methanol) in a ½ dram clear glass vial. A 25 μ L pre-irradiation sample was transferred to an HPLC sample vial. Irradiation, HPLC analysis, and data analysis were performed in the same manner described above (analysis was performed at 280 nm). Additionally, a modified, steeper gradient HPLC method (0 minutes – 35%, 15 minutes – 95%, 40 minutes – 95%, 40.083 minutes – 35%, 50 minutes – 35%) was utilized in order to shorten the overall run time required.

Assessment of background dimerization of BIST-dRap 46 in split luciferase assay. HEK293T cells were plated, transfected, counted and re-plated into a 96-well plate in 90 μ L of LCIS exactly as described above using the 3:1 plasmid ratio for transfection (2-wells were transfected identically). Working compound solutions were prepared at 10X (10 μ M – 250 nM) the desired final concentration (1 μ M – 25 nM) by diluting a 1 mM stock solution into LCIS (for 10 μ M), then using the 10 μ M stock to prepare the remaining three solutions in LCIS. To the wells of cells expressing the reporter, 10 μ L of the appropriate working solution were added in triplicate and incubated for 2.5 hours. Then, 90 μ L of BrightGlo reagent was added and luminescence was measured after a 2-minute incubation. Raw values were normalized such that DMSO equaled 1, and averages with standard deviation are reported.

Activation of BIST-Rap 47 in split luciferase assay. HEK293T cells were plated, transfected, counted and re-plated into a 96-well plate in 90 μ L of LCIS exactly as described above using the 1:1 plasmid ratio for transfection (2-wells were transfected identically). Working solutions of **21** and **47** were prepared at 10X (500 nM) the desired final concentration (50 nM) by diluting a 0.1 mM stock solution into LCIS (4 μ L into 796 μ L). To the wells of cells expressing the reporter, 10 μ L of the compound solutions were added in triplicate. A subset of wells was irradiated with a 415 or 450 nm LED set to 700 mA using a foil mask (from 0 – 180 seconds), then the plate was incubated for 2.5 hours. After, 90 μ L of BrightGlo reagent was added and luminescence was measured after a 2-minute incubation. Raw values were normalized such that DMSO equaled 1, and averages with standard deviation are reported.

5.5 ANB-caged Rapamycin Analogs

Here, we describe the development and application of an aminonitrobiphenyl-caged rapamycin analog (**53**) which represents a significant advancement over previously reported systems, since (1) it is activated with >400 nm light and (2) shows minimal background activity, enabling interfacing with existing FKBP/FRB-based switches. In recent years, several nitrobiphenyl derived caging groups have been developed by Specht and Goeldner (Figure 5-32). The para-methoxy **48**⁴⁵⁴ and para-tris-ethoxymethoxy **49**⁴⁵⁵ caging groups can be photolyzed with both one- and two-photon excitation; however, their one-photon excitation maxima is ~ 395 nm, thus optimal decaging was typically achieved with 365 nm light. Switching from a biphenylphenol to an alkylated aminobiphenyl (as in **50** and **51**) resulted in a bathochromic shift such that activation could be achieved with 405 nm light.⁴⁵⁶ All four of these analogs decay through the β -

elimination pathway like other (nitrophenyl)ethanol and (nitrophenyl)propanol cages. Most recently, the Specht group developed **52**, which has an absorption maximum at 413 nm and upon irradiation generates a keto-enol byproduct that is fluorescent.⁴⁵⁷ This analog decages through the traditional release of the α -substituent like other nitrobenzyl cages. We developed an aminonitrobiphenyl (ANB) ethanol caging group due to the synthetic accessibility, only two steps for the caging alcohol, and for its red-shifted properties compared to previous other nitrobiphenyl cages. Caged rapamycin **53** was synthesized in four steps by former lab member, Trevor Horst (Figure 5-32).

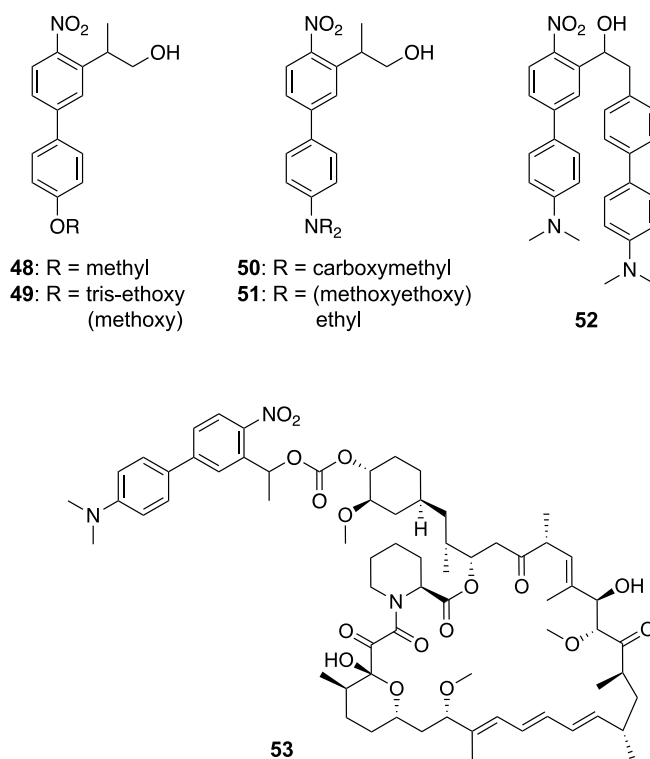


Figure 5-32 Structures of nitrobiphenyl caging groups and **53**
Structures of different nitrobiphenyl caging groups reported in the literatures. Caged rapamycin **53** was synthesized by Trevor Horst.

We first performed decaging studies to validate that **53** generates rapamycin upon irradiation with >400 nm light. An absorbance scan of **53** showed a maximum at 412 nm (Figure 5-33a) when measured in water and therefore 405, 415, and 450 nm LED irradiation was tested

for efficient decaging and the photolysis reactions were analyzed by HPLC (Figure 5-33b-d). Both the 405 and 415 nm LEDs resulted in almost complete loss of **53** (<3% remaining caged CID) with 84% and 71% recovery of rapamycin, respectively, after 10 minutes of irradiation. Marginal photolysis (~20%) was observed with the 450 nm LED after 10 minutes of irradiation. Based on these results, the remaining biological studies were performed with 405 or 415 nm irradiation. Additionally, we determined the extinction coefficient for **53** at 405 and 415 nm to be 7900 and 8100 M⁻¹cm⁻¹, respectively.

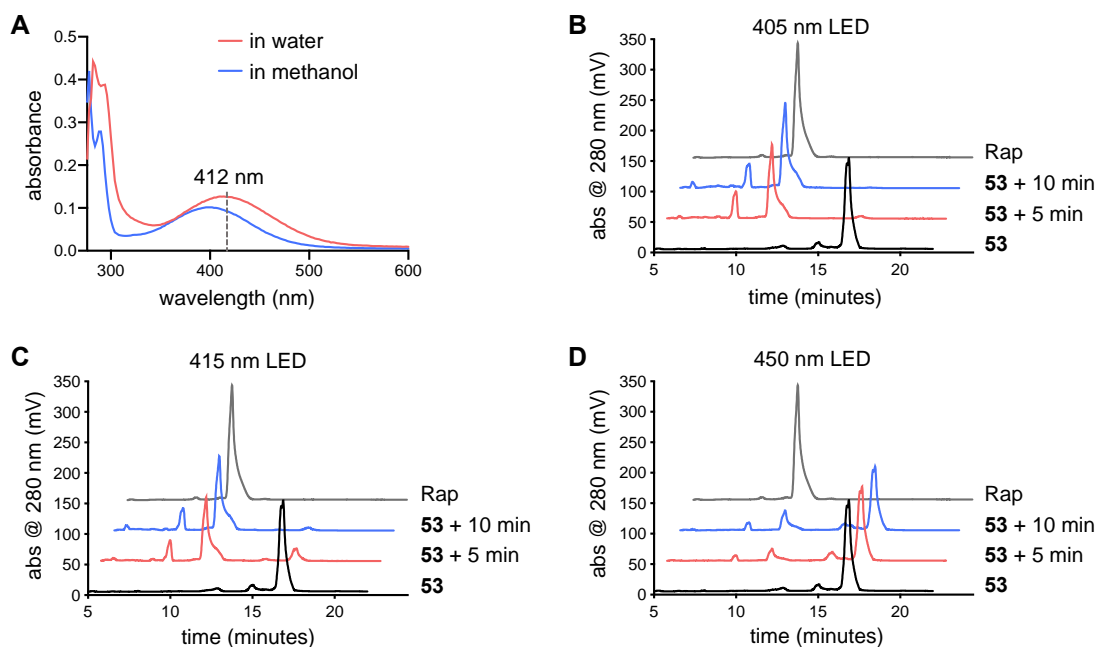


Figure 5-33 HPLC decaging analysis of caged rapamycin **53** with 405, 415, and 450 nm LEDs
a) The absorbance spectrum of **53** shows a maximum at 412 nm in water and 402 nm in methanol (50 μ M; 2% DMSO).
b-d) HPLC analysis of decaging of **53** (100 μ M; 2% DMSO in methanol) with an LED at 405 nm (b), 415 nm (c), or 450 nm (d). Successful decaging is observed with the 405 and 415 nm LEDs, while minimal decaging is observed upon 450 nm irradiation after a 10 minute irradiation.

Since the first-generation rapamycin analog, **22**, required protein engineering of FKBP to minimize background dimerization activity⁷¹ and the second-generation analog, **25**, required a second rapamycin attached to the caging group to recruit a second FKBP for increased steric bulk,²¹² we wanted to explore whether **53** would be compatible with the well-established wild-type FKBP/FRB system or if it would require additional protein engineering. For this, analysis of

ternary complex formation through gel shift assays was performed. FKBP-YFP-6xHis and FRB-CFP-6xHis were recombinantly expressed in BL21 (DE3) cells and purified using Ni-NTA resin. The two fusion proteins were combined in 1:1 molar ratios (5 μ M of each) and incubated with increasing concentrations of compound (either rapamycin [**21**], **22**, **25**, or **53**) for two hours in the dark to allow for ternary complex formation. The proteins were then resolved by native-PAGE and detected via Coomassie staining (Figure 5-34). Gratifyingly, **53** showed almost no background dimerization compared to the previous caged analogs. These results confirmed that **53** can be applied to the broadly utilized wild-type FKBP systems that have been reported and that are commercially available, thereby providing optical control without the need for any further protein engineering.

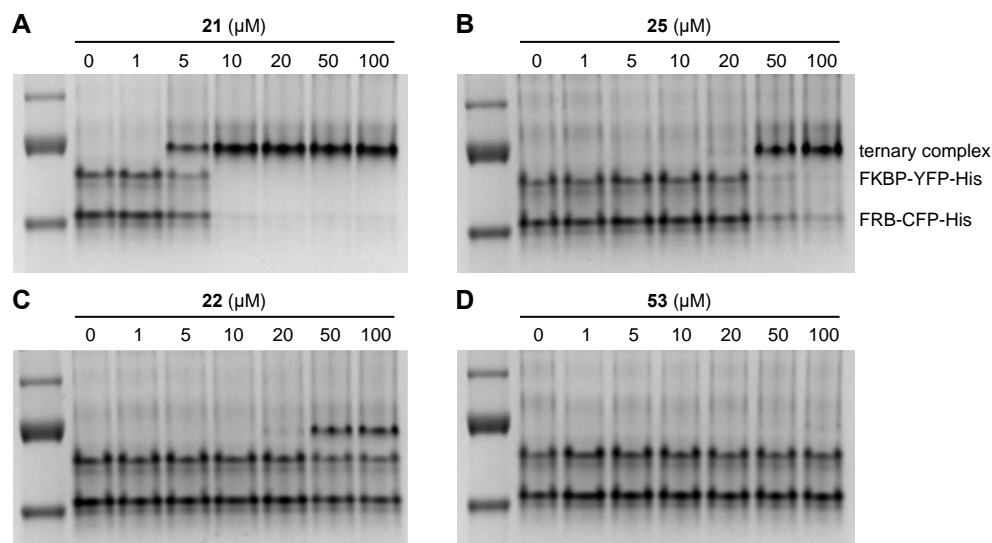


Figure 5-34 Gel shift assays with caged rapamycin **53** and previous caged analogs
Gel shift assays with 5 μ M of FKBP-YFP-6xHis and FRB-CFP-6xHis with compounds (a) rapamycin (**21**), (b) **25**, (c) **22**, and (d) **53**, allowing for the investigation of background ternary complex formation. Rapamycin shows significant ternary complex formation – as expected, while **22** and **25** show similar background levels with wild-type FKBP. Importantly, **53** shows almost no background activity up to 100 μ M.

Numerous split enzyme systems have been developed using the FKBP/FRB dimerization pair.⁴⁵⁸ Addition of rapamycin to these systems results in reconstitution of an active enzyme of interest. In order to demonstrate that **53** could be utilized in a split enzyme system, we used the

split luciferase reporter as discussed above (Figure 5-23).³⁷⁸ In this reporter, the C-terminus (residues 398 - 550) of luciferase is fused to FKBP while the N-terminus (residues 2 - 416) is fused to FRB (Figure 5-35a). When these protein fusions are co-expressed in mammalian cells, minimal interaction between FKBP/FRB or the split enzyme fragments occurs in the absence of compound; however, addition of rapamycin results in ternary complex formation and subsequent reconstitution of an active luciferase enzyme. HEK293T cells co-expressing FRB-NLuc and CLuc-FKBP at a 1:1 ratio were treated with 50 nM of **53** in the dark for one hour, then a subset of wells was irradiated for various durations (15, 30, 45, 60, or 90 seconds) with either a 405 or 415 nm LED. Cells were further incubated, and luciferase activity was read out after lysis and substrate addition. A dose-dependent response to light was observed, with minimal background activity in the absence of irradiation. (Figure 5-35b,c). These results confirmed that **53** can be used to control the activation of a split enzyme system with light.

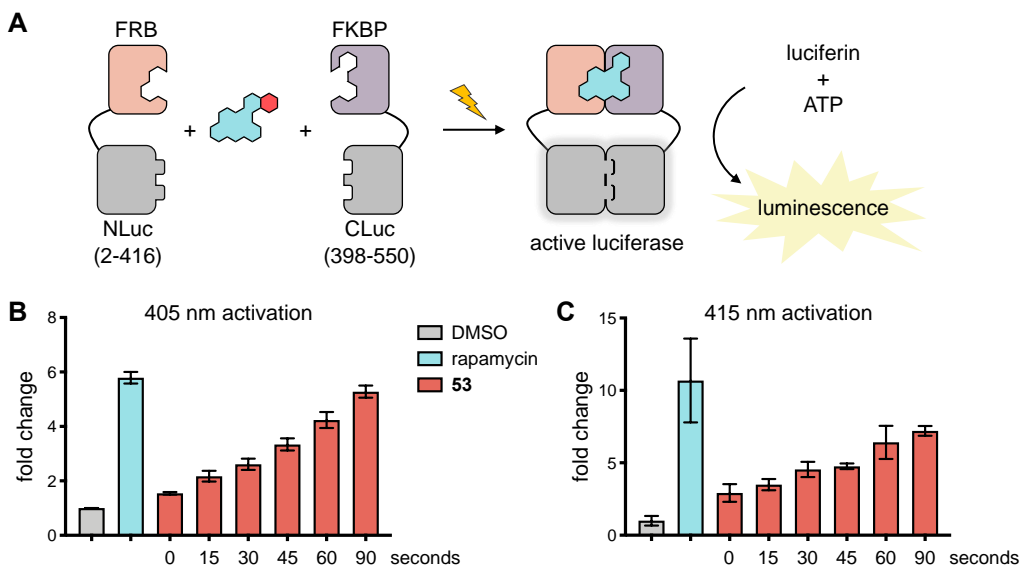


Figure 5-35 Photoactivation of caged rapamycin **53** in the split luciferase reporter assay

a) HEK293T cells co-expressing the reporter were treated with rapamycin or **53** for one hour, then irradiated with a 405 nm LED for the specified time and incubated for four hours. Almost complete photoactivation was achieved with 90 seconds of irradiation. b) The experiment was also conducted with a 415 nm LED and similar levels of activation are observed. Bars represent the average luminescence measured from three replicate wells, with error bars denoting standard deviation.

After successfully demonstrating that **53** could be applied to optical activation of split enzymes, we next wanted to demonstrate applicability toward optical control of a protein degron via a destabilized FKBP domain. The combination of F36V and L106P mutations in FKBP has been shown to generate a destabilized FKBP variant (ddFKBP), which results in subsequent protein degradation. Addition of a synthetic ligand, Shield-1 (**54**), results in stabilization of the ddFKBP protein (Figure 5-36a).⁴⁵⁹⁻⁴⁶² Fusion of ddFKBP to a protein of interest allows for small molecule-controlled temporal regulation of protein stability and was successfully applied to cyclin-dependent kinase 1, the transmembrane protein CD8 α , and the motor protein TgMyoA in cell culture and live parasites.^{459, 463}

Traditionally, **54** has been used in the literature for these stabilization assays since it only interacts with FKBP and does not induce ternary complex formation, thereby avoiding any potential interaction with endogenous calcineurin or mTOR. In the initial report, the authors did demonstrate that FK506 successfully stabilized their ddFKBP fusion (however, a 10-fold higher concentration of ligand was required compared to **54**),⁴⁵⁹ thus we hypothesized that rapamycin and photoactivated analogs could be used in a similar manner. To optically control a degron system with **53**, we fused mCherry-HA to the C-terminus of ddFKBP to utilize a fluorescent readout of protein stabilization/destabilization (Figure 5-36b). Briefly, mCherry-HA was PCR amplified, then Gibson assembled into the commercial Clontech pPTuner IRES2 system. This system co-expresses the ddFKBP fusion of interest with *acGFP* using an internal ribosomal entry site (IRES) such that the destabilized fusion is expressed in a 1:1 ratio with *acGFP* (which is utilized as a transfection and transcription control).

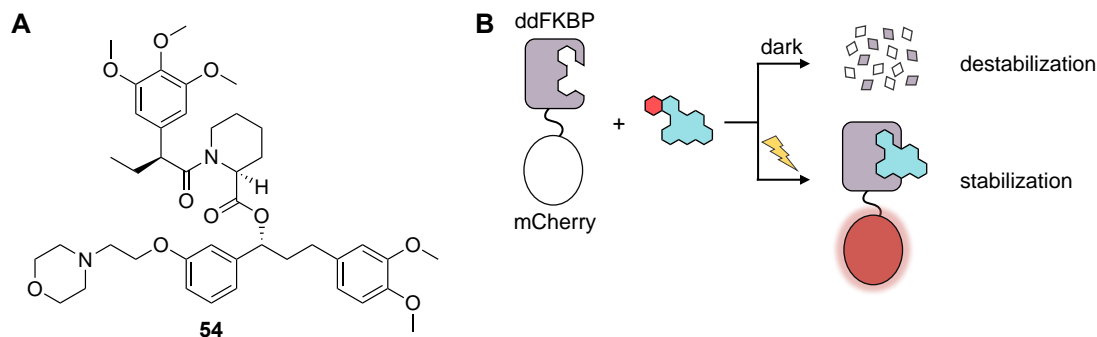


Figure 5-36 Structure of Shield-1 (**54**) and schematic of destabilized FKBP reporter

a) Structure of Shield-1 (**54**). b) The destabilized FKBP mutant was fused to mCherry-HA for visualization of stabilization via fluorescence microscopy. In the absence of stabilizing ligand, the fusion protein is degraded; however, upon addition of stabilizer (shown here as a photoactivated rapamycin analog), the reporter is stabilized and red fluorescence is observed.

In order to determine the optimal concentration of rapamycin to use in place of **54**, HEK293T cells expressing the ddFKBP-mCherry-HA-IRES-acGFP reporter were treated with DMSO, **54**, or rapamycin (**21**) at increasing concentrations (Figure 5-37a). Fluorescence micrographs acquired at 24 hours post-treatment showed that 5 and 10 μM concentrations of **21** stabilized comparably or better than the 0.5 μM of **54** control. At 25 μM , mild cytotoxicity was detected through visible patchiness of the cell monolayer. Since 5 μM most closely matched that of the control and showed no morphological changes in this assay, we utilized this concentration for follow up assays.

Literature reports using **54** for protein stabilization incubated with ligand for 24 hours, thus we were curious whether incubation with rapamycin would require the same incubation period, or if a shorter time period would afford higher protein levels. HEK293T cells were transiently transfected with the ddFKBP-mCherry-HA-IRES-acGFP reporter overnight, then the transfection media was replaced with compound treatment in media (DMSO, **54**, or **21**). Fluorescence imaging was performed periodically for 24 hours to monitor for the stabilization of mCherry (Figure 5-37b). While 5 μM of **21** showed a much faster response than the synthetic ligand, maximum protein

levels were only obtained at the 24-hour time point, thus it does appear that the 24-hour incubation is necessary for optimal protein levels.

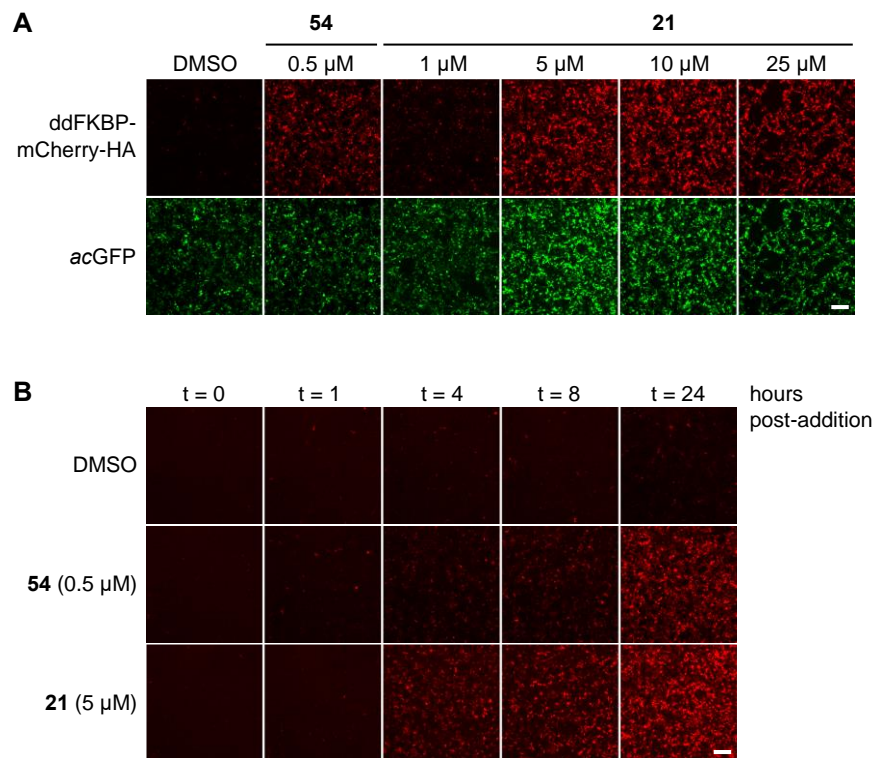


Figure 5-37 Optimization of a destabilized FKBP reporter for use with rapamycin

a) HEK293T cells expressing the ddFKBP-mCherry-HA-IRES-acGFP were treated with **54** (0.5 μ M) and a range of rapamycin (**21**) concentrations to monitor for the stabilization of mCherry-HA. Treatment with 5 μ M of **21** resulted in comparable stabilization as the **54** control; however, treatment with 25 μ M showed noticeable cytotoxicity as observed in the patchiness of the cell monolayer. Thus, 5 μ M was chosen for future experiments. b) HEK293T cells expressing the reporter were treated with DMSO, 0.5 μ M of **54**, or 5 μ M of **21** and monitored over 24 hours to determine the optimal incubation time. Maximum fluorescence intensity was observed at 24 hours, thus future incubations were performed for this length.

When the ddFKBP-mCherry-HA reporter was expressed in HEK293T cells in the absence of a small molecule stabilizer, almost no mCherry signal was detected (Figure 5-38a). Addition of rapamycin (5 μ M) resulted in significant stabilization of the reporter and subsequent mCherry fluorescence. In the presence of **53** (5 μ M), minimal background stabilization was observed. Upon increasing exposure to 415 nm light, we observed a dose-dependent response in mCherry stabilization (Figure 5-38b). Furthermore, these results suggest that the ANB caging group functions to prevent interaction with the FKBP domain (as opposed to the FRB domain, which is

absent from this system). These results are consistent with our previous findings that **22** could be rendered a suitable light-activated dimerizer through engineering FKBP (iFKBP) in order to develop a low-background optically controlled system.⁷¹

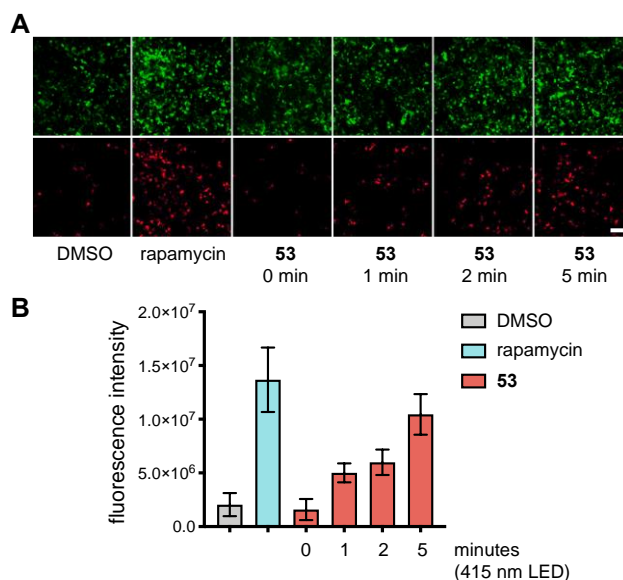


Figure 5-38 Photoactivation of caged rapamycin **53** in a destabilized FKBP reporter

a) HEK293T cells expressing the ddFKBP-mCherry-HA reporter were treated with 5 μ M of **21** or **53**, then cells were irradiated with a 415 nm LED. Fluorescence micrographs were acquired 24 hours later and show stabilization of the ddFKBP-mCherry-HA fusion for rapamycin and the photoactivated **53** samples. The acGFP images show similar levels of transfected cells across all samples, while the mCherry signal varies depending on the degree of stabilization. Scale bar equals 125 μ m. b) Quantification of fluorescence intensity shows that **53** photoactivation occurs in a dose-dependent manner. Bars represent the average mCherry fluorescence measured from three biological replicate wells, with error bars denoting standard deviation.

Subcellular protein translocation is a common mechanism in the regulation of biological processes.³⁵¹ Small molecule-based protein dimerization systems have been extensively applied to the control of sub-cellular protein localization through anchoring of one binding partner in a particular cellular compartment.^{351, 354, 464-465} We investigated whether **53** could be a useful addition to the toolbox of conditional control to subcellular protein localization. For this, we utilized a nuclear translocation reporter which consists of mCherry-NLS_{x3}-FRB and GFP-FKBP, such that mCherry is localized to the nucleus while GFP is diffuse throughout the cell (Figure 5-39a). Upon addition of rapamycin, ternary complex formation of FKBP-**21**-FRB results in co-localization of

the fluorescent proteins as seen by the nuclear translocation of GFP. When **53** is added to cells expressing the reporter, no nuclear localization of GFP is observed, again indicating no background activity in the dark state, until photoactivation with 415 nm light (Figure 5-39b-c). Quantification of the nuclear/cytoplasmic ratio over time demonstrates successful photoactivation of **53**, with ~70% efficiency compared to rapamycin. Rapamycin induces a rapid response of nuclear accumulation, while the photoactivated **53** results in a slower, more gradual nuclear localization of FKBP-GFP, which is potentially due to less efficient decaging in a complex cellular environment such that the actual concentration of released rapamycin is lower than the control sample.

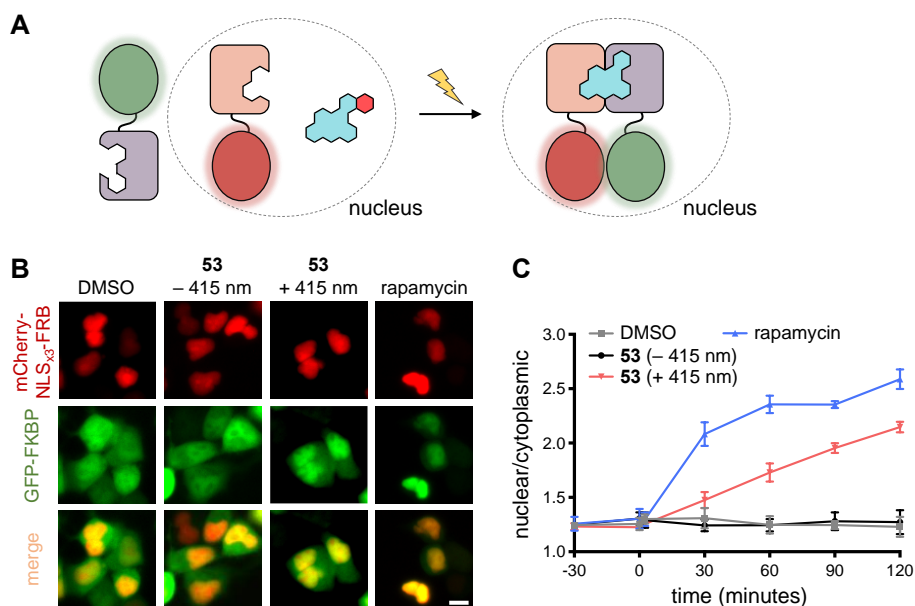


Figure 5-39 Photoactivation of caged rapamycin **53** in a nuclear translocation reporter

a) Schematic representation of the nuclear translocation reporter. GFP-FKBP (diffuse throughout the cell) and mCherry-NLS_{x3}-FRB (nuclear localized) are co-expressed. Upon addition of caged rapamycin, no translocation is observed; however, irradiation with 415 nm light results in ternary complex formation and nuclear accumulation of GFP-FKBP. b) HEK293T cells co-expressing the reporter were treated with 1 μM of **21** or **53**. Following irradiation with a 415 nm LED for 2 minutes significant nuclear accumulation of GFP-FKBP is observed after 2 hours. Scale bar equals 10 μm. c) Quantification of the nuclear/cytoplasmic ratio supports the micrograph findings. Five cells per condition were averaged and plotted with error bars representing standard error of the mean.

Next, we explored whether **53** could be used for optical control of mTOR signaling in mammalian cells, with the eventual goal of applying this as a tool in zebrafish development. We

first validated that **53** could be used for light-controlled inhibition of ribosomal protein S6, a well-established readout of mTOR activity.⁴⁶⁶ HeLa cells were treated with 5 and 10 nM **21** or **53** in the presence or absence of 405 nm irradiation for one hour. Following incubation, the samples were lysed and western blot analysis was performed using a phospho-S6 antibody, with GAPDH serving as a loading control (Figure 5-40). With 10 nM treatment, a minimal degree of background activity for **53** was observed; however, no background inhibition was observed with 5 nM treatment. Treatment with **21** at both concentrations resulted in complete inhibition. Gratifyingly, irradiation with 405 nm light resulted in inhibition of the pathway as observed by a loss of phosphorylated signal.

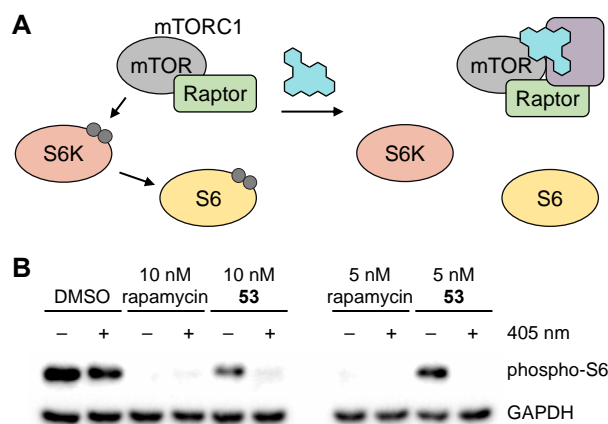


Figure 5-40 Optical control of **53** inhibition of mTOR signaling in HeLa cells

a) The mTORC1 complex results in phosphorylation of S6K and S6; however, treatment with rapamycin results in a ternary complex of mTOR-rapamycin-FKBP which blocks the kinase activity of mTOR and prevents phosphorylation of downstream targets. Grey filled circles represent phosphorylation. b) Western blot analysis using an anti-phospho-S6 antibody demonstrates complete inhibition of the pathway when treated with 10 or 5 nM of rapamycin, while treatment with **aRap** only inhibits phosphorylation following photoactivation with a 405 nm LED (30 seconds).

In zebrafish embryos, we first tested for background activity of **53** by treating with compound concentrations previously reported for rapamycin.⁴⁶⁶⁻⁴⁶⁷ Wild-type embryos were exposed to 100 nM, 400 nM, or 10 μ M of rapamycin or **53** at 4 hours post fertilization (hpf), with daily refreshing of compound treatment every 24 hours, for a total of 72 hours of treatment. Representative images show increased developmental defects with increased concentration of

rapamycin treatment (Figure 5-41a), which are consistent with literature reported phenotypes.⁴⁶⁷⁻
⁴⁶⁸ These defects include shortened body length, an enlarged yolk sac, and decreased dorsal pigmentation. Treatment with **53** from 0.1 to 10 μM showed no apparent phenotypic defects, suggesting that **53** has minimal background activity. Western blot analysis of these embryos probing for phospho-S6 levels shows complete inhibition of phosphorylation at all rapamycin concentrations tested (Figure 5-41b). Interestingly, western blot analysis of **53**-treated embryos revealed background inhibition of mTOR signaling when treated at $>0.4 \mu\text{M}$; however, treatment at 0.1 μM does not inhibit signaling. These results suggest that different thresholds exist for phenotypic effects (system level) and extent of protein phosphorylation (molecular level).

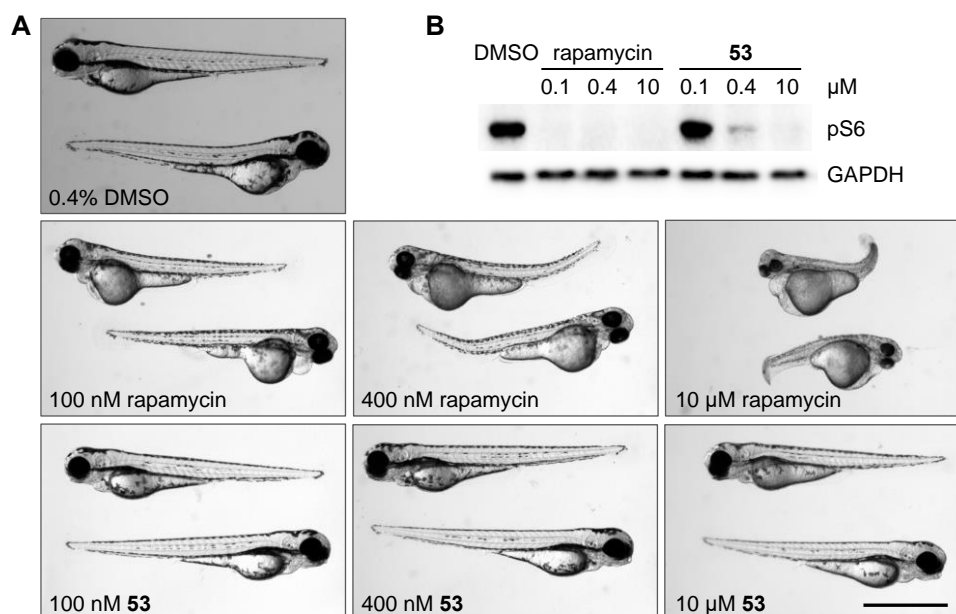


Figure 5-41 Assessment of background activity of **53** in zebrafish embryos
a) Representative images of 76 hpf zebrafish treated with increasing concentrations of rapamycin or **53**. Scale bar equals 1 mm. b) Western blot analysis shows complete inhibition of phosphorylated S6 protein at all rapamycin concentrations, while **53** only shows background inhibition at greater than 100 nM. Zebrafish treatment, image acquisition, and tissue lysis was conducted by Kristie Darrah.

In these preliminary experiments, compound was refreshed daily over the length of the experiment as is done in literature reports; however, this is not amenable to the use of light as a trigger as irradiations would need to be performed daily post-addition of fresh compound. We

modified the workflow to: (1) shorten the overall treatment time from 72 to 48 hours and (2) did not refresh compound solutions daily. Western blot analysis of these embryos probing for phospho-S6 levels shows complete inhibition of phosphorylation at all rapamycin concentrations tested (Figure 5-42a). Western blot analysis of **53**-treated embryos shows background inhibition of the mTOR pathway upon treatment $>0.4 \mu\text{M}$; however, treatment at $0.1 \mu\text{M}$ does not inhibit signaling. These blot results are consistent with the previous experimental design, suggesting that this modified workflow can be applied in light activation studies. With this earlier end time, developmental defects (at the phenotypic level) are not apparent, thus we focused on western blot analysis as the readout in our remaining experiments.

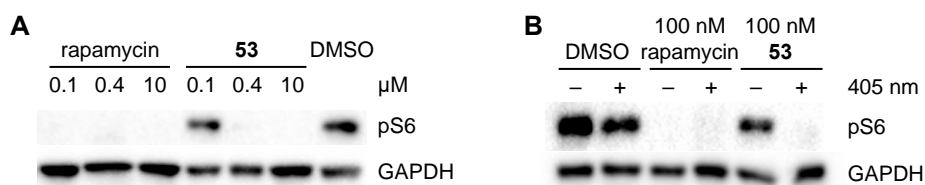


Figure 5-42 Demonstration of light activation of **53** in zebrafish embryos

a) Zebrafish embryos were treated with rapamycin or **53** at 4 hpf with varied concentrations (0.1 to $10 \mu\text{M}$) and maintained until 48 hpt. Western blot analysis probing for pS6 and GAPDH was performed. b) Western blot analysis of irradiated embryos shows light-induced mTOR inhibition for **53**, while light alone has no impact on DMSO or rapamycin treatment.

Based on this, we proceeded to test the light activation of **53** in zebrafish embryos by treating with 100 nM of compound at 4 hpf, followed by a 1-minute irradiation (405 nm) at 6 hpf, then embryos were harvested for western blot analysis at 48 hpf (Figure 5-42b). Gratifyingly, we observed light-induced inactivation of mTOR signaling with **53**-irradiated samples, while irradiated DMSO and rapamycin samples show no light-induced effects. These results demonstrate that caged rapamycin analogs can be used for regulating mTOR signaling in embryos and may enable future studies involving the effects of temporal control of mTOR inhibition.

We have successfully developed a caged rapamycin analog that does not induce FKBP/FRB heterodimerization until activated with 405 and 415 nm light. Caged rapamycin **53**

exhibits several advantages over the previously reported caged rapamycin analogs: (i) it has no background activity in the absence of light stimulation, (ii) it requires no FKBP engineering, (iii) it does not need a caging group that increases steric bulk or leads to extracellular localization, and (iv) it can be activated with visible light rather than UV light. We have demonstrated that **53** can be used to control several biological processes, including split enzyme reconstitution, stabilization of ddFKBP fusion proteins, protein translocation and localization, and inhibition of endogenous mTOR signaling. We envision that this rapamycin analog will be compatible with a wide range of biological applications and readily convey optical activation over a wide range of processes that have been placed under control of chemically induced protein dimerization by rapamycin.

5.5.1 Methods

Reagents. Rapamycin (and caged analogs) stocks were generated at 5 mM in sterile-filtered DMSO. LEDs were obtained from Mouser Electronics: 405 nm (LZ1-10UA00-00U8) and 450 nm (LXML-PR02-A900), or LuxeonStar: 415 nm (SZ-01-U8).

Photochemical analysis of 53. Five solutions of **53** were prepared at various concentrations (20, 30, 40 50, and 75 μ M) in milliQ water at a final DMSO concentration of 0.75%. A DMSO blank was also prepared. Samples were transferred to a 1.5 mL cuvette and absorbance readings at 405, 412, 415, and 450 nm were acquired on a UV spectrophotometer (Childers lab, VWR UV1600PC). The absorbance of the DMSO sample was background subtracted from all values and plots were generated in Graphpad Prism 8. Linear regression was fitted to each data set such that the slopes correspond to the extinction coefficient.

Cloning of DNA constructs. Top10 cells were used for all cloning. FRB-CFP-6xHis and FKBP-YFP-6xHis were generated using Gibson assembly. The FRB fragment (template: mCherry-

NLSx3-FRB, primers: P1/P2), the CFP fragment (template: CFP-FRBx5-His, primers P3/P4), the FKBP fragment (template: GFP-FKBP, primers P5/P6), and the YFP fragment (template: YFP-FKBP_{x5}-His, primers P7/P8) were PCR amplified using DreamTaq Green. PCR products were electrophoresed on a 0.8% agarose gel and gel extracted following the manufacturer's protocol. CFP-FRB_{x5}-His was linearized with NcoI and NotI (from NEB) to generate the backbone fragment. Equimolar amounts of backbone, FRB, and CFP were used to generate FRB-CFP-6xHis, while equimolar amounts of backbone, FKBP, and YFP were used to generate FKBP-YFP-6xHis by Gibson assembly.⁹⁹ Both constructs were confirmed by Sanger sequencing performed by Genewiz using their "T7" forward and "T7 term" reverse sequencing primers.

To generate the ddFKBP-mCherry-HA construct, an HA-tag was added to mCherry through PCR amplification using primers P9 and P10 using mCherry-actin as the template. pPTuner IRES2 (Clontech #632168) was linearized with EcoRI and BamHI. The mCherry-HA fragment was ligated into the backbone using T4 DNA ligase. The construct was verified by Sanger sequencing at Genewiz using their "CMV-forward" sequencing primer. Plasmid maps are included in Appendix A.

Table 5-3 Primer sequences for cloning constructs used with caged rapamycin **53**
Restriction sites are indicated in **bold**.

Primer	Sequence (5' → 3')
P1	gtttaactttaagaaggagatataccatgggcatcctctggcatgagatgtgg
P2	ttgctcaccataaccaccagcactagtctttgagattcgctcggaac
P3	tctcaaagactagtgtggtggtatggtgagcaagggcgagga
P4	gtggtggtggtgctgagtgccgcccctgtacagctcgccatgccg
P5	ttgtttaactttaagaaggagatataccatgggagtgagggtgaaaccatctcc
P6	cactgccataaccaccagcactttccagttttagaagctccacatcg
P7	aactgaaagtgtggtggtatggcagtgagcaagggcga
P8	gtggtggtgctgagtgccgcccctgtacagctcgccatgccgag
P9	gtat gaattc tatggtgagcaagggcgagga
P10	atat ggatcct caagcgaatctggaacatcgatgggtactgtacagctcgccatgc

HPLC analysis of decaging. A 100 μM solution of **53** was prepared using a 5 mM stock solution (10 μL of stock diluted into 490 μL of methanol) in a ½ dram clear glass vial. A 40 μL pre-irradiation sample was transferred to an HPLC sample vial. The remainder of the solution was split into 120 μL aliquots in three separate ½ dram clear glass vials (one for each irradiation wavelength). The vials were irradiated from the bottom with the LED source touching the glass surface. Handheld LEDs (405, 415, and 450 nm) operated at 700 mA output were used in increments of 5 minutes to provide 5- and 10-minute irradiation samples (40 μL was removed and transferred to an HPLC vial at each time point). A 100 μM solution of rapamycin was prepared in the same manner to use as a control for retention time and expected product peak area following irradiation. A Shimadzu HPLC equipped with an analytical scale column (Agilent, Zorbax SB-C18, 3.5 μm , 4.6 x 100 mm) was used for analysis. Solvent A was milliQ water and Solvent B was HPLC-grade acetonitrile. A 50-minute gradient method with a 1.0 mL/minute flow rate was developed and percentages listed are for Solvent B (0 minutes – 35%, 15 minutes – 95%, 40 minutes – 95%, 40.083 minutes – 35%, 50 minutes – 35%). An autosampler was utilized for injections and 25 μL of sample was injected per analysis. The UV detector was set to 280 nm (absorbance maxima for rapamycin). The raw data was extracted from the LabSolutions software (Shimadzu) and plotted in GraphPad Prism 8.

Gel shift analysis of ternary complex formation. Bacterially expressed FKBP-YFP-6xHis and FRB-CFP-6xHis (see section below for expression) were diluted to 10 μM in assay buffer (20 mM Tris-HCl pH 7.4, 100 mM NaCl, 10% glycerol). Compound stocks (5 mM) were diluted in water to 10X (1 mM – 0.01 mM) of the desired final concentrations (100 μM – 1 μM), with the exception being that the 1 mM stock was prepared in DMSO. A master mix of the two proteins was prepared by mixing 300 μL of FKBP-YFP-6xHis with 300 μL of FRB-CFP-6xHis, then 18 μL were

transferred to PCR tubes. The desired compound (2 μ L of a 10X stock) was added to the proteins to yield \sim 5 μ M of each protein partner with 1X compound. These samples were incubated at room temperature in the dark for two hours. Afterwards, 8 μ L of 4X Laemmli buffer without reducing agent or SDS (see 8.3.9, Native) was added to each sample. Native-PAGE gels (10%, 1.5 mm thick, 10-well comb) were prepared. The entire 28 μ L of sample was loaded, and the gels were electrophoresed at 60 V for 20 minutes, followed by 150 V for 70 minutes on ice. Gels were Coomassie stained and imaged on a ChemiDoc Imager.

Bacterial expression of FKBP-YFP-6xHis and FRB-CFP-6xHis. BL21 (DE3) were transformed with either FKBP-YFP-6xHis or FRB-CFP-6xHis and grown on LB agar supplemented with kanamycin (50 μ g/mL). Starter expression cultures in LB/kanamycin were prepared and incubated with shaking (250 rpm) overnight at 37 $^{\circ}$ C. Expression cultures (100 mL for each) were prepared by diluting 1 mL of the saturated starter culture in 100 mL of LB/kanamycin and cells were incubated with shaking (250 rpm) at 37 $^{\circ}$ C until OD₆₀₀ reached 0.5. Protein expression was induced by the addition of 10 μ L of 1M IPTG (for a final concentration of 0.1 mM of IPTG) and flasks were shaken at 250 rpm overnight at room temperature. After 18 hours, cells were collected into 50 mL conical tubes (2 tubes per expression) and pelleted at 4000 g for 10 minutes at 4 $^{\circ}$ C. Cell pellets were resuspended in 10 mL of PBS (pH 7.4) supplemented with 1X protease inhibitor (Sigma P8849) via vortexing and kept on ice, then the two identical samples were pooled (20 mL per sample). Cell lysis was performed using an EmulsiFlex C3 Homogenizer (Avestin) in a cold room. Cells were passed through without pressure for 5 minutes, then cycled through with pressure (\sim 20,000 psi) for 15 minutes. Cellular debris was pelleted at 21,000 g for 15 minutes at 4 $^{\circ}$ C, and the soluble protein fraction was transferred to a fresh tube and kept on ice. Ni-NTA resin (400 μ L; G-Biosciences) was added to each sample and incubated with

rocking for 90 minutes in a cold room. The immobilized protein on the resin was pelleted at 800 g for 5 minutes, then the supernatant was discarded. The resin was washed thrice with wash buffer (PBS containing 75 mM imidazole). The proteins were eluted in four fractions with PBS plus 250 mM imidazole. Protein purity was assessed using a 10% SDS-PAGE gel, followed by Coomassie staining. After confirming purity, the elution fractions were combined and buffer exchanged in storage and assay buffer (20 mM Tris-HCl pH 7.4, 100 mM NaCl, 10% glycerol) using centrifuge filters (Amicon Ultra, 10 kDa cutoff). Protein concentrations were determined using a BSA standard curve from densitometry analysis of a Coomassie stained protein gel.

Split luciferase reporter. HEK293T cells were plated at 200,000 cells/well in a 6-well clear bottom plate (Greiner) and grown at 37 °C/5% CO₂. At ~80% confluence, cells were co-transfected with CLuc-FKBP and FRB-NLuc (1000 ng each, 2000 ng total) using Lipofectamine 2000. Lipofectamine 2000 (10 µL) was diluted into OptiMEM (500 µL) and incubated at room temperature for five minutes. In a separate tube, plasmid DNA (4000 ng, for two wells) was diluted into 500 µL of OptiMEM. After the incubation, the Lipofectamine/OptiMEM solution was added to the DNA/OptiMEM solution (~1000 µL total) and mixed gently by flicking the tube, then the transfection mixture was incubated for 20 minutes at room temperature. During this time, the media was replaced with 2 mL of DMEM (+ 10% FBS, – antibiotics), then the transfection mix (500 µL/well) was added and incubated overnight. Two wells were transfected identically in order to obtain enough cells for a single assay. After ~18 hours of transfection, the transfection media was removed, the cells were lifted with TrypLe (500 µL/well) and transferred to a 15 mL conical tube, then TrypLe was inactivated by the addition of 9 mL of DMEM (+ 10% FBS, – antibiotics). Cells were pelleted at 1,000 g for 10 minutes at room temperature. The media was removed, and the cell pellet was resuspended in 1 mL of LCIS. Cells were counted using a hemocytometer in

the presence of Trypan Blue to avoid counting dead cells (combination of two wells typically yielded 1.5 – 1.8 million cells). Subsequently, cells were plated in a white, clear bottom 96-well plate at 10,000 cells per well in 90 μ L of LCIS.

To prepare the compound solutions, 5 mM stocks of **21** or **53** in DMSO were first diluted to 1 mM in DMSO, then a 0.1 mM solution was prepared by dilution of the 1 mM solution into water. For a final concentration of 50 nM, a 10X sample (500 nM) was prepared by diluting 4 μ L of the 0.1 mM solution into 796 μ L of LCIS. To each well of the 96-well plate containing cells expressing the reporter, 10 μ L of compound (either **21**, **53**, or DMSO) was added in triplicate and the plate was placed in the incubator for one hour. A subset of wells was photoactivated using either a 405 or 415 nm LED (set to 300 mA) by holding the LED directly above the well and using a foil mask to prevent undesired irradiation of neighboring wells. Irradiation times of 15, 30, 45, 60, or 90 seconds were utilized. After irradiation, the plate was incubated for an additional four hours at 37 °C/5% CO₂. Afterwards, 90 μ L of BrightGlo reagent was added to each well and incubated for two minutes, then luminescence was measured on a Tecan M1000 plate reader using an integration time of 200 msec. Raw luminescence values were normalized such that DMSO equaled 1. Average fold-change values with error bars representing standard deviation are reported.

Determination of optimal parameters for degron FKBP reporter. HEK293T cells were plated at 200,000 cells/well in a 6-well plate. At ~80% confluence, cells were transfected with 1600 ng of ddFKBP-mCherry-HA-IRES-acGFP in 200 μ L of OptiMEM using 20 μ L of LPEI (0.323 mg/mL). All six wells were transfected identically. The transfection mix was added to wells containing 2 mL of DMEM (+ 10% FBS, – antibiotics) and incubated for ~18 hours. Afterwards, the transfection media was removed and replaced with media containing various concentrations of

compound. A 0.5 μM solution of **54** was prepared by diluting 1.5 μL of a 0.5 mM stock (in ethanol) into 1.5 mL of DMEM (+10% FBS, – antibiotics, – phenol red). Rapamycin solutions were prepared at 1, 5, 10, and 25 μM in DMEM (+10% FBS, – antibiotics, – phenol red) using 100X stock solutions prepared in water (100 – 2500 μM) by diluting 15 μL into 1.485 mL. The entire 1500 μL of compound solutions was transferred to the appropriate well, including a DMSO control prepared in the same manner. The plate was maintained at 37 °C/5% CO₂ for the course of the experiment, except every few hours when the plate was removed for imaging at ambient temperature. Images were acquired on a Zeiss microscope using a 5X N-Achroplan (0.13 NA) objective equipped with an AxioCam MRm camera with mCherry and EGFP filter sets (Zeiss 43HE and 38HE, respectively).

Degron FKBP reporter with 53. HEK293T cells were plated at 50,000 cells/well in a black 96-well poly-D-lysine treated plate. At ~80% confluence, cells were transfected with 200 ng of ddFKBP-mCherry-HA-IRES-acGFP in 20 μL of OptiMEM using 2 μL of LPEI (0.5 mg/mL). The transfection mix was added to wells containing 100 μL of DMEM (+ 10% FBS, – antibiotics) and incubated for ~18 hours. Afterwards, the transfection media was removed and replaced with media containing 5 μM of compound (either **21**, **53**, or DMSO). Compound solutions were prepared by diluting 5 μL of a 1 mM stock solution into 995 μL of DMEM (+ 10% FBS, – antibiotics, – phenol-red) to prepare a 5 μM solution. One hundred microliters of compound in media was added to each well. One hour after the addition of compound, a subset of wells was irradiated for 1, 2, or 5 minutes using the 415 nm LED in conjunction with the foil mask (as described above). The plate was incubated for an additional 24 hours to allow for stabilization of the reporter. Cells were imaged at ambient temperature with an Axio Observer Z1 microscope using a 10X Plan Achromat objective equipped with an AxioCam MRm camera with mCherry and EGFP filter

sets (Zeiss 43HE and 38HE, respectively). Integrated density (mean fluorescence \times area of region) from three different wells per condition was quantified using FIJI. Averages with error bars representing the standard deviation are provided.

Nuclear translocation reporter. HEK293T cells were plated at 50,000 cells/well in a black 96-well poly-D-lysine treated plate. At 80% confluence, cells were co-transfected with 33 ng of GFP-FKBP and 66 ng of mCherry-NLS_{x3}-FRB in 20 μ L of OptiMEM using 2 μ L of LPEI (0.5 mg/mL). The transfection mix was added to wells containing 100 μ L of DMEM (+ 10% FBS, – antibiotics) and incubated for ~18 hours. The transfection media was removed and replaced with 90 μ L of LCIS. Compound stocks (10 μ M) were prepared by diluting 5 μ L of a 1 mM stock into 495 μ L of LCIS. A solution of **53** (10 μ L) was added to the desired wells and incubated in the dark for 30 minutes to check for any background dimerization activity. The plate was carefully removed from the stage, irradiated from below with the LED bulb touching the surface of the plate for 2 minutes, then immediately returned to the stage for continued imaging. Rapamycin (**21**) was added to a separate set of wells for use as a control immediately after irradiation of **53**-containing wells. Images were acquired every 30 minutes until 2 hours post-addition of light (or rapamycin). Circular ROIs were selected in the nucleus and cytoplasm of the GFP channel and mean fluorescence intensity was measured using FIJI in order to calculate the nuclear/cytoplasmic (N/C) ratio. Five cells were quantified per condition. Average N/C ratios are provided with error bars representing standard error of the mean.

Inhibition of endogenous mTOR signaling in cells. HeLa cells were plated in a clear, 24-well plate and maintained at 5% CO₂/37 °C until cells reached 90% confluency (usually 24 – 48 hours). Rapamycin and **53** solutions were prepared at 200X in DMSO (1 μ M and 2 μ M) from a 5 mM DMSO stock. Working solutions were prepared by diluting 2.5 μ L into 498 μ L of LCIS, and 250

μL was used per well (treatment performed in duplicate for \pm irradiation). A 405 nm LED (set to 700 mA) was positioned directly above the well, with the heat sink barely touching the plate and a 15 second irradiation was performed for each of the samples. The plate was placed in the incubator for one hour. Lysis buffer was prepared as follows: 500 μL of RIPA + 5 μL of 100X Halt Protease Inhibitor Cocktail + 10.5 μL of 50X phosphatase inhibitors (100 mM each of sodium fluoride and sodium orthovanadate). The plate was placed on ice, the compound solutions were removed, cells were carefully washed once with cold PBS, followed by addition of 40 μL of lysis buffer. The plate still on ice was placed on an orbital shaker at 250 rpm for 15 minutes for cell lysis. The lysate was collected into 1.7 mL tubes, 17 μL of 4X loading dye was added, and samples were boiled for 10 minutes at 95 °C. Lysate was stored at -80 °C. Western blot analysis was performed using 12 μL of lysate per sample, as described previously for gel electrophoresis and transfer. Membranes were blocked for 1 hour with 5% milk in TBST, then washed thrice with TBST for 5 minutes each time. Phospho-S6 antibody was used at 1:1,000 dilution (2 μL in 2 mL of 5% BSA in TBST) and GAPDH was used at 1:5,000 (1 μL in 5 mL of 5% milk in TBST). Membranes were incubated overnight in a cold room with rocking. Primary antibody solutions were discarded, the membranes were washed thrice with TBST for 5 minutes each time, followed by incubation with secondary goat anti-rabbit at 1:10,000 in TBST for one hour at room temperature with rocking. The antibody was discarded, the membrane was again washed thrice as before, and a chemiluminescent substrate was added.

Western blot analysis of zebrafish lysates. All zebrafish manipulations (treatment, imaging, and lysis) were performed by Kristie Darrah in accordance with IACUC regulations. A detergent compatible Bradford assay (Pierce – 23246) was performed using 2.5 μL of lysate diluted with 2.5 μL of T-PER (Thermo Scientific – 78510) and 150 μL of Bradford reagent (5 μL of eight different

BSA concentrations was used for generating a standard curve), followed by a 10 minute incubation with 50 rpm orbital shaking at room temperature. Absorbance measurements were acquired on a Tecan M1000 at 595 nm. Following background subtraction of a buffer only sample, concentrations were determined using the standard curve. The volume necessary for 20 and 15 μg was determined by dividing by the concentration. Western blot analysis was performed as described above, except the appropriate volume of lysate was loaded per lane to obtain 20 μg and 15 μg (used for phospho-S6 and GAPDH, respectively). The remainder of the process was repeated identically to the above section.

6.0 Optical Deactivation of Rapamycin-Induced Protein Dimerization

While we have demonstrated the ability to use light to turn-on dimerization using rapamycin analogs, we hypothesized we could develop an analog to enable turn-off behavior. In Nature, biological processes undergo rapid association and dissociation as a means of regulating signaling pathways and other cellular responses, thus we envisioned the ability to break open or disassemble the ternary complex would be beneficial to the field.¹⁰ The use of light to inactivate biological processes (via CALI) is well-established and has been introduced in detail in Chapter 3. Initially, we hypothesized that attachment of a small molecule ROS generator to rapamycin would lead to one of two outcomes following light-induced oxidation: (1) oxidation/degradation of rapamycin and the two FKBP/FRB fusion proteins, or (2) oxidation/inactivation of rapamycin alone such that the intact FKBP/FRB fusions could undergo an additional dimerization event upon addition of more compound (Figure 6-1).

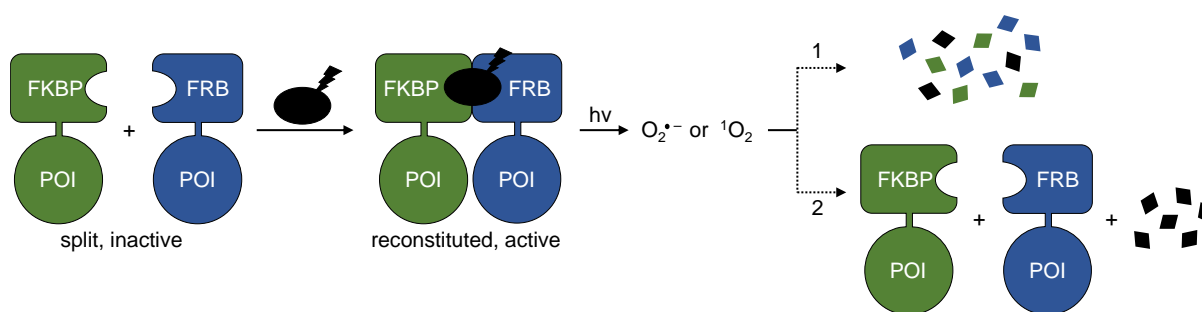


Figure 6-1 Schematic representation of ROS-induced ternary complex disruption
Rapamycin was modified with a ROS generator (indicated with a lightning bolt). After addition of compound, dimerization is achieved. Upon irradiation, singlet oxygen is generated which we propose can result in one of two pathways shown in the figure: 1) complete degradation of the entire complex, or 2) degradation of ROS-rap to yield free FKBP and FRB which could then be re-dimerized upon a second addition of compound.

6.1 Development and Application of Optically-Deactivated Rapamycin Analog

While there are several small molecule-based ROS generators reported in the literature, we initially chose the iodinated-BODIPY chromophore due to its red-shifted (>500 nm) activation wavelength and high quantum yield. Trevor Horst synthesized the BODIPY-modified rapamycin **55** (Figure 6-2a) and validated this analog generated ROS using a small molecule reporter (data not shown). BODIPY-rapamycin **55** was initially tested in the split luciferase assay to demonstrate ternary complex formation before trying to test its degradation ability. Briefly, HEK293T cells were doubly transfected with CLuc-FKBP and FRB-NLuc in a 1:1 plasmid ratio and treated with increasing concentrations of **55** (Figure 6-2b). After a two-hour incubation with compound, a BrightGlo assay was performed and raw luminescence values were normalized to DMSO. Unfortunately, **55** functioned very inefficiently as a dimerizer. Even with 10 and 25 μM of **55**, only a $\sim 1/3$ activation was observed compared to the 1 μM of rapamycin control. Higher concentrations (up to 50 μM) were also tested with no improvement in dimerization. Being concerned that the split luciferase assay wasn't providing the full picture, we also tested **55** in the nuclear translocation assay but observed the same lack of dimerization ability (not shown).

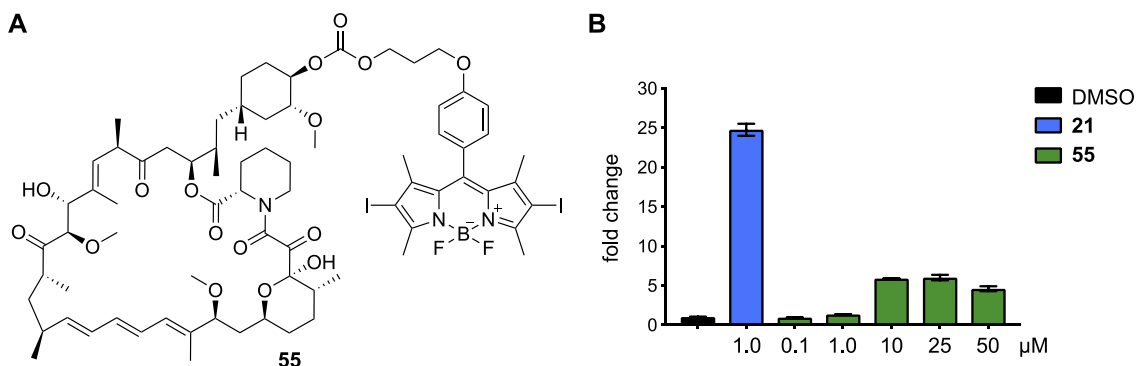


Figure 6-2 Structure of BODIPY-rapamycin **55** and testing in split luciferase reporter
a) Structure BODIPY-rapamycin **55** which was synthesized by Trevor Horst. b) BODIPY-rapamycin **55** was initially tested in the split luciferase assay using a 1:1 FKBP:FRB ratio to check for dimerization activity prior to performing

ROS generation experiments. Unfortunately, even at moderate micromolar concentrations (due to poor solubility, higher concentrations were not possible), no dimerization is detected.

We hypothesized that the BODIPY group is too sterically demanding to allow for efficient dimerization in the current design and decided to introduce a PEG-3 linker between the BODIPY group and rapamycin in order to generate a longer, more flexible linker that would hopefully be more efficient at dimerization. Trevor Horst synthesized a PEG-BODIPY-rapamycin **57** using a click reaction with **56** and an alkynyl-modified iodinated-BODIPY (Figure 6-3).

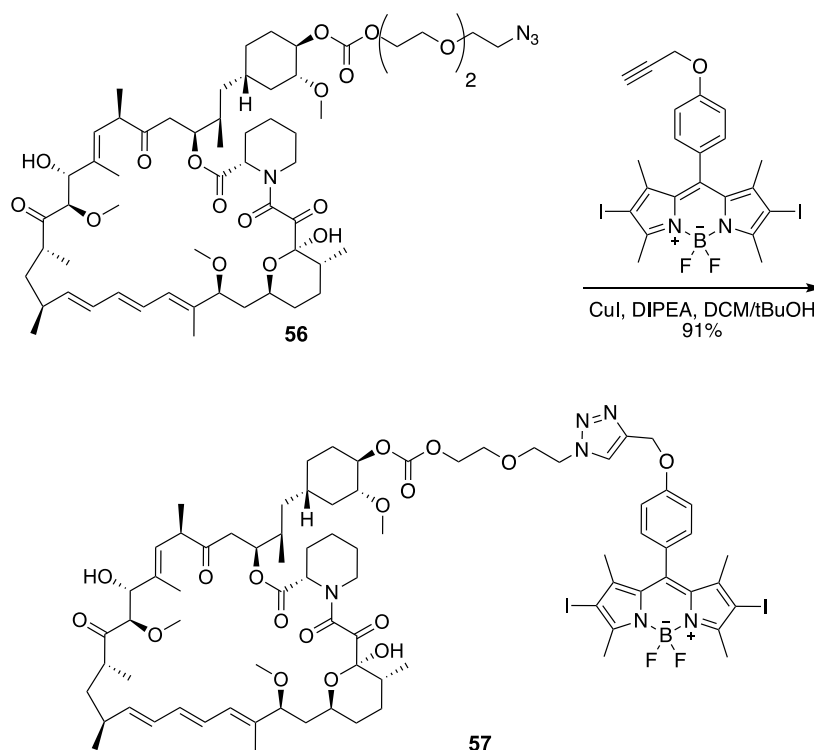


Figure 6-3 Structures of **56** and PEG-BODIPY-rapamycin **57**
Trevor Horst synthesized **57** using **56** and an alkynyl-modified iodinated-BODIPY.

In order to determine if **57** was capable of generating ROS, the singlet oxygen sensor, **4** was used (Figure 6-4a).⁴⁶⁹ A solution of **4** with and without **57** (10:1 **4**:**57**) was irradiated for 0, 10, 30, or 60 seconds using a 530 nm LED. With increasing irradiation times, a concomitant decrease in fluorescence was observed in samples containing **57**, thus demonstrating that **57** does generate ROS (Figure 6-4b).

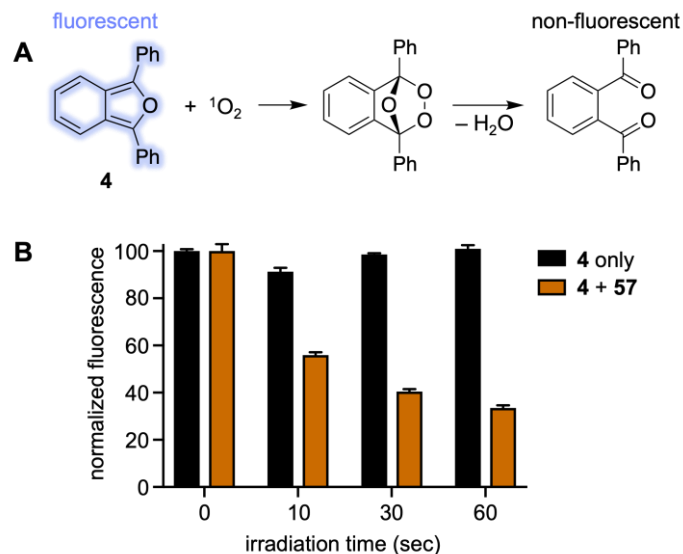


Figure 6-4 Testing of **57** with the singlet oxygen sensor **4**

a) The fluorescent sensor, **4**, reacts with singlet oxygen to generate an unstable peroxide intermediate that rapidly decomposes into a non-fluorescent product. b) Sensor **4** was utilized to measure the singlet oxygen generation capabilities of **57**. The sensor was kept in 10-fold excess of **57** such that 100 μM of **4** and 10 μM of **57** was used. Irradiation of the sensor alone with increasing amounts of 530 nm light showed minimal change in fluorescence; however, upon increasing irradiation of the sample containing **57** and the sensor, a significant decrease in fluorescence was observed, thus demonstrating that **57** generates reactive oxygen species.

Prior to testing in a biological setting, we first characterized the stability of **57** in physiological buffers. The stability of **57** was tested in phosphate buffered saline at pH 7.4 (Figure 6-5a) or 10% fetal bovine serum (FBS) in phosphate buffered saline at pH 7.4 (Figure 6-5b) over an 8-hour period at 37 $^{\circ}\text{C}$ to closely mimic physiological conditions. Monitoring the peak area by HPLC, we found **57** to be completely stable over this time period in both scenarios, suggesting this compound should be stable in cells over the time frame required for inactivation experiments.

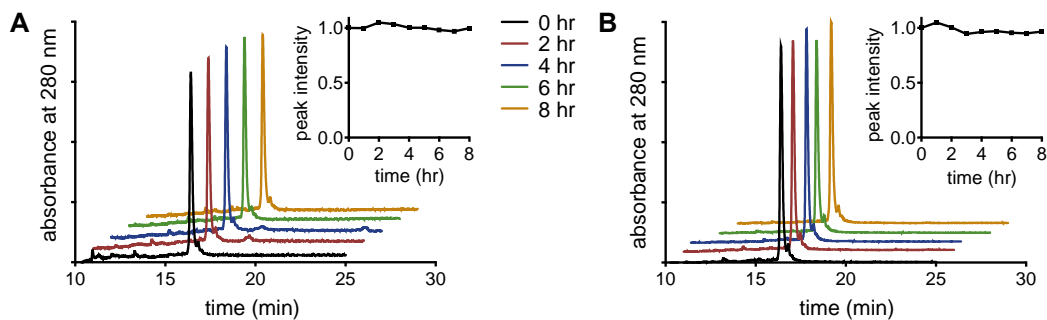


Figure 6-5 HPLC analysis of **57** stability in physiological buffers

Compound **57** was diluted in phosphate buffered saline at 20 μ M in the absence (a) and presence (b) of 10% fetal bovine serum (FBS) and maintained at 37 $^{\circ}$ C for 8 hours. Each hour, an aliquot of this solution was analyzed by HPLC. The integration of each peak was normalized to the initial reading and plotted over time (subset). Compound **57** is stable with and without FBS over 8 hours. Experiment was performed by Chasity Hankinson.

Next, we validated that **57** functions to dimerize FKBP and FRB *in vitro*. Ternary complex formation was assessed through a gel shift assay using bacterially expressed FKBP and FRB fusion proteins (as discussed previously in Section 5.5). Purified FKBP-YFP-His and FRB-CFP-His were incubated with rapamycin (**21**) or **57** (with increasing concentrations) for two hours to allow for ternary complex formation. The samples were resolved by Native-PAGE and Coomassie stained to monitor for the appearance of a higher molecular weight band for the ternary complex. Ternary complex formation is achieved using **57**; unfortunately, it does not have as high of an affinity as the rapamycin (**21**) control (Figure 6-6a,b). We predicted that the BODIPY group was functioning to decrease the affinity, even with the introduction of a longer linker, thus we also tested **56** in the same assay and found that it functions as efficiently as rapamycin (Figure 6-6c). Based on these results, it appears the BODIPY chromophore is primarily responsible for the significant decrease in ternary complex formation efficiency. Although **57** is a less efficient dimerizer than **21**, we proceeded with further cell-based experiments to explore its ability to induce ROS-mediated oxidation and/or degradation of FKBP/FRB fusions.

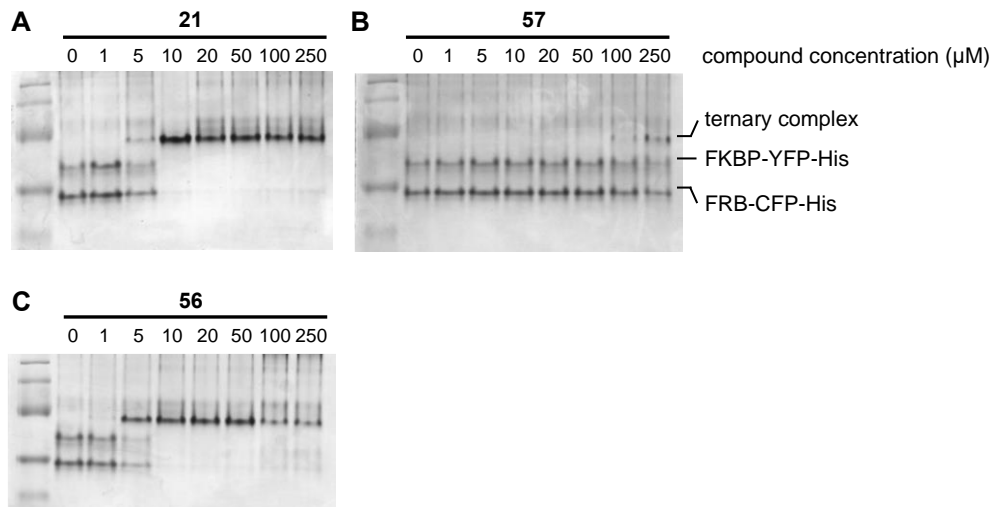


Figure 6-6 Gel shift assays using **21**, **56**, and **57**

Recombinant FKBP-YFP-His and FRB-CFP-His were used in a 1:1 ratio at 5 μM each for *in vitro* gel shift assays. Solutions of FKBP/FRB were incubated with rapamycin [**21**] (A), **57** (B), or **56** (C) at the specified concentrations for two hours, then analyzed via Native-PAGE to assess for dimerization which is apparent through a gel shift to a higher molecular weight. Compound **57** does result in a gel shift; however, a ~10-fold higher concentration than rapamycin is needed to obtain a similar shift. Compound **56** functions as efficiently as rapamycin, thus suggesting that the BODIPY-chromophore is the main contributor for the decreased affinity of **57**.

A split luciferase reporter (described in Figure 5-23a) was used to test dimerization of FKBP and FRB in response to **57** in HEK293T cells. Chasity Hankinson performed preliminary experiments to determine the optimal concentration of **21** and **57** in this assay, then used those concentrations (100 nM – **21**, 10 μM – **57**) to demonstrate optical inactivation of luciferase activity upon increasing irradiation with a 530 nm LED (Figure 6-7b). A significant reduction in enzymatic activity was observed upon a 90 second irradiation with **57**-treated samples, while an irradiated rapamycin control showed no decrease, suggesting that this reduction was a result of light-induced oxidation.

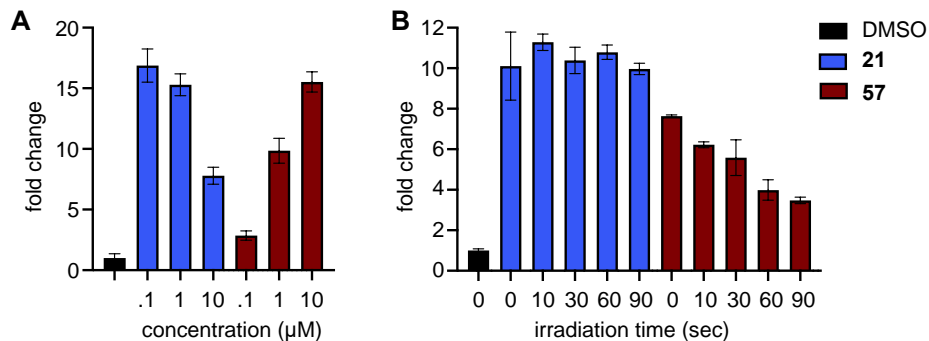


Figure 6-7 Application of **57** in a split luciferase reporter

a) Rapamycin analog **57** was validated as a functional dimerizer in cells by testing a range of concentrations in the split luciferase reporter. We found that 100 nM of **21** and 10 µM of **15** elicited optimal activity, and as such, were used in the subsequent experiment. b) Cells were treated with the optimal concentration of each compound and irradiated with 530 nm light for various amounts of time. A decrease in luminescence was observed with increasing irradiation times for **57**-treated cells, while no light-induced effect was seen in the **21**-treated control. Average signal intensity is plotted with error bars representing standard deviation. Experiment was performed by Chasity Hankinson.

After demonstrating we could control a split enzyme, we wanted to further showcase the utility in a translocation-based assay. We utilized the membrane reporter consisting of Lyn₁₁-FKBP_{x2}-CFP and YFP-FRB (introduced in Figure 5-16a) to visualize dimerization of FKBP and FRB through monitoring co-localization of CFP and YFP at the plasma membrane.⁴³⁹ When cells expressing the reporter were treated with **21** or **57**, YFP-FRB translocated to the membrane as a result of ternary complex formation as observed in epifluorescence imaging (Figure 6-8). Treatment with 20 µM of **21** or **57** resulted in the most efficient translocation to the membrane within a reasonable time frame, so this concentration was used in all subsequent translocation assays.

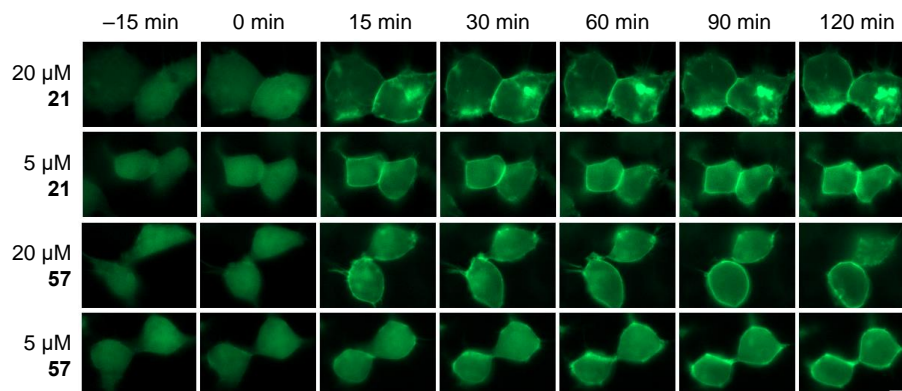


Figure 6-8 Validation of the dimerization efficiency of **57** in the membrane translocation reporter HEK293T cells expressing both YFP-FRB and Lyn₁₁-FKBP_{x2}-CFP in a 1:1 ratio were treated with either **21** or **57** at both 5 and 20 μ M concentrations. Epifluorescent images were acquired over the course of two hours to monitor for membrane translocation and the YFP images are provided here pseudocolored in green. Treatment with 20 μ M of **57** resulted in the most rapid membrane accumulation, thus this concentration was utilized in subsequent experiments. Scale bar = 10 μ M.

Next, light-inactivation experiments with **57** in the membrane reporter were performed by Chasity Hankinson. Briefly, HEK293T cells expressing the reporter were treated with 20 μ M of **21** or **57**, followed by a 2-hour incubation period to allow for ternary complex formation and two 1-hour washes to remove any excess, unbound dimerizer. Irradiations were performed using a DsRed filter (550/25 nm) on the microscope and images were acquired for two hours. Quantification of mean fluorescence intensity over time revealed a \sim 30% decrease in the irradiated, **57**-treated sample, but no change in any of the controls (Figure 6-9). This experiment validates that both compound treatment with **57** and irradiation with 530 nm light are necessary for deactivation of the ternary complex to occur.

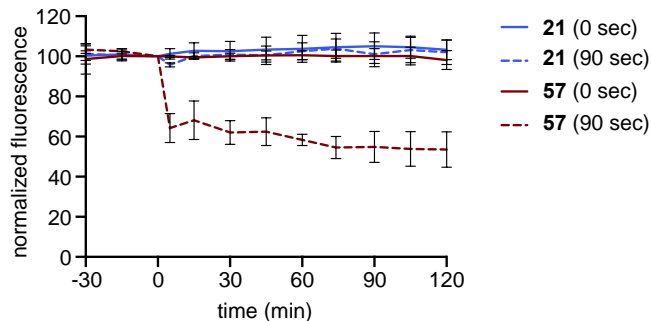


Figure 6-9 Light-induced deactivation of fluorescent membrane reporter proteins using **57**

HEK293T cells expressing the membrane reporter in a 3:1 FKBP:FRB ratio were treated with either **21** or **57** at 20 μ M concentrations for two hours, followed by two one-hour washes, and then irradiated with a DsRed filter to monitor for disappearance of fluorescence. Quantification of the mean CFP signal intensity over times shows a reduction of fluorescence upon a 90 second irradiation of **57**-treated cells, while all other conditions showed no decrease in fluorescent signal. Average signal intensity is plotted with error bars representing standard deviation. Data was collected and analyzed by Chasity Hankinson.

To further investigate the effects of **57** using the membrane reporter, protein levels were analyzed via western blot. HEK293T cells expressing the membrane reporter system were treated with 20 μ M of **21** or **57**, followed by a 2-hour incubation period and two 1-hour washes. Cells were irradiated using a 530 nm LED and incubated for an additional 2 hours. Following cell lysis and protein denaturation, western blot analysis was performed. To visualize the levels of Lyn₁₁-FKBP_{x2}-CFP and YFP-FRB, a GFP antibody was utilized, and to monitor two housekeeping proteins, GAPDH and nucleolin, their corresponding antibodies were employed. Both Lyn₁₁-FKBP_{x2}-CFP and YFP-FRB signals decrease in response to increasing irradiation time when treated with **57**, but not rapamycin. This data suggests **57** is selectively deactivating the proteins of interest (Figure 6-10a).

To further validate the results of decreased fluorescence observed in the micrographs, a similar experiment as just described was performed; however, the samples were not boiled in order to avoid denaturing the fluorescent proteins. The samples were analyzed by SDS-PAGE and imaged using a ChemiDoc equipped with a GFP filter (560/50 nm) to visualize in-gel fluorescence.

For both Lyn₁₁-FKBP_{x2}-CFP and FRB-YFP the same trend applies in which an increase in irradiation time corresponds to a decrease in protein signal (Figure 6-10b).

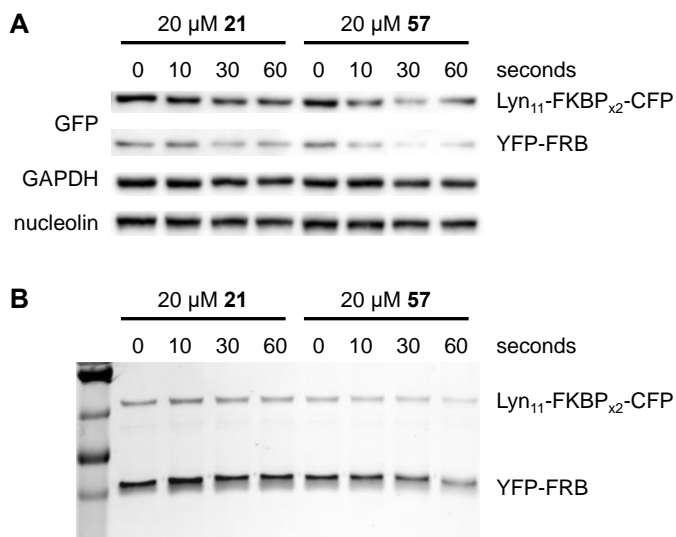


Figure 6-10 Western blot analysis of light-induced oxidation using **57** in a membrane reporter

a) HEK293T cells expressing the membrane reporter in 3:1 ratio were treated with 20 μM of **21** or **57** for two hours, followed by two one-hour washes prior to irradiating with 530 nm light. Western blot analysis using anti-GFP, anti-GAPDH, and anti-Nucleolin antibodies was performed. A decrease in signal is observed with **57**, but not the rapamycin treatment. b) Prior to denaturing samples for western blot, an aliquot of native proteins was collected and used to analyze in-gel fluorescence. As above, a decrease in signal is observed with **57**, but not the rapamycin treatment. Data in Panel b was generated by Chasity Hankinson.

Next, we wanted to elucidate the mechanism through which deactivation and/or degradation was occurring. We hypothesized that the oxidized and inactive proteins might be shuttled to the proteasome to result in degradation, thus explaining the decrease in signal we observe by blotting. To investigate this, two known proteasome inhibitors MG132⁴⁷⁰ and epoxomicin⁴⁷¹ were employed. If protein degradation was occurring via an active proteasome, no decrease in signal would be observed in the presence of an inhibitor. HEK293T cells expressing the membrane reporter were treated with 20 μM of **57** for two hours, then washed twice for one hour each time (with and without 10 μM of inhibitor), then irradiated as described previously. The same sample preparation was followed, and protein levels were detected via western blot. When treated with either MG132 or epoxomicin, a decrease in signal is still observed for the proteins of

interest (Figure 6-11), thus suggesting that an active proteasome is not required for the decreased signal we observed.

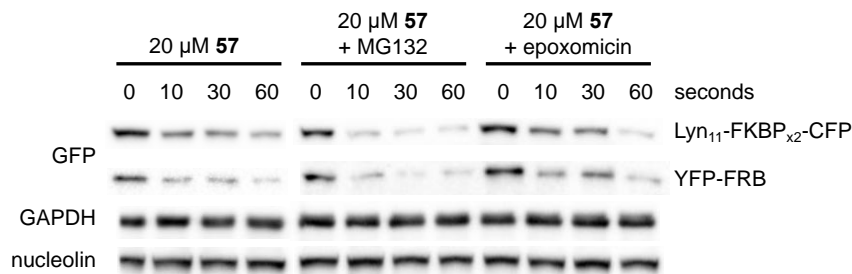


Figure 6-11 Western blot analysis of **57** in the membrane reporter with a proteasome inhibitor. Proteasome inhibitors MG132 and epoxomicin were used in the membrane reporter assay to test if an active proteasome was required for the observed loss of signal. A decrease in both Lyn₁₁-FKBP_{x2}-CFP and YFP-FRB were still observed in the presence of inhibitor, thus suggesting that an active proteasome is not required.

We hypothesized that the proteins are simply being rendered inactive through oxidation, but not to an extent as to trigger rapid degradation, and therefore are not recognized efficiently by the antibodies. Since oxidation could be occurring via singlet oxygen generation or by superoxide radical formation, we tested whether protein levels would be retained in the presence of different ROS scavengers. Sodium azide and sodium pyruvate act as quenchers of singlet oxygen⁴⁷² and hydrogen peroxide,⁴⁷³ respectively. HEK293T cells expressing the membrane reporter were treated with 20 μM of **57** for two hours, followed by two 1-hour washes (with and without 10 mM of scavenger), followed by irradiation. Western blot analysis was performed as before. When treated with **57** in the presence of sodium azide, no decrease in GFP or nucleolin signal was observed (Figure 6-12). This validates that singlet oxygen is required for the observed protein oxidation. Sodium pyruvate does not appear to block degradation as efficiently as sodium azide.

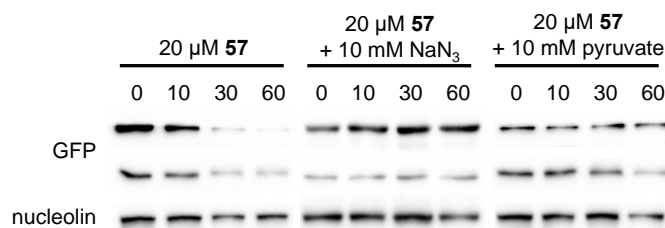


Figure 6-12 Determination of type of ROS being generated upon light-induced oxidation in the membrane reporter. To validate whether oxidation proceeds through the Type I or II pathways, two different scavengers were employed. HEK293T cells expressing the membrane reporter were treated with **57** in the presence and absence of NaN₃ or sodium pyruvate. Following irradiation with 530 nm light to induce oxidation, western blot analysis was performed. Sodium azide functions to block loss of signal, while sodium pyruvate has less of an effect, thus supporting that **57**-induced signal loss requires the generation of singlet oxygen.

An XTT cell viability assay was performed to ensure the generation of ROS has no effect on overall cell health. This assay showed **57** has no effect on cell viability up to 72 hours. Non-transfected HEK293T cells and HEK293T cells expressing the membrane reporter were treated with 20 μM of **21** or **57**, followed by a 2-hour incubation period and two 1-hour washes. Cells were irradiated using a 530 nm LED, followed by a 72-hour incubation period, then an XTT assay was performed (Figure 6-13). Absorbance values were normalized such that non-irradiated **57**-treated cells were equal to 100%. No decrease in normalized absorbance is observed in cells treated with **57** even upon irradiation and oxidation. A decrease in rapamycin cell viability was observed for non-transfected cells, but no effect due to the LED was seen. This is consistent with literature reports of rapamycin-induced cell toxicity in a variety of different cell lines upon prolonged treatment.⁴⁷⁴⁻⁴⁷⁶

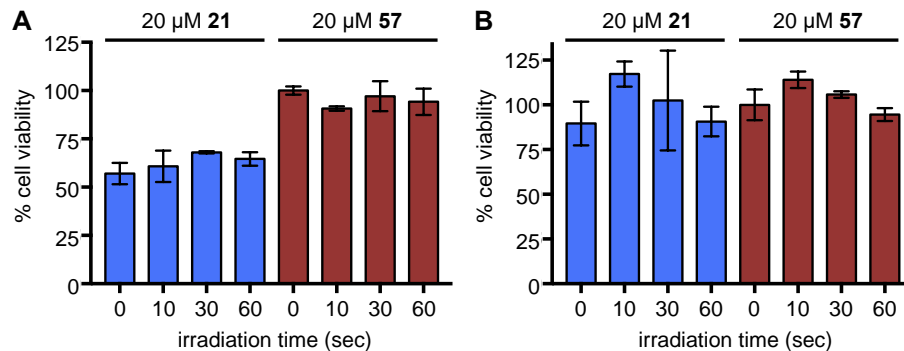


Figure 6-13 XTT cell viability assay with **57** in non-transfected and membrane reporter transfected cells. Non-transfected (a) or membrane reporter transfected (b) HEK293T cells were incubated with 20 μ M of **21** or **57** for two hours, then washed twice for one hour each time, and irradiated for the indicated time. Cells were maintained in the incubator for an additional 72 hours prior to cell viability testing with an XTT assay. No apparent toxicity was observed for the irradiated **57**-treated samples. Average signal intensity is plotted with error bars representing standard deviation.

6.2 Summary and Outlook

In summary, we have developed a BODIPY-modified rapamycin analog **57** capable of generating singlet oxygen to oxidize an FKBP-FRB induced protein-protein interaction upon irradiation with 530 nm light. While formation of the FKBP-rapamycin-FRB ternary complex has proven to be a useful tool for activating split-proteins or inducing protein-protein interactions, this has up until this point been an essentially irreversible process. By harnessing the ROS-generating capability of the BODIPY chromophore, we demonstrate that oxidation by singlet oxygen can inactivate a split luciferase enzyme and a fluorescent membrane reporter in HEK293T cells.

6.3 Methods

Reagent preparation. Stock solutions of **21** and **57** were generated at 2.86 mM (5 mg/mL for the BODIPY-PEG-rapamycin) in sterile-filtered DMSO and stored at -20°C . Unfortunately, due to limited solubility, the typical 5 mM stock solution could not be prepared for **57**.

DPBF singlet oxygen assay. DPBF (**4**, Acros) was prepared at 100 mM in DMSO and aliquots were frozen at -20°C . A working stock solution (10 mM) was prepared by diluting 10 μL of the 100 mM solution into 90 μL of DMSO. The “**4** only” sample was prepared by combining 15 μL of 10 mM DPBF, 60 μL of DMSO, and 1425 μL of 1X PBS (pH 7.4). The “**4** + **57**” sample was prepared by combining 15 μL of 10 mM **4**, 5 μL of 2.86 mM **57**, 55 μL of DMSO, and 1425 μL of 1X PBS (pH 7.4). This preparation yielded 100 μM **4** \pm 10 μM **57** in a 5% DMSO solution. To a black 96-well flat-bottomed plate, 100 μL of each prepared solution was transferred to 12 separate wells (24 wells total). Wells were irradiated for 0, 10, 30, or 60 seconds in triplicate using a 530 nm LED (Mouser Electronics, LUMILEDS LXML-PM01-0100) set at 700 mA. DPBF fluorescence was monitored using ex. 417/5 and em. 487/5 nm on a Tecan M1000 plate reader. The three independent wells were averaged and values were normalized such that the 0 second sample was equal to 100 percent. Error bars represent standard deviation of the three replicates.

Gel-shift dimerization assay. Bacterial expression of FKBP-YFP-His and FRB-CFP-His were performed as described in Section 5.5.1. FKBP-YFP-His and FRB-CFP-His were diluted to 10 μM in assay buffer (20 mM Tris-HCl pH 7.4, 100 mM NaCl, 10% glycerol). A master mix of 1:1 FKBP-YFP-His and FRB-CFP-His was prepared by mixing 300 μL of each 10 μM protein sample (600 μL total of 5 μM FKBP/FRB) and 18 μL were transferred to 0.2 mL tubes. Compound solutions (**21**, **56** or **57**) were prepared at 10X (2.5 mM to 0.01 mM) in water (except 1 and 2.5 mM were in DMSO) of the desired final concentrations (250 μM to 1 μM) and 2 μL was added to

the protein mixture. Samples were incubated for 2 hours at room temperature. After, 8 μ L of 4X Laemmli buffer without reducing agent (200 mM Tris-HCl pH 6.8, 8% SDS, 40% glycerol, 0.08% bromophenol blue) was added to each sample. The entire 28 μ L of sample was loaded and resolved on 10% native-PAGE gels with a 5% stacking gel on ice for 20 minutes at 60 V followed by 80 minutes at 150 V. The gel was Coomassie stained and imaged using a BioRad ChemiDoc system. Images were processed using the BioRad Image Lab software.

Split-luciferase reporter assays. HEK293T cells were plated at 200,000 cells per well in a 6-well clear bottom plate and grown at 37 °C, 5% CO₂ in 2 mL per well of Dulbecco's modified Eagle's media (DMEM) supplemented with 10% FBS and 1% streptomycin/penicillin. At 80% confluence, the media on the cells was replaced with 2 mL of DMEM (+ 10% FBS) in preparation for transfection. CLuc-FKBP and FRB-NLuc in a 2:1 ratio (2667 ng FKBP:1333 ng FRB) at 4000 total ng (2000 ng/well) were diluted into 500 μ L of OptiMEM. Lipofectamine 2000 (10 μ L) was diluted into 500 μ L of OptiMEM in a separate tube. These two solutions were incubated at room temperature for 5 minutes, the Lipo/OptiMEM solution was mixed into the DNA/OptiMEM solution and mixed by inverting. Following a 20 minute room temperature incubation, 500 μ L of transfection mix was added to each well (two wells were transfected identically). Approximately 18 hours after transfection, the media was carefully removed, and the cells were lifted with 500 μ L of TrypLe and combined in a 15 mL conical tube. The addition of 9 mL of DMEM inactivated TrypLe. Cells were pelleted at 1,000 g for 10 minutes at room temperature. DMEM was removed and cells were resuspended in 1 mL of Live Cell Imaging Solution (LCIS). Cells were counted on a hemocytometer using Trypan Blue (to avoid counting dead cells). Cells were re-plated at 10,000 cells per well in a black, clear bottom 96-well plate in 90 μ L of LCIS.

Membrane translocation reporter – validation of dimerization. HEK293T cells were plated at 10,000 cells per well in a PDK-treated black, clear bottom 96-well plate and grown at 37 °C, 5% CO₂ in 100 µL per well of DMEM (+ 10% FBS, + 1% streptomycin/penicillin). At 80 confluency, cells were transfected using linear polyethyleneimine (LPEI). The media on the cells was replaced with 100 µL of DMEM (+ 10% FBS) in preparation of transfection. A batch transfection mix was prepared for 12 wells as to avoid pipetting small volumes of reagents. Lyn₁₁₁-FKBP_{x2}-CFP and YFP-FRB in a 3:1 ratio (1800 ng FKBP:600 ng FRB) at 2400 total ng (200 ng/well) were diluted into 240 µL of OptiMEM. LPEI (24 µL of a 0.5 mg/mL stock solution) at 12,000 total ng (1000/well) was added and the transfection solution was mixed by inverting, followed by a 20-minute room temperature incubation. Transfection mix (20 µL) was added to each well (12 wells were transfected identically). Approximately 18 hours after transfection, a 10X stock solution of each **21** and **57** were made at both 50 µM and 200 µM in DMEM (– phenol red, + 10% FBS). The media was carefully removed and replaced with 90 µL of DMEM (– phenol red, + 10% FBS). The plate was imaged on a Zeiss Axio Observer Z1 microscope (20X objective, NA 0.8 Plan-Apochromat) with a GFP (filter set 38 HE; ex. BP 470/40; em. BP 525/50 nm) filter cube, with an HBO 100 lamp as a light source. Images were acquired every 15 minutes (from 15 minutes pre-treatment to 120 minutes post-addition). Cells were treated at 5 µM and 20 µM concentrations of each compound by carefully adding 10 µL of the appropriate 10X stock solution to each well. Image processing and analysis was performed in FIJI.

Western blot analysis of light-induced deactivation. HEK293T cells were plated at 100,000 cells per well in 8 wells of a clear bottom 12-well plate and grown at 37 °C, 5% CO₂ in 1 mL per well of DMEM (+ 10% FBS, + 1% streptomycin/penicillin) until 80% confluent. Media was replaced with 1 mL of DMEM (+ 10% FBS) in preparation for transfection. A batch transfection

mix was prepared for each treatment condition (4 wells per condition) as to avoid any variation in transfection efficiency. Lyn₁₁-FKBP_{x2}-CFP and YFP-FRB in a 3:1 ratio (3000 ng FKBP:1000 ng FRB) at 4000 total ng (1000 ng/well) were diluted into 400 μ L of OptiMEM. LPEI (40 μ L of a 0.5 mg/mL stock solution) at 20,000 total ng (5000/well) was added and the transfection solution was mixed by inverting, followed by a 20-minute room temperature incubation. Transfection mix (100 μ L) was added to each well. Approximately 18 hours after transfection, 20 μ M solutions of **21** and **57** were made in DMEM (– phenol red, + 10% FBS) to allow for 500 μ L of compound solution for each well. The media was carefully removed and replaced with 500 μ L of the appropriate compound solution, followed by a 2-hour incubation period. Media was carefully removed and replaced with 1 mL of LCIS for two 1-hour washes to remove any residual unbound compound. Cells were irradiated for 0, 10, 30 or 60 seconds using a 530 nm LED (using a foil mask to ensure illumination of only the specified well), followed by a 2-hour incubation period in the absence of light.

After this time, the 12-well plate was placed on ice and the cells were lifted and transferred to Eppendorf tubes using the 1 mL of media, and cells were pelleted at 10,000 g for 2 minutes at 4 °C and the supernatant discarded. Cells were resuspended in 100 μ L of ice-cold RIPA lysis buffer (150 mM NaCl, 1.0% NP-40, 0.5% sodium deoxycholate, 0.1% SDS, 50 mM Tris pH 8.0) with 1X Halt protease inhibitor cocktail and placed on an orbital shaker (still on ice) for 15 minutes to completely lyse cells. Cellular debris was pelleted at 15,000 g for 7.5 minutes at 4 °C and 72 μ L of each supernatant was transferred to a 0.2 mL tube. Samples were mixed with 30 μ L of 4X Laemmli sample buffer (recipe above + 4% β -mercaptoethanol). At this point, 15 μ L of each sample was removed for in-gel fluorescence analysis. The remaining samples were then heated at 95 °C for 10 minutes to denature proteins. Each sample (15 μ L) was resolved on a 10% SDS-

PAGE gel with a 4% stacking gel on ice at 60 V for 20 minutes followed by 150 V for 80 minutes, then transferred to a 0.45 μ M PVDF membrane at 80 V for 105 minutes in Towbin buffer (25 mM Tris-HCl, 192 mM glycine, 20% methanol). Membranes were blocked for 2 hours with 5% milk in TBST (0.1% Tween-20 in 1X tris-buffered saline). After this time, one membrane was cut in half horizontally at the 70 kDa marker. The top half of the membrane was probed with anti-nucleolin and the bottom half was probed with anti-GAPDH, while another entire membrane was probed with anti-GFP. Anti-GFP was diluted 1:5,000 and anti-GAPDH was diluted 1:5,000 in 5% milk in TBST, while anti-nucleolin was diluted 1:2,000 in TBST (6 mL of each were prepared). The membranes were incubated with the appropriate primary antibodies overnight with rocking in a cold room. The following day, membranes were washed with TBST (3 x 10 mL), then a secondary antibody solution (goat anti-rabbit HRP) was prepared using 1:10,000 dilution in TBST (10 mL). The secondary antibody solution was applied, and membranes were incubated at room temperature for 1 hour with rocking. Membranes were again washed with TBST (3 x 10 mL). Membranes were then developed using SuperSignal West Pico PLUS Chemiluminescent Substrate for 5 minutes and imaged on a BioRad ChemiDoc system using the Chemi Hi Sensitivity setting. Images were processed using the BioRad Image Lab software.

Cell viability assay. HEK293T cells were plated at 10,000 cells per well in a PDK-treated black, clear bottom 96-well plate and grown at 37 °C, 5% CO₂ in 100 μ L per well of DMEM (+ 10% FBS, + 1% streptomycin/penicillin). At 80 confluence, half of the plate of cells was transfected using LPEI as detailed previously. The other half of the plate had the media changed and was maintained as a non-transfected sample. The next day, cells were treated with 20 μ M of **21** or **57** for two hours, followed by two 1-hour washes. The media was replaced with 100 μ L of DMEM (–phenol red, + 10% FBS), then a subset of wells was irradiated for 0, 10, 30, or 60 seconds (in

both the membrane reporter transfected wells and the non-transfected samples). The plate was maintained in the 37 °C, 5% CO₂ incubator for an additional 72 hours. An XTT cell viability assay was performed by adding 40 µL of the activated XTT reagent (8 µL of 1.7 mg/mL menadione diluted into 1 mL of 1 mg/mL XTT reagent solution) to each well. Absorbance was measured at 450 nm and 630 nm (background) on a Tecan M1000 plate reader immediately following reagent addition. Cells were placed back in the incubator for four hours, then final absorbance measurements were taken. The background absorbance was subtracted from each well, then absorbance was normalized such that the non-irradiated sample equaled 100% cell viability. Averages are reported with standard deviation.

7.0 Reversible Optical Switching of Rapamycin-Induced Protein Dimerization

The material in Section 7.1 was reprinted in its entirety with permission from **Courtney, T. M.**; Horst, T. J.; Hankinson, C. P.; Deiters, A. *Org. Biomol. Chem.* **2019**, *17*, 8348–8353.

7.1 Arylazopyrazole-modified Rapamycin Analogs

Since most biological processes occur reversibly in a highly-regulated spatiotemporal manner (for example, regulation of the MEK/ERK pathway by protein phosphatases),⁴⁷⁷⁻⁴⁷⁸ it would be beneficial to develop tools that enable chemical biologists to control cycles of protein dimerization/localization with light. To date, truly reversible control of rapamycin-induced dimerization has yet to be achieved in mammalian cells. Wandless and Crabtree demonstrated reversibility through addition of a large excess of FK506M, which acts by outcompeting rapamycin and inducing proteasomal degradation, requiring 9 hours for depletion in mice.⁴⁴¹ Lee utilized a similar approach of outcompeting with a 50-fold excess of FK506 and observed slightly faster loss of dimerization.⁴⁷⁹ Interestingly, in yeast, formation of rapamycin-induced dimerization can be reversed in 20 minutes by removal of rapamycin from the cells by switching to drug-free media.^{443, 480} Taken together, these approaches allow for a single on-then-off cycle of dimerization, but at a timescale that is often not amenable for dissecting dynamic biological processes. Additionally, several photocaged rapamycin analogs have been developed that allow for off-to-on control of dimerization (discussed extensively in sections 5.1.2, 5.4, and 5.5).

Therefore, we aimed to develop the first rapamycin analogs that would enable multiple cycles of activation and deactivation of ternary complex formation that could be applied to existing FKBP/FRB systems. In order to render rapamycin reversibly switchable, we envisioned that addition of a diazobenzene or arylazopyrazole (AAP) light-switchable moiety to rapamycin would enable reversible control using light. Azobenzenes have been applied to a wide range of biological processes including reversible control of transcription factors, protein-protein interactions of α -helices, cell membrane receptors, catabolite-binding proteins, DNA duplex formation, RNA aptamers and several others.^{13, 222, 229, 234, 481-484} However, the arylazopyrazole (discussed previously in Section 4.2) is a recently developed photoswitchable group with improved photostationary states and slower thermal reversion compared to traditional azobenzenes.²³⁷ Arylazopyrazoles utilize switching wavelengths of *trans*-to-*cis* (365 nm) and *cis*-to-*trans* (530 nm) and we decided to focus on developing arylazopyrazole modified rapamycin analogs. Although non-methylated arylazopyrazoles provide longer thermal stability (1000 days with 3,5-H vs 10 days with 3,5-CH₃), we decided to use dimethylated analogs as they display near quantitative switching between the two stereoisomers.²⁴⁰ Since prediction of the molecular interactions of the *cis*- vs *trans*-AAP modified-rapamycin analogs with FKBP/FRB is impossible, we made no initial assumptions regarding which isomer, if either, would allow for ternary complex formation.

We synthesized five AAP-modified rapamycin analogs for subsequent biological testing. Both alkyl and aryl substituents were utilized in order to cover a broad steric range from a small methyl to a bulky naphthyl group. Modification at the *N*-1 position was selected due the synthetic versatility of using various hydrazines to generate a small panel of analogs. Although the methyl groups at positions 3 and 5 could be varied depending on the dione used in the condensation reaction, we avoided modifying these positions with bulkier substituents which could adversely

affect *trans*-to-*cis* switching. The five analogs were synthesized following similar procedures by Trevor Horst, a fellow Deiters lab member (Figure 7-1).

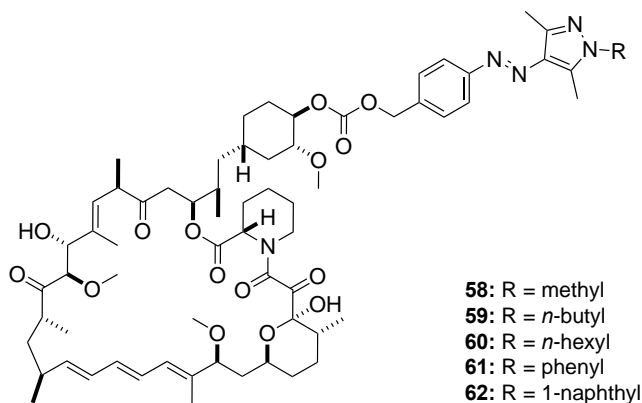


Figure 7-1 Five arylazopyrazole-modified rapamycin analogs were synthesized. A combination of both alkyl and aryl substituents at the *N*-1 position were synthesized by Trevor Horst.

The photostationary states and thermal stabilities were determined by $^1\text{H-NMR}$ (Table 7-1). Solutions of the five AAP analogs were prepared in 20% D_2O :80% $\text{d}_6\text{-DMSO}$ at 4 mM concentration. Unfortunately, due to the poor aqueous solubility of rapamycin, we were unable to generate more physiologically-relevant solvent conditions for these photoswitching studies. A UV transilluminator (365 nm) was used for irradiations when determining the photostationary state (PSS) of the *trans*-to-*cis* conversion. A 530 nm LED was utilized for the *cis*-to-*trans* isomerization. For *cis*-thermal stability studies, the solutions were irradiated with 365 nm light until the PSS was reached, then maintained at 37 °C and NMR spectra were acquired every 24 hours. This data was collected by Trevor Horst and Chasity Hankinson, also a Deiters lab member.

Table 7-1 Characterization of the PSS at 365 nm and 530 nm irradiation and thermal stability of the AAP-rapamycin analogs

	<i>trans</i> : <i>cis</i> (365 nm)	<i>trans</i> : <i>cis</i> (530 nm)	<i>cis</i> half-life at 37 °C
58	6 : 94	93 : 7	1.3 days
59	13: 87	91 : 9	1.7 days
60	16 : 84	92 : 8	2.8 days
61	11 : 89	98 : 2	1.7 days
62	10 : 90	94 : 6	3.6 days

The AAP-rapamycin analogs were tested in cells using a split luciferase reporter. The split luciferase reporter was chosen because activity can easily be quantified with high sensitivity and linearity across several orders of magnitude. Additionally, the reporter works well with low (nanomolar) concentrations of rapamycin as opposed to translocation reporters which require micromolar ligand (data not shown). This reporter utilizes the N-terminus of a split firefly luciferase fused to FRB, while the C-terminus is attached to FKBP.³⁷⁸ When co-expressed in HEK293T cells, addition of rapamycin generates the FKBP-rapamycin-FRB ternary complex and brings the two luciferase halves in close proximity in order to reconstitute the active enzyme (Figure 7-2a).

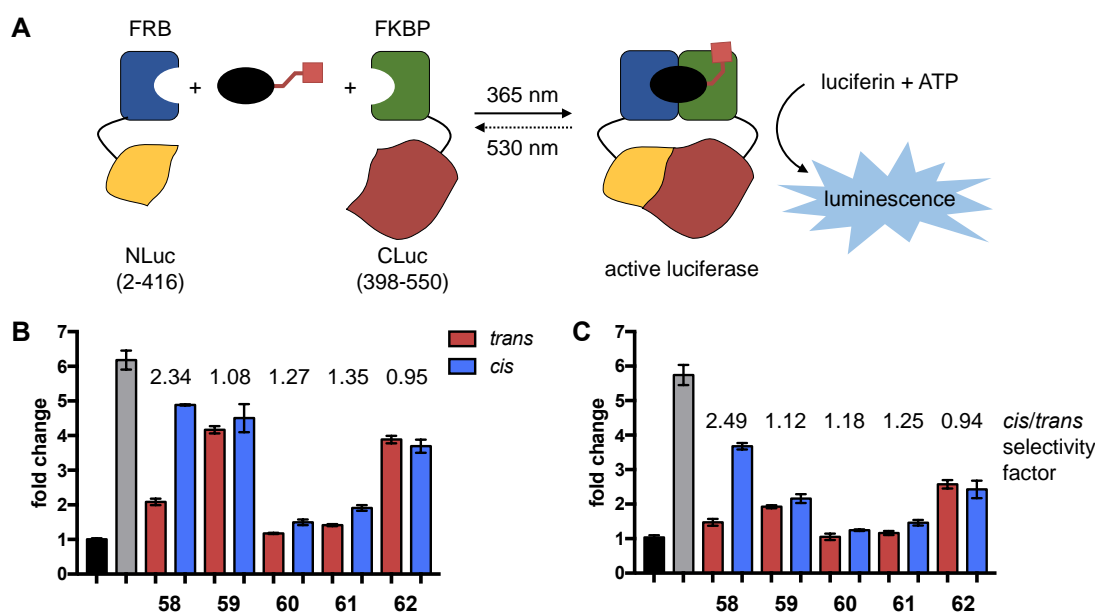


Figure 7-2 A split luciferase reporter was used to test the efficacy of the photoswitchable rapamycin analogs a) A schematic of the split luciferase reporter is provided. In the presence of the *trans*-isomer, minimal ternary complex formation is expected; however, upon generation of the *cis*-isomer and ternary complex formation, an active luciferase is formed. In theory, irradiation with 530 nm light should regenerate the inactive, *trans*-isomer (indicated with a dotted arrow). b-c) HEK293T cells expressing the split luciferase reporter were treated with pre-formed *cis*- or *trans*-isomers at 100 nM (b) or 25 nM (c) for 2.5 hours, then luciferase substrates were added and luminescence was measured. Black bars represent the DMSO control and grey bars represent rapamycin. Raw values were normalized to DMSO and error bars represent standard deviations from experiments conducted in triplicate. Reproduced from Courtney *et. al.*, *Org. Biomol. Chem.* **2019**, 17, 8348-8353. Copyright 2019 The Royal Society of Chemistry.

HEK293T cells expressing the split luciferase reporter were treated with pre-formed *cis*- and *trans*-isomers of the five AAP-analogs, incubated for 2.5 hours, and lysed. Luciferase substrates were added and recorded luminescence values were normalized to DMSO (negative control) (Figure 7-2b-c). While most the stereoisomers of **59-62** did not show significant differential activity, the methyl analog **58** was >2-fold more active as the *cis*-isomer compared to the *trans* isomer at both 100 nM and 25 nM concentrations. The larger alkyl and aryl modifications resulted in a loss of isomer selectivity, and the *n*-butyl and 1-naphthyl isomers only allowed for moderate ternary complex formation for both the *cis*- and *trans*-isomers. Overall, *cis*-**58** displayed 80% and 65% activity compared to unmodified rapamycin at 100 nM and 25 nM, respectively.

Based on the encouraging results of our preliminary testing with wild-type FKBP, we wanted to explore whether FKBP protein engineering would result in further improved enhancement of ternary complex formation for one isomer over the other. Based on our previous experience with iFKBP,^{71, 400} we generated the corresponding CLuc-iFKBP expression construct to use in the split enzyme reporter. When cells co-expressing the CLuc-iFKBP and FRB-NLuc reporter were treated with rapamycin or the pre-formed *cis*- or *trans*-**58** for 2.5 hours, no dimerization was observed for either isomer at concentrations as high as 5 μ M (Figure 7-3). iFKBP requires higher compound concentration due to the decreased affinity for rapamycin.

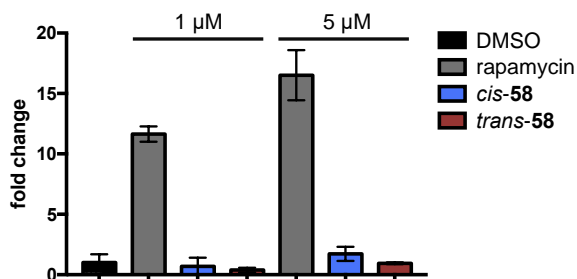


Figure 7-3 Split luciferase variant (iFKBP) was used for testing **58**
a) HEK293T cells expressing the split luciferase reporter (with CLuc-iFKBP and FRB-NLuc) were treated with pre-formed *cis*- or *trans*-isomers of **58** at 1 and 5 μ M for 2.5 hours, then luciferase substrates were added and luminescence was measured. Black bars represent the DMSO control and grey bars represent rapamycin. Raw values were

normalized to DMSO and error bars represent standard deviation of three replicates. Reproduced from Courtney *et al.*, *Org. Biomol. Chem.* **2019**, 17, 8348-8353. Copyright 2019 The Royal Society of Chemistry.

Since no improvement in selectivity was achieved with iFKBP, we looked into alternative approaches to modify FKBP. We analyzed the crystal structure of FKBP-rapamycin-FRB (PDB: 1FAP)³⁶³ to find residues that were proximal to the C-40 hydroxyl of rapamycin (the position where the AAP-moiety was appended). We selected glutamine 53 to mutate to phenylalanine and to tryptophan with two different rationales in mind: (1) increase in steric bulk would reduce the background binding of the *trans*-isomer or (2) introduction of π - π stacking opportunities would preferentially stabilize one isomer over the other (Figure 7-4a). Cells co-expressing either CLuc-FKBP Q53F or Q53W with FRB-NLuc were treated with rapamycin or pre-formed *cis*- or *trans*-**58** at 25 nM for 2.5 hours (Figure 7-4b). No significant reduction in *trans*-**58** background activity was observed and no significant increase in *cis/trans* preferential complexation was obtained. Unfortunately, neither of these approaches resulted in any improvement, thus we proceeded with additional testing of the methyl-AAP analog **58** with wild-type FKBP.

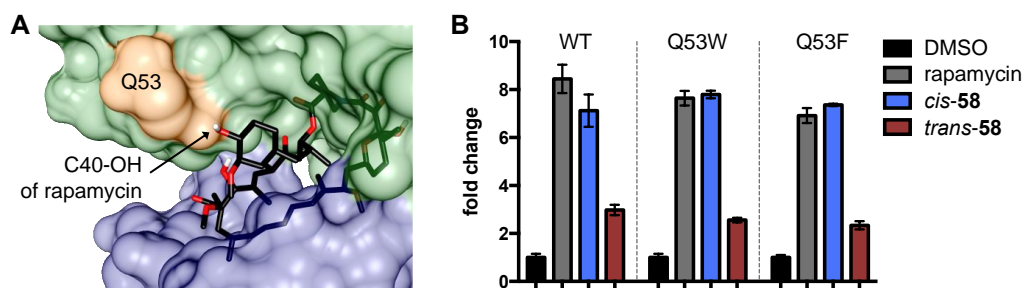


Figure 7-4 Split luciferase variants (point mutations made in FKBP) were used for testing **58**. Either CLuc-FKBP, CLuc-FKBP_{Q53F}, or CLuc-FKBP_{Q53W} were co-expressed with FRB-NLuc, and treated with 25 nM of pre-formed *cis*- and *trans*-**58**. Black bars represent the DMSO control and grey bars represent rapamycin. Raw values were normalized to DMSO and error bars represent standard deviation of three replicates. Reproduced from Courtney *et al.*, *Org. Biomol. Chem.* **2019**, 17, 8348-8353. Copyright 2019 The Royal Society of Chemistry.

Since the methyl analog displayed the highest degree of *cis/trans* selectivity when added to cells as the pre-formed isomers, we next tested whether this analog would allow for activation and/or deactivation of ternary complex formation by irradiating cells following the addition of

compound. We first validated that **58** could undergo multiple cycles of photoswitching without displaying fatigue or degradation (Figure 7-5). Reversible switching was performed four times by irradiating the sample alternatingly with 365 and 530 nm light, with ^1H NMR analysis performed after every irradiation step (experiment conducted by Chasity Hankinson).

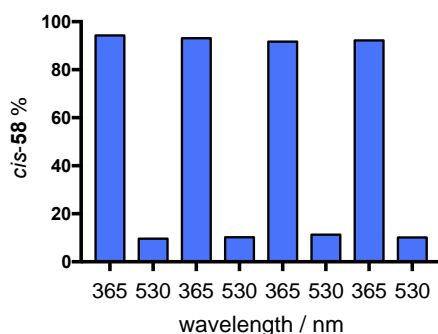


Figure 7-5 The photocycling stability of **58** was analyzed. Photoswitching of analog **58** in $\text{D}_2\text{O}/d_6\text{-DMSO}$ (1:4) demonstrated robust switching with fatigue resistance following irradiations with both 365 and 530 nm light over four cycles, as measured by NMR. Experiment was performed by Chasity Hankinson. Reproduced from Courtney *et. al.*, *Org. Biomol. Chem.* **2019**, 17, 8348-8353. Copyright 2019 The Royal Society of Chemistry.

To test the turn-on ability of **58**, cells expressing the split luciferase reporter were treated with the *trans*-isomer for one hour. A fraction of the cells was irradiated using a 365 nm UV transilluminator for 0.5, 1, or 2 minutes. Incubation was performed for an additional 90 minutes (for 2.5 hours total) to allow for ternary complex formation, then cells were lysed, luciferase substrates were added, and luminescence was measured. Gratifyingly, we observed significant off-to-on activation in this experiment with minimal adverse effect of the UV exposure as seen by the irradiated rapamycin control (Figure 7-6a).

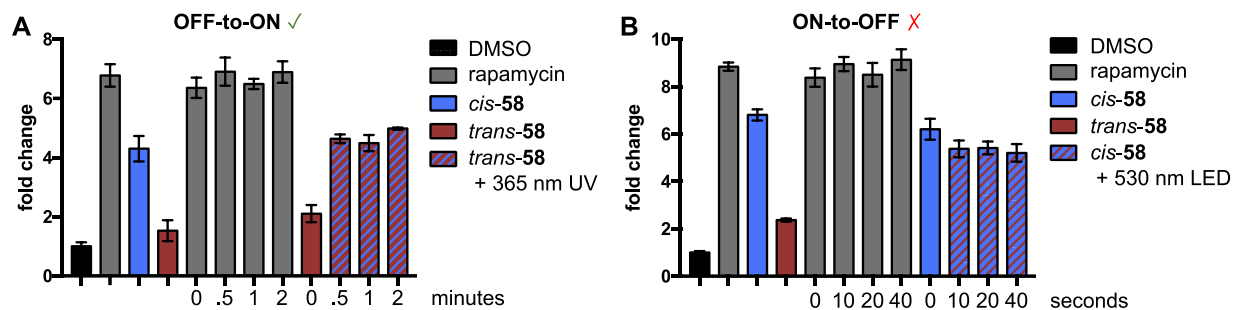


Figure 7-6 Assessment of reversibly controlled ternary complex formation with **58** in the split luciferase assay a) HEK293T cells expressing the split luciferase reporter were treated with the pre-formed *trans*-isomer for one hour. Irradiation to generate the *cis*-isomer was performed using a UV transilluminator and cells were incubated for an additional 90 minutes to allow for ternary complex formation. Successful off-to-on activation was achieved. b) HEK293T cells expressing the split luciferase reporter were treated with the pre-formed *cis*-isomer for one hour. A handheld 530 nm LED was used to convert to the *trans*-isomer and cells were incubated for an additional 90 minutes. Interestingly, minimal on-to-off activity was observed. Reproduced from Courtney *et al.*, *Org. Biomol. Chem.* **2019**, 17, 8348-8353. Copyright 2019 The Royal Society of Chemistry.

After demonstrating that the system could be turned on in cells, we wanted to explore the turn-off nature of this analog. For this, cells expressing the split luciferase reporter were treated with the pre-formed *cis*-isomer for one hour to allow for uptake and initial complex formation. Irradiations were then performed with a 530 nm LED for 10, 20, or 40 seconds to intracellularly generate the *trans*-isomer, followed by incubation for an additional 90 minutes. Interestingly, the luminescence readout showed no significant decrease in signal, indicating the inability to optically break up the FKBP-rapamycin-FRB complex (Figure 7-6b). We hypothesize that isomerization to the *trans*-isomer does not provide sufficiently unfavorable steric interactions to disrupt an already formed ternary complex that involves very high-affinity protein-ligand and protein-protein interactions with a K_d of 12 nM.³⁶⁴ A split luciferase reporter system with FKBP/FRB replaced with a kinase/kinase interacting peptide has previously been utilized for screening kinase inhibitors as detected by loss of luciferase activity,⁴⁸⁵ thus implicating that the inability to detect a decrease in luminescence here is a direct result of the FKBP-**58**-FRB complex remaining intact. Alternatively, the ternary complex that is formed with the *cis*-isomer could be oriented in such a way that *trans* isomerization is inhibited or minimized, although this is less likely to be the case.

Unfortunately, since these experiments are performed at very low compound concentrations in cells, monitoring absorbance to confirm isomerization is not possible.

In conclusion, five arylazopyrazole-modified rapamycin analogs were synthesized and their photoswitching properties were characterized. These analogs exhibit favorable switching properties with photostationary states that result in almost complete *cis* or *trans*-isomer formation depending on the irradiation wavelength. Moreover, they provided very high thermal stability with half-lives of greater than 1 day for the *cis*-isomer of all five analogs. Additionally, we demonstrated that the AAP results in fatigue resistance over eight alternating irradiations. In a split luciferase reporter, the methyl-substituted derivative provided ~2.5 fold enhancement in the FKBP-rapalog-FRB ternary complex formation for the photoswitched *cis*-isomer over the ground-state *trans*-isomer, comparing favorably to negative (DMSO) and positive (natural rapamycin) controls. The remaining four analogs did not induce ternary complex formation with any significant preference for one isomer over the other. We explored the methyl analog as a potential on/off light-switch and found that we could successfully turn on dimerization activity in cells through irradiation with 365 nm light; however, once the protein complex was formed, we were unable to turn off dimerization with this analog. The FRB-rapamycin-FKBP complex is extremely stable, which allows complete dimerization of a wide range of fusion proteins at low rapamycin concentration. Since previous reports had to use 50-fold excess of competing ligand to reverse the ternary complex over the course of several hours,⁴⁷⁹ reversing the complex through photoswitching of a small molecule ligand may not be achievable. In order to further develop systems that can undergo multiple cycles of dimerization activation/deactivation, we hypothesize that a weaker ternary complex may need to be engineered (e.g., through further mutational analysis of the protein-protein interface) in order to successfully achieve reversible complex formation. While protein

engineering to reduce the binding affinity should, in theory, be possible for this CID system, one should keep in mind that the high binding affinity is often an attractive feature of this system. Thus, a fine balance of weaker affinity to allow for reversibility and high affinity to hold together proteins of interest must be achieved. Additionally, alternative photoswitchable handles could be appended to rapamycin in an effort to improve the preferential binding through chemical means, as opposed to biological optimization. Although our current system does not afford reversibility, further development to achieve reversibility of the FKBP-rapamycin-FRB complex is certainly worthwhile. Unlike photoswitchable protein dimerizers (*e.g.* LOV domains, PhyB/PIF, CRY2/CIB),⁴¹⁵ FKBP and FRB are significantly smaller and are less likely to interfere with the biological question being addressed. Additionally, small molecule photoswitches typically don't require pulsed (or even constant) irradiation like their optogenetic counterparts, thus minimizing the potential for phototoxicity.

7.2 Spiropyran-modified Rapamycin Analog

In addition to the azobenzene and arylazopyrazole photoswitches described previously, the spiropyran (SP) is another commonly utilized photoswitch.⁴⁸⁶ Spiroyrans are a unique class of photoswitch in that their two isomers have vastly differing properties. Upon irradiation with UV light, the spiropyran undergoes a heterolytic cleavage of the C-O bond to generate a merocyanine (MC) form (Figure 7-7).

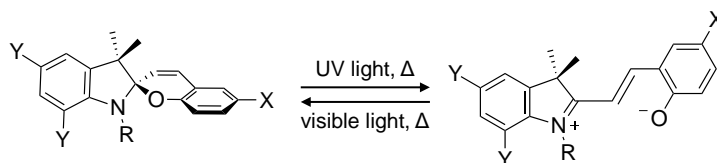


Figure 7-7 The spiroopyran photoswitch exists in both a spiroopyran and merocyanine form. The spiroopyran (closed) form can be isomerized to the merocyanine (open) form with UV light, while the reverse isomerization can be induced with visible light. Various substituents have been explored in order to modify isomerization wavelengths, solubility, and preferential stability of one form.

The merocyanine form can be reverted back to the spiroopyran thermally in the dark or upon irradiation with visible light due to electronic excitation of the phenolate. The structural change induced upon SP and MC isomerization is less significant than that of azobenzenes or arylazopyrazoles; however, a unique feature of this class of photoswitch is the >10 D difference in dipole moment between the SP and MC forms.⁴⁸⁶⁻⁴⁸⁸ Another unique feature is the conversion between a non-planar and planar molecule. The thermal equilibrium for spiroopyrans usually consists of a mixture of the SP and MC forms, with a spiroopyran being the predominant species in most cases.⁴⁸⁹ Thermal half-lives for the MC form are strongly dependent on the surrounding environment and polar solvents tend to favor the MC form. Additionally, as a result of the formation of a phenolate in the MC form, the ability to isomerize to the SP form can be greatly diminished in low pH environments, because protonation of the phenol prevents nucleophilic attack.

Spiroopyrans have been employed in a wide range of materials: (i) polymeric chains (for reversible micelle formation⁴⁹⁰ and micellular drug delivery,⁴⁹¹ for control of microfluidic device valves,⁴⁹²⁻⁴⁹³ and for control of metal ion chelation⁴⁹⁴⁻⁴⁹⁵), (ii) biomacromolecules (controlled folding of polypeptide chains,⁴⁹⁶⁻⁴⁹⁷ control of enzymatic activity,⁴⁹⁸⁻⁴⁹⁹ and control of DNA hybridization⁵⁰⁰), and (iii) solid supports (control of protein⁵⁰¹ and cell adhesion⁵⁰²⁻⁵⁰³). We hypothesized that introduction of a spiroopyran at the C-40 position of rapamycin would enable us to optically control ternary complex formation in a complementary manner to that of our

arylazopyrazole-modified derivatives. Trevor Horst synthesized the spiropyran conjugated rapamycin analog, **63** (Figure 7-8).

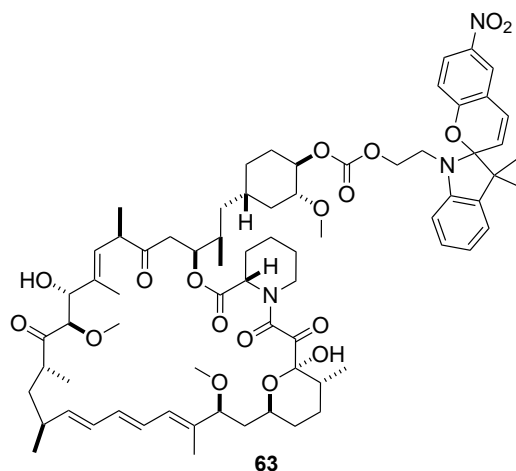


Figure 7-8 Structure of the spiropyran-modified rapamycin **63**
Compound **63** was synthesized by Trevor Horst.

Photoswitching of **63** was performed in DMSO using NMR by Trevor Horst and confirmed successful switching using white light and UV (365 nm) illumination using a dual white/UV transilluminator. Additionally, the change in absorbance of the two forms was analyzed. A 10 μM sample of **63** was prepared in phosphate buffered saline (pH 7.4). Irradiation with UV light to generate the merocyanine form shows an absorbance maximum at 565 nm (Figure 7-9), while irradiation with white light shows near complete loss of this peak.

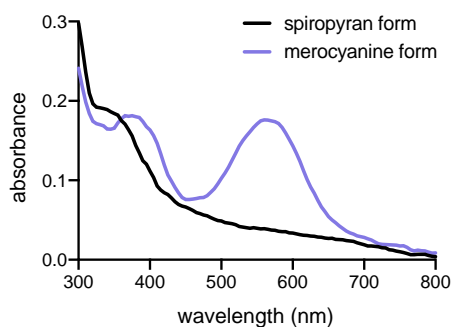


Figure 7-9 Absorbance spectra of spRap in the spiropyran and merocyanine forms

A 10 μM solution of **63** in PBS at pH 7.4 was irradiated for 5 minutes with white light to obtain an absorbance spectrum of the predominant spiropyran form (black line). Following a 5 minute irradiation with UV light, the absorbance spectrum of the merocyanine form was recorded (purple line). Appearance of a peak with maximum at 565 nm is characteristic of the open form.

After validating that **63** undergoes photoisomerization into two different forms, we proceeded to test this in the split luciferase reporter described previously in Figure 7-2a. HEK293T cells expressing the split luciferase reporter at a 1:2 FKBP:FRB ratio (as used in the previous section) were treated with pre-formed spiropyran and merocyanine forms, incubated for 2.5 hours, and lysed. Luciferase substrates were added, and recorded luminescence values were normalized to DMSO (Figure 7-10a). At all concentrations tested, the merocyanine form appeared to function slightly better than the spiropyran; however, overall dimerization efficiency relative to that of rapamycin (**21**) was quite poor.

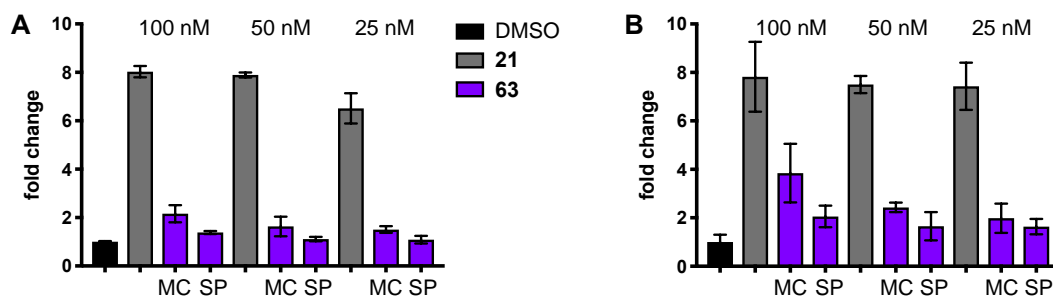


Figure 7-10 A split luciferase reporter was used to test the spiropyran-modified rapamycin analog **63** HEK293T cells expressing the split luciferase reporter in 1:2 FKBP:FRB ratio (a) or 2:1 FKBP:FRB ratio (b) were treated with pre-formed MC or SP forms of **63** at 100 nM, 50 nM and 25 nM for 2.5 hours, then luciferase substrates were added and luminescence was measured. Black bars represent the DMSO control and gray bars represent rapamycin. Raw values were normalized to DMSO and error bars represent standard deviations from experiments conducted in triplicate.

Next, we repeated the assay with an inverted plasmid ratio (2:1) and observed a slightly higher response for both the spiropyran and merocyanine forms (Figure 7-10b). Unfortunately, the selectivity for one form over the other was still lower than we had observed previously for the arylazopyrazole-modified rapamycin analogs. Additionally, the overall response relative to rapamycin was still low, suggesting that neither form is an optimal substrate for dimerization.

Since this analog proved to function worse than our previous photoswitchable analogs, we did not proceed with further optimization of the split luciferase testing. Theoretically, FKBP engineering could be performed to introduce positively and negative charged residues to stabilize

the zwitterionic merocyanine form; however, it is likely that a series of FKBP mutants would need to be screened to find one that functions as a dimerizer and stabilizes the merocyanine form.

7.3 Methods

Reagents and equipment. Rapamycin (and photoswitchable analogs) stocks were generated at 5 mM in sterile-filtered DMSO. Working solutions of 1 mM were prepared in sterile-filtered DMSO and stored at $-20\text{ }^{\circ}\text{C}$. Live Cell Imaging Solution (LCIS) was purchased from Molecular Probes/Invitrogen. Chemically competent bacterial cells (Top10) were prepared in-house. HEK293T cells were obtained from ATCC and monitored every three months to ensure the absence of mycoplasma contamination. The 530 nm LED was obtained from Mouser Electronics (LUMILEDS LXML-PM01-0100) and was mounted on a heat sink by the University of Pittsburgh Electronics Shop.

Cloning of DNA constructs. All cloning was performed using Top10 cells (Invitrogen). DreamTaq Green DNA polymerase (Thermo) was used for PCR amplification, while Phusion DNA polymerase (Thermo) was used for site directed mutagenesis.

Site directed mutagenesis was performed using CLuc-FKBP as the template to generate CLuc-FKBP_{Q53F} (primers Q53F F/R) and CLuc-FKBP_{Q53W} (primers Q53W F/R) mutations in FKBP. Both mutations were validated by Sanger sequencing at Genewiz using their BGHR sequencing primer.

To generate CLuc-iFKBP, a Gibson assembly strategy was utilized. CLuc was PCR amplified from CLuc-FKBP using primers CLuc F/R, while the iFKBP sequence (a truncated form of FKBP, residues 22 – 108) was PCR amplified from CLuc-FKBP using primers iFKBP F/R.

CLuc-FKBP was linearized with BamHI and NotI to generate the backbone. The backbone, CLuc insert, and iFKBP insert were Gibson assembled, and verified by Sanger sequencing at Genewiz using their BGHR sequencing primer. For maps of all plasmids used, see Appendix A.

Table 7-2 List of primers used to generate constructs for AAP-rapamycin analogs testing
Base mutations are indicated with CAPITALIZATION.

Primer	Sequence (5' → 3')
Q53F F	aagttatgctaggcaagTTCgaggtgatccgaggctgg
Q53F R	ccagcctcggatcacctcGAActgcctagcataaactt
Q53W F	aagttatgctaggcaagTGGgaggtgatccgaggctgg
Q53W R	ccagcctcggatcacctcCCActgcctagcataaactt
CLuc F	ttgtaccgagctcggatccactagtccagtgtggtggaa
CLuc R	gtgtagtgcaccacgcaggtgcccccgggacgcgtacgaga
iFKBP F	tctgtacgcgtcccggggcacctgcgtggtgactacac
iFKBP R	ctctagactcgagcggccgccactgtgctggatatctgca

Split luciferase reporter with AAP-analogs. HEK293T cells were plated at 200,000 cells/well in a 6-well clear bottom plate (Greiner) and grown at 37 °C/5% CO₂. At ~80% confluence, cells were co-transfected with CLuc-FKBP (wild-type, Q53F, Q53W or iFKBP) and FRB-NLuc (666 ng FKBP and 1333 ng FRB, 2000 ng total per well) using Lipofectamine 2000 following the manufacturer's protocol. The media on the cells was replaced with 2 mL of DMEM supplemented with 10% FBS (minus antibiotics), then the transfection mix (all 500 µL) was added to the cells and incubated overnight. Two wells were transfected identically in order to obtain enough cells for a single assay. After ~18 hours of transfection, the media was removed, the cells were lifted with 0.5 mL of TrypLe and transferred to a 15 mL conical tube, then TrypLe was inactivated by the addition of 9.5 mL of media. Cells were pelleted at 1,000 g for 10 minutes at room temperature. The media was removed and the cells were resuspended in 1 mL of LCIS. Cells were counted using a hemocytometer in the presence of Trypan Blue to avoid counting dead cells (combination of two wells typically yielded 1.5 – 1.8 million cells). Subsequently, cells were plated in a white, clear bottom 96-well plate at 10,000 cells per well in 90 µL of LCIS.

To prepare the compound solutions, 1 mM stocks of the five analogs were diluted to 0.1 mM in milliQ water (10 μ L of stock into 90 μ L). Two identical 0.1 mM solutions were prepared and transferred to a clear, glass $\frac{1}{2}$ dram vial. One vial was irradiated using a UV transilluminator set at 365 nm for 10 minutes, while the other vial was irradiated with the 530 nm LED (output set to 700 mA) for two minutes. In order to obtain final concentrations of 100 and 25 nM once added to cells, a 10X solution (1 μ M and 0.25 μ M) was prepared for each of the five analogs for both the *cis*- (365 nm) and *trans*-isomers (530 nm). To each well of the 96-well plate containing cells expressing the reporter, 10 μ L of compound (either rapamycin, AAP-analog, or DMSO) was added in triplicate and placed in the incubator for two and a half hours. Afterwards, 90 μ L of BrightGlo reagent was added to each well and incubated for two minutes, then luminescence was measured on a Tecan M1000. Raw luminescence values were normalized such that DMSO equaled 1. Average fold-change values with error bars representing standard deviation of triplicates are reported.

For experiments with photoswitching in cells, HEK293T cells were transfected the same as above. Cells were counted and plated in a white, 96-well plate just as above. For the turn-on experiment: analog **58** was prepared at 250 nM (maintained in the dark), then 10 μ L of this solution was added to the cells in 90 μ L LCIS (final concentration of 25 nM). Cells were incubated with compound for one hour in the dark, then a subset of wells were irradiated with 365 nm (UV transilluminator) for either 30, 60, or 120 seconds. After an additional 1.5-hour incubation, luciferase substrates were added and luminescence was measured. For the turn-off experiment: analog **58** was pre-irradiated at 100 μ M for 10 minutes with 365 nm light, then diluted to 250 nM. To the cells in 90 μ L of LCIS, 10 μ L of compound was added and incubated for an hour. Then, a subset of wells was irradiated with a 530 nm LED using a foil mask to prevent undesired irradiation

of neighboring wells. After another 90-minute incubation, luciferase substrates were added and luminescence was measured. Normalization to DMSO was performed as described above.

Split luciferase reporter with spiropyran-modified rapamycin 63. HEK293T cells were plated at 200,000 cells/well in a 6-well clear bottom plate (Greiner) and grown at 37 °C/5% CO₂. At ~80% confluence, cells were co-transfected with CLuc-FKBP and FRB-NLuc (666 ng and 1333 ng, 2000 ng total per well, in either a 2:1 or 1:2 FKBP:FRB plasmid ratio) using Lipofectamine 2000 following the manufacturer's protocol. The media on the cells was replaced with 2 mL of DMEM supplemented with 10% FBS (without antibiotics), then the transfection mix (all 500 µL) was added to the cells and incubated overnight. Two wells were transfected identically in order to obtain enough cells for a single assay. After ~18 hours of transfection, the cells were lifted, counted and re-plated as described in the section above in 90 µL of LCIS.

To prepare the compound solutions, a 1 mM stock of **63** was diluted to 100 µM in milliQ water (10 µL of stock into 90 µL). The 100 µM solution was split into two clear, glass ½ dram vials (50 µL each). One vial was irradiated using a UV transilluminator set at 365 nm for 5 minutes, while the other vial was irradiated on a white light transilluminator for 5 minutes. The 100 µM pre-irradiated solutions were used to generate 1000, 500, and 250 nM (10X) working solutions, such that a final concentration of 100, 50, and 25 nM were achieved following addition to cells. To each well of the 96-well plate containing cells expressing the reporter, 10 µL of compound (either rapamycin (**21**), **63**, or DMSO) was added in triplicate and placed in the incubator for two and a half hours. Afterwards, 90 µL of BrightGlo reagent was added to each well and incubated for two minutes, then luminescence was measured on a Tecan M1000. Raw luminescence values were normalized such that DMSO equaled 1. Average fold-change values with error bars representing standard deviation of triplicates are reported.

8.0 Expanded Methods

8.1 General Techniques – Molecular Biology

8.1.1 Polymerase Chain Reaction (PCR)

For fragments <2000 bp, DreamTaq polymerase (Thermo EP0711) was utilized, while Phusion polymerase (Thermo F530S) was utilized for anything >2000 bp. A 10 mM dNTP solution was prepared by mixing 10 μ L of each of the four dNTPs (100 mM each, Thermo FERR0181) with 60 μ L of autoclaved milliQ water. Primers were ordered from either Sigma or Integrated DNA Technologies (IDT) and were resuspended at 100 μ M using autoclaved milliQ water and a working 10 μ M dilution was prepared by diluting 10 μ L of the 100 μ M stock into 90 μ L of autoclaved milliQ water.

DreamTaq Reaction Setup:

5 μ L of 10X DreamTaq Green Buffer
2 μ L of 10 mM dNTPs
2.5 μ L of 10 μ M forward primer
2.5 μ L of 10 μ M reverse primer
1 μ L of DNA template (1 – 100 ng)
0.5 μ L of DreamTaq
36.5 μ L of autoclaved milliQ water

Phusion Reaction Setup:

10 μ L of 5X Phusion-HF Buffer
1 μ L of 10 mM dNTPs
2.5 μ L of 10 μ M forward primer
2.5 μ L of 10 μ M reverse primer
1 μ L of DNA template (1 – 100 ng)
0.5 μ L of Phusion
32.5 μ L of autoclaved milliQ water

DreamTaq Cycling Conditions:

95 $^{\circ}$ C 1 minute
95 $^{\circ}$ C 30 seconds
 $T_m - 5$ $^{\circ}$ C 30 seconds
72 $^{\circ}$ C 1 minute
Repeat step 2 – 4 30 times
72 $^{\circ}$ C 5 minutes
cool to 12 $^{\circ}$ C, hold at room temperature

Phusion Cycling Conditions:

98 $^{\circ}$ C 1 minute
98 $^{\circ}$ C 30 seconds
 $T_m - 5$ $^{\circ}$ C 30 seconds
72 $^{\circ}$ C 30 seconds per kilobase
Repeat step 2 – 4 30 times
72 $^{\circ}$ C 10 minutes
cool to 12 $^{\circ}$ C, hold at room temperature

After completion of the PCR reaction, 5.55 μ L of CutSmart Buffer (NEB) and 0.5 μ L of DpnI were added, followed by a two-hour incubation at 37 °C to digest the parental template. To the crude Phusion PCR product, 15 μ L of 6X Gel Loading Dye (NEB B7024S) was added and mixed. The DreamTaq PCR product contains a proprietary loading dye mixture and was used as-is. The entire volume was loaded onto a 0.8% agarose gel and electrophoresed at 80 V for 45 minutes. The desired bands were purified using E.Z.N.A Gel Extraction Kit (Omega Biotek D2500-02) or GeneJET Gel Extraction Kit (Thermo Scientific K0692) following the manufacturer's recommended protocol using nuclease-free water for elution. All fragments purified before March 2020 used the Omega kit, while all preps since were performed with GeneJET brand.

8.1.2 Introduction of Point Mutations (Site-Directed Mutagenesis and QuikChange)

Two different methods were utilized for introducing point mutations: (1) site-directed mutagenesis design (SDM) or (2) QuikChange design. The SDM approach utilizes forward and reverse primers with partial overlapping (15 bases) and non-overlapping (~17 to 25 bases) regions. The mutation site is included in the middle of the overlapping region, such that there are 6 fully complementary bases, followed by the three bases being mutated, followed by another 6 fully complementary bases (15 total). The non-overlapping region was designed to have a T_m of 5 – 10 °C higher than that of the overlapping region. The two non-overlapping regions of the forward and reverse primers may have different lengths; however, the annealing temperatures should be within two degrees Celsius of one another, where possible. The QuikChange design utilizes completely complementary primers designed using the Agilent QuikChange Primer Design Tool online. The

SDM approach allows for exponential amplification, while the QuikChange protocol does not. Between the two approaches the SDM design was typically utilized first. However, upon failure to introduce the desired mutation, a QuikChange design was attempted. *Note: when setting up the PCR reactions for either approach, a negative control reaction was assembled identically to the experimental one but without dNTPs or polymerase and was substituted with 2 μ L of autoclaved milliQ water.*

SDM Setup:

5 μ L of 5X Phusion-HF Buffer
 1 μ L of 10 mM dNTPs
 2.5 μ L of 10 μ M forward primer
 2.5 μ L of 10 μ M reverse primer
 1 μ L of DNA template (5 ng)
 1 μ L of Phusion
 12 μ L of autoclaved milliQ water

SDM Cycling Conditions:

95 °C 5 minute
 95 °C 1 minute
 T_m whole – 5 °C 1 minute
 72 °C 1 minute per 500 bases
 Repeat step 2 – 4 15 cycles
 T_m overlap – 5 °C 1 minute
 72 °C 30 minutes
 cool to 12 °C, hold at room temperature

QuikChange Reaction Setup:

10 μ L of 5X Phusion-HF Buffer
 1 μ L of 10 mM dNTPs
 2.5 μ L of 10 μ M forward primer
 2.5 μ L of 10 μ M reverse primer
 1 μ L of DNA template (1 – 100 ng)
 0.5 μ L of Phusion
 32.5 μ L of autoclaved milliQ water

QuikChange Cycling Conditions:

98 °C 1 minute
 98 °C 30 seconds
 T_m – 5 °C 30 seconds
 72 °C 30 seconds per kilobase
 Repeat step 2 – 4 15 cycles
 72 °C 10 minutes
 cool to 12 °C, hold at room temperature

After completion of the PCR reaction, 2.78 μ L of CutSmart Buffer and 0.5 μ L of DpnI were added to the experimental and negative control samples and incubated at 37 °C for four hours. Following DpnI treatment, 5 μ L of the PCR reaction was transformed into Top10 or DH5 α following the protocol in section 8.1.9.

Typically, a ratio of 5:1 (or greater) number of colonies for experimental:negative control was obtained; however, if 2:1 or 1:1 was obtained, additional DpnI treatment was performed and transformations were repeated. If that did not resolve the background issue, then PCR conditions

were optimized. Three cultures per mutation were grown up, miniprepped, and analyzed by Sanger sequencing.

8.1.3 Restriction Enzyme Digest

All restriction enzymes were purchased from New England Biolabs. When possible, the enzymes were ordered as the HF variant to minimize star activity and for their improved compatibility in CutSmart Buffer. Antarctic Phosphatase (AP) was from NEB also. All digestions were carried out in 50 μL total volume. For backbone generation, the DNA template (usually 8 – 10 μg , occasionally 3 μg for low copy plasmids with low miniprep yields), plus 5 μL of CutSmart Buffer, plus 1 μL of each restriction enzyme, and autoclaved milliQ water to 50 μL were combined. Digestion reactions were incubated at 37 °C for 4 – 5 hours. For backbones that would be used in restriction enzyme cloning (as opposed to Gibson assembly), after 1 hour of digestion, samples were removed from the incubator, 5.55 μL of Antarctic Phosphatase Buffer was added, followed by the addition of 1 μL of Antarctic Phosphatase, and samples were returned to 37 °C. In the rare instances where the two restriction enzymes were not compatible in the same buffer, rather than performing sequential digestions as recommended on NEB's website, 5 μL of each of the optimal buffers was used in the double digestion reaction, and the reaction time was extended to eight hours.

For digestion of inserts generated by PCR, 44 μL of the purified PCR product was combined with 5 μL of CutSmart Buffer and 0.5 μL of each restriction enzyme and incubated at 37 °C for two hours.

After incubation, the samples were heat inactivated at 80 °C for 20 minutes, then cooled to room temperature. Following the addition of 15 μL of 6X Gel Loading Dye, the entire sample

volume was loaded onto a 0.8% agarose gel and electrophoresed at 80 V for 45 minutes. The desired bands were gel extracted as discussed in 8.1.1.

8.1.4 Plasmid Assembly – Ligation

Backbone DNA fragments were generated as described in 8.1.3 in most cases; however, occasionally Phusion PCR was used to introduce restriction site overhangs (8.1.1). Inserts were most commonly obtained from PCR amplification as described in 8.1.1, where the appropriate restriction sites were included as overhangs in the primer design, and followed by digestion and purification. All ligations were performed using T4 DNA ligase from NEB (M0203S). Ligations were typically performed with a 1:3 molar ratio of backbone:insert (except in cases where the insert was as large as the backbone and a 1:1 ratio was used), and the amounts were calculated such that DNA accounted for 8.5 μ L (this typically provided anywhere from ~1 to 100 ng of backbone). A negative control sample was prepared using the same volume of backbone as the experimental sample, but the insert volume was replaced with an equal amount of autoclaved milliQ water. Following addition of 1 μ L of T4 DNA Ligase Buffer and 0.5 μ L of T4 DNA Ligase, the samples were incubated in the fridge (~4 °C) overnight. Two microliters of the ligation mixture were transformed in Top10 or DH5 α .

If a colony ratio of 3:1 experimental:negative control was obtained, three colonies from the experimental plate were grown up in liquid culture to process for miniprep and subsequent sequencing. If the ratio was lower, a PCR screen was performed as described in 8.1.6 (this is really only helpful if the ligated insert is a different size than the piece previously cut out of the backbone). Three successful hits from the PCR screen were then grown up in liquid culture.

8.1.5 Plasmid Assembly – Gibson Isothermal Assembly

The backbone used for Gibson assemblies was either prepared by restriction enzyme digest (8.1.3) or PCR amplification (8.1.1). The insert(s) was/were prepared through PCR amplification in order to introduce sufficient complementarity on both the 5' and 3' ends. In a typical Gibson reaction, 25-100 ng of backbone was used with a 1:3 backbone:insert ratio (in some cases equimolar amounts were used). The volume of DNA needs to be maintained at or below 5 μ L, so if 100 ng required too much volume of the individual pieces, the reaction was scaled down to ensure that the DNA was only in 5 μ L. Then, 15 μ L of pre-prepared Gibson Isothermal Master Mix (8.3.20) was added to the PCR tube (for 20 μ L total), and the assembly was incubated in a heat block at 50 °C for one hour. Afterwards, 2 μ L of the reaction mixture was transformed in Top10 or DH5 α . Typically, three colonies were grown up in liquid culture to process for miniprep and Sanger sequencing. Gibson assemblies tended to work in an all-or-nothing manner meaning that the colonies obtained were usually correct and if there were no colonies, something was wrong with the fragments combined. As such, a PCR screen was typically skipped.

8.1.6 PCR Screen

Many protocols exist for a PCR screen; however, the following is the protocol that I employed for the sake of completeness. On average, I found that screening 14 colonies provided at least one (and usually more) hit(s) to grow up for analysis.

To start, 14 colonies were selected and numbered on the plate. Ten microliters of autoclaved milliQ water was transferred to 14 PCR tubes (numbered 1 – 14). Using a 10 μ L pipette tip, a small portion of the colony was collected and resuspended in the 10 μ L of water. These

samples were boiled at 95 °C for 5 minutes while preparing the PCR master mix. The master mix was prepared for 15 samples (but was scaled up or down linearly for more or fewer samples). The forward primer was selected to anneal in the promoter region (T7 forward, pBAD forward, or CMV forward) and the reverse primer was the same as the reverse primer used in amplifying the insert.

PCR Screen Master Mix:

30 μ L of 10X DreamTaq Green Buffer
6 μ L of 10 mM dNTPs
3 μ L of 100 μ M forward primer
3 μ L of 100 μ M reverse primer
1.5 μ L of DreamTaq
257 μ L autoclaved milliQ water

PCR Screen Cycling Conditions:

95 °C	1 minute
95 °C	30 seconds
45 °C	30 seconds
72 °C	2 minutes
Repeat steps 2 – 4	30 cycles
72 °C	5 minutes
Cool to 12 °C, hold at room temperature	

Prepare the Master Mix and maintain on ice. Label 14 more PCR tubes and place tube rack (with tubes) on ice. Transfer 19 μ L of the Master Mix to each tube. After the five-minute boil, cool those samples on ice, then transfer 1 μ L of the boiled culture to the appropriately numbered tube containing the PCR reaction components. Place samples in thermocycler and use the thermocycler settings above. The low annealing temp is necessary since the forward primers tend to have a lower melting temperature (the goal here is to check for appearance of a band at the expected size, thus some background from non-specific primer binding isn't usually an issue).

Afterward, directly load 10 μ L of the PCR reaction on 0.8% agarose gel (prepared with a 15-well comb) and load ladder in the remaining well. Electrophorese at 80 V for 30 minutes to check for appearance of the appropriate band size. Select clones with the correct band size and grow up in liquid culture.

8.1.7 Calcium Competent Cell Preparation (for Cloning)

Empirically, it was found that the Krantz lab (U.C. Berkeley) [protocol](#) for making calcium competent cells worked significantly better than any other protocols that were tested. A few minor modifications were made and are detailed below.

Day 1

1. Streak out frozen glycerol stock of bacterial cells (Top10 or DH5 α) onto an LB plate (no antibiotics). Work sterile. Grow plate overnight at 37 °C. This streak plate can be used to select a colony for up to 7 days.

Day 2

1. Syringe sterile filter:
 - a. 50 mL of 100 mM CaCl₂
 - b. 50 mL of 100 mM MgCl₂
 - c. 10 mL of 85 mM CaCl₂, 15% glycerol v/v (made by mixing 8.5 mL of 100 mM CaCl₂ with 1.5 mL of glycerol)
2. Chill solutions overnight at 4 °C: 100 mM CaCl₂, 100 mM MgCl₂, and 85 mM CaCl₂, 15% glycerol v/v.
3. Prepare starter culture of cells. Select a single colony of *E. coli* from the plate and inoculate a 10 mL starter culture of LB (no antibiotics) using a 50 mL conical for proper aeration. Grow culture at 37 °C in shaker (250 rpm) overnight.

Day 3

1. Inoculate 50 mL of LB media in a 250 mL Erlenmeyer flask with 500 μ L of starter culture and grow in 37 °C shaker (250 rpm). Measure the OD₆₀₀ every hour, then every 15-20 minutes when the OD gets above 0.2.

2. When the OD₆₀₀ reaches 0.35-0.4, immediately put the cells on ice. Chill the culture for 20-30 minutes, swirling occasionally to ensure even cooling. Place a 50 mL conical on ice at this time. *NOTE: It is important not to let the OD get any higher than 0.4.* The OD should be carefully monitored and checked often, especially when it gets above 0.2, as the cells grow exponentially. It usually takes about 3 hours to reach an OD of 0.35 when using a 10 mL starter culture. It is also very important to keep the cells on ice for the remainder of this procedure. The cells, and any bottles or solutions that they come in contact with, must be pre-chilled.
3. Pour the cells into an ice-cold 50 mL conical tube. Harvest the cells by centrifugation at 3000 g for 15 minutes at 4 °C.
4. Decant the supernatant and gently resuspend the pellet in 20 mL of ice cold MgCl₂ using a wide orifice pipette tip.
5. Harvest the cells by centrifugation at 2000 g for 15 minutes at 4 °C.
6. Decant the supernatant and resuspend the pellet in 10 mL of ice cold CaCl₂ using a wide orifice pipette tip. Keep this suspension on ice for at least 20 minutes (up to 40 minutes works fine too). Start putting 1.7 mL microfuge tubes on ice.
7. Harvest the cells by centrifugation at 2000 g for 15 minutes at 4 °C.
8. Decant the supernatant and resuspend the pellet in 5 mL of ice cold 85 mM CaCl₂, 15% glycerol using a wide orifice pipette tip.
9. Harvest the cells by centrifugation at 1000 g for 15 minutes at 4 °C.
10. Decant the supernatant and resuspend the pellet in 2.5 mL of ice cold 85 mM CaCl₂, 15% glycerol using a wide orifice pipette tip.
11. Aliquot 50 µL into sterile 1.7 mL microfuge tubes and snap freeze with liquid nitrogen. Store frozen cells in the -80 °C freezer.

8.1.8 KCM Competent Cell Preparation (for Protein Expression)

For recombinant protein expression using BL21 (DE3) cells, a faster method of making competent cells was utilized. Typically, the competency of cells prepared in this manner were lower than those prepared following the protocol in 8.1.7. This protocol was obtained from the Childers lab (University of Pittsburgh).

Protocol:

1. Streak cells from a glycerol stock on an LB agar plate (– antibiotic). Grow overnight at 37 °C.
2. Pick an isolated colony and grow up in 5 mL of LB broth overnight at 37 °C with shaking (250 rpm). Prepare TSB solution (see 8.3.17) for tomorrow and pre-chill at 4 °C overnight.
3. Transfer 1 mL of starter culture into 100 mL of LB broth in a 500 mL Erlenmeyer flask and grow at 37 °C with shaking (250 rpm) to OD₆₀₀ of 0.4–0.5.
4. Place culture on ice for 5 minutes. Pellet cells at 4000 g for 10 minutes at 4 °C in pre-chilled 50 mL conical tubes. Gently resuspend cells in 1/10 volume of TSB (pre-chilled) using a wide orifice pipette tip and incubate on ice for 5 minutes.
5. Aliquot into pre-chilled 1.7 mL tubes (100 µL each) and snap freeze in liquid nitrogen. Store at –80 °C.

8.1.9 Transformation of Calcium Competent Cells

Competent cell stocks (50 µL aliquots) were thawed on ice. Plasmid DNA (10 – 100 ng) or cloning reaction mix (typically 2 – 5 µL, see sections 8.1.2, 8.1.4, and 8.1.5 for more details) was added to the tube of cells. Gently flick tube to mix contents, then flick down to bring contents of tube to the bottom. Incubate on ice for 30 minutes. Place tube(s) in a foam rack, then heat shock

at 42 °C in a water bath for 45 seconds. Place tube(s) back on ice for two minutes. Add 250 µL of SOC (TekNova), then parafilm lids to ensure they're sealed. Place tube(s) in a beaker, then insert the beaker into a flask rack in the 37 °C shaker at 250 rpm and grow for 45 minutes to allow cells to recover. For plasmid DNA propagation, 50 µL of cell suspension was plated on LB agar supplemented with the correct antibiotic at the concentration specified in Table 8-1; for cloning reactions, the entire 300 µL of cell suspension was plated on LB agar supplemented with antibiotics. To plate, the appropriate volume of cells was pipetted onto an LB-agar plate, then 12-15 plating beads (Zymo S1001) were added and using a horizontal shaking motion, cells were evenly spread across the plate, then the beads were poured off. Plates were left with the lids open to dry for ~5 – 10 minutes, then the lids were placed on, and plates were placed in the 37 °C incubator upside down for overnight growth. The plating beads were collected in a 250 mL flask containing 10% ethanol in water. To clean the beads (when the bottle was down to ~10% clean beads remaining), the ethanol solution was poured off, the beads were washed with water to remove residual ethanol, then they were soaked in a 20% bleach solution for one hour, then the beads were poured into a Buchner funnel and washed several times with water. The beads were dried by pulling air through the funnel by connecting to a PIAB system and once dried were transferred to a clean 50 mL bottle and autoclaved for reuse in plating.

To prepare LB-agar plates, melt a 500 mL autoclaved bottle of LB-agar in the microwave (only melt what is needed, the entire bottle doesn't need to be melted). Flame the lid and place face down on the benchtop, then flame the lip of the bottle and pour the needed amount into a 50 mL conical, then flame both the lid and lip and close the bottle (if working carefully under the flame, the stock bottle should not become contaminated). Cool the LB-agar in the conical tube until ~50 °C, then add the appropriate volume of antibiotics, then pour 10 mL into plates. Allow

to cool/solidify without the lids proximal to the Bunsen burner flame, then replace lids and store upside down until ready to plate cells.

Table 8-1 Antibiotic stocks and dilutions

Antibiotic	Stock Concentration	Final Concentration	Solvent used in stock prep
Kanamycin	50 mg/mL	50 µg/mL	milliQ water
Ampicillin	100 mg/mL	100 µg/mL	milliQ water
Tetracycline	5 mg/mL	25 µg/mL	70% ethanol
Chloramphenicol	34 mg/mL	25 µg/mL	milliQ water
Spectinomycin	50 mg/mL	50 µg/mL	milliQ water

8.1.10 Transformation of KCM Competent Cells

Competent cell aliquots (100 µL) were thawed on ice. In a separate 1.7 mL tube, 20 µL of 5X KCM (see 8.3.18) + 10 – 100 ng of plasmid DNA (volume depends on concentration) + milliQ water to fill to 100 µL were combined. To the tube of diluted DNA, 100 µL of competent cells was added and gently mixed. Tubes were incubated on ice for 20 minutes, then heat shocked at 42 °C for 90 seconds and placed on ice for 1 minute. After, 400 µL of SOC was added to the cells and the lids were parafilmmed to prevent leakage. The tubes of cells were shaken (250 rpm) at 37 °C for 1 hour, then 250 µL of cell suspension was plated on LB agar supplemented with antibiotic (see section 8.1.9 for preparing LB-agar plates).

8.1.11 Plasmid Purification

Plasmids were purified from bacterial cultures generated in the above sections. When a glycerol stock was needed (typically the first time a plasmid culture was grown), 564 µL of the saturated culture was removed and transferred to a sterile 1.7 mL tube (and 189 µL of autoclaved glycerol was added for 750 µL of a 25% glycerol sample), then 564 µL of water was placed back

into the culture so it could be pelleted with the remaining 5 mL samples. Pellet cells at 4 °C in a swinging bucket rotor at 4000 g for 10 minutes, then discard the supernatant. Stand tubes upside down on a KimWipe for 5 minutes such that residual media drains off the pellet. Cap the tubes and freeze at –80 °C for at least 15 minutes (a freeze-thaw cycle seems to improve plasmid yield). The tubes can be maintained frozen for up to 6 months with no observable decrease in plasmid yield or quality. Following the manufacturer’s protocol (E.Z.N.A. Plasmid Mini Kit I Q-spin from Omega Bio-Tek [before March 2020] or GeneJET Plasmid Miniprep Kit from Thermo Scientific [post March 2020]), the samples were purified. Elutions were performed with 50 µL of nuclease-free water (pre-warmed to 65 °C in a heat block). Plasmid concentration (ng/µl) was determined using a NanoDrop ND-1000 spectrophotometer. Typically, 50 – 800 ng/µL solutions were obtained, depending on low versus high copy plasmids.

8.1.12 Sanger Sequencing

Prior to April 2016, sequencing samples were submitted to Beckman Coulter Genomics; however, after they were acquired by Genewiz (April 2016), we continued using the services provided by Genewiz. The amount (in ng) depends on the plasmid size (e.g., 600 ng was used for a 6000 bp plasmid). The volume was filled to 10 µL with autoclaved milliQ water. In most cases, [free universal primers from Genewiz](#) were utilized (with them adding it), but sometimes they didn’t have a suitable primer, so 5 µL of a 5 µM sequencing primer (ordered from Sigma or IDT) was pre-mixed before submission. Sequencing analysis was performed using the open-source software, A Plasmid Editor (ApE), and sequencing alignments were performed using NCBI nucleotide BLAST (for two samples) or Clustal Omega > Multiple Sequence Alignments (for more than two samples).

8.1.13 Agarose Gel Electrophoresis

When preparing an agarose gel, first determine the number of samples needed to analyze. The 7 x 7 cm cassette can be used for up to 15 samples, while a 7 x 10 cm cassette can accommodate up to 30 samples. If using the 7 x 7 cm one, 40 mL is needed, while 60 mL is sufficient for the 7 x 10 cm one. For a standard 0.8% (w/v) agarose gel, 0.32 g (or 0.48 g) of agarose was weighed into a 125 mL Erlenmeyer flask, followed by the addition of 40 mL (or 60 mL) of 1X TBE (8.3.4). The mixture was heated at max power in a microwave for 33 seconds, followed by swirling, then 22 and 11 second microwave segments (with swirling after each). After ensuring that the agarose was fully dissolved, the sample was cooled by running under cold tap water to lower the temperature to ~50 °C. Once cooled, 2 µL (or 3 µL) of 10 mg/mL ethidium bromide in water was added and the solution was swirled to ensure even distribution. The agarose solution was poured into the gel caster cassette and an appropriate well comb was added. The gel was then allowed to solidify at room temperature (for ~30 minutes) and the comb was carefully removed. The gel was placed in a Sub-Cell GT Cell from BioRad and filled with 1X TBE. Samples were carefully loaded into the wells. The 2-well preparative comb can safely hold ~100 µL, while the 8-well comb can hold ~40 µL, and the 15-well comb can hold ~20 µL. A 1 kb TriDye DNA ladder (NEB N3272S) was loaded (5 µL for the 15-well and 2-well prep sizes, and 10 µL for the 8-well comb). Typically, the gel was electrophoresed at 80 V for 45 minutes, but for samples with bands of similar size, 60 V for 90 minutes was used to improve resolution. Gels were imaged on a ChemiDoc XRS+ from BioRad, then bands were visualized on a UV transilluminator (365 nm) for band excision.

8.2 General Techniques – Cell Biology

8.2.1 Protein Expression (and UAA incorporation) in *E. coli*

Typically, the wild-type protein was expressed first to ensure that conditions were optimal, prior to performing the UAA incorporation experiment. The conditions detailed here were used for the majority of all expressions performed, and any modifications are noted in the detailed methods section above. The pBAD-POI-TAG-pylT plasmid (protein of interest = POI), often sfGFP, was co-transformed with pBK-MbPylRS containing the appropriate mutations (using the EV series numbering) into chemically-competent Top10 cells using ~50 ng of each plasmid, and plated on LB-agar (+ 25 µg/mL tetracycline, + 50 µg/mL kanamycin). A single colony was grown in LB broth supplemented with both antibiotics overnight at 37 °C with 250 rpm shaking to generate a saturated starter culture. In some cases (most often for sfGFP), a glycerol stock of this double transformed cell culture was prepared and stored at –80 °C. In a 125 mL Erlenmeyer flask, 25 mL of LB broth was supplemented with antibiotics and the expression culture was inoculated with 250 µL of saturated overnight culture and grown at 37 °C with 250 rpm until OD₆₀₀ reached 0.4 to 0.6 (the OD₆₀₀ was checked regularly using the NanoDrop). Protein expression was induced using 125 µL of a 20% arabinose solution prepared in water, for a final 0.1% arabinose induction. Unnatural amino acid was added from a 100 mM stock in either DMSO or water, depending on the amino acid, at a final 1 mM concentration (a few poorly soluble UAAs were used at 0.5 mM). Overnight expression was performed at 37 °C with 250 rpm shaking. The next day, cells were harvested by centrifugation at 4000 g for 10 minutes at 4 °C in a 50 mL conical and the supernatant was discarded. [At this point, cell pellets could be frozen at –80 °C for up to 6 months if samples weren't immediately needed.]

In some cases, when the overall goal of bacterial protein expression was simply high-resolution mass spectrometry confirmation of UAA incorporation, a 5 mL expression culture scale was utilized to avoid unnecessarily wasting the UAA. For this, all volumes were divided by five, and the expression was performed in a 15 mL conical tube. The 25 mL expression was typically only used when significant amounts of protein were needed for a functional assay.

8.2.2 Lysis of Bacterial Cells – for sfGFP Mutants

When expressing sfGFP bearing an unnatural amino acid, a unique three-phase partitioning (TPP) lysis protocol was used. For this, 5 mL expression cell pellets were thawed on ice. All samples, WT, +UAA, and –UAA were treated in the same manner. The cell pellets were resuspended in 300 μ L of Tris buffer (25 mM Tris-HCl pH 8.0) and transferred to 1.7 mL tubes, followed by the addition of 200 μ L of saturated ammonium sulfate and 500 μ L of tert-butanol. Samples were capped and the tubes were shaken vigorously by hand for one minute. The tubes were centrifuged at 4000 g for 10 minutes at room temperature (do not use 4 °C as the butanol will solidify). At this point, three layers (hence the name) should be apparent: (1) ~500 μ L top layer consisting of the butanol, (2) a middle, precipitated disk that separates the two layers, about 1 mm thick, and (3) ~500 μ L aqueous solution containing ammonium sulfate and Tris, with the sfGFP protein. Carefully pipette away the butanol layer into a waste receptacle, then using a fresh pipette tip, pierce through the precipitated layer to reach the bottom solution, and aspirate/transfer this to a fresh 1.7 mL tube. Add 1 mL of bacterial lysis buffer (8.3.21) so that there is a low imidazole concentration present to minimize background binding during Ni-NTA resin purification (8.2.4).

8.2.3 Lysis of Bacterial Cells – for Non-sfGFP Proteins

For small scale (5 mL) expressions, cell pellets were resuspended in 1.2 mL of bacterial lysis buffer (8.3.21), followed by the addition of 12 μL of lysozyme (10 mg/100 μL in water), 12 μL of 10% (v/v) Triton X-100, and 1.2 μL of bacterial protease inhibitor (Sigma P8849). Samples were gently mixed and incubated on ice for 1 hour. Cell resuspensions were sonicated (Fisher Scientific 550 Sonic Dismembrator) at 50% output using the microtip for 3 minutes with cycles of 20 seconds on, and 30 seconds off. Cell lysates were centrifuged at 4 °C at 15000 g for 15 minutes to pellet cellular debris. Successful and complete lysis was monitored based on the appearance of the obtained pellet. If the pellet looked similar to the original cell pellet, this was indicative of incomplete lysis, therefore the samples were resuspended and the sonication process repeated. A typical fully lysed pellet should be significant lighter (tan/off-white) and smaller than the original cell pellet. At this point, the soluble protein fraction (supernatant) was transferred to a 1.7 mL tube for Ni-NTA resin purification (8.2.4).

For the 25 mL scale expressions, the sonication protocol detailed above could be employed (with 5X volumes as written); however, longer sonication times are needed to ensure complete lysis. As such, an Avestin EmulsiFlex-C3 homogenizer (in the Childers lab) was more commonly used out of personal preference. For this, the cell pellets were thawed on ice and resuspended in 10 mL of bacterial lysis buffer (8.3.21) with vortexing. *Note: 10 mL is the smallest working volume compatible with the EmuliFlex, if using a larger scale expression size, the cell pellet should be resuspended in 1/5 of expression volume.* Following the addition of 10 μL of bacterial protease inhibitor, the samples were transported to the cold room on ice. Following the detailed instructions guide at the instrument for prepping it for sample use. Pour the sample into the sample collector and make sure to create a continuous loop by connecting drain tubing back to the sample collector

(otherwise your sample will drain to waste). Flow the sample through with no pressure for 5 minutes to ensure that it is homogeneous and clump-free, then flow through with pressure added (17000 – 20000 psi) for 12 minutes to lyse cells. After this time, reduce pressure setting back to zero and collect sample in a fresh 50 mL conical tube. Make sure to clean the instrument appropriately. Pellet cellular debris at 15000 g in the 4 °C centrifuge with the fixed angle rotor for 15 minutes. Transfer supernatant to fresh 15 mL conical tube for Ni-NTA resin purification (8.2.4).

8.2.4 Ni-NTA Protein Purification

Four different Ni-NTA resin/agarose vendors were used in the lab over the last several years (Qiagen 30210, 05/2015 to 02/2017; Invitrogen R90115, 02/2017 to 03/2018; EMD Millipore 70666, 03/2018 to 02/2019; G-Biosciences 786939, 02/2019 to present). Unfortunately, the quality and binding capacity of the resins do vary quite a bit between vendors. The protocol detailed here is based on the most recent work performed using G-Biosciences; however, the only difference is the volume of resin slurry used. All resins were obtained as a 50% slurry in 20% ethanol. The volumes used are for total volume pipetted (not the actual volume of resin). For expression at 5 mL (25 μ L of resin), for 25 mL (125 μ L of resin), and for 100 mL (400 μ L of resin) was used per sample. Before adding to the sample, the resin was washed thrice with the lysis buffer to remove the 20% ethanol solution (centrifuge at 4 °C for 5 minutes at 1000 g, remove supernatant, resuspend resin in equi-volume of lysis buffer, repeat 3 times). After washing, the resin was resuspended in lysis buffer and added to the samples. The tubes were placed on a multi-direction rocker in the cold room for 2 – 3 hours (unless specified otherwise). The resin was collected by centrifugation at 4 °C for 5 minutes at 1000 g, and the supernatant was collected into a new tube. Volumes provided for wash and elution steps are for 25 mL scale and can be scaled up/down

linearly for the other expression sizes. Each wash and elution was collected in a separate, fresh 1.7 mL tube. The resin was washed once with 250 μ L of lysis buffer (8.3.21), then thrice with 250 μ L of wash buffer (8.3.22), then eluted four times with 200 μ L of elution buffer (8.3.23). For analysis of purity, 20 μ L of the wash and elution fractions were transferred to PCR tubes, and mixed with 8 μ L of 4X Laemmli Sample Buffer. Samples were mixed thoroughly, then boiled at 95 °C for 10 minutes. The samples were maintained at -20 °C until analyzed by gel. SDS-PAGE gels were cast as described in 8.2.5 (the percent of acrylamide was chosen based on the molecular weight of the protein). Typically, 10 μ L of sample was loaded onto the gel (unless a low yield was expected, or very low visual fluorescence was observed in the sample, then the entire volume was used). The gels were electrophoresed at 60 V for 20 minutes, then 150 V for 80 minutes, followed by Coomassie staining. Gels were imaged on a ChemiDoc system with a preset Coomassie setting. To quantify purity, images were exported from the ChemiDoc software (ImageLab) and saved as a tiff file for analysis in FIJI. The entire lane was analyzed using the “gels” tool in FIJI, then the gel lane was plotted using the “plot lanes” feature, all peaks (anything detectable above background) were selected with the “wand” tool to measure the area under the curve. Purity was calculated by the following: peak area of desired molecular weight band/(sum of all peak areas extracted)*100.

For high-resolution mass spectrometry analysis of samples, an aliquot was taken directly from the most concentrated elution and submitted to the Department of Chemistry Mass Spectrometry Facility. For proteins/enzymes to be used in any other manner, elution fractions that were deemed “pure” were pooled and buffer exchanged (to remove the high imidazole concentration) into the suitable assay buffer.

8.2.5 SDS-PAGE Preparation and Electrophoresis

SDS-PAGE gels were prepared in-house using the volumes detailed in Table 8-2. The 40% acrylamide (19:1) solution was purchased from Fisher, TEMED (tetramethylethylenediamine) was purchased from Acros, and the remaining solutions were prepared as common-use lab solutions. The volumes listed make 5 mL of the resolving gel, which is enough for pouring a 0.75 mm thick gel using the Mini-PROTEAN Tetra Cell system from BioRad. Most gels were prepared using the 1.5 mm thick cassettes and required doubling of the volumes in the table. When considering molecular weight of proteins and the necessary percentage of acrylamide gel, the following ranges were employed such that the protein of interest fell in the middle of the range: 8% gel (20 – 100 kDa), 10% gel (15 – 70 kDa), 12% gel (8 – 60 kDa), and 15% gel (<30 kDa). For most proteins, the 10% gel provided sufficient resolution.

Table 8-2 Preparation of various percentage of SDS-PAGE gels

Resolving					Stacking	
	8% gel	10% gel	12% gel	15% gel		5% gel
water	2.645 mL	2.4 mL	2.15 mL	1.775 mL	water	3.0 mL
40% acrylamide (19:1)	1.0 mL	1.25 mL	1.5 mL	1.875 mL	40% acrylamide	0.5 mL
1.5 M Tris pH 8.8	1.25 mL	1.25 mL	1.25 mL	1.25 mL	1.0 M Tris pH 6.8	0.5 mL
10% SDS	50 μ L	50 μ L	50 μ L	50 μ L	10% SDS	40 μ L
10% APS	50 μ L	50 μ L	50 μ L	50 μ L	10% APS	40 μ L
TEMED	3 μ L	3 μ L	3 μ L	3 μ L	TEMED	4 μ L

The appropriate volumes of gel components (based on Table 8-2) were combined in a 15 or 50 mL conical, followed by gentle inversion to fully mix. The solution was poured into the gel caster between the glass faceplate and backplate. To make sure the top of the gel was flat, 2 mL of milliQ was gently pipetted onto the top of the gel solution. After allowing the resolving gel to polymerize (~25 minutes), the top water layer was poured off and residual water was removed

with Kimwipe. A 5% stacking gel was prepared and poured to obtain a ~5 mm tall gel (4 mL for one 1.5 mm thick gel), and the appropriate comb (either 10- or 15-well) was added and allowed to polymerize for ~20 minutes. [Typically, gels were prepared as needed; however, gels were successfully stored (with the comb still in) overnight wrapped in a wet paper towel and sealed in a zipper bag with no negative effects observed.] The gel comb was carefully removed, and the wells were gently rinsed with deionized H₂O to remove any unpolymerized gel solution. Using the Mini-PROTEAN Tetra Electrode assembly, the gel and a buffer dam (if using one gel) or two gels were loaded into the gel chamber. Fresh 1X SDS-PAGE running buffer (8.3.6) was used to fill the chamber between the gels/buffer dam (~200 mL needed), and used 1X SDS-PAGE running buffer was used to fill the rest of the tank. For low molecular weight proteins (<20 kDa – *e.g.*, myoglobin), 1X MES-SDS-PAGE running buffer (8.3.7) was used instead. An ice pack was placed in the buffer reservoir to keep the gel cool during electrophoresis. Protein samples were carefully loaded with 10 µL pipette tips to ensure that the sample entered the appropriate well. Prestained protein ladder (Thermo 26617) was loaded at 8 µL for a 10-well gel or 5 µL for a 15-well gel. Any wells that did not have samples were filled with an equi-volume of 1X Laemmli Sample Buffer (300 µL of milliQ water + 100 µL of 4X Laemmli Sample Buffer) to ensure even migration of samples through the gel. Electrophoresis was performed at 60V for 20 minutes to move samples through the stacking gel, then the samples were pushed through the resolving gel at 150V for 80 minutes or 175V for 60 minutes (no observable difference in final band shape was detected between the two voltages/times, but gels could be sped up when needed).

Following electrophoresis, gels were either: (1) stained overnight in Coomassie stain solution (8.3.10), then destained the following day with regular changes of destain buffer (8.3.11),

(2) further processed in a western blot (8.2.11), or (3) imaged on the ChemiDoc for in-gel fluorescence, when applicable.

8.2.6 Mammalian Cell Maintenance

All mammalian cell lines were grown and maintained at 37 °C/5% CO₂ in tissue culture-treated 10 cm plates (Corning 353003) with 10 mL of media. HEK293T (CRL-11268) and HeLa (CCL-2) cell lines were obtained from ATCC, and grown in Dulbecco's Modified Eagle Medium (DMEM, see recipe 8.3.16) supplemented with 10% fetal bovine serum (FBS; Sigma-Aldrich, through 03/2019; HyClone, 03/2019 – present). For general cell passaging and plating into well-plates for experiments, DMEM plus antibiotics (1% penicillin/streptomycin, Corning) was used; and for all transfections and compound treatments, minus-antibiotic DMEM was used. Every three months, media from a confluent plate of cells, as well as samples of sterile medias, were tested using Genlantis MycoScope PCR Detection Kit (MY01100) to check for mycoplasma contamination.

Cell passaging and plating was performed in a biosafety cabinet once 10 cm plates reached 90 – 100% confluence (typically 2 – 4 days). Cells were passaged by carefully removing the 10 mL of media, washing gently with 1 mL of TrypLe (Gibco 12604021), then incubating with 1 mL of TrypLe for ~ 2 minutes at room temperature for HEK293T and at 37 °C/5% CO₂ incubator for HeLa cells. Following the incubation, using a 1 mL pipette tip, cells were gently pipetted to aid in complete lifting of cells from the plate, and 9 mL of media was added to inactivate TrypLe. To a fresh 10 cm plate, 9 mL of media was added, followed by the addition of 1 mL of the cell suspension (for a 1:10 dilution). Cells were labeled with date, cell line, and passage number. Cells were discarded after reaching passage 25, and new cell stocks were thawed. *Note: To avoid having*

a gap in useable cells, new cell stocks were thawed upon reaching passage 23, so the new ones would be ready when needed.

Cells were thawed by removing the desired vial from an LN₂ dewar (preferably Dewar 1), thawing in the 37 °C water bath until completely thawed (but not longer than absolutely necessary), then cells were poured into a 10 cm plate containing 10 mL of media. Typically, pouring is forbidden due to risk of contamination; however, thawed cells tend to be quite fragile and do not tend to recover as well when a 1 mL pipette is used for transferring. The following day, the media was removed (transferred to a new 10 cm plate and labeled as “supernatant”) and fresh 10 mL of media was added to remove the DMSO used in storage. In rare cases, so few cells will have adhered prior to media change that it might be necessary to use the “supernatant” plate 48 – 72 hours post thaw in order to revive cell stocks.

When taking the second-to-last vial of any cell line, or upon obtaining a new cell line from ATCC or another lab, cells stocks should be frozen down. For this, upon the next passage, plate 3 mL of cell suspension into a 15 cm plate containing 20 mL of media. On the day of freezing cells, prior to starting, ensure that the Mr. Frosty Freezing Container (Thermo Scientific 5100-0001) is at room temperature and filled with the appropriate volume of isopropanol. Cells were grown to ~100% confluence, then rinsed with 2 mL of TrypLe, lifted with 2 mL of TrypLe and transferred to a 15 mL conical tube, and diluted with 12 mL of media (14 mL total). A sample (10 µL) was taken for counting, then the remainder was pelleted at 1000 g for 10 minutes at room temperature. The media was discarded, and the cell pellet was resuspended in a volume of media such that cells were stored at 1 million cells per mL (1 mL per cryogenic tube). [Typically, 6 tubes of HeLa cells and 8 tubes of HEK293T cells were obtained from a single 15 cm plate.] For example, given a count of 8 million total cells, a total volume of 8 mL is needed, consisting of 7.6 mL of media and

0.4 mL of DMSO (5% final). At this step, 3 mL of media was added first, and used to gently resuspend the cells with a 1 mL pipette, then the remaining needed volume was added (if all volume is added at once, gentle resuspension is challenging). Add the necessary volume of DMSO, then mix by gently inverting the conical ~5 times. Quickly transfer 1 mL of the cell suspension to cryogenic tubes, then place tubes in Mr. Frosty and close the lid, then place in the -80°C freezer. After ~24 hours, vials should be transferred to an LN_2 dewar.

8.2.7 Poly-D-Lysine Treatment

For any imaging experiments or experiments requiring several wash steps, the plate was treated with poly-D-lysine (MP Biomedicals 0215017550, 70 – 150 kDa) prior to plating cells in order to maintain adherence. A stock solution of 10 mg/mL was prepared by dissolving 12 mg in 1.2 mL of sterile-filtered autoclaved milliQ water. This stock was stored in the cell culture 4°C fridge until depleted (up to 12 months sometimes). A working solution of 0.1 mg/mL in sterile-filtered autoclaved milliQ water was prepared immediately prior to use. The volumes needed per well for various plate types are as follows: 96-well plate, 40 μL ; 8-well chamber slide, 150 μL ; 12-well plate, 400 μL . The 0.1 mg/mL solution was added to the plate and incubated for ~15 minutes at room temperature. The solutions were removed, and wells were washed twice with sterile-filtered autoclaved milliQ water, 2X the volume of poly-D-lysine solution. The plate(s) were dried in the biosafety hood for ~1 hour with the plate lids opened slightly.

8.2.8 Mammalian Cell Transfection – Linear Polyethyleneimine

Linear polyethyleneimine (LPEI, from Polysciences, 23966-1) was prepared following the [Polysciences protocol](#) at a 0.5 mg/mL concentration scaled down to a 20 mL preparation. Following preparation, the entire volume was sterile-filtered using a 0.2 μm cellulose acetate syringe filter. The solution was aliquoted into 1.7 mL tubes at 200 μL each (~100 tubes) and the stocks were stored at $-20\text{ }^{\circ}\text{C}$. When performing an LPEI transfection, a single aliquot was thawed and used for that day only, then any remaining volume was discarded. A 0.5 mg/mL concentration was selected because it simplified the transfection calculations since DNA (μg): LPEI (μg) was maintained at a 1:5 ratio. Thus, for 1000 ng of DNA, 10 μL of LPEI was needed. The amount of DNA used for each transfection was optimized when starting a new assay, and the values reported in each section are the optimal values for that specific assay. Here, I have provided the starting points used for different plate formats in Table 8-3, as a guide for optimizing transfections for new targets.

Table 8-3 LPEI transfection reagent volumes for various plate formats

Plate format	Volume of media	Volume of OptiMEM	Amount of DNA	Volume of LPEI
96-well plate	100 μL	20 μL	200 ng	2 μL
8-well chamber slide	250 μL	20 μL	200 ng	2 μL
12-well plate	1 mL	100 μL	1000 ng	10 μL
6-well plate	2 mL	200 μL	2000 ng	20 μL

When multiple identical wells were needed, the transfection mix was prepared in bulk such that there would be less well-to-well variability. Typically, calculations were performed to prepare 2 – 3 extra wells so that there was enough material for the needed wells. When cells were ~80% confluent, the media was removed and replaced with antibiotic-free DMEM. The transfection mix was prepared by transferring OptiMEM (Gibco 22600050) to a 1.7 mL tube, followed by the

addition of DNA, then LPEI. The tube was flicked to mix, then the contents were quickly spun down in a tabletop minifuge, and the solution was incubated at room temperature for 20 minutes. Then, the “Volume of OptiMEM” was added to each well since the contributions from DNA/LPEI were usually negligible. Cells were incubated with the transfection mix overnight (or occasionally up to 48 hours) depending on the experiment.

8.2.9 Mammalian Cell Transfection – Lipofectamine 2000

Lipofectamine 2000 (L2K) transfections were typically only used after LPEI transfections failed to provide significant protein expression. The values provided in Table 8-4 show the starting point for Lipofectamine 2000 transfections. If a different plate size is needed, the [protocols website](#) for L2K has recommended volumes for scaling up or down. The volume of media used for culturing cells during transfection is the same for both transfection methods.

Table 8-4 Lipofectamine 2000 transfection reagent volumes for various plate formats

Plate format	Volume of OptiMEM (x 2 tubes)	Amount of DNA	Volume of L2K
96-well plate	25 μ L	200 ng	0.5 μ L
12-well plate	100 μ L	1000 ng	2.5 μ L
6-well plate	250 μ L	2000 ng	5 μ L

As was true for LPEI transfections, if multiple wells were needed, the transfection mix was prepared in bulk. Per the manufacturer’s recommendation, a 2.5:1 ratio of L2K (μ L): DNA (μ g) was utilized. When cells reached ~80% confluence, the media was removed and replaced with antibiotic-free DMEM. In a 1.7 mL tube, OptiMEM and L2K were combined and incubated at room temperature for 5 minutes. In a separate 1.7 mL tube, OptiMEM and DNA were combined. After the incubation, the OptiMEM/L2K solution was mixed into the OptiMEM/DNA solution, the solution was flicked to mix, then briefly spun down to bring contents to the bottom. The

transfection solutions were incubated at room temperature for 20 minutes, then the solution (twice the original OptiMEM volume, *e.g.*, 50 μ L for 96-well format) was added to the wells. Cells were incubated with the transfection mix overnight (or occasionally up to 48 hours) depending on the experiment.

8.2.10 Mammalian Cell Lysis

Cells in either 6- or 12-well format that were transfected as described above were lysed for western blot analysis ~24 – 48 hours post transfection. A working solution of RIPA buffer (8.3.8) with 1X Halt Protease Inhibitor Cocktail (from 100X, Thermo Scientific 78429) was prepared. For 6-well plate, 200 μ L per well was used; for 12-well format, 100 μ L was used per well; prepare enough working solution for # of wells + 1 to ensure each well gets the correct amount. Place the plate of cells on ice, carefully remove the media, rinse gently with 1 mL of ice-cold 1X PBS, then add 200 μ L of RIPA buffer. Place plate on ice on an orbital shaker for 15 minutes with 250 rpm shaking. Collect total lysate into 1.7 mL tubes, then centrifuge at 15000 g for 10 minutes to pellet cellular debris. The supernatant (84 μ L) was carefully collected, avoiding the pellet, and transferred to 0.2 mL PCR tubes, followed by the addition of 35 μ L of 4X Laemmli Sample buffer (8.3.9). For western blot analysis, the regular buffer was used, the samples were mixed, then boiled and denatured for 10 minutes in a 95 °C heat block. These samples were frozen at –20 °C (for up to 6 months) until used for further analysis. For in-gel fluorescence experiments, the minus β -mercaptoethanol buffer was used, the samples were mixed thoroughly, but were NOT boiled. These samples were electrophoresed on SDS-PAGE gels immediately to avoid any loss of fluorescence signal due to freeze-thaw effects. For a single well, 15 μ L of sample was typically

used and the remaining sample was again frozen (the prep volume above allows for 7 gels/blots from a single PCR tube).

8.2.11 Western Blot Analysis

As soon as the SDS-PAGE gels were resolving (8.2.5), 1 L of 1X western blot transfer buffer (8.3.13) was prepared and placed in the $-80\text{ }^{\circ}\text{C}$ for the entirety of time the gels were electrophoresed. Using a spare faceplate as a template, four pieces of Whatman filter paper (GE Healthcare 100115) were cut to the exact size of the gel minus the stacking gel/wells. Next, the $0.45\text{ }\mu\text{m}$ PVDF membrane (MilliporeSigma IPVH00010) was cut to size using the filter paper as a guide. With ~ 5 minutes remaining on the SDS-PAGE gel, the PVDF membrane was soaked in 100% methanol to activate the membrane. Using a larger Nalgene pan, an ice moat was created around a gel tank equipped with a Mini Trans-Blot Cell (BioRad). The pre-chilled 1 L of transfer buffer was poured into the gel tank, and an ice pack was placed in the gap between the Cell and wall of the tank. When finished electrophoresing, the gel was removed from the glass plates and the stacking gel/wells were cut off with a clean razor blade. A glass baking dish was used for assembly of the transfer cassette. One liter of used transfer buffer was poured into the baking dish, and the cassette assembly (plastic portion and two sponges) was submerged with the black side down. The transfer assembly was built like a sandwich from the bottom up on the black plastic piece in the following manner: pre-wetted sponge, two pieces of filter paper, gel, activated PVDF membrane, two pieces of filter paper, and pre-wetted sponge. After each layer was added, the pieces were carefully smoothed out to avoid any bubbles between the layers, mostly importantly with no bubbles between the gel and membrane. The cassette was closed and the locking clip was used to hold the assembly together. The cassette was placed in the Trans-Blot Cell by matching

black-to-black and clear-to-red to ensure proper directionality of transfer. The transfer was performed at 80 V for 90 minutes (or occasionally 105 minutes for larger proteins). Following transfer, the cassette was disassembled and the membrane was placed in a clear plastic box (choose a box that is closest in size to the membrane to avoid wasting antibody [see Table 8-5]; typically blocking was performed in a large box, then the membrane was cut as needed and transferred to either a medium or small box). From here on, make sure that the membrane does not dry out due to excessive periods of time without solution in the box.

Table 8-5 Volumes of antibody solution and wash steps for various membrane box sizes

Size	Dimensions (in cm) W x L x H	Volume of Antibody Solution	Volume for Washes
small	9.0 x 3.0 x 1.6	3 mL	6 mL
medium	7.0 x 5.0 x 3.0	4 mL	8 mL
large	9.0 x 6.4 x 2.1	6 mL	10 mL

Block the membrane with 5% milk in TBST (or 5% BSA in TBST, depending on the recommendation of the antibody vendor) for a minimum of 2 hours at room temperature with rocking. Primary antibody solutions were prepared in the recommended diluent (see specific chapters for exact preparation), and were incubated overnight with rocking in a cold room. The following day, the primary antibody solution was discarded and the membrane was washed thrice with TBST with a 5-minute incubated rocking period per wash. The secondary antibody was prepared in TBST (dilution factor again depends on the antibody) and was incubated with rocking at room temperature for one hour. After, the antibody solution was discarded and the membrane was again washed thrice with TBST. SuperSignal West Pico PLUS Chemiluminescent Substrate (Thermo Scientific 34580) was prepared by mixing the “Luminol” and “Enhancer” solutions at 1:1 v/v ratio. The volume used per membrane was ½ of the volume of antibody solution (this was to avoid wasting the costly substrate), and this solution was incubated on the membrane with rapid rocking for 5 minutes to ensure complete coverage of the membrane with the minimal volume.

The membrane was immediately placed between two sheets of plastic (cut fresh from a zipper bag), then imaged on a ChemiDoc with “Chemi Resolution” or “Chemi Sensitivity” (no significant difference was observed between these preset programs) using the auto-exposure feature, or occasionally a manual exposure time if signal intensity was low. The blot was also imaged with the Cy3 and Cy5 settings in order to image the stained protein ladder. Using the ImageLab software (BioRad version 5.2.1), blot images were exported using the “Export for Publication” feature.

8.2.12 AmidoBlack 10B Staining

After membranes were imaged, the chemiluminescent substrate was removed by washing the membrane for one hour with PBST (refreshed every 30 minutes) on a rocking platform. The AmidoBlack 10B stain (8.3.14) was incubated with rocking for 5 minutes at room temperature. The stain was discarded and the membrane was destained (8.3.15) with refreshment of solution every 5 minutes until the background became off-white. A cell phone camera was used to image stained membranes in lieu of the camera on the ChemiDoc.

8.3 Common Buffers and Solutions Recipes

When searching for and preparing common buffers, there are numerous sources that provide a range of different preparations, all of which may yield differing final concentrations of reagents. The exact recipes of common laboratory buffers are detailed below to ensure clarity for reproduction of any experiments described within.

As there is often a high degree of variability between batches of unnatural amino acids, Table 8-6 comprises the UAAs used in this work, the chemist who synthesized the batch used, and the solvent used for preparation of stock solutions.

Table 8-6 Preparation of UAA stock solutions

UAA	Synthesized by	Stock concentration	Solvent used
AAPF	Trevor Horst	100 mM	DMSO
AllocK	commercial	100 mM	milliQ water
AzoF	Trevor Horst	100 mM	DMSO
HCK	Subhas Samanta	100 mM	DMSO
oPyrAzoF	Trevor Horst	100 mM	DMSO
ONBY	Jessica Torres	100 mM	0.25 M NaOH
NorK	Anirban Bardhan	100 mM	milliQ water
NVC	Taylor Courtney	100 mM	DMSO

8.3.1 10X Phosphate Buffered Saline (PBS)

- 80 g NaCl
- 2.0 g KCl
- 14.4 g Na₂HPO₄
- 2.4 g KH₂PO₄

Dissolve in 800 mL of milliQ water. Adjust pH to 7.4 with 7.8 M HCl (referred to colloquially as “65% HCl” in the lab). Fill to 1 liter with milliQ water, store at room temperature indefinitely. Dilute to 1X with milliQ water and store at room temperature. For 1X PBS used with mammalian cells, a small volume was sterile filtered on an as-needed basis. Unless specified otherwise, 1X PBS was used without sterile filtering. Protocol taken from [Cold Spring Harbor](#).

8.3.2 10X Tris Buffered Saline (TBS)

- 88 g NaCl

- 12.1 g Tris-base

Dissolve in 800 mL milliQ water. Adjust to pH 7.4 with 10 M HCl, requires a bit of time and patience. Fill to 1 liter with milliQ water. It can be stored at room temperature indefinitely. Dilute to 1X prior to use with milliQ water (100 mL of 10X into 900 mL of milliQ water), store at room temperature. *Note: Various TBS recipes can be found online, but this one yields 10 mM Tris, 150 mM NaCl when diluted to 1X.*

8.3.3 1X Tris Buffered Saline + Tween-20 (TBST)

- 50 mL of 10X TBS
- 450 mL of milliQ water
- 0.5 mL of Tween-20

Mix thoroughly. Prepare fresh for each western blot. Use TBST to prepare 5% milk (2.5 g of powdered milk into 50 mL of TBST) as blocking solution and primary antibody solution for western blots.

8.3.4 10X Tris-Boric Acid-EDTA (TBE)

- 108 g Tris base
- 55 g boric acid
- 40 mL of 0.5 M EDTA pH 8.0

Add salts and EDTA solution, fill to 1 liter with milliQ water. Autoclave to fully dissolve (and to help minimize precipitation over time). Store at room temperature. Dilute to 1X before using with milliQ water (100 mL of 10X into 900 mL of water). *Note: The quality of the boric acid that was purchased varied significantly over time. Empirically, I found that certain vendors*

caused the 10X stock to precipitate much faster than others. Once a significant degree of precipitation was noticed (typically occurred when ~300 mL remained), the 10X stock was discarded and fresh was made. This was to ensure that a true 1X was achieved upon dilution. Protocol taken from [OpenWetWare](#).

8.3.5 0.5 M EDTA pH 8.0 Solution

- 9.31 g EDTA disodium salt

Add 40 mL milliQ water. Add NaOH pellets individually, one at a time until each dissolves. EDTA does not go into solution until the pH reaches ~8.0. Continue adding NaOH pellets until all of the EDTA has gone into solution (can take roughly 1 hour). Check the pH and adjust back to ~8.0 with 7.8 M HCl if greater than pH 8.2. Store at room temperature indefinitely. Protocol taken from [Cold Spring Harbor](#).

8.3.6 10X SDS-PAGE Running Buffer

- 30.3 g NaCl
- 144 g Tris base
- 10 g sodium dodecyl sulfate (or sodium lauryl sulfate, depending on the vendor)

Fill to 1 liter with milliQ water. Mix thoroughly. Should prepare at least one day prior to needing this, as it can take a significant amount of time to completely dissolve. Dilute to 1X prior to use with milliQ water. Both 10X and 1X can be stored at room temperature indefinitely. To minimize the frequency in which the 1X needs to be prepared, the used 1X running buffer was collected in a separate 1 L bottle and used in the outside portion of the running tank, and fresh 1X

(~ 200 mL) was used inside the chamber during electrophoresis. Every couple of weeks, the used running buffer was discarded. Protocol taken from [Cold Spring Harbor](#).

8.3.7 20X MES-SDS-PAGE Running Buffer

- 97.6 g of MES
- 60.6 g of Tris base
- 10 g of sodium dodecyl sulfate
- 20 mL of 0.5 M EDTA

Combine all solids and the EDTA solution, then fill to 1 liter with milliQ water. Mix thoroughly. Dilute to 1X prior to use (50 mL of 20X into 950 mL of milliQ water). This running buffer was used for electrophoresis of proteins <20 kDa for improved resolution, instead of the recipe in 8.3.6. No modifications were made to electrophoresis voltages or run times. This recipe is based on a product sold by Thermo Scientific (NP00020).

8.3.8 Radioimmunoprecipitation Assay (RIPA) Lysis Buffer – for Mammalian Cells

Initially, RIPA buffer was ordered from Thermo Scientific (100 mL, 89900) for use through December 2018. The exact composition is detailed on their [website](#), so rather than ordering again, 100 mL was made in-house. Final concentration for all components are: 25 mM Tris-HCl pH 7.6, 150 mM NaCl, 1% NP-40, 1% sodium deoxycholate, and 0.1% SDS.

- 2.5 mL of 1 M Tris-HCl pH 7.6
- 5 mL of 3 M NaCl
- 10 mL of 10% NP-40 (borrow solid from Islam lab)
- 10 mL of 10% sodium deoxycholate
- 1 mL of 10% sodium dodecyl sulfate

Combine reagents in 100 mL bottle (re-used original Thermo Nalgene polypropylene bottle). Fill to 100 mL with autoclaved milliQ water, and store indefinitely at 4 °C.

8.3.9 4X Laemmli Sample Buffer

- 2 mL of 1 M Tris-HCl pH 6.8
- 0.8 g sodium dodecyl sulfate
- 4 mL of glycerol
- 400 μ L of β -mercaptoethanol
- 8 mg bromophenol blue

Combine all components in a 15 mL conical tube, then fill to 10 mL with water. Prepare a couple of days in advance since it takes a significant amount of time for everything to go into solution. Two variations of this recipe were prepared: (1) a non-reducing buffer which contains everything except β -mercaptoethanol, and (2) a Native-PAGE buffer which only has Tris, glycerol and dye. All three of the 4X buffers were stored at room temperature indefinitely. Protocol adapted from [OpenWetWare](#).

8.3.10 Coomassie Stain Solution

- 1 g Brilliant Blue G-250
- 700 mL of milliQ water
- 100 mL of glacial acetic acid
- 200 mL of methanol

Mix together in this order in a 1 L bottle. It may take overnight for the dye to completely dissolve. This staining solution can be reused ~10 times. To stain an SDS-PAGE gel, remove the gel from the glass plates, rinse briefly with water to remove residual running buffer, then place in gel box with ~ 50 mL of staining solution. Rock at room temperature overnight.

8.3.11 Coomassie Destain Solution

- 700 mL of milliQ water
- 100 mL of glacial acetic acid
- 200 mL of methanol

Mix together. Destain solution can be reused once filtered over decolorizing carbon to remove the dye. Decolorized destain solution can be reused up to 5 times. To destain a gel, remove (and recollect) the staining solution, then replace with ~50 mL of destaining solution. Rock at room temperature with regular refreshing of destain solution. Continue this process until the bands are visibly detectable above background (typically takes 8 to 12 hours).

8.3.12 10X Western Blot Transfer Buffer

- 30.3 g NaCl
- 144 g Tris base

Fill to 1 liter with milliQ water. Mix thoroughly. Store at 4 °C indefinitely.

8.3.13 1X Western Blot Transfer Buffer

- 100 mL of 10X transfer buffer
- 200 mL of methanol
- 700 mL of milliQ water

Mix thoroughly. Prepare fresh each time for every western blot. One liter is enough for a single tank that can hold two transfer cassettes. *Note: Some protocols recommend adding SDS to the transfer buffer; however, in my experience this causes undesired artifacts on the membrane following the transfer.* Unless otherwise noted in the specific protocol, western blots were always

performed in the absence of SDS. The 1X transfer buffer was pre-chilled for ~1 hour in a –80 °C freezer until used for transfer.

8.3.14 Amido Black 10B Stain (for PVDF Membrane)

- 100 mg Amido Black 10B
- 45 mL of methanol
- 15 mL of glacial acetic acid
- 40 mL of milliQ water

Add dye to 250 mL glass bottle. Add water, followed by methanol and acetic acid. Mix thoroughly. Store at room temperature in the dark.

8.3.15 Amido Black 10B Destain (for PVDF Membrane)

- 90 mL of methanol
- 2 mL of glacial acetic acid
- 8 mL of milliQ water

Mix together in a 250 mL glass bottle.

8.3.16 DMEM (for Culturing Mammalian Cells)

- 6.7 g DMEM (GE catalog #: SH3000303)
- 1.85 g sodium bicarbonate
- 55 mg sodium pyruvate

Combine these three solids in an autoclaved 500 mL glass bottle. Add 445 mL of milliQ water and mix thoroughly until completely dissolved. In a tissue culture hood, carefully pour the media into a 500 mL sterile filter flask (0.2 µm PES filter), then add 5 mL of 100X

penicillin/streptomycin and 50 mL of FBS. If making antibiotic-free media, use 450 mL of milliQ water when dissolving the solids. After sterile filtering, store media in the 4 °C fridge in the cell culture room. Warm to 37 °C in the tissue culture room water bath prior to using for any cell work.

8.3.17 Transformation Storage Buffer (TSB)

- 20.5 mL of 2X LB Broth pH 6.5
- 10 mL of 50% PEG (3,350 molecular weight)
- 2.5 mL of neat DMSO
- 0.5 mL of 1 M MgCl₂
- 0.5 mL of 1 M MgSO₄
- 16 mL of autoclaved milliQ water

Autoclave the LB broth solution, then transfer 20.5 mL to a 50 mL conical tube. Add the remaining solutions and water for 50 mL final volume. Use a 0.2 µm sterile syringe filter to sterilize the solution, then store at 4 °C indefinitely.

8.3.18 5X KCM Solution (for KCM Transformations)

- 6 mL of 2.5 M KCl
- 4.5 mL of 1 M CaCl₂
- 7.5 mL of 1 M MgCl₂
- 12 mL of milliQ water

Thoroughly mix all four together. Sterilize by syringe filtering (0.2 µm), then store aliquots at -20 °C. Once thawed, aliquots can be stored at 4 °C indefinitely.

8.3.19 5X Isothermal Gibson Assembly Buffer

- 3 ml of 1 M Tris-HCl pH 7.5
- 150 μ l of 2 M MgCl₂
- 600 μ l of 10 mM dNTPs
- 300 μ L of 1 M DTT
- 1.5 g of PEG-8000
- 20 mg of NAD⁺ hydrate

Combine all reagents in a 15 mL conical tube and fill to 6 mL with autoclaved milliQ water.

Store at -20 °C in 320 μ L aliquots.

8.3.20 Gibson Assembly Master Mix

- 320 μ L of 5X Isothermal Gibson Assembly Buffer
- 0.64 μ L of T5 Exonuclease (10U/ μ L) [NEB M0363S]
- 20 μ L of Phusion polymerase (2U/ μ L) [Thermo Scientific F530L]
- 160 μ L of Taq DNA ligase (40U/ μ L) [Applied Biomedical Materials E090]
- 699 μ L of autoclaved milliQ water

Combine all components in a 1.7 mL tube. Mix well by inverting, do not vortex. Keep all working solutions on ice during preparation. Aliquot 15 μ L into pre-chilled PCR tubes on ice (makes 80 tubes). Store at -20 °C until needed.

8.3.21 Lysis Buffer (for Bacterial Protein Expression)

- 24 mL of 3 M NaCl
- 11.185 mL of 1 M Na₂HPO₄
- 0.815 mL of 1 M NaH₂PO₄
- 10 mL of Elution buffer
- 65 μ L of 10 M NaOH

Combine all of the above into a 250 mL glass bottle. Fill to 250 mL with autoclaved milliQ water. Check that the pH is ~8.0. Store at room temperature indefinitely. This contains 10 mM imidazole to help minimize background binding during purification with Ni-NTA resin.

8.3.22 Wash Buffer (for Bacterial Protein Expression)

- 10 mL of Lysis buffer
- 435 μ L of Elution buffer

Mix the two buffers together to generate a 20 mM imidazole wash buffer. If more stringent washes are needed, a 78.5 mM imidazole wash buffer can be prepared by mixing 5 mL of Lysis buffer with 2 mL of Elution buffer.

8.3.23 Elution Buffer (for Bacterial Protein Expression)

- 0.3 g NaH_2PO_4
- 0.877 g NaCl
- 0.85 g imidazole
- 107 μ L of 10 M NaOH

Combine all solids in a 50 mL conical tube. Add 40 mL of autoclaved milliQ water. Vortex to dissolve all reagents. Add the sodium hydroxide solution. Then fill to 50 mL with autoclaved milliQ water. This yields a 250 mM imidazole solution.

8.3.24 FKBP/FRB Storage and Assay Buffer

- 600 μ L of 1 M Tris-HCl pH 7.4
- 1 mL of 3 M NaCl
- 3 mL of glycerol

Combine all three components into a 50 mL conical tube. Then fill to 30 mL with milliQ water. Final buffer concentration is 20 mM Tris pH 7.4, 100 mM NaCl, and 10% glycerol.

8.3.25 TEV Protease Lysis and Storage Buffer

- 5 mL of 1 M Tris-HCl pH 8.0
- 8.3 mL of 3 M NaCl
- 0.25 mL of 1 M DTT
- 50 μ L of 0.5 M EDTA

Combine all reagents in a 50 mL conical. Fill to 50 mL with autoclaved milliQ water. As DTT is unstable in solution, this should be prepared fresh as needed.

8.3.26 1 M Dithiothreitol (DTT) – for Gel Band Sample Preparation

- 1.54 g of dithiothreitol

Dissolve in B&J water (to 10 mL final volume). Transfer 12 μ L into 0.65 mL eppendorf tubes and store at -20 °C. Working solutions were prepared fresh by diluting 10 μ L of the 1 M solution into 990 μ L of 25 mM ammonium bicarbonate.

8.3.27 450 mM Iodoacetamide (IAA) – for Gel Band Sample Preparation

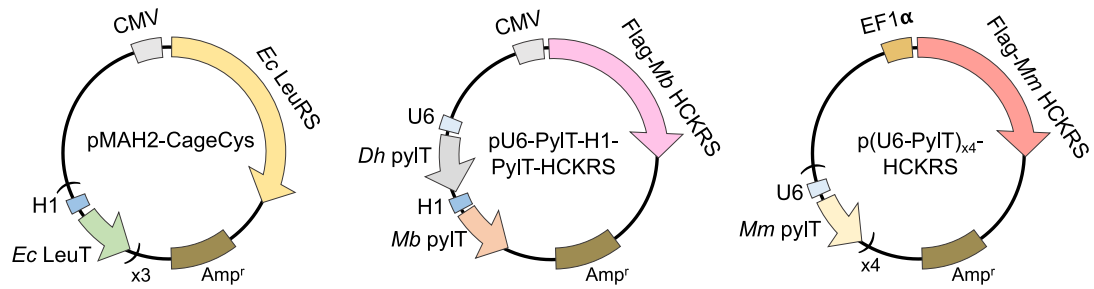
- 416 mg of iodoacetamide

Dissolve in 5 mL of B&J water. Transfer 65 μ L into 0.65 mL eppendorf tubes and store at -20 °C. Working solutions were prepared fresh and stored in the dark. Dilute 61 μ L of the 450 mM solution into 439 μ L of 25 mM ammonium bicarbonate.

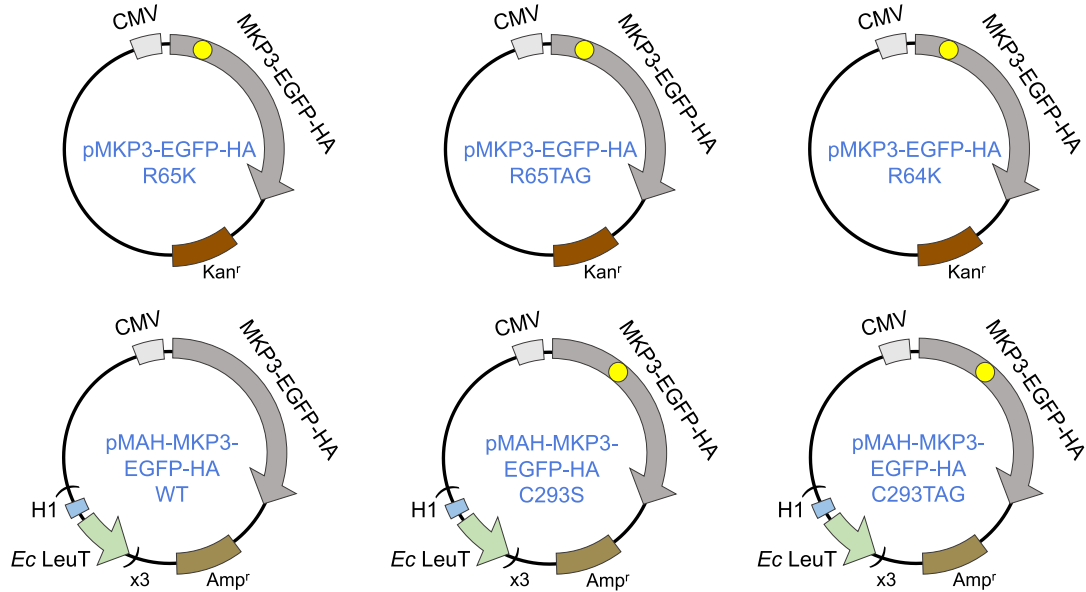
Appendix A – Plasmid Maps

Maps of all plasmids used within this document are included in this Appendix section. Plasmids assembled by myself are denoted with a blue color-coded plasmid name, while plasmids assembled by fellow lab members or those that were purchased are denoted in black.

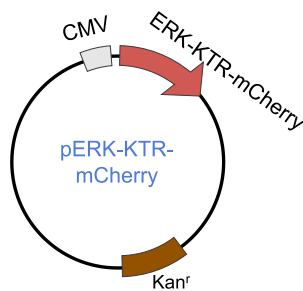
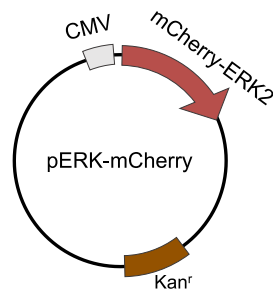
Synthetase/tRNA constructs:



Phosphatase constructs:



Reporter constructs:



Bacterial expression:

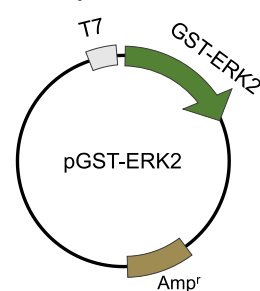


Figure A-1 Plasmids used in Chapter 2

Plasmids pMAH2-CageCys and pGST-ERK2 were purchased from Addgene #71404 and #47573, respectively. Plasmids pU6-PylT-H1-PylT-HCKRS and p(U6-PylT)_{x4}-HCKRS were provided by Jihe Liu. Plasmid pERK-mCherry was a gift from Jason Haugh at North Carolina State University.

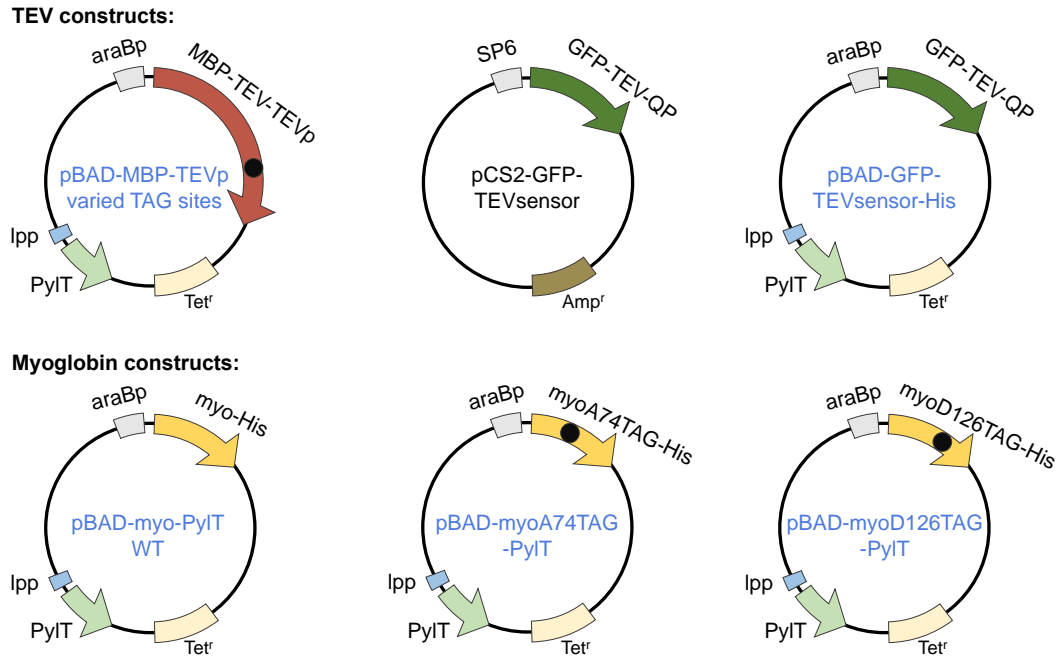


Figure A-2 Plasmids used in Chapter 3
 Plasmid pCS2-GFP-TEVsensor was provided by Kristie Darrah.

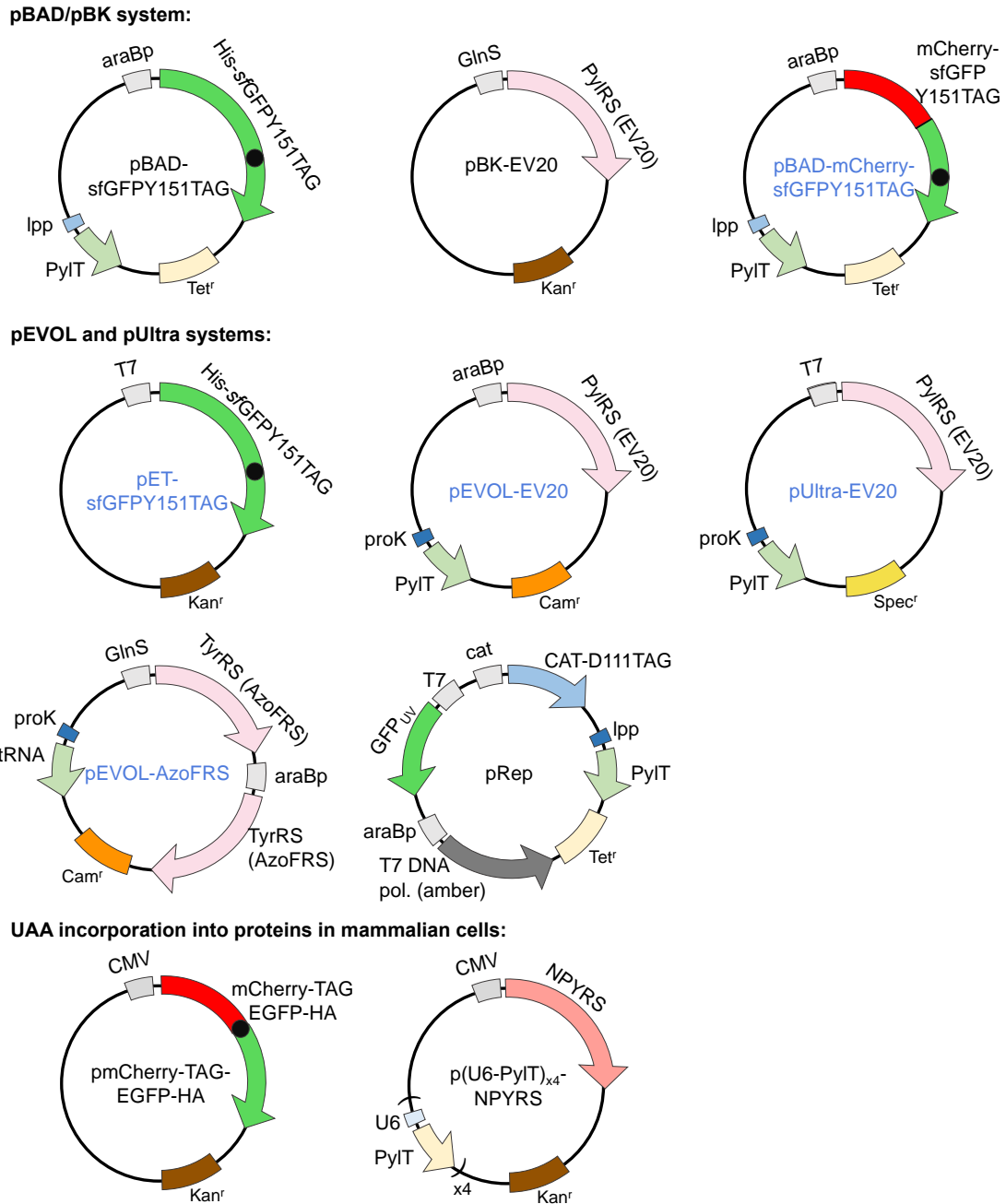
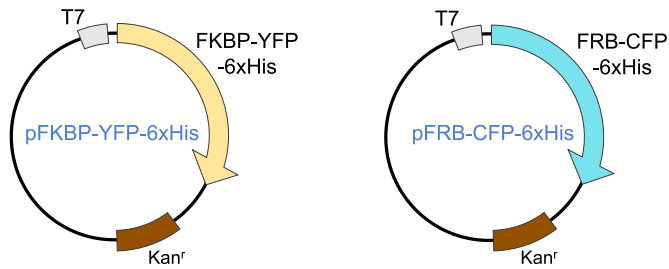


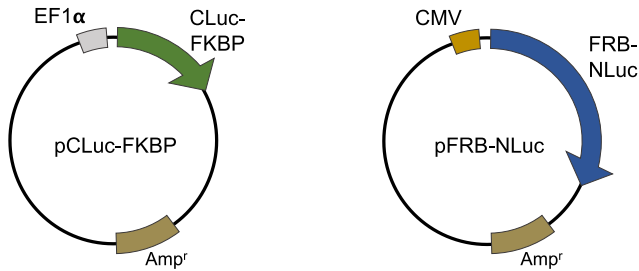
Figure A-3 Plasmids used in Chapter 4

Plasmids pBAD-sfGFPY151TAG and pBK-EV20 were obtained from Jihe Liu. pRep was a gift from Ashton Cropp at Virginia Commonwealth University. UAA incorporation plasmids pmCherry-TAG-EGFP-HA and p(U6-PyIT)_{x4}-NPYRS were provided by Jihe Liu and Ji Luo, respectively. The NPYRS sequence is a mammalian codon optimized version of the EV20 synthetase containing mutations L270F, L274M, N311G, C313G, and Y349F.

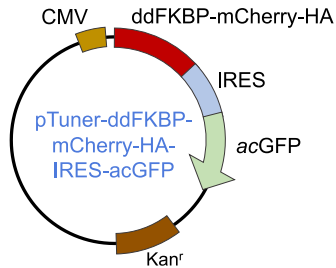
Bacterial FKBP/FRB constructs:



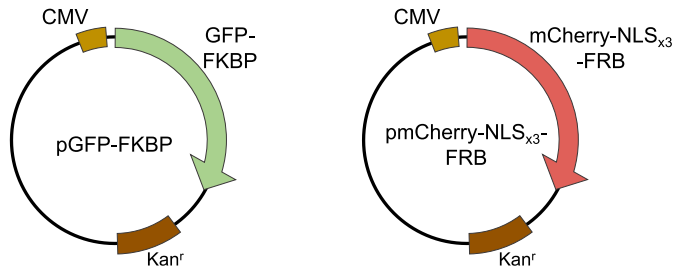
Split Luciferase Reporter:



FKBP degenron:



Nuclear Translocation:



Membrane Translocation:

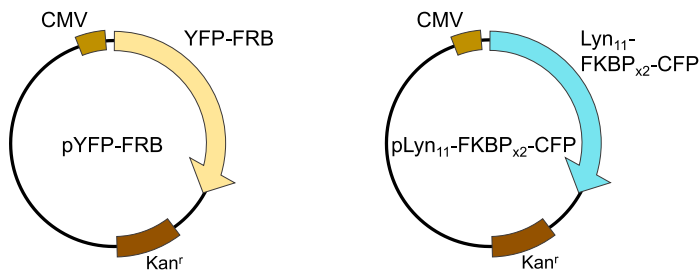


Figure A-4 Plasmids used in Chapters 5 and 6

Plasmids pCLuc-FKBP, pFRB-NLuc, pYFP-FRB, and pLyn₁₁-FKBP_{x2}-CFP were purchased from Addgene #31184, #31181 #20148, and #20149, respectively. Plasmids pGFP-FKBP and pmCherry-NLS_{x3}-FRB were gifts from Takamari Inoue at Johns Hopkins.

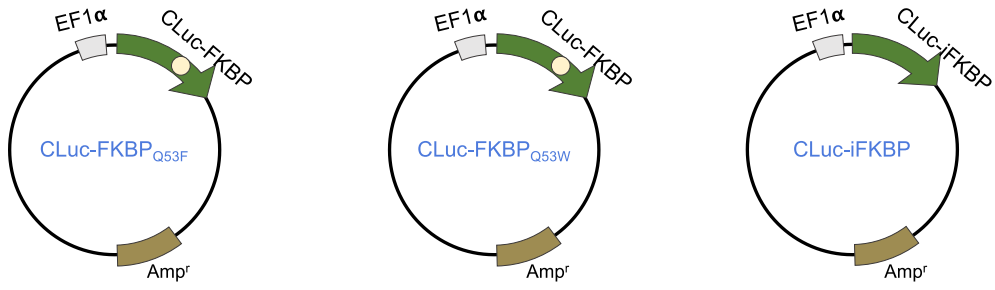


Figure A-5 Plasmids used in Chapter 7

Appendix B – Synthetase Panel Mutants

	301	302	305	306	309	346	348	350	384	<i>M. mazei</i> numbering
Name	266	267	270	271	274	311	313	315	349	<i>M. barkeri</i> numbering
wild-type	L	A	L	Y	L	N	C	M	Y	
EV16_1				A		A	A			
EV16_2					V	A	A			
EV16_3						A	A			F
EV16_4				A		A	A			F
EV16_5				M	A	A	A			F
EV16-7		T				A	A			
EV16-8		S				A	A			
EV17				M	A					F
EV18_1				M	A	G	G			F
EV18_2			F	M	A	G	G			F
EV19_1						G	G			F
EV19_2			F			G	G			F
EV20			F		M	G	G			F

Figure A-6 Synthetase panel mutations

This is not a comprehensive list of synthetase mutants available in the lab, but only contains mutants that were included in the synthetase panel screens performed in Chapter 4.

Appendix C – ITC Binding Curves

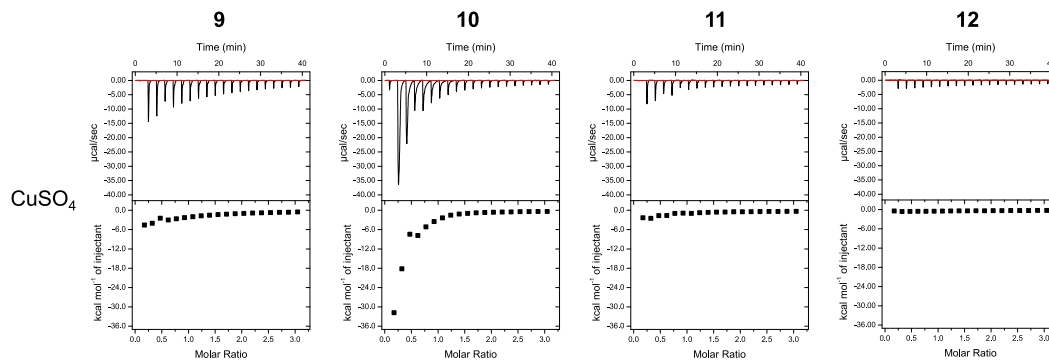


Figure A-7 Raw data corresponding to the heat maps shown in Figure 4-27

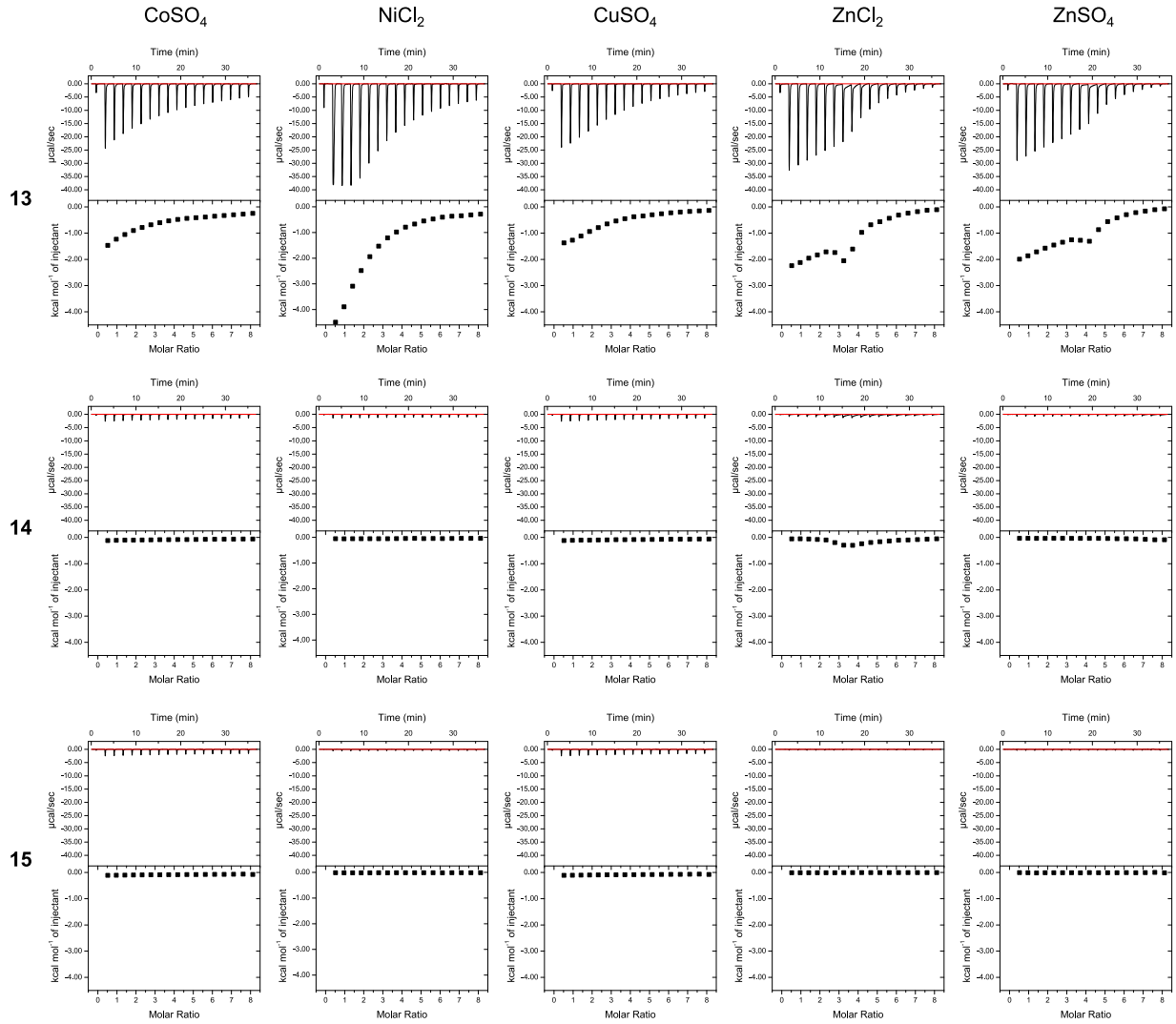


Figure A-8 Raw data corresponding to the heat maps shown in Figure 4-28

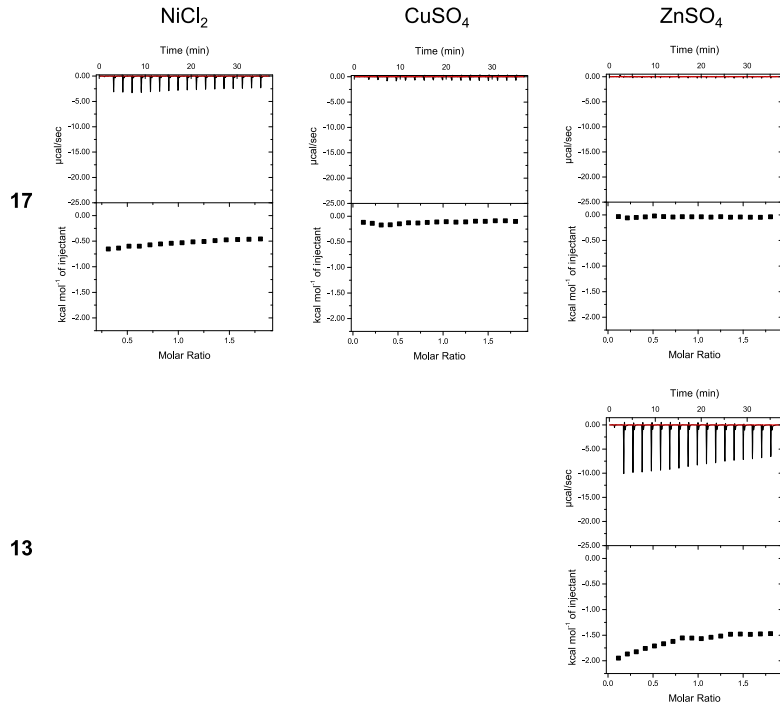


Figure A-9 Raw data corresponding to the heat maps shown in Figure 4-29

Appendix D – Description of LEDs

The University of Pittsburgh Electronics Shop constructed the LED systems used in experiments described in this document. The LEDs were obtained from Mouser Electronics: 405 nm (LZ1-10UA00-00U8), 450 nm (LXML-PR02-A900), 530 nm (LXML-PM01-0100) or LuxeonStar: 415 nm (SZ-01-U8) or 470 nm (SP-01-B4). Heat sinks (to which the LEDs were mounted) were purchased from Digi-Key Electronics (501503B00000G).

Bibliography

1. Khoury, G. A.; Baliban, R. C.; Floudas, C. A., Proteome-wide post-translational modification statistics: frequency analysis and curation of the swiss-prot database. *Sci Rep* **2011**, *1*.
2. Bock, A.; Forchhammer, K.; Heider, J.; Leinfelder, W.; Sawers, G.; Veprek, B.; Zinoni, F., Selenocysteine: the 21st amino acid. *Mol. Microbiol.* **1991**, *5* (3), 515-20.
3. Atkins, J. F.; Gesteland, R., Biochemistry. The 22nd amino acid. *Science* **2002**, *296* (5572), 1409-10.
4. Wan, W.; Tharp, J. M.; Liu, W. R., Pyrrolysyl-tRNA synthetase: An ordinary enzyme but an outstanding genetic code expansion tool. *Biochim. Biophys. Acta* **2014**, *1844* (6), 1059-1070.
5. Young, T. S.; Schultz, P. G., Beyond the canonical 20 amino acids: expanding the genetic lexicon. *J. Biol. Chem.* **2010**, *285* (15), 11039-44.
6. Wang, L.; Brock, A.; Herberich, B.; Schultz, P. G., Expanding the genetic code of *Escherichia coli*. *Science* **2001**, *292* (5516), 498-500.
7. Liu, C. C.; Schultz, P. G., Adding New Chemistries to the Genetic Code. *Annual Review of Biochemistry* **2010**, *79* (1), 413-444.
8. Xie, J.; Schultz, P. G., An expanding genetic code. *Methods* **2005**, *36* (3), 227-238.
9. Davis, L.; Chin, J. W., Designer proteins: applications of genetic code expansion in cell biology. *Nat. Rev. Mol. Cell Biol.* **2012**, *13* (3), 168-82.
10. Ankenbruck, N.; Courtney, T.; Naro, Y.; Deiters, A., Optochemical Control of Biological Processes in Cells and Animals. *Angew. Chem. Int. Ed.* **2018**, *57*, 2-33.
11. Baker, A. S.; Deiters, A., Optical control of protein function through unnatural amino acid mutagenesis and other optogenetic approaches. *ACS Chem Biol* **2014**, *9* (7), 1398-407.
12. Tsai, Y.-H.; Essig, S.; James, J. R.; Lang, K.; Chin, J. W., Selective, rapid and optically switchable regulation of protein function in live mammalian cells. *Nature chemistry* **2015**, *7* (7), 554-561.
13. Broichhagen, J.; Damijonaitis, A.; Levitz, J.; Sokol, K. R.; Leippe, P.; Konrad, D.; Isacoff, E. Y.; Trauner, D., Orthogonal Optical Control of a G Protein-Coupled Receptor with a SNAP-Tethered Photochromic Ligand. *ACS Cent Sci* **2015**, *1* (7), 383-93.

14. Deisseroth, K., Optogenetics: 10 years of microbial opsins in neuroscience. *Nat. Neurosci.* **2015**, *18* (9), 1213-1225.
15. Zhang, K.; Cui, B., Optogenetic control of intracellular signaling pathways. *Trends Biotechnol.* **2015**, *33* (2), 92-100.
16. Weitzman, M.; Hahn, K. M., Optogenetic approaches to cell migration and beyond. *Curr. Opin. Cell Biol.* **2014**, *30*, 112-20.
17. Repina, N. A.; Rosenbloom, A.; Mukherjee, A.; Schaffer, D. V.; Kane, R. S., At Light Speed: Advances in Optogenetic Systems for Regulating Cell Signaling and Behavior. *Annual Review of Chemical and Biomolecular Engineering* **2017**, *8* (1), 13-39.
18. Hemphill, J.; Borchardt, E. K.; Brown, K.; Asokan, A.; Deiters, A., Optical Control of CRISPR/Cas9 Gene Editing. *J. Am. Chem. Soc.* **2015**, *137* (17), 5642-5.
19. Hemphill, J.; Chou, C.; Chin, J. W.; Deiters, A., Genetically encoded light-activated transcription for spatiotemporal control of gene expression and gene silencing in mammalian cells. *J. Am. Chem. Soc.* **2013**, *135* (36), 13433-9.
20. Luo, J.; Arbely, E.; Zhang, J.; Chou, C.; Uprety, R.; Chin, J. W.; Deiters, A., Genetically encoded optical activation of DNA recombination in human cells. *Chem Commun (Camb)* **2016**, *52* (55), 8529-32.
21. Gautier, A.; Deiters, A.; Chin, J. W., Light-Activated Kinases Enable Temporal Dissection of Signaling Networks in Living Cells. *Journal of the American Chemical Society* **2011**, *133* (7), 2124-2127.
22. Liu, J.; Hemphill, J.; Samanta, S.; Tsang, M.; Deiters, A., Genetic Code Expansion in Zebrafish Embryos and Its Application to Optical Control of Cell Signaling. *J. Am. Chem. Soc.* **2017**, *139* (27), 9100-9103.
23. Liaunardy-Jopeace, A.; Murton, B. L.; Mahesh, M.; Chin, J. W.; James, J. R., Encoding optical control in LCK kinase to quantitatively investigate its activity in live cells. *Nat. Struct. Mol. Biol.* **2017**, *24* (12), 1155-1163.
24. Walker, O. S.; Elsasser, S. J.; Mahesh, M.; Bachman, M.; Balasubramanian, S.; Chin, J. W., Photoactivation of Mutant Isocitrate Dehydrogenase 2 Reveals Rapid Cancer-Associated Metabolic and Epigenetic Changes. *J. Am. Chem. Soc.* **2016**, *138* (3), 718-21.
25. Engelke, H.; Chou, C.; Uprety, R.; Jess, P.; Deiters, A., Control of protein function through optochemical translocation. *ACS Synth Biol* **2014**, *3* (10), 731-6.
26. Erickson, S. B.; Mukherjee, R.; Kelemen, R. E.; Wrobel, C. J.; Cao, X.; Chatterjee, A., Precise Photoremovable Perturbation of a Virus-Host Interaction. *Angew. Chem. Int. Ed. Engl.* **2017**, *56* (15), 4234-4237.

27. Luo, J.; Uprety, R.; Naro, Y.; Chou, C.; Nguyen, D. P.; Chin, J. W.; Deiters, A., Genetically encoded optochemical probes for simultaneous fluorescence reporting and light activation of protein function with two-photon excitation. *J. Am. Chem. Soc.* **2014**, *136* (44), 15551-8.
28. Luo, J.; Kong, M.; Liu, L.; Samanta, S.; Van Houten, B.; Deiters, A., Optical Control of DNA Helicase Function through Genetic Code Expansion. *ChemBioChem* **2017**, *18* (5), 466-469.
29. Stanley, M.; Virdee, S., Genetically Directed Production of Recombinant, Isosteric and Nonhydrolysable Ubiquitin Conjugates. *ChemBioChem* **2016**, *17* (15), 1472-80.
30. Pace, N. J.; Weerapana, E., Diverse functional roles of reactive cysteines. *ACS Chem Biol* **2013**, *8* (2), 283-96.
31. Wu, N.; Deiters, A.; Cropp, T. A.; King, D.; Schultz, P. G., A genetically encoded photocaged amino acid. *J. Am. Chem. Soc.* **2004**, *126* (44), 14306-7.
32. Nguyen, D. P.; Mahesh, M.; Elsasser, S. J.; Hancock, S. M.; Uttamapinant, C.; Chin, J. W., Genetic encoding of photocaged cysteine allows photoactivation of TEV protease in live mammalian cells. *J. Am. Chem. Soc.* **2014**, *136* (6), 2240-3.
33. Ren, W.; Ji, A.; Ai, H. W., Light activation of protein splicing with a photocaged fast intein. *J. Am. Chem. Soc.* **2015**, *137* (6), 2155-8.
34. Tyszkiewicz, A. B.; Muir, T. W., Activation of protein splicing with light in yeast. *Nat. Methods* **2008**, *5*, 303.
35. Bocker, J. K.; Friedel, K.; Matern, J. C.; Bachmann, A. L.; Mootz, H. D., Generation of a genetically encoded, photoactivatable intein for the controlled production of cyclic peptides. *Angew. Chem. Int. Ed. Engl.* **2015**, *54* (7), 2116-20.
36. Uprety, R.; Luo, J.; Liu, J.; Naro, Y.; Samanta, S.; Deiters, A., Genetic encoding of caged cysteine and caged homocysteine in bacterial and mammalian cells. *ChemBioChem* **2014**, *15* (12), 1793-9.
37. Mousa, R.; Notis Dardashti, R.; Metanis, N., Selenium and Selenocysteine in Protein Chemistry. *Angew. Chem. Int. Ed. Engl.* **2017**, *56* (50), 15818-15827.
38. Gupta, N.; DeMong, L. W.; Banda, S.; Copeland, P. R., Reconstitution of Selenocysteine Incorporation Reveals Intrinsic Regulation by SECIS Elements. *J. Mol. Biol.* **2013**, *425* (14), 2415-2422.
39. Mukai, T.; Englert, M.; Tripp, H. J.; Miller, C.; Ivanova, N. N.; Rubin, E. M.; Kyrpides, N. C.; Soll, D., Facile Recoding of Selenocysteine in Nature. *Angew. Chem. Int. Ed. Engl.* **2016**, *55* (17), 5337-41.

40. Metanis, N.; Hilvert, D., Harnessing selenocysteine reactivity for oxidative protein folding. *Chem Sci* **2015**, *6* (1), 322-325.
41. Rakauskaite, R.; Urbanaviciute, G.; Ruksenaite, A.; Liutkeviciute, Z.; Juskenas, R.; Masevicius, V.; Klimasauskas, S., Biosynthetic selenoproteins with genetically-encoded photocaged selenocysteines. *Chem Commun (Camb)* **2015**, *51* (39), 8245-8.
42. Deiters, A.; Groff, D.; Ryu, Y.; Xie, J.; Schultz, P. G., A genetically encoded photocaged tyrosine. *Angew. Chem. Int. Ed. Engl.* **2006**, *45* (17), 2728-31.
43. Edwards, W. F.; Young, D. D.; Deiters, A., Light-activated Cre recombinase as a tool for the spatial and temporal control of gene function in mammalian cells. *ACS Chem Biol* **2009**, *4* (6), 441-5.
44. Chou, C.; Young, D. D.; Deiters, A., A light-activated DNA polymerase. *Angew. Chem. Int. Ed. Engl.* **2009**, *48* (32), 5950-3.
45. Chou, C.; Young, D. D.; Deiters, A., Photocaged t7 RNA polymerase for the light activation of transcription and gene function in pro- and eukaryotic cells. *ChemBioChem* **2010**, *11* (7), 972-7.
46. Chou, C.; Deiters, A., Light-Activated Gene Editing with a Photocaged Zinc-Finger Nuclease. *Angew. Chem. Int. Ed. Engl.* **2011**, *50* (30), 6839-42.
47. Arbely, E.; Torres-Kolbus, J.; Deiters, A.; Chin, J. W., Photocontrol of tyrosine phosphorylation in mammalian cells via genetic encoding of photocaged tyrosine. *J. Am. Chem. Soc.* **2012**, *134* (29), 11912-5.
48. Luo, J.; Torres-Kolbus, J.; Liu, J.; Deiters, A., Genetic Encoding of Photocaged Tyrosines with Improved Light-Activation Properties for the Optical Control of Protease Function. *ChemBioChem* **2017**, *18* (14), 1442-1447.
49. Jiang, F.; Doudna, J. A., CRISPR–Cas9 Structures and Mechanisms. *Annual Review of Biophysics* **2017**, *46* (1), 505-529.
50. Hsu, Patrick D.; Lander, Eric S.; Zhang, F., Development and Applications of CRISPR-Cas9 for Genome Engineering. *Cell* **157** (6), 1262-1278.
51. Zhou, W.; Deiters, A., Conditional Control of CRISPR/Cas9 Function. *Angew. Chem. Int. Ed. Engl.* **2016**, *55* (18), 5394-9.
52. Brown, W.; Liu, J.; Tsang, M.; Deiters, A., Cell Lineage Tracing in Zebrafish Embryos with an Expanded Genetic Code. *ChemBioChem* **2018**, *19* (12), 1244-1249.
53. Rahman, S. M. T.; Zhou, W.; Deiters, A.; Haugh, J. M., Optical control of MAP kinase kinase 6 (MKK6) reveals that it has divergent roles in pro-apoptotic and anti-proliferative signaling. *J. Biol. Chem.* **2020**, *295* (25), 8494-8504.

54. Kang, J. Y.; Kawaguchi, D.; Coin, I.; Xiang, Z.; O'Leary, D. D.; Slesinger, P. A.; Wang, L., In vivo expression of a light-activatable potassium channel using unnatural amino acids. *Neuron* **2013**, *80* (2), 358-70.
55. Kang, J. Y.; Kawaguchi, D.; Wang, L., Optical Control of a Neuronal Protein Using a Genetically Encoded Unnatural Amino Acid in Neurons. *J Vis Exp* **2016**, (109), e53818.
56. Larson, A. S.; Hergenrother, P. J., Light activation of Staphylococcus aureus toxin YoeBSa1 reveals guanosine-specific endoribonuclease activity. *Biochemistry* **2014**, *53* (1), 188-201.
57. Day, E. K.; Sosale, N. G.; Lazzara, M. J., Cell Signaling Regulation by Protein Phosphorylation: A Multivariate, Heterogeneous, and Context-dependent Process. *Curr. Opin. Biotechnol.* **2016**, *40*, 185-92.
58. Caunt, C. J.; Keyse, S. M., Dual-specificity MAP kinase phosphatases (MKPs): Shaping the outcome of MAP kinase signalling. *FEBS J.* **2013**, *280* (2), 489-504.
59. Wang, J.; Liu, Y.; Liu, Y.; Zheng, S.; Wang, X.; Zhao, J.; Yang, F.; Zhang, G.; Wang, C.; Chen, P. R., Time-resolved protein activation by proximal decaging in living systems. *Nature* **2019**, *569* (7757), 509-513.
60. Zhou, X. X.; Fan, L. Z.; Li, P.; Shen, K.; Lin, M. Z., Optical control of cell signaling by single-chain photoswitchable kinases. *Science* **2017**, *355* (6327), 836-842.
61. Toettcher, J. E.; Weiner, O. D.; Lim, W. A., Using optogenetics to interrogate the dynamic control of signal transmission by the Ras/Erk module. *Cell* **2013**, *155* (6), 1422-34.
62. Johnson, H. E.; Goyal, Y.; Pannucci, N. L.; Schupbach, T.; Shvartsman, S. Y.; Toettcher, J. E., The Spatiotemporal Limits of Developmental Erk Signaling. *Dev. Cell* **2017**, *40* (2), 185-192.
63. Levskaya, A.; Weiner, O. D.; Lim, W. A.; Voigt, C. A., Spatiotemporal control of cell signalling using a light-switchable protein interaction. *Nature* **2009**, *461* (7266), 997-1001.
64. Dagliyan, O.; Tarnawski, M.; Chu, P. H.; Shirvanyants, D.; Schlichting, I.; Dokholyan, N. V.; Hahn, K. M., Engineering extrinsic disorder to control protein activity in living cells. *Science* **2016**, *354* (6318), 1441-1444.
65. Wu, Y. I.; Frey, D.; Lungu, O. I.; Jaehrig, A.; Schlichting, I.; Kuhlman, B.; Hahn, K. M., A genetically encoded photoactivatable Rac controls the motility of living cells. *Nature* **2009**, *461* (7260), 104-8.
66. Yi, J. J.; Wang, H.; Vilela, M.; Danuser, G.; Hahn, K. M., Manipulation of endogenous kinase activity in living cells using photoswitchable inhibitory peptides. *ACS Synth Biol* **2014**, *3* (11), 788-95.

67. Priestman, M. A.; Sun, L.; Lawrence, D. S., Dual wavelength photoactivation of cAMP- and cGMP-dependent protein kinase signaling pathways. *ACS Chem Biol* **2011**, *6* (4), 377-84.
68. Bardhan, A.; Deiters, A., Development of photolabile protecting groups and their application to the optochemical control of cell signaling. *Curr. Opin. Struct. Biol.* **2019**, *57*, 164-175.
69. Leopold, A. V.; Chernov, K. G.; Verkhusha, V. V., Optogenetically controlled protein kinases for regulation of cellular signaling. *Chem. Soc. Rev.* **2018**, *47* (7), 2454-2484.
70. Idevall-Hagren, O.; Dickson, E. J.; Hille, B.; Toomre, D. K.; De Camilli, P., Optogenetic control of phosphoinositide metabolism. *Proceedings of the National Academy of Sciences* **2012**, *109* (35), E2316-E2323.
71. Karginov, A. V.; Zou, Y.; Shirvanyants, D.; Kota, P.; Dokholyan, N. V.; Young, D. D.; Hahn, K. M.; Deiters, A., Light regulation of protein dimerization and kinase activity in living cells using photocaged rapamycin and engineered FKBP. *J. Am. Chem. Soc.* **2011**, *133* (3), 420-3.
72. Fahs, S.; Lujan, P.; Köhn, M., Approaches to Study Phosphatases. *ACS Chemical Biology* **2016**, *11* (11), 2944-2961.
73. Cargnello, M.; Roux, P. P., Activation and Function of the MAPKs and Their Substrates, the MAPK-Activated Protein Kinases. *Microbiol. Mol. Biol. Rev.* **2011**, *75* (1), 50-83.
74. Low, H. B.; Zhang, Y., Regulatory Roles of MAPK Phosphatases in Cancer. *Immune Netw* **2016**, *16* (2), 85-98.
75. Owens, D. M.; Keyse, S. M., Differential regulation of MAP kinase signalling by dual-specificity protein phosphatases. *Oncogene* **2007**, *26* (22), 3203-13.
76. Seternes, O.-M.; Kidger, A. M.; Keyse, S. M., Dual-specificity MAP kinase phosphatases in health and disease. *Biochim. Biophys. Acta* **2019**, *1866* (1), 124-143.
77. Kidger, A. M.; Keyse, S. M., Dual-Specificity Map Kinase (MAPK) Phosphatases (MKPs) and Their Involvement in Cancer. In *Protein Tyrosine Phosphatases in Cancer*, Neel, B. G.; Tonks, N. K., Eds. Springer New York: New York, NY, 2016; pp 201-231.
78. Ahmad, M. K.; Abdollah, N. A.; Shafie, N. H.; Yusof, N. M.; Razak, S. R. A., Dual-specificity phosphatase 6 (DUSP6): a review of its molecular characteristics and clinical relevance in cancer. *Cancer Biology & Medicine* **2018**, *15* (1), 14-28.
79. Zhou, B.; Wu, L.; Shen, K.; Zhang, J.; Lawrence, D. S.; Zhang, Z. Y., Multiple regions of MAP kinase phosphatase 3 are involved in its recognition and activation by ERK2. *J. Biol. Chem.* **2001**, *276* (9), 6506-15.

80. Camps, M.; Nichols, A.; Gillieron, C.; Antonsson, B.; Muda, M.; Chabert, C.; Boschert, U.; Arkinstall, S., Catalytic activation of the phosphatase MKP-3 by ERK2 mitogen-activated protein kinase. *Science* **1998**, *280* (5367), 1262-5.
81. Bose, A. K.; Janes, K. A., A high-throughput assay for phosphoprotein-specific phosphatase activity in cellular extracts. *Molecular & cellular proteomics : MCP* **2013**, *12* (3), 797-806.
82. Ahmed, S.; Grant, K. G.; Edwards, L. E.; Rahman, A.; Cirit, M.; Goshe, M. B.; Haugh, J. M., Data-driven modeling reconciles kinetics of ERK phosphorylation, localization, and activity states. *Mol. Syst. Biol.* **2014**, *10* (1).
83. Brunet, A.; Roux, D.; Lenormand, P.; Dowd, S.; Keyse, S.; Pouyssegur, J., Nuclear translocation of p42/p44 mitogen-activated protein kinase is required for growth factor-induced gene expression and cell cycle entry. *EMBO J.* **1999**, *18* (3), 664-74.
84. Karlsson, M.; Mathers, J.; Dickinson, R. J.; Mandl, M.; Keyse, S. M., Both nuclear-cytoplasmic shuttling of the dual specificity phosphatase MKP-3 and its ability to anchor MAP kinase in the cytoplasm are mediated by a conserved nuclear export signal. *J. Biol. Chem.* **2004**, *279* (40), 41882-91.
85. Zhou, B.; Zhang, J.; Liu, S.; Reddy, S.; Wang, F.; Zhang, Z. Y., Mapping ERK2-MKP3 binding interfaces by hydrogen/deuterium exchange mass spectrometry. *J. Biol. Chem.* **2006**, *281* (50), 38834-44.
86. Costa, M.; Marchi, M.; Cardarelli, F.; Roy, A.; Beltram, F.; Maffei, L.; Ratto, G. M., Dynamic regulation of ERK2 nuclear translocation and mobility in living cells. *J. Cell Sci.* **2006**, *119* (23), 4952.
87. Regot, S.; Hughey, J. J.; Bajar, B. T.; Carrasco, S.; Covert, M. W., High-sensitivity measurements of multiple kinase activities in live single cells. *Cell* **2014**, *157* (7), 1724-34.
88. Brown, W.; Liu, J.; Tsang, M.; Deiters, A., Cell-Lineage Tracing in Zebrafish Embryos with an Expanded Genetic Code. *ChemBioChem* **2018**, *19* (12), 1244-1249.
89. Courtney, T.; Deiters, A., Recent advances in the optical control of protein function through genetic code expansion. *Curr. Opin. Chem. Biol.* **2018**, *46*, 99-107.
90. Liu, S.; Sun, J. P.; Zhou, B.; Zhang, Z. Y., Structural basis of docking interactions between ERK2 and MAP kinase phosphatase 3. *Proc Natl Acad Sci U S A* **2006**, *103* (14), 5326-31.
91. Zhang, J.; Zhou, B.; Zheng, C.-F.; Zhang, Z.-Y., A Bipartite Mechanism for ERK2 Recognition by Its Cognate Regulators and Substrates. *J. Biol. Chem.* **2003**, *278* (32), 29901-29912.

92. MacKeigan, J. P.; Murphy, L. O.; Dimitri, C. A.; Blenis, J., Graded Mitogen-Activated Protein Kinase Activity Precedes Switch-Like c-Fos Induction in Mammalian Cells. *Mol. Cell. Biol.* **2005**, *25* (11), 4676-4682.
93. Whitehurst, A.; Cobb, M. H.; White, M. A., Stimulus-coupled spatial restriction of extracellular signal-regulated kinase 1/2 activity contributes to the specificity of signal-response pathways. *Mol. Cell. Biol.* **2004**, *24* (23), 10145-50.
94. Shindo, Y.; Iwamoto, K.; Mouri, K.; Hibino, K.; Tomita, M.; Kosako, H.; Sako, Y.; Takahashi, K., Conversion of graded phosphorylation into switch-like nuclear translocation via autoregulatory mechanisms in ERK signalling. *Nature Communications* **2016**, *7*, 10485.
95. Gautier, A.; Nguyen, D. P.; Lusic, H.; An, W.; Deiters, A.; Chin, J. W., Genetically Encoded Photocontrol of Protein Localization in Mammalian Cells. *Journal of the American Chemical Society* **2010**, *132* (12), 4086-4088.
96. Liu, H.; Naismith, J. H., An efficient one-step site-directed deletion, insertion, single and multiple-site plasmid mutagenesis protocol. *BMC Biotechnol.* **2008**, *8* (1), 91.
97. Schmied, W. H.; Elsässer, S. J.; Uttamapinant, C.; Chin, J. W., Efficient Multisite Unnatural Amino Acid Incorporation in Mammalian Cells via Optimized Pyrrolysyl tRNA Synthetase/tRNA Expression and Engineered eRF1. *Journal of the American Chemical Society* **2014**, *136* (44), 15577-15583.
98. Ahmed, S.; Grant, K. G.; Edwards, L. E.; Rahman, A.; Cirit, M.; Goshe, M. B.; Haugh, J. M., Data-driven modeling reconciles kinetics of ERK phosphorylation, localization, and activity states. *Mol. Syst. Biol.* **2014**, *10*, 718.
99. Gibson, D. G.; Young, L.; Chuang, R.-Y.; Venter, J. C.; Hutchison Iii, C. A.; Smith, H. O., Enzymatic assembly of DNA molecules up to several hundred kilobases. *Nat. Methods* **2009**, *6*, 343.
100. Ankenbruck, N.; Kumbhare, R.; Naro, Y.; Thomas, M.; Gardner, L.; Emanuelson, C.; Deiters, A., Small molecule inhibition of microRNA-21 expression reduces cell viability and microtumor formation. *Biorg. Med. Chem.* **2019**, *27* (16), 3735-3743.
101. Sano, Y.; Watanabe, W.; Matsunaga, S., Chromophore-assisted laser inactivation--towards a spatiotemporal-functional analysis of proteins, and the ablation of chromatin, organelle and cell function. *J. Cell Sci.* **2014**, *127* (Pt 8), 1621-9.
102. Jacobson, K.; Rajfur, Z.; Vitriol, E.; Hahn, K., Chromophore-assisted laser inactivation in cell biology. *Trends Cell Biol.* **2008**, *18* (9), 443-450.
103. Xiong, Y.; Tian, X.; Ai, H.-w., Molecular Tools to Generate Reactive Oxygen Species in Biological Systems. *Bioconjugate Chemistry* **2019**, *30* (5), 1297-1303.

104. Abrahamse, H.; Hamblin, M. R., New photosensitizers for photodynamic therapy. *Biochem J* **2016**, *473* (4), 347-64.
105. Straight, R.; Spikes, J., Photosensitized oxidation of biomolecules. *Singlet O2* **1985**, *4* (91), 143.
106. Davies, M. J., Singlet oxygen-mediated damage to proteins and its consequences. *Biochem. Biophys. Res. Commun.* **2003**, *305* (3), 761-770.
107. Kuimova, M. K.; Yahioglu, G.; Ogilby, P. R., Singlet oxygen in a cell: spatially dependent lifetimes and quenching rate constants. *J. Am. Chem. Soc.* **2009**, *131* (1), 332-40.
108. Baker, A.; Kanofsky, J. R., Quenching of singlet oxygen by biomolecules from L1210 leukemia cells. *Photochem. Photobiol.* **1992**, *55* (4), 523-8.
109. Sokolov, V. S.; Batishchev, O. V.; Akimov, S. A.; Galimzyanov, T. R.; Konstantinova, A. N.; Malingriaux, E.; Gorbunova, Y. G.; Knyazev, D. G.; Pohl, P., Residence time of singlet oxygen in membranes. *Sci Rep* **2018**, *8* (1), 14000.
110. Dysart, J. S.; Patterson, M. S., Characterization of Photofrin photobleaching for singlet oxygen dose estimation during photodynamic therapy of MLL cells in vitro. *Phys Med Biol* **2005**, *50* (11), 2597-616.
111. Baier, J.; Maier, M.; Engl, R.; Landthaler, M.; Bäuml, W., Time-Resolved Investigations of Singlet Oxygen Luminescence in Water, in Phosphatidylcholine, and in Aqueous Suspensions of Phosphatidylcholine or HT29 Cells. *The Journal of Physical Chemistry B* **2005**, *109* (7), 3041-3046.
112. Skovsen, E.; Snyder, J. W.; Lambert, J. D.; Ogilby, P. R., Lifetime and diffusion of singlet oxygen in a cell. *J. Phys. Chem. B* **2005**, *109* (18), 8570-3.
113. Hatz, S.; Poulsen, L.; Ogilby, P. R., Time-resolved singlet oxygen phosphorescence measurements from photosensitized experiments in single cells: effects of oxygen diffusion and oxygen concentration. *Photochem. Photobiol.* **2008**, *84* (5), 1284-90.
114. Moan, J.; Berg, K., The photodegradation of porphyrins in cells can be used to estimate the lifetime of singlet oxygen. *Photochem. Photobiol.* **1991**, *53* (4), 549-53.
115. Ozog, L.; Aebischer, D., Singlet oxygen lifetime and diffusion measurements. *European Journal of Clinical and Experimental Medicine* **2018**, *16* (2), 123-126.
116. Jay, D. G., Selective destruction of protein function by chromophore-assisted laser inactivation. *Proceedings of the National Academy of Sciences* **1988**, *85* (15), 5454.
117. Liao, J. C.; Roeder, J.; Jay, D. G., Chromophore-assisted laser inactivation of proteins is mediated by the photogeneration of free radicals. *Proc Natl Acad Sci U S A* **1994**, *91* (7), 2659-63.

118. Linden, K. G.; Liao, J. C.; Jay, D. G., Spatial specificity of chromophore assisted laser inactivation of protein function. *Biophys. J.* **1992**, *61* (4), 956-962.
119. Kou, J.; Dou, D.; Yang, L., Porphyrin photosensitizers in photodynamic therapy and its applications. *Oncotarget* **2017**, *8* (46), 81591-81603.
120. Zhang, J.; Jiang, C.; Figueiró Longo, J. P.; Azevedo, R. B.; Zhang, H.; Muehlmann, L. A., An updated overview on the development of new photosensitizers for anticancer photodynamic therapy. *Acta Pharmaceutica Sinica B* **2018**, *8* (2), 137-146.
121. Jakubaszek, M.; Goud, B.; Ferrari, S.; Gasser, G., Mechanisms of action of Ru(ii) polypyridyl complexes in living cells upon light irradiation. *Chem. Commun.* **2018**, *54* (93), 13040-13059.
122. Prieto-Montero, R.; Prieto-Castañeda, A.; Sola-Llano, R.; Agarrabeitia, A. R.; García-Fresnadillo, D.; López-Arbeloa, I.; Villanueva, A.; Ortiz, M. J.; de la Moya, S.; Martínez-Martínez, V., Exploring BODIPY Derivatives as Singlet Oxygen Photosensitizers for PDT. *Photochem. Photobiol.* **2020**, *96* (3), 458-477.
123. Tour, O.; Meijer, R. M.; Zacharias, D. A.; Adams, S. R.; Tsien, R. Y., Genetically targeted chromophore-assisted light inactivation. *Nat. Biotechnol.* **2003**, *21* (12), 1505-1508.
124. Kohler, L.; Nease, L.; Vo, P.; Garofolo, J.; Heidary, D. K.; Thummel, R. P.; Glazer, E. C., Photochemical and Photobiological Activity of Ru(II) Homoleptic and Heteroleptic Complexes Containing Methylated Bipyridyl-type Ligands. *Inorg. Chem.* **2017**, *56* (20), 12214-12223.
125. Lee, J.; Udugamasooriya, D. G.; Lim, H. S.; Kodadek, T., Potent and selective photo-inactivation of proteins with peptoid-ruthenium conjugates. *Nat. Chem. Biol.* **2010**, *6* (4), 258-60.
126. Takemoto, K.; Matsuda, T.; McDougall, M.; Klaubert, D. H.; Hasegawa, A.; Los, G. V.; Wood, K. V.; Miyawaki, A.; Nagai, T., Chromophore-Assisted Light Inactivation of HaloTag Fusion Proteins Labeled with Eosin in Living Cells. *ACS Chemical Biology* **2011**, *6* (5), 401-406.
127. Keppler, A.; Ellenberg, J., Chromophore-Assisted Laser Inactivation of α - and γ -Tubulin SNAP-tag Fusion Proteins inside Living Cells. *ACS Chemical Biology* **2009**, *4* (2), 127-138.
128. Zou, J.; Yin, Z.; Ding, K.; Tang, Q.; Li, J.; Si, W.; Shao, J.; Zhang, Q.; Huang, W.; Dong, X., BODIPY Derivatives for Photodynamic Therapy: Influence of Configuration versus Heavy Atom Effect. *ACS Applied Materials & Interfaces* **2017**, *9* (38), 32475-32481.
129. Wang, L.; Bai, J.; Qian, Y., Synthesis of a triphenylamine BODIPY photosensitizer with D-A configuration and its application in intracellular simulated photodynamic therapy. *New J. Chem.* **2019**, *43* (43), 16829-16834.

130. Durantini, A. M.; Heredia, D. A.; Durantini, J. E.; Durantini, E. N., BODIPYs to the rescue: Potential applications in photodynamic inactivation. *Eur. J. Med. Chem.* **2018**, *144*, 651-661.
131. Gu, K.; Lin, G.; Zhu, Y.; Ji, X.; Li, J.; Dong, X.; Zhao, W., Anchoring BODIPY photosensitizers enable pan-microbial photoinactivation. *European Journal of Medicinal Chemistry* **2020**, *199*, 112361.
132. Kamkaew, A.; Lim, S. H.; Lee, H. B.; Kiew, L. V.; Chung, L. Y.; Burgess, K., BODIPY dyes in photodynamic therapy. *Chem. Soc. Rev.* **2013**, *42* (1), 77-88.
133. Epelde-Elezcano, N.; Martínez-Martínez, V.; Peña-Cabrera, E.; Gómez-Durán, C. F. A.; Arbeloa, I. L.; Lacombe, S., Modulation of singlet oxygen generation in halogenated BODIPY dyes by substitution at their meso position: towards a solvent-independent standard in the vis region. *RSC Advances* **2016**, *6* (48), 41991-41998.
134. Pefkianakis, E. K.; Christodouleas, D.; Giokas, D. L.; Papadopoulos, K.; Vougioukalakis, G. C., A Family of RuII Photosensitizers with High Singlet Oxygen Quantum Yield: Synthesis, Characterization, and Evaluation. *Eur. J. Inorg. Chem.* **2013**, *2013* (26), 4628-4635.
135. Amat-Guerri, F.; López-González, M. M. C.; Martínez-Utrilla, R.; Sastre, R., Singlet oxygen photogeneration by ionized and un-ionized derivatives of Rose Bengal and Eosin Y in diluted solutions. *J. Photochem. Photobiol. A: Chem.* **1990**, *53* (2), 199-210.
136. Szent-Gyorgyi, C.; Schmidt, B. F.; Creeger, Y.; Fisher, G. W.; Zakel, K. L.; Adler, S.; Fitzpatrick, J. A.; Woolford, C. A.; Yan, Q.; Vasilev, K. V.; Berget, P. B.; Bruchez, M. P.; Jarvik, J. W.; Waggoner, A., Fluorogen-activating single-chain antibodies for imaging cell surface proteins. *Nat. Biotechnol.* **2008**, *26* (2), 235-40.
137. He, J.; Wang, Y.; Missinato, M. A.; Onuoha, E.; Perkins, L. A.; Watkins, S. C.; St Croix, C. M.; Tsang, M.; Bruchez, M. P., A genetically targetable near-infrared photosensitizer. *Nat. Methods* **2016**, *13* (3), 263-8.
138. Bulina, M. E.; Chudakov, D. M.; Britanova, O. V.; Yanushevich, Y. G.; Staroverov, D. B.; Chepurnykh, T. V.; Merzlyak, E. M.; Shkrob, M. A.; Lukyanov, S.; Lukyanov, K. A., A genetically encoded photosensitizer. *Nat Biotech* **2006**, *24* (1), 95-99.
139. Shu, X.; Lev-Ram, V.; Deerinck, T. J.; Qi, Y.; Ramko, E. B.; Davidson, M. W.; Jin, Y.; Ellisman, M. H.; Tsien, R. Y., A genetically encoded tag for correlated light and electron microscopy of intact cells, tissues, and organisms. *PLoS Biol.* **2011**, *9* (4), e1001041.
140. Wojtovich, A. P.; Foster, T. H., Optogenetic control of ROS production. *Redox Biology* **2014**, *2* (Supplement C), 368-376.
141. Takemoto, K.; Matsuda, T.; Sakai, N.; Fu, D.; Noda, M.; Uchiyama, S.; Kotera, I.; Arai, Y.; Horiuchi, M.; Fukui, K.; Ayabe, T.; Inagaki, F.; Suzuki, H.; Nagai, T., SuperNova, a

- monomeric photosensitizing fluorescent protein for chromophore-assisted light inactivation. **2013**, *3*, 2629.
142. Rajfur, Z.; Roy, P.; Otey, C.; Romer, L.; Jacobson, K., Dissecting the link between stress fibres and focal adhesions by CALI with EGFP fusion proteins. *Nat. Cell Biol.* **2002**, *4* (4), 286-293.
 143. Monier, B.; Péliissier-Monier, A.; Brand, A. H.; Sanson, B., An actomyosin-based barrier inhibits cell mixing at compartmental boundaries in *Drosophila* embryos. *Nat. Cell Biol.* **2010**, *12* (1), 60-65.
 144. Liao, Z. X.; Li, Y. C.; Lu, H. M.; Sung, H. W., A genetically-encoded KillerRed protein as an intrinsically generated photosensitizer for photodynamic therapy. *Biomaterials* **2014**, *35* (1), 500-8.
 145. Buckley, C.; Carvalho, M. T.; Young, L. K.; Rider, S. A.; McFadden, C.; Berlage, C.; Verdon, R. F.; Taylor, J. M.; Girkin, J. M.; Mullins, J. J., Precise spatio-temporal control of rapid optogenetic cell ablation with mem-KillerRed in Zebrafish. *Scientific Reports* **2017**, *7* (1), 5096.
 146. Williams, Daniel C.; El Bejjani, R.; Ramirez, Paula M.; Coakley, S.; Kim, S. A.; Lee, H.; Wen, Q.; Samuel, A.; Lu, H.; Hilliard, Massimo A.; Hammarlund, M., Rapid and Permanent Neuronal Inactivation In Vivo via Subcellular Generation of Reactive Oxygen with the Use of KillerRed. *Cell Reports* **2013**, *5* (2), 553-563.
 147. Riani, Y. D.; Matsuda, T.; Takemoto, K.; Nagai, T., Green monomeric photosensitizing fluorescent protein for photo-inducible protein inactivation and cell ablation. *BMC Biol.* **2018**, *16* (1), 50.
 148. Sarkisyan, K. S.; Zlobovskaya, O. A.; Gorbachev, D. A.; Bozhanova, N. G.; Sharonov, G. V.; Staroverov, D. B.; Egorov, E. S.; Ryabova, A. V.; Solntsev, K. M.; Mishin, A. S.; Lukyanov, K. A., KillerOrange, a Genetically Encoded Photosensitizer Activated by Blue and Green Light. *PLOS ONE* **2015**, *10* (12), e0145287.
 149. Makhijani, K.; To, T.-L.; Ruiz-González, R.; Lafaye, C.; Royant, A.; Shu, X., Precision Optogenetic Tool for Selective Single- and Multiple-Cell Ablation in a Live Animal Model System. *Cell Chemical Biology* **2017**, *24* (1), 110-119.
 150. Mironova, K. E.; Proshkina, G. M.; Ryabova, A. V.; Stremovskiy, O. A.; Lukyanov, S. A.; Petrov, R. V.; Deyev, S. M., Genetically encoded immunophotosensitizer 4D5scFv-miniSOG is a highly selective agent for targeted photokilling of tumor cells in vitro. *Theranostics* **2013**, *3* (11), 831-40.
 151. Xu, S.; Chisholm, A. D., Highly efficient optogenetic cell ablation in *C. elegans* using membrane-targeted miniSOG. *Scientific Reports* **2016**, *6* (1), 21271.

152. Qi, Y. B.; Garren, E. J.; Shu, X.; Tsien, R. Y.; Jin, Y., Photo-inducible cell ablation in *Caenorhabditis elegans* using the genetically encoded singlet oxygen generating protein miniSOG. *Proceedings of the National Academy of Sciences* **2012**, *109* (19), 7499.
153. Ruiz-González, R.; Cortajarena, A. L.; Mejias, S. H.; Agut, M.; Nonell, S.; Flors, C., Singlet Oxygen Generation by the Genetically Encoded Tag miniSOG. *Journal of the American Chemical Society* **2013**, *135* (26), 9564-9567.
154. Wojtovich, A. P.; Wei, A. Y.; Sherman, T. A.; Foster, T. H.; Nehrke, K., Chromophore-Assisted Light Inactivation of Mitochondrial Electron Transport Chain Complex II in *Caenorhabditis elegans*. *Scientific Reports* **2016**, *6*, 29695.
155. Lin, J. Y.; Sann, S. B.; Zhou, K.; Nabavi, S.; Proulx, C. D.; Malinow, R.; Jin, Y.; Tsien, R. Y., Optogenetic inhibition of synaptic release with chromophore-assisted light inactivation (CALI). *Neuron* **2013**, *79* (2), 241-53.
156. Onukwufor, J. O.; Trewin, A. J.; Baran, T. M.; Almast, A.; Foster, T. H.; Wojtovich, A. P., Quantification of reactive oxygen species production by the red fluorescent proteins KillerRed, SuperNova and mCherry. *Free Radical Biol. Med.* **2020**, *147*, 1-7.
157. Panieri, E.; Santoro, M. M., ROS homeostasis and metabolism: a dangerous liason in cancer cells. *Cell Death & Disease* **2016**, *7* (6), e2253-e2253.
158. Krumova, K.; Cosa, G., Chapter 1 Overview of Reactive Oxygen Species. In *Singlet Oxygen: Applications in Biosciences and Nanosciences, Volume 1*, The Royal Society of Chemistry: 2016; Vol. 1, pp 1-21.
159. Bhattacharyya, A.; Chattopadhyay, R.; Mitra, S.; Crowe, S. E., Oxidative stress: an essential factor in the pathogenesis of gastrointestinal mucosal diseases. *Physiol. Rev.* **2014**, *94* (2), 329-54.
160. Bae, Y. S.; Oh, H.; Rhee, S. G.; Yoo, Y. D., Regulation of reactive oxygen species generation in cell signaling. *Mol Cells* **2011**, *32* (6), 491-509.
161. Schieber, M.; Chandel, N. S., ROS function in redox signaling and oxidative stress. *Curr. Biol.* **2014**, *24* (10), R453-62.
162. Cecarini, V.; Gee, J.; Fioretti, E.; Amici, M.; Angeletti, M.; Eleuteri, A. M.; Keller, J. N., Protein oxidation and cellular homeostasis: Emphasis on metabolism. *Biochim. Biophys. Acta* **2007**, *1773* (2), 93-104.
163. Wright, A.; Bubb, W. A.; Hawkins, C. L.; Davies, M. J., Singlet oxygen-mediated protein oxidation: evidence for the formation of reactive side chain peroxides on tyrosine residues. *Photochem. Photobiol.* **2002**, *76* (1), 35-46.
164. Zhang, W.; Xiao, S.; Ahn, D. U., Protein oxidation: basic principles and implications for meat quality. *Crit. Rev. Food Sci. Nutr.* **2013**, *53* (11), 1191-201.

165. Pajares, M.; Jiménez-Moreno, N.; Dias, I. H. K.; Debelec, B.; Vucetic, M.; Fladmark, K. E.; Basaga, H.; Ribaric, S.; Milisav, I.; Cuadrado, A., Redox control of protein degradation. *Redox Biol* **2015**, *6*, 409-420.
166. Sletten, E. M.; Bertozzi, C. R., Bioorthogonal chemistry: fishing for selectivity in a sea of functionality. *Angew. Chem. Int. Ed. Engl.* **2009**, *48* (38), 6974-98.
167. Prescher, J. A.; Bertozzi, C. R., Chemistry in living systems. *Nat. Chem. Biol.* **2005**, *1* (1), 13-21.
168. Lang, K.; Chin, J. W., Bioorthogonal Reactions for Labeling Proteins. *ACS Chemical Biology* **2014**, *9* (1), 16-20.
169. Devaraj, N. K., The Future of Bioorthogonal Chemistry. *ACS Central Science* **2018**, *4* (8), 952-959.
170. Lee, K. J.; Kang, D.; Park, H. S., Site-Specific Labeling of Proteins Using Unnatural Amino Acids. *Mol Cells* **2019**, *42* (5), 386-396.
171. Lang, K.; Chin, J. W., Cellular incorporation of unnatural amino acids and bioorthogonal labeling of proteins. *Chem Rev* **2014**, *114* (9), 4764-806.
172. Deiters, A.; Cropp, T. A.; Mukherji, M.; Chin, J. W.; Anderson, J. C.; Schultz, P. G., Adding Amino Acids with Novel Reactivity to the Genetic Code of *Saccharomyces Cerevisiae*. *Journal of the American Chemical Society* **2003**, *125* (39), 11782-11783.
173. Liu, W.; Brock, A.; Chen, S.; Chen, S.; Schultz, P. G., Genetic incorporation of unnatural amino acids into proteins in mammalian cells. *Nat. Methods* **2007**, *4*, 239.
174. Tsao, M.-L.; Tian, F.; Schultz, P. G., Selective Staudinger Modification of Proteins Containing p-Azidophenylalanine. *ChemBioChem* **2005**, *6* (12), 2147-2149.
175. Yu, Z.; Pan, Y.; Wang, Z.; Wang, J.; Lin, Q., Genetically encoded cyclopropene directs rapid, photoclick-chemistry-mediated protein labeling in mammalian cells. *Angew. Chem. Int. Ed. Engl.* **2012**, *51* (42), 10600-4.
176. Elliott, T. S.; Townsley, F. M.; Bianco, A.; Ernst, R. J.; Sachdeva, A.; Elsässer, S. J.; Davis, L.; Lang, K.; Pisa, R.; Greiss, S.; Lilley, K. S.; Chin, J. W., Proteome labeling and protein identification in specific tissues and at specific developmental stages in an animal. *Nat. Biotechnol.* **2014**, *32* (5), 465-472.
177. Lang, K.; Davis, L.; Torres-Kolbus, J.; Chou, C.; Deiters, A.; Chin, J. W., Genetically encoded norbornene directs site-specific cellular protein labelling via a rapid bioorthogonal reaction. *Nature Chemistry* **2012**, *4* (4), 298-304.
178. Borrmann, A.; Milles, S.; Plass, T.; Dommerholt, J.; Verkade, J. M.; Wiessler, M.; Schultz, C.; van Hest, J. C.; van Delft, F. L.; Lemke, E. A., Genetic encoding of a

- bicyclo[6.1.0]nonyne-charged amino acid enables fast cellular protein imaging by metal-free ligation. *ChemBioChem* **2012**, *13* (14), 2094-9.
179. Lang, K.; Davis, L.; Wallace, S.; Mahesh, M.; Cox, D. J.; Blackman, M. L.; Fox, J. M.; Chin, J. W., Genetic Encoding of bicyclononynes and trans-cyclooctenes for site-specific protein labeling in vitro and in live mammalian cells via rapid fluorogenic Diels-Alder reactions. *J. Am. Chem. Soc.* **2012**, *134* (25), 10317-20.
 180. Plass, T.; Milles, S.; Koehler, C.; Szymański, J.; Mueller, R.; Wießler, M.; Schultz, C.; Lemke, E. A., Amino Acids for Diels–Alder Reactions in Living Cells. *Angew. Chem. Int. Ed.* **2012**, *51* (17), 4166-4170.
 181. Hoffmann, J.-E.; Plass, T.; Nikić, I.; Aramburu, I. V.; Koehler, C.; Gillandt, H.; Lemke, E. A.; Schultz, C., Highly Stable trans-Cyclooctene Amino Acids for Live-Cell Labeling. *Chemistry – A European Journal* **2015**, *21* (35), 12266-12270.
 182. Li, J.; Jia, S.; Chen, P. R., Diels-Alder reaction-triggered bioorthogonal protein decaging in living cells. *Nat. Chem. Biol.* **2014**, *10* (12), 1003-1005.
 183. Uttamapinant, C.; Howe, J. D.; Lang, K.; Beránek, V.; Davis, L.; Mahesh, M.; Barry, N. P.; Chin, J. W., Genetic Code Expansion Enables Live-Cell and Super-Resolution Imaging of Site-Specifically Labeled Cellular Proteins. *Journal of the American Chemical Society* **2015**, *137* (14), 4602-4605.
 184. Nikić, I.; Plass, T.; Schraidt, O.; Szymański, J.; Briggs, J. A. G.; Schultz, C.; Lemke, E. A., Minimal Tags for Rapid Dual-Color Live-Cell Labeling and Super-Resolution Microscopy. *Angew. Chem. Int. Ed.* **2014**, *53* (8), 2245-2249.
 185. Beliu, G.; Kurz, A. J.; Kuhlemann, A. C.; Behringer-Pliess, L.; Meub, M.; Wolf, N.; Seibel, J.; Shi, Z.-D.; Schnermann, M.; Grimm, J. B.; Lavis, L. D.; Doose, S.; Sauer, M., Bioorthogonal labeling with tetrazine-dyes for super-resolution microscopy. *Communications Biology* **2019**, *2* (1), 261.
 186. Fang, Y.; Judkins, J. C.; Boyd, S. J.; am Ende, C. W.; Rohlfing, K.; Huang, Z.; Xie, Y.; Johnson, D. S.; Fox, J. M., Studies on the stability and stabilization of trans-cyclooctenes through radical inhibition and silver (I) metal complexation. *Tetrahedron* **2019**, *75* (32), 4307-4317.
 187. Fang, Y.; Zhang, H.; Huang, Z.; Scinto, S. L.; Yang, J. C.; am Ende, Christopher W.; Dmitrenko, O.; Johnson, D. S.; Fox, J. M., Photochemical syntheses, transformations, and bioorthogonal chemistry of trans-cycloheptene and sila trans-cycloheptene Ag(i) complexes. *Chemical Science* **2018**, *9* (7), 1953-1963.
 188. Lam, S. S.; Martell, J. D.; Kamer, K. J.; Deerinck, T. J.; Ellisman, M. H.; Mootha, V. K.; Ting, A. Y., Directed evolution of APEX2 for electron microscopy and proximity labeling. *Nat. Methods* **2015**, *12* (1), 51-4.

189. Roux, K. J.; Kim, D. I.; Raida, M.; Burke, B., A promiscuous biotin ligase fusion protein identifies proximal and interacting proteins in mammalian cells. *J. Cell Biol.* **2012**, *196*, 801.
190. Trinkle-Mulcahy, L., Recent advances in proximity-based labeling methods for interactome mapping. *F1000Res* **2019**, *8*.
191. Miller, G.; Hahn, S., A DNA-tethered cleavage probe reveals the path for promoter DNA in the yeast preinitiation complex. *Nat. Struct. Mol. Biol.* **2006**, *13* (7), 603-10.
192. Ugur, Z.; Coffey, C. M.; Gronert, S., Comparing the efficiencies of hydrazide labels in the study of protein carbonylation in human serum albumin. *Anal. Bioanal. Chem.* **2012**, *404* (5), 1399-411.
193. Mukherjee, K.; Chio, T. I.; Bane, S. L., Chapter Eight - Visualization of oxidative stress-induced carbonylation in live mammalian cells. In *Methods Enzymol.*, Chenoweth, D. M., Ed. Academic Press: 2020; Vol. 641, pp 165-181.
194. Kang, K.; Park, J.; Kim, E., Tetrazine ligation for chemical proteomics. *Proteome Sci* **2016**, *15*, 15.
195. Jun, M. E.; Roy, B.; Ahn, K. H., "Turn-on" fluorescent sensing with "reactive" probes. *Chem Commun (Camb)* **2011**, *47* (27), 7583-601.
196. Chan, J.; Dodani, S. C.; Chang, C. J., Reaction-based small-molecule fluorescent probes for chemoselective bioimaging. *Nat Chem* **2012**, *4* (12), 973-84.
197. Hanna, R. D.; Naro, Y.; Deiters, A.; Floreancig, P. E., Alcohol, Aldehyde, and Ketone Liberation and Intracellular Cargo Release through Peroxide-Mediated α -Boryl Ether Fragmentation. *Journal of the American Chemical Society* **2016**, *138* (40), 13353-13360.
198. Loredó, A.; Tang, J.; Wang, L.; Wu, K.-L.; Peng, Z.; Xiao, H., Tetrazine as a general phototrigger to turn on fluorophores. *Chemical Science* **2020**, *11* (17), 4410-4415.
199. Wu, H.; Devaraj, N. K., Advances in Tetrazine Bioorthogonal Chemistry Driven by the Synthesis of Novel Tetrazines and Dienophiles. *Acc. Chem. Res.* **2018**, *51* (5), 1249-1259.
200. Cao, D.; Zhu, L.; Liu, Z.; Lin, W., Through bond energy transfer (TBET)-based fluorescent chemosensors. *Journal of Photochemistry and Photobiology C: Photochemistry Reviews* **2020**, *44*, 100371.
201. Chen, Y.; Tsao, K.; Keillor, J. W., Fluorogenic protein labelling: a review of photophysical quench mechanisms and principles of fluorogen design. *Can. J. Chem.* **2014**, *93* (4), 389-398.
202. Linden, G.; Zhang, L.; Pieck, F.; Linne, U.; Kosenkov, D.; Tonner, R.; Vázquez, O., Conditional Singlet Oxygen Generation through a Bioorthogonal DNA-targeted Tetrazine Reaction. *Angew. Chem. Int. Ed.* **2019**, *58* (37), 12868-12873.

203. Dalle-Donne, I.; Carini, M.; Orioli, M.; Vistoli, G.; Regazzoni, L.; Colombo, G.; Rossi, R.; Milzani, A.; Aldini, G., Protein carbonylation: 2,4-dinitrophenylhydrazine reacts with both aldehydes/ketones and sulfenic acids. *Free Radic Biol Med* **2009**, *46* (10), 1411-9.
204. Weber, D.; Davies, M. J.; Grune, T., Determination of protein carbonyls in plasma, cell extracts, tissue homogenates, isolated proteins: Focus on sample preparation and derivatization conditions. *Redox Biol* **2015**, *5*, 367-380.
205. Suzuki, Y. J.; Carini, M.; Butterfield, D. A., Protein carbonylation. *Antioxid. Redox Signal.* **2010**, *12* (3), 323-5.
206. Colombo, G.; Clerici, M.; Garavaglia, M. E.; Giustarini, D.; Rossi, R.; Milzani, A.; Dalle-Donne, I., A step-by-step protocol for assaying protein carbonylation in biological samples. *J Chromatogr B Analyt Technol Biomed Life Sci* **2016**, *1019*, 178-90.
207. Guedes, S.; Vitorino, R.; Domingues, R.; Amado, F.; Domingues, P., Oxidation of bovine serum albumin: identification of oxidation products and structural modifications. *Rapid Commun. Mass Spectrom.* **2009**, *23* (15), 2307-2315.
208. Waugh, D. S., An overview of enzymatic reagents for the removal of affinity tags. *Protein Expr Purif* **2011**, *80* (2), 283-93.
209. Cesaratto, F.; Burrone, O. R.; Petris, G., Tobacco Etch Virus protease: A shortcut across biotechnologies. *J. Biotechnol.* **2016**, *231*, 239-249.
210. Kapust, R. B.; Tözsér, J.; Fox, J. D.; Anderson, D. E.; Cherry, S.; Copeland, T. D.; Waugh, D. S., Tobacco etch virus protease: mechanism of autolysis and rational design of stable mutants with wild-type catalytic proficiency. *Protein Eng.* **2001**, *14* (12), 993-1000.
211. Phan, J.; Zdanov, A.; Evdokimov, A. G.; Tropea, J. E.; Peters, H. K.; Kapust, R. B.; Li, M.; Wlodawer, A.; Waugh, D. S., Structural Basis for the Substrate Specificity of Tobacco Etch Virus Protease. *J. Biol. Chem.* **2002**, *277* (52), 50564-50572.
212. Brown, K. A.; Zou, Y.; Shirvanyants, D.; Zhang, J.; Samanta, S.; Mantravadi, P. K.; Dokholyan, N. V.; Deiters, A., Light-cleavable rapamycin dimer as an optical trigger for protein dimerization. *Chem Commun (Camb)* **2015**, *51* (26), 5702-5.
213. Nicholls, S. B.; Chu, J.; Abbruzzese, G.; Tremblay, K. D.; Hardy, J. A., Mechanism of a Genetically Encoded Dark-to-Bright Reporter for Caspase Activity. *J. Biol. Chem.* **2011**, *286* (28), 24977-24986.
214. Palmer, I.; Wingfield, P. T., Preparation and extraction of insoluble (inclusion-body) proteins from *Escherichia coli*. *Curr Protoc Protein Sci* **2004**, *Chapter 6*, Unit 6.3.
215. Gay, C.; Collins, J.; Gebicki, J. M., Hydroperoxide Assay with the Ferric–Xylenol Orange Complex. *Anal. Biochem.* **1999**, *273* (2), 149-155.

216. Bettinger, J. Q.; Welle, K. A.; Hryhorenko, J. R.; Ghaemmaghami, S., Quantitative Analysis of in Vivo Methionine Oxidation of the Human Proteome. *Journal of proteome research* **2020**, *19* (2), 624-633.
217. Madian, A. G.; Regnier, F. E., Proteomic identification of carbonylated proteins and their oxidation sites. *J Proteome Res* **2010**, *9* (8), 3766-80.
218. Afiuni-Zadeh, S.; Rogers, J. C.; Snovida, S. I.; Bomgarden, R. D.; Griffin, T. J., AminoxyTMT: A novel multi-functional reagent for characterization of protein carbonylation. *BioTechniques* **2016**, *60* (4), 186-196.
219. Verrastro, I.; Pasha, S.; Jensen, K. T.; Pitt, A. R.; Spickett, C. M., Mass spectrometry-based methods for identifying oxidized proteins in disease: advances and challenges. *Biomolecules* **2015**, *5* (2), 378-411.
220. Liu, Q. Identification and Quantification of Protein Carbonylation by Mass Spectrometry. Virginia Commonwealth University, Richmond, VA, 2012.
221. Shcherbakova, I.; Mitra, S.; Beer, R. H.; Brenowitz, M., Fast Fenton footprinting: a laboratory-based method for the time-resolved analysis of DNA, RNA and proteins. *Nucleic Acids Res.* **2006**, *34* (6), e48-e48.
222. Beharry, A. A.; Woolley, G. A., Azobenzene photoswitches for biomolecules. *Chem. Soc. Rev.* **2011**, *40* (8), 4422-4437.
223. Lubbe, A. S.; Szymanski, W.; Feringa, B. L., Recent developments in reversible photoregulation of oligonucleotide structure and function. *Chem. Soc. Rev.* **2017**, *46* (4), 1052-1079.
224. Lerch, M. M.; Hansen, M. J.; van Dam, G. M.; Szymanski, W.; Feringa, B. L., Emerging Targets in Photopharmacology. *Angew. Chem. Int. Ed. Engl.* **2016**, *55* (37), 10978-99.
225. Broichhagen, J.; Trauner, D., The in vivo chemistry of photoswitched tethered ligands. *Curr. Opin. Chem. Biol.* **2014**, *21*, 121-127.
226. Hüll, K.; Morstein, J.; Trauner, D., In Vivo Photopharmacology. *Chem. Rev.* **2018**, *118* (21), 10710-10747.
227. Broichhagen, J.; Frank, J. A.; Trauner, D., A roadmap to success in photopharmacology. *Acc. Chem. Res.* **2015**, *48* (7), 1947-60.
228. Toettcher, J. E.; Voigt, C. A.; Weiner, O. D.; Lim, W. A., The promise of optogenetics in cell biology: interrogating molecular circuits in space and time. *Nat Meth* **2011**, *8* (1), 35-38.
229. Bose, M.; Groff, D.; Xie, J.; Brustad, E.; Schultz, P. G., The incorporation of a photoisomerizable amino acid into proteins in E. coli. *J. Am. Chem. Soc.* **2006**, *128* (2), 388-9.

230. Padilla, M. S.; Young, D. D., Photosensitive GFP mutants containing an azobenzene unnatural amino acid. *Bioorg Med Chem Lett* **2015**, *25* (3), 470-3.
231. Hoppmann, C.; Maslennikov, I.; Choe, S.; Wang, L., In Situ Formation of an Azo Bridge on Proteins Controllable by Visible Light. *J. Am. Chem. Soc.* **2015**, *137* (35), 11218-21.
232. Hoppmann, C.; Lacey, V. K.; Louie, G. V.; Wei, J.; Noel, J. P.; Wang, L., Genetically encoding photoswitchable click amino acids in Escherichia coli and mammalian cells. *Angew. Chem. Int. Ed. Engl.* **2014**, *53* (15), 3932-6.
233. Hoppmann, C.; Wang, L., Genetically encoding photoswitchable click amino acids for general optical control of conformation and function of proteins. *Methods Enzymol.* **2019**, *624*, 249-264.
234. Klippenstein, V.; Hoppmann, C.; Ye, S.; Wang, L.; Paoletti, P., Optocontrol of glutamate receptor activity by single side-chain photoisomerization. *eLife* **2017**, *6*, e25808.
235. John, A. A.; Ramil, C. P.; Tian, Y.; Cheng, G.; Lin, Q., Synthesis and Site-Specific Incorporation of Red-Shifted Azobenzene Amino Acids into Proteins. *Org. Lett.* **2015**, *17* (24), 6258-61.
236. Luo, J.; Samanta, S.; Convertino, M.; Dokholyan, N. V.; Deiters, A., Reversible and Tunable Photoswitching of Protein Function through Genetic Encoding of Azobenzene Amino Acids in Mammalian Cells. *ChemBioChem* **2018**, *19* (20), 2178-2185.
237. Weston, C. E.; Richardson, R. D.; Haycock, P. R.; White, A. J.; Fuchter, M. J., Arylazopyrazoles: azoheteroarene photoswitches offering quantitative isomerization and long thermal half-lives. *J. Am. Chem. Soc.* **2014**, *136* (34), 11878-81.
238. Wendler, T.; Schütt, C.; Näther, C.; Herges, R., Photoswitchable Azoheterocycles via Coupling of Lithiated Imidazoles with Benzenediazonium Salts. *The Journal of Organic Chemistry* **2012**, *77* (7), 3284-3287.
239. Otsuki, J.; Suwa, K.; Narutaki, K.; Sinha, C.; Yoshikawa, I.; Araki, K., Photochromism of 2-(Phenylazo)imidazoles. *The Journal of Physical Chemistry A* **2005**, *109* (35), 8064-8069.
240. Calbo, J.; Weston, C. E.; White, A. J.; Rzepa, H. S.; Contreras-Garcia, J.; Fuchter, M. J., Tuning Azoheteroarene Photoswitch Performance through Heteroaryl Design. *J. Am. Chem. Soc.* **2017**, *139* (3), 1261-1274.
241. Jain, S.; Singh, R.; Gupta, M. N., Purification of recombinant green fluorescent protein by three-phase partitioning. *J. Chromatogr. A* **2004**, *1035* (1), 83-6.
242. Misal, S. A.; Gawai, K. R., Azoreductase: a key player of xenobiotic metabolism. *Bioresources and Bioprocessing* **2018**, *5* (1), 17.
243. Ryan, A., Azoreductases in drug metabolism. *Br J Pharmacol* **2017**, *174* (14), 2161-2173.

244. Stricker, L.; Bockmann, M.; Kirse, T. M.; Doltsinis, N. L.; Ravoo, B. J., Arylazopyrazole Photoswitches in Aqueous Solution: Substituent Effects, Photophysical Properties, and Host-Guest Chemistry. *Chemistry* **2018**, *24* (34), 8639-8647.
245. Smith, S.; Bou-Abdallah, F., The Kinetics of the Cis-to-Trans Thermal Isomerization of 4-Anilino-4'-Nitroazobenzene are Highly Influenced by Solvent Polarity. *Journal of Thermodynamics and Catalysis* **2017**, *8* (1).
246. Berthet, J.; Agouridas, L.; Chen, S.; Allouchi, H.; Melnyk, P.; Champagne, B.; Delbaere, S., Synthesis and switching properties of new derivatives of azoresveratrol. *Dyes and Pigments* **2019**, *171*, 107666.
247. Stricker, L.; Fritz, E. C.; Peterlechner, M.; Doltsinis, N. L.; Ravoo, B. J., Arylazopyrazoles as Light-Responsive Molecular Switches in Cyclodextrin-Based Supramolecular Systems. *J. Am. Chem. Soc.* **2016**, *138* (13), 4547-54.
248. Hammill, M. L.; Isaacs-Trépanier, C.; Desaulniers, J.-P., siRNAzOs: A New Class of Azobenzene-Containing siRNAs that Can Photochemically Regulate Gene Expression. *ChemistrySelect* **2017**, *2* (30), 9810-9814.
249. Hammill, M. L.; Islam, G.; Desaulniers, J. P., Reversible control of RNA interference by siRNAzOs. *Org Biomol Chem* **2019**, *18* (1), 41-46.
250. Matsunaga, D.; Asanuma, H.; Komiyama, M., Photoregulation of RNA digestion by RNase H with azobenzene-tethered DNA. *J. Am. Chem. Soc.* **2004**, *126* (37), 11452-3.
251. Wu, L.; He, Y.; Tang, X., Photoregulating RNA digestion using azobenzene linked dumbbell antisense oligodeoxynucleotides. *Bioconjug Chem* **2015**, *26* (6), 1070-9.
252. Ando, H.; Furuta, T.; Tsien, R. Y.; Okamoto, H., Photo-mediated gene activation using caged RNA/DNA in zebrafish embryos. *Nat. Genet.* **2001**, *28* (4), 317-25.
253. Zhang, D.; Zhou, C. Y.; Busby, K. N.; Alexander, S. C.; Devaraj, N. K., Light-Activated Control of Translation by Enzymatic Covalent mRNA Labeling. *Angew. Chem. Int. Ed. Engl.* **2018**, *57* (11), 2822-2826.
254. Ogasawara, S., Control of cellular function by reversible photoregulation of translation. *ChemBioChem* **2014**, *15* (18), 2652-5.
255. Ogasawara, S., Duration Control of Protein Expression in Vivo by Light-Mediated Reversible Activation of Translation. *ACS Chem Biol* **2017**, *12* (2), 351-356.
256. Akahoshi, A.; Doi, Y.; Sisido, M.; Watanabe, K.; Ohtsuki, T., Photo-dependent protein biosynthesis using a caged aminoacyl-tRNA. *Bioorg Med Chem Lett* **2014**, *24* (23), 5369-72.

257. Ohtsuki, T.; Kanzaki, S.; Nishimura, S.; Kunihiro, Y.; Sisido, M.; Watanabe, K., Phototriggered protein syntheses by using (7-diethylaminocoumarin-4-yl)methoxycarbonyl-caged aminoacyl tRNAs. *Nature Communications* **2016**, *7* (1), 12501.
258. Sheldon, J. E.; Dcona, M. M.; Lyons, C. E.; Hackett, J. C.; Hartman, M. C., Photoswitchable anticancer activity via trans-cis isomerization of a combretastatin A-4 analog. *Org Biomol Chem* **2016**, *14* (1), 40-9.
259. Dong, M.; Babalhavaeji, A.; Samanta, S.; Beharry, A. A.; Woolley, G. A., Red-Shifting Azobenzene Photoswitches for in Vivo Use. *Acc. Chem. Res.* **2015**, *48* (10), 2662-2670.
260. Samanta, S.; McCormick, T. M.; Schmidt, S. K.; Seferos, D. S.; Woolley, G. A., Robust visible light photoswitching with ortho-thiol substituted azobenzenes. *Chem. Commun.* **2013**, *49* (87), 10314-10316.
261. Fahey, R. C.; Brown, W. C.; Adams, W. B.; Worsham, M. B., Occurrence of glutathione in bacteria. *J. Bacteriol.* **1978**, *133* (3), 1126-9.
262. Forman, H. J.; Zhang, H.; Rinna, A., Glutathione: overview of its protective roles, measurement, and biosynthesis. *Mol Aspects Med* **2009**, *30* (1-2), 1-12.
263. Santos, A. L.; Oliveira, V.; Baptista, I.; Henriques, I.; Gomes, N. C.; Almeida, A.; Correia, A.; Cunha, A., Wavelength dependence of biological damage induced by UV radiation on bacteria. *Arch. Microbiol.* **2013**, *195* (1), 63-74.
264. El Najjar, N.; van Teeseling, M. C. F.; Mayer, B.; Hermann, S.; Thanbichler, M.; Graumann, P. L., Bacterial cell growth is arrested by violet and blue, but not yellow light excitation during fluorescence microscopy. *BMC Mol Cell Biol* **2020**, *21* (1), 35.
265. Cestari, I.; Stuart, K., A Spectrophotometric Assay for Quantitative Measurement of Aminoacyl-tRNA Synthetase Activity. *J. Biomol. Screen.* **2012**, *18* (4), 490-497.
266. Chatterjee, A.; Sun, S. B.; Furman, J. L.; Xiao, H.; Schultz, P. G., A versatile platform for single- and multiple-unnatural amino acid mutagenesis in Escherichia coli. *Biochemistry* **2013**, *52* (10), 1828-37.
267. Wang, W. W.; Angulo-Ibanez, M.; Lyu, J.; Kurra, Y.; Tong, Z.; Wu, B.; Zhang, L.; Sharma, V.; Zhou, J.; Lin, H.; Gao, Y. Q.; Li, W.; Chua, K. F.; Liu, W. R., A Click Chemistry Approach Reveals the Chromatin-Dependent Histone H3K36 Deacylase Nature of SIRT7. *Journal of the American Chemical Society* **2019**, *141* (6), 2462-2473.
268. Kuhn, S. M.; Rubini, M.; Fuhrmann, M.; Theobald, I.; Skerra, A., Engineering of an Orthogonal Aminoacyl-tRNA Synthetase for Efficient Incorporation of the Non-natural Amino Acid O-Methyl-L-tyrosine using Fluorescence-based Bacterial Cell Sorting. *J. Mol. Biol.* **2010**, *404* (1), 70-87.

269. Kwok, H. S.; Vargas-Rodriguez, O.; Melnikov, S. V.; Söll, D., Engineered Aminoacyl-tRNA Synthetases with Improved Selectivity toward Noncanonical Amino Acids. *ACS Chem Biol* **2019**, *14* (4), 603-612.
270. Owens, A. E.; Grasso, K. T.; Ziegler, C. A.; Fasan, R., Two-Tier Screening Platform for Directed Evolution of Aminoacyl-tRNA Synthetases with Enhanced Stop Codon Suppression Efficiency. *Chembiochem : a European journal of chemical biology* **2017**, *18* (12), 1109-1116.
271. Fottner, M.; Brunner, A.-D.; Bittl, V.; Horn-Ghetko, D.; Jussupow, A.; Kaila, V. R. I.; Bremm, A.; Lang, K., Site-specific ubiquitylation and SUMOylation using genetic-code expansion and sortase. *Nat. Chem. Biol.* **2019**, *15* (3), 276-284.
272. Sharma, V.; Zeng, Y.; Wang, W. W.; Qiao, Y.; Kurra, Y.; Liu, W. R., Evolving the N-Terminal Domain of Pyrrolysyl-tRNA Synthetase for Improved Incorporation of Noncanonical Amino Acids. *Chembiochem : a European journal of chemical biology* **2018**, *19* (1), 26-30.
273. Sharma, V. The Engineering and Optimization of Pyrrolysyl Synthetase as a Tool for Noncanonical Amino Acid Incorporation. Texas A&M University, College Station, TX, 2017.
274. Wilson, D. S.; Keefe, A. D., Random Mutagenesis by PCR. *Current Protocols in Molecular Biology* **2000**, *51* (1), 8.3.1-8.3.9.
275. Agilent GeneMorph II Random Mutagenesis Kit. <https://www.agilent.com/cs/library/usermanuals/public/200550.pdf> (accessed 06/01/2020).
276. Bryson, D. I.; Fan, C.; Guo, L. T.; Miller, C.; Soll, D.; Liu, D. R., Continuous directed evolution of aminoacyl-tRNA synthetases. *Nat. Chem. Biol.* **2017**, *13* (12), 1253-1260.
277. Melzer, S.; Sonnendecker, C.; Föllner, C.; Zimmermann, W., Stepwise error-prone PCR and DNA shuffling changed the pH activity range and product specificity of the cyclodextrin glucanotransferase from an alkaliphilic *Bacillus* sp. *FEBS open bio* **2015**, *5*, 528-534.
278. Cherry, J. R.; Lamsa, M. H.; Schneider, P.; Vind, J.; Svendsen, A.; Jones, A.; Pedersen, A. H., Directed evolution of a fungal peroxidase. *Nat. Biotechnol.* **1999**, *17* (4), 379-84.
279. Lu, Y., Metal ions as matchmakers for proteins. *Proceedings of the National Academy of Sciences* **2010**, *107* (5), 1811.
280. Waldron, K. J.; Robinson, N. J., How do bacterial cells ensure that metalloproteins get the correct metal? *Nat. Rev. Microbiol.* **2009**, *7* (1), 25-35.

281. Andreini, C.; Bertini, I.; Cavallaro, G.; Holliday, G. L.; Thornton, J. M., Metal ions in biological catalysis: from enzyme databases to general principles. *JBIC Journal of Biological Inorganic Chemistry* **2008**, *13* (8), 1205-1218.
282. Shimazaki, Y.; Takani, M.; Yamauchi, O., Metal complexes of amino acids and amino acid side chain groups. Structures and properties. *Dalton Transactions* **2009**, (38), 7854-7869.
283. Sigel, H.; Martin, R. B., Coordinating properties of the amide bond. Stability and structure of metal ion complexes of peptides and related ligands. *Chem. Rev.* **1982**, *82* (4), 385-426.
284. Dürrenberger, M.; Ward, T. R., Recent achievements in the design and engineering of artificial metalloenzymes. *Curr. Opin. Chem. Biol.* **2014**, *19*, 99-106.
285. DeGrado, W. F.; Summa, C. M.; Pavone, V.; Natri, F.; Lombardi, A., De novo design and structural characterization of proteins and metalloproteins. *Annu Rev Biochem* **1999**, *68*, 779-819.
286. Lu, Y.; Yeung, N.; Sieracki, N.; Marshall, N. M., Design of functional metalloproteins. *Nature* **2009**, *460* (7257), 855-62.
287. Pordea, A., Metal-binding promiscuity in artificial metalloenzyme design. *Curr. Opin. Chem. Biol.* **2015**, *25*, 124-132.
288. Natri, F.; Chino, M.; Maglio, O.; Bhagi-Damodaran, A.; Lu, Y.; Lombardi, A., Design and engineering of artificial oxygen-activating metalloenzymes. *Chem. Soc. Rev.* **2016**, *45* (18), 5020-5054.
289. Wieszczycka, K.; Staszak, K., Artificial metalloenzymes as catalysts in non-natural compounds synthesis. *Coord. Chem. Rev.* **2017**, *351*, 160-171.
290. Schwizer, F.; Okamoto, Y.; Heinisch, T.; Gu, Y.; Pellizzoni, M. M.; Lebrun, V.; Reuter, R.; Köhler, V.; Lewis, J. C.; Ward, T. R., Artificial Metalloenzymes: Reaction Scope and Optimization Strategies. *Chem. Rev.* **2018**, *118* (1), 142-231.
291. Koder, R. L.; Anderson, J. L.; Solomon, L. A.; Reddy, K. S.; Moser, C. C.; Dutton, P. L., Design and engineering of an O(2) transport protein. *Nature* **2009**, *458* (7236), 305-9.
292. Dieckmann, G. R.; McRorie, D. K.; Tierney, D. L.; Utschig, L. M.; Singer, C. P.; O'Halloran, T. V.; Penner-Hahn, J. E.; DeGrado, W. F.; Pecoraro, V. L., De Novo Design of Mercury-Binding Two- and Three-Helical Bundles. *Journal of the American Chemical Society* **1997**, *119* (26), 6195-6196.
293. Matzapetakis, M.; Farrer, B. T.; Weng, T. C.; Hemmingsen, L.; Penner-Hahn, J. E.; Pecoraro, V. L., Comparison of the binding of cadmium(II), mercury(II), and arsenic(III) to the de novo designed peptides TRI L12C and TRI L16C. *J. Am. Chem. Soc.* **2002**, *124* (27), 8042-54.

294. Wegner, S. V.; Boyaci, H.; Chen, H.; Jensen, M. P.; He, C., Engineering a uranyl-specific binding protein from NikR. *Angew. Chem. Int. Ed. Engl.* **2009**, *48* (13), 2339-41.
295. Lewis, J. C., Metallopeptide catalysts and artificial metalloenzymes containing unnatural amino acids. *Curr. Opin. Chem. Biol.* **2015**, *25*, 27-35.
296. Yu, Y.; Hu, C.; Xia, L.; Wang, J., Artificial Metalloenzyme Design with Unnatural Amino Acids and Non-Native Cofactors. *ACS Catalysis* **2018**, *8* (3), 1851-1863.
297. Hu, C.; Chan, S. I.; Sawyer, E. B.; Yu, Y.; Wang, J., Metalloprotein design using genetic code expansion. *Chem. Soc. Rev.* **2014**, *43* (18), 6498-6510.
298. Imperiali, B.; Prins, T. J.; Fisher, S. L., Chemoenzymic synthesis of 2-amino-3-(2,2'-bipyridinyl)propanoic acids. *The Journal of Organic Chemistry* **1993**, *58* (6), 1613-1616.
299. Xie, J.; Liu, W.; Schultz, P. G., A Genetically Encoded Bidentate, Metal-Binding Amino Acid. *Angew. Chem. Int. Ed.* **2007**, *46* (48), 9239-9242.
300. Lee, H. S.; Spraggon, G.; Schultz, P. G.; Wang, F., Genetic incorporation of a metal-ion chelating amino acid into proteins as a biophysical probe. *J. Am. Chem. Soc.* **2009**, *131* (7), 2481-3.
301. Park, S. H.; Wang, V. S.; Radoicic, J.; De Angelis, A. A.; Berkamp, S.; Opella, S. J., Paramagnetic relaxation enhancement of membrane proteins by incorporation of the metal-chelating unnatural amino acid 2-amino-3-(8-hydroxyquinolin-3-yl)propanoic acid (HQA). *J. Biomol. NMR* **2015**, *61* (3-4), 185-96.
302. Jin, S.; Lee, H.-J.; Lee, S.; Lee, H. S., Genetic Incorporation of Phenanthroline- Containing Amino Acid in Escherichia coli. **2014**, 35.
303. Liu, X.; Li, J.; Dong, J.; Hu, C.; Gong, W.; Wang, J., Genetic incorporation of a metal-chelating amino acid as a probe for protein electron transfer. *Angew. Chem. Int. Ed. Engl.* **2012**, *51* (41), 10261-5.
304. Lee, H. S.; Schultz, P. G., Biosynthesis of a site-specific DNA cleaving protein. *J. Am. Chem. Soc.* **2008**, *130* (40), 13194-5.
305. Koga, N.; Tatsumi-Koga, R.; Liu, G.; Xiao, R.; Acton, T. B.; Montelione, G. T.; Baker, D., Principles for designing ideal protein structures. *Nature* **2012**, *491* (7423), 222-7.
306. Baker, D., What has de novo protein design taught us about protein folding and biophysics? *Protein Sci.* **2019**, *28* (4), 678-683.
307. Huang, P. S.; Boyken, S. E.; Baker, D., The coming of age of de novo protein design. *Nature* **2016**, *537* (7620), 320-7.
308. Mills, J. H.; Khare, S. D.; Bolduc, J. M.; Forouhar, F.; Mulligan, V. K.; Lew, S.; Seetharaman, J.; Tong, L.; Stoddard, B. L.; Baker, D., Computational design of an

- unnatural amino acid dependent metalloprotein with atomic level accuracy. *Journal of the American Chemical Society* **2013**, *135* (36), 13393-13399.
309. Mills, J. H.; Sheffler, W.; Ener, M. E.; Almhjell, P. J.; Oberdorfer, G.; Pereira, J. H.; Parmeggiani, F.; Sankaran, B.; Zwart, P. H.; Baker, D., Computational design of a homotrimeric metalloprotein with a trisbipyridyl core. *Proc Natl Acad Sci U S A* **2016**, *113* (52), 15012-15017.
310. Rohl, C. A.; Strauss, C. E. M.; Misura, K. M. S.; Baker, D., Protein Structure Prediction Using Rosetta. In *Methods Enzymol.*, Academic Press: 2004; Vol. 383, pp 66-93.
311. Baliza, P. X.; Ferreira, S. L.; Teixeira, L. S., Application of pyridylazo and thiazolylazo reagents in flow injection preconcentration systems for determination of metals. *Talanta* **2009**, *79* (1), 2-9.
312. Meredith, N. A.; Volckens, J.; Henry, C. S., Paper-based microfluidics for experimental design: screening masking agents for simultaneous determination of Mn(ii) and Co(ii). *Analytical Methods* **2017**, *9* (3), 534-540.
313. Cheng, K. L.; Bray, R. H., 1-(2-Pyridylazo)-2-naphthol as Possible Analytical Reagent. *Anal. Chem.* **1955**, *27* (5), 782-785.
314. Kocyła, A.; Pomorski, A.; Krężel, A., Molar absorption coefficients and stability constants of metal complexes of 4-(2-pyridylazo)resorcinol (PAR): Revisiting common chelating probe for the study of metalloproteins. *J. Inorg. Biochem.* **2015**, *152*, 82-92.
315. Vittaya, L.; Leesakul, N.; Saithong, S.; Phongpaichit, S.; Chumponanomakun, P.; Boonprab, T.; Chainok, K.; Tantirungrotechai, Y., Synthesis, characterization, and biological studies of novel Ni(II) and Zn(II) complexes with 5-chloro-2-(phenylazo)pyridine. *ScienceAsia* **2017**, *43*, 175-185.
316. Seth, S.; Chakraborty, S., Structure of bis(2'-[α -(2-pyridyl)benzylidene]salicyclohydrazidonickel(II) monohydrate. *Acta Crystallographica Section C* **1984**, *40* (9), 1530-1533.
317. Hotze, A. C. G.; Bacac, M.; Velders, A. H.; Jansen, B. A. J.; Kooijman, H.; Spek, A. L.; Haasnoot, J. G.; Reedijk, J., New Cytotoxic and Water-Soluble Bis(2-phenylazopyridine)ruthenium(II) Complexes. *J. Med. Chem.* **2003**, *46* (9), 1743-1750.
318. Velders, A. H.; Kooijman, H.; Spek, A. L.; Haasnoot, J. G.; de Vos, D.; Reedijk, J., Strong Differences in the in Vitro Cytotoxicity of Three Isomeric Dichlorobis(2-phenylazopyridine)ruthenium(II) Complexes. *Inorg. Chem.* **2000**, *39* (14), 2966-2967.
319. Wang, Z.; Cook, M. J.; Nygård, A.-M.; Russell, D. A., Metal-Ion Chelation and Sensing Using a Self-Assembled Molecular Photoswitch. *Langmuir* **2003**, *19* (9), 3779-3784.

320. Suwa, K.; Otsuki, J.; Goto, K., Syntheses of shuttlecock- and bowl-equipped phenylazopyridines and photomodulation of their coordination ability to Zn-porphyrin. *Tetrahedron Lett.* **2009**, *50* (18), 2106-2108.
321. Thies, S.; Sell, H.; Bornholdt, C.; Schütt, C.; Köhler, F.; Tucek, F.; Herges, R., Light-Driven Coordination-Induced Spin-State Switching: Rational Design of Photodissociable Ligands. *Chemistry – A European Journal* **2012**, *18* (51), 16358-16368.
322. Yasui, T.; Mizuno, Y.; Maeda, K.; Yamada, H.; Yuchi, A., Selectively Enhanced Retention of Neutral Iron(II) Complex in RP-LC with o-Hydroxy Pyrimidylazo Compounds as Precolumn Derivatizing Reagent. *Chromatographia* **2008**, *68* (5), 387-391.
323. Pilipenko, A.; Savranskii, L.; Sheptun, V., Structure and stability of metal oxyazo reagent complexes. *Koord. Khim.* **1988**, *14* (11), 1482-1489.
324. Siroki, M.; Koren-Marković, M., Extraction and Characterization of Palladium 4-(2-pyridylazo) resorcinol Complexes. *Solvent Extr. Ion Exch.* **1988**, *6* (5), 771-783.
325. Hussain, G.; Abass, N.; Shabir, G.; Athar, M.; Saeed, A.; Saleem, R.; Ali, F.; Khan, M. A., New acid dyes and their metal complexes based on substituted phenols for leather: Synthesis, characterization and optical studies. *Journal of Applied Research and Technology* **2017**, *15* (4), 346-355.
326. Li, Y.; Yang, Z.; Zhou, M.; Li, Y.; He, J.; Wang, X.; Lin, Z., Ni(ii) and Co(ii) complexes of an asymmetrical aroylhydrazone: synthesis, molecular structures, DNA binding, protein interaction, radical scavenging and cytotoxic activity. *RSC Advances* **2017**, *7* (66), 41527-41539.
327. Wu, W.-N.; Wu, H.; Wang, Y.; Mao, X.-J.; Liu, B.-Z.; Zhao, X.-L.; Xu, Z.-Q.; Fan, Y.-C.; Xu, Z.-H., A simple hydrazone as a multianalyte (Cu²⁺, Al³⁺, Zn²⁺) sensor at different pH values and the resultant Al³⁺ complex as a sensor for F⁻. *RSC Advances* **2018**, *8* (10), 5640-5646.
328. Chen, L.; Tian, X.; Xia, D.; Nie, Y.; Lu, L.; Yang, C.; Zhou, Z., Novel Colorimetric Method for Simultaneous Detection and Identification of Multimetal Ions in Water: Sensitivity, Selectivity, and Recognition Mechanism. *ACS Omega* **2019**, *4* (3), 5915-5922.
329. Mata, F. E. Phenylazopyridines as photoswitchable and metal chelating motifs in supramolecular chemistry. The University of Manchester, The University of Manchester, 2013.
330. Ho, T.-L., Hard soft acids bases (HSAB) principle and organic chemistry. *Chem. Rev.* **1975**, *75* (1), 1-20.
331. Pal, S., Pyridine: A Useful Ligand in Transition Metal Complexes. In *Pyridine*, 2018.

332. Olson, E. J.; Bühlmann, P., Getting More out of a Job Plot: Determination of Reactant to Product Stoichiometry in Cases of Displacement Reactions and n:n Complex Formation. *The Journal of Organic Chemistry* **2011**, *76* (20), 8406-8412.
333. MacCarthy, P., Simplified experimental route for obtaining Job's curves. *Anal. Chem.* **1978**, *50* (14), 2165-2165.
334. Wolfgang, B., Metal Complexes of Biologically Important Ligands. Metal Ions and Metal Complexes as Protective Groups of Amino Acids and Peptides – Reactions at Coordinated Amino Acids. *Zeitschrift für Naturforschung B* **2009**, *64* (11-12), 1221-1245.
335. Xuereb, D. J.; Raja, R., Design strategies for engineering selectivity in bio-inspired heterogeneous catalysts. *Catalysis Science & Technology* **2011**, *1* (4), 517-534.
336. Chin, J.; Lee, S. S.; Lee, K. J.; Park, S.; Kim, D. H., A metal complex that binds α -amino acids with high and predictable stereospecificity. *Nature* **1999**, *401* (6750), 254-257.
337. Kahrovic, E.; Zahirovic, A.; Kraljevic Pavelic, S.; Turkusic, E.; Harej, A., In vitro anticancer activity of binuclear Ru(II) complexes with Schiff bases derived from 5-substituted salicylaldehyde and 2-aminopyridine with notably low IC50 values. *J. Coord. Chem.* **2017**, *70* (10), 1683-1697.
338. Abdel-Rahman, L. H.; Abu-Dief, A. M.; Newair, E. F.; Hamdan, S. K., Some new nano-sized CrIII, FeII, CoII, and NiII complexes incorporating 2-((E)-(pyridine-2-ylimino)methyl)naphthalen-1-ol ligand: Structural characterization, electrochemical, antioxidant, antimicrobial, antiviral assessment and DNA interaction. *J. Photochem. Photobiol. B: Biol.* **2016**, *160*, 18-31.
339. Trofimenko, S., Coordination chemistry of pyrazole-derived ligands. *Chem. Rev.* **1972**, *72* (5), 497-509.
340. Bagley, M. J.; Nicholls, D.; Warburton, B. A., Pyrazole complexes of cobalt(II). *Journal of the Chemical Society A: Inorganic, Physical, Theoretical* **1970**, (0), 2694-2697.
341. Enke, M.; Jehle, F.; Bode, S.; Vitz, J.; Harrington, M. J.; Hager, M. D.; Schubert, U. S., Histidine–Zinc Interactions Investigated by Isothermal Titration Calorimetry (ITC) and their Application in Self-Healing Polymers. *Macromol. Chem. Phys.* **2017**, *218* (5), 1600458.
342. Robinson, S. G.; Burns, P. T.; Miceli, A. M.; Grice, K. A.; Karver, C. E.; Jin, L., Calorimetric studies of the interactions of metalloenzyme active site mimetics with zinc-binding inhibitors. *Dalton Transactions* **2016**, *45* (29), 11817-11829.
343. Cragnell, C.; Staby, L.; Lenton, S.; Kragelund, B. B.; Skepö, M., Dynamical Oligomerisation of Histidine Rich Intrinsically Disordered ProteinS Is Regulated through Zinc-Histidine Interactions. *Biomolecules* **2019**, *9* (5), 168.

344. Zhang, Y.; Akilesh, S.; Wilcox, D. E., Isothermal Titration Calorimetry Measurements of Ni(II) and Cu(II) Binding to His, GlyGlyHis, HisGlyHis, and Bovine Serum Albumin: A Critical Evaluation. *Inorg. Chem.* **2000**, *39* (14), 3057-3064.
345. Perego, L. A.; Blicek, R.; Michel, J.; Ciofini, I.; Grimaud, L.; Taillefer, M.; Monnier, F., Copper-Catalyzed Hydroamination of N-Allenylazoles: Access to Amino-Substituted N-Vinylazoles. *Adv. Synth. Catal.* **2017**, *359* (24), 4388-4392.
346. Bai, S.-Q.; Kwang, J. Y.; Koh, L. L.; Young, D. J.; Hor, T. S. A., Functionalized 1,2,3-triazoles as building blocks for photoluminescent POLOs (polymers of oligomers) of copper(i). *Dalton Transactions* **2010**, *39* (10), 2631-2636.
347. Wong, C. M.; Vuong, K. Q.; Gatus, M. R. D.; Hua, C.; Bhadbhade, M.; Messerle, B. A., Catalyzed Tandem C–N/C–C Bond Formation for the Synthesis of Tricyclic Indoles using Ir(III) Pyrazolyl-1,2,3-Triazolyl Complexes. *Organometallics* **2012**, *31* (21), 7500-7510.
348. Mukherjee, R., Coordination chemistry with pyrazole-based chelating ligands: molecular structural aspects. *Coord. Chem. Rev.* **2000**, *203* (1), 151-218.
349. Neumann, H.; Hazen, J. L.; Weinstein, J.; Mehl, R. A.; Chin, J. W., Genetically Encoding Protein Oxidative Damage. *Journal of the American Chemical Society* **2008**, *130* (12), 4028-4033.
350. Hammill, J. T.; Miyake-Stoner, S.; Hazen, J. L.; Jackson, J. C.; Mehl, R. A., Preparation of site-specifically labeled fluorinated proteins for ¹⁹F-NMR structural characterization. *Nature Protocols* **2007**, *2* (10), 2601-2607.
351. Putyrski, M.; Schultz, C., Protein translocation as a tool: The current rapamycin story. *FEBS Lett.* **2012**, *586* (15), 2097-105.
352. Voss, S.; Klewer, L.; Wu, Y. W., Chemically induced dimerization: reversible and spatiotemporal control of protein function in cells. *Curr. Opin. Chem. Biol.* **2015**, *28*, 194-201.
353. Fegan, A.; White, B.; Carlson, J. C.; Wagner, C. R., Chemically controlled protein assembly: techniques and applications. *Chem Rev* **2010**, *110* (6), 3315-36.
354. DeRose, R.; Miyamoto, T.; Inoue, T., Manipulating signaling at will: chemically-inducible dimerization (CID) techniques resolve problems in cell biology. *Pflugers Arch* **2013**, *465* (3), 409-17.
355. Stanton, B. Z.; Chory, E. J.; Crabtree, G. R., Chemically induced proximity in biology and medicine. *Science (New York, N.Y.)* **2018**, *359* (6380), eaao5902.
356. Ali, J. A.; Jackson, A. P.; Howells, A. J.; Maxwell, A., The 43-kilodalton N-terminal fragment of the DNA gyrase B protein hydrolyzes ATP and binds coumarin drugs. *Biochemistry* **1993**, *32* (10), 2717-2724.

357. Farrar, M. A.; Olson, S. H.; Perlmutter, R. M., Coumermycin-induced dimerization of GyrB-containing fusion proteins. *Methods Enzymol.* **2000**, *327*, 421-9.
358. Pruschy, M. N.; Spencer, D. M.; Kapoor, T. M.; Miyake, H.; Crabtree, G. R.; Schreiber, S. L., Mechanistic studies of a signaling pathway activated by the organic dimerizer FK1012. *Chem. Biol.* **1994**, *1* (3), 163-72.
359. Spencer, D. M.; Belshaw, P. J.; Chen, L.; Ho, S. N.; Randazzo, F.; Crabtree, G. R.; Schreiber, S. L., Functional analysis of Fas signaling in vivo using synthetic inducers of dimerization. *Curr. Biol.* **1996**, *6* (7), 839-847.
360. Yang, J.-x.; Symes, K.; Mercola, M.; Schreiber, S. L., Small-molecule control of insulin and PDGF receptor signaling and the role of membrane attachment. *Curr. Biol.* **1998**, *8* (1), 11-18.
361. Stockwell, B. R.; Schreiber, S. L., Probing the role of homomeric and heteromeric receptor interactions in TGF- β 2 signaling using small molecule dimerizers. *Curr. Biol.* **1998**, *8* (13), 761-773.
362. Almawi, W. Y.; Melemedjian, O. K., Clinical and mechanistic differences between FK506 (tacrolimus) and cyclosporin A. *Nephrology Dialysis Transplantation* **2000**, *15* (12), 1916-1918.
363. Choi, J.; Chen, J.; Schreiber, S. L.; Clardy, J., Structure of the FKBP12-rapamycin complex interacting with the binding domain of human FRAP. *Science* **1996**, *273* (5272), 239-42.
364. Banaszynski, L. A.; Liu, C. W.; Wandless, T. J., Characterization of the FKBP.rapamycin.FRB ternary complex. *J. Am. Chem. Soc.* **2005**, *127* (13), 4715-21.
365. Pecot, M. Y.; Malhotra, V., Golgi Membranes Remain Segregated from the Endoplasmic Reticulum during Mitosis in Mammalian Cells. *Cell* **2004**, *116* (1), 99-107.
366. Zoncu, R.; Perera, R. M.; Balkin, D. M.; Pirruccello, M.; Toomre, D.; De Camilli, P., A Phosphoinositide Switch Controls the Maturation and Signaling Properties of APPL Endosomes. *Cell* **2009**, *136* (6), 1110-1121.
367. Robinson, M. S.; Sahlender, D. A.; Foster, S. D., Rapid inactivation of proteins by rapamycin-induced rerouting to mitochondria. *Dev. Cell* **2010**, *18* (2), 324-31.
368. Goulden, B. D.; Pacheco, J.; Dull, A.; Zewe, J. P.; Deiters, A.; Hammond, G. R. V., A high-avidity biosensor reveals plasma membrane PI(3,4)P2 is predominantly a class I PI3K signaling product. *J. Cell Biol.* **2019**, *218* (3), 1066-1079.
369. Kohler, J. J.; Bertozzi, C. R., Regulating Cell Surface Glycosylation by Small Molecule Control of Enzyme Localization. *Chem. Biol.* *10* (12), 1303-1311.
370. Diaz, J. E.; Morgan, C. W.; Minogue, C. E.; Hebert, A. S.; Coon, J. J.; Wells, J. A., A Split-Abl Kinase for Direct Activation in Cells. *Cell Chem Biol* **2017**.

371. Zetsche, B.; Volz, S. E.; Zhang, F., A split-Cas9 architecture for inducible genome editing and transcription modulation. *Nat. Biotechnol.* **2015**, *33* (2), 139-42.
372. Williams, D. J.; Puhl, H. L.; Ikeda, S. R., Rapid modification of proteins using a rapamycin-inducible tobacco etch virus protease system. *PLoS One* **2009**, *4* (10), e7474.
373. Gray, D. C.; Mahrus, S.; Wells, J. A., Activation of specific apoptotic caspases with an engineered small-molecule-activated protease. *Cell* **2010**, *142* (4), 637-46.
374. Cabantous, S.; Nguyen, H. B.; Pedelacq, J. D.; Koraichi, F.; Chaudhary, A.; Ganguly, K.; Lockard, M. A.; Favre, G.; Terwilliger, T. C.; Waldo, G. S., A new protein-protein interaction sensor based on tripartite split-GFP association. *Sci Rep* **2013**, *3*, 2854.
375. Galarneau, A.; Primeau, M.; Trudeau, L. E.; Michnick, S. W., Beta-lactamase protein fragment complementation assays as in vivo and in vitro sensors of protein protein interactions. *Nat. Biotechnol.* **2002**, *20* (6), 619-22.
376. Jullien, N.; Sampieri, F.; Enjalbert, A.; Herman, J. P., Regulation of Cre recombinase by ligand-induced complementation of inactive fragments. *Nucleic Acids Res.* **2003**, *31* (21), e131.
377. Jones, K. A.; Kentala, K.; Beck, M. W.; An, W.; Lippert, A. R.; Lewis, J. C.; Dickinson, B. C., Development of a Split Esterase for Protein-Protein Interaction-Dependent Small-Molecule Activation. *ACS Cent Sci* **2019**, *5* (11), 1768-1776.
378. Luker, K. E.; Smith, M. C. P.; Luker, G. D.; Gammon, S. T.; Piwnica-Worms, H.; Piwnica-Worms, D., Kinetics of regulated protein-protein interactions revealed with firefly luciferase complementation imaging in cells and living animals. *Proceedings of the National Academy of Sciences of the United States of America* **2004**, *101* (33), 12288-12293.
379. Pratt, M. R.; Schwartz, E. C.; Muir, T. W., Small-molecule-mediated rescue of protein function by an inducible proteolytic shunt. *Proc Natl Acad Sci U S A* **2007**, *104* (27), 11209-14.
380. Vezina, C.; Kudelski, A.; Sehgal, S. N., Rapamycin (AY-22,989), a new antifungal antibiotic. I. Taxonomy of the producing streptomycete and isolation of the active principle. *J Antibiot (Tokyo)* **1975**, *28* (10), 721-6.
381. Sehgal, S. N.; Baker, H.; Vezina, C., Rapamycin (AY-22,989), a new antifungal antibiotic. II. Fermentation, isolation and characterization. *J Antibiot (Tokyo)* **1975**, *28* (10), 727-32.
382. Baker, H.; Sidorowicz, A.; Sehgal, S. N.; Vezina, C., Rapamycin (AY-22,989), a new antifungal antibiotic. III. In vitro and in vivo evaluation. *J Antibiot (Tokyo)* **1978**, *31* (6), 539-45.
383. Law, B. K., Rapamycin: an anti-cancer immunosuppressant? *Crit Rev Oncol Hematol* **2005**, *56* (1), 47-60.

384. Dumont, F. J.; Su, Q., Mechanism of action of the immunosuppressant rapamycin. *Life Sci.* **1996**, *58* (5), 373-95.
385. Li, J.; Kim, S. G.; Blenis, J., Rapamycin: one drug, many effects. *Cell Metab* **2014**, *19* (3), 373-9.
386. Seto, B., Rapamycin and mTOR: a serendipitous discovery and implications for breast cancer. *Clin Transl Med* **2012**, *1* (1), 29.
387. Hidalgo, M.; Rowinsky, E. K., The rapamycin-sensitive signal transduction pathway as a target for cancer therapy. *Oncogene* **2000**, *19* (56), 6680-6686.
388. Bjornsti, M.-A.; Houghton, P. J., The tor pathway: a target for cancer therapy. *Nature Reviews Cancer* **2004**, *4* (5), 335-348.
389. Georgakis, G. V.; Younes, A., From Rapa Nui to rapamycin: targeting PI3K/Akt/mTOR for cancer therapy. *Expert Review of Anticancer Therapy* **2006**, *6* (1), 131-140.
390. Xie, J.; Wang, X.; Proud, C. G., mTOR inhibitors in cancer therapy. *F1000Res* **2016**, *5*.
391. Hua, H.; Kong, Q.; Zhang, H.; Wang, J.; Luo, T.; Jiang, Y., Targeting mTOR for cancer therapy. *Journal of Hematology & Oncology* **2019**, *12* (1), 71.
392. Brown, E. J.; Albers, M. W.; Bum Shin, T.; Ichikawa, K.; Keith, C. T.; Lane, W. S.; Schreiber, S. L., A mammalian protein targeted by G1-arresting rapamycin-receptor complex. *Nature* **1994**, *369* (6483), 756-758.
393. Sabatini, D. M.; Erdjument-Bromage, H.; Lui, M.; Tempst, P.; Snyder, S. H., RAFT1: a mammalian protein that binds to FKBP12 in a rapamycin-dependent fashion and is homologous to yeast TORs. *Cell* **1994**, *78* (1), 35-43.
394. Sabatini, D. M., Twenty-five years of mTOR: Uncovering the link from nutrients to growth. *Proceedings of the National Academy of Sciences* **2017**, *114* (45), 11818.
395. Francavilla, A.; Starzl, T. E.; Scotti, C.; Carrieri, G.; Azzarone, A.; Zeng, Q. H.; Porter, K. A.; Schreiber, S. L., Inhibition of liver, kidney, and intestine regeneration by rapamycin. *Transplantation* **1992**, *53* (2), 496-8.
396. Hall, M. N., An Amazing Turn of Events. *Cell* **2017**, *171* (1), 18-22.
397. Thomson, A. W.; Turnquist, H. R.; Raimondi, G., Immunoregulatory functions of mTOR inhibition. *Nature Reviews Immunology* **2009**, *9* (5), 324-337.
398. Raimondi, G.; Sumpter, T. L.; Matta, B. M.; Pillai, M.; Corbitt, N.; Vodovotz, Y.; Wang, Z.; Thomson, A. W., Mammalian target of rapamycin inhibition and alloantigen-specific regulatory T cells synergize to promote long-term graft survival in immunocompetent recipients. *J. Immunol.* **2010**, *184* (2), 624-36.

399. Molina, L.; Yang, H.; Adebayo Michael, A. O.; Oertel, M.; Bell, A.; Singh, S.; Chen, X.; Tao, J.; Monga, S. P. S., mTOR inhibition affects Yap1- β -catenin-induced hepatoblastoma growth and development. *Oncotarget* **2019**, *10* (15), 1475-1490.
400. Karginov, A. V.; Ding, F.; Kota, P.; Dokholyan, N. V.; Hahn, K. M., Engineered allosteric activation of kinases in living cells. *Nat. Biotechnol.* **2010**, *28* (7), 743-7.
401. Umeda, N.; Ueno, T.; Pohlmeier, C.; Nagano, T.; Inoue, T., A photocleavable rapamycin conjugate for spatiotemporal control of small GTPase activity. *J. Am. Chem. Soc.* **2011**, *133* (1), 12-4.
402. Harwood, K. R.; Miller, S. C., Leveraging a small-molecule modification to enable the photoactivation of rho GTPases. *ChemBioChem* **2009**, *10* (18), 2855-7.
403. Sadovski, O.; Jaikaran, A. S. I.; Samanta, S.; Fabian, M. R.; Dowling, R. J. O.; Sonenberg, N.; Woolley, G. A., A collection of caged compounds for probing roles of local translation in neurobiology. *Biorg. Med. Chem.* **2010**, *18* (22), 7746-7752.
404. Ballister, E. R.; Aonbangkhen, C.; Mayo, A. M.; Lampson, M. A.; Chenoweth, D. M., Localized light-induced protein dimerization in living cells using a photocaged dimerizer. *Nat Commun* **2014**, *5*, 5475.
405. Ballister, E. R.; Ayloo, S.; Chenoweth, D. M.; Lampson, M. A.; Holzbaur, E. L. F., Optogenetic control of organelle transport using a photocaged chemical inducer of dimerization. *Curr. Biol.* **2015**, *25* (10), R407-R408.
406. Jing, C.; Cornish, V. W., Chemical tags for labeling proteins inside living cells. *Acc. Chem. Res.* **2011**, *44* (9), 784-92.
407. Zimmermann, M.; Cal, R.; Janett, E.; Hoffmann, V.; Bochet, C. G.; Constable, E.; Beaufile, F.; Wymann, M. P., Cell-Permeant and Photocleavable Chemical Inducer of Dimerization. *Angew. Chem. Int. Ed.* **2014**, *53* (18), 4717-4720.
408. Wright, C. W.; Guo, Z. F.; Liang, F. S., Light control of cellular processes by using photocaged abscisic acid. *ChemBioChem* **2015**, *16* (2), 254-61.
409. Schelkle, K. M.; Griesbaum, T.; Ollech, D.; Becht, S.; Buckup, T.; Hamburger, M.; Wombacher, R., Light-induced protein dimerization by one- and two-photon activation of gibberellic acid derivatives in living cells. *Angew. Chem. Int. Ed. Engl.* **2015**, *54* (9), 2825-9.
410. Miyazono, K.; Miyakawa, T.; Sawano, Y.; Kubota, K.; Kang, H. J.; Asano, A.; Miyauchi, Y.; Takahashi, M.; Zhi, Y.; Fujita, Y.; Yoshida, T.; Kodaira, K. S.; Yamaguchi-Shinozaki, K.; Tanokura, M., Structural basis of abscisic acid signalling. *Nature* **2009**, *462* (7273), 609-14.
411. Liang, F.-S.; Ho, W. Q.; Crabtree, G. R., Engineering the ABA plant stress pathway for regulation of induced proximity. *Science signaling* **2011**, *4* (164), rs2-rs2.

412. Ueguchi-Tanaka, M.; Ashikari, M.; Nakajima, M.; Itoh, H.; Katoh, E.; Kobayashi, M.; Chow, T.-y.; Hsing, Y.-i. C.; Kitano, H.; Yamaguchi, I.; Matsuoka, M., Gibberellin Insensitive Dwarf1 encodes a soluble receptor for gibberellin. *Nature* **2005**, *437* (7059), 693-698.
413. Miyamoto, T.; DeRose, R.; Suarez, A.; Ueno, T.; Chen, M.; Sun, T. P.; Wolfgang, M. J.; Mukherjee, C.; Meyers, D. J.; Inoue, T., Rapid and orthogonal logic gating with a gibberellin-induced dimerization system. *Nat. Chem. Biol.* **2012**, *8* (5), 465-70.
414. Pathak, G. P.; Vrana, J. D.; Tucker, C. L., Optogenetic Control of Cell Function Using Engineered Photoreceptors. *Biology of the cell / under the auspices of the European Cell Biology Organization* **2013**, *105* (2), 59-72.
415. Spiltoir, J. I.; Tucker, C. L., Photodimerization systems for regulating protein–protein interactions with light. *Curr. Opin. Struct. Biol.* **2019**, *57*, 1-8.
416. Niu, J.; Ben Johny, M.; Dick, I. E.; Inoue, T., Following Optogenetic Dimerizers and Quantitative Prospects. *Biophys. J.* **2016**, *111* (6), 1132-1140.
417. Klewer, L.; Wu, Y.-W., Light-Induced Dimerization Approaches to Control Cellular Processes. *Chemistry – A European Journal* **2019**, *25* (54), 12452-12463.
418. de Mena, L.; Rizk, P.; Rincon-Limas, D. E., Bringing Light to Transcription: The Optogenetics Repertoire. *Front Genet* **2018**, *9*, 518.
419. Shcherbakova, D. M.; Cox Cammer, N.; Huisman, T. M.; Verkhusha, V. V.; Hodgson, L., Direct multiplex imaging and optogenetics of Rho GTPases enabled by near-infrared FRET. *Nat. Chem. Biol.* **2018**, *14* (6), 591-600.
420. Strickland, D.; Lin, Y.; Wagner, E.; Hope, C. M.; Zayner, J.; Antoniou, C.; Sosnick, T. R.; Weiss, E. L.; Glotzer, M., TULIPs: tunable, light-controlled interacting protein tags for cell biology. *Nat. Methods* **2012**, *9* (4), 379-84.
421. Pathak, G. P.; Strickland, D.; Vrana, J. D.; Tucker, C. L., Benchmarking of optical dimerizer systems. *ACS Synth Biol* **2014**, *3* (11), 832-8.
422. Aoki, K.; Kumagai, Y.; Sakurai, A.; Komatsu, N.; Fujita, Y.; Shionyu, C.; Matsuda, M., Stochastic ERK activation induced by noise and cell-to-cell propagation regulates cell density-dependent proliferation. *Mol. Cell* **2013**, *52* (4), 529-40.
423. Shimizu-Sato, S.; Huq, E.; Tepperman, J. M.; Quail, P. H., A light-switchable gene promoter system. *Nat. Biotechnol.* **2002**, *20* (10), 1041-1044.
424. Kennedy, M. J.; Hughes, R. M.; Peteya, L. A.; Schwartz, J. W.; Ehlers, M. D.; Tucker, C. L., Rapid blue-light-mediated induction of protein interactions in living cells. *Nat. Methods* **2010**, *7* (12), 973-5.

425. Taslimi, A.; Zoltowski, B.; Miranda, J. G.; Pathak, G. P.; Hughes, R. M.; Tucker, C. L., Optimized second-generation CRY2-CIB dimerizers and photoactivatable Cre recombinase. *Nat. Chem. Biol.* **2016**, *12* (6), 425-430.
426. Kawano, F.; Okazaki, R.; Yazawa, M.; Sato, M., A photoactivatable Cre-loxP recombination system for optogenetic genome engineering. *Nat. Chem. Biol.* **2016**, *12* (12), 1059-1064.
427. Nihongaki, Y.; Kawano, F.; Nakajima, T.; Sato, M., Photoactivatable CRISPR-Cas9 for optogenetic genome editing. *Nat. Biotechnol.* **2015**, *33* (7), 755-60.
428. Han, T.; Chen, Q.; Liu, H., Engineered Photoactivatable Genetic Switches Based on the Bacterium Phage T7 RNA Polymerase. *ACS Synth Biol* **2017**, *6* (2), 357-366.
429. Ozkan-Dagliyan, I.; Chiou, Y. Y.; Ye, R.; Hassan, B. H.; Ozturk, N.; Sancar, A., Formation of Arabidopsis Cryptochrome 2 photobodies in mammalian nuclei: application as an optogenetic DNA damage checkpoint switch. *J. Biol. Chem.* **2013**, *288* (32), 23244-51.
430. Bugaj, L. J.; Choksi, A. T.; Mesuda, C. K.; Kane, R. S.; Schaffer, D. V., Optogenetic protein clustering and signaling activation in mammalian cells. *Nat. Methods* **2013**, *10* (3), 249-52.
431. Chang, K. Y.; Woo, D.; Jung, H.; Lee, S.; Kim, S.; Won, J.; Kyung, T.; Park, H.; Kim, N.; Yang, H. W.; Park, J. Y.; Hwang, E. M.; Kim, D.; Heo, W. D., Light-inducible receptor tyrosine kinases that regulate neurotrophin signalling. *Nat Commun* **2014**, *5*, 4057.
432. Kim, N.; Kim, J. M.; Lee, M.; Kim, C. Y.; Chang, K. Y.; Heo, W. D., Spatiotemporal control of fibroblast growth factor receptor signals by blue light. *Chem. Biol.* **2014**, *21* (7), 903-12.
433. Lee, S.; Park, H.; Kyung, T.; Kim, N. Y.; Kim, S.; Kim, J.; Heo, W. D., Reversible protein inactivation by optogenetic trapping in cells. *Nat. Methods* **2014**, *11* (6), 633-6.
434. Zhou, X. X.; Zou, X.; Chung, H. K.; Gao, Y.; Liu, Y.; Qi, L. S.; Lin, M. Z., A Single-Chain Photoswitchable CRISPR-Cas9 Architecture for Light-Inducible Gene Editing and Transcription. *ACS Chem Biol* **2018**, *13* (2), 443-448.
435. O'Banion, C. P.; Lawrence, D. S., Optogenetics: A Primer for Chemists. *ChemBioChem* **2018**, *19* (12), 1201-1216.
436. Laplante, M.; Sabatini, D. M., mTOR signaling in growth control and disease. *Cell* **2012**, *149* (2), 274-93.
437. Liberles, S. D.; Diver, S. T.; Austin, D. J.; Schreiber, S. L., Inducible gene expression and protein translocation using nontoxic ligands identified by a mammalian three-hybrid screen. *Proceedings of the National Academy of Sciences* **1997**, *94* (15), 7825-7830.

438. Bayle, J. H.; Grimley, J. S.; Stankunas, K.; Gestwicki, J. E.; Wandless, T. J.; Crabtree, G. R., Rapamycin Analogs with Differential Binding Specificity Permit Orthogonal Control of Protein Activity. *Chem. Biol.* **2006**, *13* (1), 99-107.
439. Inoue, T.; Heo, W. D.; Grimley, J. S.; Wandless, T. J.; Meyer, T., An inducible translocation strategy to rapidly activate and inhibit small GTPase signaling pathways. *Nat. Methods* **2005**, *2* (6), 415-8.
440. Yang, W.; Digits, C. A.; Rozamus, L.; Holt, D. A., 28-epirapalogs. Google Patents: 2001.
441. Stankunas, K.; Bayle, J. H.; Gestwicki, J. E.; Lin, Y. M.; Wandless, T. J.; Crabtree, G. R., Conditional protein alleles using knockin mice and a chemical inducer of dimerization. *Mol. Cell* **2003**, *12* (6), 1615-24.
442. Stankunas, K.; Bayle, J. H.; Havranek, J. J.; Wandless, T. J.; Baker, D.; Crabtree, G. R.; Gestwicki, J. E., Rescue of degradation-prone mutants of the FK506-rapamycin binding (FRB) protein with chemical ligands. *ChemBioChem* **2007**, *8* (10), 1162-9.
443. Patury, S.; Geda, P.; Dobry, C. J.; Kumar, A.; Gestwicki, J. E., Conditional nuclear import and export of yeast proteins using a chemical inducer of dimerization. *Cell Biochem Biophys* **2009**, *53* (3), 127-34.
444. Goguen, B. N.; Aemissegger, A.; Imperiali, B., Sequential activation and deactivation of protein function using spectrally differentiated caged phosphoamino acids. *J. Am. Chem. Soc.* **2011**, *133* (29), 11038-41.
445. San Miguel, V.; Bochet, C. G.; del Campo, A., Wavelength-selective caged surfaces: how many functional levels are possible? *J. Am. Chem. Soc.* **2011**, *133* (14), 5380-8.
446. Agarwal, H. K.; Janicek, R.; Chi, S. H.; Perry, J. W.; Niggli, E.; Ellis-Davies, G. C., Calcium Uncaging with Visible Light. *J. Am. Chem. Soc.* **2016**, *138* (11), 3687-93.
447. Deiters, A.; Hahn, K.; Karginov, A., Light mediated regulation of protein dimerization. Google Patents: 2012.
448. Pasini, D., The click reaction as an efficient tool for the construction of macrocyclic structures. *Molecules* **2013**, *18* (8), 9512-30.
449. Rostovtsev, V. V.; Green, L. G.; Fokin, V. V.; Sharpless, K. B., A stepwise Huisgen cycloaddition process: copper(I)-catalyzed regioselective "ligation" of azides and terminal alkynes. *Angew. Chem. Int. Ed. Engl.* **2002**, *41* (14), 2596-9.
450. Ruan, B.; Pong, K.; Jow, F.; Bowlby, M.; Crozier, R. A.; Liu, D.; Liang, S.; Chen, Y.; Mercado, M. L.; Feng, X.; Bennett, F.; von Schack, D.; McDonald, L.; Zaleska, M. M.; Wood, A.; Reinhart, P. H.; Magolda, R. L.; Skotnicki, J.; Pangalos, M. N.; Koehn, F. E.; Carter, G. T.; Abou-Gharbia, M.; Graziani, E. I., Binding of rapamycin analogs to calcium channels and FKBP52 contributes to their neuroprotective activities. *Proc Natl Acad Sci U S A* **2008**, *105* (1), 33-8.

451. Carosso, S.; Miller, M. J., Nitroso Diels–Alder (NDA) reaction as an efficient tool for the functionalization of diene-containing natural products. *Organic & Biomolecular Chemistry* **2014**, *12* (38), 7445-7468.
452. Richers, M. T.; Passlick, S.; Agarwal, H.; Ellis-Davies, G. C. R., Dendrimer Conjugation Enables Multiphoton Chemical Neurophysiology Studies with an Extended π -Electron Caging Chromophore. *Angew. Chem. Int. Ed.* **2019**, *58* (35), 12086-12090.
453. Komori, N.; Jakkampudi, S.; Motoishi, R.; Abe, M.; Kamada, K.; Furukawa, K.; Katan, C.; Sawada, W.; Takahashi, N.; Kasai, H.; Xue, B.; Kobayashi, T., Design and synthesis of a new chromophore, 2-(4-nitrophenyl)benzofuran, for two-photon uncaging using near-IR light. *Chem. Commun.* **2016**, *52* (2), 331-334.
454. Gug, S.; Charon, S.; Specht, A.; Alarcon, K.; Ogden, D.; Zietz, B.; Léonard, J.; Haacke, S.; Bolze, F.; Nicoud, J.-F.; Goeldner, M., Photolabile Glutamate Protecting Group with High One- and Two-Photon Uncaging Efficiencies. *ChemBioChem* **2008**, *9* (8), 1303-1307.
455. Warther, D.; Bolze, F.; Leonard, J.; Gug, S.; Specht, A.; Puliti, D.; Sun, X. H.; Kessler, P.; Lutz, Y.; Vonesch, J. L.; Winsor, B.; Nicoud, J. F.; Goeldner, M., Live-cell one- and two-photon uncaging of a far-red emitting acridinone fluorophore. *J. Am. Chem. Soc.* **2010**, *132* (8), 2585-90.
456. Donato, L.; Mourot, A.; Davenport, C. M.; Herbivo, C.; Warther, D.; Léonard, J.; Bolze, F.; Nicoud, J.-F.; Kramer, R. H.; Goeldner, M.; Specht, A., Water-Soluble, Donor–Acceptor Biphenyl Derivatives in the 2-(o-Nitrophenyl)propyl Series: Highly Efficient Two-Photon Uncaging of the Neurotransmitter γ -Aminobutyric Acid at $\lambda=800$ nm. *Angew. Chem. Int. Ed.* **2012**, *51* (8), 1840-1843.
457. Abou Nakad, E.; Bolze, F.; Specht, A., o-Nitrobenzyl photoremovable groups with fluorescence uncaging reporting properties. *Organic & Biomolecular Chemistry* **2018**, *16* (33), 6115-6122.
458. Shekhawat, S. S.; Ghosh, I., Split-protein systems: beyond binary protein-protein interactions. *Curr. Opin. Chem. Biol.* **2011**, *15* (6), 789-97.
459. Banaszynski, L. A.; Chen, L.-c.; Maynard-Smith, L. A.; Lisa Ooi, A. G.; Wandless, T. J., A Rapid, Reversible, and Tunable Method to Regulate Protein Function in Living Cells Using Synthetic Small Molecules. *Cell* **2006**, *126* (5), 995-1004.
460. Liu, Y.-C.; Singh, U., Destabilization domain approach adapted for regulated protein expression in the protozoan parasite *Entamoeba histolytica*. *Int. J. Parasitol.* **2014**, *44* (10), 729-735.
461. Lampson, M. A.; Kapoor, T. M., Targeting Protein Stability with a Small Molecule. *Cell* **2006**, *126* (5), 827-829.

462. Banaszynski, L. A.; Wandless, T. J., Conditional Control of Protein Function. *Chem. Biol.* **2006**, *13* (1), 11-21.
463. Herm-Götz, A.; Agop-Nersesian, C.; Münter, S.; Grimley, J. S.; Wandless, T. J.; Frischknecht, F.; Meissner, M., Rapid control of protein level in the apicomplexan *Toxoplasma gondii*. *Nat. Methods* **2007**, *4* (12), 1003-1005.
464. Komatsu, T.; Kukelyansky, I.; McCaffery, J. M.; Ueno, T.; Varela, L. C.; Inoue, T., Organelle-specific, rapid induction of molecular activities and membrane tethering. *Nat. Methods* **2010**, *7* (3), 206-8.
465. Ding, L.; Laor, D.; Weisman, R.; Forsburg, S. L., Rapid regulation of nuclear proteins by rapamycin-induced translocation in fission yeast. *Yeast (Chichester, England)* **2014**, *31* (7), 253-264.
466. Khor, E.-S.; Noor, S. M.; Wong, P.-F., Expression of zTOR-associated microRNAs in zebrafish embryo treated with rapamycin. *Life Sci.* **2016**, *150*, 67-75.
467. Sucularli, C.; Shehwana, H.; Kuscu, C.; Dungul, D. C.; Ozdag, H.; Konu, O., Functionally conserved effects of rapamycin exposure on zebrafish. *Mol Med Rep* **2016**, *13* (5), 4421-30.
468. Makky, K.; Tekiela, J.; Mayer, A. N., Target of rapamycin (TOR) signaling controls epithelial morphogenesis in the vertebrate intestine. *Dev. Biol.* **2007**, *303* (2), 501-513.
469. Carloni, P.; Damiani, E.; Greci, L.; Stipa, P.; Tanfani, F.; Tartaglino, E.; Wozniak, M., On the use of 1,3-diphenylisobenzofuran (DPBF). Reactions with carbon and oxygen centered radicals in model and natural systems. *Res. Chem. Intermed.* **1993**, *19* (5), 395-405.
470. Kisselev, A. F.; Goldberg, A. L., Proteasome inhibitors: from research tools to drug candidates. *Chem. Biol.* **2001**, *8* (8), 739-758.
471. Kim, K. B.; Myung, J.; Sin, N.; Crews, C. M., Proteasome inhibition by the natural products epoxomicin and dihydroeponemycin: insights into specificity and potency. *Bioorg Med Chem Lett* **1999**, *9* (23), 3335-40.
472. Bancirova, M., Sodium azide as a specific quencher of singlet oxygen during chemiluminescent detection by luminol and Cypridina luciferin analogues. *Luminescence* **2011**, *26* (6), 685-688.
473. Wang, X.; Perez, E.; Liu, R.; Yan, L.-J.; Mallet, R. T.; Yang, S.-H., Pyruvate protects mitochondria from oxidative stress in human neuroblastoma SK-N-SH cells. *Brain Res.* **2007**, *1132*, 1-9.
474. Molnar, Z.; Millward, A. B.; Tse, W.; Demaine, A. G., p21(WAF1/CIP1) Expression is Differentially Regulated by Metformin and Rapamycin. *Int J Chronic Dis* **2014**, *2014*, 327640.

475. Bell, E.; Cao, X.; Moibi, J. A.; Greene, S. R.; Young, R.; Trucco, M.; Gao, Z.; Matschinsky, F. M.; Deng, S.; Markman, J. F.; Naji, A.; Wolf, B. A., Rapamycin has a deleterious effect on MIN-6 cells and rat and human islets. *Diabetes* **2003**, *52* (11), 2731-9.
476. Leisching, G. R.; Loos, B.; Botha, M. H.; Engelbrecht, A. M., The role of mTOR during cisplatin treatment in an in vitro and ex vivo model of cervical cancer. *Toxicology* **2015**, *335*, 72-8.
477. Volmat, V.; Pouyssegur, J., Spatiotemporal regulation of the p42/p44 MAPK pathway. *Biol. Cell* **2001**, *93* (1-2), 71-9.
478. Caunt, C. J.; Armstrong, S. P.; Rivers, C. A.; Norman, M. R.; McArdle, C. A., Spatiotemporal regulation of ERK2 by dual specificity phosphatases. *J. Biol. Chem.* **2008**, *283* (39), 26612-23.
479. Lee, K. B.; Hwang, J. M.; Choi, I. S.; Rho, J.; Choi, J. S.; Kim, G. H.; Kim, S. I.; Kim, S.; Lee, Z. W., Direct Monitoring of the Inhibition of Protein-Protein Interactions in Cells by Translocation of PKC δ Fusion Proteins. *Angew. Chem. Int. Ed.* **2011**, *50* (6), 1314-1317.
480. Geda, P.; Patury, S.; Ma, J.; Bharucha, N.; Dobry, C. J.; Lawson, S. K.; Gestwicki, J. E.; Kumar, A., A small molecule-directed approach to control protein localization and function. *Yeast* **2008**, *25* (8), 577-94.
481. Mart, R. J.; Allemann, R. K., Azobenzene photocontrol of peptides and proteins. *Chem. Commun.* **2016**, *52* (83), 12262-12277.
482. Zhu, M.; Zhou, H., Azobenzene-based small molecular photoswitches for protein modulation. *Organic & Biomolecular Chemistry* **2018**, *16* (44), 8434-8445.
483. Lotz, T. S.; Halbritter, T.; Kaiser, C.; Rudolph, M. M.; Kraus, L.; Groher, F.; Steinwand, S.; Wachtveitl, J.; Heckel, A.; Suess, B., A light-responsive RNA aptamer for an azobenzene derivative. *Nucleic Acids Res.* **2018**, *47* (4), 2029-2040.
484. Asanuma, H.; Liang, X.; Yoshida, T.; Komiyama, M., Photocontrol of DNA Duplex Formation by Using Azobenzene-Bearing Oligonucleotides. *ChemBioChem* **2001**, *2* (1), 39-44.
485. Jester, B. W.; Cox, K. J.; Gaj, A.; Shomin, C. D.; Porter, J. R.; Ghosh, I., A Coiled-Coil Enabled Split-Luciferase Three-Hybrid System: Applied Toward Profiling Inhibitors of Protein Kinases. *Journal of the American Chemical Society* **2010**, *132* (33), 11727-11735.
486. Klajn, R., Spiropyran-based dynamic materials. *Chem. Soc. Rev.* **2014**, *43* (1), 148-184.
487. Bluemmel, P.; Setaro, A.; Maity, C.; Hecht, S.; Reich, S., Tuning the interaction between carbon nanotubes and dipole switches: the influence of the change of the nanotube-spiropyran distance. *J Phys Condens Matter* **2012**, *24* (39), 394005.

488. Russew, M.-M.; Hecht, S., Photoswitches: From Molecules to Materials. *Adv. Mater.* **2010**, *22* (31), 3348-3360.
489. Lukyanov, B. S.; Lukyanova, M. B., Spiroprans: Synthesis, Properties, and Application. (Review). *Chemistry of Heterocyclic Compounds* **2005**, *41* (3), 281-311.
490. Lee, H. I.; Wu, W.; Oh, J. K.; Mueller, L.; Sherwood, G.; Peteanu, L.; Kowalewski, T.; Matyjaszewski, K., Light-induced reversible formation of polymeric micelles. *Angew. Chem. Int. Ed. Engl.* **2007**, *46* (14), 2453-7.
491. Son, S.; Shin, E.; Kim, B. S., Light-responsive micelles of spiropyran initiated hyperbranched polyglycerol for smart drug delivery. *Biomacromolecules* **2014**, *15* (2), 628-34.
492. Coleman, S.; ter Schiphorst, J.; Ben Azouz, A.; Bakker, S.; Schenning, A. P. H. J.; Diamond, D., Tuning microfluidic flow by pulsed light oscillating spiropyran-based polymer hydrogel valves. *Sensors Actuators B: Chem.* **2017**, *245*, 81-86.
493. Sugiura, S.; Sumaru, K.; Ohi, K.; Hiroki, K.; Takagi, T.; Kanamori, T., Photoresponsive polymer gel microvalves controlled by local light irradiation. *Sensors and Actuators A: Physical* **2007**, *140* (2), 176-184.
494. Fries, K. H.; Driskell, J. D.; Samanta, S.; Locklin, J., Spectroscopic analysis of metal ion binding in spiropyran containing copolymer thin films. *Anal. Chem.* **2010**, *82* (8), 3306-14.
495. Suzuki, T.; Kato, T.; Shinozaki, H., Photo-reversible Pb²⁺-complexation of thermosensitive poly(N-isopropyl acrylamide-co-spiropyran acrylate) in water. *Chem Commun (Camb)* **2004**, (18), 2036-7.
496. Ciardelli, F.; Fabbri, D.; Pieroni, O.; Fissi, A., Photomodulation of polypeptide conformation by sunlight in spiropyran-containing poly(L-glutamic acid). *Journal of the American Chemical Society* **1989**, *111* (9), 3470-3472.
497. Cooper, T. M.; Natarajan, L. V.; Miller, C. G., Control by Ring Substitution of the Conformation Change Dynamics in Photochromic Polypeptides. *Photochem. Photobiol.* **1999**, *69* (2), 173-176.
498. Aizawa, M.; Namba, K.; Suzuki, S., Light-induced enzyme activity changes associated with the photoisomerization of bound spiropyran. *Arch. Biochem. Biophys.* **1977**, *182* (1), 305-310.
499. Weston, D. G.; Kirkham, J.; Cullen, D. C., Photo-modulation of horseradish peroxidase activity via covalent attachment of carboxylated-spiropyran dyes. *Biochimica et Biophysica Acta (BBA) - General Subjects* **1999**, *1428* (2), 463-467.

500. Asanuma, H.; Shirasuka, K.; Yoshida, T.; Takarada, T.; Liang, X.; Komiyama, M., Spiropyran as a Regulator of DNA Hybridization with Reversed Switching Mode to That of Azobenzene. *Chem. Lett.* **2001**, *30* (2), 108-109.
501. Blonder, R.; Levi, S.; Tao, G.; Ben-Dov, I.; Willner, I., Development of Amperometric and Microgravimetric Immunosensors and Reversible Immunosensors Using Antigen and Photoisomerizable Antigen Monolayer Electrodes. *Journal of the American Chemical Society* **1997**, *119* (43), 10467-10478.
502. Edahiro, J.; Sumaru, K.; Tada, Y.; Ohi, K.; Takagi, T.; Kameda, M.; Shinbo, T.; Kanamori, T.; Yoshimi, Y., In situ control of cell adhesion using photoresponsive culture surface. *Biomacromolecules* **2005**, *6* (2), 970-4.
503. Kikuchi, K.; Sumaru, K.; Edahiro, J.-I.; Ooshima, Y.; Sugiura, S.; Takagi, T.; Kanamori, T., Stepwise assembly of micropatterned co-cultures using photoresponsive culture surfaces and its application to hepatic tissue arrays. *Biotechnol. Bioeng.* **2009**, *103* (3), 552-561.